E. Aprile, A.E. Bolotnikov,
A.I. Bolozdynya, T. Doke

WILEY-VCH

Noble Gas Detectors

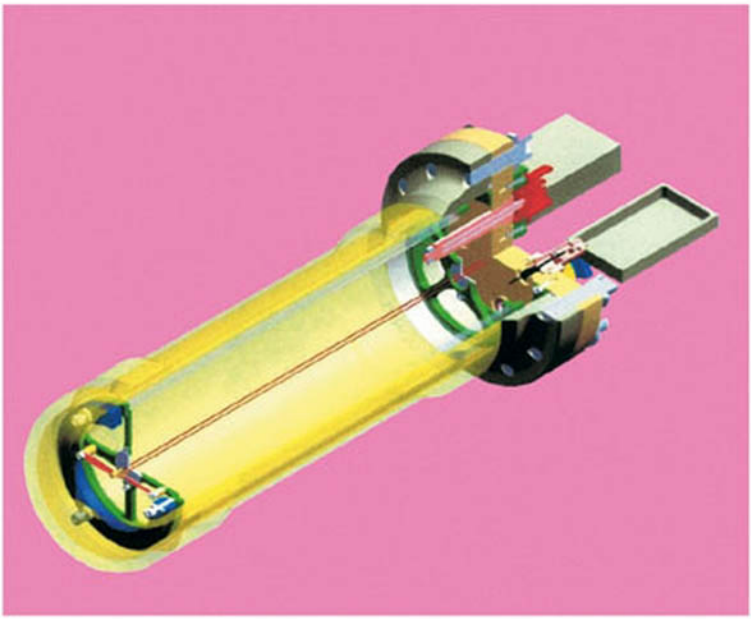

Elena Aprile, Aleksey E. Bolotnikov,
Alexander I. Bolozdynya,
and Tadayoshi Doke

Noble Gas Detectors

WILEY-VCH Verlag GmbH & Co. KGaA

Elena Aprile, Aleksey E. Bolotnikov,
Alexander I. Bolozdynya,and
Tadayoshi Doke

Noble Gas Detectors

Related Titles

Grob, R. L., Barry, E. F. (eds.)

Modern Practice of Gas Chromatography

1045 pages
2004. Hardcover
ISBN 0-471-22983-0

Tschulena, G., Lahrmann, A. (eds.)

Sensors in Household Appliances

Sensors Applications Vol. 5

310 pages with 153 figures and 32 tables
2003. Hardcover
ISBN 3-527-30362-6

O'Hanlon, J. F.

A User's Guide to Vacuum Technology

550 pages
2003. Hardcover
ISBN 0-471-27052-0

Knoll, G. F.

Radiation Detection and Measurement

816 pages
2000. Hardcover
ISBN 0-471-07338-5

Turner, J. E.

Atoms, Radiation, and Radiation Protection

575 pages
1995. Hardcover
ISBN 0-471-59581-0

Zucker, R. D., Biblarz, O.

Fundamentals of Gas Dynamics

512 pages
2002. Hardcover
ISBN 0-471-05967-6

Elena Aprile, Aleksey E. Bolotnikov,
Alexander I. Bolozdynya,
and Tadayoshi Doke

Noble Gas Detectors

WILEY-VCH Verlag GmbH & Co. KGaA

The Authors

Dr. Alexander I. Bolozdynya
Case Western Reserve University
Department of Physics
10900 Euclid Avenue
Cleveland, OH 44106-7079
USA

Prof. Elena Aprile
Columbia University
Physics Department & Astrophysics Laboratory
550 West 120th Street
New York, NY 10027
USA

Dr. Aleksey E. Bolotnikov
Brookhaven National Lab.
Bldg. 197-D
Upton, NY 11793
USA

Prof. Tadayoshi Doke
Waseda University
1-104 Totsukamach
Shinjuku-ku
169-8050 Tokyo
Japan

Library of Congress Card No.:
applied for

British Library Cataloguing-in-Publication Data
A catalogue record for this book is available from the British Library.

Bibliographic information published by the Deutsche Nationalbibliothek
The Deutsche Nationalbibliothek lists this publication in the Deutsche Nationalbibliografie; detailed bibliographic data are available in the Internet at http://dnb.d-nb.de.

Typesetting Uwe Krieg, Berlin
Printing Strauss GmbH, Mörlenbach
Binding Littges & Dopf Buchbinderei GmbH, Heppenheim

Printed in the Federal Republic of Germany
Printed on acid-free paper

ISBN-13: 978-3-527-40597-8
ISBN-10: 3-527-40597-6

Foreword

This book is a welcome addition to the literature available to those of us interested in the spectroscopy and imaging of ionizing radiation. The subset of detectors based on dense noble gases as the active medium has grown in diversity and importance over the past several decades. The material included here is both comprehensive and authoritative. Each of the authors has a distinguished research record that has helped advance the field. They provide a unique perspective and expertise that is reflected in the high-quality discussions of principles and devices that will be found throughout the book.

Noble gases in compressed or liquid form are regarded as an attractive detection medium from several standpoints. Detector volume is not limited by the need for crystal growth required in many alternative approaches, and the statistical limit on energy resolution is quite small due to moderate values for average ionization energy and a relatively low Fano factor. These media also show a scintillation yield that can be a primary or supplemental output signal. These properties are reviewed and thoroughly documented throughout the book with useful and current literature citations. The types of detectors discussed cover the use of noble gases in liquid, high pressure, and two-phase states. These media are incorporated into devices based on various strategies to generate output signals, including direct collection of ionization charges, proportional multiplication of that charge, or the collection of scintillation light.

The world of radiation detection and imaging has historically been dominated by requirements set by the physics and medical imaging communities. With the emergence of new needs for environmental monitoring and remote detection of radiation, there is an increasing need to expand the horizon of technologies and instruments available for these applications. This monograph will play an important role in providing a basic scientific and technical foundation for some of the development efforts that will be required in the future.

Ann Arbor, Michigan, June 2006 *Glenn F. Knoll*

Contents

Preface

This book is the first monograph exclusively dedicated to a new class of radiation detectors developed in the past three or four decades. Pure compressed noble gases (He, Ne, Ar, Kr, and Xe) and their liquids have a unique combination of physical properties such as high stopping power, small Fano factor, and relatively low energy required for electron–ion pair and photon production (xenon), high thermal neutron absorption cross section (^{3}He), low Doppler broadening in Compton scatter (neon) etc., making them very suitable radiation detection media. Moreover, pure noble gases are available in large quantities and noble gas detectors are scalable, allowing the construction of large detectors that operate in accordance with principles explored using small prototypes. Noble gases are relatively cheap (the current market price of the most expensive of them, pure xenon, is about $1 per gram), and their annual production levels are measured in many tons.

For the last two decades of the twentieth century, considerable efforts were devoted to developing noble gas gamma ray spectrometers, gamma ray and X-ray imaging devices, Compton cameras, luminescence cameras, high-energy electromagnetic calorimeters based on liquefied noble gases, and two-phase emission detectors. New challenges of the twenty-first century, related to nonproliferation and antiterrorism, have drawn more attention to noble fluid detectors. The detection and monitoring of nuclear materials demand highly reliable and sensitive nuclear radiation detection systems. Recently, it was demonstrated that high-pressure xenon ionization chambers could tolerate the full range of environmental extremes seen in nature and operate as gamma spectrometers, approaching room temperature semiconductor detectors in performance. Recent advances in the development of noble fluid detectors and associated technologies have led to the planning of several new experiments of fundamental scientific significance such as the search for cold dark matter in the universe, the measurement of neutrino mass through neutrino-less double beta decay, the measurement of the neutrino magnetic moment.

This book is primarily addressed to physicists and graduate students involved in the preparation of the next generation of experiments in fundamental physics, nuclear engineers developing instrumentation for nuclear security, and for monitoring nuclear materials. The book may serve as a textbook for beginners as well as a practical manual for experienced detector physicists planning construction of noble gas detectors with extremely pure, dense and massive working media. Detector physics is a subject of interest in nuclear engineering, experimental nuclear and high-energy physics courses in several distinguished universities, among which can be counted Columbia University, MIT, Princeton University, UCLA, and the University of Michigan in United States, Waseda University in Japan, MEPI in Russia. This book will also provide students in health physics, environmental protection, radiation biology, and nuclear chemistry with a useful glimpse into an exciting and important area of modern radiation detector technology.

August 2006 *E. Aprile, A. E. Bolotnikov, A. I. Bolozdynya, and T. Doke*

Acknowledgements

This book represents a distillation of more than 120 years of total experimental experience of the authors distributed over almost 40 calendar years, beginning from the 1960s. The authors would be happy to individually acknowledge all the colleagues who shared the hard work in the development of the technology of noble gas detectors over this period. However, they cannot be absolutely sure that all names are recalled. For this reason, they would like to dedicate this monograph to all experimentalists working on novel detector developments.

Daniel McKinsey, Vitaly Chepel and Pavel P. Brusov, Robert Austin, Karl-Ludwig Giboni, Carl E. Dahl, Toshinori Mori, Satoshi Suzuki are thanked for their critical reading of the book and many valuable suggestions. Satoshi Mihara and Guillaume Plante are thanked for helping prepare illustrations in Chapter 9. The input of the graduating students in the US, Russia, and Japan is difficult to overestimate.

Many figures and tables in this monograph have been previously published elsewhere as indicated in captions and references. The authors acknowledge cooperation of the following publishers in granting permissions for reproduction of these materials:

Nuclear Instruments and Methods in Physics Research
Copyright © by Elsevier. Figures 2.5, 2.11, 2.12, 2.13, 3.47, 3.50, 4.5, 4.6, 4.7, 4.15, 4.16, 4.21, 4.22, 5.7, 5.8, 5.9, 5.12, 5.14, 5.15, 5.17, 5.18, 5.19, 5.30, 6.4, 6.5, 6.6, 6.7, 6.9, 6.10, 6.11, 6.18, 6.19, 6.20, 6.21, 6.26, 6.27, 7.5, 7.8, 7.10, 8.2, 8.3, 8.5, 8.6, 8.7, 8.8, 8.9, 8.10, 8.12, 9.7, 9.8, 9.9, 9.10, 9.12. Tables 5.1, 8.2.

Physics Letters
Copyright © by Elsevier. Figure 3.24.

Nuclear Physics B – Proceedings Supplements
Copyright © by Elsevier. Figure 9.8.

IEEE Transactions
Copyright © by The Institute of Electrical and Electronics Engineers, Inc., New York. Figures 2.3, 2.4, 3.2, 3.19, 3.23, 3.25, 3.53, 3.54, 4.2, 4.3, 4.8, 4.9, 4.10, 4.11, 4.12, 4.13, 4.14, 4.17, 4.18, 4.19, 4.20, 4.21, 5.19, 5.20, 5.21, 5.22, 5.23, 5.24, 5.25, 6.1, 6.12, 6.13, 6.14, 6.17, 7.9, 7.11, 9.11, 9.15. Tables 3.8, 8.4.

Physical Review
Copyright © by the American Physical Society, New York. Figures 3.14, 3.30, 3.31, 3.34, 3.35, 3.36, 3.37, 3.42, 3.44, 3.45, 3.46, 3.48, 3.49, 5.26, 9.9. Tables 3.10, 3.14, 3.15.

Journal of Chemical Physics
Copyright © by the American Physical Society, New York. Figure 3.33.

Japanese Journal of Applied Physics
Copyright © by the Japan Society of Applied Physics. Figures 4.22, 4.23, 4.24, 4.25, 4.26, 5.27. Table 8.3.

Journal Physics B: Atomic, Molecular and Optical Physics
Copyright © by the Institute of Physics and 10P Publishing Limited 2006. Figure 3.26.

In addition, a number of figures were obtained courtesy of individuals as indicated in captions and borrowed from archives of the authors. These include Figs. 6.19, 7.6, 7.8, 9.11, 9.21, 9.22.

1
Introduction

Progress in experimental nuclear and particle physics and their applications in medicine, geological exploration, and industry has always been closely linked with improved methods of radiation measurement.

This book will review the physical properties of noble fluids, operational principles of detectors based on these media, and the most innovative technical design approaches yet developed to optimize these detectors. This subject area has developed through the research of many groups from different countries and continents. Many outstanding physicists and nuclear engineers have contributed to the development of noble fluid detectors. Among them there are Nobel laureates Glaser (1960), Alvarez (1964), and Charpak (1992).

In this monograph, extensive attention is devoted to detector technology: purification and purity monitoring methods, information readout methods, electronics, detection of far ultraviolet light emission, selection of materials, cryogenics, etc. This book is intended to provide all the information necessary for understanding the construction of pure noble gas-filled detectors, it might serve as a handbook on the properties of noble gases and liquids. Numerous cited publications are provided to allow readers to delve more deeply into any of the subjects touched upon in this book.

1.1
Units and Definitions

SI is the favored system of units throughout this text, although in experimental nuclear and elementary particle physics, energy is conventionally measured in units of electron volts and gas pressure is measured in Torr, bar or atmospheres, and these units will be frequently employed when describing these quantities. To aid readers wishing to cross reference values encountered in their reading, we have tabulated many of the physical quantities used throughout the text in Table 1.1.

Tab. 1.1 Fundamental constants, symbols and units used in the book.

Quantity	Symbol, equation	Value or conversion formula
Avogadro's number	N_A	$6.0221\times10^{23}\,\mathrm{mol}^{-1}$
Bohr magneton	μ_B	$9.27\times10^{-24}\,\mathrm{J/T} = 5.79\times10^{-5}\,\mathrm{eV\,T}^{-1}$
Boltzman constant	k	$1.381\times10^{-23}\,\mathrm{JK}^{-1} = 8.617\times10^{-5}\,\mathrm{eV\,K}^{-1}$
Capacitance	C	$1\,\mathrm{F} = 1\,\mathrm{C\,V}^{-1} = 10^{12}\,\mathrm{pF}$
Concentration	K	1 ppm = 10^{-6}; 1 ppb = 10^{-9}; 1 ppt = 10^{-12}
Density	ρ	$1\,\mathrm{kg\,m}^{-3} = 0.001\,\mathrm{g\,cm}^{-3} = 6.243\times10^{-2}\,\mathrm{lb\,ft.}^{-3}$
Electric field strength	E	$1\,\mathrm{kV\,cm}^{-1} = 10^5\,\mathrm{V\,m}^{-1} = 10^5\,\mathrm{N\,C}^{-1}$
Elementary charge	e	$1.60\times10^{-19}\,\mathrm{C}$
Electron rest mass	m_e	$9.11\times10^{-31}\,\mathrm{kg}$
Energy	E	$1\,\mathrm{eV} = 1.602\times10^{-19}\,\mathrm{J} = 1.60\times10^{-12}\,\mathrm{erg}$
		$1\,\mathrm{J} = 0.2388\,\mathrm{cal}$
Length	l	1 m = 39.4 in. = 3.28 ft.
		1 in. = 2.54 cm = 25.4 mm; 1 mi = 1.61 km
Magnetic field	B	$1\,\mathrm{T} = 1\,\mathrm{Wb\,m}^{-2} = 10^4$ gauss
Mass	m	$1\,\mathrm{g} = 10^{-3}\,\mathrm{kg} = 10^{-6}$ ton (metric) $= 6.02\times10^{23}$ u
		$1\,\mathrm{u} = 1.661\times10^{-27}\,\mathrm{kg}$
Permittivity constant	ε_0	$1.26\times10^{-6}\,\mathrm{F\,m}^{-1}$
Pressure	p	1 atm = 1.013 bar = 760 Torr = 1.03×10^5 Pa = 14.7 psi
		1 Torr = 1 mmHg = 133.32 Pa
		$1\,\mathrm{Pa} = 1\,\mathrm{N\,m}^{-2} = 9.869\times10^{-6}\,\mathrm{atm} = 1.45\times10^{-4}\,\mathrm{lb\,in.}^{-2}$
Radioactivity	$\mathrm{d}N/\mathrm{d}t$	$1\,\mathrm{Bq} = 1\,\mathrm{disintegration/s} = 2.703\times10^{-11}\,\mathrm{Ci}$
Speed	v	$1\,\mathrm{m\,c}^{-1} = 100\,\mathrm{cm\,s}^{-1} = 3.6\,\mathrm{km\,h}^{-1} = 2.237\,\mathrm{mi\,h}^{-1}$
Speed of light	c	$299\,792\,458\,\mathrm{m\,s}^{-1}$
Temperature	T	K = °C + 273.16; °F = 1.8×(°C) + 32; °R = °F + 459.67
Time	t	1 s = 1/60 min = 1/3600 h; 1 d = 86 400 s
		1 y = 365.2 d = 3.16×10^7 s; 1 ns = 10^{-9} s; 1 µs = 10^{-6} s
Volume	V	$1\,\mathrm{m}^3 = 103\,\mathrm{L} = 106\,\mathrm{cm}^3 = 264.2$ US gallons
Wavelength	λ	$1\,\mathrm{nm} = 10^{-9}\,\mathrm{m} = 10\text{Å}$

1.2 Brief History of Noble Gas Detectors

The first device used to detect ionizing radiation was the eighteenth century gas (air) ionization chamber known as a gold-leaf electroscope. Since Becquerel's discovery of radioactivity in 1896, the electroscope has been used to measure the integral flux of ionizing radiation. Thomson received a Noble Prize in Physics in 1906 for his study of the electrical conductivity of ionized gases. In 1897, Thomson reported on the increasing conductivity of Vaseline oil irradiated by X-rays [1]. This was the first example of an ionization cham-

ber working with a condensed dielectric. Soon thereafter, Curie observed a similar effect due to the influence of radium radiation in several nonpolar liquids [2]. In 1908, Rutherford and Geiger developed a cylindrical pulse ionization chamber for the detection of individual subatomic particles. A few years later, Geiger built his very sensitive gas-discharge particle counter [3, 4] that was used in experiments leading to the identification of the alpha particle with the nucleus of the helium atom [5] and to the development of Rutherford's model of the atom. Between 1928 and 1929 Geiger and Mueller constructed large sensitive area counters, and they have since been called Geiger–Mueller counters [6, 7]. The next important step was the development of proportional counters that provided a means to identify particles based on their inherent ionization ability [8].

The first position-sensitive device for particle track visualization was the "cloud" chamber built by Wilson in 1912, which for decades served as a workhorse in experimental particle physics. Later, diffusion, spark, and streamer cameras were developed to visualize individual particle tracks in gases at atmospheric pressure. Noble gases played an important role in all these developments, serving as "fast" fill gases. With the ever-increasing energies of particle interactions being explored, coupled with the development of sensitive electronic amplifiers, detectors with liquid and solid working media were gradually introduced into elementary particle research. The development of imaging detectors culminated with the introduction of bubble chambers (including some employing liquid xenon) by Glaser, who received the Noble Prize in Physics in 1960 for this development.

Noble gas detector development entered a new era beginning in the late 1940s when Davidson and Larsh observed the appearance of electron conductivity in liquid argon that was initiated by the absorption of radiation in that medium [9]. Almost immediately thereafter, Hutchinson (1949) confirmed the observation of highly mobile ionization electrons drifting in liquid and solid argon and for the first time reported on detection particles in a two-phase electron emission detector [10].

At the beginning of the 1950s, liquid (LAr) ionization chambers, employing a Frisch grid, were used in a major nuclear physics experiment [11, 12]. Attention later focused on the excellent scintillation properties of condensed noble gases [13, 14].

During the 1950s and 1960s, significant effort was expended on investigations into the electron transport properties of pure noble gases and gas mixtures used for efficient electron multiplication in wire chambers. The multiwire proportional chamber (MWPC), invented by Charpak in 1968, has undergone tremendous development after the introduction of digital signal processing, integrated electronic circuits and computers. Since that time practically every experimental installation in high-energy physics incorporates MWPCs,

allowing for the discovery of new particles such as J/Ψ by Ting and Richter or the W and Z by Rubbia, who won Nobel Prizes in 1976 and 1984, respectively. For the invention of these electronic detectors Charpak was awarded a Noble Prize in Physics in 1992.

Charpak and his collaborators (Sauli, Majewski, Policarpo, Ypsilantis, Breskin) have originated many innovative noble gas detectors such as gas-filled drift chambers, proportional scintillation chambers, parallel plate avalanche chambers, and they pioneered the development of X-ray digital imagers for medicine, biology and industry.

The advantages of condensed noble gases for precision imaging and for the development of high-energy particle and radiation detectors was recognized by Alvarez in 1968 [15]. Following the development of liquid xenon ionization chambers by Alvarez, Zaklad, Derenzo and others during the 1960s and 1970s, it was realized that such devices could be utilized in the field of nuclear medicine due to their potential for imaging 140-511 keV gamma rays.

Independently of Alvarez and his colleagues in the West, Russian and Japanese scientists explored condensed noble gases as working media of particle detectors. Doke and coworkers initiated a study of the fundamental properties of liquid rare gases that led to their determination of the W-values and values of the Fano factor, decay times and light yield of scintillations for heavy noble gases, etc. Dolgoshein and coworkers, in the course of their attempts to develop a liquid noble gas streamer chamber, observed secondary electron emission and electroluminescence, leading them to propose using these processes to develop new, highly sensitive instrumentation with imaging capabilities.

During the 1970s and 1980s, liquid noble gas calorimeters were constructed to detect high-energy electromagnetic radiation at several major laboratories around the world, among these were: the Institute of High-Energy Physics (Serpukhov, Russia), CERN, and the Budker Institute (Novosibirsk). The ICARUS group headed by Rubbia developed a LAr TPC for solar neutrino detection. Later, a few groups from the US, Russia, Japan, and Europe (CERN) investigated the possibility of building homogeneous electromagnetic calorimeters, where passive particle absorption and signal detection are combined within one material.

At the beginning of the 1980s, it was recognized that the energy resolution of noble liquid ionization detectors is much worse at low energies than predicted from ionization statistics, and researchers turned their attention to the development of high-pressure gas detectors, which have better intrinsic resolution at low energies. Two methods were developed for extracting information from these detectors. The more conventional technique is to measure the charge liberated by ionizing radiation. Alternatively, one can measure the light emitted by ionization electrons drifting in sufficiently high electric

fields. This process, called electroluminescence (EL) or proportional scintillation, was originally investigated by Policarpo and Conde in the 1960s.

Initially, the difficulty of achieving sufficient noble gas purity necessary for transporting electrons over large distances inhibited the development of noble fluid based detector technology. A solution to the problem of effective xenon purification in the 1990s opened the way for developing precision gamma ray spectrometric instrumentation for observational astronomy, nuclear safeguard applications, and medical imaging. At the beginning of the twenty-first century, huge noble liquid ionization calorimeters are working at many accelerator laboratories across the world, liquid argon time projection chambers containing many tons of fluid are used for the study of solar neutrinos, scintillation detectors and two-phase emission detectors containing tons of noble fluid are under intensive development for rare events and exotic particles searches, and several groups continue to pursue the development of new instrumentation for nuclear medicine imaging. The authors of this book believe that the best pages of the history of noble gas detectors are yet to be written.

2
Noble Fluids as Detector Media

Properties of noble fluids from the point of view of their ability to absorb radiation and transform the absorbed energy into charge carriers or/and photon emission are described in this chapter.

2.1
Physical Properties of Dense Noble Gases

Noble gases have several advantages that make them very attractive as detection media for ionization detectors. First of all, they are available in large amounts as byproducts of the oxygen production for the steel industry. Argon is the third most abundant gas in the atmosphere following nitrogen and oxygen. The world production of xenon is about 27 tons per year. The second, noble gases can be relatively easy purified. For detection of penetration radiation, the most popular are heavy noble gases: argon (Ar), krypton (Kr) and xenon (Xe) because of their inherent high stopping power. Physical properties of noble gases are represented in Table 2.1 and Figs. 2.1 and 2.2. Excellent reviews of the properties of noble gases are available in monographs [16,17] and particular physical data can be found at the "Gas Data" page of Air Liquide website (http://www.airliquide.com). The specific properties of noble gases and their importance for noble gas detectors are discussed below.

Solid noble gases have relatively high density achieving 4 g cm^{-3} for solid xenon at cryogenic temperatures (Fig. 2.1). However, in the vicinity of the triple point the noble solids are mechanically very soft. For example, one of the authors observed the drift of charged macroscopic ($\sim$ 0.1-mm diameter) gas bubbles through the solid xenon near its triple point with velocity of $\sim$ 1 cm per hour in the laboratory of Obodovsky in 1975. This kind of soft crystal built up due to the weak van der Waals force is sometimes referred to as molecular crystals. The molecular structure is specific for condensed noble gases as well as for oxygen, nitrogen, methane, and for saturated hydrocarbon solids. In molecular crystals, molecules (atoms) can easily change their orientations, which explains the fact that the noble gas solids have dielectric constant larger than that of liquids. Since noble atoms are relatively mobile

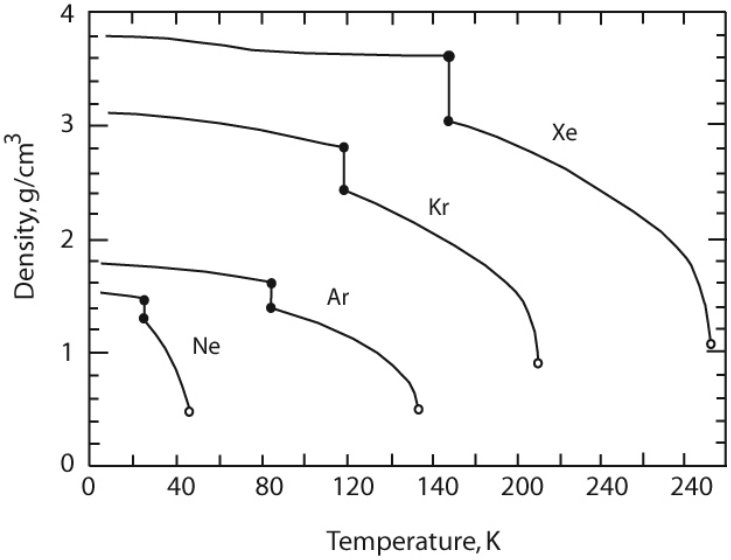

Fig. 2.1 Density of condensed noble gases dependence on temperature (open circles mark critical points, closed circles mark triple points). Redrawn from [18].

in their crystal lattice, the luminescence spectra of the condensed phases and dense gases are similar (see Chapter 4). Noble gases crystallize in the face-centered cubic (fcc) lattice at normal pressure. However, at high pressures and temperatures there is a possibility of phase transitions to body-centered cubic (bcc) structure in solid xenon without changing the volume [19]. Some molecular crystals such as methane perform fcc-bcc transitions at temperatures below the triple point.

The microstructure of the free surface of condensed noble gases is often described as a continuous transition of the gas through the critical point [20]. The average width of the transition is about 2 to 3 times the intermolecular distance. Diffraction investigations of thin samples of crystal xenon confirmed that the 5-nm thick surface layer is structureless having a distance between atoms that was larger than that found in the bulk crystal.

Xenon is a highly compressible, deviating significantly from the ideal gas at densities exceeding 0.2 $\mathrm{g\,cm^{-3}}$ (3 MPa pressure at 300 K). The density of xenon gas can reach $\sim$ 1.5–1.8 $\mathrm{g\,cm^{-3}}$ at comparably low pressures (6–7 MPa). The extremely high solubility of xenon in water which exceeds, for example, the solubility of nitrogen implies that trace amounts of water impurities are difficult to remove from xenon. Indeed, recent chromatographic analysis of highly purified xenon confirmed that water is the dominant impurity limiting performance of liquid xenon scintillation detectors [21].

Tab. 2.1 Physical properties of noble gases.

	He	Ne	Ar	Kr	Xe
Mol. mass μ, g mol^{-1}	4.0026	20.183	39.948	83.80	131.3
Boil. point at 1 atm T_S, K		27.102	87.26	119.74	169
Liq. dens. ρ_S at T_S, kg m^{-3}	0.13(4.2)	1204	1399	2413	3100
Gas dens. (273 K, 1 atm), kg m^{-3}	0.17850	0.8881	1.7606	3.696	5.8971
Latent heat of vaporiz.					
l_S at T_S, J kg^{-1}	20.3	87.20	163.2	107.7	96.29
Latent heat of fusion					
l_T at T_T, kJ kg^{-1}		16.60	29.44	19.52	17.48
Min. energy					
of liquefaction A, kJ kg^{-1}		1376	480	2	2
Debye temp. θ_D, K (T)		64 (<20)	80(<10)	63(<10)	64 (0)
Triple point:	None				
Temperature T_T, K		24.559	83.78	115.76	161.31
Vapor density ρ_G, kg m^{-3}		5	4.05	6.2	12
Liquid density ρ_L, kg m^{-3}		1200	1400	2450	3100
Solid density ρ_S, kg m^{-3}		1442	1622	2830	3640
Pressure p_T, 10^{-2} MPa		4.34	6.876	7.34	8
Liq. surf. tension σ_L, mN m^{-1} (T)		5.54	13.33	16.31	18.74
		(T_T)	(84)	(116)	(162)
Critical point:					
Temperature T_C, K	5.25	44.39	150.86	209.38	289.74
Density ρ_C, kg m^{-3}	69.64	483.5	530.8	908.5	1155
Pressure p_C, MPa	0.226	2.686	4.898	5.427	5.764
Mol. vol. V_C, cm^3 mol^{-1}		41.7	75.2	92.2	119.5
Heat cap. c_P, kJ kg^{-1} K^{-1}:					
Gas at 273 K & 1 atm	5.193	1.030	0.521	0.248	0.158
	(298)				(298K)
Vapor at T_S		1.030	0.521	0.248	
Liquid at T_S	2.47 (3)	1.84	1.05	0.538	
Solid at T_T	1.087(1)	1.302	0.833	0.428	
Viscosity η, 10^{-7} kg m^{-1} s^{-1}:					
Gas at 273 K & 1 atm	196.14	296.2	209.8	233	211
	(293)				
Gas at T_K		74.8	123.1	182.0	
Vapor at T_S		46	73		
Liquid at T_S		1240	2760	1600	
Therm. conduct. λ, mW m^{-1} K^{-1}:					
Gas at 273 K & 1 atm	142.64	46.1	16.4	8.78	5.192
Gas at T_K			10.1		
Vapor at T_S			6.5		
Liquid at T_S	0.016(3)	113	125	90	71
Refractive index					
at 293 K & 1 atm, n_D	1.000035	1.000067	1.000284	1.000427	1.000702
liquid at T_T for (λ_{sc}, nm)		1.233(80)			1.566(180)

Tab. 2.1 Physical properties of noble gases. (Continued)

	He	Ne	Ar	Kr	Xe
Diel. constant ε:					
Gas at 273 K & 1 atm	1.000127	1.000554	1.00076	1.000768 (298)	
Vapor at T_S	1.00129	1.00175			
Liquid at (T)	1.19(25)	1.59 (87)	1.63(129)	1.93(164)	
Solid at 20 K	1.230	1.67	1.80	2.23	
Isotherm. compressibility χ_T at T_S, 10^{-9}m^2 N^{-1}		1.92	1.53	1.1	
Solubility in water at n.p. (T, °C), vol/vol	0.0089(20)	0.014(0)	0.0537 (0)	0.099(0)	0.203(0)
Concentr. in air, vol ppm		18	9340	1.14	0.09

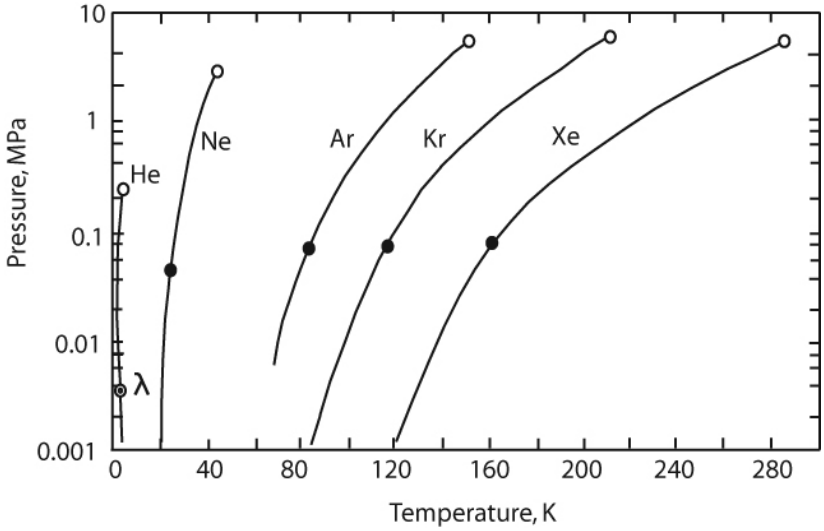

Fig. 2.2 Vapor pressure dependence on temperature of condensed phases of noble gases (open circles mark critical points, closed circles mark triple points, double circle marks lambda point of liquid helium). Redrawn from [18].

2.2 Energy Dissipation in Noble Gases

The most important characteristic of the detecting medium is its ability to stop and absorb nuclear radiation. This ability is characterized by the particle's absorption cross section. Interactions of radiation with noble atoms depend on

the nature of the ionizing particles. Charged particles such as electrons or positively charged nuclei (protons, alpha particles, etc.) interact with matter via electrostatic forces. They ionize and excite atoms leaving behind the tracks of positively charged ions and free electrons. Rapidly moving particles also generate bremsstrahlung radiation while passing through matter. If X-rays and gamma rays interact with matter they generate energetic electrons via three primary processes: photoelectric absorption, Compton scattering, and pair production with interaction probabilities that are proportional to $Z^5/E_\gamma^{7/2}$, Z/E_γ and $Z^2\ln(2E_\gamma)$, respectively. Considering its high atomic number ($Z = 54$), Xe is an excellent candidate for a detection medium, especially in the energy range where photoelectric absorption is the dominant process.

The energy of an energetic particle is transferred to the atoms in two ways: ionization and excitation. During the ionization process, an electron is removed from an atom resulting in the formation of a positively charged ion and an electron (an electron–ion pair). The excitation process raises an electron to a higher energy state; it subsequently returns to its original state via a cascade process resulting in the emission of photons having characteristic energies. The secondary electrons from the ionization process may have sufficient kinetic energy to generate more electron–ion pairs or excitations. To understand this process schematically, consider an ionization particle R, which generates electron–ion (holes in solids) pairs e and A^+, and excited atomic states, A^*, as follows:

$$\begin{aligned} R + A &\longrightarrow e + A^+ + R' \\ R + A &\longrightarrow A^* + R' \\ e + A^+ &\longrightarrow A^* \end{aligned} \tag{2.1}$$

The excitation energy released during these processes is manifested in the emission of a VUV photon (radiative process)

$$A^* \longrightarrow A + h\nu_a \tag{2.2}$$

or through the production of heat (nonradiative energy relaxation). In collisions with other atoms, the excitation energy can be released to form an electron–ion pair. In pure gases at low pressures, the characteristic photons, $h\nu_a$, may escape from the gas volume. If the pressure (density) of the gas increases the probability of the absorption of the characteristic photons rapidly increases. As a result, these photons become "trapped" in the volume at a pressure of $\sim 10^3$–10^4 Pa. In dense noble gases ($n \sim 10^{19}$ cm^{-3}), a probability of triple collisions is increased and it takes 10^{-11}–10^{-12} s to produce excited molecules in the reaction of

$$A^* + 2A \longrightarrow A_2^* + A \tag{2.3}$$

Tab. 2.2 Parameters of the energy balance equation for condensed heavy noble gases [23].

	$<E_i>$, eV	N_{ex}/N_i, eV	$<E_{ex}>$, eV	ξ_{se}, eV
Ar	15.4	0.21	12.7	5.15
Kr	13	0.08	10.5	5.50
Xe	10.5	0.06	8.4	4.45

Radiative decay of the excited states leads to the generation of a new population in the emission spectra, so-called molecular continuum

$$A_2^* \longrightarrow 2A + h\nu_m \tag{2.4}$$

Photons emitted at radiative decays of excited atoms $h\nu_a$ diffuse in the dense media and eventually become absorbed by walls and electrodes. However, dense noble gases and their liquid and solid phases are practically transparent for photons $h\nu_m$ from the molecular continuum; such photons can propagate far enough to be used for detection purposes (see Chapter 4).

In general, energy E deposited in the media is distributed between atoms (ions), $<\eta>$, and electrons liberated from neutral atoms, $<\nu>$

$$E = <\eta> + <\nu> \tag{2.5}$$

In case of light particle interactions such as electrons and photons, $E = <\nu>$, and the part of energy loss due to inelastic interaction with atomic electrons can be expressed via Platzman's [22] equation

$$<\nu>(E) = N_i < E_i > + N_{ex} < E_{ex} > + N_i < \xi_{se} > \tag{2.6}$$

where N_i is the number of electron–ion pairs ultimately produced with an average energy expenditure $<E_i>$, N_{ex} is the number of atoms excited at an average energy expenditure $<E_{ex}>$, and $<\xi_{se}>$ is the average kinetic energy of subexcitation electrons, whose energy is lower than the excitation potential and eventually goes into heat.

Parameters of Eq. (2.6) for different aggregate states of the most popular noble gases used as detector media are presented in Table 2.2.

2.3 Ionization Clusters and Principal Limitations on Position Resolution of Noble Gas Detectors

After many interactions the energetic particles eventually slowdown and become thermalized at some distances from the origin. The distance traveled by a charged particle (ranges) in condensed media depends on its charge, mass,

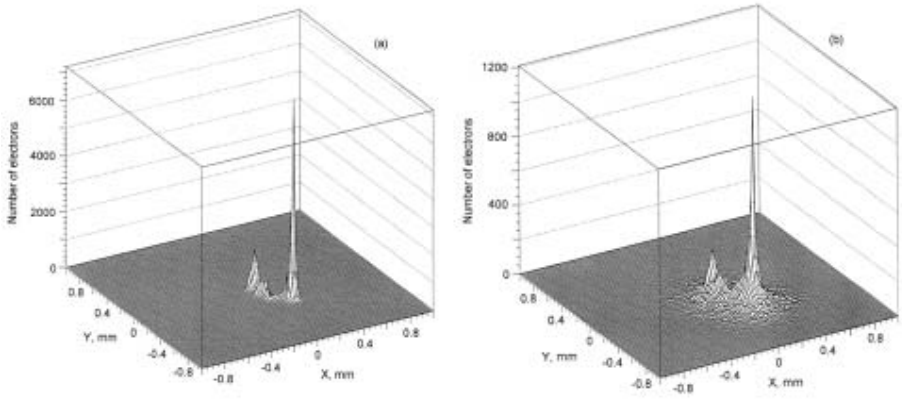

Fig. 2.3 Distribution of secondary ionization electrons in an ionization blob originated with a 50 keV primary electron incoming perpendicularly to the xy-plane in the point of $x = 0$, $y = 0$ immediately after stopping in 2 MPa argon (left) and after 0.8 μs drift at 2 kV cm^{-1} bar^{-1} reduced electric field (right) as simulated with GEANT by Morgunov [24].

and initial energy. Low mass particles like electrons and positrons follow curved trajectories caused by the multiple scattering on atoms. The ionization electrons are distributed along the trajectory of the primary particle to form an ionization blob as shown, for example, in Fig. 2.3.

The largest part of the energy of the primary electron is deposited at the end of the path. One can see that the center of gravity of the electron blob is shifted from the point of original interaction. This effect causes the principal limitation for the position resolution of gas detectors and may be reduced in more dense media or more heavy gases. Figure 2.4 shows average sizes of ionization blobs (spurs) created by 20 to 50 keV electrons in Ne, Ar, and Xe dependent on pressure. In real detectors, the effect of diffusive broadening blobs drifting under the influence of the electric field should be taken into account (compare Fig. 2.3a and Fig. 2.3b).

For detection of X-rays and soft gamma rays, relatively low-pressure noble gas (xenon) detectors are often used. If position sensitivity with high resolution is required, the effect of possible emission of secondary fluorescence photons should be considered. For gamma ray interactions with deposited energies above 34.5 keV, the probability that photoabsorption occurs in the K shell is 86% while the probability that the atom relaxes via a K_α(29.7 keV) or a K_β(33.8 keV) fluorescence photon is as high as 87% (see Table 2.3). Depending on the geometry of the detector, filling pressure and energy of the original X-ray event the fluorescence photon can be reabsorbed in the sensitive volume of the detector, generating a second localized electron cloud at a different point with respect to the primary photoelectron cloud. If the pres-

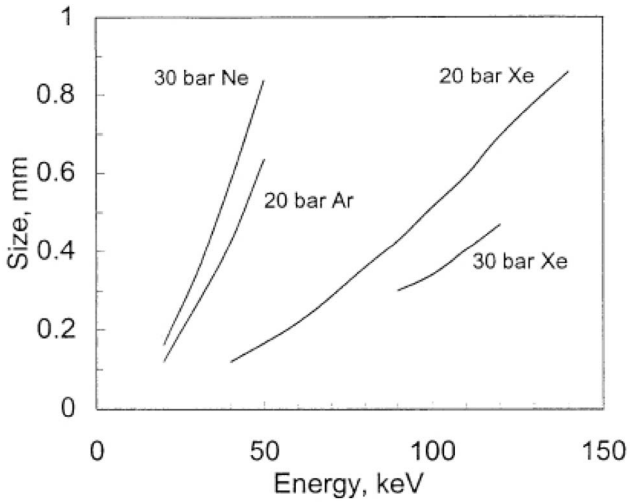

Fig. 2.4 Average sizes of ionization blob generated by the energetic electron stopping in pressurized noble gases as a function of its initial energy [24].

ence of two or more clouds cannot be recognized, their distribution over the detector volume may essentially affect the position sensitivity. For example, in a detector filled with xenon under normal conditions, a K-shell photon has a mean penetration depth of 19.5 cm and if it did not escape, the point of original photoabsorption may be significantly different from the position defined as the average of the positions of two clouds.

In time projection chambers the two electron clouds from the double interaction may be distinguished by measuring the arrival times, their separation and identification of the cloud corresponding to the absorption of the fluorescence photon. Since the energy of the fluorescence photon E_f is exactly known

Tab. 2.3 X-ray fluorescence properties of xenon [27].

Edge energies, keV	Edge jumps	Fluorescence yield
K 34.5820007	**K** 6.07753229	**K** 0.890999973
$\mathbf{L}_1$ 5.45200014	$\mathbf{L}_1$ 1.15944588	$\mathbf{L}_1$ 0.0460000001
$\mathbf{L}_2$ 5.0999999	$\mathbf{L}_2$ 1.40999997	$\mathbf{L}_2$ 1.14300001
$\mathbf{L}_3$ 4.78100014	$\mathbf{L}_3$ 2.87899995	$\mathbf{L}_3$ 29.802
M 1.14300001		
K-alpha 29.802		
K-beta 33.644001		
L-alpha 4.11100006		
L-beta 4.42199993		

($E_f = const$), this part of the total deposited energy E_t is assigned the tabulated value E_f, which is used in data analysis instead of the measured value. Then the statistical fluctuations will be due only to the cloud of residuals with reduced energy ($E_t - E_f$), and the energy determination of E_t will be improved. This so-called fluorescence gated technique is often used to improve the energy resolution of noble gas detectors working with gamma radiation in the energy range just above the xenon K-shell [25,26].

2.4 Ionization and Recombination

The production and recombination of electron–ion pairs affects the amplitudes of the output signals in the detectors operating in the electron collection mode such as ionization, proportional and electroluminescent chambers. To characterize the transfer efficiency of the absorbed energy into the measurable number of electron–ion (electron-hole) pairs, one often uses a value of the energy acquired for production of an electron–ion pair defined as

$$W_i = < \nu > (E)/N_i \tag{2.7}$$

or, with Eq. (2.6), one can obtain

$$W_i = < E_i > + (N_{ex}/N_i)E_{ex} + < \zeta_{se} > \tag{2.8}$$

The average energy loss per ionizing collision, $<E_i>$, exceeds the ionization potential of the atom, I, since some part of the ionization energy goes into excited ions and multiply charged ions.

For noble gases, the ratio W_i/I_{gas} is about 1.7 (see Table 2.4). It means roughly 40% of the absorbed energy is converted into free charge carriers. In the condensed phase, this ratio is close to 1.6 [23], i.e., about 60% of the absorbed energy is converted into ionization.

As seen from the Table 2.4, the ionization potential is sensitive to the aggregate state, decreasing by 10–30% in transition from the gas phase to the condensed phase. This effect is associated with polarization of the media. For example, the relationship between the gas ionization potential I_{gas} and the liquid ionization potential I_{liq} is regulated by the following equation:

$$I_{liq} = I_{gas} + P_+ + V_0 + \Gamma \tag{2.9}$$

where P_+ is the polarization energy of the liquid by the electric field of a positive ion, V_0 is the energy of the ground state of electron in the liquid, and Γ is the split in the valence band of the atom (molecule) [28–30]. Usually, the polarization energy is about -1 to -2 eV and may be defined as

$$P_+ = -\frac{1}{4\pi\varepsilon_0}(e^2/2R)(1 - 1/\varepsilon) \tag{2.10}$$

Tab. 2.4 Atom ionization and first excitation potentials, average energies of scintillation photons, energies for production of electron–ion pairs measured with fast electrons and scintillation photons measured with relativistic heavy ions, and Fano factors for noble gases at normal conditions and for their condensed phases near triple points.

		I_i, eV	I^e_{ex}, eV	$h\nu^e_m$, eV	W_i, eV	W_{sc}, eV	F
He							
	Gas	24.587[e]	20.62		41.3[r]		0.21[t]
							0.24±0.02[u]
	Liquid			15.5; 20			
	Solid						
Ne							
	Gas	21.565[e]	16.62		29.2[r]		0.13[t]
	Liquid			16.02			
	Solid	21.4[n]					
Ar							
	Gas	15.75[e]	11.55		26.4[r]		0.16[t]
							$0.20^{+0.01}_{-0.02}$[u]
	Liquid	13.4[d]		9.57	23.6±0.3[a]	19.5±1[e]	0.107[f]
	Solid	14.2[m]					
Kr							
	Gas	14.00[e]	9.91		24.2[r]	∼ 30	
	Liquid	11.55[d]		8.42	20.5±1.5[h]	15[i]	0.057[f]
					18.4±0.3[q]		
	Solid	11.6[m]					
Xe							
	Gas	12.13[e]	8.32		22.1[r]	∼ 28	0.13±0.01[s]
	Liquid	11.67[d]		7.02	15.6±0.3[v]	13.8±0.9[e]	0.041[f]
					14.2±0.3[p]		
	Solid	9.28[e]			12.4±0.3[p]		

Notes: *a* - [36,37], *b* - [38], *c* - [39], *d* - calculated [29,32], *e* - [31], *f* - [40], *h* - [41], *i* - [42], *k* - [43], *m* - [44], *n* - [45], *p* - [46], *r* - [47], *q* - [48], *s* - [49], *t* - [50,51], *u* - [52], *v* - [23].

where e is the elementary charge, R is the radius of the ion, and ε is the optical dielectric constant of the liquid. For noble liquids with high electron mobility, $V_0 = 0.1$–1 eV and $\Gamma \approx -1$ eV (compare with $\Gamma \approx -0.4$ to -0.5 eV for liquid hydrocarbons). In general, the transition from the gas to the liquid phase leads to the reduction of the ionization potential of 1–3 eV (Table 2.4).

In the absence of an electric field, the recombination process is 100% efficient and all electrons and ions liberated by absorbed radiation eventually recombine and generate a flash of UV light or scintillation. Assuming that one ionization act produces one photon and one excitation also produces one

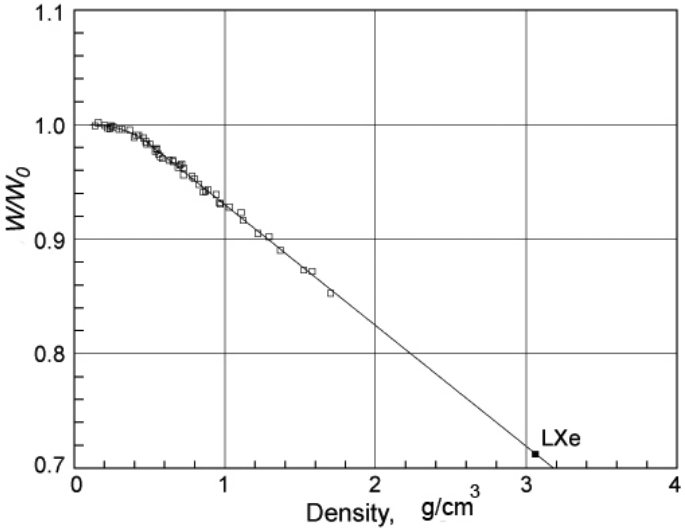

Fig. 2.5 Density dependence of W/W_0, for 662 keV gamma rays. $W_0 = 21.5$ eV is the low-density limit [33].

photon, the total number of scintillation photons may be described as

$$N_{\rm sci} = N_{\rm i} + N_{\rm ex} = N_{\rm i}(1 + N_{\rm ex}/N_{\rm i}) \tag{2.11}$$

Taking into account Eq. (2.7), one can obtain [31,32] the following equation for the average energy required for production of the scintillation photon:

$$W_{\rm sc} = E/N_{\rm sci} = W_{\rm i}/(1 + N_{\rm ex}/N_{\rm i}) \tag{2.12}$$

The values of $W_{\rm sc}$ measured for LAr and LXe with relativistic particles are in a good agreement with Eq. (2.12) if parameters $N_{\rm ex}/N_{\rm i}$ and $W_{\rm i}$ presented in Tables 2.2 and 2.4 are used.

The value of $W_{\rm i}$ is sensitive to density of the media, e.g., Fig. 2.5 shows that the energy for electron–ion pair production decreases by $\sim 15\%$ when the density of xenon gas increases from 0.12 to 1.7 $\mathrm{g\,cm^{-3}}$ [33]. Extrapolation of the reduced value $W_{\rm i}/W_0$, where W_0 is the low-density limit for $W_{\rm i}$, to the density of liquid Xe, 3.06 $\mathrm{g\,cm^{-3}}$, gives a value of $W_{\rm i}/W_0 = 0.72$, which is very close to the ratio measured in the liquid [23]. The sensitivity of $W_{\rm i}$ to the density of the gas may be understood by suggesting the formation and evolution of the electronic bands of noble gases at elevated densities. This suggestion is supported by the fact [34,35] that already at densities between 10^{19} and 10^{21} $\mathrm{cm^{-3}}$ indirect ionization of xenon atoms occurred via reactions

$$\begin{aligned} Xe + Xe + h\nu &\longrightarrow Xe_2^* \\ Xe_2^* &\longrightarrow Xe_2^+ + e^- \end{aligned} \tag{2.13}$$

The minimum energy, E_0, required for this process is the energy difference between the ground state of the molecular ion and the ground state of the free atom (11.10 eV in Xe). As soon as the band structure starts to form, the electrons can be directly excited from the valence band into the conduction band with an energy expenditure of less than 11.10 eV. Thus, the change in the slope of W_i/W_0 above 0.5 g cm^{-3} could be attributed to a decrease of the photoconductivity threshold and to the change of the ratio of the excited and ionized states with density.

2.4.1 Jaffe Model of Recombination

At the final stage of the dissipation of the energy absorbed in the media, the kinetic energy of the secondary electrons becomes smaller than that required to produce electron–ion pairs but still enough to travel large distances in dense media. Such hot electrons continue dissipating their energy via inelastic scattering with atoms and molecules. This process is called electron thermalization. The electrons continue to lose their energies until thermodynamic equilibrium with the surrounding medium is reached. Diffusion or drift-diffusion processes govern the electron transitions when an externally applied electric field exists in the medium. In the absence of the electric field, practically all thermalized electrons recombine with positive charge carriers and the dissipation process of the absorbed energy of radiation will be completed

$$\begin{aligned} A^+ + e &\longrightarrow A^* \\ A^+ + 2A &\longrightarrow A_2^+ + A \\ A_2^+ + e &\longrightarrow A^{**} + A \\ A^{**} &\longrightarrow A^* + heat \end{aligned} \tag{2.14}$$

In detectors filled with dense noble gases, the recombination rates are usually very high, and a strong electric field is needed to reduce the charge loss due to recombination. This is reflected by the so-called saturation curve-dependence of collected charge on the electric field strength. A great deal of experimental and theoretical work has been conducted to better understand this process. Two theoretical models that describe two limited cases of electron–ion recombination in fluid media have been developed and applied to the different substances in their gaseous and liquefied phases. The first model, proposed by Jaffe [53] and later improved by Lee [54] and Kramers [55], is based on the assumption that a dense plasma of positive and negative ions is formed along tracks of ionizing particles. Both the electrons and ions are described by the same special distribution function and recombination takes place in a finite volume. This theory of columnar recombination provides good agreement with experimental data when thermalized electrons are rapidly trapped by

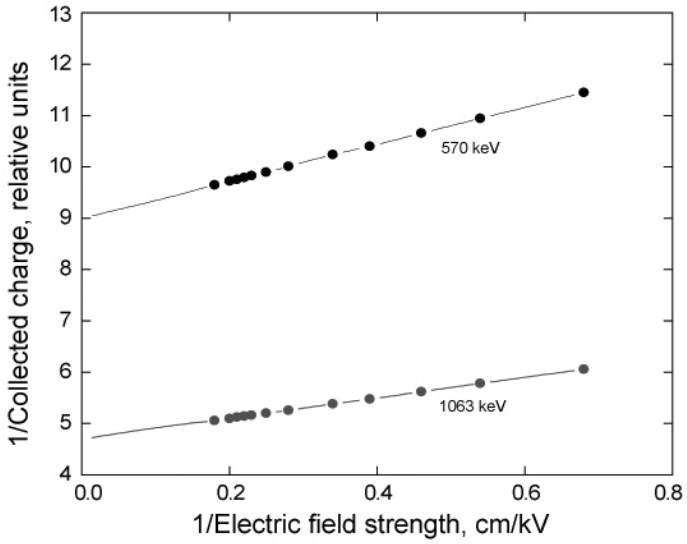

Fig. 2.6 Dependence of $1/Q$ versus $1/E$ measured in a Xe + 0.7% H_2 mixture at 1.27 g cm^{-3} for two gamma ray energies: 570 and 1063 keV [57].

electronegative ions that then locally recombine with positive ions. The theory predicts the dependence of the free ion yield on the electric field in form of

$$Q = Q_0/(1 + K/E) \tag{2.15}$$

where Q_0 is the total produced charge and K is the recombination coefficient. The experimental data acquired from ionization chambers filled with dense noble gases and irradiated with relativistic electrons accurately follow this dependence at elevated electric field strength E. As an example, Fig. 2.6 shows the saturation curves measured for a Xe + 0.7% H_2 mixture at density of 1.27 g cm^{-3} [56]. As can be seen, in the inverted coordinates, the experimental points lie on the straight lines described by Eq. (2.15). The slopes of the lines give values of recombination coefficients that are usually used to characterize the recombination rate in detection media. Higher K values mean a higher recombination rate.

Figure 2.7 shows changes of the recombination coefficient with Xe density evaluated at different concentrations of H_2. As seen, K increases with density as a parabolic function and saturates at a density of ~ 0.8 g cm^{-3}. This behavior, which is only qualitatively explained in Ref. [56], reflects a general tendency of K to increase with the electron–ion pair concentration which itself increases with the medium density. The coefficient K also increases with the concentration of H_2, explained by the fact that the addition of H_2 increases

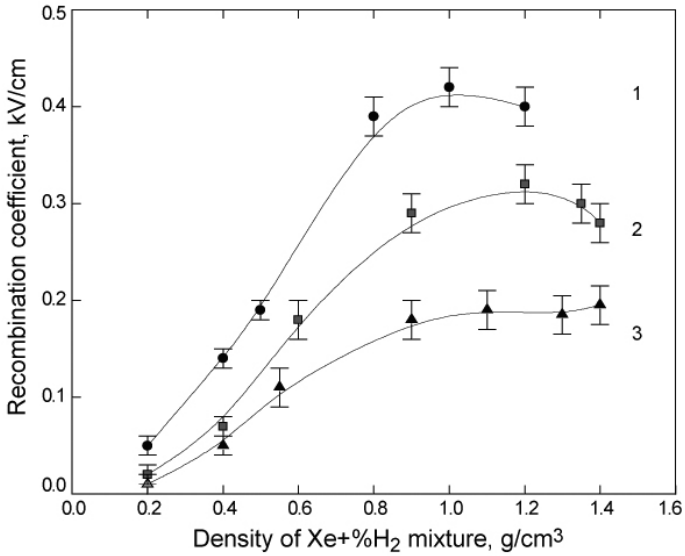

Fig. 2.7 Dependence of the recombination coefficient K on density in Xe + H_2 mixture: 0.7% (1), 0.5% (2), and 0.1% (3). The measurements were taken for 1063 keV gamma rays [56].

the probability that the electrons lose their energies more rapidly in inelastic collisions. As a result, the hot electrons travel shorter distances before they become thermalized, which means a higher density of electron–ion plasma in the tracks of ionizing particles.

Using a parallel plate ionization chamber, Bolotnikov et al. [58] measured the electron–ion recombination in pure Xe with densities between 0.05 and 1.7 g cm^{-3}. As follows from Fig. 2.8, they found that K is practically independent of gamma ray energy at $E > 0.2$ kV cm^{-1}, but it is sensitive to the density and to the electric field strength in the low energy range (below $\sim$ 400 keV).

2.4.2 Onsager Model of Recombination

The model proposed by Onsager [59], assumes that some electrons produced by an ionizing particle can be thermalized very close, within the spheres of Coulomb attraction, to their parent ions and undergo initial or geminate recombination. These electrons will totally recombine, unless a strong electric field is applied to separate them from the parent ions. The radius of these spheres is defined as the distance from the parent ion at which the Coulomb energy becomes equal to the thermal energy. However, in fluid noble gases, due to the high polarization of the medium, the effective radius of the Coulomb sphere could be significantly reduced [39]. The amount of

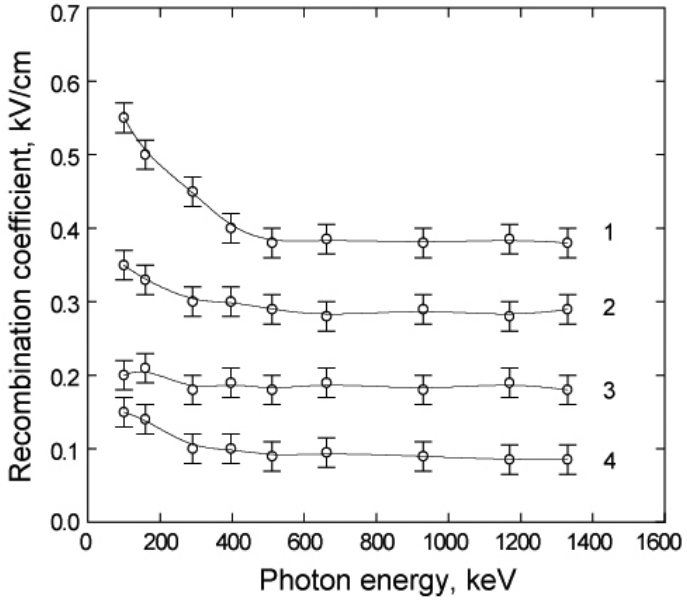

Fig. 2.8 Dependence of the recombination coefficient K versus gamma ray energy measured at several Xe densities: 1.35 (1), 0.74 (2), 0.6 (3), 0.5 g cm^{-3} (4) [58].

charge avoiding the geminate recombination can be derived by describing an electron's Brownian motion under the action of the external field and the Coulomb attraction of the parent ion. In addition, it is assumed that an average distance between parent ions is significantly larger than an electron–ion separation.

Some of the electrons become thermalized beyond the sphere of the Coulomb attraction and they are capable of escaping the recombination even in the absence of the external electric field. However, these free electrons, involved in the random thermal motion, can eventually approach ions and recombine, or they can leave the volume where ionization took place. It is clear, that in this case the recombination probability depends on how long the electrons stay in the vicinity of an ion. This type of recombination is a much slower process than initial recombination, resulting in the presence of long scintillation decay times (see Chapter 4).

Based on Onsager's formalism another approach was proposed to evaluate the electric field dependence of the collected charge taking into account a nonuniform distribution of thermalized electrons around a positive ion core [58].

2.4.3 Influence of δ-Electrons

Both the Jaffe and Onsager models describe the recombination process in a quite simplified manner. For example, they both assume a uniform distribution of ionization along the track of the ionizing particle. That is not realistic because of sharp nonuniformities introduced by the random emission of δ-electrons (secondary ionization electrons with very large transferred momentum). The introduction of two types of ionization with very different recombination coefficients provided a better description of the shape of ionization saturation curves and explained unusually poor energy resolution observed with liquid xenon ionization chambers [57]. Using Jaffe's formalism, Aprile et al. [60] reconstructed Eq. (2.15) in a two-component form

$$Q = (Q_0 - Q_\delta)/(1 + K/E) + Q_\delta/(1 + K_\delta/E) \tag{2.16}$$

where Q_0 is the total charge of free carriers produced by relativistic electrons in liquid argon and K is the recombination constant for relativistic electrons, Q_δ is the charge of electrons produced by δ-electrons and K_δ is the recombination constant corresponding to this charge. Fitting the saturation curve of the 976 keV electrons in liquid argon (Fig. 2.9) with Eq. (2.16) gives the following parameters: Q_0-Q_δ = 5.68±0.04 fC, $K = 0.03$ kV cm^{-1}, Q_δ = 1.28±0.15 fC, K_δ = 12±3 kV cm^{-1}. As it was shown in [57], there are a few tens of δ-electrons of 1–20 keV energy generated along the beta particle track; on average, 10 to 20% of the absorbed energy is deposited in δ-electrons. Statistical fluctuations in the number of generated δ-electrons may significantly affect the energy resolution of liquid xenon ionization chambers.

The idea that δ-electron production statistics affect the energy resolution was further developed when Thomas et al. [61] took into consideration the charge distribution nonuniformity along tracks of high-energy δ-electrons. Indeed, as one can see in Fig. 2.3, high-energy electron tracks have a minimum ionizing portion and a high charge density blob at their endpoints. A simplified, double density ionization model proposed by Thomas et al. [61] provided a more accurate description of the ionization curves in LAr and LXe [62]. However, the energy resolution calculated in the framework of this model did not agree with experimental data. Shibamura et al. [62] proposed the idea that all of the recombination models have limited application, because they do not take into account the structure of the condensed phase, which could be essentially nonuniform due to the presence of variously sized density clusters.

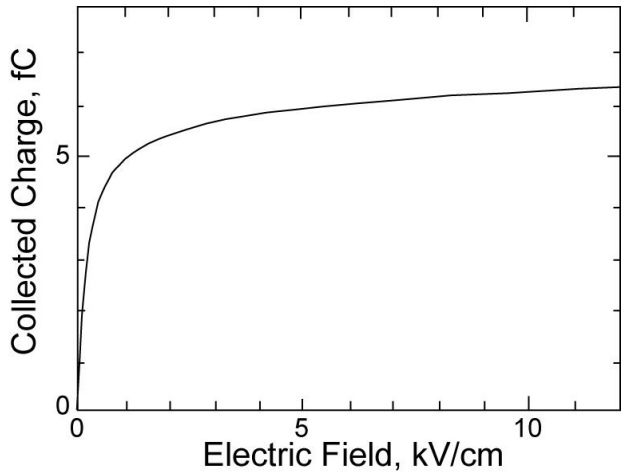

Fig. 2.9 Field dependence of the charge collected from liquid argon ionization chamber irradiated with 976 keV electrons. Redrawn from [60].

2.5 Principal Limitations for Energy Resolution

Since the energy needed for the production of electrons (ions) or photons is well-defined (see Section 2.3), the energy E deposited by ionizing radiation into a detector can be defined via the number N of generated electrons or photons: $E = NW$. Fluctuations in the number of primary energy information carriers (electrons or photons) cause uncertainty in the determination of the absorbed energy. In 1947, Fano [63] demonstrated that the standard deviation δ in the fluctuation of the number N of electron–ion pairs produced by an ionization particle, when all of its energy is absorbed in the detector, is different from the Poisson distribution by factor F

$$\delta^2 =< (N - N_\mathrm{i})^2 >= F \times N_\mathrm{i} \tag{2.17}$$

The Fano factor is an expression of the deviation of the ionization process away from independent, identically distributed ionization events; for a Poisson process $F = 1$, for ionization process with identical ionization events $F = 0$ [61].

According to [64], in the first approximation the Fano factor depends on the ratio between the number of excitations to ionizations as the following:

$$F \approx \frac{N_\mathrm{ex}}{N_\mathrm{i}} \cdot \left\{1 + \frac{N_\mathrm{ex}}{N_\mathrm{i}}\right\} \cdot \left(\frac{< E_\mathrm{ex} >}{W_\mathrm{i}}\right)^2 \tag{2.18}$$

Values of Fano factors for noble gases are presented in Table 2.4. Analyzing these data, one can observe that higher F is always connected to higher W.

This fact along with observation that in gases the value of F increases toward 1, as the initial energy of an incident particle decreases toward the ionization potential of a gas I, led Bronic [65] to the conclusion that the Fano factor F may be represented as a linear function of W_i at least for $E > 50$ eV

$$F = a(W_i/I) + b$$
$$a = 0.188 \pm 0.006$$
$$b = -0.15 \pm 0.02 \tag{2.19}$$

Figure 2.10 represents the plot of the Fano factor against the ratio W_i/I for pure gases and some gas mixtures. The empirical relation (2.19) can serve as a practical guide for gases where no data either on F or on W_i is available.

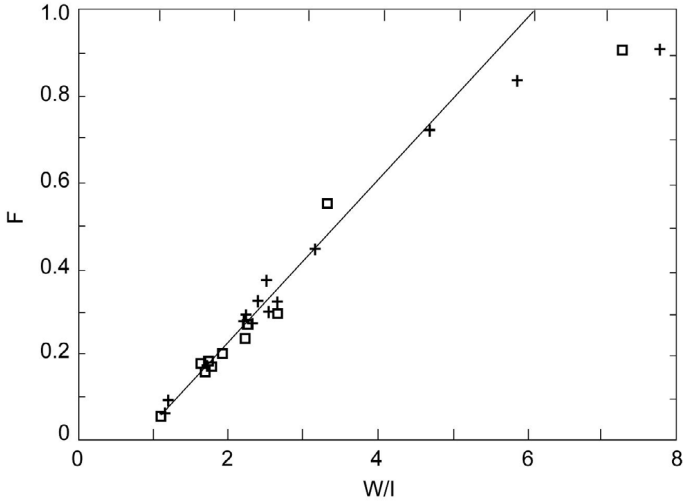

Fig. 2.10 The correlation between the Fano factor and the ratio W_i/I in noble gases and gas mixtures at normal conditions. Redrawn from [65].

A detector's ability to measure energy is characterized by its energy resolution. The energy resolution is measured as the energy peak width in a pulse height distribution of signals acquired from the detector absorbing monoenergetic ionizing particles. There are several ways to evaluate the peak width, the most common way is to measure the so-called full width at half maximum of the peak (FWHM). In general, FWHM of the full energy deposition peak, ΔE_{tot}, is determined by many factors that can be broken down into the following three terms:

$$\Delta E_{tot} = (\Delta E_0^2 + \Delta E_{el}^2 + \Delta E_c^2)^{1/2} \tag{2.20}$$

Where ΔE_{el} is electronic noise (the width of the test-pulse generator peak), and ΔE_c represents fluctuations associated with electron or light, in the case

of scintillation detectors, collection. The latter factor, called the geometrical width of the device response function, is specific for the device geometry and operating mode. In the case of ionization detectors working in the charge collection mode, ΔE_c is defined by shielding inefficiency, a parameter that characterizes the contribution of the positive ions in the output signal. Electronic noise in ionization detectors (charge collection mode) is determined by the noise generated by the input FET transistor. The noise is directly proportional to the input capacitor of the device, typically on the order of 10–50 pF. The first term of Eq. (2.20) is an intrinsic characteristic of the detecting medium, giving the lowest achievable energy resolution

$$E_0 = 2.355(FE/W_i)^{1/2} \tag{2.21}$$

The W_i value and Fano factor determine statistical fluctuations in the total amount of charge generated by an ionizing particle and, thus, the intrinsic energy resolution of the ionization detector. One can expect that the best energy resolution can be achieved in the liquid phase where the density has the maximum value. However, as the gas density increases the fluctuations of the electron–ion recombination in ionizing particles' tracks becomes more important than fluctuations due to primary ionization.

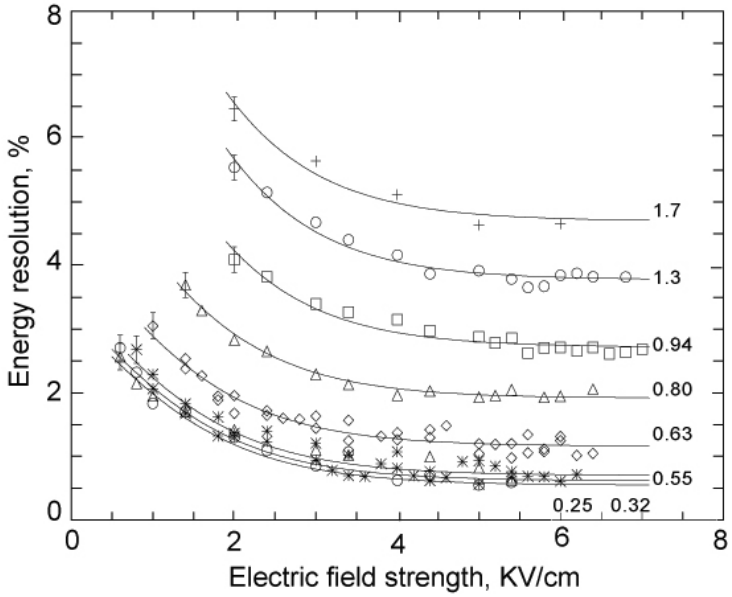

Fig. 2.11 Field dependence of the intrinsic energy resolution (% FWHM) measured for 662 keV gamma rays from high-pressure xenon ionization chamber filled with different densities (g cm^{-3}) shown at right of the curves [33].

Bolotnikov and Ramsey [33] reported the field dependence of the intrinsic energy resolution of high-pressure xenon gas ionization chamber for 662 keV gamma rays at different Xe densities (Fig. 2.11). As is seen, the resolution at first becomes better with the field and then, above 2–6 kV cm^{-1} (depending on the density), it remains practically unchanged. At low densities ($<$0.55 g cm^{-3}) the resolution almost saturates to the same limit, determined by the statistics of ion production, while at high densities ($>$0.55 g cm^{-3}) it continues to slowly deteriorate even at the maximum applied field, but still remains far above the statistical limit. This is seen more clearly in Fig. 2.12 which gives the intrinsic energy resolution ΔE_0 versus density obtained for 662 keV gamma rays at a field of 7 kV cm^{-1}.

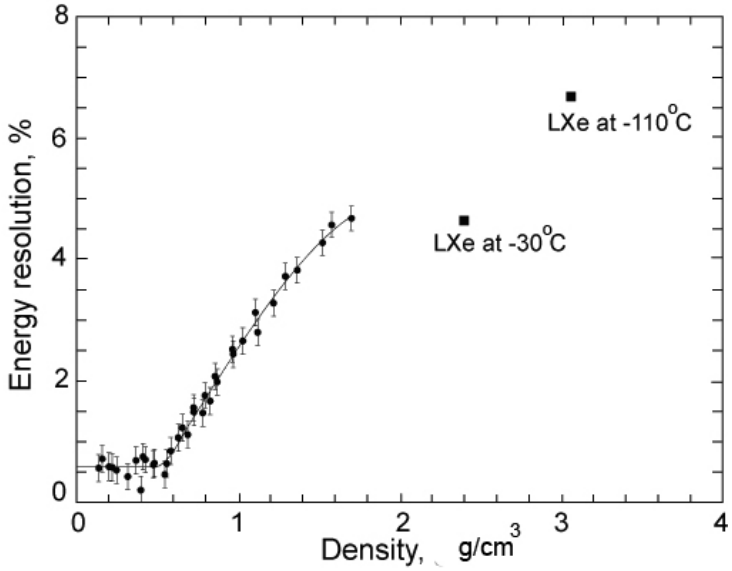

Fig. 2.12 Density dependencies of the intrinsic energy resolution (% FWHM) obtained for 662 keV gamma rays [33].

For the density range between 0.12 g cm^{-3} and 0.6 g cm^{-3} the intrinsic energy resolution is almost constant. The authors gave the value of the intrinsic energy resolution to be 0.6% FWHM that is very close to the statistical limit with a Fano factor of 0.14 [66]. Note, that the absolute value of the intrinsic resolution received by subtracting the noise from the measured energy resolution may include a big systematic error associated, for example, with uncertainty in the calculation of the shielding inefficiency. But, for the present considerations, it is important to note that the intrinsic resolution does not depend on the xenon density in the low-density range in sharp contrast with higher densities, where the energy resolution quickly deteriorates with growing den-

sity. This tendency is also consistent with results obtained by Dmitrenko's group [67] and the measurements by Levin et al. [68].

The degradation of the energy resolution above 0.55 g cm^{-3} may be explained by the δ-electron model, originally proposed to explain the poor energy resolution observed for liquid Xe ionization chambers [57, 60]. The location of the step around 0.55 g cm^{-3} density (see Fig. 2.12) corresponds to the threshold of appearance of the first exciton band formed inside a cluster of at least 10 atoms bonded together due to stochastic density fluctuations [69]. Delta electrons interact with whole clusters to produce an exciton or free electron. This could be an additional channel of energy loss that would result in a sharp decrease in the size of delta electron tracks and, consequently, in a sharp rise of the number of tracks with high density of ionization above 0.55 g cm^{-3}. A similar behavior of the intrinsic resolution was obtained in the range of gamma ray energies between 0.3 and 1.4 MeV. Below 0.55 g cm^{-3}, the intrinsic energy resolution saturates to its statistical limit, determined by $(FW/E_\gamma)^{1/2}$.

The formation of the band structure and appearance of excitons depends on the temperature, since heating brings the properties of the high-pressure gas closer to those observed for an ideal gas. Figure 2.13 shows the relative changes of the collected charge and the intrinsic resolution ΔE_0 with temperature measured at 5 kV cm^{-1} for two densities of 0.55 and 0.69 g cm^{-3}. At low densities, no changes were observed between the condensation point of Xe and 70 °C. At higher densities the resolution starts to degrade after the temperature exceeds some threshold, for instance, 37 °C at 0.69 g cm^{-3}. The collected charge decreases with temperature and this can be attributed to changes of both the W value and the recombination rate. As for the energy resolution, it stays unchanged up to some temperature that depends on density and, then, starts to degrade.

We have to note, that the observed density effects in the intrinsic energy resolution may be explained by the model of the nonuniform condensed phase. Clusterization of high-density heavy noble gases may explain the observed high scattering of the emission light, and fluctuations in charge yield from tracks of short-range protons and tritons in dense xenon [70, 71].

Masuda et al. [72] observed the fluctuations of energy deposition of heavy ions in liquid argon doped with allene (C_3H_4) to be 2 to 3 times worse than those predicted by the theory. They suggested that nonuniform density of liquid argon may be responsible for deterioration of the energy resolution.

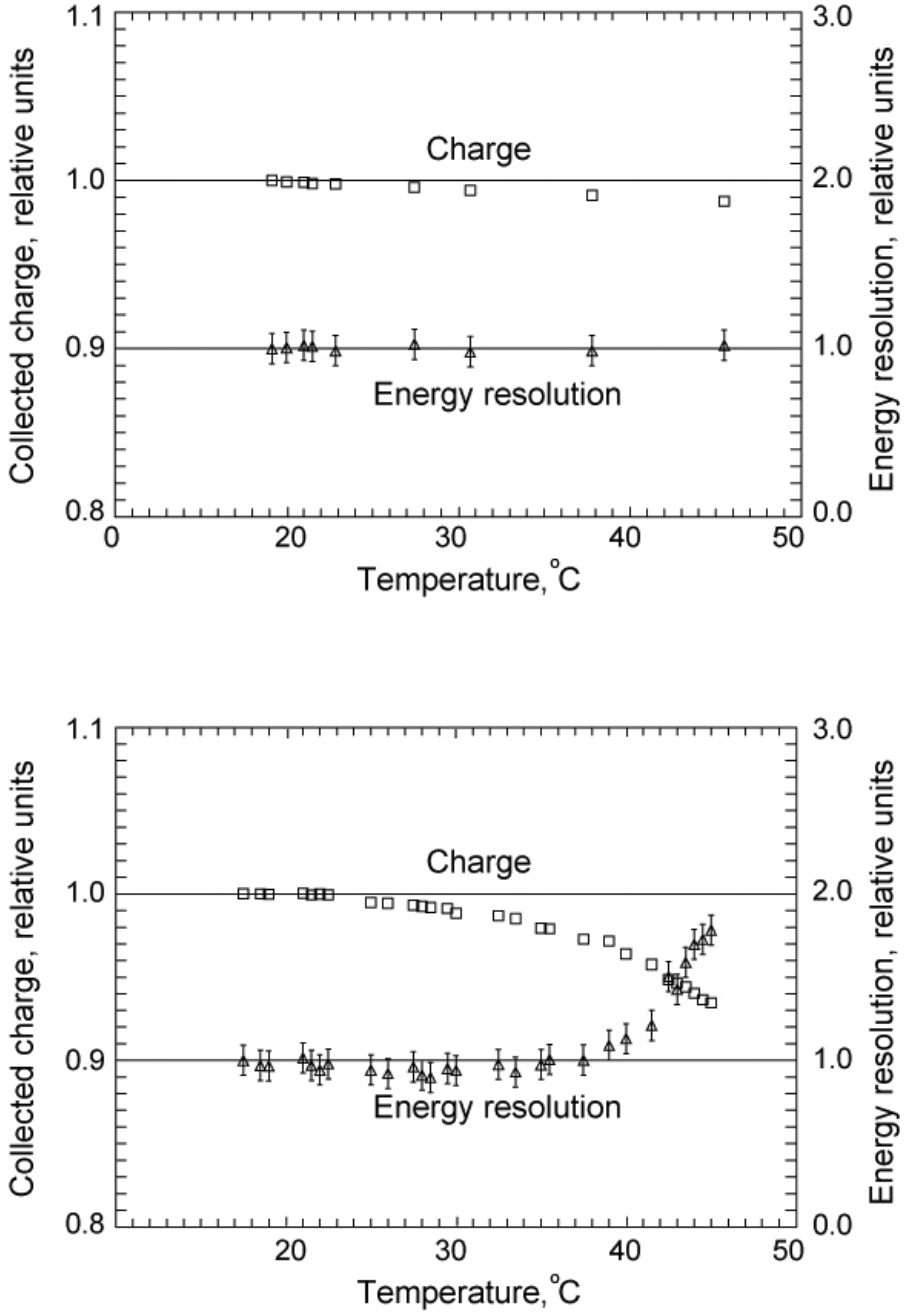

Fig. 2.13 The relative changes of the collected charge and the intrinsic resolution ΔE_0 with temperature measured at 5 kV cm^{-1} for two densities: 0.55 g cm^{-3} (top) and 0.69 g cm^{-3} (bottom) [33].

2.6
Detection of Nuclear Recoils

For applications such as the detection of massive particles, such as WIMPs of dark matter, scattering from nuclei becomes an important application for modern noble gas detectors (see Chapter 9). There are important effects that should be taken into account when nonrelativistic heavy particles are detected via nuclear recoils in heavy noble gases. Formally, this case is represented by $<\nu> \longrightarrow 0$ in Eq. (2.5) and the energy deposited in the detector $E = <\eta>$.

When the momentum transfer q is low enough that the de Broglie wavelength of the particle h/q is no longer large compared to the nuclear radius r_{n}, the cross section of scattering from the nuclei $\sigma(qr_{\mathrm{n}})$ is reduced by factor $F^2(qr_{\mathrm{n}})$

$$\sigma(qr_{\mathrm{n}}) = \sigma_0 F^2(qr_{\mathrm{n}}) \tag{2.22}$$

where σ_0 is the cross section at zero momentum transfer and the form factor $F(qr_{\mathrm{n}})$ is the Fourier transform of the ground mass density [73]. The form factor results in a loss of the detector sensitivity at particular energy depositions.

Figure 2.14 presents a form factor of ^{131}Xe calculated by Lewin and Smith [74]. The form factor reduces the cross section of elastic interactions

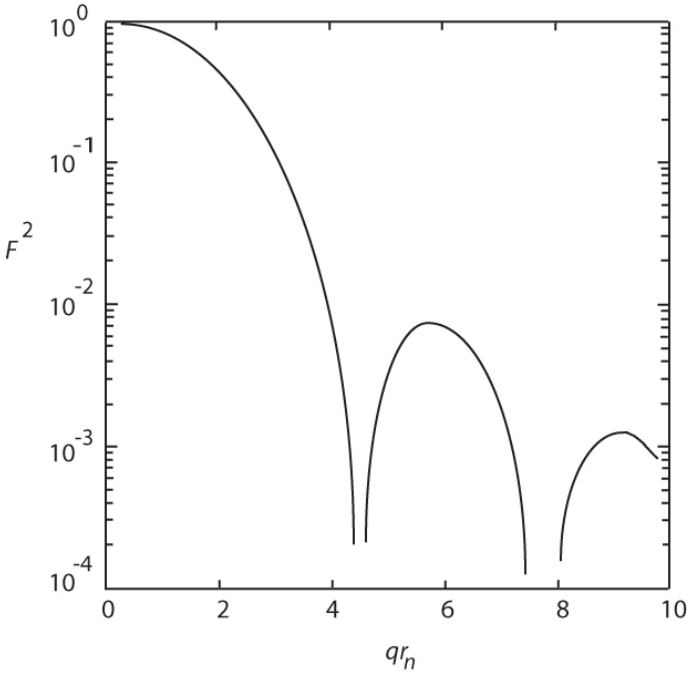

Fig. 2.14 Calculated form factor for ^{131}Xe. Redrawn from [74].

of scalar particles by several orders of magnitude especially for particular energies, for example, with $\sim$ 100 GeV mass at energies of about 100 keV ($qr_n \approx$ 4–5) and 250 keV ($qr_n \approx$ 7–8); the effect should not be observed in detectors filled with light media such as LNe [75]. However, the total drop of the cross section with increasing energy transfer makes reduction of the detection threshold for nuclear recoil detectors an extremely important task.

Another important effect, which should be taken into account when designing a detector for nuclear recoils is the so-called quenching factor. The quenching factor, q, for nuclear recoil is an empirical value defined as a ratio of the amount of ionization or light produced by a recoil nucleus to the amount of ionization or light produced by an electron (or a gamma ray) for the same deposited energy. The effect is associated with a much higher ionization density produced by nuclei and much more efficient recombination processes in comparison with electrons. The effect was observed in crystal scintillators [76] and in liquid xenon ionization detectors (Table 2.5).

Tab. 2.5 Quenching factor for nuclear recoils in LXe.

Quenching factor	Energy range, keV	Ref.
0.2	50–100	[77]
0.22$\pm$0.01	40–70	[78]
0.13–0.24	10–60	[79]

2.7 Detection of High-Energy Particles

Electrons and photons of sufficiently high energy ($\geq$ 1 GeV) interact with matter mainly through bremsstrahlung and pair production, respectively; through these interactions, secondary photons and electron-positron pairs produce more particles, developing a cascade of charged and uncharged particles (electromagnetic showers) [80]. The growth of the cascade will stop when the energies of the secondary particles fall below the critical energy, ε, where radiation losses are dominant. The length of the cascade may be characterized in terms of radiation length, X_0, which represents the average distance, x, that an electron needs to travel in a material to reduce its energy to $1/e$ of its original energy E_0

$$< E(x) >= E_0 \exp(-x/X_0) \tag{2.23}$$

The radiation length for different materials can be calculated as

$$X_0(\mathrm{g\,cm^{-2}}) \approx 716 \mathrm{g\,cm^{-2}} A/[Z(Z+1)\ln(287/\sqrt{Z})] \tag{2.24}$$

Tab. 2.6 Properties of materials used in high energy calorimeters.

Medium	A	ρ, g cm^{-3}	λ, cm	$\rho\lambda$, g cm^{-2}	X_0, cm	X_0, g cm^{-2}
Al	26.98	2.70	39.4	106.4	8.9	24.01
LAr	39.95	1.40	83.7	117.2	14.0	19.55
Fe	55.85	7.87	16.8	131.9	1.76	13.84
Cu	63.55	8.96	15.1	134.9	1.43	12.86
LKr	83.8	2.45	60	147	4.72	11.6
LXe	131.29	3.059	55.2	169	2.77	8.48
W	183.85	19.3	9.59	185	0.35	6.76
Pb	195.08	11.35	17.0	193.7	0.56	6.37
U	238.03	18.95	10.5	199	0.32	6.00
BGO		7.1	22.0	156	1.12	7.98

The shower maximum is reached after $\sim 9X_0$; about 90% of the shower energy is contained in a radius R_M. The Moliere radius, R_M, can be approximated as

$$R_M(\mathrm{g\,cm^{-2}}) \approx 21\ \mathrm{MeV}[X_0/\varepsilon(\mathrm{MeV})] \tag{2.25}$$

This represents the average lateral deflection of electrons at the critical energy after traversing one radiation length. After the shower maximum, the electromagnetic cascade decays exponentially with the attenuation length, which is practically independent of energy, and its value is close to the material-dependent minimum attenuation for photons; the photons in the tail of the shower dissipate their energy mainly through Compton scattering and photoabsorption [81]. Usually, thickness of the electromagnetic calorimeter is selected based on desirable energy resolution in the range of 22–26 X_0. The parameters of noble liquids considered for homogeneous electromagnetic calorimeters are collected in Table 2.6. The large light output and relatively short radiation length (2.8 cm) of liquid xenon make it most attractive. The ratio of the light output per unit energy for alpha and beta particles has been measured to be 1.1 in sharp contrast to traditional materials for scintillation calorimeters such as BaF_2, NaI, BGO, which have a ratio of no larger than 0.5. Computer simulations have shown that with liquid xenon an energy resolution of $3\%/\sqrt{E}(\mathrm{GeV})$ can be achieved.

The hadronic showering process is dominated by a succession of inelastic interactions of strongly interacting particles. At high energy, these are characterized by multiparticle production and particle emission originating from nuclear decay of excited nuclei. Due to the relatively frequent generation of neutral pions, there is also an electromagnetic component presented in hadronic showers. Secondary particles are mostly pions and nucleons. The hadronic multiplication process scales according to the nuclear interaction length or mean free pass λ, which is defined by the inelastic (neither elastic nor diffrac-

tive) cross section, $\sigma = \sigma_{\text{total}}$-$\sigma_{\text{elastic}} - \sigma_{\text{diffractive}}$, which is essentially energy-independent. The mean free path can be defined as

$$\lambda = A/(\sigma N_A \rho) \tag{2.26}$$

where Avogadro's number $N_A = 6.022 \times 10^{23}$ mol^{-1}, atomic weight A measured in [g mol^{-1}] units and density ρ [g cm^{-3}]. Numerical values for λ of different detector materials are given in Table 2.6. At high energies some characteristic of hadronic showers can be described [82] by a simple parameterization in terms of λ:

- hadronic shower achieves its maximum intensity at $l_{\max} \approx [0.6 \log(E[\text{GeV}]) - 0.2]\lambda$;
- shower depth for 95% longitudinal containment $l_{95\%} \approx l_{\max} + 4E^{0.15}\lambda$;
- shower radius for 95% radial containment $R_{95\%} \approx \lambda$.

In general, one can conclude that the hadronic cascade has a more poorly defined structure than an EM cascade because of leakage outside of neutrons; a typical value of the energy resolution of hadronic calorimeters is $\geq 50\%/\sqrt{E}(\text{GeV})$. Another distinguishing property of hadronic cascades is that they develop slowly. In contrast to electromagnetic showers that develop on a subnanosecond time scale due to atomic ionization and charged particle stoppage, hadronic showers are characterized by different processes that develop on different time scales, the slowest of which (deexcitation of heavy nuclei) may take as long as a microsecond.

3
Elementary Processes Affecting Generation of Signals

Signals acquired with noble gas detectors are generated as a result of motion of charge carriers and/or collection of photons produced during dissipation of absorbed energy of ionizing radiation, as described in Chapter 2. Processes of electron avalanche multiplication and excitation of the media by drifting electrons are often used to amplify signals. Both original and secondary electrons, and photons can be used to acquire data on absorbed energy, transferred momentum, position, time of interactions and also identification of ionizing particles. In this chapter, we will consider elementary processes associated with charge carrier transport in noble gases in different aggregate states. Particular principles of operation of different detectors will be considered in other chapters, while various technical aspects of charge carrier and photon collection will be considered in Chapter 8, devoted to the noble gas detector technology.

3.1
Collection of Charge Carriers

Drift is a process of motion of charge carriers under the influence of an electric field. In absence of external forces in gas, electrons move around with a Maxwellian energy distribution with the most probable value kT (about 0.04 eV at room temperature). Under an applied electric field, $\overrightarrow{E}$, carriers acquire a net motion in the direction of the electric field with a stationary drift velocity, $\overrightarrow{v_{\mathrm{d}}}$, which is the average of the instantaneous velocities as $\overrightarrow{v_{\mathrm{d}}} = < \overrightarrow{v}(t) >$. In presence of sufficiently low electric fields, when the carriers elastically collide with atoms and molecules of medium, the drift velocity is proportional to the electric field

$$\overrightarrow{v} = \mu \overrightarrow{E} \tag{3.1}$$

The proportionality factor, μ, is called the mobility. The mobility of electrons is a constant in a low electric field range. The mobility of ions is a constant in all cases relevant from the practical point of view. Probability of inelastic collisions of ions becomes substantial when instantaneous velocities become comparable with the electron velocity in the atom $v(t) \approx 10^8\ \mathrm{cm\,s^{-1}}$. That said,

the ion should possess an energy of more than 10 keV to collide inelastically, somewhat practically impossible at realistic electric fields.

Distribution of carriers in the ionization detector volume is largely nonuniform. The concentration gradient gives rise to spread of carriers over the entire volume, the process known as diffusion. Typically, the density of carriers is sufficiently low so that one can neglect the mutual Coulomb interaction, in which case the carrier current density can be presented in the following form:

$$\overrightarrow{J} = -D\overrightarrow{\nabla n} + n\overrightarrow{v_{\mathrm{d}}} \tag{3.2}$$

In weak electric fields and at small carrier concentrations the mobility is independent of the electric field, E, and is given by the Nernst–Einstein equation

$$\mu = eD/kT \tag{3.3}$$

The *weak electric field* condition implies that the carriers exist in a thermodynamic equilibrium with the medium, otherwise meaning that the carriers are thermalized. This condition is practically always valid for ions. When the charge carriers are not thermalized, the mobility becomes dependent of the electric field and the drift cannot be described within the above simplified model. In that case, the diffusion coefficient is a tensor with a D_T value in directions perpendicular to the electric field and D_L in the drift direction. It should be noted, that a nonzero magnetic field introduces even more anisotropy into the diffusion coefficient tensor. In many practical applications, distribution of carriers in the originally (at $t = 0$) point-like cluster containing n_0 carriers may be given as

$$N(t) = \frac{n_0}{e(4\pi D_T t)(4\pi D_L t)^{1/2}} \exp\left[-\frac{(x^2+y^2)}{4D_T t}\right] \exp\left[-\frac{(z+v_{\mathrm{d}}t)^2}{4D_L t}\right], \tag{3.4}$$

Equation (3.4) suggests that the electric field is directed opposite of the z-direction [83].

In the following discussion of transport properties of noble gases we prefer to present the transport coefficients as functions of E/N, where E is the electric field strength and N is the number of molecules per unit volume. Although small for measurements at temperatures close to 300 K (room temperature), the temperature effect should be taken into account when calculating N. The term E/N is often taken in units of Townsend (Td), where 1 Td = 10^{-21} V m^2 = 10^{-17} V cm^2. Some works made use of another alternative E/p, where p represents the gas pressure.

3.1.1
Charge Carrier Drift in Gases Under High Pressure

Transport properties of charge carriers in noble gases have been extensively investigated (see, for example, a monograph by Huxley [83]). In pure no-

ble gases, negative carriers are electrons while positive carriers are ions. Due to their low mass, between collisions electrons are easily accelerated by an electric field loosing a small fraction of their energy $\sim m/M$. Here, m is the electron mass, and M is the atomic mass. As a result, electrons have high drift velocities and diffusion coefficients. The electrons easily achieve high energies and inelastically collide with atoms exciting them, generating electroluminescence and charge multiplication. This is why electrons are often used for generation of signals in radiation detectors. However, low mobility ions may essentially influence the detector performance, for example, in accumulation of spatial charge or initiating secondary ionization processes.

3.1.1.1 Drift of Electrons in Gases

035 The electron drift velocity in gases V does depend on the electric field strength, the transport cross section, $q_t(\varepsilon)$, and the energy distribution function, $F(\varepsilon)$, according to

$$V = \frac{eE}{3N}(2/m)^{1/3} \cdot \int_0^\infty \frac{\varepsilon}{q_t(\varepsilon)} \cdot \frac{\partial F(\varepsilon)}{\partial(\varepsilon)}\, d\varepsilon \tag{3.5}$$

where E is electric field strength, N is the number of scattering centers per unit volume, m is the mass of an electron, and ε is the kinetic energy of an electron. The above relation is valid assuming electrons are in a thermal equilibrium with the medium and can be described by the Maxwellian distribution. Clearly, the drift velocity in gases is a linear function of the reduced electric field E/N. It is often more convenient to use the mobility and the reduced mobility defined as $\mu = V/E$ and μN, respectively

$$\mu N = \frac{e}{3}(2/m)^{1/3} \cdot \int_0^\infty \frac{\varepsilon}{q_t \varepsilon} \cdot \frac{\partial F(\varepsilon)}{\partial(\varepsilon)}\, d\varepsilon \tag{3.6}$$

$$D_T/\mu = -e^{-1} \cdot \frac{\int_0^\infty \frac{\varepsilon \cdot F(\varepsilon)}{q_m(\varepsilon)}\, d\varepsilon}{\int_0^\infty \frac{\varepsilon}{q_m(\varepsilon)(\frac{dF(\varepsilon)}{d\varepsilon})}\, d\varepsilon} \tag{3.7}$$

For electrons experiencing elastic collisions only, Robson's semiempirical expression [84] relates D_T and D_L according to

$$D_L/D_T = \partial(\ln \nu_d)/\partial(\ln E) = \partial(\ln \nu_d)/\partial(\ln E/N) \tag{3.8}$$

This implies that the ratio, D_L/D_T, may be obtained as a slope of an experimental curve for the electron drift velocity, $\nu(E/N)$, plotted on a double logarithmic scale. Such data is presented in Fig. 3.1 for He, Ne, Ar, Kr and Xe at nearly normal conditions. One can see that in low electric fields the electron drift velocity linearly depends on the electric field. In this range, the electrons are still in thermodynamic equilibrium with the media (thermalized) and the

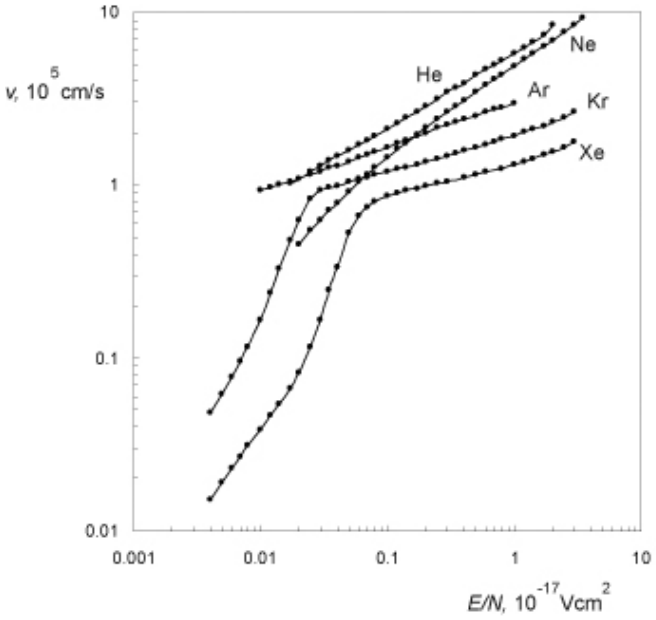

Fig. 3.1 Electron drift velocities plotted against a reduced electric field at a normal pressure in helium, neon, argon at $T = 293$ K (adopted from [83]) and in krypton, xenon at $T = 301$ K (adopted from [85]).

field dependence of the drift velocity follows Eq. (3.1) with "zero field" mobility $\mu_0 = \lim_{E\to 0} \nu(E)/E$.

When $E/N > 10^{19}$ V cm^2, the kinetic energy of electrons exceeds kT and the mobility becomes a function of the reduced electric field E/N. The Nernst–Einstein equation ((3.3)) can be presented in the following form:

$$eD(E)/\mu(E) = \mathcal{F} < E > \tag{3.9}$$

where <E> is the average kinetic energy (eV) of the drifting electrons. Factor $\mathcal{F}$ has a numerical value between 1 and 1/2 depending on the distribution function of the electrons ($\mathcal{F}_{\mathcal{M}}$ = 2/3 for a Maxwellian distribution). From Eq. (3.9) one can see that eD/μ defines the average energy of the electrons with an accuracy factor of 1 to 2 and because of this it often called the characteristic energy.

A nice compilation of kinetic parameters of electrons may be found in Ref. [86]. For a reference, electron drift velocities and diffusion coefficients at a reduced electric field of $E/N = 0.303\times10^{-17}$ V cm^2 (0.1 V cm Torr) for some noble gases of low density are presented in Table 3.1. In high-density gases, electron behavior becomes more sophisticated (for a reference, see Ref. [87]).

Tab. 3.1 Kinetic parameters of electrons in noble gases under normal conditions and a reduced electric field of 0.303×10^{-17} V cm^2 [83, 86].

	V, 10^5 cm s^{-1}	eD_T/μ, eV	eD_L/μ, eV
He	2.8	0.25	0.16
Ne	3.5	1	
Ar	2.3	3.0	0.3
Kr	1.6	2.0	0.22
Xe	1.05	2.7	0.27

In the limit $E \longrightarrow 0$, the kinetic theory predicts that the density-normalized mobility $\mu_0 N$ of electrons in a noble gas at constant temperature is independent of the density N. However, experimental data reveals that this statement is valid only for low densities of $N < 1$ nm^{-3}, as shown in Fig. 3.2 [88].

Horizontal lines shown in Fig. 3.2, indicate the prediction of the classic kinetic theory. Approaching the critical point from the low-density region, the reduced zero-field mobility is slowly decreasing in He and Ne before the critical points and, above the critical points, drops down by more than four orders of magnitude. In sharp contrast, the reduced mobility in Ar and Xe increases passing from low densities through the critical point when the aggregate state of noble gases changes from gaseous to liquid. Such a dramatic difference

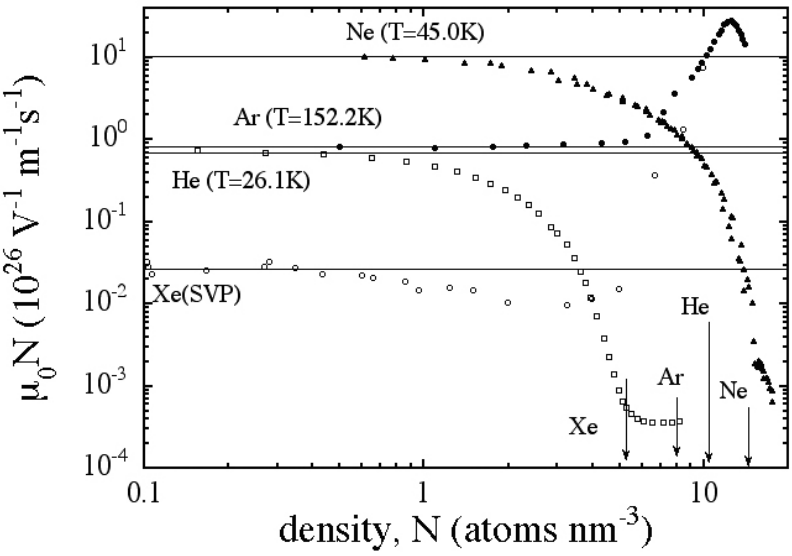

Fig. 3.2 Zero-field density normalized mobility $\mu_0 N$ as a function of N for noble gases: arrows indicate the critical densities; horizontal lines are predictions of kinetic theory [88].

is associated with significant differences in between-atom interactions among light and heavy atoms of noble gases. Interaction of an excess electron with light noble gas atoms is mainly repulsive, such that $V_0 < 0$. The electrons may lower their free energy by trapping in lower-than-average density fluctuations, known as bubbles, which have very low hydrodynamic mobility. For example, the mobility of electrons of 0.012 $cm^2\ V^{-1}\ s^{-1}$ may be estimated as that due to a charged sphere of radius $R_0 = 22$ Å moving in a viscous medium according to Stokes law

$$\mu = e/(6\pi\eta R_0) \tag{3.10}$$

where the viscosity of liquid helium is $\eta = 31.7\ \mu g\,cm^{-1}\ s^{-1}$ [89].

Increasing mobility in heavy noble gases in the vicinity of the critical density is associated with effective interactions of the neighboring atoms forming a band structure of the media. In the case of the fluid Xe, comprehensive analysis of the experimental and theoretical results are presented in Ref. [90].

Gas Mixtures

To increase the electron drift velocities in noble gases different molecular admixtures such as H_2, He, N_2, CH_4, CO_2, and other organic compounds, have been proposed and investigated. However, in the case of HPXe, the practical use on any particular gas mixture is restricted by the viability of employing the spark discharge technique for its purification. Because of this, the commonly used accelerating admixtures are H_2, N_2 and recently He. A significant contribution in detailed studies of Xe mixtures with small percentages of H_2 and N_2 were carried by a group of MEPhI in the early 1980s [67, 91]. In these works, it was shown that H_2 is the most efficient drift accelerating agent among the practical admixtures.

Figure 3.3 shows electric field dependencies of the electron drift velocities measured at the threshold density, 0.6 $g\,cm^{-3}$, and different concentrations of H_2 determined as a ratio of Xe H_2 molecules to Xe atoms. As was mentioned before, this density is close to the maximum operating density of high-energy resolution ionization chambers. As seen from Fig. 3.3, even a small percentage of H_2 added to Xe increases the drift velocity by a factor of 2.5 and higher. At the same time, a stronger electric field is required to achieve such an improvement. The optimal concentration of H_2 depends on several factors and a drift velocity is one of them. It was found that the optimal concentration should be within 0.3–0.6%. Cooling electrons lead to reduction in diffusion. Note, that other molecular admixture such as CH_4 [92] could be used as well but the use of H_2 is the most significant, because it can be used in discharge purifiers.

Admixture of helium to xenon also can be used for cooling and acceleration of drifting electrons. For example, at gas pressure 0.4 MPa admixture of 15% ^{4}He in xenon increases the electron drift velocity and reduces transverse diffusion about three times at reduced electric field of about 3×10^{-18} $V\,cm^2$

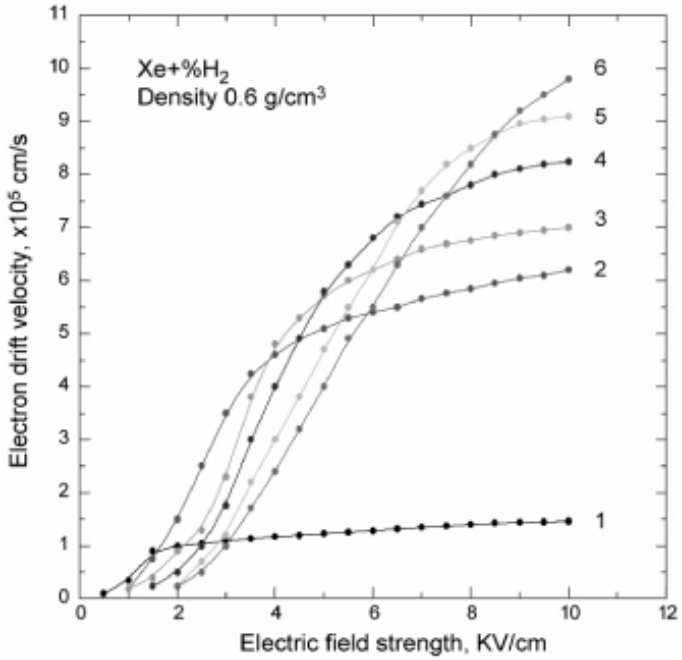

Fig. 3.3 Dependencies of electron drift velocities versus electric field strength in Xe+%H_2 mixture at 0.6 g cm^{-3}. (1) - pure Xe, (2) - 0.2%, (3) - 0.3%, (4) - 0.5%, (5) - 0.7%, (6) - 1.0%. Redrawn from [91].

(0.1 V cm^{-1} Torr^{-1} [93]. Similar observations were made at 2 MPa pressure and concentration of 13% ^{4}He [94] and 3% ^{3}He in xenon at reduced electric fields in the range of 2–5.5$\times$10^{-18} V cm^2 (results from A. Bolozdynya).

3.1.1.2 **Drift of Ions in Gases**

In the practice of noble gas detectors, we usually deal with single charged ions: positive ions of atoms or molecules of noble gases and negative ions of electronegative impurities. However, it may be useful to keep in a mind that the number of ion species produced in heavy noble gases is much greater and more complex than was earlier thought. For example, xenon ions Xe^{n+} have been identified for n = 1 to 13. The mobility hardly varies with the charge of the ion: a doubly charged ion having practically the same mobility as a singly charged ion of either sign. Mobility of dimer ions in xenon and krypton is a factor of 1.5 higher than that of atomic ions in the parent gas [95]. The drift velocities of atomic ions dependent on the reduced electric field in krypton and xenon gases at normal conditions are presented in Fig. 3.4. Mobility of ions in their parent gas and alkali ions in noble gases at normal conditions are presented in Tables 3.2 and 3.3.

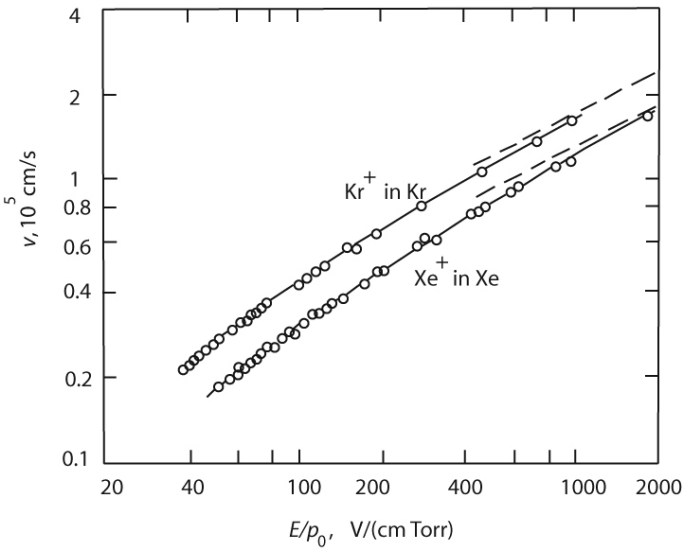

Fig. 3.4 The drift velocity of atomic ions in krypton and xenon at normal conditions. The broken lines show a slope of $1/2$. Redrawn from [95].

Tab. 3.2 Mobility μ_0 [10^{-4} $m^2s^{-1}V^{-1}$] of ions in their parent gas at a gas density of 2.69×10^{25} m^{-3} [96].

Ionic species	He	Ne	Ar	Kr	Xe
Atomic positive ion	10.2	4.2	1.53	0.9	0.6
Molecular positive ion	20.3	6.5	2.3	1.2	0.8

Tab. 3.3 Mobility μ_0 [10^{-4} $m^2s^{-1}V^{-1}$] of alkali ions in noble gases [96].

Ion	He	Ne	Ar	Kr	Xe
Li^+	25.6	12	4.99	4.0	3.04
Na^+	23.4	8.70	3.23	2.34	1.80
K^+	22.7	8.0	2.81	1.98	1.44
Rb^+	21.2	7.18	2.40	1.59	1.10
Cs^+	19.1	6.50	2.23	1.42	0.99

The mobility of ions in noble gases is constant at low values of E/N, the departure from constancy occurring when the ions attain drift velocities comparable with the agitation velocity of the gas molecule. Mobility can be critically dependent on gas purity because polar impurity molecules tend to cluster around the ion and so reduce its mobility. The mobility has been shown to vary as (gas number density)$^{-1}$ for pressures from 10 to 6×10^6 Nm^{-2}. The

mobility of positive ions in gas mixtures is given by Blanc's law

$$\mu = 1/\Sigma_i f_i/\mu_i \tag{3.11}$$

where f_i is the fractional composition of the ith gas.

3.1.2 Drift of Charge Carriers in Condensed Phases

There are a broad variety of transport properties of charge carriers in condensed noble gases. At the same time, there are a lot of similarities in behavior of electrons and ions (holes) in comparison with those in gas phases. A reason for the similarities is that atoms in condensed noble gases are weakly bonded and compose very soft structures, in some sense, similar to the gaseous phase. A reason for the differences is that light and heavy noble atoms have very different polarizability. Xenon atoms have the highest polarizability among other atoms of noble gases (except Rd): $\alpha_{Xe} = 4.0\times10^{-24}$ cm^3 (for comparison, $\alpha_{Ar} = 1.66\times10^{-24}$ cm^3, $\alpha_{He} = 0.21\times10^{-24}$ cm^3).

3.1.2.1 Drift of Electrons in Condensed Phases

Electrons behave very differently in different condensed noble gases at different conditions. Obviously, their behavior is classified via the value of mobility in zero limit of the electric field [97]. Generally, there are three classes of electron states classified via the mobility in the zero-field approximation:

1. $\mu_0 > 10$ cm^2 V^{-1} s^{-1}
2. $\mu_0 < 0.1$ cm^2 V^{-1} s^{-1}
3. 0.1 cm^2 V^{-1} s^{-1} $< \mu_0 <$ 10 cm^2 V^{-1} s^{-1}

Electrons with mobilities $\mu_0 > 10$ cm^2 V^{-1} s^{-1} are usually classified as *quasifree*. This term suggests that *free* electrons exist only in a vacuum; however, in some condensed noble gases electrons are very mobile and comparable in this parameter with low-density gases. Electrons with mobility $\mu_0 < 0.1$ cm^2 V^{-1} s^{-1} are considered as being *localized* in deep traps or density fluctuations which develop into deep traps. The third class is a transition class where different states are possible with different probabilities.

In dense media electrons interact with a few atoms simultaneously. If atoms have high polarizability, being polarized by electrons, they become attractive to electrons and interact with each other via dipole-dipole interaction. The balance between these two effects defines a potential energy of the ground state of electrons V_0 in the condensed media. Experimentally, V_0 is most often measured as a difference between work function electron emission from metal photocathode in a vacuum (or low-density gas) and in the tested medium.

Summary of measured ground state energies (relatively vacuum) of electrons in different media are shown along with zero-field mobilities in Table 3.4. A value of V_0 is a characteristic of a potential barrier existing at the interface between condensed and rarefied phases.

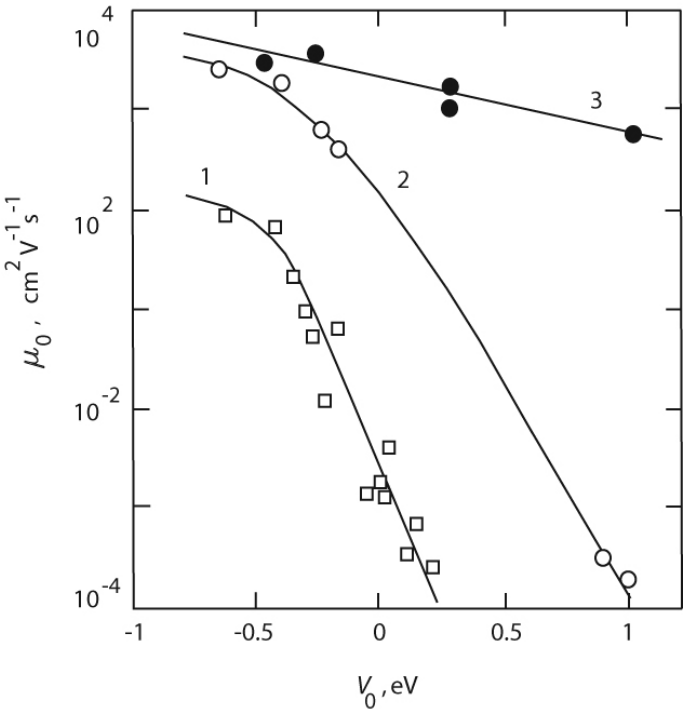

Fig. 3.5 Correlation between zero-field mobilities and the ground states of electrons in liquid hydrocarbons (1), liquid noble gases (2) and noble solids (3) (see Table 3.4 for condensed noble gases and Ref. [98] for liquid saturated hydrocarbons). Lines drawn for better reading of the data. Redrawn from [18].

There is a very certain correlation between V_0 and μ_0: μ_0 is reducing with increasing V_0 (Fig. 3.5). From Table 3.4 one can see that in liquid noble gases, changing V_0 from -0.5 eV to +0.5 eV leads to μ_0 changing in several orders of value.

Quasifree Electrons

In heavy noble (Ar, Kr, Xe) liquids and solids, due to high atom polarizability and strong interaction between atoms polarized in the electron field, electrons predominantly exist in a quasifree state, which is characterized with high drift velocities even exceeding drift velocities in the gas phase at the same reduced electric field E/N (Fig. 3.6).

Tab. 3.4 Energy of ground state of excess electrons V_0 and zero-field mobilities μ_0 in condensed noble gases.

	T, K	V_0, K [99, 100]	μ_0, $cm^2\,V^{-1}\,s^{-1}$ [101–103]
^4He			
Liquid	3		0.03
Liquid	4.2	+1.05	
Ne			
Solid	4	+1.1±0.1	600
Liquid	25	+0.67±0.05	
	27		0.001
Ar			
Solid	4	+0.3±0.1	
	80		1600±30
Liquid	84	-0.2±0.03	
	85		625±15
	87.5	-0.21±0.03	
Kr			
Solid	20	-0.25±0.1	
	113		3700
Liquid	116	-0.40±0.05	
	117		1200±150
	123	-0.45±0.05	

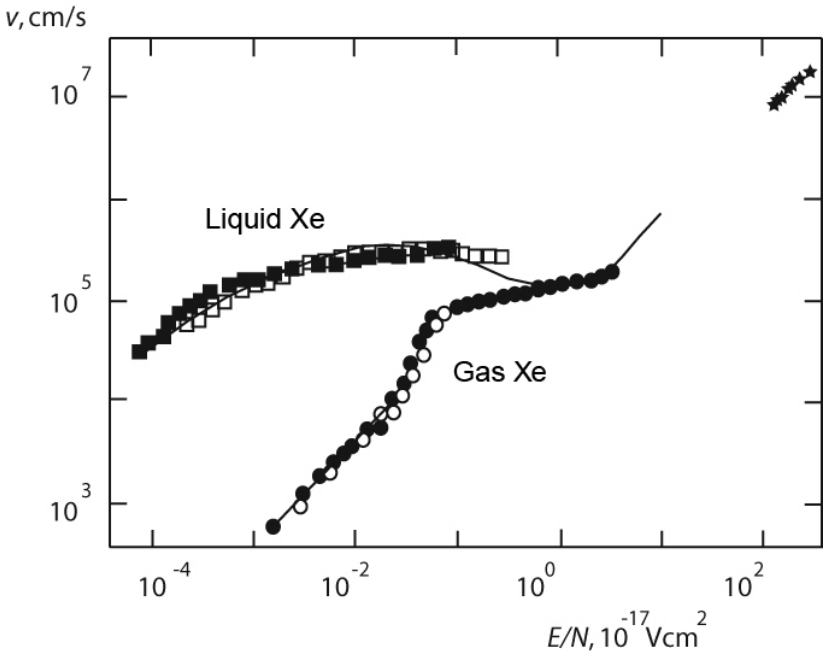

Fig. 3.6 Electron drift velocity in liquid and gaseous Xe: experimental data (points), calculations (curve). Redrawn from [104].

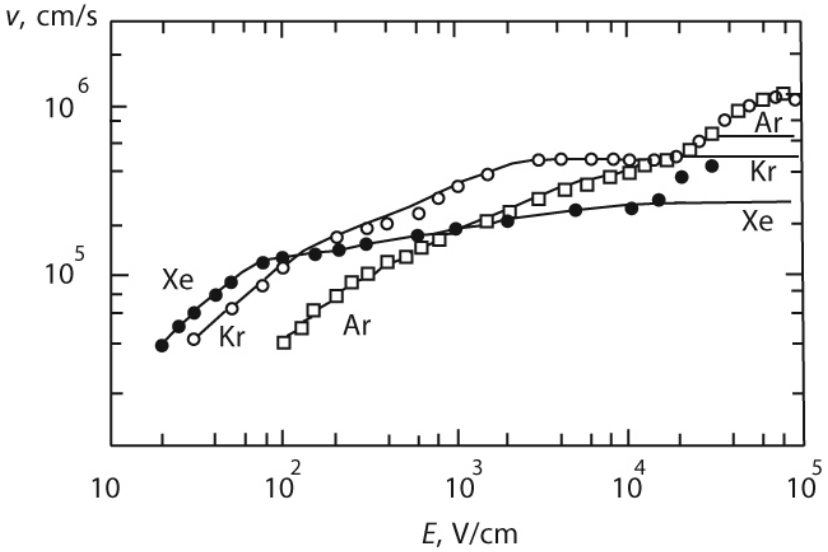

Fig. 3.7 Electron drift velocity as a function of the electric field strength in liquid argon ($T = 87$ K), krypton ($T = 120$ K) and xenon ($T = 165$ K): pure (solid lines) and solutions with nitrogen (symbols). Redrawn from [103].

Heating of electrons by the electric field in the liquid starts for smaller values of the E/N parameter compared with those in the gas. The mobility in the gas remains constant up to $E/N = 2\times10^{-19}$ V cm^2, while the mobility in the liquid begins to decrease already at $E/N = 10^{-21}$ V cm^2. This is a result of small cross section of electron scattering in the liquids compared to the cross section in gas. The drift velocity of electrons in the liquid is limited for high electric fields and approaches the drift velocity in the gas with the increasing field. The characteristic energy in the liquid is larger than the electron mean energy but the difference is smaller in the liquid. Adding molecular impurity increases electron drift velocity at high electric fields (Fig. 3.7).

Figures 3.8, 3.9, and 3.10 show the electrons drift velocity as a function of electric field strength measured in condensed phases of heavy noble gases at different temperatures.

Figure 3.11 presents data on zero-field mobility of electrons in liquid argon, liquid and solid xenon as a function of temperature in the range between triple and critical points. In the liquids, the mobility has a maximum; in the solid xenon the mobility is a monotonic function of temperature increasing with reducing temperature. The highest mobility (8500 cm^2 V^{-1} s^{-1}) was measured in liquid xenon at 220 K. Complicated behaviors of the temperature dependence of the transport properties in the liquids may indicate certain evolution of the liquid structure.

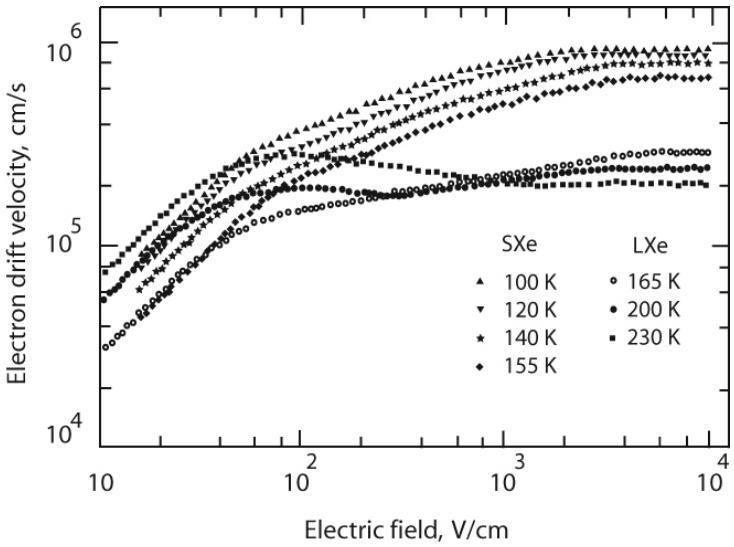

Fig. 3.8 Electron drift velocity in solid and liquid xenon at different temperatures in the range between 100 K and 230 K. Redrawn from [102].

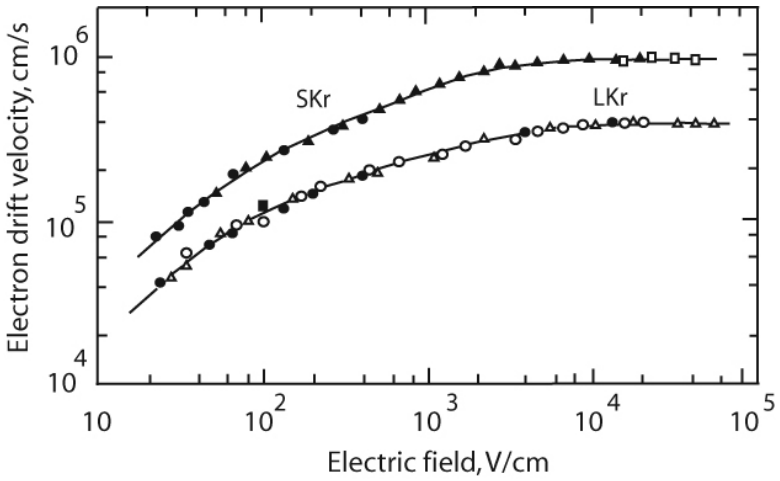

Fig. 3.9 Electron drift velocity in solid krypton (SKr) at 113 K and liquid krypton (LKr) at 117 K. Different symbols represent results for different specimen as described in Ref. [101]. Redrawn from [101].

Diffusion of electrons in condensed noble gases was not so thoroughly investigated as drift velocity and mobility. There are very few publications on this subject. Figure 3.12 represents data measured by Doke, Shibamura et al., and Derenzo for liquid argon and xenon [40, 107, 108].

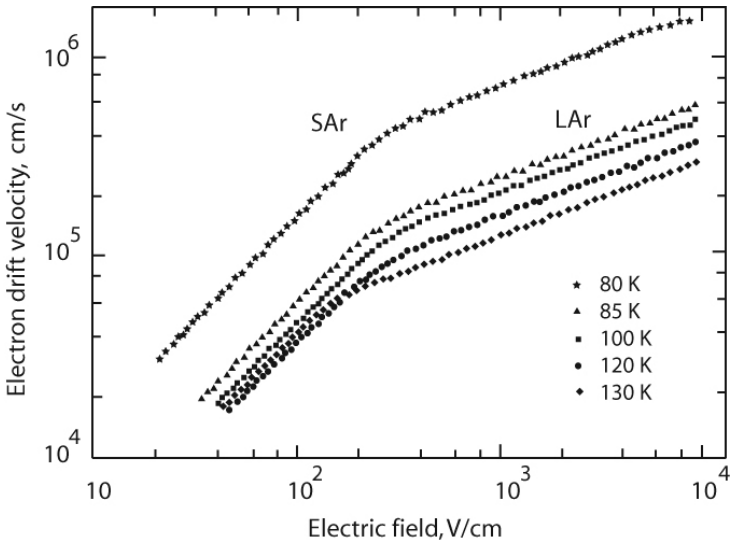

Fig. 3.10 Electron drift velocity in solid (SAr) and liquid (LAr) argon at different temperatures. Redrawn from [102].

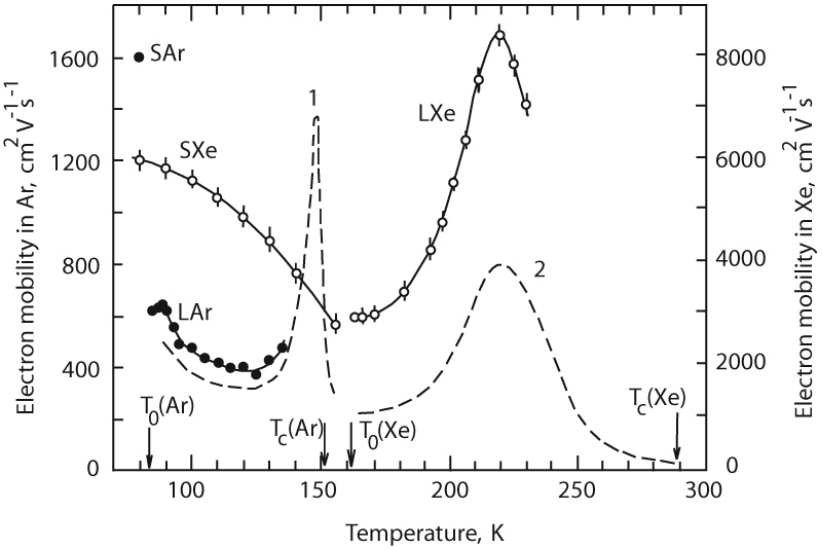

Fig. 3.11 Zero-field mobility of electrons dependent on temperature in liquid argon, liquid and solid xenon: T_0 triple point temperature, T_c critical temperature. (1) Data adopted from [105], (2) Data adopted from [106], experimental points are measured by Guschin et al. [102]. Redrawn from [102].

The theory of hot electrons in condensed noble gases was developed by Lekner and Cohen [109, 110] and used until now [104] for explanation of the

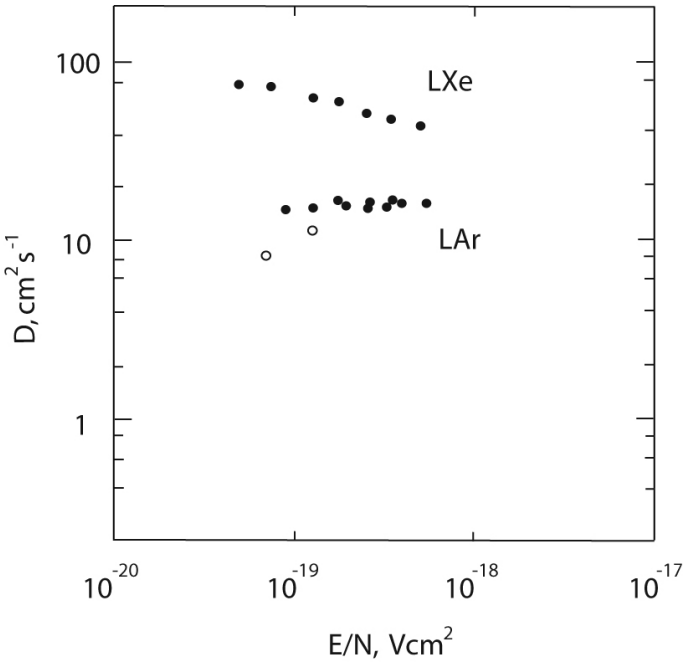

Fig. 3.12 Diffusion coefficient of electron in dependence on reduced electric field in liquid xenon and argon: the full circles represent data measured by Doke [40, 107], the open circles measured by Derenzo [108]. Redrawn from [40].

dependence of the drift velocity, mobilities, diffusion coefficients on the electric field in pure condensed noble gases and in the presence of molecular admixtures [103]. The theory is based on the formal consideration of the electron drift as a consequence of single elastic scatterings on effective potentials of the muffin-tin type defined by Lekner, taking in account the interference of scattered electron waves. The Cohen–Lekner theory accurately describes transport properties of electrons in liquid argon near the triple point, however agreement between predictions of the theory for other noble liquids (krypton) was not so good [111].

Another approach was proposed by Ascarelli [112], who suggested that the observed variation of the drift velocity with the electric field is a result of the time spent by the electron in shallow traps rather than the effect of energy transfers during collisions. This approach easy explains similarities in variations of the dependence of the drift velocity on the electric field when different molecular admixtures are added as well as the square root field dependence of the enhancement of the drift velocity. Similar models of part-time free electrons time-to-time trapped in density fluctuations is used to describe $\nu(E)$ in liquid saturated hydrocarbons [113].

The suggestion that shallow traps may be formed by density fluctuations makes the approach of Ascarelli to be relative to the hypothesis discussed above about the influence of density fluctuations on measured values of the Fano factor, temperature variations of the electron mobility in liquids, and density effects in pressurized xenon. However, similarity in behavior of electrons in liquids and solids noble can be better understood in the frame of the Cohen–Lekner theory. Maybe these two approaches could be unified in the future.

Localized Electrons

In condensed noble gases with $V_0 > 0$, electrons usually demonstrate low mobility (see Table 3.4). Moreover, in superfluid ^{4}He, electrons were found to be even less mobile than positive ions (Fig. 3.13). Low mobile or localized electrons have also been observed in normal liquid helium, liquid neon (Fig. 3.13) and liquid hydrogen (for references, see review of properties of localized electrons in Ref. [114]. Localization of electrons was observed in cold high-density ($n > 10^{21}$ cm^{-3}) helium gas as well [115].

It was found that due to the strong electron (small He atom) exchange repulsion, a void or bubble of macroscopic size is created around an electron in condensed light noble gases. In presence of an electric field, the bubble

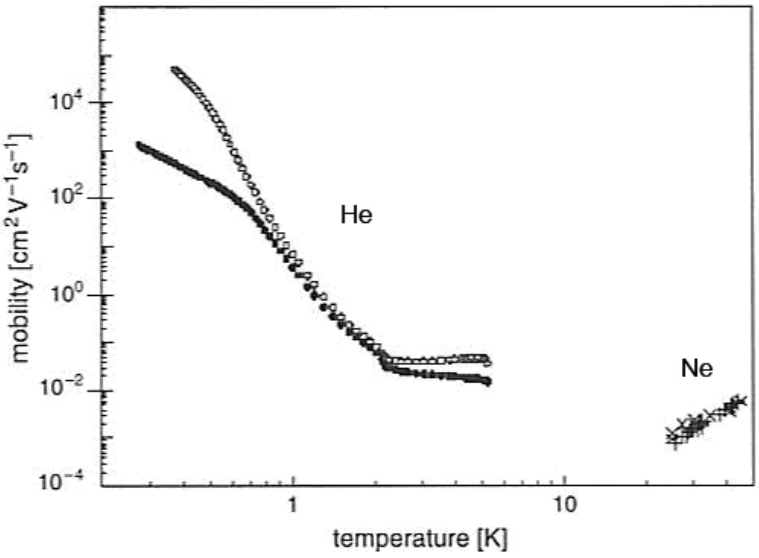

Fig. 3.13 Mobility of positive ions (open circles) and electrons (closed circles) in liquid helium and electrons in liquid neon dependent on temperature (adopted from [114]).

moves as a single entity with an electron inside and a total mobility of about 10^{-2}–10^{-3} $cm^2\,V^{-1}\,s^{-1}$. The drifting electron bubble experiences hydrodynamic resistance and the mobility can be calculated according to Stokes equation (Eq. (3.10)). In normal liquid ^{4}He at normal pressure, the radius is about 2.2 nm, in liquid neon around its triple point, about 0.7 nm, in liquid hydrogen $\sim$ 1 nm at 19 K. In superfluid helium, mobility of localized electrons is essentially increased but still remains smaller than that of positive ions (Fig. 3.13).

3.1.2.2 Drift of Ions and Holes in Condensed Noble Gases

In liquid dielectrics, ion mobility is usually about 10^{-2}–10^{-4} $cm^2\,V^{-1}\,s^{-1}$ that is close to the mobility of ions in electrolytes, a thousand times smaller than the ion mobility in the noble gases, and a million times smaller than the mobility of quasifree electrons in heavy noble liquids. The ion mobility depends on a viscosity of the liquid as $\mu \sim \eta^{-\alpha}$, where parameter α equals 1–2 for different ions and $\alpha \approx 1$ for atom ions and for quasispherical molecular ions. In the latter case ($\alpha \approx 1$), the mobility of ions follows Eq. (3.10). Mobility of positive ions in liquid helium follows Stokes law only in suggestion [116] that the ions drag about 50 ^{4}He atoms. Atkins suggested that electrostriction effects increase the liquid density over a large region surrounding the ion. The size of this ion complex (Atkins' snowball) is about 10–15 a_0 ($a_0 = 5.3\times10^{-9}$ cm is the Bohr radius). Experimental data on mobility of ions and holes in condensed noble gases are presented in Table 3.5. Diffusion coefficients of ions may be calculated with the Nernst–Einstein equation (Eq. (3.9)) using the tabulated values of mobility.

Positive holes were observed in noble solids [117] and liquid xenon [119]. The results of measurements of the hole mobilities as a function of the temperature are presented in Figs. 3.14 and 3.15. As seen from Table 3.5, holes demonstrate significantly higher mobility than positive ions in the liquids but approximately five orders lower than electrons in the solids. The magnitude of the hole mobility and its temperature dependence can be described via the hopping model of charge carrier transport. In this model, the charge propagates in result of thermally activated jumps from one trap to another and the mobility is given as

$$\mu = (eb^2/kT)\omega \tag{3.12}$$

where b is the average jump distance and ω is the jumping frequency, which can be expressed as $\omega = P(\omega_0/2\pi)\exp(-E_a/kT)$, where P is the tunneling probability for the case where adjacent sites have the same energy level, E_a is activation energy, and ω_0 is the phonon frequency. The hole may be self-trapped in a potential well between two rare atoms, produced by the resulting lattice and electronic distortions. This formation called a *polaron* is similar to the molecular ion R_2^+. The localized hole will occasionally tunnel to a neighboring atom,

Tab. 3.5 Mobility of ions and holes in condensed noble gases.

	T, K	μ_+, $cm^2\,V^{-1}\,s^{-1}$	μ_-, $cm^2\,V^{-1}\,s^{-1}$	Ref.
^{3}He				
Liquid	1.21	7.65	3.64	[121]
	2.94	9.36	3.50	[121]
^{4}He				
Liquid	0.371	5.19×10^4	540	[122]
	0.510	6420	209	[122]
	1.132	2.57	1.51	[122]
	2.20	0.0472	0.0326	[122]
	4.16	0.0470	0.0196	[122]
	5.18	0.0376	0.0157	[122]
Ne				
Solid	25	0.0105 (holes)		[117]
Ar				
Solid	84	0.023 (holes)		[117]
Liquid	90.1	6.61×10^{-4}		[123]
	111.5	12.2×10^{-4} (Ar_2^+)		[123]
	145.0	26.1×10^{-4} (Ar_2^+)		[123]
Kr				
Solid	116	0.04 (holes)		[117]
Liquid	120	6.45×10^{-4}		[124]
	145.0	6.67×10^{-4} (Kr_2^+)		[123]
	168.5	12.19×10^{-4} (Kr_2^+)		[123]
	184.3	10.6×10^{-4} (Kr_2^+)		[123]
Xe				
Solid	157	0.020 (holes)		[101]
	161	0.018 (holes)		[117]
Liquid	161	35×10^{-4} (holes)		[118]
	230	46×10^{-4} (holes)		[118]
	280	41×10^{-4} (holes)		[118]
	162	2×10^{-4} ($TMSi^+$)	7×10^{-4} (O_2^-)	[119]
	192	3×10^{-4} ($TMSi^+$)	10×10^{-4} (O_2^-)	[119]
	162	2.4×10^{-4} ($^{226}Th^+$)		[125]
	163.0	1.33×10^{-4} ($^{208}Tl^+$)		[126]
	184.2	2.85×10^{-4} (Xe_2^+)		[123]
	192.1	3.17×10^{-4} (Xe_2^+)		[123]

where it will reestablish an R_2^+ formation. A great review of hole transport properties can be found in a classic review of hole transport in solids [120] and in a recent review of transport properties of localized electrons, ions, and holes [114].

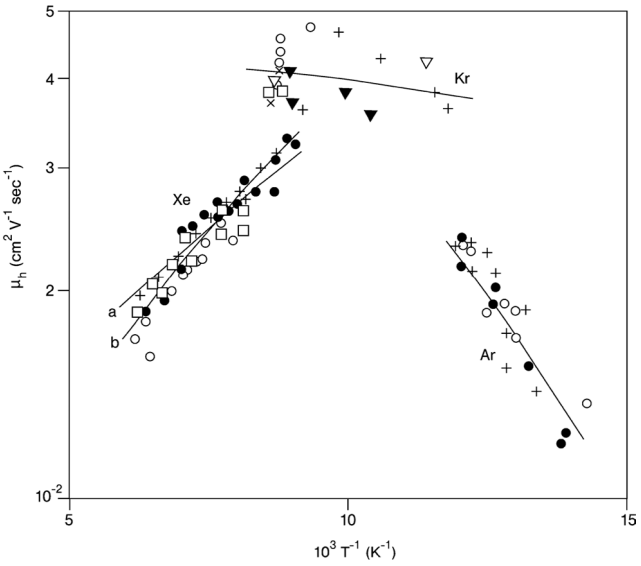

Fig. 3.14 The drift mobility of holes in solid Xe, Kr, Ar dependent on reciprocal temperature. The points were measured in a number of experiments using samples ranging in thickness from 250 to 385 μm in Xe, from 60 to 130 μm in Kr, from 50 to 85 μm in Ar; the solid lines are theoretical predictions from the nonadiabatic theory [117].

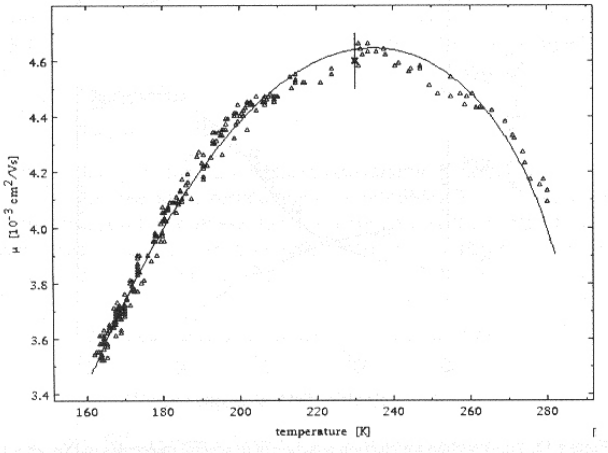

Fig. 3.15 The drift mobility of holes in liquid xenon as function of temperature [118].

3.1.3 Charge Carrier Trapping

The attachment of electrons to electronegative impurities in condensed phases is the most important process limiting performance of noble gas detectors such as ionization chambers, electroluminescence detectors, and time projection chambers (TPCs).

3.1.3.1 Electron Attachment in Liquids

Drifting ionization electrons may be trapped and cannot contribute further to the signal acquired from noble gas detectors based on the collection of the ionization charge. Collisions between electronegative impurities and free electrons may result in attachment, in which the electron is captured by the neutral atom or molecule AB producing a negative ion. There are three types of attachment considered most often:

1. Radiative attachment

$$e + AB \longrightarrow AB^- + h\nu \tag{3.13}$$

2. Dissociative attachment

$$e + AB \longrightarrow AB^* + e \longrightarrow A^+ + B^- + e \tag{3.14}$$

$$e + AB \longrightarrow AB^- \longrightarrow A^+ + B^- \tag{3.15}$$

3. Three-body attachment realized as the two-stage Bloch–Bradbury [127] reaction

$$\begin{aligned} e + AB &\longleftrightarrow (AB^-)^* \\ (AB^-)^* + X &\longrightarrow AB^- + X \end{aligned} \tag{3.16}$$

In the latter reactions, molecule or atom X representing the majority of gas population plays a role of the third body carrying out the binding energy of the electron and electronegative molecule AB. Usually, the reaction of the radiative Eq. (3.13) has a small cross section and we will not discuss it here. The energy released in Eq. (3.16) is known as the *electron affinity*. The positive sign of the electron affinity means electronegativity of the atom or molecule, i.e., that the suitable negative ion is stable. Examples of electronegative atoms and molecules are tabulated in Table 3.7. Noble gases and alkali metals have negative electron affinities.

The dissociative attachment is the threshold process. In Eq. (3.15) electrons may be captured even by nonelectronegative molecules. At relatively small

energies of drifting electrons in dense gases ($p > 100$ Pa), the basic mechanism of the electron attachment is the three-body Eq. (3.16) in collisions from electronegative impurities. The rate of the process may be described as

$$\mathrm{d}n_{AB^-}/\mathrm{d}t = -k_3 n_{AB} n_X n_\mathrm{e} \tag{3.17}$$

where k_3 is the constant of the reaction, n_{AB}, n_X and n_e are the densities of electronegative impurity, atoms of the medium, and electrons, respectively. Table 3.8 presents the constants of the attachment of thermalized electrons to oxygen impurities in the most popular gases including noble gases.

The electron lifetime is the average period of time an electron stays free before it gets trapped by an electronegative molecule and cannot be used in generation of measurable signal. Formally, the capture process can be described in terms of the number of free electrons $N(t)$ changing over time as

$$N(t) = N_0 \exp(-t/\tau_\mathrm{e}) \tag{3.18}$$

where N_0 is the number of original electrons, for example generated by ionization radiation, and τ_e is the electron lifetime.

The electron lifetime is related to the concentration of different electronegative impurities, n_i, as

$$\tau_\mathrm{e} = (\Sigma k_i n_i)^{-1} \tag{3.19}$$

The factors, k_i, characterize efficiency of electron capture (cross section) by different electronegative molecules. The electron capture is often described in terms of so-called attenuation drift length $L = \nu_\mathrm{d}\tau_\mathrm{d}$, where ν_d is the electron drift velocity. The total impurities concentration is often express in terms of concentration of oxygen or O_2 *equiv*. This value for some *i* of the impurity may be defined as

$$c_{O_2} = k_i n_i / k_{O_2}$$

Generally, the coefficient of the electron capture depends on electron energy or electric field strength $k_i = k_i(E)$. Bakale et al. [128] studied attachment of electrons to molecules of O_2, SF_6, N_2O dependent on the electric field strength in liquid Ar, Kr, Xe, and CH_4 (Fig. 3.16).

It was found that the rate constant for attachment to SF_6 is extremely high: at 10 V cm^{-1} it is well above 10^{14} M^{-1}s^{-1} and it decreases with increasing field strength by almost an order of magnitude. The rate constant for electron attachment to O_2 is a factor of 10^3 smaller and also decreases with increasing field strength in the range of 0.1–10 kV cm^{-1}. The rate constant for electron attachment to N_2O is comparable to the rate constant for attachment to O_2; however, it increases with increasing field strength by more than one order of magnitude. The rate constant for electron attachment to CO_2 in liquid argon

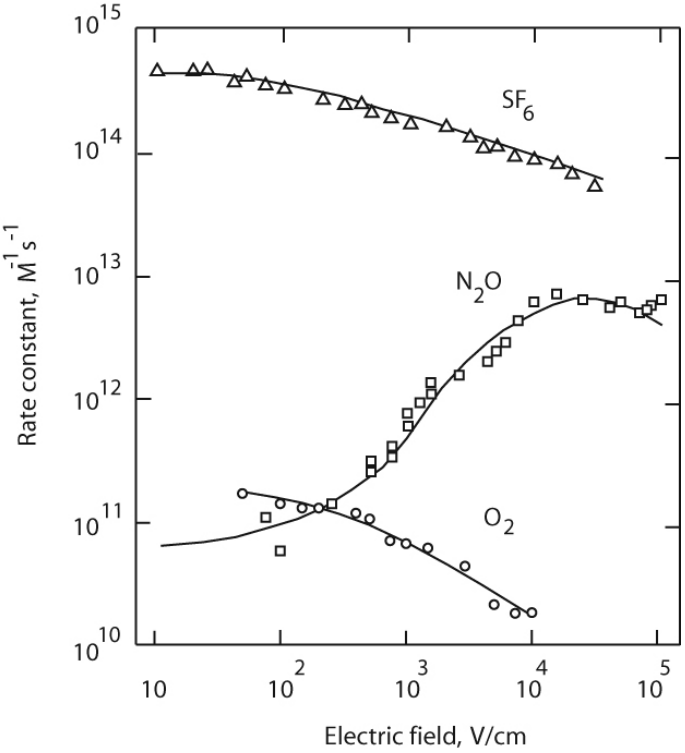

Fig. 3.16 The dependence of the rate constant for the electron attachment to several solutes on the electric field strength in liquid xenon at $T = 165$ K. Redrawn from [128].

also has been reported to be increasing at high electric drift fields [129]. The similar behavior of the attachment rate constant was observed for unidentified residue impurity in liquid krypton [130] and in liquid xenon [131] both purified in gas phase with hot calcium getter. Zaklad [132] suggested that the calcium getter absorbing O_2, N_2, H_2O molecules may play a role of catalyst for production of N_2O, NO, NH_3 impurities. More efficient getters or combination of several types of chemical absorbers help to solve the problem (see Chapter 8).

It was shown [18] that the dependence of the coefficient of the electron capture by oxygen on the electric field strength in the noble liquids may be approximated as

$$k_{O_2} = aE^{-b}$$

where a is measured in (ppm mm)$^{-1}$, and E is measured in kV cm^{-1}. Parameters a and b were defined as fitting parameters of the experimental data and their values for some particularly cases are shown in Table 3.6. Practically, the

concentration of such electronegative impurities as oxygen in large LXe detectors of below 1 ppb is required. Here, a and b depend on the temperature of the liquids and their values for some particular cases are shown in Table 3.6. Practically, the concentration of such electronegative impurities as oxygen in large LXe detectors is required to be below 1 ppb.

Tab. 3.6 Parameters of the dependence of the oxygen electron capture coefficient on the electric field strength [18].

Liquid	T, K	Electric field range, kV cm^{-1}	a, mol^{-1}s^{-1}	b
LAr	87	0.2–4	0.95	0.8
	100		1.1	0.8
LXe	165	0.1–10	0.75	0.7
LCH_4	120	0.18–1.8	1.4	1

A more detailed review of experimental data on electron attachment in condensed noble gases can be found, for example, in a review by Obodovskiy [133] and in monographs [89] and [18].

3.1.3.2 Charge Trapping in Solids

Electron trapping in noble solids has been poorly investigated. Increasing electron drift velocity in the solids against the liquids may lead to increasing drift path. On the other hand, imperfections in solids may play a role of additional structure traps. Investigators indicated that in condensed krypton at a 7 kV cm^{-1} drift field [130] and in condensed xenon in the range of a 1–10 kV cm^{-1} electric field [131] the drift path, controlled by electronegative impurities presented at the level of 10^{-6}–10^{-9} O_2 equivalent, is increasing a few times during transition from the liquid to the solid phase. For very pure argon (2×10^{-10} O_2 eqv.), the opposite effect was observed, but in a low field range of 20–300 V cm^{-1} [134]. As we have mentioned above (Section 3.1.2.2), the drift mobility of excess holes in noble solids is several orders of magnitude smaller than that of electrons. The hopping mechanism of the hole transfer takes place in these media with part-time self-localization of holes in polaron states. It may happen that the count rate of useful events in the detectors is exceeding the collection time of holes and, then, a positive space charge build-up may affect the normal operation of the detector.

Tab. 3.7 Electron affinities of some atoms and molecules and thresholds of dissociative attachment for some molecules [135, 136].

	Electron affinity, eV	Threshold of dissociative attachment ($T = 296$ K), eV
F_2	2.96	~ 0
NO_2	2.43	
SO_2	1.097	
SF_6	0.6	~ 0
O_2	0.44	3.65
N_2O	0.22	0.1
NO	0.024	7.5
NH_3	<0	5.3
H_2O	<0	4.36
H_2	<0	3.75
CO_2	<0	3.99
CO	<0	9.7
N_2	<0	9.7

Tab. 3.8 Constants of three-body attachment of thermalized electrons by oxygen in gases [137].

	He	Ne	Ar	Kr	Xe	N_2	CH_4	H_2	CO_2	H_2O
k_3, 10^{-30} cm^6 s^{-1}	0.033	0.023	0.05	0.05	0.085	0.085	0.34	0.48	3	14

3.2 Electron Multiplication and Electroluminescence

In the absence of an electric field, electrons injected in gas are quickly thermalized. In the presence of an electric field, electrons can gain a sufficient amount of energy from the field between two collisions to cause ionization or excitation of atoms. The secondary electrons can also gain energy for the next ionization. This process can lead to avalanche multiplication of electrons. If drifting electron can ionize atoms per unit length, increasing number of electrons is calculated from $\mathrm{d}N = \alpha N_0 \mathrm{d}x$ to be

$$N(x) = N_0 \exp(\alpha x) \tag{3.20}$$

if α does not depend on N_0, the initial concentration of electrons. The coefficient α is called the first Townsend coefficient. The first Townsend coefficient α depends on the field strength. The reduced coefficient α/p has about one ion pair per cm drift per Torr at reduced electric field strength $E/p = 100$ V cm^{-1} Torr^{-1} for all pure noble gases. The gas gain (amplification factor) of up to

10^6 is possible only in noble gases doped with quenching molecular impurities. Despite many attempts, in pure noble gases, liquids and solids, only poor gas gain of < 100 has been achieved and no detectors of practical importance have been developed with electron multiplication (see review [18] and recent experiments described in [138, 139]).

If energy of drifting electrons slightly below ionization threshold they effectively excite atoms in collisions and generate electroluminescence (or proportional scintillation) in processes similar to the generation of scintillation by high energy particles

$$\begin{aligned} e + A &\longrightarrow e + A^* \\ A^* + 2A &\longrightarrow A_2^* + A \\ A_2^* &\longrightarrow 2A + h\nu \end{aligned} \tag{3.21}$$

Note, that the second equation of the array is valid at gas densities $n > 10^{10}$ cm^{-3}.

The emission spectra of electroluminescence are similar to those of scintillation (see below Section 3.4.1 for details). There are data showing that some part of the photon emission is released in the infrared (IR) range [140]. In dense and heavy noble gases such as xenon, additional mechanism of the electroluminescence generation can occur because of growing concentration of free dimers or clusters or even formation of the conduction band. With increasing pressure and decreasing temperature, the direct excitation of predominant dimers A_2 becomes likely according to the following processes:

$$\begin{aligned} e + A_2 &\longrightarrow A_2^* + e \\ A^* + A_2 &\longrightarrow A_2^* + A \\ A_2^* &\longrightarrow 2A + h\nu \end{aligned} \tag{3.22}$$

That increases electroluminescence light output at the cost of increased photon attenuation due to the resonance absorption by dimers. The last effect was observed in xenon at densities $> 10^{21}$ cm^3 [141, 142]. If the energy of electrons has achieved the ionization threshold, an additional recombination channel is opened to increase the electroluminescence light output

$$\begin{aligned} e + A &\longrightarrow A^+ + 2e \\ A^+ + 2A &\longrightarrow A_2^+ + A \\ A_2^+ + e &\longrightarrow A_2^* \\ A_2^* &\longrightarrow 2A + h\nu \end{aligned} \tag{3.23}$$

However, electron multiplication introduces significant fluctuations in the process and degrades the energy resolution of electroluminescence detectors.

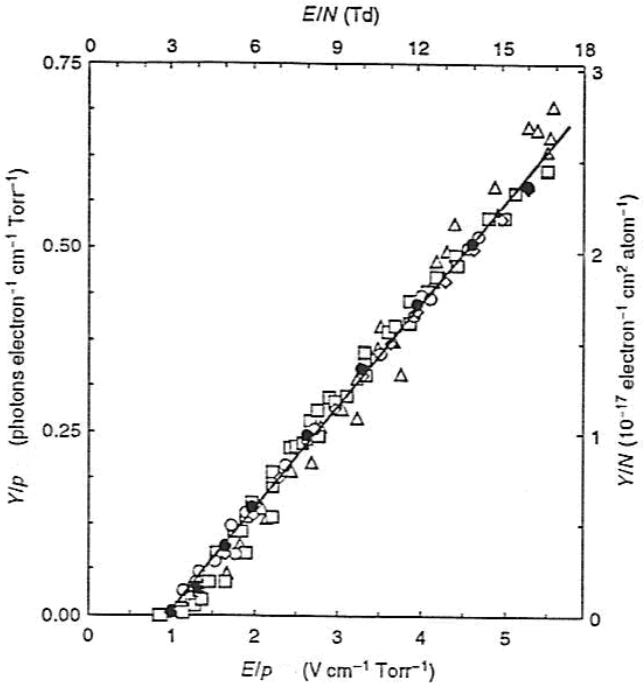

Fig. 3.17 Reduced light output of electroluminescence of xenon gas at 293 K temperature and normal pressure as a function of the reduced electric field strength (compilation of experimental and computer simulation data by Conde [143]).

The electroluminescence is a threshold process (Figs. 3.17 and 3.18). The value of the threshold is about the same ($\sim 3\times10^{-17}$ V cm^2) in xenon and krypton gas. The emission of photons observed below the threshold (Fig. 3.18) is predominantly bremsstrahlung.

In a uniform electric field, the number of photons generated by one drifting electron N_{ph}, is proportional to the drift path x [cm] and for xenon gas at room temperature may be defined via the reduced electric field strength E/p [kV cm^{-1} bar^{-1}] and the gas pressure p [bar] using the empirical equation [144] as

$$\mathrm{d}N_{ph}/\mathrm{d}x = 70(E/p - 1.0)p \qquad (\text{UV photons/e cm drift}) \tag{3.24}$$

The intensity of electroluminescence (EL) up to 1700 photons/cm in xenon at 0.5 MPa pressure has been demonstrated [144]. Taking into account that the energy of a single photon of 172 nm wavelength is about 8.4 eV, one can calculate the efficiency of conversion of the energy of the electric field into the photon emission: $\xi = (1700\times8.4)/(3400\times5) = 84\%$. The rest of the energy ac-

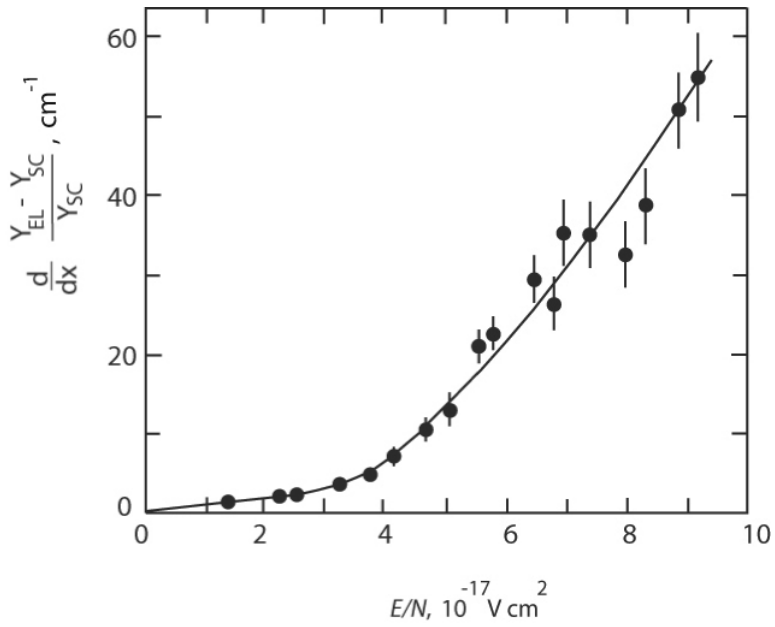

Fig. 3.18 Reduced light output of electroluminescence of krypton gas relatively light output of scintillation at 290 K temperature and 0.108 MPa pressure as a function of the reduced electric field strength. Redrawn from [18].

quired by drifting electrons from the electric field is probably converted into IR radiation. Taking into account that at extremely high electric fields in pure Xe the charge multiplication factor can be about 10, we may estimate the conversion efficiency of the EL process to be $\sim$ 8%.

Electroluminescence has been observed in all noble gases and noble gas mixtures. In mixtures containing >0.1% Xe, the light output and spectrum of EL is very similar to that one in pure xenon. Note, that EL has been observed in different aggregate states of noble gases but it is practically used only in gas. The process of EL is linear, in contrast to the avalanche-like charge (electron) multiplication. That is because the energy of drifting electrons is mostly dissipated via the emission of photons, which do not participate further in the process. Due to this circumstance, EL can provide lower fluctuations and better energy resolution than the gas gain amplification process. More details about practical applications of electroluminescence can be found in Chapter 6.

3.3
Charge Carrier Transfer at Interfaces

Since the dielectric constant of condensed phases of noble gases is different from that of the saturated vapor, charge carriers experience an image potential A near the interface acting against their transition into the less dense phase

$$A_{1,2} = -e(\varepsilon_1 - \varepsilon_2)/4\varepsilon_{1,2}(z + \beta z/|z|)(\varepsilon_1 + \varepsilon_2) \tag{3.25}$$

where $\varepsilon_1 E_1 = \varepsilon_2 E_2$ is the dielectric constant and indices 1 and 2 are related to the condensed phase and the equilibrium gas phase, respectively; z is a Cartesian coordinate perpendicular to the interface, β is the cutting parameter of about thickness of the interphase transition layer. The image potential is temperature-dependent approaching zero at temperatures close to the critical temperature. At favorable conditions as described in this section, some charge carriers can be extracted from condensed phases of noble gases through the free interface surface and collected in the equilibrium gas phase.

3.3.1
Quasifree Electron Emission

At the electric field E, applied to extract electrons from the condensed dielectric, and the energy of the ground state of quasifree electrons V_0, the total potential energy of electrons in the vicinity of the interphase surface may be described in terms of a one-dimensional potential (Fig. 3.19)

$$\begin{aligned} V_1(z) &= V_0 - eE_1 z + eA_1, \quad z < 0 \\ V_2(z) &= -eE_2 z + eA_2, \qquad z > 0 \end{aligned} \tag{3.26}$$

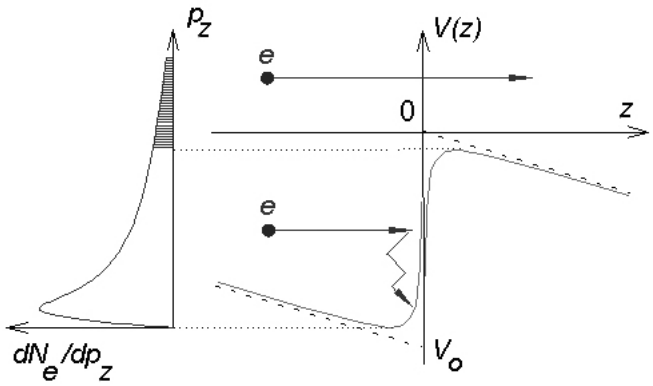

Fig. 3.19 Emission of hot quasifree electrons from condensed ($Z < 0$) into rarefied ($Z > 0$) noble gas.

In terms of this one-dimensional consideration, an electron approaching the interface can penetrate the interface if its momentum projection along the z-direction p_z is higher than $p_0 \approx (2m_e \mid V_0 \mid)^{1/2}$. If $p_z < p_0$, it is reflected by the potential barrier back to the condensed phase and may be thermalized after several collisions. Trapped under the surface electrons stay in thermodynamic equilibrium with the condensed dielectric and can be emitted as thermal electrons. For an average extraction time t_e much greater than the relaxation time of the electron momentum distribution function $f(\mathbf{p})$, the thermal electron emission can be considered as a stationary process and the number of electrons under the surface is described as

$$N(t) = N_0 \exp(-t/t_e) \tag{3.27}$$

If the lifetime of quasifree electrons is limited by t_c

$$N(t) = N_0 \exp(-t/t_e - t/t_c) \tag{3.28}$$

The total number of emitted electrons within a time t is then obtained by integrating the emission rate $dN(t)/dt$

$$N_e(t) = N_0 t_c (t_e + t_c)^{-1} 1 - \exp[-(t_e + t_c)t/t_e t_c] \tag{3.29}$$

Then, the probability (coefficient) of emission is given as

$$K = N_e(\infty)/N_0 = (1 + t_e/t_c)^{-1} \tag{3.30}$$

The total number of all emitted thermal electrons is controlled by the lifetime of excess electrons before their attachment to electronegative impurities or capture into other deep traps.

Effective emission of quasifree electrons has been observed from condensed noble gases, methane and some other liquid saturated hydrocarbons (Table 3.9). In general, the emission looks like a threshold process with strong correlation between the observed threshold electric field E_0 and the energy of the ground state of excess electrons V_0 as shown in Fig. 3.20.

3.3.1.1 Thermal Electron Emission

In liquid argon and liquid saturated hydrocarbons such as isooctane and n-hexane, the height of the interface potential barrier is comparable with a kinetic energy of quasifree electrons, which are in thermodynamic equilibrium with the medium (Table 3.9). Electrons from the high-momentum tail ($p_z > p_0$) of the momentum distribution (Fig. 3.19) have sufficient energy for emission. In this case of thermoactivated electron emission from saturated hydrocarbons, it was found that the emission time t_e depends on the applied electric field approximately as $\sim 1/E$ ranging about 10^{-3}–10^{-6} s at

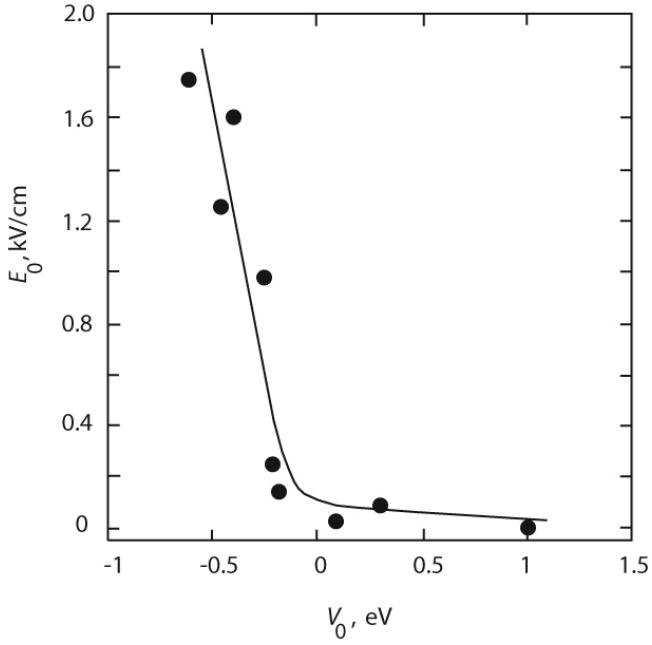

Fig. 3.20 Correlation between observed threshold of emission and ground state energy of excess electrons in liquid and solid nonpolar dielectrics; the curve is shown for a better reading of the data. Redrawn from [38].

0.1–1 kV cm^{-1} [145, 146]. For noble liquids, the trapping time of quasifree electrons under the surface may be calculated as

$$t_e \sim (\Lambda/\nu_d) \exp\left[V_0 - 2eA_1^{1/2}(1 + A_2^{1/2}/A_1^{1/2})E^{1/2}\right] \tag{3.31}$$

where Λ and ν_d are the electron momentum free path and the drift velocity, respectively [147]. In general, emission of quasifree electrons from heavy noble liquids and solids is a combination of thermal and hot electron emission. That explains the observation of *fast* and *slow* components in electron emission from liquid argon (Fig. 3.21).

3.3.1.2 **Hot Electron Emission**

In condensed Kr and Xe, the potential barrier is so high ($|V_0| \gg kT$) that at temporarily achievable levels of purification the lifetime is much shorter than the emission time and the thermoactivated electron emission from these liquids and solids has not been observed. On the other hand, in these media it is easy to achieve the electric field strength E_c in which drifting electrons have average kinetic energy exceeding the temperature of the media. Then, hot electrons with momentum $p_z > p_0$ escape the condensed phase without delay.

Tab. 3.9 Electronic properties of liquid and solid (s) nonpolar dielectrics used in emission detectors [163].

	T, K	μ_0, $cm^2\,V^{-1}\,s^{-1}$	V_0, eV	E_c, $kV\,cm^{-1}$	E_0, $kV\,cm^{-1}$	t_e
Emitters of cold electrons						
^4He	1–2	0.03	+1			10 s (100 $V\,cm^{-1}$)
$n-H$	300	0.09	+0.09	100	0.03	
$iso-O$	300	7	-0.18	90	0.15	20 μs (1 $kV\,cm^{-1}$)
TMP	297	24	-0.3	50		
Ar	84	475	-0.21	0.2		700 μs (100 $V\,cm^{-1}$)
sNe	24	600	+1.1			
Emitters of hot electrons						
CH_4	100	400	-0.18	1.5	<4	
sCH_4	77	∼ 1000	0		<1.5	<0.1 μs (>1 $kV\,cm^{-1}$)
Ar	84	475	-0.21	0.2	0.25	<0.1 μs (>0.3 $kV\,cm^{-1}$)
sAr	83	1000	+0.3 (6 K)		0.1	<0.1 μs (>100 $V\,cm^{-1}$)
Kr	116	1800	-0.4	0.08	1.6	<0.1 μs (>1.6 $kV\,cm^{-1}$)
sKr	116	3700	-0.25 (20 K)		0.98	<0.1 μs (>1 $kV\,cm^{-1}$)
Xe	161	2200	-0.61	0.05	1.75	<0.1 μs (>1.8 $kV\,cm^{-1}$)
sXe	161	4500	-0.46 (40 K)		1.25	<0.1 μs (>1.3 $kV\,cm^{-1}$)

Notes: n-H - normal hexane, *iso* - isooctane, TMP - tetramethylepentane.

Effective and fast electron emission from these media has been observed at $E > E_c$ (Fig. 3.21). Note that electrons that are not emitted cannot continue their drift and, thus, cannot be heated by the applied electric field; then, they are quickly (∼ 1 ps) thermalized.

An experimental confirmation of the described model is presented in Ref. [149]. Quasifree electron emission from liquid krypton has been analyzed from the point of view of following the basic law describing the emission current from hot cathodes. According to the Richardson–Dushman equation, the emitted electron current density J (A m^{-2}) is related to temperature, T, and the work function, W, as

$$J = AT^2 e^{-w/kT} \tag{3.32}$$

where A is the Richardson constant. Since quasifree electrons in condensed krypton can be heated by the electric field, Eq. (3.32) can be modified for the

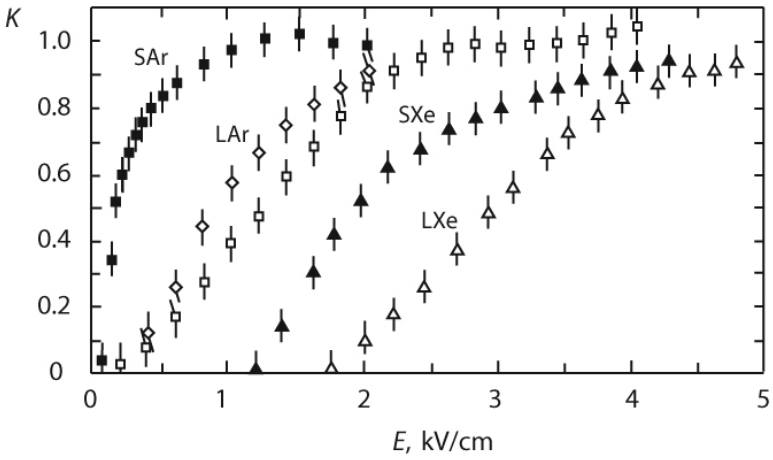

Fig. 3.21 Coefficients of quasifree electron emission from solid argon (SAr, $T = 80$ K), liquid argon (LAr, $T = 90$ K), closed circles is the fast component, open circles is the slow component, solid xenon (SXe, $T = 160$ K), and liquid xenon (LXe, $T = 165$ K) dependent on the electric field in the condensed phases. Redrawn from [148].

coefficient emission as the following:

$$K = I_e/I_i = < E_e >^2 \exp[-w/(2/3) < E_e >] \tag{3.33}$$

where I_e and I_i are the electron emission current and electron ionization current, respectively, and $< E_e >$ is the average electron energy dependent on the applied electric field. Using the measured $I_e(E)$ and $I_i(E)$ and calculated $E_e(E)$ dependent on the electric field E applied to the liquid krypton, the graph of $\ln(K/< E_e >^2)$ versus $< E_e >^{-1}$ has been built as shown in Fig. 3.22.

The slope of the linear part of this curve allows to define the work function of krypton to be $w = 0.39 \pm 0.07$ eV, which matches very well the value of $V_0 = -0.4$ eV measured in other experiments (Table 3.9). The nonlinear part of the curve is a result of saturation of the ionization yield from tracks of X-ray photoelectrons used in this study.

3.3.1.3 **Transition of Quasifree Electrons Along Interface**

Trapped under the interface surface quasifree electrons may be again heated by the electric field applied along the surface of the condensed phase. In [150], it was shown that such conditions may be realized if the interface surface of vapor–liquid krypton is not coplanar to the electrodes of the parallel plate ionization chamber and the electric field pressing electrons to the interface $E < E_0$.

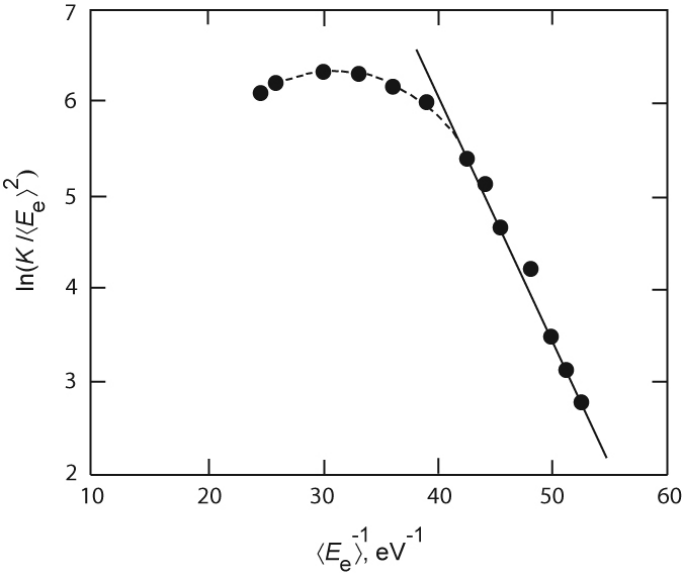

Fig. 3.22 Coefficient of electron emission from liquid krypton at 120 K in dependence on the average electron energy; electrons are generated with a pulsed X-ray tube. Redrawn from [149].

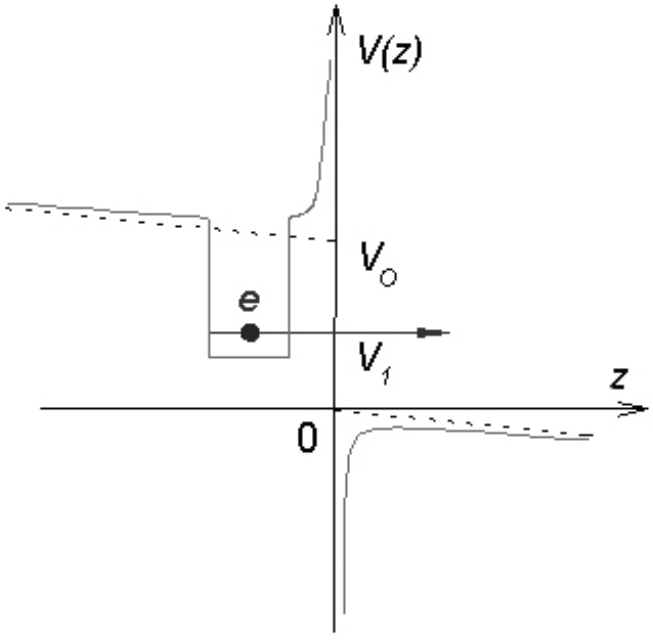

Fig. 3.23 Emission of electrons from the localized state.

3.3.2 Electron Emission From Localized States

In dielectrics with relatively small atoms and $V_0 > 0$ (liquid helium, hydrogen, and neon), excess electrons exist in low-mobile, auto-localized states: bubbles. The potential well of localized electrons should be superimposed on the potential $V(z)$ (Eq. (3.26)), as shown in Fig. 3.23. The emission of electrons from bubbles in liquid helium and neon was observed in several experiments [151–154]. The mechanism of electron emission from the localized states is a combination of thermal emission and quantum effects. The superpositioned electrical potential, suppressing the electron to the free surface in the condensed medium, and the image potential, attracting the electron inside the dense dielectric, provide a shallow minimum located several tens of nanometers under the surface, depending on the value of E. When the electron, due to its thermal motion comes sufficiently close to the surface (less than 23 nm according to Anciolotto and Toigo [155]), the potential barrier between the bubble and the surface is essentially deviated and the electron can easy tunnel from the localized state into the gas phase. The process is thermoactivated: below the λ point, the measured current of emitted electrons decreases rapidly with decreasing temperature as $\exp(-\Phi/kT)$ where the effective barrier Φ/k ranging from 30 K to 40 K depending on the electric field. At 1 to 2-K temperature liquid ^{4}He and ^{3}He, the characteristic time of the barrier penetration (emission time) is 10–100 s at 100–10 V cm^{-1} suppressing the electric field [153]. At lower temperatures, the probability of electron tunneling is very low but at fields of > 100 V cm^{-1} the electronic bubble drifting in the superfluid helium forms a vortex, which drags electrons through the surface without delay or overcoming any noticeable barrier [152, 156]. This kind of emission may be generated by mechanical rotation of a cryostat filled with superfluid helium in such a way that generates quantized vortex lines perpendicular to the free liquid surface [157].

Figure 3.24 shows a schematic drawing of the test cell and a dependence of the current measured at a collector C versus the temperature at different rotation frequencies ω. Ionization electrons generated by a radioactive source S are drifting between a grid G and an anode A in a direction, which is parallel to the free liquid surface and perpendicular to vortex lines generated, when the cryostat is rotating. The emission current $J_{\text{not imm}}$ was detected with a collector C placed above the liquid surface and, with accuracy of about 1%, it was identical to the current J_{imm} measured with the collector immersed in the liquid. Without rotation no current ($<10^{-14}$ A) at C was detectable.

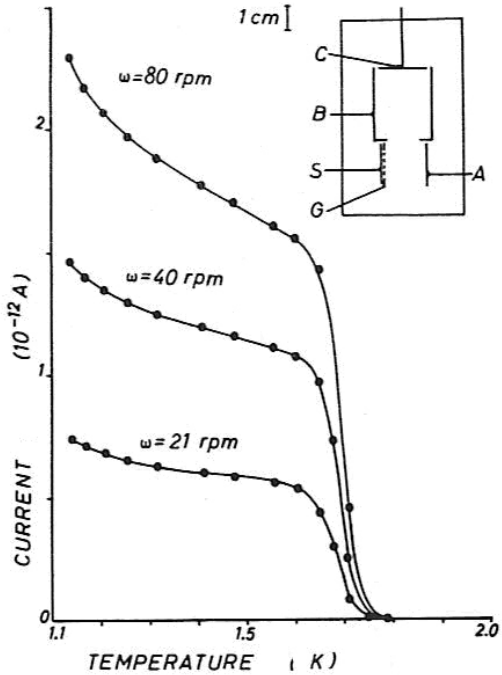

Fig. 3.24 Temperature dependence of current of electrons, captured by vortex cores at different frequencies of rotation ω, and measured at collector C test cell as shown at insert [157].

3.3.3
Transitions Between Different Media

Transitions of excess electrons between different materials can be beneficial for detector technology as well as transitions between different phases of the same dielectric.

Charge Carrier Penetrating Liquid–Liquid Interface of ^{3}He-^{4}He Mixture

Charge carriers can be trapped at the liquid–liquid interface of the two coexisting phases of ^{3}He-^{4}He mixture: a superfluid ^{4}He-rich phase floating on top of a normal ^{3}He-rich phase [158]. There is a potential barrier at the interface associated with a lower surface tension of the ^{3}He-rich phase. The effective value of the barrier was found to be $\Phi/k \approx 220$ K at temperatures below 0.3 K. However, on approaching to the tricritical point $T_t = 0.867$ K the barrier becomes comparable to kT and the bubbles are able to penetrate the barrier by thermal activation. The trapping time in seconds range has been measured in 10^{-2}–10^{-3} K range of T–T_t and electrical holding fields ~ 100 V cm^{-1} [159]. More details on properties of the liquid–liquid interface of ^{3}He-^{4}He mixture are reviewed in Ref. [114].

Electron Transition from Condensed Noble Gases Into Superconductive Metals

Transitions of excess electrons between different materials can be as advantageous for detector development as transitions between different phases of the same dielectric [160]. Let us suppose that a single free electron, or a single electron in the conduction band, is created as a result of scattering of an incident particle off a Xe nucleus (Fig. 3.25).

The threshold energy for this process is about the band gap $\sim E_g$. An electric field is applied to collect electrons from the bulk solid xenon (SXe) to a quasiparticle transition edge sensor (TES), consisting of a superconductive aluminum-fin connected to a superconductive tungsten quasiparticle trap. The ground state of electrons in the conduction band of SXe is about $V_0 = -0.45$ eV relative to the vacuum level. The Fermi level of Al is $E_F = -4.54$ eV. So, the electron falling down into the Al anode deposits $V_0 + E_F \approx 4$ eV energy. The deposited energy may destroy several Cooper pairs (0.36 meV bonding energy) and generate a bunch of quasiparticles (QP in Fig. 3.25). The quasiparticles diffuse into the superconductive tungsten (transition temperature <100 mK) QP trap and, breaking Cooper pairs there, deposit a heat pulse measured with SQUID in the scheme for example described in Ref. [161].

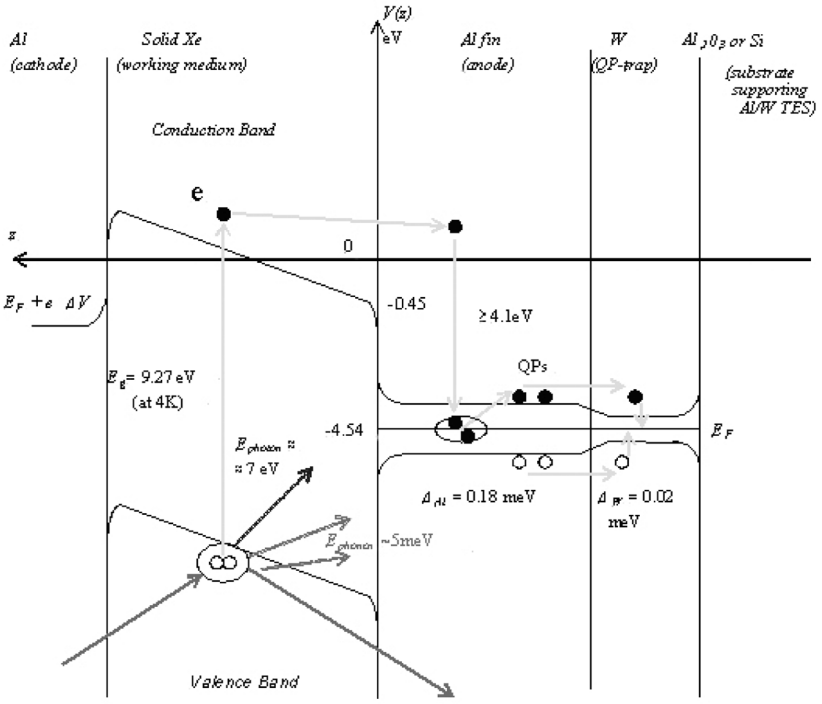

Fig. 3.25 Concept of operation of Cryogenic Solid Xenon Detector with Transition Edge Sensors [149].

At the moment of interaction, prompt phonons and excitons will be generated. Prompt phonons and scintillation photons (emitted by decaying excitons) can be measured with the TES as well as electrons. Then, a few signals from a single act of particle interaction in SXe can be measured. Comparison of different signals could be used to distinguish useful events from the background. Drifting electrons could be *heated* by the applied electric field in order to amplify the ionization signal and generate additional phonons by the Neganov–Trofimov–Luke effect, which is similar to the electroluminescence in noble gases (see, for example, Ref. [162]). Note, that other solid noble gases can be used in this detection scheme providing even larger potential drops across the solid gas-aluminum boundary (for example, $V_0(SNe) - E_F(Al) = 5.6$ eV). However, solid xenon is the most attractive because of its inherent high density, low E_g, and low excitation energies. Unfortunately, properties of solid heavy noble gases at cryogenic temperatures are poorly explored. In particular, there is no available data on propagation of phonons through the bulk crystals and through the boundary with TES. This subject may concern the next generation of researchers.

3.3.4
Ion Emission from Nonpolar Dielectrics

It was shown that in the presence of high enough extraction electric fields, ions can be extracted from liquid nonpolar dielectrics due to gravitational instability of the charged liquid surface [154,164]. A simple model assuming that microwaves of the liquid surface cause hemispherical shaped protrusions, which under the influences of an ion-extracting electric field acting against the gravitational force and the surface tension may develop into a droplet, allowing for the definition [164] of a critical field of the extraction

$$E_0 = (32\pi)^{1/2}(\Delta\rho\sigma g/3)^{1/4} \tag{3.34}$$

and a droplet radius $r_0 = (3\sigma/\Delta\rho g)^{1/2}$, where $\Delta\rho$ is the difference between densities of the condensed phase and of the equilibrium gas phase, σ is the surface tension, and g is the acceleration of gravity. Extraction of positive ions from dielectric liquids due to microgravity nonstability of the charged interphase surface may be described in the following consequence of events: a drifting ion approaches the liquid surface; the ion is captured inside a microwave; extracting electrical force deforms the surface; a droplet containing the ion separates from the surface and begins to evaporate; extracted ion departs from the liquid surface. Available experimental data and calculations of the critical electric field for some popular nonpolar dielectrics are presented in Table 3.10.

Tab. 3.10 Critical electric field of ion extraction from some nonpolar liquids.

	T, K	σ, erg cm^{-2}	ρ, g cm^{-3}	E_0, kV cm^{-1}	Ref.
CH_4	91	17	0.44	21.1	*calc*
N_2	77	8.3	0.808	19	[164]
He	3.2–5.1	0.007–0.2	0.14–0.1	1–4	[164]
Ne	25	5.54	1.2	20.5	*calc*
Ar	83.81	13.45	1.40	26.6	*calc*
Kr	115.78	16.1	2.451	32.0	*calc*
Xe	161.36	19.3	3.1	35.5	*calc*

3.3.5 Electron Emission into Nonpolar Dielectrics

Generation of electrons in condensed phases by ionizing radiation has certain disadvantages for some particular applications. First, positive carriers are unavoidably generated as well. Second, it is difficult to generate a large density of the electron current in this way. There are at least two methods that allow overcoming these disadvantages.

3.3.5.1 Electron Emission From Cathodes

Normally, this method is used for research and measurements of V_0 values in condensed gases and liquid saturated hydrocarbons. For example, Halpern and Gomer [165] used autoelectron emission from tungsten tips to inject 10^{-10}–10^{-6} A electron currents in H_2, D_2, He, Ne, Ar , N_2, O_2, and C_6H_6 liquids. The current was limited with space charge at $>10^{-9}$ A and only in liquid H_2, D_2 can they build Fowler–Nordheim plots in order to define the work function. The photoemission efficiency in dense media is quite low ($<10^{-4}$) because of backscatter of electrons and that intensive light sources need to be used in order to generate good signals. In dielectrics with $V_0 < 0$, a barrier to overcome by photoelectrons ($w + V_0$) is essentially reduced and the photoemission from photocathodes used in most experiments on determination of V_0 presented in Table 3.4.

3.3.5.2 Electron Injection Through the Free Interface

This method is most convenient for dielectrics with $V_0 < 0$. At this case, electrons can easy penetrate the narrow barrier of the imaging potential and drop into the potential well. The method allows injecting high-density electron currents generated in the gas phase, for example, with thermocathodes [166]. In the past, the similar technique was used for generation of ion currents in dielectric liquids for measurement of their mobilities [121]. In the case of $V_0 > 0$, electrons cannot easily penetrate the potential barrier and they localize on the

interface. However, the electric field strength overcomes the critical value

$$E_{\text{crit}} = [16\pi^2\sigma(\rho_1 - \rho_2)g]^{1/4} \tag{3.35}$$

where σ is the surface tension, ρ_1 and ρ_2 are the densities of the liquid and gas phases, respectively, and g is the acceleration due to gravity. Stability of the surface may be lost at $E > E_{\text{crit}}$ and the electrons drop down in the liquid [167]. Practically, the condition in Eq. (3.35) may be realized with light liquids when the difference $\rho_1 - \rho_2$ is small. This was used for injection of electrons in liquid He, Ne, and H_2 [168].

3.4 Properties of Noble Gas Scintillators

3.4.1 Primary Processes

The energy of ionization radiation absorbed in a noble gas is divided into three branches: energy of ionization, the energy of atomic excitation, and kinetic energy given to electrons with energy lower than the excitation threshold. The average energy required to produce an electron–ion pair in the detector medium W is a measure of the ionization efficiency of the material, and can be defined as

$$W = K_{\text{i}} I_{\text{i}} + < I_{\text{ex}} >< N_{\text{ex}} > / < N_{\text{i}} > + < \Im > \tag{3.36}$$

where I_{i} is the ionization potential, $<I_{\text{ex}}>$ is the average energy of atom excitation, $<N_{\text{ex}}>$ is the average number of excited atoms, $<N_{\text{i}}>$ is the average number of electron–ion pairs, K_{i} is factor taking into account multiple acts of ionization, and $<\Im>$ is the average kinetic energy of subexcitation electrons. Parameters of Eq. (3.36) for noble gases could be found by Platzman [22] and for the liquid state in Doke et al. [39] and Aprile et al. [48]. The experimental values of W and the ionization potentials for major noble gases in different phases are presented in Chapter 2. For gaseous xenon, the W value is practically constant at densities below 0.2 g cm^{-3} and gradually decreases by $\sim 15\%$ when the density approaches 1.7 g cm^{-3}. This is an effect of formation and evolution of the electronic bands in dense xenon [33].

Passing though the noble gas, the ionization radiation R generates electrons, ions A^+, and excited atoms A^* as follows:

$$R + A \longrightarrow e + A^+ + R'; \quad R + A \longrightarrow A^* + R'; \quad e + A^+ \longrightarrow A^* \tag{3.37}$$

In dense noble gases ($n > 10^{19}$ cm^{-3}), it takes 10^{-11}–10^{-12} s to produce excited molecules in the reaction of $A^* + 2A \longrightarrow A_2^* + A$.

Photons emitted through the radiative decay of excited atoms are effectively scattered and absorbed in dense media, so this light is not typically detected, making them unusable in detectors. But dense noble gases and their liquid and solid phases are transparent for photons emitted through the radiative decay of excited molecules or excitons. Such photons from a so-called molecular continuum of noble gas scintillation spectra can be used for detection purposes.

Note, that the description of the processes leading to emission of light in a molecular continuum is rather primitive and is based on a simplified few-body model. In condensed phases, such as liquid helium, more complicated entities are involved such as He_3^+ self-trapped in a snowball of about 30 He atoms and the He_2 excimers existing in stable cavities [169]. In any case, the final states include excited molecules or self-trapped excitons, which are responsible for the formation of a molecular continuum in the emission spectra of dense noble gases. A structure of the formations is responsible for the observed moderate spectral shifts and broadening of transitions within excimer manifolds.

3.4.2 Emission Spectra

Emission spectra of noble gases are formed in result of deexcitation and ion recombination processes. There are several excitation levels and transitions involved [170]:

1. *Optical levels.* The excited atom returns to the ground state by successive transitions to lower excitation levels, with the emission of photons of corresponding energies, thus yielding an atomic line spectrum. The lifetime of the optical levels is typically 10^{-7}-10^{-8} s.

2. *Resonance levels.* The atom returns directly to the ground state without passing through intermediate excited states, with lifetime $< 10^{-9}$ s. In the case of noble gases, the resonance radiation occurs in the far ultraviolet range. The resonance radiation may be reabsorbed and reemitted by many atoms in dense noble gases. This effect known as the trapping of resonance radiation or diffusion of the light. The total lifetime of propagation of this light depends on the density and geometry of the scintillator.

3. *Metastable levels.* In a metastable level the transition is forbidden by quantum mechanical selection rules. The lifetime is only limited by collisions with neutral or excited atoms or ions, which may lead to the formation of excited dimmers or molecular ions in gases or excimers and polarons in condensed phases. In gases the lifetime depends strongly on

the temperature and pressure of the gas. For example, in room temperature argon gas, the lifetime of metastable states varies from $\sim$ 20 s at 10^{-2} Pa to $\sim$ 5 ms at 100 Pa and $\sim$ 200 ns at 10^5 Pa.

4. *Excited atomic ions*. Corresponding levels and transitions may occur in any excited atomic ions produced in the gas.

5. *Excited dimers and molecular ions.* Such species are formed by double and triple collisions with metastable excited atoms in dense noble gases. Since the dimer in gaseous phase or exciton in condensed phase cannot exist in the ground state, the photon emission accompanying its dissociation yields a spectral continuum, which has the most practical use in dense noble scintillators. Excited dimers can also be metastable states, for example all triplet excimers.

6. *Impurity emission.* Any impurity molecules present may quench the emission of hard UV light, and their own emission may be stimulated by transfer of excitation energy. This is of practical importance in the xenon, which is used as a wavelength-shifter the emission from helium or argon, which excitation energies are higher than the minimum xenon excitation level. At relative concentration of 10^{-5}, nitrogen is adequate for efficient energy transfer from all the noble gases at atmospheric pressure. At relative concentration of 10^{-3}, Xe can be used as a wavelength shifter, for example in ^{3}He scintillator at 3.5 MPa pressure [171]. Sometimes, impurities have nonradiative transitions or emit in regions where the sensitivity of photodetectors is limited. This effect may dramatically reduce the observed light yield of noble gas scintillators.

Figure 3.26 shows an example of the kinetic scheme of excitation of xenon considered by Salamero et al. [172]. There are three characteristic emissions of xenon at 129, 147 and 173 nm. The emission at 129 nm is associated with formation of an upper atomic state responsible for the formation of radiative molecular states by three-body collisions. This line is resonance absorbing and does not play an important role in photon emission from the dense xenon. The relaxation of the molecular state $^3P_2$ is responsible for the second molecular continuum, playing the leading role in photon emission from condensed xenon. The radiative decay of the atomic 6p[1/2] state is responsible for infrared emission recently observed in scintillations of liquid argon and xenon [140, 173] and scintillation of gaseous xenon at near atmospheric pressure [174]. To summarize, the scintillation emission spectrum of a noble gas is a complex system of lines, bands and continua, originating from many excited states and from various collision and transfer processes. The spectrum extends from the infrared into the far ultraviolet. In general, a tendency

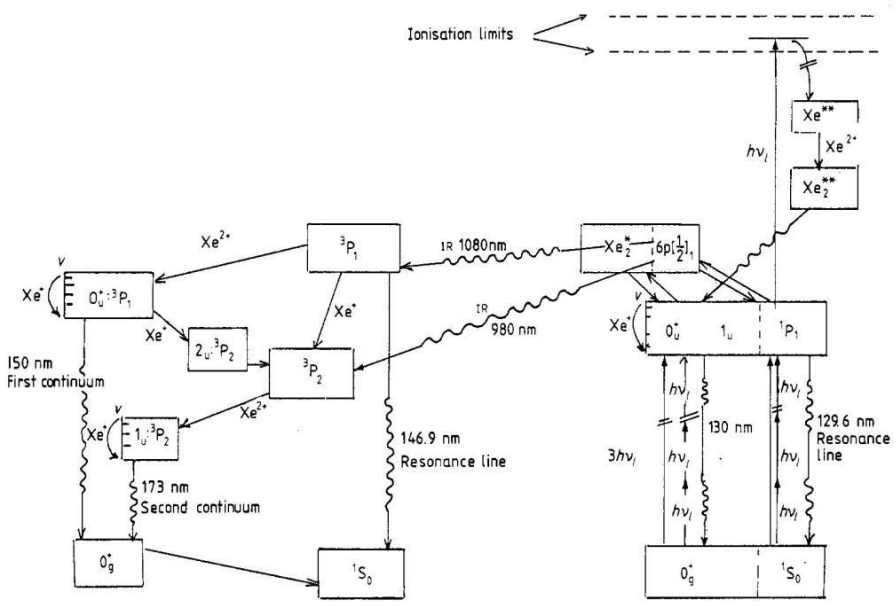

Fig. 3.26 Kinetic scheme of excitation of Xe considered by Salamero et al. [172].

is that the spectrum shifts towards longer wavelengths as the atomic number is increased. From a practical point of view, xenon is the most favorable scintillation material for relatively compact detectors and it is often used as a wavelength shifting admixture into lighter noble gases. For very massive detectors, liquid argon should be considered as less expensive and the most available scintillation material.

3.4.2.1 Emission Spectra of Gases

The emission spectrum of neon gas at different temperatures and pressures are described by Packard et al. [175]. At low densities ($p < 5$ kPa, $T = 55$ K) the spectrum consists of a single atomic line near 74.3 nm. At higher densities ($p > 10$ kPa) this line broadens to longer wavelengths and a second broader peak appears near 80 nm. As the pressure is increased, the second peak grows in intensity while the intensity of the atomic line decreases. At lower temperatures (near 25 K) and comparable densities the narrow line near 74.3 nm persists, but the peak at 80 nm does not appear. At room temperature and a pressure of more than 60 Torr, the principal continuum maximum is located at 822 nm while the continuum spreads between 74 and 100 nm [176].

Emission spectra of low-density He, Ar, Kr, and Xe are well-known (see, for example, Ref. [174]). An important tendency of scintillation spectra of gas

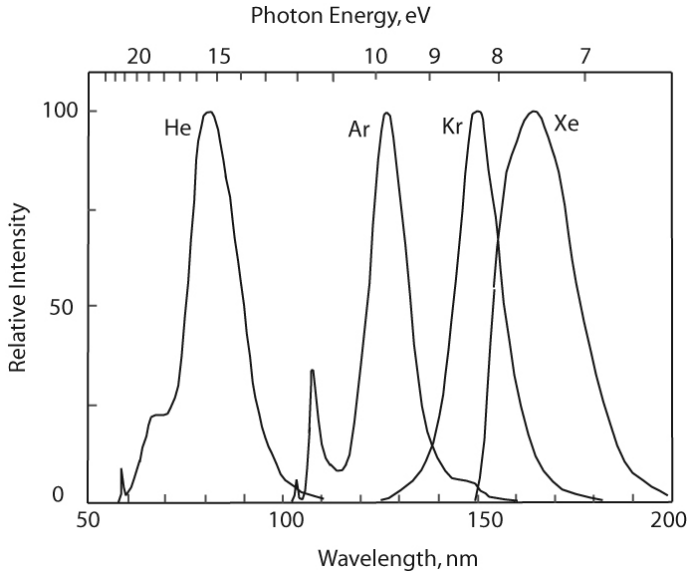

Fig. 3.27 Noble gas continua of helium, argon, krypton, and xenon normalized to the same intensity of the maximum. Redrawn from [176].

phases is that in noble gases with densities of $> 10^{19}$ cm^{-3} the resonance levels and metastable states are not practical to observe and most of the emission spectra is associated with the molecular continua. At elevated densities approaching those of condensed phases, only red shifted continua remain observable, as shown in Fig. 3.27. Weak atomic lines can be seen on the left from the He and Ar continua.

Time-integrated emission spectra of Xe and Ar at 34 bar pressure shown in Fig. 3.28 contain only the continua associated with transitions from the $^3P_2$ state (Fig. 3.26). The Xe emission peaks at 170.9 nm; in addition to the UV continuum, very weak emissions at 310 nm and 540 nm are also observed; the emission of Ar peaks at 126.5 nm. Absorption peaks superimposed onto the emission spectra are associated with contamination of the gases with hydrocarbons from the vacuum system: for example, the absorption line at 165.7 nm is attributed to carbon, other attributed to H, C, N, and O. The width (FWHM) of the molecular continuum depends on pressure, changing from $\sim$ 15 nm at 0.1 MPa Xe pressure to 12 nm at 3.5 MPa Xe pressure and from 12 nm at 0.1 MPa bar Ar pressure to 8.5 nm at 6.5 MPa Ar pressure [177].

3.4.2.2 **Emission Spectra of Liquids and Solids**

Vacuum-ultraviolet luminescence from condensed phases of noble gases have been studied with UV light, X-rays, and ionizing charged particle excitations. In all of these investigations, scintillation was observed with spectra very similar to those observed in dense gases.

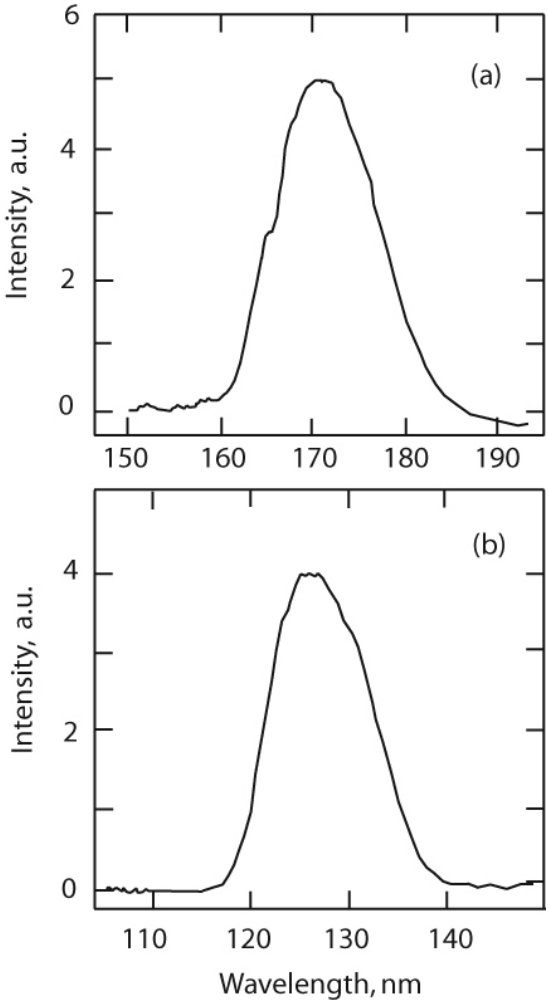

Fig. 3.28 Emission spectra of Xe (a) and Ar (b) gas at 34 bar pressure and excited with relativistic electrons. Redrawn from [177], the absorption lines of impurities are omitted.

For example, Fig. 3.29 presents emission spectra of liquid helium in normal and superfluid states measured by Stockton et al. [178]. In this plot the dotted curve represents the shorter wavelength atomic bands, which are absorbed within the first few millimeters of the ground state liquid. At these very low wavelengths the light is usually referred to as *extreme ultraviolet* or EUV. For the first time, a strong absorption of the EUV below 60 nm was reported in 1970 [179]. It was shown that the liquid is transparent at wavelengths greater than about 60.5 nm but it is absorbing in the range up to 82.5 nm at presence of 0.2–0.6% N_2 impurities.

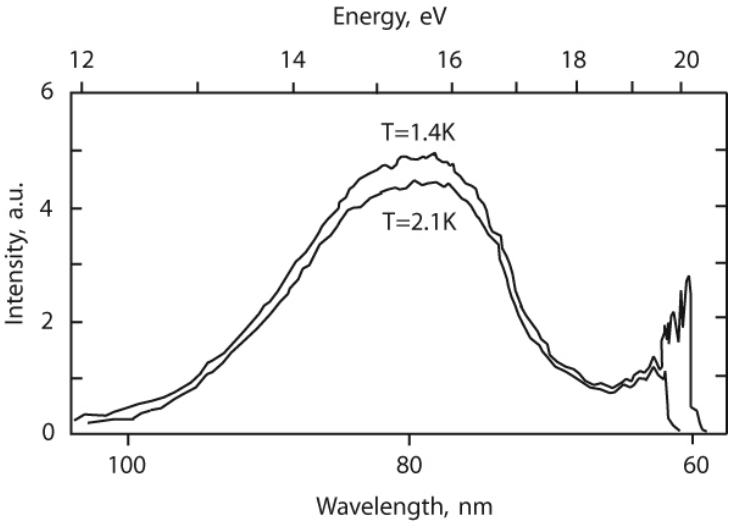

Fig. 3.29 Emission spectrum of electron-bombarded superfluid helium. Redrawn from [178].

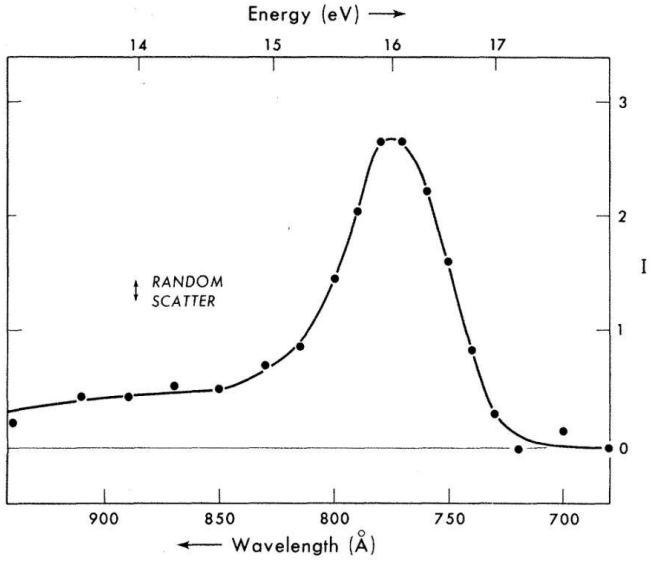

Fig. 3.30 Emission spectrum of liquid neon activated by tritium beta decay at 25.4 K and measured with a resolution of 4 Å [175].

The emission spectrum of liquid neon (Fig. 3.30) is characterized by a main peak located at 77.4 nm, with a width of about 3 nm FWHM [175]. The liquid thickness from 3 to 10 mm does not affect the spectrum. The intensity of the emission integrated over the spectrum is considerably smaller than that in solid neon (Fig. 3.31).

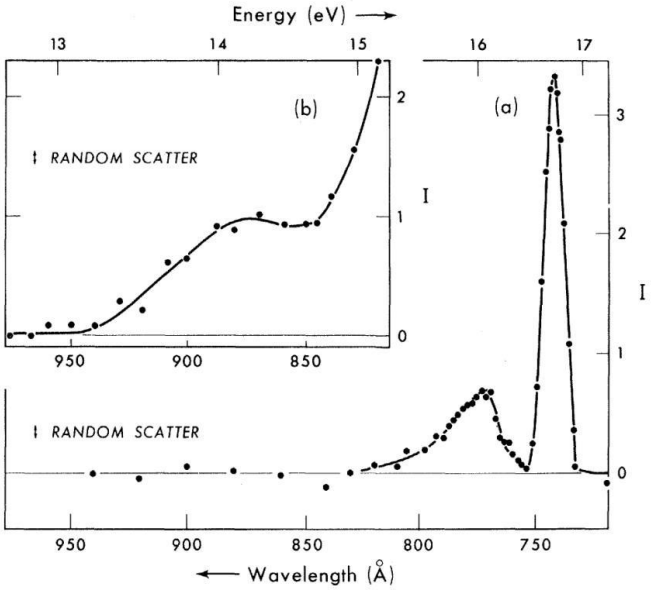

Fig. 3.31 Emission spectrum of solid neon activated by tritium beta decay at 14 K and measured with 12 Å (a) and 24 Å(b) resolution [175].

In the solid neon spectrum, there are two broad lines at 77.4 and 89.0 nm. The first of these lines appears in the liquid; there are indications that the second one appears there too. The presence of these line in both dense phases suggests that these lines are due to transitions of the Ne_2 molecule. However, in contrast to the other rare gases, the positions of these lines do not correspond to those observed in the discharge spectrum of neon gas. The greatest difference between the spectra of solid and liquid neon is the presence of the narrow line at 74.3 nm in the solid, which corresponds to the lowest frequency transition at 74.37 nm observed in the Ne atomic spectrum. The line has no analog in the known spectra of other rare-gas solids or liquids. Its small width (< 3.6 nm FWHM) confirms the atomic origin of the line.

Spectra of solid neon and its mixtures with xenon at 4.2 K were reported by Fugol [180]. Emission spectra of xenon impurity states in solid and liquid krypton were reported by Chesnovsky [181]. It was shown that alpha-induced scintillation consists of three emission bands, which are assigned to the host Kr_2^* molecule, the guest $XeKr^*$ heteronuclear molecules, and the Xe_2^* molecule. Electronic energy transfer occurs via dipole-dipole coupling between Kr_2^* and Xe single impurity states. The emission spectra of liquid and solid krypton were found to be sensitive to the presence of xenon impurities already at concentrations as low as 25 ppm; the emission spectra are dominated by xenon impurities at concentrations of $> 2.5\%$ [42, 182].

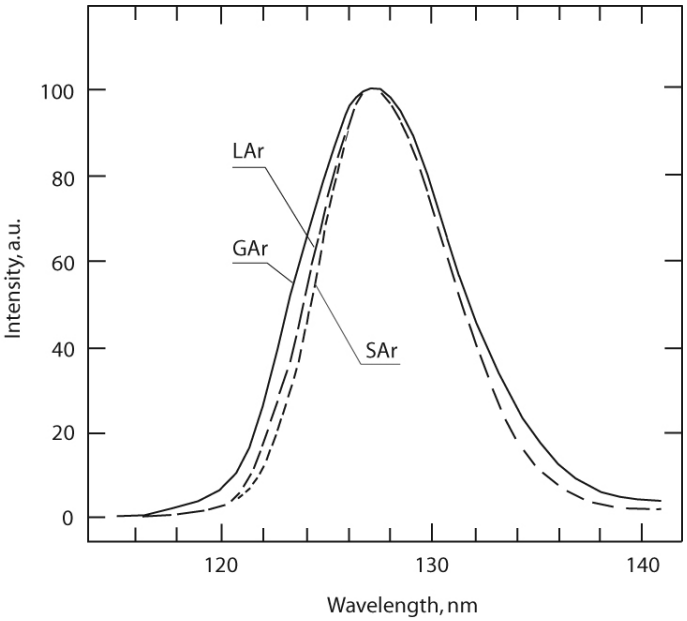

Fig. 3.32 Emission spectra of argon in gas (200 K), liquid (87 K) and solid (80 K) phase measured with a resolution of 2.5 nm. Redrawn from [183].

Figure 3.32 shows spectra of three phases of argon including a dense gas [183]. Figure 3.33 shows spectra of three phases of xenon reported by Jortner et al. [184]. On passing from the gas phase to the solid phase, the emission spectrum is blue shifted; but on passing from the gas phase to the liquid phase, the emission spectrum is red shifted. The fact is consistent with the greater ease of atomic displacement in a liquid than in a solid. Similar trends are evident, but less marked, in the spectra of other noble gases.

From the above observations, one can conclude: (a) the emission spectra of all noble liquids and solids consist of broad structureless bands, considerably displaced toward lower energy from the corresponding atomic absorption lines; (b) the efficiency of energy conversion in noble scintillators is very high: between 10 and 100% of the energy of ionization particles is converted into emission light in condensed phases, compared to a few percent in gas phases.

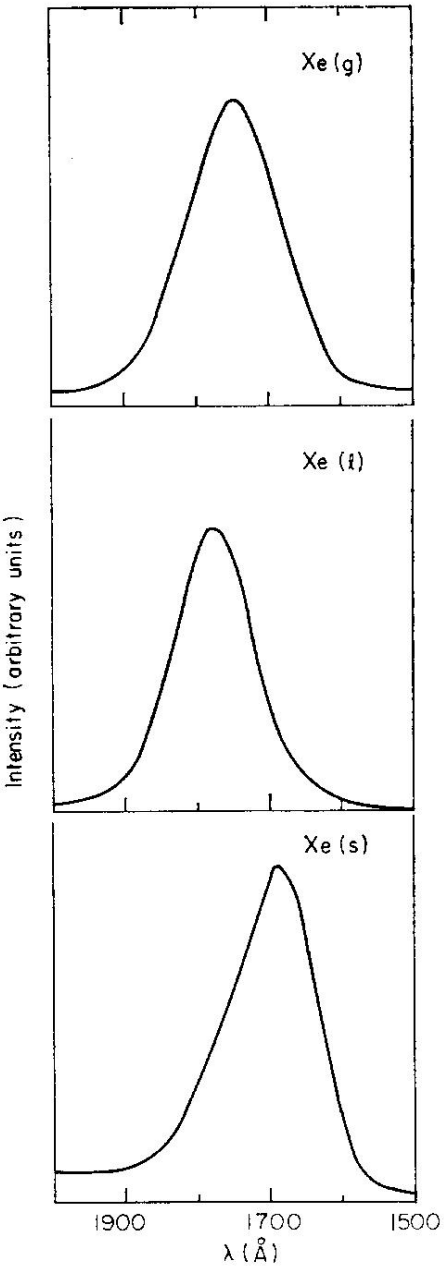

Fig. 3.33 Emission spectra of α-particle excited Xe in different states of aggregation [184].

3.4.3
Absorption and Scattering

3.4.3.1 Self-Absorption

Measurements of the self-absorption spectra of condensed noble gases is a difficult task because there are no optical materials transparent in the range of interest (the best one, LiF, has a cutoff at 11.8 eV) and samples must be investigated in a vacuum monochromator.

Boursey et al. [185] measured the absorption spectrum of solid neon condensed onto a sapphire substrate held near 4.2 K and coated with sodium salicylate. The emission ultraviolet light is converted into visible light after transversing the sample. A triggered vacuum spark source was used as a windowless source of UV radiation. Three peaks are apparent in the absorption spectrum (Fig. 3.34). Due to the low polarizability of Ne, the spectrum of the solid Ne is very close to the spectrum of the free atom.

Baldini condensed samples onto a phosphor-coated cooled substrate [186]. In this way he recorded the absorption spectra of solid Xe, Kr, and Ar (Figs. 3.35, 3.36 and 3.37) up to about 14 eV, limited by the emission spectrum of the hydrogen discharge lamp. He used an annealing procedure for outgassing hydrogen. The absorption doublets in solid argon, krypton, and xenon are found at energies close to those of the atomic resonance doublets. There appear slightly weaker absorption lines in the neighborhood of the

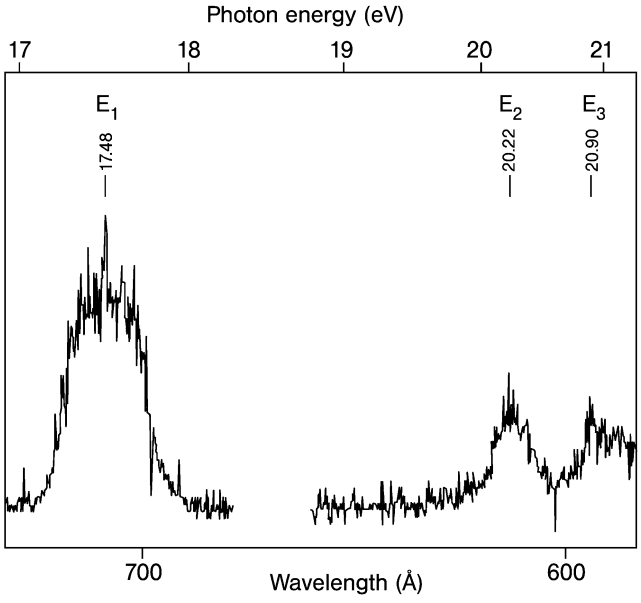

Fig. 3.34 Absorption spectrum of solid neon near 4.2 K [185].

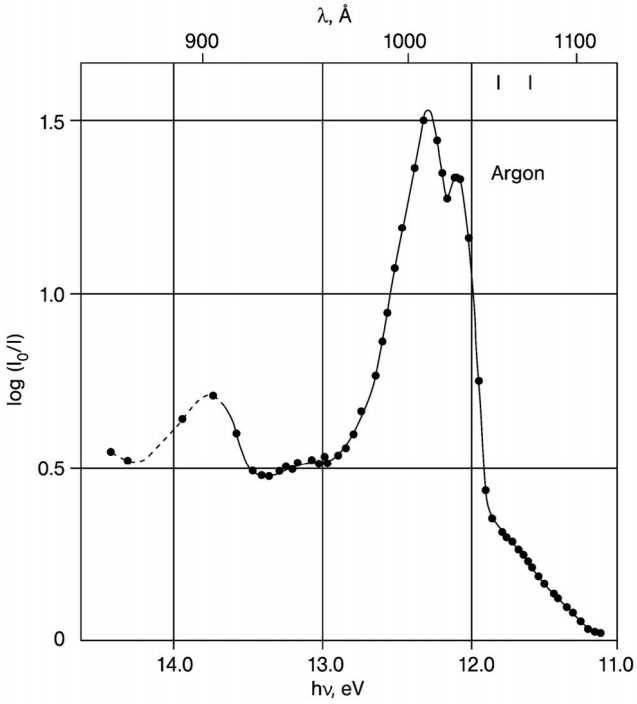

Fig. 3.35 Absorption spectrum of solid argon at 20 K [186]. The two vertical lines show the energy of the resonance doublets in the free atom. Bandpass 2 Å.

doublets. For example, the peak at 9.07 eV in solid xenon is 0.38 eV below the closest atomic level ($^3P_0$) while the peak at 9.53 eV, apparently corresponding to the $^1P_1$ level has a shift of only -0.04 eV. In solid krypton, absorption lines occur very close to the doublet on the high-energy side.

The observed spectra allow one to estimate the band gap between the higher valence band and the conduction band as well as the binding energy of excitons in the solids. The peak energies of the absorption peaks correspond to the Rydberg series

$$E_n = E_G - G/n^2 \tag{3.38}$$

where E_n is the peak energy, E_G is the energy gap at the Γ point of the Brillouin zone, G is the binding energy of the exciton, and n is the quantum number.

In Table 3.11, the values of E_G and G are compared for the noble gas solids.

3.4.3.2 **Impurity Absorption**

One of the important parameters for practical scintillators is the attenuation length for scintillation photons in the medium itself. Since the second molec-

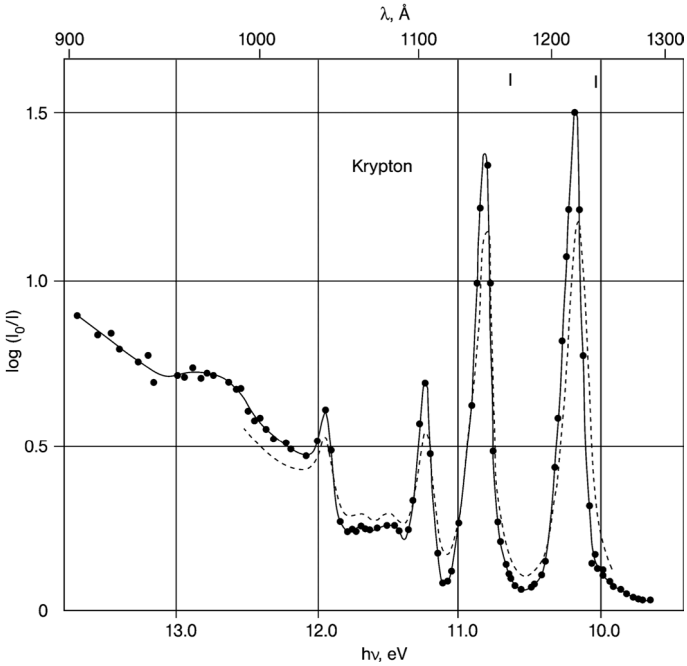

Fig. 3.36 Absorption spectrum of solid krypton at 20 K and annealed at 44 K (solid line) and at 40 K (dashed line) measured by Baldini [186]. The two vertical lines show the energy of the resonance doublets in the free atom. Bandpass 2 Å.

Tab. 3.11 Band gaps and exciton binding energies of solid noble gases [185, 186].

	E_G, eV		G, eV	
	Γ (3/2)	Γ(1/2)	Γ (3/2)	Γ (1/2)
Ne, 4.2 K	21.42		4.89	
Ar, 20 K	14.16	4.25	2.30	2.06
Kr, 20 K	11.67	12.33	1.73	1.52
Xe, 19 K	9.28		0.86	

ular continuum in noble gases is well separated from the absorption spectra, the self absorption of the emission photons from the continuum should be negligible. However, presence of dissolved molecular impurities leads to significant absorption of the UV light. This is a primary reason for limited transparency of condensed noble gases to emission photons even originated from the molecular continuum [179]. One of the first observations to confirm this high transparency was reported by Simmons and Perkins [187], who found that liquid helium scintillation light passes through 10 cm of liquid helium almost without attenuation. Due to low operation temperatures, the most pos-

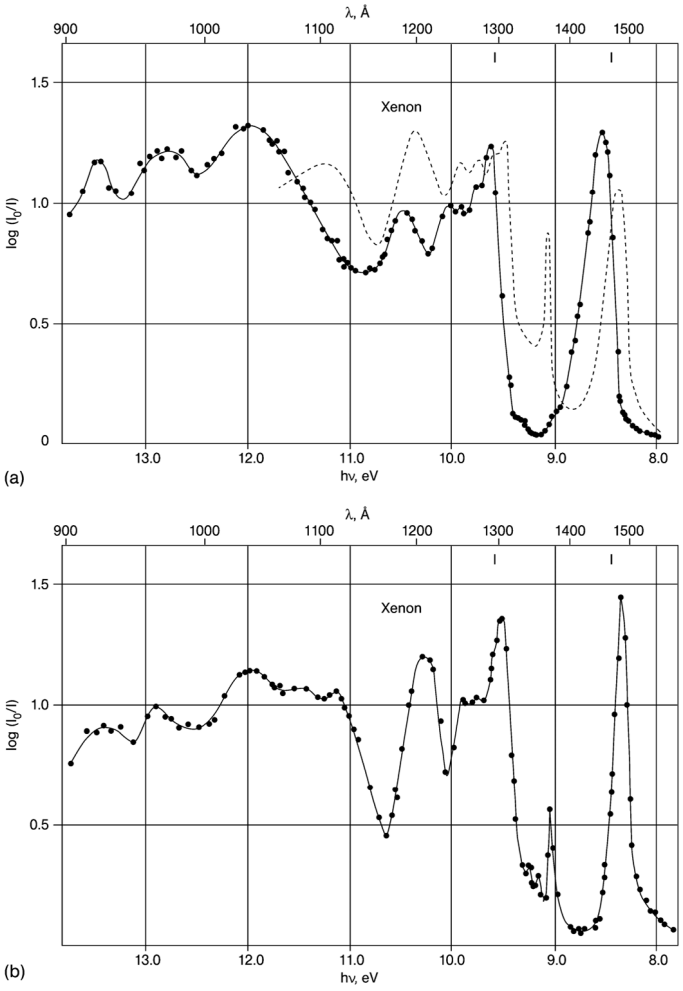

Fig. 3.37 (a) Absorption spectrum of unannealed solid xenon at 19 K (solid line) and at 53 K (dashed line) and (b) absorption spectrum of solid xenon at 21 K annealed at 53 K. The two vertical lines show the energy of the resonance doublets in the free atom. Bandpass 1 Å [186].

sible impurities are frozen, and liquid helium is inherently pure liquid and does not require very special purification. For heavier noble gases, it took two decades longer in order to achieve the attenuation length above 10 cm.

One of the first breakthroughs was reported by Anisimov et al. in 1984 [188], when they achieved 32 cm attenuation length in LKr as a result of multiple circulation of the gas through a hot metal (calcium) getter. Yet, the attenuation length of solid krypton was found to be a few times less than that in the orig-

inal liquid sample even though the total light yield of the scintillation was twice that of the the liquid. In the 1990s, several groups reported achievement of highly transparent liquid xenon, krypton, and argon with attenuation length approaching 1 m (see Table 3.13 and references therein). Recently, it was shown by Baldini et al. [21, 189] that water at a ppm level is the most likely impurity responsible for the absorption processes in liquid xenon and that the attenuation length may be drastically increased using continuous circulation of xenon through a purifier to reduce the concentration of water to < 100 ppb.

3.4.3.3 **Scattering**

In the course of development of the LXe/LKr scintillating calorimeter, it was found that thermodynamic motion of the liquid essentially affects efficiency of the light collection through LXe/LKr layers of >10-cm thickness [190, 191]. The best attenuation length of the scintillation light was achieved when temperature gradients were minimized below 0.1 K cm^{-1} and convection fluxes in the bulk liquid were eliminated [182]. More detail concerning the light collection process in condensed noble gases raised an issue about scattering of the UV light on density fluctuations [192, 193]. The inverse of the Rayleigh scattering length can be written in the following form:

$$h = (\omega^4/6\pi c^4)\left[kT\rho^2 k_T\left(\frac{\partial\varepsilon}{\partial\rho}\right)_{T^2} + (kT^2/\rho c_v)\left(\frac{\partial\varepsilon}{\partial T}\right)_{\rho^2}\right] \tag{3.39}$$

where ω is the angular frequency of the radiation, c is the velocity of light, k is the Boltzmann's constant, T is the temperature, ρ is the liquid density, k_T is the isothermal compressibility, c_v is the heat capacity at constant volume, and ε is the dielectric constant. The theory confirms that the presence of gradients of density and dielectric constant increases the scattering and in some radical cases may cause reduced transparency of the samples. The effect found to be competitive to practically achievable attenuation on residue impurities. For example, the scattering length in LXe is calculated to be 30 cm at 174 nm wavelength, which is close to the majority of available experimental data on attenuation length of the scintillation light in LXe. Variations in the density introduced by convection of the liquid should essentially decrease this value.

It may be interesting to note, that according to Eq. (3.39) one can conclude that the reduction of the temperature can help to suppress the scattering. Rayleigh scattering may also be essentially suppressed if the wave-shifting technique used. For example, adding 3% Xe to LKr or LAr significantly reduces the scattering [192]. Seidel et al. [193] also pointed out that one could add fluorine to liquid xenon to wave shift the spectrum. Reduced light yield of scintillations observed in pressurized xenon at densities above 0.2 g cm^{-3}

(see Section 3.4.4) may be associated with the growing probability of scattering due to density fluctuations or clusters [71]. Calculated Rayleigh scattering lengths for noble liquids are presented in Table 3.12. The major uncertainty in the calculations arises from the determination of the dielectric constant; Seidel et al. [193] estimated those uncertainties to be a factor of 2 in the case of helium, 40% for neon, 35% for argon, 25% for krypton, and 20% for xenon.

Tab. 3.12 Calculated Rayleigh scattering length (SL) [193] and measured attenuation length (AL) for liquefied noble gases.

Liquid	Wavelength, nm	Dielectric constant	SL (calc.), cm	AL (meas.), cm
He at 4.2 K	78	1.007	600	> 10 [e]
He at 0.1 K	78	1.089	20 000	
Ne	80	1.52	60	
Ar	128	1.90	90	66 [a]
Kr	147	2.27	60	32 [b], 82 [a]
Xe	174	2.85	30	29 [a], 40 [c], 50 [d]

References: [a] - [192], [b] - [188], [c] - [194], [d] - [195,196], [e] - [187]

3.4.4 Scintillation Light Yield

Even in the first studies, it was shown that the scintillation yields of the condensed noble gases are comparable with that of the gaseous phases [13, 14]. For all noble gases, it was shown that the yield of scintillation photons increases [197] but the decay time declines [177] with increasing pressure in the range between normal and several tens of bar pressure. In xenon, it was found that the light output of scintillations generated by alpha particles is reduced at densities $> 0.1\ \mathrm{g\,cm^{-3}}$ as shown in Fig. 3.38.

Since the scintillation yield of liquid xenon is higher than the scintillation yield of the gas phase, this decrease in the observed light output must be changed to increase in order to meet the light output of the liquid xenon. The effect may be understood in suggestion that there is a significant light scattering at certain, relatively high, densities of xenon gas [198].

In 1986 and 1987, the ionization and scintillation yields in liquid argon for relativistic heavy particles were simultaneously measured [199–201]. Using these data, the results of the scintillation yields obtained for the individual particles are shown as a function of the linear energy transfer (LET) of an incident particle in Fig. 3.39.

From the figure, one can see a flat maximum response level for relativistic heavy particles except for Au particles. The scintillation yields for relativistic electrons and for relativistic protons and helium ions are shown to be below

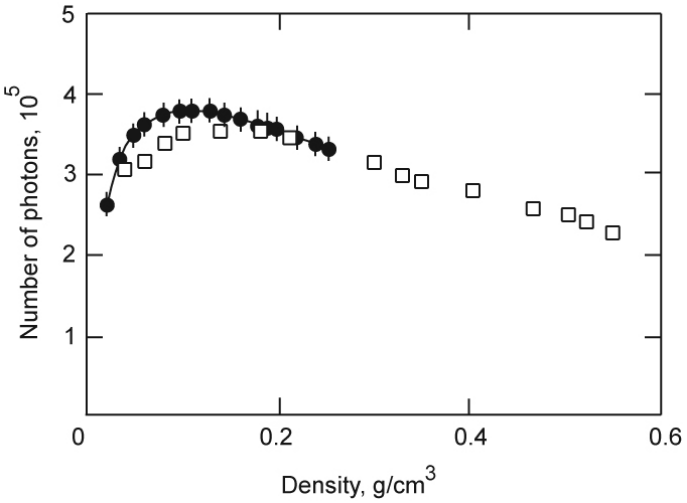

Fig. 3.38 Dependence of light output of scintillations excited by alpha particles on the density of high-pressure xenon: open squares represent data of Bolotnikov and Ramsey [33], closed circles represent data of Kobayashi et al. [198]. Redrawn from [198].

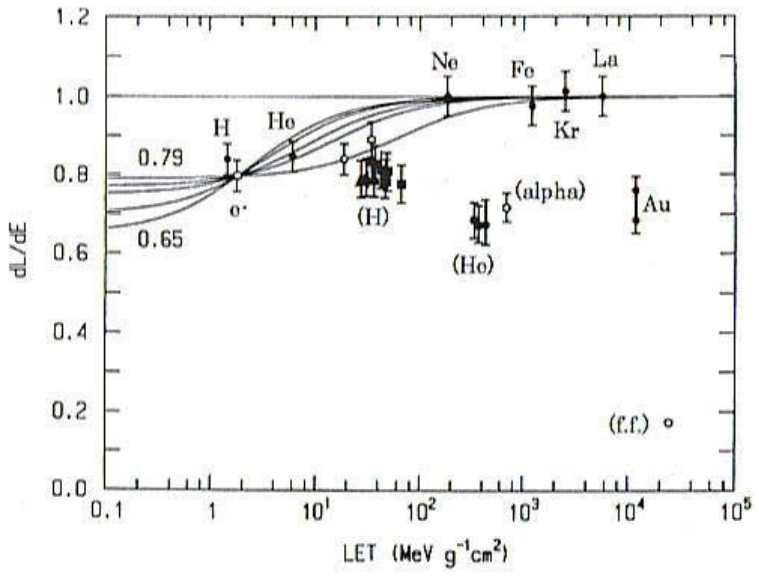

Fig. 3.39 LET dependence of scintillation yields in liquid argon for various ionizing particles.

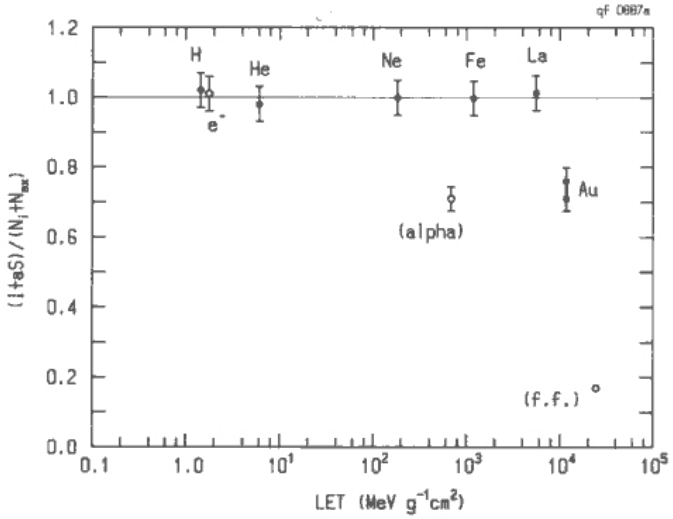

Fig. 3.40 LET dependence of the ratio of $I + aS$ to $N_\mathrm{i} + N_\mathrm{ex}$ in liquid argon for various ionizing particles.

the flat maximum response level. If the scintillation intensity, aS, is taken to be the number of emitted photons, that is, $\Delta E/W_\mathrm{ph}$, where ΔE is the energy deposited in the sensitive volume and W_ph is the average energy required to produce one photon, and I is the number of electrons, then their sum, $aS + I$, should be equal to $N_\mathrm{i} + N_\mathrm{ex}$ which expresses the sum of the number of electron ion pairs produced by an ionizing particle, N_i, and the number of excited atoms produced by an ionizing particle N_ex. Therefore, the fact that the ratio of $(I + aS)/(N_\mathrm{i} + N_\mathrm{ex})$ is unity means that the scintillation yield is 100%.

Figure 3.40 shows the variation of the ratio of $(I + aS)/(N_\mathrm{i} + N_\mathrm{ex})$ as a function of particle LET obtained from the data in Fig. 3.39 [202]. In this figure, the ratio on the low LET side is almost unity. On the high LET side, however, the ratio decreases from unity. The change in the low LET side in Fig. 3.40 occurs as a result of electrons that escaped recombination [202] but which are finally collected by the anode. As a result, $(I + aS)/(N_\mathrm{i} + N_\mathrm{ex}) = 1$ does not change. In contrast, the reduction of scintillation yield on the high LET side occurs due to the so-called quenching effect [203, 204] because the quenching loss means a real loss of photons. Figure 3.40 also shows that the scintillation yields for alpha particles and fission fragments are lower than unity. This is also due to the quenching effect. The flat part between them corresponds to 100% scintillation yield. In liquid xenon, we have no data for ionization and scintillation signals observed for relativistic heavy particles but we do have data for the variation of scintillation yields for relativistic heavy particles as a function of particle LET, which is very similar to that of liquid argon. Thus, we assumed

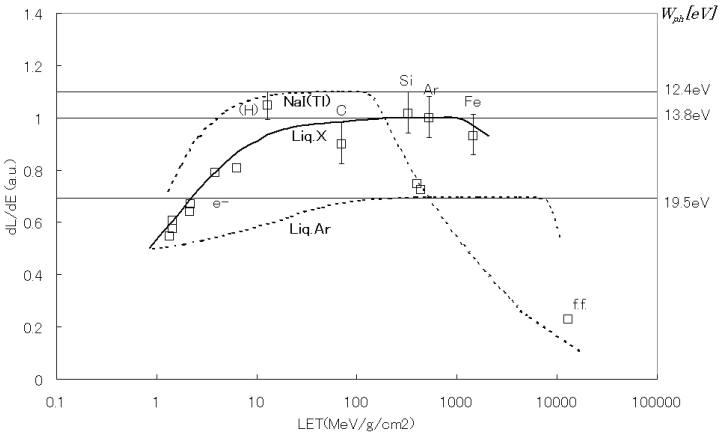

Fig. 3.41 Three LET dependences of scintillation yield curves, the upper curve is that of NaI(Tl) crystal, the lower curve is liquid argon and the middle curve is liquid xenon. The abscissa on the right side shows the value of W_{ph}.

that the flat part of the LET response corresponds to a 100% scintillation level as shown in liquid argon. From this assumption, we can estimate $W_{ph}(\beta)$ for relativistic electrons.

Figure 3.41 depicts the LET dependences of scintillation yield in liquid argon, xenon and NaI(Tl) [32, 202, 204, 205]. The vertical axis on the right side is given by W_{ph}. From this figure, we know that the ratio of the scintillation yield of liquid xenon to that of NaI(Tl) for MeV electrons is about 80%. The $W_{ph}(\beta)$, $W_{ph}(\alpha)$, and $W_{ph}(\max)$ are listed in Table 3.13.

Michniak et al. [208] investigated the scintillation yield of liquid and solid neon and liquid helium. It was found that the light yield of condensed neon is sensitive to temperature and the aggregate state. The transition from the solid to liquid state reduces the light yield about two times. The light yield of the solid neon was measured to be comparable with that of the liquid helium. Note, that according to D. McKinsey (private communication, 2006), there are data with liquid neon that show a much higher light yield, comparable to liquid argon.

Tab. 3.13 Experimental data on average energy needed for production of a scintillation photon in noble gases and NaI(Tl) for comparison.

	Relativistic electrons	α-particles	Relativistic heavy particles	Ref.
LAr	25.1±2.5	27.5±2.8	19.5±2.0	[206]
LKr		15		[42]
LXe	23.7±2.4	19.6±2.0	14.7±1.5	[206]
NaI(Tl)	16.7±0.6			[207]

Effect of Electrical Field on Light Yield

Experiments with electrical field applied to the condensed noble gases have demonstrated that 67% of the scintillation produced in LAr and 74% of the scintillation produced in LXe is due to the excited molecules that are produced through the recombination process of molecular ions R_2^+ and free electrons, and that 33% in LAr and and 26% in LXe is due to the emission from self-trapped excitons (Fig. 3.42).

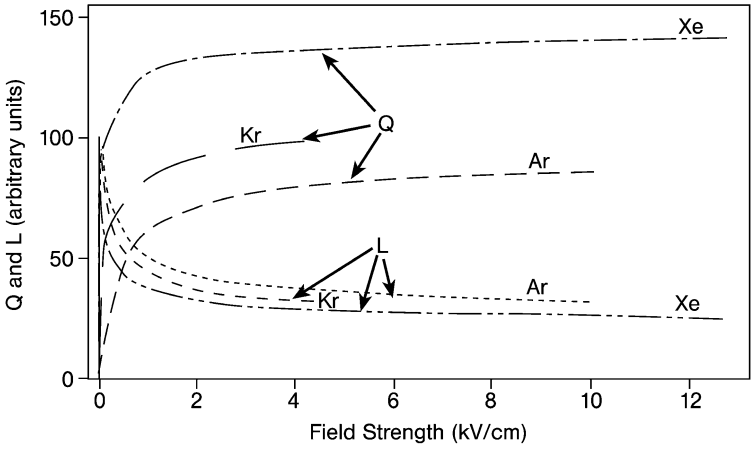

Fig. 3.42 Variation of luminescence intensity L and collected charge Q in liquid argon, krypton and xenon near their triple points vs. applied electric field for 1 MeV electrons [209].

These types of luminescence, which have the same photon energy, are called recombination luminescence and self-trapped exciton luminescence. An applied electric field quenches the luminescence from free electron recombination. Self-trapped exciton luminescence has two components: a fast one corresponds to ${}^1\Sigma_u^+ \longrightarrow {}^1\Sigma_g^+$ transition, a slow one corresponds to ${}^3\Sigma_u^+ \longrightarrow {}^1\Sigma_g^+$ transition. Information about the dynamics of the recombination process associated with free electrons has been derived from the difference in the decay curves observed at zero and high electric field.

Roberts and Hereford [210] investigated electrical field and temperature dependence of the scintillation yield from liquid helium; they have shown that the light output of scintillation is a complex function of temperature (Fig. 3.43).

They observed also the luminescence in liquid ^{3}He produced by alpha particles. The total light output found to be independent on temperature in the range between 0.3 and 2.4 K, which indicates that complex behavior of light output is peculiar to the superfluid. The temperature dependence can be accounted by collision-induced radiative destruction of He_2 triplet molecules. They found that the light output is independent on field direction at tem-

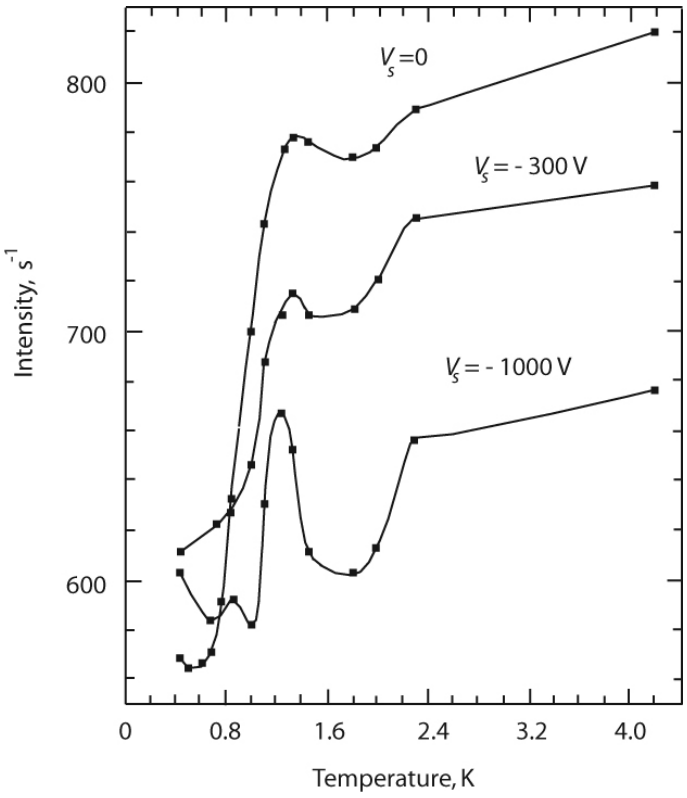

Fig. 3.43 Total intensity of scintillation of LHe vs. temperature for different applied voltages corresponding to the electric field strength 4 and 13.3 kV cm^{-1}. Redrawn from [210].

peratures above 1.5 K. However, as temperature drops lower, the intensity of scintillation for negative voltage (electrons pulled out into the bath) starts to exceed that for positive voltage. A strong peak appears at 1.25 K for negative voltage. Since in this temperature range only electrons form stably charged vortex rings, the data support the suggestion that the metastables are radiatively destroyed through interaction with charged vorticity. Below about 1 K, both species of ions are known to form stably charged vorticity. The enhancement of the luminescence upon establishment of charged vorticity in the He II bath for temperatures less than 0.8 K indicated that the interaction of the metastable with vortex-trapped ions increases their rate of the radiative destruction. Note, that Hereford only looked at scintillation light with emission time of less than 1 μs, and so missed a lot of the liquid helium signal associated with long-living metastables.

3.4.5
Refractive Index

Properties of scintillation detectors are affected by the refractive index of scintillators. Difficulties of using the standard methods of refractive index measurement of condensed heavy noble gases are a result of the short wavelengths of the scintillations and the expected large refractive index for heavy liquids such as liquid xenon.

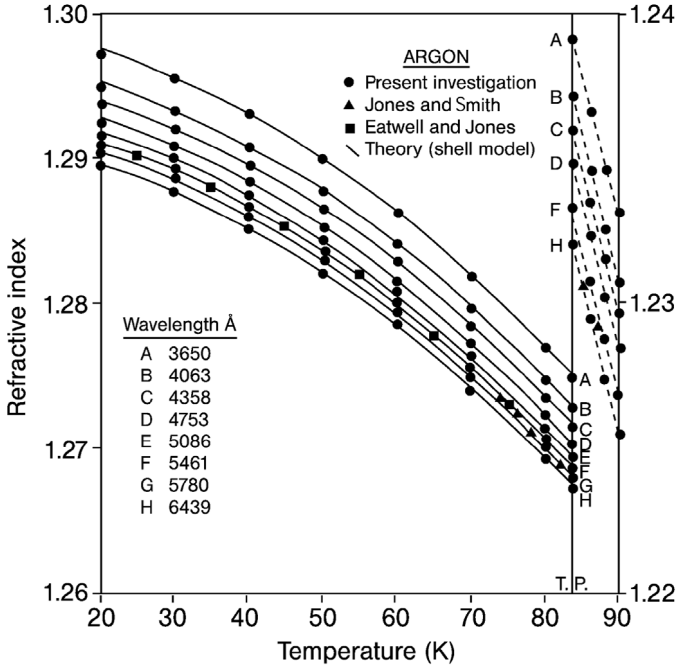

Fig. 3.44 Refractive indices of liquid and solid argon vs. wavelength at different temperatures [211].

Measurements of refractive indices of liquid argon, krypton, and xenon in the wavelength range of 350–650 nm are reported by Sinnok and Smith [211] and presented in Figs. 3.44, 3.45 and 3.46 for wide temperature range and in Table 3.14 for emission peak wavelength at triple points.

Tab. 3.14 Indices of refraction for liquid and solid heavy noble gases around their triple points at 5461Å wavelength [211].

	Ar	Kr	Xe
Liquid	1.2316	1.298	1.385
Solid	1.2334	1.346	1.443

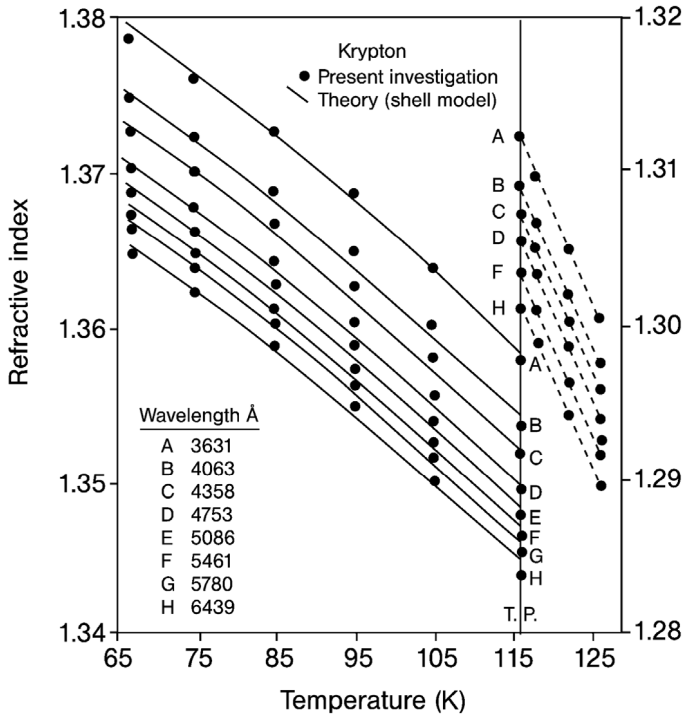

Fig. 3.45 Refractive indices of liquid and solid krypton vs. wavelength at different temperatures [211].

Data of Sinnok and Smith [211] have been extrapolated down to UV wavelength by Braem et al. [194] for liquid xenon as presented in Fig. 3.47.

The extrapolation was confirmed by direct measurement of the LXe refractive index at 180 nm carried out by Barkov et al. [212]. The value obtained at 180 nm is equal to $1.5655 \pm 0.0024 \pm 0.0078$ for the xenon triple point, where the first error is due to the reproducibility of the experimental conditions, and the second error is a result of some differences in light collection during LXe measurements and calibration measurement with BGO crystal. Recently (S. Nakamura, private communication) the refractive index was measured at 175 nm to be 1.61.

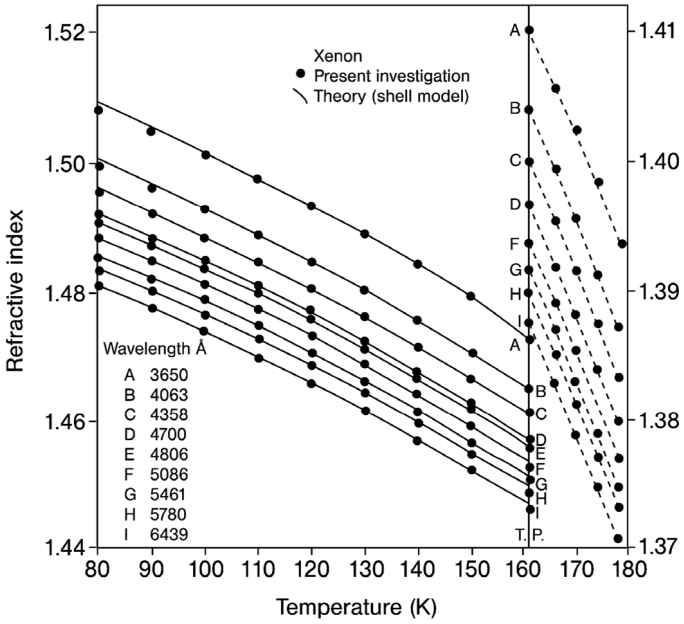

Fig. 3.46 Refractive indices of liquid and solid xenon plotted against wavelength at different temperatures [211].

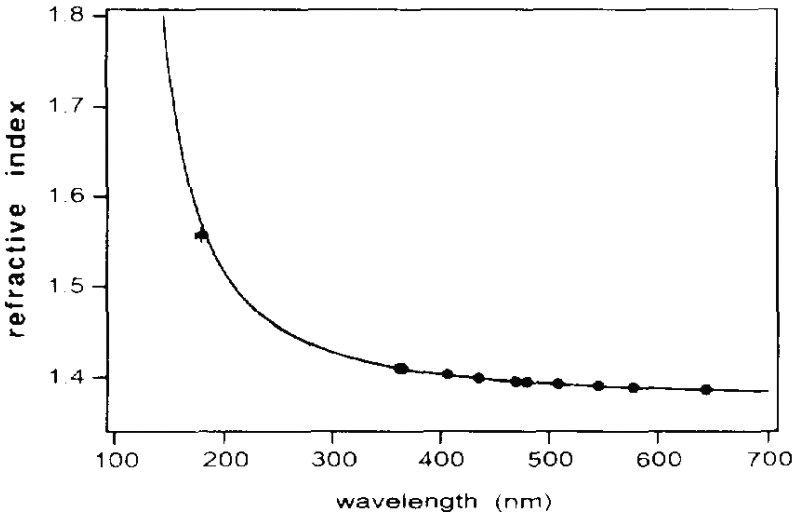

Fig. 3.47 Liquid xenon refractive index in dependence on wavelength, measured by Sinnock and Smith [211] (circles), Barkov et al. [212] (squares), and calculated by Braem et al. [194] (solid line) at the triple point. Adopted from [194].

3.4.6 Decay Times

The scintillation decay time is the average over all observed emission components with wavelength λ_n weighted according to their relative intensities a_n and the relative efficiency of detection of radiation of wavelength λ_n. An intensity of the scintillation may be described as a superposition of a few exponential terms

$$I(t) = \sum_{i=1}^{n} Y_i(t) = \sum_{i=1}^{n} a_i \cdot \exp(-t/\tau_i) \tag{3.40}$$

For example, in low-pressure xenon gas three terms ($n = 3$) are needed to describe the decay curve [172, 177]. Three terms used for description of the scintillation decay of mixtures of pure noble gases. In dense noble gases, the first two excited states of the noble gas molecules are the most important in description of scintillations. More specifically, the states that are relevant and the ground singlet state and the ground triplet state.

In a typical experiment using a pulsed beam technique or using a nuclide-emitting two prompt gamma quanta, a delayed coincidence curve is measured. A start pulse coincident in time with a radiation activation of the scintillator is fed into one channel of a time-to-amplitude converter; the stop pulse is derived from a photodetector detecting a random single photon from the scintillation flash. The experimental data take the form of total counts in a number of channels of a multichannel pulse amplitude analyzer fed by the time-to-amplitude converter. The measured pulse height spectrum is called a decay curve. Recent experiments just digitize the PMT pulses, without use of a TAC.

In the case where the transitions of deexcitation are comparable with time characteristics of photodetector and wavelength shifters used to detect UV photons, the time resolution of the photodetector and decay time of the wavelength shifter should be taken into account. For example, describing decay curves of liquid krypton, xenon, and their mixtures, Akimov et al. [182] used modified Gale's formula [213] instead of simple exponential terms in Eq. (3.40)

$$\begin{aligned} Y_i(t) = a_i\{&\exp(A_i)(1 + erf[ht - (1/2h\tau_i)]) \\ &- \exp(A_w(1 + erf[ht - (1/2h\tau_w)])\} \end{aligned} \tag{3.41}$$

where $A_i = (1/2h\tau_i)^2 - (t/\tau_i)$ and $A_w = (1/2h\tau_w)^2 - (t/\tau_w)$, τ_i is a decay time of a component with amplitude a_i, τ_w is a decay time of wavelength shifter, $h = (1/2)^{1/2}\sigma$, where σ is the time resolution of the photodetector. In fact, the time dependence is not always exponential: one can see $1/t$ or $1/t^2$ terms as well. This can come from recombination (in liquid argon and liquid xenon) or from Penning ionization (in liquid helium).

3.4.6.1 Decay Times of Gases

Heron et al. [214, 215] measured the lifetime of certain excited atomic states of helium at low pressures (1–10 mTorr) in the range of 400–800 nm for transitions from several levels: 3^1P, 68 ns; 4^3S, 115 ns; 4^3P, 153 ns; 3^3D, 10 ns. The large amount of light emitted in the visible and near-infrared wavelength regions is specific for low-density noble gases. In high-pressure (3.5 MPa) ^{3}He+0.5%Xe gas mixture a single component with decay time of 200 ns has been observed recently [171].

The emission spectrum of neon at about 0.1 MPa pressure when it is excited by alpha particles consists of a number of atomic lines in the wavelength range of 580–750 nm with decay times of about 30 ns; the most intensive line emission at 337.8 nm has a ≈ 1.2 ns decay time. The decay curve is well described with two exponents [216].

Decay time constants, build-up constants, and amplitudes of scintillations of Xe and Ar gases at different pressures when excited by 1.3 MeV electrons have been obtained by fitting oscilloscope traces [177] with a sum of exponential terms (Eq. (3.39)); the data are presented in Tables 3.15 and 3.16. A negative amplitude a_1 characterizes intensity build-up; a positive amplitude characterizes intensity of decay. Below 0.3 MPa, one build-up term and two decay terms were adequate to fit the data. The build-up time constants are sensitive to pressure as $p^{-1.5}$ in the low pressure range ($<$ 0.2–0.3 MPa). Above 0.3 MPa pressure, the build-up constants could not be measured accurately since the build-up time was comparable to the duration of the excitation pulse. Data taken on a slow time scale were fit with three (Xe) and two (Ar) decay components. The slowest third component was relatively weak and had a pressure-independent time constant of about 280 ns. The time constants and ratio of intensities of faster components were not sensitive to pressure at elevated pressures both for Ar and Xe. In contrast to Ar, the amplitudes of fast and slow components decreased rapidly with pressure above 2.4 MPa in Xe. This effect may be associated with forming light scattering entities such as large atomic clusters in gas xenon at densities $> 10^{20}$ cm^{-3} [71].

3.4.6.2 Decay Times of Liquids and Solids

Liquid Helium

The kinetics of scintillations generated in liquid helium by ^{210}Po alpha particles was investigated recently by McKinsey et al. [217]. They found that the scintillation pulse is 10 ns wide and yields about two-thirds of the total scintillation signal (Fig. 3.48).

At later times, the pulse exhibits an exponential decay with ≈ 1.6 μs time constant followed by a slower decay proportional to t^{-1} (Fig. 3.49).

Tab. 3.15 Decay time constants, τ_i (ns), and amplitudes, a_i (a.u.), for Xe gas at different pressures [177].

Pressure, bar	$-a_1$	a_2	a_3	a_4	a_5	τ_1	τ_2	τ_3	τ_4	τ_5
0.27	0.015		0.053	0.01		140		60	440	
0.54	0.15		0.055	0.10		74		28	160	
0.95	0.54		0.29	0.23		20		10	80	
1.4	1.0	0.07		0.55		12	300		49	
2.0	2.4	0.12		1.6		6	250		39	
2.7	7.1	0.4		4.0	3.8	5	250		35	10
4.1	30			8.3	9.8	3			31	8
5.4	44			17	26	2			27	4.4
8.5	190			27	48	1.2			26	5.5
13.6				26	48				23	5.5
20.4				24	52				20	4.5
29.3				32	56				13	3.5
41.0				11	36				18	4.0
42.5				9.6	20				15	3.5
47.6				3.6	9				17	4.0
54.4				1.1	2.4				15	3.5

Tab. 3.16 Decay time constants, τ_i (ns), and amplitudes, a_i (a.u.), for argon gas at different pressures [177].

Pressure, MPa	a_1	a_2	τ_1	τ_2
0.68	6	5.5	6	37
1.0	20	8	6	32
1.4	22	10	6.5	35
1.7	30	13	6.5	37
2.0	30	15	5.5	30
2.4	27	16	6.0	30
3.0	36	24	5.5	25
3.7	42	18	7.0	30
4.4	45	17	6.5	36
5.1	42	22	6.0	25
5.8	40	17	6.5	28
6.5	46	20	6.5	28

The exponential fluorescence decay is different for a cold helium gas sample than for a liquid helium sample. The fastest component of the scintillation is associated with the recombination process. The short-time afterpulsing derives from metastable states such as atomic He(2^1S). The slowest compo-

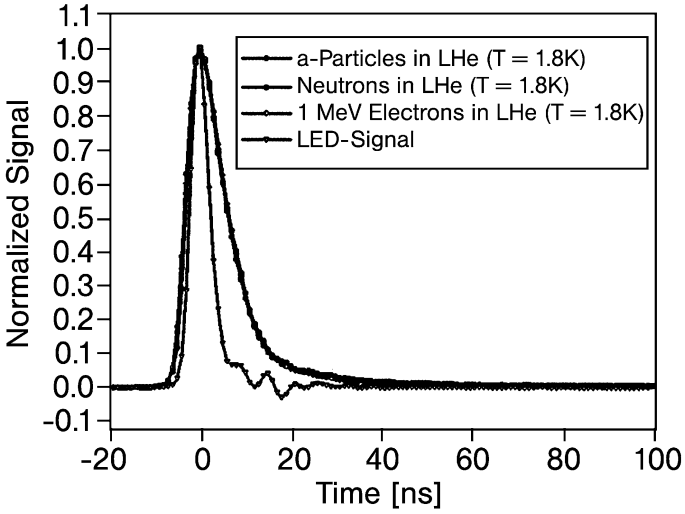

Fig. 3.48 Decay curves of liquid helium [217].

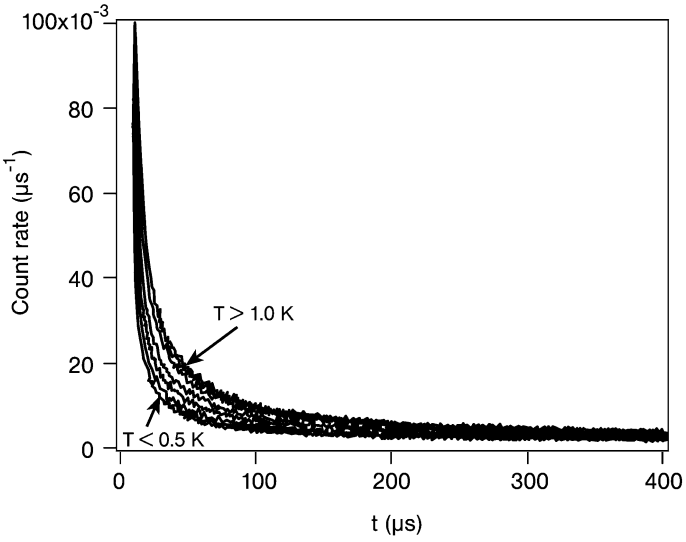

Fig. 3.49 Liquid helium scintillation afterpulse intensity excited by alpha particles at different temperatures (220 mK, 360 mK, 500 mK, 670 mK, 780 mK, 830 mK, 880 mK, 960 mK, 1060 mK, and 1140 mK): the intensity of the afterpulsing increases as the temperature is raised from 500 mK to 960 mK [217].

nent is probably associated with multibody interactions such as metastable-metastable interactions. Metastable-metastable interaction can result in Penning ionization, which can then lead to the formation of singlet molecules, which then decay.

Following the t^{-1} component, no further decay is found on millisecond time scales. However, there is a large rate of single-photon events, probably related to $He_2(a^3\Sigma_u^+)$ decay. Triplet $He_2(a^3\Sigma_u^+)$ molecules diffuse out of the ionization track and radiatively decay with a lifetime of 13 s [218]. At low temperatures the metastables should be quenched on the container walls, however this has not yet been verified experimentally.

Liquid and Solid Neon

Data from 364 keV beta (^{113}Sn) decay events is shown in Fig. 3.50. At earlier times, the decay is exponential with a lifetime of 3.9 ± 0.5 μs in the liquid and 3.3 ± 0.3 μs in the solid. These lifetimes agree roughly with a previously measured lifetime for the excited triplet neon dimer in liquid and solid neon [219].

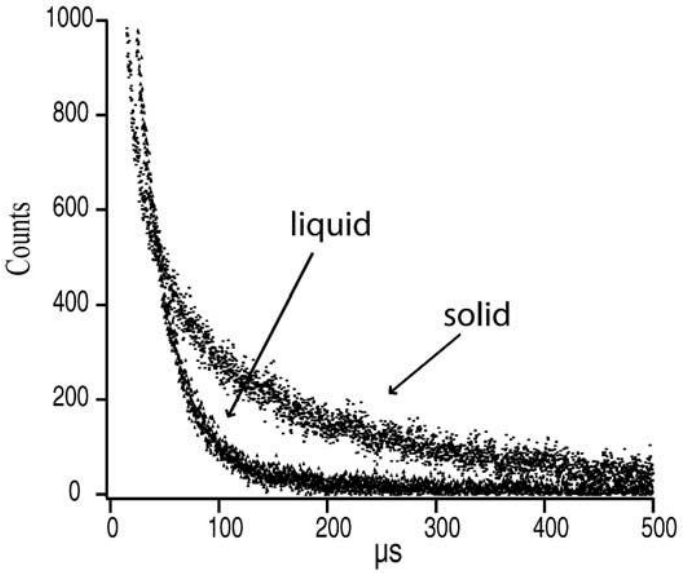

Fig. 3.50 Decay curves of liquid (25 K) and solid (16 K) neon [208].

In the solid, there is a long time component to the decay with a lifetime of several hundred microseconds. Spectroscopy of excitations in solid neon detected lines due to transitions from excited states of the neon atoms. The intensities of these lines were found to decay with a lifetime of 560 μs in the solid while in the liquid, these lines showed nonexponential decay and disappeared within several microseconds.

Liquid and Solid Argon

Liquid and solid argon and nitrogen-doped argon excited by electrons and alpha particles decay times and scintillation intensity investigated by Himi et al. [220]. Two exponential decays are observed for $[N_2] < 10^3$ ppm in

liquid and solid, which result from transitions $Ar_2^*(^1\Sigma_u^+) \longrightarrow 2Ar + h\nu(\text{UV})$ and $Ar_2^*(^3\Sigma_u^+) \longrightarrow 2Ar + h\nu(\text{UV})$. The $Ar_2^*(^3\Sigma_u^+)$ states are quenched by doping nitrogen in liquid argon but not in solid phase for concentrations of nitrogen $[N_2] < 500$ ppm. The scintillation intensity excited by alpha particles decreases with increasing $[N_2]$. The second positive emission $N_2^*(C^3\Pi_u) \longrightarrow N_2^*(B^3\Pi_g) + h\nu(\text{visible})$, which is the main emission in a argon-nitrogen gas scintillator, has not been observed for 5 ppm $<[N_2] <$13% nitrogen in liquid and solid argon.

Liquid and Solid Xenon

The time response of scintillation from liquid xenon is comparable to that of a plastic scintillator. However, its details differ significantly from plastic scintillators. The scintillation from liquid xenon for alpha particles and fission fragments consists of two decay components from singlet and triplet states as in plastic scintillators. In liquid xenon, the recombination component is added as the third component.

Figure 3.51 illustrates typical decay shapes when liquid xenon is excited by relativistic electrons, alpha particles and fission fragments without an electric field [221]. The decay time of scintillation from the singlet state is about 4 ns and that from triplet state is about 22 ns but the decay time for relativistic electrons does not have two components and exhibits only a single decay component of approximately 45 ns. This time is needed for recombination between electrons and ions. If an electric field is applied, this component disappears.

Figure 3.52 displays two decay components of scintillation when the electric field is applied [222]. A list of decay time constants of scintillation pulses in liquid xenon is shown in Table 3.17. The disadvantage of liquid xenon is its relatively low density, which is half or less than half of those of crystal scintillators. However, this disadvantage can be overcome because it is very easy to expand its sensitive volume freely because of its homogeneity.

Decay curves of solid xenon measured by Baum et al. [223] are shown in Fig. 3.53.

There was a certain difference found in kinetics of scintillations excited with nuclear particles and relativistic high-energy particles in liquid xenon (Table 3.17). This correlates to observations of the quenching effect in scintillation yield from liquid xenon excited with short-range nuclear recoils (see Section 2.6).

Liquid Krypton

Decay curves of liquid krypton have been measured by Kubota et al. [209,222] and Akimov et al. [182,224]. Figures 3.54 and 3.55 present data measured by Akimov et al. [182] as described in the introduction to this section.

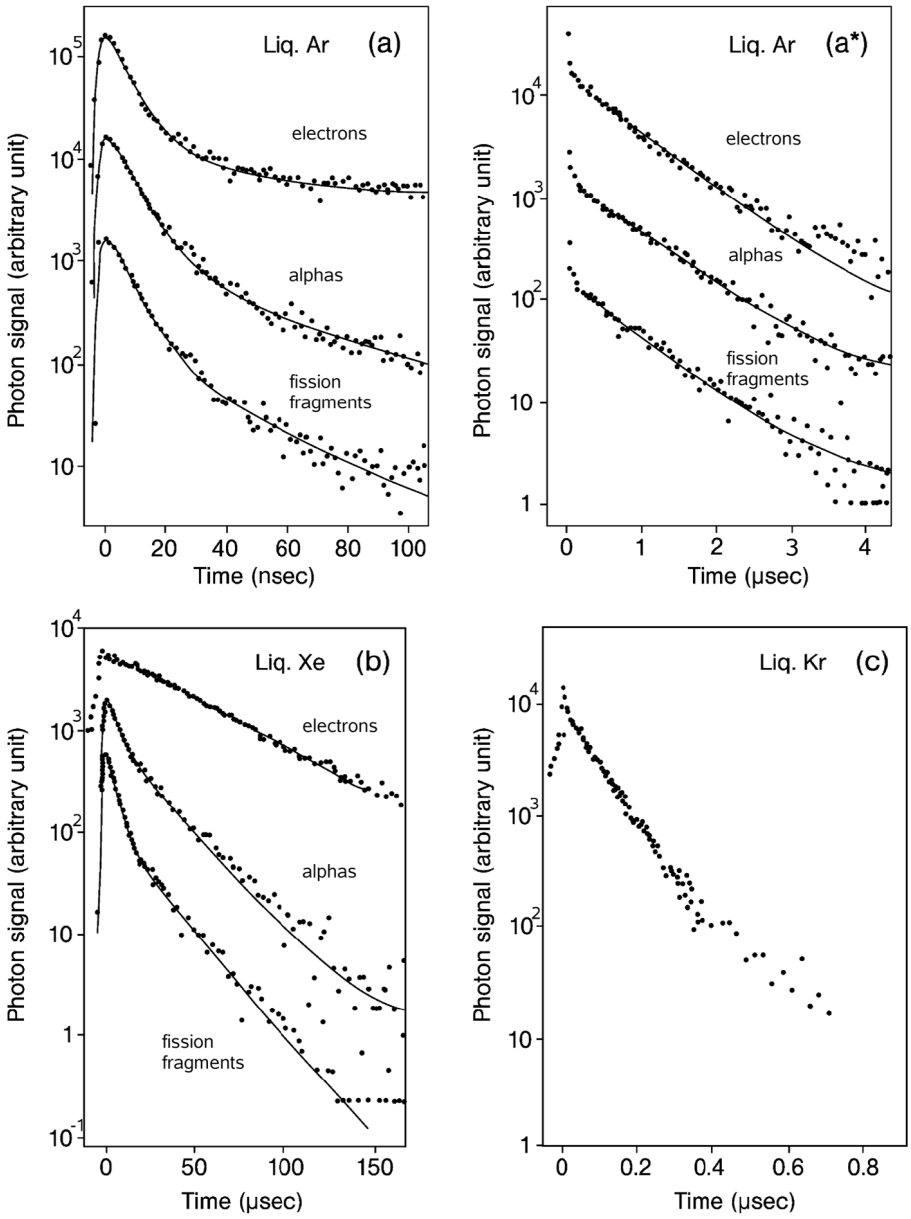

Fig. 3.51 Decay curves of liquid argon, krypton, and xenon [221, 222].

The data were analyzed using Eqs. (3.40) and (3.41). The decay time of p-terphenyl wavelength shifter was suggested to be $\tau_w = 2.0 \pm 0.6$ ns; the time resolution of the PMT was suggested to be $\sigma = 2.4 \pm 0.5$ ns. The third term of the decay curves was considered as a recombination component following

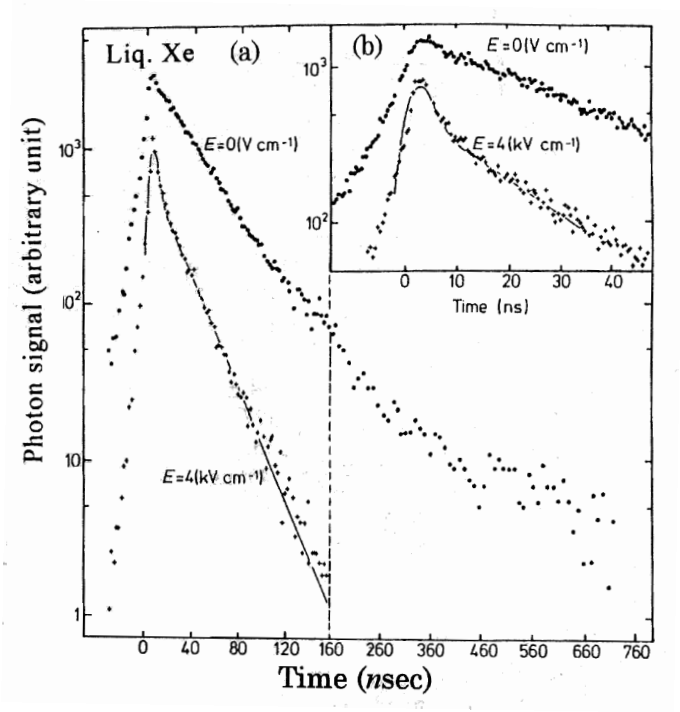

Fig. 3.52 (a) Decay curves of scintillation light from liquid xenon excited by electrons with and without an electric field. The long time range (a) and the short time range (b) without electric field are indicated [222].

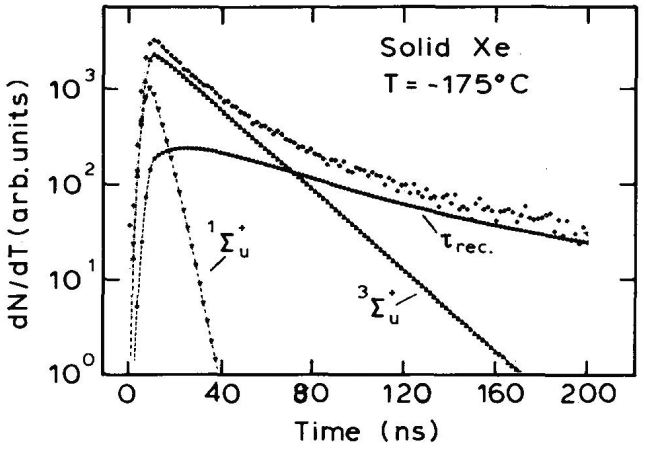

Fig. 3.53 Decay curve of scintillations in solid xenon excited by ^{239}U ions of 1.4 MeV amu^{-1} and fitting terms of the fast singlet state decay, of the slow triplet state decay, and of the recombination [223].

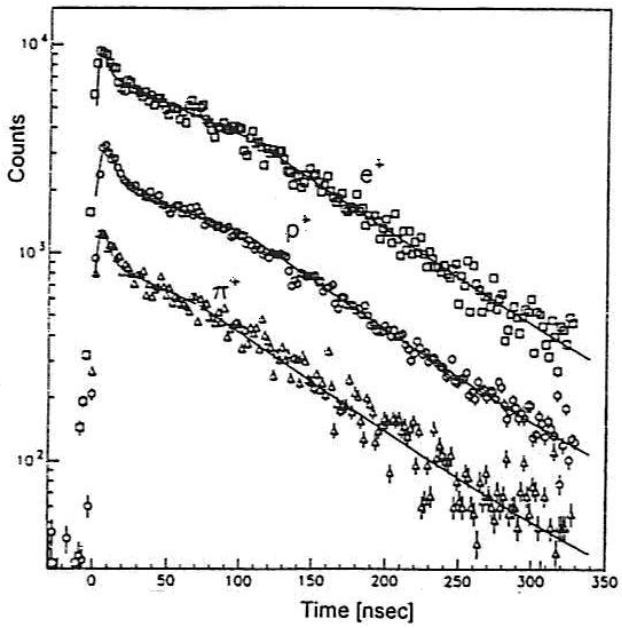

Fig. 3.54 Decay curves of LKr excited with relativistic 0.35 GeV c^{-1} positrons, protons, and positive pions at $T = 120$ K [182].

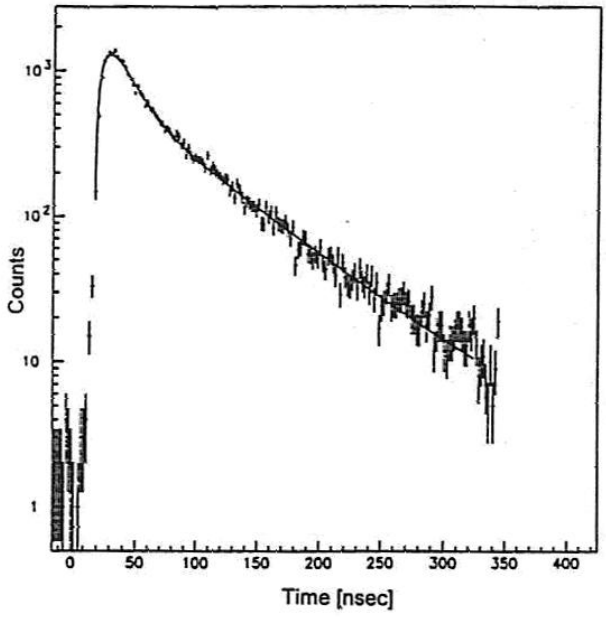

Fig. 3.55 Decay curve of scintillation excited by 0.8 GeV c^{-1} positive pions in liquid Kr+1.7%Xe [182].

Kubota [225]. The results of measurements are presented in Table 4.1 along with other available data on decay times of condensed noble gases excited by different radiations. There was not found a significant difference in scintillation kinetics of liquid krypton on the kind of relativistic particles in the range of 0.5–2.1 GeV c^{-1} momentum.

The influence of 1.7–5.3%Xe doping on LKr scintillation decay times was reported by Akimov et al. [42, 182, 224]. As a result of the doping the slow decay time of Kr is decreased to 29 ± 2 ns and the intensity of the fast component (8.7 ± 0.6 ns) is increased making LKr scintillator more likely LXe scintillator. This may be important for construction of large detectors such as EM calorimeters for high-energy physics. In this study, a detector with glass PMT FEU-85 coated with 0.5 mg cm^{-2} p-terphenyl has been used (see Section 4.2.2.1). The detector was installed at a secondary beam of the ITEP proton synchrotron. The photomultiplier was operated in a single-photon mode. The measured signal was normalized to the signal from a low intensity reference alpha source located in the vicinity of the PMT window. The detector was triggered with time-of-flight system and magnetic spectrometer selecting certain particles from the secondary beam of the accelerator. In decay time measurements, a single-photon signal from the PMT was used as a stop signal for time-to-digital converter. The attenuation length of the generic UV light was about 10 cm. The temperature of the detector was carefully controlled and stabilized with gradient temperature < 0.5 K over the samples. A xenon dope in LKr increases intensity of the fast component of scintillations and decreases decay time of slow component. Dominated contribution of the fast component in the LKr+Xe mixture excited with high energy particles is a very positive argument in support of development of scintillation calorimeters based on this mixture for high-luminosity accelerators of the next generation.

Table 3.17 presents data on parameters of scintillations measured for condensed heavy noble gases and their mixtures.

Tab. 3.17 Parameters of scintillations measured with different radiation in condensed noble gases near their triple points if there is no indicated temperature.

	Excitation	τ_1, ns	τ_2,ns	τ_3, ns	a_1/a_2	a_2/a_3	Ref.
LAr	α, ^{210}Po	7.7±1.0	1660±100				(e)
	α, ^{210}Po	5	1200±100				(a)
	β, ^{207}Bi	6.3±0.2	1020±60		-		(e)
	β, ^{207}Bi	6±2	1590±100				(a)
	β, ^{207}Bi	6	1200				(g)
+37ppmN_2	β, ^{207}Bi	5	170		(20)		(g)
+890ppmN_2	β, ^{207}Bi	4	90	550	(20)		(g)
SAr	β, ^{207}Bi	5	1100	-	(5)	-	(g)
+37ppmN_2		3	900		(16)		(g)
+890ppmN_2		4	1000				(g)
LKr	β, ^{207}Bi	2±0.2	91±2	-	0.4±0.2	-	(a)
	β, ^{207}Bi	2	85	-	0.49	-	(b)
	γ, ^{60}Co	-	80±10	-	-	-	(c)
	e^+, 0.35 GeV c^{-1}	2.0±0.1	95±3	11±2	0.18±0.01		(d)
	π^+, 0.8 GeV c^{-1}	2.9±0.1	95±3	13±2	0.23±0.01		(d)
	π^+, 1.5 GeV c^{-1}	3.0±0.1	92±3	12±2	0.22±0.01		(d)
	π^+, 2.1 GeV c^{-1}	3.3±0.1	95±3	12±2	0.22±0.03		(d)
	p, 0.8 GeV c^{-1}	2.8±0.1	87±4	-	-		(d)
	p, 1.5 GeV c^{-1}	2.8±0.1	95±3	12±2	0.20		(d)
	p, 2.1 GeV c^{-1}	3.3±0.1	95±3	12±2	0.22±0.03		(d)
SKr, 5.3 K	hν, 10.42 eV	5	100		10		(h)
LXe	α, ^{210}Po	3	22	-	25	-	(b)
	α, ^{252}Cf	4.3±0.6	22±1.5	-	0.45±0.07	-	(e)
	f, ^{252}Cf	4.3±0.5	21±2	-	1.6±0.2	-	(e)
	β, ^{207}Bi	-	34±2	-	-	-	(a)
	β, ^{207}Bi	-	33±1	-	-	-	(b)
	γ, ^{60}Co	-	25±3	-	-	-	(c)
	e, 0.6 GeV c^{-1}	-	46.1	-	-	-	(f)
	π^+, 1.5 GeV c^{-1}	3.0±0.1	39±2	11±2	2.0±0.3		(d)
	π^+, 2.1 GeV c^{-1}	2.8±0.2	34±2	12±2	1.9±0.6		(d)
SXe, 4.2 K	hν, 8.86 eV	6	50		100		(h)
98 K	α, ^{241}Am	3.5	20.0	34.9	0.3	3	(i)
LKr+1.7%Xe	γ, ^{60}Co	8.7±0.6	29±2	-	2	-	(c)
	e^+, 0.35 GeV c^{-1}	2.5	63	10	2	0.1–0.2	(d)
	π^+, 0.8 GeV c^{-1}	2.7	73	12	5	0.1–0.2	(d)
	π^+, 1.5 GeV c^{-1}	1	61	12	10	0.1–0.2	(d)
	π^+, 2.1 GeV c^{-1}	3.0	62	10	10	0.1–0.2	(d)
	p, 0.8 GeV c^{-1}	3.3	63	10	5	0.1–0.2	(d)
	p, 1.5 GeV c^{-1}	1.9	90	16	5	0.1–0.2	(d)
	d^+, 1.5 GeV c^{-1}	2.3	60	17	10	0.1–0.2	(d)

References: a - [222]; b - [209]; c - [224]; d - [182]; e - [221]; f - [226]; g - [220]; h - estimated from data from [227]; i - [223]; intensities estimated from picture are shown in brackets.

4
Scintillation Detectors

The liquefied noble gases attracted attention as scintillation materials over fifty years ago. According to Birks [170], the first noble gas scintillation counter was constructed by Grün and Schopper in 1951 [228]. Scintillations of condensed heavy noble gases Ar, Kr, and Xe were first observed by Northrop [13]. Liquid helium scintillations were first reported by Thorndike and Shlaer [229] and by Fleishman et al. [230], while liquid scintillations were observed by Packard et al. [175]. Since that time many scientists have worked on development of these technologies. Among the most important steps were the exploration of scintillation properties of condensed noble gases, the development of spectrometers for nuclear radiation and homogeneous calorimeters for high-energy physics, and the exploration of the possibility of construction of liquid Xenon PET systems for medical imaging. In this chapter, we review the properties of condensed noble gas scintillators and the developments mentioned above.

4.1
High-Pressure Noble Gas Scintillation Detectors

Gas scintillation detectors are attractive because of the following [170]:

1. the near linearity of its scintillation response over a wide range of dE/dx and E;
2. the fast scintillation decay times;
3. the simplicity of obtaining good 2π and 4π geometry;
4. the flexibility of shape and size of the scintillation volume;
5. the control of stopping power obtained by variation of the gas pressure, which enables the conditions to be adjusted so that the charged particles of interest dissipate their energy completely in the gas while the sensitivity to more penetrating particles is limited.

However, to achieve reasonable detection efficiency it is necessary to use gases at high pressures. In the past, gas scintillators have been extensively used for the detection and spectroscopy of heavily charged particles, including fission fragments, low-energy nuclear reactions, etc. With the development of solid semiconductor detectors, these new techniques replaced the use of gas scintillators due to their significantly better energy resolution, less bulky devices, thin input windows and easy operation. Presently, the only area of continuing interest is the detection of thermal neutrons in pressurized ^{3}He. Thermal neutrons are effectively absorbed in ^{3}He, yielding a triton and proton, which share 764 keV nuclear fission reaction energy plus the kinetic energy of the incident neutron (actually, negligible for thermal neutrons). The absorption cross section of thermal neutrons is $\sigma_{th}(^3\text{He}) = 5333$ barns at 2200 m s^{-1}. The ^{3}He nucleus has the highest cross section for thermal neutron absorption, neglecting nuclides with resonance (n, γ) capture at thermal energy, as well as a relatively high cross section for elastic interactions of fast neutrons, demonstrating an advantage even over hydrogen in the range of > 3 MeV of neutron energy. Detection efficiency via elastic scattering is proportional to the gas pressure. Typically, gas pressures of < 2 MPa are used in proportional counters because of the technical difficulty of applying sufficiently high voltages to provide effective charge amplification.

In comparison to other ionization detectors, scintillation detectors do not require a high voltage bias, and much higher pressures can be used. Fast scintillation signals are convenient for the nanosecond range time measurements and can be used to trigger a few readout channels operating in coincidence. All these features help to suppress the gamma ray background.

4.1.1 Single-Channel Gas Scintillation Detectors

In his pioneering research, Engelke [231] had shown that a high-pressure gas counter filled with 1.8 MPa ^{3}He + 0.36 MPa Xe functions as an efficient neutron detector in the range of 0.1–6.0 MeV. A resonance reaction of ^{14}N(n,p)^{14}C has been used by Engelke in a sharp threshold scintillation detector of 0.5 MeV neutrons filled with 2.8 MPa Xe and 0.7 MPa N_2; the energy resolution of 29.5% FWHM was obtained. Observing a 3.2 MeV neutron resonance in the Ne(n, α) nuclear reaction with the detector filled with 1.8 MPa Ne + 0.36 MPa Xe, he demonstrated the pulse height resolution of 6.7%.

Soon after that, Baldin and Matveev [232] developed a counter containing 90% ^{3}He + 10% Xe at a pressure of 2 MPa. They found that the energy resolution is independent on energy in the range up to 2–3 MeV and consists of 14% FWHM. Aamodt et al. [233] constructed a ^{3}He scintillation neutron detector of 38 cm^3 volume working at room temperature and 24 MPa

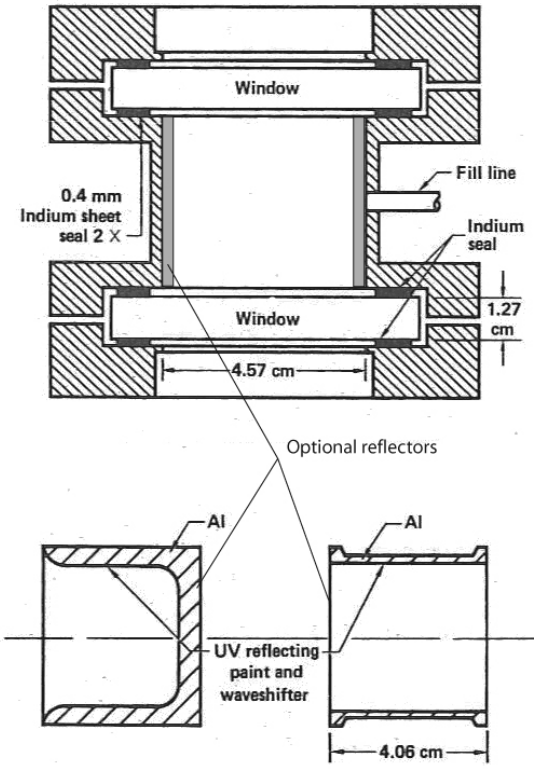

Fig. 4.1 High-pressure ^{3}He scintillation detector with two windows and optional reflectors for single (left) and two-channel readout [236].

pressure or 0.03 g cm^{-3} gas density, which is about half the density of liquid ^{3}He. However, the detector demonstrated relatively low energy resolution, probably because of poor efficiency of light collection from the large sensitive volume while not using any wavelength shifter. Better performance was demonstrated with the high-pressure scintillation detector developed by Evans [234, 235], who used an admixture of 0.5–1% xenon as a wavelength shifter. The parameters of this and some following developments are presented in the Table 4.1.

An example of typical construction of high-pressure ^{3}He scintillation neutron detector of this type is shown in Fig. 4.1. The high-pressure chamber is designed for both the one-window and two-window geometries. The active volume is defined by the aluminum reflectors, shown at the bottom. The surfaces of the reflectors were first coated with VUV high-reflectance paint and then with an optically thick p-terphenyl wavelength shifter coating. A thin layer of p-terphenyl was also applied to the internal window surfaces. The best results were achieved with quartz windows coated with p-terphenyl. The

detector was assembled with metal gaskets. Both ^{3}He and Xe were supplied from vessels maintained at 80 K and extended gettering was accomplished with titanium. To reduce personnel hazard in the event of window failure, the detector chamber and phototubes were placed inside a secondary containment constructed of aluminum. The chamber was lined with mu-metal to reduce external magnetic fields and by cadmium to shield against thermal neutrons.

In all those pioneering works, the use of photomultipliers as photoreceivers imposed the upper limit on gas pressure and made the construction bulky and hazardous. These first detectors were unsuitable because of the low efficiency of gamma background rejection compared to the gamma ray discrimination obtainable in proportional counter tubes. A new approach using solid state photodiodes mounted directly inside the high-pressure ^{3}He gas scintillator is investigated by Arodzero et al. [171]. Detectors of this type may operate at very high pressures and still be compact and rugged.

4.1.2
Multichannel Gas Scintillation Detectors

There have been at least two attempts in order to construct a two-channel ^{3}He scintillation detector. Derzon et al. [236] described the construction of a two-window scintillation detector, that potentially could be used as two-channel detectors, however, no results of testing the detector in two-channel mode were reported. A compact, two-channel, high-pressure ^{3}He scintillation detector (HeSD) with avalanche photodiode readout was constructed by Arodzero et al. [171]. The detector consists of two photodetectors with a 7-mm gap between them, which are mounted inside a stainless steel shell with ~1.5-mm thick and 25-mm diameter input windows. A schematic design of the detector is shown in Fig. 4.2.

The gap is filled with ^{3}He + 0.5%Xe gas under a pressure of 3.5 MPa. No electric field is applied to the gap. A para-terphenyl (p-TP) wave shifter with a thickness of 0.5 mg cm^{-2} was deposited on the surfaces of 16-mm diame-

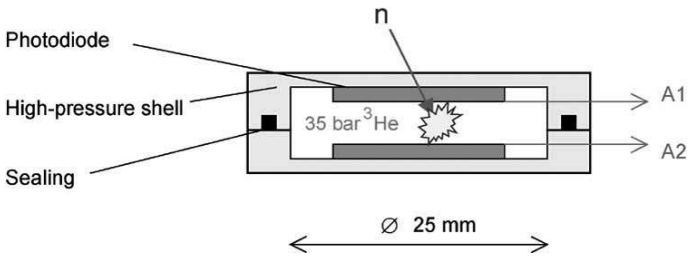

Fig. 4.2 Two-channel ^{3}He scintillation detector with avalanche photodiode readout [171].

ter silicon avalanche photodiodes of model SD7911 produced by Advanced Photonix, Inc. The photodiodes were operated at a gain of 300. The products of the ^{3}He(n,p) reaction are effectively stopped in the detector volume of ~ 1 cm^3 at 3.5 MPa pressure and higher. In the case of elastically scattered fast neutrons, the range of ^{3}He recoils is about 2 cm at 1 MeV. This requires the use of ~ 15 cm^3 detectors or a moderator to reduce the wall effect. The coincidence mode of operation of the detector makes it possible to analyze the correlation between values of scintillation signals received from different photodiodes.

Figure 4.3 presents two-dimensional distributions of individual signals measured in coincidence from the two photodiodes. The "fish-tail" area observed in Fig. 4.3a is associated with absorption of thermal neutrons at different points between the photodiodes. Events close to APD1, for instance, register higher on the APD1 axis, compared with the APD2 axis. The shape of the fishtail distribution represents position sensitivity of the detector to the location of thermal neutron absorption points. Different event concentrations in the two fans of the tail are a result of the location of the neutron source on the APD1 side of the device for this experiment.

The detector was also irradiated with a ^{137}Cs (662 keV) gamma source in order to estimate the sensitivity of the detector to gamma rays. It was found that gamma rays generate signals with average amplitude comparable to scintillations associated with absorption of thermal neutrons. However these gamma events result in a pulse height distribution without peaks. The two-dimensional distribution of gamma events has a completely different configuration (Fig. 4.3b) from that produced by thermal neutrons, probably because scintillating tracks of photoelectrons and Compton-scattered electrons bridge the gap between the photodiodes. Using the location of an event in the two-dimensional plot, the rejection of gamma rays can be further enhanced. The ability of the detector to reject events associated with direct interactions with photodiodes may be understood from Fig. 4.3c, representing the *A1 vs. A2* distribution in the anticoincidence mode.

4.2
Condensed Noble Gas Scintillation Detectors

4.2.1
Scintillation Detectors Using Liquid Helium and Condensed Neon

Liquid helium scintillators were investigated during the very early stages of the noble gas scintillators R&D. A reason is that due to very low operation temperature liquid helium is inherently pure because all organic and compli-

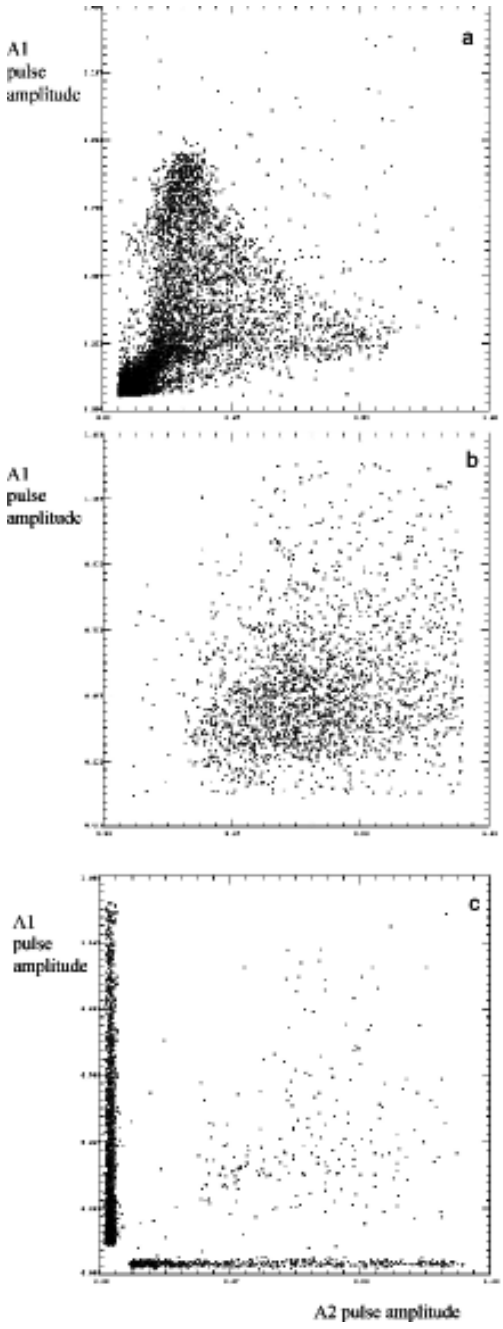

Fig. 4.3 Plot of A1 pulse amplitude vs. A2 pulse amplitude of scintillations generated by (a) neutrons and (b) ^{137}Cs gamma rays in coincidence mode and (c) anticoincidence mode measured by Arodzero et al. [171].

Tab. 4.1 High-pressure noble gas scintillation detectors.

	Pressure (MPa), size(cm)	WLS	Particle, Energy(MeV)	En. Res., % FWHM	Ref.
^{4}He	13.8; 5 I.D.×8.6	7%Xe, DPS	n, 1.0	36	[234]
Ne	1.7	20%Xe	n, 3.5	6.7	[231]
^{3}He	2.0	10%Xe	n, < 3	14	[232]
	3.5; 1.7×0.5	0.5%Xe, p-TP	n_{th}	18	[171]
	24.8; 38 cm^3	DPS	n_{th}	54	[233]
			α, 5.15	16	
	20.0; 4 I.D.×4	5%Xe, p-TP	n, 2.5	4.8	[236]
	13.8; 5 I.D.×8.6	2%Xe, DPS	n_{th}	31	[235]
Xe	2.8	25%N_2	n, 0.5	29.5	[231]

Note: WLS - wavelength shifting; DPS - trans p,p'-diphenylstilbene; p-TP - paraterphenyl; n_{th} - thermal neutrons.

cated molecular admixtures are frozen out at these temperatures. First observations of the liquid helium as a scintillator date to 1959 [229, 230]. Emission spectra of scintillations of LHe excited by $\alpha(^{233}U)$ located at different depths in the liquid (0.5 mm (a), 10 mm (b), and 19 mm (c)) are shown in comparison with CsI spectrum (d) in Fig. 4.4. In the spectra observed by Fleishman, about 20% FWHM compares to 13% FWHM for CsI placed in the same light collection system. Absorption of wave-shifted light in the Lucite light guide was estimated to be 25%, so the possible energy resolution might be better.

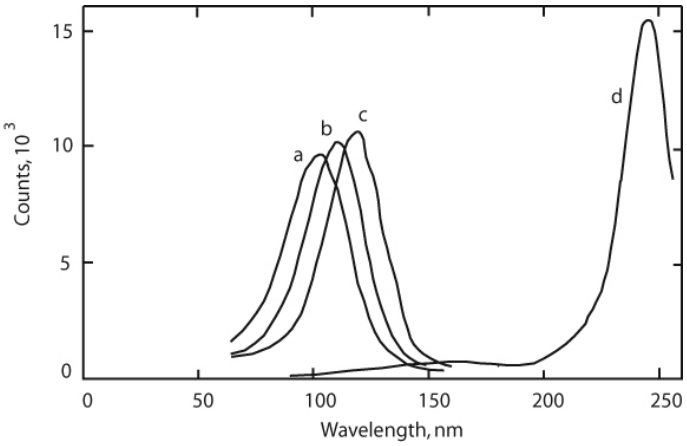

Fig. 4.4 Emission spectra of LHe excited by $\alpha(^{233}U)$ located at depths of (a) 0.5 mm, (b) 10 mm, and (c) 19 mm, shown in comparison with CsI spectrum (d). Redrawn from [230].

Soon after the first experiments, the liquid helium scintillator has been considered as an active neutron target for polarization experiments at energies near 20 MeV [187]. Their detector consisted of a LHe scintillator of about 3″×3″Dia [1] dimensions enclosed in a glass cryostat and viewed by an outside mounted photomultiplier tube through two Pyrex windows and aluminum light guide. The internal surface of the Pyrex windows contacted LHe was coated with 50–100 μg cm^{-2} p,p′-diphenylstylbene (DPS) wavelength shifter. The pulse height distribution from a source of ^{239}Pu alpha particles placed inside the flask with LHe was measured to be 25% FWHM. With this detector, the observation of Fleishman et al. [230] that the light output of wave-shifted scintillations in LHe is almost as strong as that of scintillations in CsI(Tl) scintillator has been confirmed. It was also found that the helium scintillation light suffers little, if any, attenuation in the liquid at distances of 10 cm. The detector was used to measured the neutron polarization from the T(d,n)^{4}He reaction. In these experiments, the LHe scintillation detector was operating in coincidence with a plastic scintillator and provided a time resolution of about 6 ns FWHM.

Accurate measurement of the lifetime of a neutron (which is unstable due to beta decay) is important for understanding the weak nuclear forces and creation of the matter from the Big Bang. Huffman et al. [237] investigated trapping of neutrons in liquid helium. The trapping region of a static magnetic trap was filled with superfluid ^{4}He, which is used to load neutrons into the trap and as a scintillator to detect their decay. Neutrons in the trap have a lifetime of 750^{+330}_{-200} s, largely limited by their beta decay rather than losses on trap walls. When a trapped neutron decays into an electron, a proton and an antineutrino, the scintillation flash is generated in liquid helium. The superfluid helium filled trapping region was surrounded by an acrylic tube coated with a thin layer of polysterene doped with organic fluor tetraphenyl butadiene (TPB). The TPB was used to shift the EUV scintillation light into blue light, a fraction of which was internally reflected down the length of the tube. The tube was optically coupled to a solid acrylic light guide that transported light to a window and into the second light guide which exited the dewar. The light was split into two guides that were each coupled to a photomultiplier tube. Background from uncorrelated photons was suppressed through requirement of coincident detection of at least two photoelectrons in each photomultiplier tube. The authors stated that the use of this technique would allow one to achieve a relative accuracy of 10^{-5} in determination of the neutron lifetime.

Solid and liquid neon scintillations excited by alpha (^{210}Po) and beta (^{113}Sn) particles were investigated by Michniak et al. [208]. The experimental cell containing the neon or helium and the radioactive source consisted of oxygen-free copper (alloy 101) tube connected via an indium seal to a thin stainless steel

1) A cylinder of 3″ height and 3″ in diameter

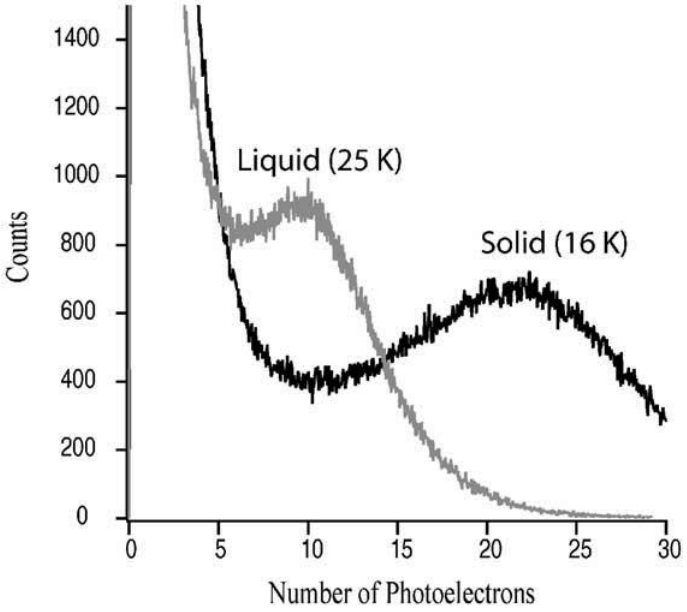

Fig. 4.5 Pulse height spectra of scintillations in liquid (25 K) and solid (16 K) neon excited by a ^{113}Sn beta source (364 keV) reported by Michiniak et al. [208].

tube hung vertically from a standard metal LHe cryostat. The cell was thermoinsulated from LHe bath via helium exchange gas jacket. The temperature was regulated with heater wrapped around the cell and pressure of the exchange gas. This design repeated a design of CRISA detector developed a few years before for investigation of the properties of LKr + Xe scintillators and light collection cells. A new construction element was a long acrylic light guide delivering the light from tetraphenyl butadiene (TPB) wavelength shifter at input surface immersed in the liquid to glass window at room temperature optically coupled to a photomultiplier. The sources have been placed at a distance of a few millimeters from the TPB-coated input window of the light guide. To maximize light collection, the light guide was wrapped with highly reflective Tyvek paper. The detector has been used for study of scintillation properties of the condensed neon and comparison liquid and solid neon scintillators with liquid helium scintillator. Figure 4.5 illustrates measured pulse height distributions from scintillations excited in liquid and solid neon by beta particles. The detector was used for investigation of properties of solid and liquid neon such as decay times and light output and comparison with that of liquid helium.

Liquid helium and neon are attractive candidates for large low-background detectors. Their low boiling points and weak interactions with surfaces allow

for them to be purified very efficiently using distillation and cold traps. Unlike other scintillators, there are no long-lived radioactive isotopes that could create a background in the detector.

4.2.2 Scintillation Detectors Using Liquid Argon, Krypton and Xenon

Liquid argon, krypton and xenon are considered as massive working media for large detectors such as high-energy ionization calorimeters, underground detectors for solar neutrino, and, most recently, for weakly-interacting massive particles (WIMPs), strong candidates for cold dark matter. Argon is the least expensive and most abundant noble gas available in large amounts from rectification of air. Xenon is the most massive of the stable noble gases, and is attractive for detection of gamma radiation (photoabsorption) and heavy particles (recoil nuclei) such as from WIMPs. Krypton in some particular cases may be considered as a less expensive substitution of xenon, though it is not suitable for low background measurements because of the large activities of ^{85}Kr and ^{81}Kr.

The detection process in the scintillation detectors includes the absorption of detected radiation and conversion of the absorbed energy into a number of photons, the collection of scintillation photons at the photodetector, and the conversion of the photons into the photoelectrons. The conversion efficiency of the scintillator, efficiency and uniformity of light collection, and the efficiency of detection of photons all directly affect performance of scintillation detectors. In particularly, variations in the output signals can deteriorate the energy resolution.

In 50 years of research and development in condensed noble gas detectors there have been constructed many different apparatuses utilizing the scintillation effect. Some of them have been used to measure energy of radiation, some to detect spatial coordinates directly from scintillation, and some of them use scintillation light as a trigger. In this section, we describe quite original or typical constructions and redirect readers looking for more detailed information to special reviews. The recent developments in condensed noble gas scintillation detectors have been reviewed by Doke and Masuda [206] and Lopes and Chepel [238].

4.2.2.1 Single-Channel Noble Liquid Scintillation Detectors

It is clear from previous consideration, that xenon is the best scintillator among other noble gases: it has the highest light yield, emits at longer wavelength, and it has the most intensive and fast scintillation and highest atomic number that makes it to be a very efficient absorber of electromagnetic radia-

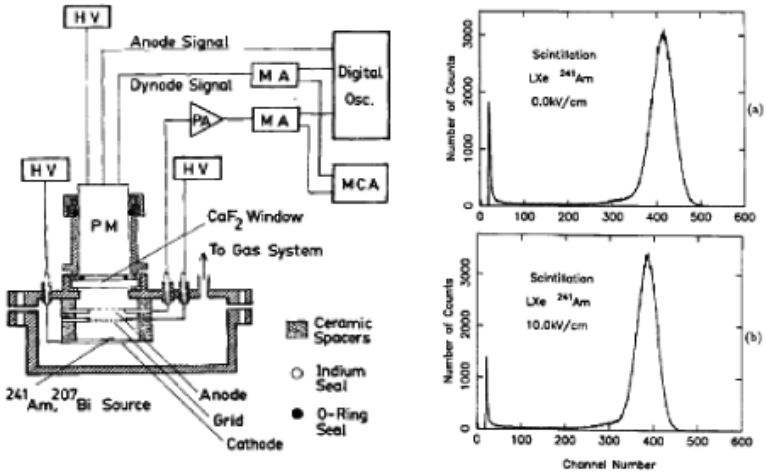

Fig. 4.6 Schematic view of the LXe detector and the associated electronics (left) used to measured pulse height spectra of scintillations excited by alpha particles (a) in absence and (b) in presence of a 10 kV cm^{-1} electric field [239].

tion: X-rays, gamma rays, and high-energy photons. The liquid phase allows construction of some of the most transparent massive scintillators. As the light yield of liquid xenon is similar to that of NaI(Tl), a similar energy resolution would be expected. In reality, the energy resolution of LXe scintillation spectrometers is always worse than that of the best crystal scintillators of equivalent mass and dimensions. This effect is mostly associated with technical difficulties in providing effective and uniform light collection of UV photons from the bulk condensed noble gas scintillators.

Single-channel scintillation detectors have been mostly used at earlier R&D stages, for investigation of scintillation properties of the noble gases, development of effective light collection structures, and for triggering time projection chambers. For example, Aprile et al. [239] used a UV-sensitive photomultiplier installed behind a CaF_2 window viewing a gridded ionization chamber filled with liquid xenon as shown in Fig. 4.6. The detector has been used to investigate the influence of electric field on scintillation signal generated by alpha and beta particles in liquid xenon. With this detector, one of the best energy resolutions for alpha particles was measured. A similar detector design was used by Baum et al. [223] for investigation and comparison of scintillation properties of liquid and solid xenon scintillators and Arneodo et al. [77] for demonstration of linearity of response of a liquid xenon scintillator with

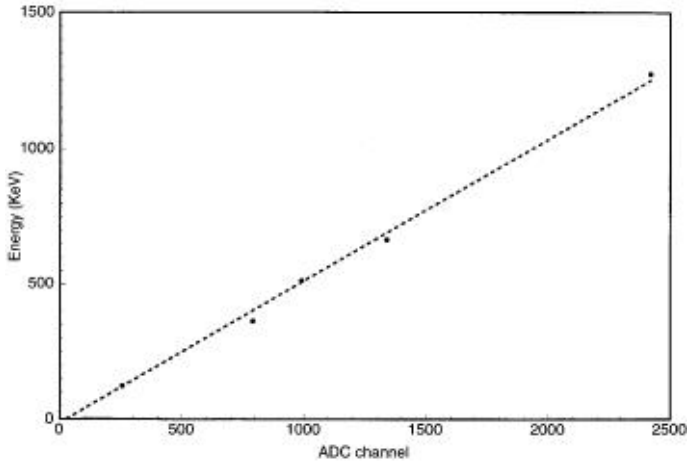

Fig. 4.7 Linearity of deposited energy vs. scintillation response acquired from a detector filled with liquid xenon and excited with gamma radiation from ^{57}Co (122 keV), ^{133}Ba (356 keV), ^{22}Na (511 and 1275 keV), and ^{137}Cs (662 keV) gamma ray sources placed outside the detector [77].

radioactive sources (Fig. 4.7) and the scintillation efficiency of nuclear recoils produced in the elastic scattering of neutrons.

The difference is that Arneodo et al. [77] used a bottom mounted photomultiplier viewing the LXe scintillator through a window that was optically coupled to the liquid. This resulted in an improved detector efficiency, estimated to be about 1 photoelectron per keV of the absorbed energy. A "quenching factor" (for details, see Section 2.6) was obtained by comparing the LXe scintillation response to xenon nuclear recoil of given energy with LXe scintillation response to gamma rays of the same energy in the energy range between 50 and 110 keV.

In the detector shown in Fig. 4.8, photomultipliers have been directly immersed in liquid noble gas scintillators [182]. This detector has been used for study of the decay times of LKr, LXe and their mixtures excited by high-energy particles and for the development of the light collection cell for EM calorimeter with uniform response function. A vertical chamber of about 70 cm in length and 5 cm in diameter allowed for the studying of a full scale cell for EM calorimeters with a PMT installed on one side of the cell. For the investigation of decay times and attenuation length the cell had UV absorbing walls. Calorimeter cells made of aluminized Mylar with deposited wavelength shifter were used. For decay time measurements, a diaphragm was installed in front of the PMT operating in single photon mode. A data-acquisition system was triggered with a telescope of plastic counters, time-of-flight spectrometer, and magnetic spectrometer in order to select certain par-

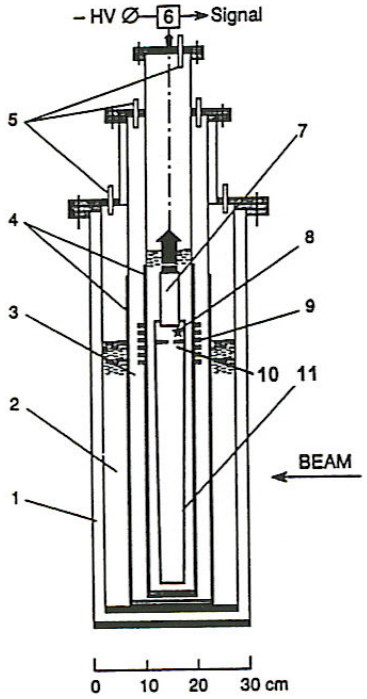

Fig. 4.8 Detector CRISA, used for measurements of scintillation in LXe, LKr, and their mixtures excited by relativistic particles at ITEP accelerator. 1 - vacuum cryostat, 2 - liquid nitrogen jacket, 3 - nitrogen gas jacket, 4 - copper screens, 5 - gas inlets, 6 - PMT base, 7 - 30-mm diameter FEU-85 photomultiplier with p-terphenyl coated glass window, 8 - reference alpha source, 9 - heater, 10 - optical diaphragm, 11 - optical cell with UV light absorbing walls [182].

ticles with certain momenta. A single-photon signal from the PMT served as a stop signal for time-to-digital converter. An alpha source installed near the PMT window was used for calibration. The chamber was surrounded with a gaseous nitrogen heat-exchange jacket and liquid nitrogen bath. The temperature was controlled with accuracy better than 0.5 K with heater and pressure of the nitrogen gas. A motion table allowed for scanning of the detector with a high-energy particle beam in order to measure light attenuation and response function of light-collecting cells. A few different PMTs have been used in the detector including a 1-inch diameter PMT with MgF_2 window and glass PMT FEU-85.

The energy and time resolution properties of the above and some other single-channel scintillation detectors are presented in Table 4.2.

Tab. 4.2 Detection properties of single-channel condensed noble gas scintillation detectors.

	Size and WLS	Particle	Time res., ns	ER (% FWHM)	Ref.
LHe	3″×3″	n, 22 MeV	6	30	[187]
	DPS	$\alpha(^{239}Pu)$		25	
LNe	200 cm^3	$\alpha(^{210}Po)$		50	[208]
	TPB	$\beta(^{113}Sn)$			
SNe		$\alpha(^{210}Po)$		∼50	
LAr+2%Xe	35mm ϕ	$\alpha(^{241}Am)$		26	[240]
	MnF_2/Q-PMT				
LKr	(15×15)×40×(29×29)	*e*, 300	0.9	11.8/	[182]
	cm^5	MeV		/(E, GeV)$^{1/2}$	
LXe	40 mm ϕ/p-TP	$\alpha(^{212}Pb)$		10.7	[223]
	40 mm ϕ PMT	$\alpha(^{241}Am)$		13	[239]
	CaF_2 window				
	50 mm ϕ PMT	$\alpha(^{210}Po)$		8.6	[241]
	Pirex/*ss*				
	35 mm ϕ	$\alpha(^{241}Am)$		22	[240]
	MnF_2/Q-PMT				
	16 mm ϕ	$\alpha(^{241}Am)$	0.6	10 (G=120)	[242]
	Windowless LAAPD		(G=605)		
	16 mm ϕ	$\alpha(^{241}Am)$		6.1 (G=57)	[243]
	Windowless LAAPD	$\beta(^{207}Bi)$		17.6 (G=146)	

Note: WLS - wavelength shifter; ER - energy resolution; ϕ - diameter; *ss* - sodium salicylate; DPS - p,p′-diphenylstilbene; TPB - tetraphenyl butadiene; p-TP - *para*-terphenyl; G - gain in avalanche photodiode; Q-PMT - photomultiplier with quartz window.

4.2.2.2 **Multichannel Noble Liquid Scintillation Detectors**

The first successful two-channel scintillation detector filled with liquid xenon and working in coincidence mode was developed by Barabanov et al. [244]. They used a cylindrical quartz vessel coated inside with a Teflon reflector. Both ends of the cylinder were sealed with photomultipliers with quartz windows. The dimensions of the cylindrical volume filled with liquid xenon were a 27-mm diameter and 12 to 30-mm length. The detector was tested as a gamma spectrometer in the range of energies between 26 keV and 1275 keV. With the Teflon reflector, an energy resolution of 12% FWHM was measured at 122 keV (^{57}Co), scaling approximately as $1/(E_\gamma)^{1/2}$ for the lower energies measured. However, for higher energies, the energy resolution was worse than expected in accordance with this dependence. That is a result of nonuniformity in light collection that affects mostly the high-energy range of gamma

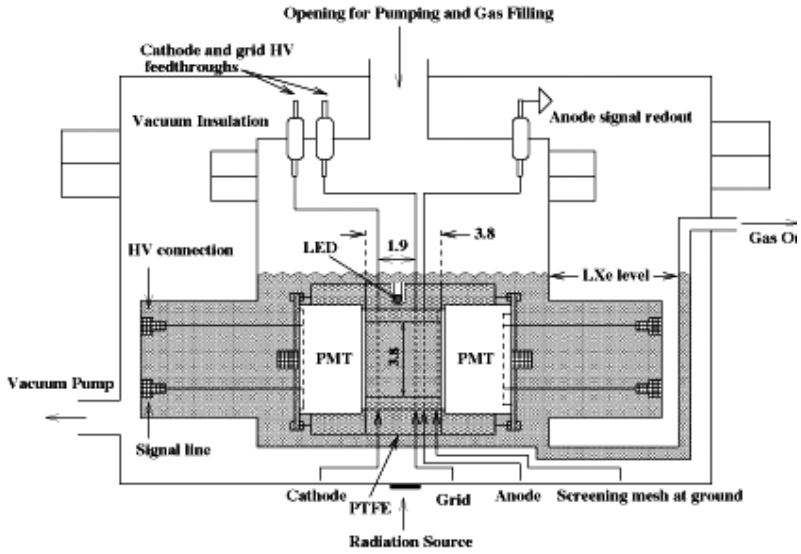

Fig. 4.9 Schematic view of the two-channel LXe scintillation detector with PMTs immersed in the liquid xenon; the vacuum cryostat is not shown, all dimensions are given in millimeters [246].

radiation absorbed over the bulk liquid xenon. Nevertheless, this approach was used in a real experiment, setting the best limit on the lifetime of neutrinoless beta decay of the ^{136}Xe isotope. The detector used in the experiment consisted of a vessel of 110-mm diameter and 33-mm length with a Teflon reflector viewed by two quartz window photomultipliers of model Hamamatsu R877. The energy resolution of the detector at the energy of $2\beta0\nu$-decay of ^{136}Xe (2.278 MeV) was obtained to be 10% FWHM [245].

The idea of using two-channel coincidence readout from cylindrical detector has been further explored in the course of development of liquid xenon detectors for ZEPPLIN, XENON, and XMASS experiments searching for cold dark matter in the form of weakly-interacting massive particles (WIMPs).

A schematic view of the detector used by Aprile et al. [246] for studying the quenching factor in the liquid xenon is presented in Fig. 4.9. The detector allows simultaneous measurement of ionization and scintillation signals produced by radiation in 21 cm^3 active volume. The volume is defined by three transparent wire meshes as cathode, grid and anode of an ionization chamber with a 2 cm drift gap. The scintillation is detected by two VUV sensitive compact metal channel photomultipliers directly coupled to the sensitive LXe volume. The data acquired with a digital sampling oscilloscope LeCroy LT374 triggered by NIM coincidence logic. The analog signals from the LXe

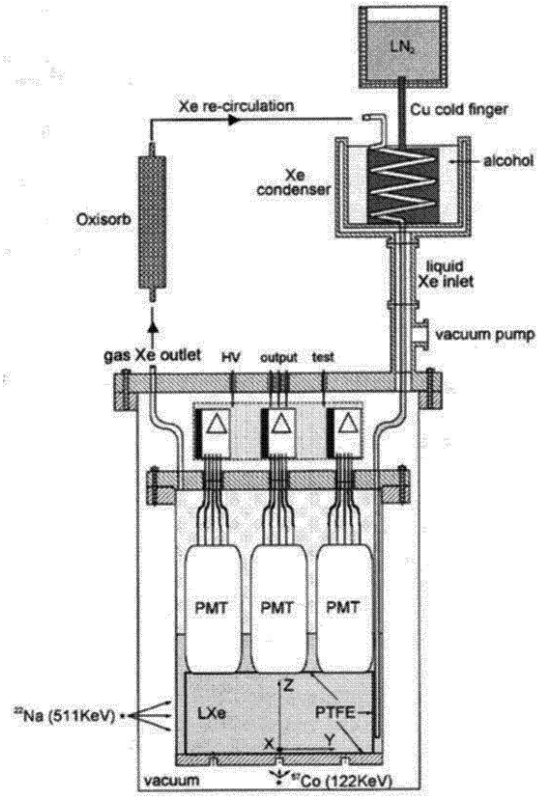

Fig. 4.10 Schematic drawing of the seven-channel LXe scintillation detector constructed by Neves et al. [247] for investigation of the scintillation efficiency and decay time due to nuclear recoils and gamma rays.

PMTs and the outside located PMT were split, with one copy going to a discriminator for each channel. The amplification and discrimination on the LXe channels was set to achieve a single photoelectron threshold. The triple coincidence among the two LXe PMTs and the outside PMT within 150 ns was used to trigger the oscilloscope. The recorded waveforms were transferred to a computer for off-line analyses. The detector was used for simultaneous measurements of scintillation and ionization signals from nuclear and electron recoils in LXe. Correlations between these two sorts of signals are expected to provide a power tool for discrimination of the background in XENON experiment. The sensitivity of the light collection system was found to be 6 photoelectron per keV allowing measurement of the scintillation efficiency of Xe recoils with energies down to 10.4 keV.

Increasing detector dimensions and mass of active detector volume requires increasing the size of photodetectors. The natural step in development of such

a detector is the exploration of the detectors with an array of PMTs. Neves et al. [247] built a detector with array of seven photomultipliers in order to improve light collection efficiency. The active volume of liquid xenon (about 1.2 L) is defined by PTFE cylindrical reflector with a diameter of 163 mm and 55 mm high, a flat bottom PTFE sheet, and the top PTFE disk with seven openings for Hamamatsu R2154 photomultipliers placed in direct contact with liquid xenon (Fig. 4.10). The photomultipliers have a 2″ diameter quartz window and bialkaline photocathodes kept at ground potential. An energy resolution of about 18% FWHM and 22% FWHM was obtained for 122 keV and 511 keV, respectively. The time resolution was measured with 511 keV gamma rays and consisted of values between 3.0 and 4.4. ns FWHM for deposited energies ranging from 105 to 20 keV. Analyzing amplitude distributions for the seven PMTs allows for reconstructing scintillation images in the plane of the PMT photocathodes (Fig. 4.11). Reconstruction of images for two positions of 122 keV gamma ray source was used to estimate the position resolution to be $\sigma = 6.9$ mm. The detector was used to study the scintillation efficiency and decay times due to nuclear recoils and gamma rays.

A significant improvement of the efficiency of light collection may be achieved in a detector with totally active walls or detectors with arrays of PMTs covering all inside surfaces. Mihara et al. [248] reported development of a prototype for detection of high-energy photons in the MEGA experiment searching for $\mu \longrightarrow e\gamma$-decay forbidden in the standard model, using a continuous muon beam at a PSI accelerator facility.

The detector has an active volume of 2.3 L ($11.6 \times 11.6 \times 17.4\,\mathrm{cm}^3$) viewed by 32 UV-sensitive PMTs assembled in a rectangular shape vessel as shown in Fig. 4.12. The PMT has a fused silica window with an effective diameter of 4.6 cm and is capable of stable operation at a temperature of 165 K. The quantum efficiency at 175 nm and normal temperature of operation is about 7%. A metal channel dynode structure of the PMT allows for reduction of the overall length of the PMT. Signals from PMTs are processed with charge-sensitive analog-to-digital converters (ADCs) and high-resolution time-to-digital converters (TDCs) after pulse discrimination. The summed signal from several PMTs is used as a trigger. The detector was placed inside a large chamber filled with liquid xenon as shown in Fig. 4.12b. Liquefaction of xenon is achieved by transferring liquid nitrogen through the copper pipe installed inside the detector.

In order to study the energy, position, and time resolution of the detector, several gamma ray sources ranging from 320 keV to 1835 keV in energy were placed in the center of one side of the array as shown in Fig. 4.12a. For monitoring and calibration of PMTs, the α-source (^{241}Am) and light flashed from the light-emitting diode fed into the detector through fibers have been used.

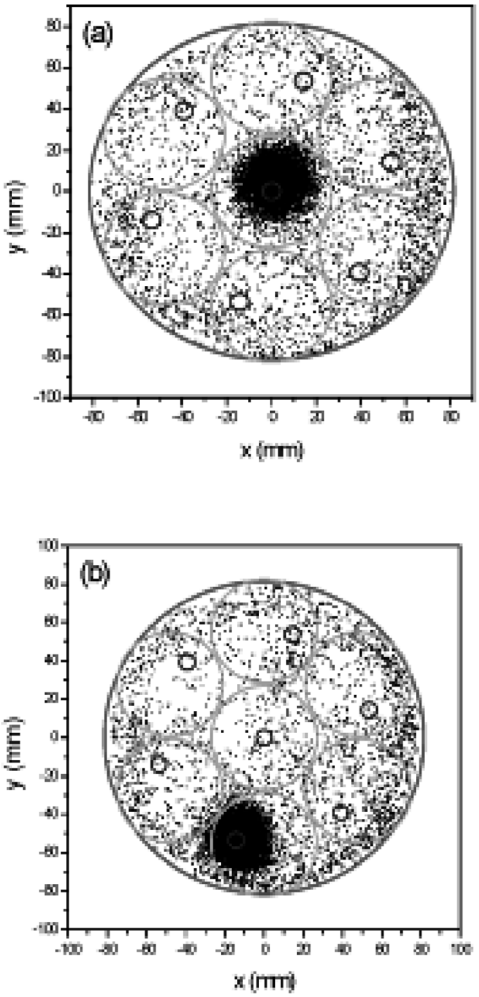

Fig. 4.11 Reconstructed position of the scintillation points due to 122 keV γ-rays from a ^{57}Co source, placed (a) at the bottom of the chamber below the central collimator hole and (b) below a noncentral position. The large circle corresponds to the active volume of the liquid xenon, medium circles outline the photomultipliers and the small circles indicate the holes in the collimator [247].

The results presented in Figs. 4.13 and 4.14 reveal that, speaking in terms of a sigma of Gaussian distribution, it is feasible to achieve an energy resolution of 0.76%, the position resolution better than 3 mm, and a time resolution of better than 50 ps for 52.8 MeV gamma rays.

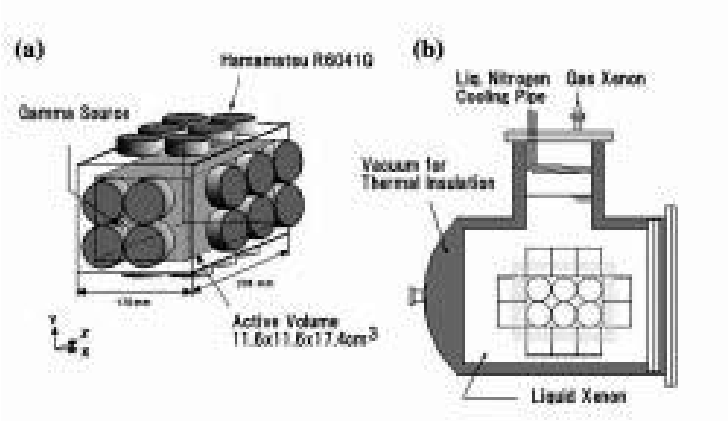

Fig. 4.12 Schematic drawing of the detector prototype for MEG experiment at PSI [248].

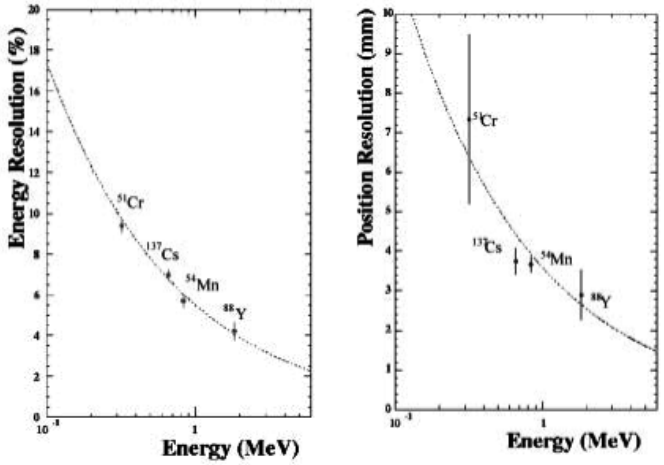

Fig. 4.13 Energy (left) and position (right) resolution of the MEG prototype detector measured with radioactive sources in comparison with simulations (dashed line) as reported by Mihara et al. [248].

4.3 Development of Scintillation Calorimeters

Calorimeters are detectors used to measure the energy of high-energy particles. In order to achieve good energy resolution, calorimeters should provide high stopping power, i.e., they should effectively absorb high-energy particles and the products of their interactions with the detection medium. In the process of absorption *showers* are generated by cascades of interactions, hence the occasionally used name *shower counter* for a calorimeter. The calorimeters transfer the absorbed energy into measurable quantities such as free elec-

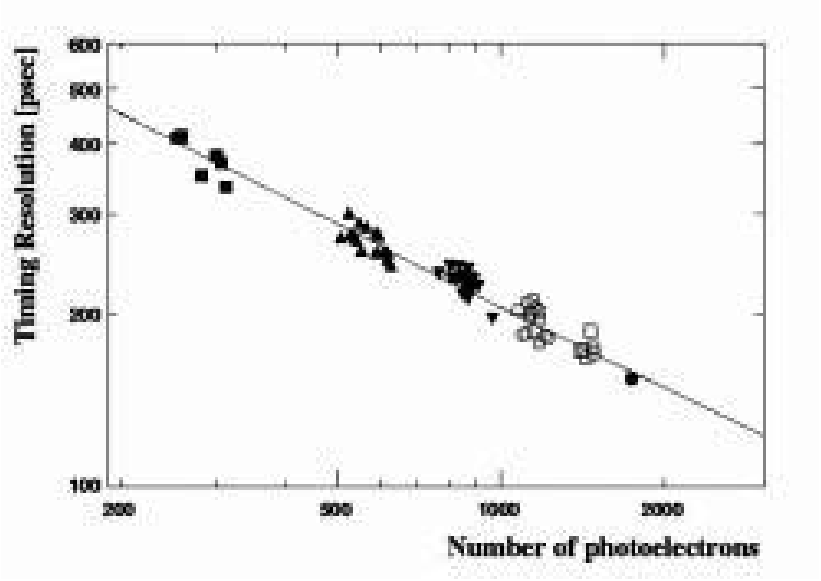

Fig. 4.14 Time resolution of the MEG prototype detector as a function of the observed number of photoelectrons [248].

trons or light photons that can be effectively collected and measured with modern electronics. Calorimetry is the only practicable way to measure the energy of neutral particles among the secondaries produced in high-energy collisions. In their dependence on their measured interactions of the measured radiation, calorimeters are divided into electromagnetic, used mainly to measure electrons and gamma rays through their electromagnetic interactions (bremsstrahlung, pair production, Compton effect, photoabsorption), and hadronic calorimeters, used to measure mainly hadrons through their strong and electromagnetic interactions. They can be further classified according to their construction technique into sampling calorimeters and homogeneous calorimeters (for details, see review of Fabian and Gianotti [80]). Sampling calorimeters consist of alternating layers of an absorber, a dense material used to effectively absorb the energy of measured particles, and an active medium that provides the detectable signal. Homogeneous calorimeters use only one type of material that performs both the energy absorption and the generation of measurable signal. The homogeneous calorimeters usually provide better energy resolution (no "lost" energy deposited into the sampling materials) at the cost of a more expensive detector medium and more bulky construction. Heavy noble liquid scintillators are considered to be among the most promising media for homogeneous and very fast calorimeters. Applications of noble liquids in different types of calorimeters are reviewed in the Section 9.3.

In this section we will review R&D efforts on development of homogeneous electromagnetic calorimeters utilizing excellent scintillation properties of condensed noble gases.

Since heavy noble gases scintillate in the UV range, there are practical difficulties in light collection and point-to-point uniform response from the calorimeter bulk medium. There are two basic strategies that can be used for improving uniformity of light collection:

1. minimizing light losses on the walls of the scintillation cell or correcting response function from the cell with pattern of wavelength shifter;
2. surrounding scintillator with photodetectors (wall-less calorimeter).

4.3.1 Granulated Scintillation Calorimeters

With growing energy and luminosity of accelerators, the calorimeter spatial resolution becomes more important than energy resolution of the jets in reconstructing the invariant masses [249].

Fine-granulated calorimeters are needed for high-energy accelerator experiments in order to provide measurements of several showers at once. It is well known that very fine electromagnetic showers are needed for identification of neutral pions at energies of above a few GeV [250]. As the mass of new particles become larger, the weak bosons from the decay of these particles become more energetic and their decay products also more collimated with opening angle of about 10°, for example, for 1 TeV Higgs. In general [81], the grain specific size is chosen to be about R_{M} (in order to minimize the number of active cells and still provide good position sensitivity) and the thickness of the calorimeter should be $> 20\ X_0$ (in order to minimize the leakage of the energy out of the calorimeter). Most of the light will suffer several reflections in light collection cells. For this reason, internal surfaces of high reflectivity are needed. Attenuation and scattering of light in the medium will also lead to nonuniformities in light collection, which degrades the energy resolution.

4.3.1.1 UV Light-Collecting Cells

There are several known attempts to construct effective UV light-collecting cells with uniform response function. One of those is described by Braem et al. [194]. They used an apparatus shown in Fig. 4.15 for testing a rectangular light collection cell of dimensions $7.4\times7.4\times60$ cm^3 with a beam of 5 GeV electrons.

The light-collecting cell walls were made of 3-mm thick aluminum plates. The plates were lacquered to create a smooth surface and made into mirrors by vacuum depositing a layer of 70-nm thick aluminum. The aluminized sur-

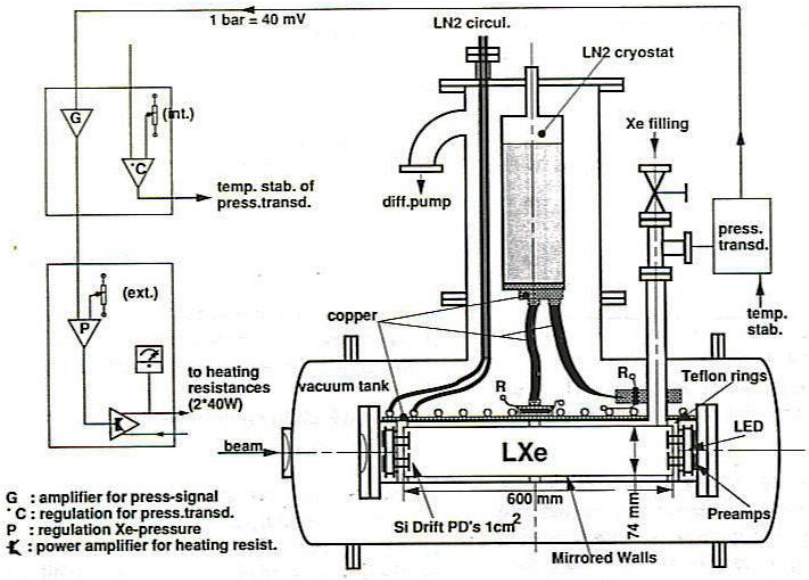

Fig. 4.15 Scintillation detector for investigation of light collection properties of reflective cells and UV photodiodes immersed in liquid xenon [194].

faces were then protected from oxidation by vacuum depositing 30 nm of MgF_2. The reflectivity was measured to be greater than 85% at 175 nm for all surfaces. Four silicone drift photodiodes of 1 cm^2 active area each were used for light collection. The light yield of scintillation in liquid xenon was found to be $(1.5\pm0.6)\times10^4$ photons per MeV of deposited energy. The data favor a light attenuation length of around 40 cm at wavelength of 175 nm. Experimental testing at a high-energy electron beam (CERN-PS T7) and Monte Carlo computer simulation agreed on the experimentally observed energy resolution $\sigma/E = 9.5\%$. The intrinsic energy resolution in liquid xenon is expected to be much better.

Chen et al. [251] used a similar apparatus and tested UV reflectors made of Kapton, aluminum, aluminum-coated glass, and Cu clad printed circuit board that was 0.29 mm thick and coated with Al and MgF_2 to obtain the reflectivity in the range of 85–90%. The best results have been achieved with thick (> 4 wavelength) coatings of MgF_2 providing an internal reflection effect in LXe. And still it was not good enough to support a uniform response along the cell of $(2.4\times2.4)\times27\times(3.5\times3.5)$ cm^5.

In order to improve the response function, a light collimator made of aluminum 8×8 grid (each of size $3\times3\times12$ mm^3) or 16×16 grid (each of size $1\times1\times3$ mm^3) were installed in front of the photodiode. However, as noted

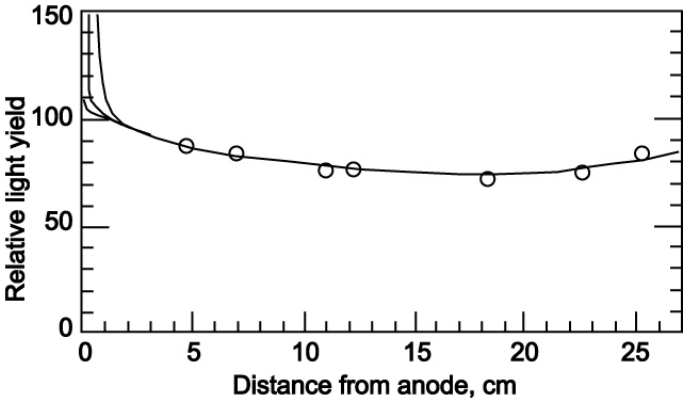

Fig. 4.16 Light collection efficiency of a light collection cell with internal reflection on MgF_2 vs. the distance to the photodiode for different light collimators installed in front of the photodiode (from top to bottom 8×8 grid and 12 mm deep, 32×32 grid and 3 mm deep, and 128×128 and 1 mm deep). Redrawn from [251].

by Doke and Mazuda [206], the flat response function (Fig. 4.16) was received by the cost of the loss of a large amount of scintillation light and it is in doubt that this method may be capable of supporting a precise energy resolution, especially at relatively low energy depositions.

4.3.1.2 Light-Collecting Cells with Wavelength Shifter

Another approach to achieving a uniform response from narrow and long light-collecting cell of granulated EM calorimeters has been developed by Akimov, and Bolozdynya et al. [42, 182, 190, 224]. The basic ideas of this approach are the following:

1. UV generic scintillation emission is wave-shifted into the visible wavelength range.
2. The photodetector is not sensitive to UV light but is sensitive to visible light.
3. Light-collecting cell is made of highly reflective material in the visible range.
4. Wavelength shifter distribution over the cell selected in order providing uniform light collection.

There are several advantages in this approach. First of all, the uniform response function can be relatively easily achieved (see below). Second, the purity of the working medium may be very moderate and relatively inexpensive glass PMTs may be used allowing construction of very large calorimeters

for very reasonable cost. And the third, maybe the most important, the light collection in very large volumes of LXe is essentially affected by Rayleigh scattering and the most effective way to reduce this effect is to shift 178 nm to a longer wavelength. For example, p-terphenyl wavelength shifter changes the spectrum to one around 340 nm; applying Eq. (3.39) we may estimate that this action increases the scattering length by $(340/178)^4 \approx 13$ times.

In the course of experimental investigation with the CRISA detector (see description in Section 4.2), a pyramidal reflector made of 50-μm aluminized Mylar with dimensions of $(2.1\times2.1)\times40\times(4.15\times4.15)$ cm^5 was developed. In order to provide longitude uniformity of the response function, each trapezoidal side of the pyramidal cell was coated with a single strip of p-terphenyl wavelength shifter as shown in Fig. 4.17.

The shape and dimensions of the strips were experimentally found to provide uniformity of the light collection along the cell. The longitudinal response function for two different cells is shown in the bottom of Fig. 4.17. The average yield in photoelectrons per MeV was defined to be 7 and 9.5 on average for LKr and LXe fillings, respectively. Very good longitudinal uniformity was achieved by the cost of essentially reduced integral light collection efficiency. Such a method can be accepted for precision calorimeters working with high-energy electromagnetic radiation. The performance of the developed light collection structure was limited because of inherent local transverse nonuniformity in the vicinity of the strips as shown in Fig. 4.18. This imperfection limits energy resolution achievable with this kind of distribution of the wavelength shifter in the low-energy range (< 1 GeV).

Computer simulations [182] revealed that a better result could be achieved using different patterns of the wavelength shifting strips, namely, perpendicular to the cell axis. In a more sophisticated approach, high uniformity may be achieved by deposition of WLS with a variable concentration along the cell.

4.3.1.3 **Scintillation Calorimeter LIDER**

Using Mylar light collection cells with wavelength shifter and a glass PMT detecting visible light, the full scale model of electromagnetic calorimeter LIDER has been constructed as shown in Fig. 4.19.

Forty-five 50-μm aluminized Mylar made cells of $(2.1\times2.1)\times40\times(4.15\times4.15)$ cm^5 dimensions were glued together. Wavelength shifting p-terphenyl strips deposited inside each cell provided the uniform response function as described in the previous section. An aluminum supplementer (not shown) supported the reflector structure and was used to reduce the volume of unused Xe (the useful volume of LXe was about 35 L). The heaters provided thermostabilization with an accuracy of 0.5 K. The temperature was measured at several points with copper-constantan thermocouples. The stability of each spectrometric cell was monitored with a pulsed nitrogen laser. The

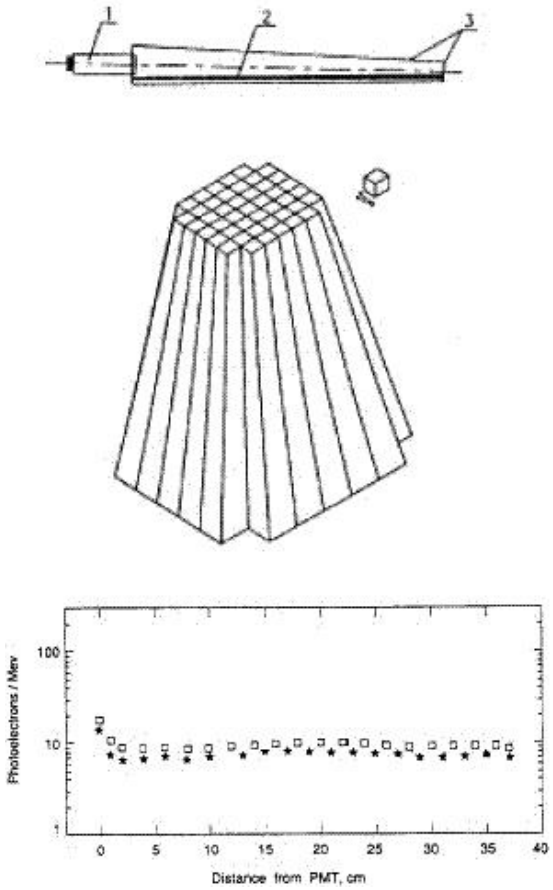

Fig. 4.17 Light-collecting pyramidal cell with p-terphenyl strip deposited at aluminized Mylar walls (top). Note: 1 - glass PMT FEU-85; 2 - p-terphenyl strip deposited at four sides of the pyramidal cell; 3 - aluminized Mylar. Pyramidal reflection structure consisted of 45 cells (middle), and the longitudinal response function for two cells of the reflector structure (bottom) [190].

laser pulse activated the plastic scintillator installed outside the cryostat. The intensity of the scintillation flash was monitored by a PMT. The flash of the scintillation light was delivered inside the cryostat through two (warm and cold) sapphire windows and accepted by a bundle of plastic optical fibers inside the cryostat. The fiber delivered the calibration signal to each of 45 photomultipliers viewing the reflector structure.

The LIDER was tested with LKr filling at 400 MeV electron beam at the ITEP (Moscow) accelerator and with LXe filling at a 106–348 MeV electron beam at BATES MIT accelerator. The energy resolution was measured to be $\sigma_E / E_e =$

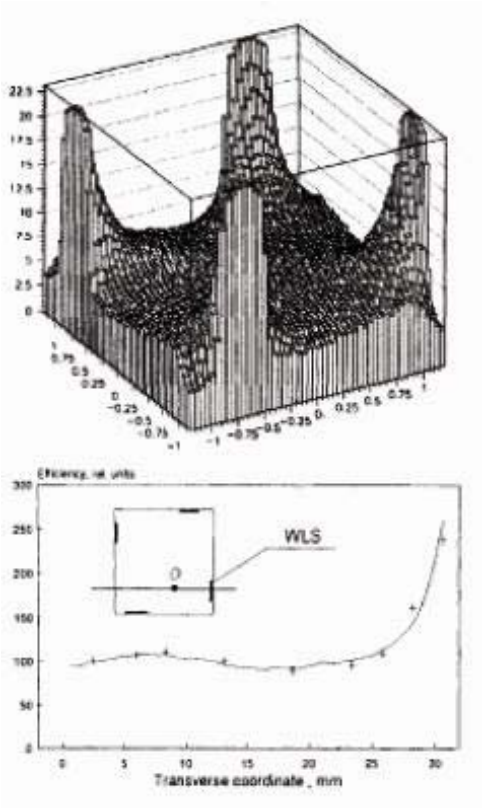

Fig. 4.18 Computer simulation of the transverse response function of the Mylar cell with longitudinal wave shifter strip (top) and the transverse response function measured with an alpha source driven across the cell (bottom) as reported by Akimov et al. [182, 190].

$5\%/\sqrt{E}$; the coordinate resolution for position of the core of the single shower was measured to be $\sigma_x = 0.7$ cm, the time resolution was $\sigma_t = 0.6$ ns for a single cell.

The experimental tests demonstrated good time properties and good position resolution in agreement with computer simulations. However, energy resolution was found to be worse than expected from GEANT simulations based on measured longitude response function for light-collecting cells. This was a result of inherent transversal nonuniformity for the chosen "one-strip-per-wall" light-collecting structure, which was not taken into account in the course of the simulations. Nevertheless, the experiments have shown that scintillation LXe EM calorimeters with fine-granulated light collection structure can be built for the next generation of high-energy accelerator experiments.

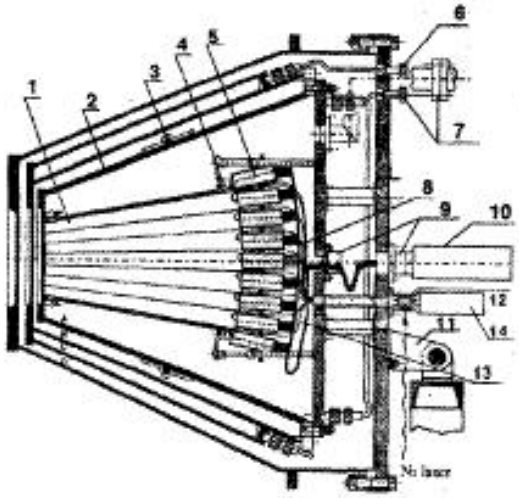

Fig. 4.19 Schematic drawing of the LKr/LXe scintillation calorimeter LIDER. Note: 1 - Mylar reflector; 2 - LKr/LXe vessel; 3 - heater; 4 support of Mylar reflector; 5 - PMT in the μ-metal magnetic shield; 6 - liquid nitrogen input; 7 - Kr/Xe gas input; 8 - PMT connection light; 9 - multipin metal-glass feedthrough; 10 - PMT divider; 11 - support; 12 - plastic scintillator; 13 - optical fiber; 14 - monitoring photomultiplier; A - vessel filled with LKr or LXe; B - nitrogen gas jacket; C - liquid nitrogen jacket; D - vacuum insulation [190].

At the R&D stage, a forward calorimeter called KryptonWall was proposed by the ITEP group for the Wide Angle Shower Apparatus (WASA) detector, currently installed at the CELSIUS accelerator of The Svedberg Laboratory (TSL) in Uppsala, Sweden (Fig. 4.20).

The KryptonWall was suggested to fill 700 L of mixture of LKr and Xe. The scintillation properties of the mixture have been shown to be similar to that of pure LXe [182]. Since the Molier radius of krypton is close to that of xenon, the transversal resolution of the calorimeter should not be dependent on the mixture composition. The thickness of the calorimeter is 40 cm of active medium, i.e., 8.5 X_0, if the LKr filling is used, and 14 X_0, if the LXe filling is used. The energy resolution is expected to be about $2\%/\sqrt{E(\mathrm{GeV})}$ if the transversal pattern of WLS strips is used. The expected time resolution should be similar to that measured with the prototype: 0.6 ns FWHM.

4.3.2
Barrel Scintillation Calorimeters

In 1996 Doke proposed a calorimeter, which has a sensitive volume completely surrounded by many photomultipliers in liquid xenon. In early 1997, Orito and Mori presented computer simulation showing that the energy resolution of this type of calorimeter for high-energy gamma rays will be better than

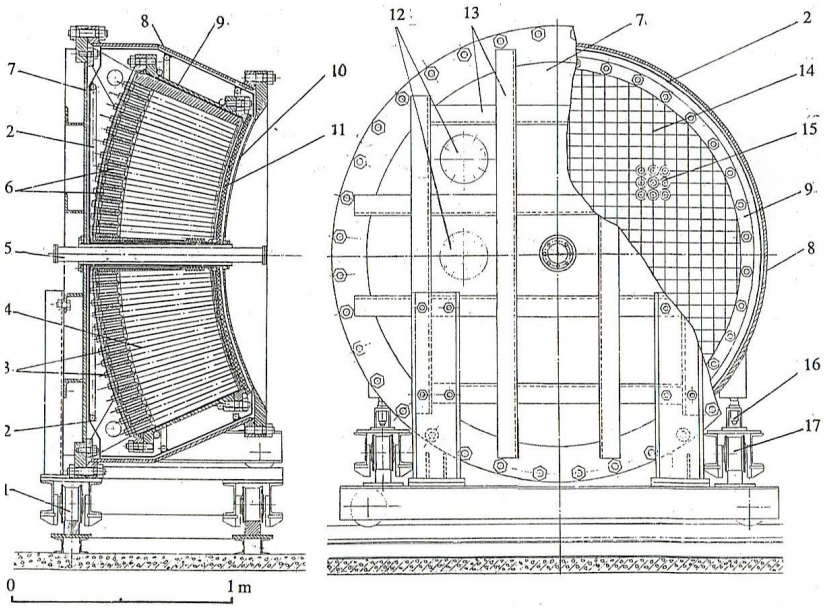

Fig. 4.20 Forward LKr+Xe scintillation calorimeter designed for the WASA installation: 1 - car for motion in direction normal to the beam; 2 - cold screen; 3 and 15 - feedthroughs; 4 - Mylar reflector coated with p-TP strips for uniform light collection; 5 - beam pipe; 6 - PMT array assembled with FEU-85 glass PMTs; 7 - back mounting plate supporting the PMT array; 8 - vacuum vessel; 9 - cooling jacket; 10 - input beryllium window; 11 - front cold screen; 12 - multipin feedthroughs; 13 - aluminum enforcing structure; 14 - frame supporting the PMT array; 15 - PMTs; 16 - leveling device; 17 - car for motion along the beam.

that obtained by crystal scintillators because of excellent liquid xenon homogeneity. In addition, this calorimeter can determine the interaction point with a gamma ray in the sensitive volume from differences in pulse heights from individual photomultipliers [252]. The idea was adopted for the $\mu \longrightarrow e\gamma$ decay search experiment at Paul Scherrer Institute, which is being made by the collaboration MEG [248, 252–254]. The decay is forbidden in the standard model of the electroweak and strong interactions. The present limit on this decay branching ratio is set to BR $< 1.2\times10^{-11}$ by the MEGA experiment [255]. The MEG experiment is aimed to achieve BR in the range of 10^{-12}–10^{-14} as predicted by supersymmetric theories of grand unification [256].

Recently, Baldini et al. [21, 189] reported results of the testing of the prototype for the MEG experiment. The detector uses approximately 100 L of LXe viewed by 240 PMTs inside the $40\times40\times50$ cm^3 box; the box is immersed in liquid xenon, which is kept cold by a high-power pulse tube refrigerator (Fig. 4.21). The box is equipped with blue LEDs for the PMT gain evaluation and monitoring, and with ^{210}Po alpha sources deposited on thin (100-μm di-

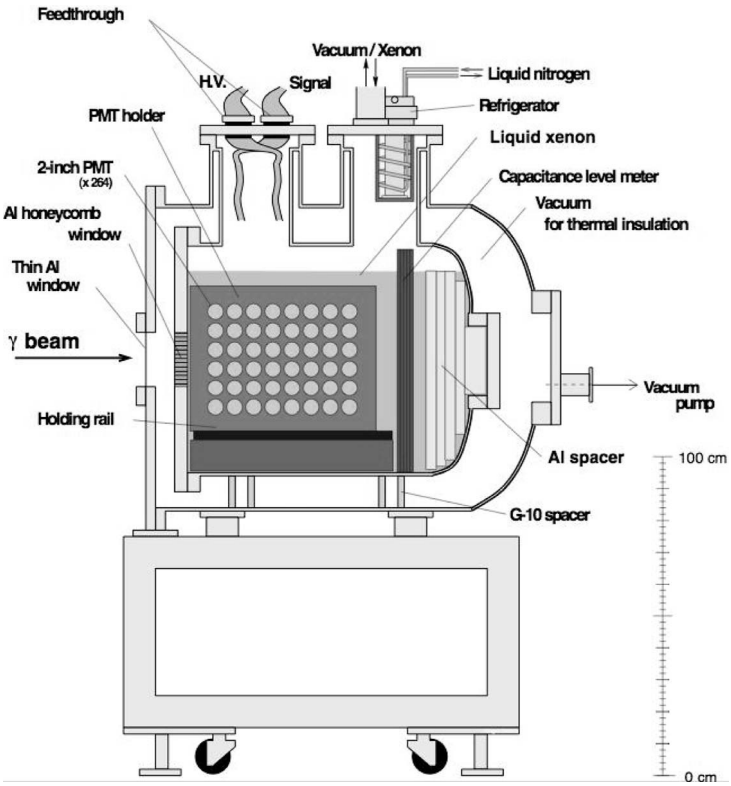

Fig. 4.21 A schematic view of the large prototype of the LXe scintillation calorimeter of barrel type for MEG experiment [21, 189].

ameter) tungsten wires suspended inside the detector volume. Xenon is continuously evaporated, passed through an Oxisorb cartridge, a molecular sieve and a hot metal getter and condensed back in the detector. During several weeks of operation, the absorption length of scintillation light was increasing and has reached $>$150 cm in four weeks. Mass-spectrometric analysis has shown the presence of water as a dominant impurity in xenon. Monte Carlo simulations have shown that the obtained purity level is sufficient to achieve an energy resolution better than 5% FWHM at 52.8 MeV. The detector was tested with 55 MeV photons from π^0 decays. Negative pions from πE5 beam line at the Paul Scherrer Institute were stopped on a liquid hydrogen target. Monochromatic neutral pions produced in the charge-exchange reaction $\pi^- p \longrightarrow \pi^0 n$ eventually decay in two photons. One of the photons is detected with the LXe detector while the other photon is detected by a crystal scintillation detector on the opposite side. Triggering the system on 83 MeV photons in the crystal scintillation detector, the 55 MeV photons were selected to hit the LXe calorimeter. The measured spectrum of 55 MeV photons was cleaned in

the following procedure. The photon conversion point inside liquid xenon was defined by fitting the charge distributions of the PMTs of the front face in order to select the photons inside the lead collimator acceptance. Then, those photons were discarded which convert at less than 2 cm in front of the PMTs. The resulting peak is shown in Fig. 4.22. A resolution of 4.9±0.4% FWHM was obtained.

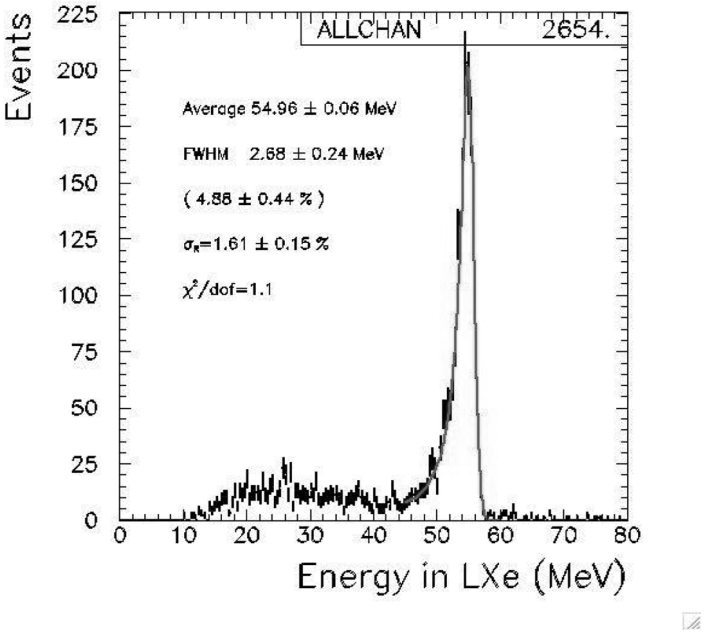

Fig. 4.22 Reconstructed spectrum of the 55 MeV photons measured with 100-L barrel scintillation calorimeter [21, 189].

With this result along with expectations for the other subdetectors, it was estimated that for a muon stopping rate on target of $1.2\times10^7\mu^+$ s^{-1} and a data-taking time of 3.5×10^7 s, the observation of no candidate for $\mu^+ \longrightarrow e^+\gamma$ decay set a limit on the branching ratio BR($\mu^+ \longrightarrow e^+\gamma$) $< 1.2\times10^{-13}$.

4.4 Time-of-Flight Scintillation Detectors

In 1976, Lavoie attracted attention to the fact that the fast response and high scintillation yield of liquid xenon could be used in the positron emission tomography (PET) and with the application of time-of-flight techniques, the recovery of additional spatial information would be possible [257]. At that time, most scientists were developing PET based on new crystals with fast re-

sponse, and high scintillation yield would be found in the near future. During the 1980s, the studies of scintillation decay shape in liquid xenon were mostly completed. It was found that the short decay time constants and the high scintillation yield of liquid xenon are superior to those of crystal scintillators. In 1997, Kikuchi proposed the use of a liquid xenon scintillator for time-of-flight position emission tomography (TOF-PET) and the Waseda group constructed and tested a prototype system [258, 259]. Doke, Nishikido and Kikuchi [260] have shown that the great merit of this approach is the reduction of background events.

A similar approach was explored by Gallin-Martel et al. [261] for development of a compact high-resolution PET camera based on position-sensitive PMTs and dedicated to small animal imaging. The combined method, with scintillation of LXe used for triggering a time projection chamber (TPC) was explored by Chepel [262] for PET application and a few different groups developing two-phase emission detectors for cold dark matter search in the form of weakly-ionizing massive particles [263–265]. We discuss these developments in the Chapter 9 devoted to applications of the noble gas detector technology.

The Waseda apparatus consisted of a pair of liquid xenon chambers 70 cm apart containing 32 photomultipliers each as shown in Fig. 4.23. Xenon for this apparatus was purified in convection circulation through a Ti-Ba getter. In the test, a ^{22}Na point source was put in the center of both chambers.

Figure 4.24 shows a block diagram of the electronic circuits used in the test. When two 511 keV photons from ^{22}Na were detected in both liquid xenon chambers, output signals from 32 PMTs were recorded with charge-sensitive analog-to-digital converters (QADCs) and the TOF information was recorded with time-to-digital converters (TDCs). The sum signals of 32 PMT outputs from each chamber were used as TDC stop signals. The nonuniformities of PMT characteristics were corrected by the following method before the interaction position was calculated. The number of photoelectrons in each PMT produced by scintillation light from a point alpha source in liquid xenon was calculated by a Monte Carlo simulation. The product of the quantum efficiency and the gain of each PMT were corrected so that the experiment data corresponds to the simulation data.

The positions in which a gamma ray interacts are determined by calculating the center of gravity of light outputs from individual PMTs after the calibration by alpha source. The positions of X, Y and Z are defined by the following equations:

$$X = (1/N)\sum X_j N_j, \quad Y = (1/N)\sum Y_j N_j, \quad Z = (1/N)\sum Z_j N_j \qquad (4.1)$$

where the total number of photoelectrons is $N = \sum Nj$, Nj is the number of photoelectrons, and X_j, Y_j, and Z_j are the positions of individual PMTs. The

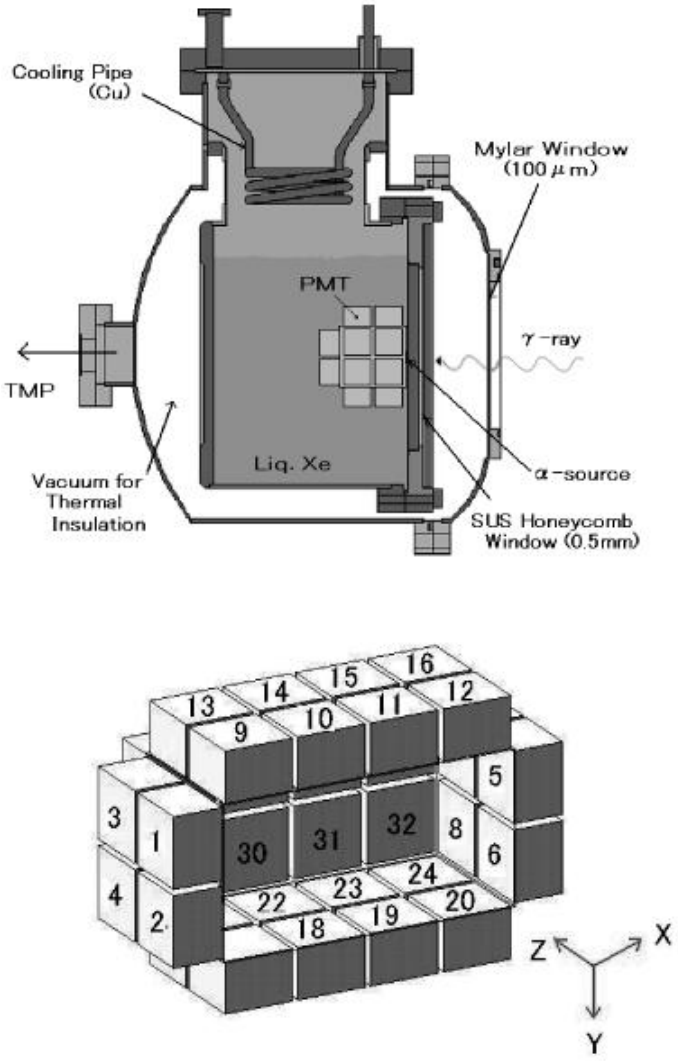

Fig. 4.23 Cross sectional view of the prototype of liquid Xe TOF-PET chamber (top) and array of 32 PMTs (bottom) used in this apparatus [258, 259].

position distributions for annihilation gamma rays in XY, XZ and YZ planes inside the effective area are shown in Fig. 4.25.

The energy spectrum was measured by summing the signals from all 32 PMT outputs in each liquid xenon chamber. The PMT outputs depend on the solid angles of individual PMTs from interaction points. The energy resolution in the central volume (-2.5 mm $< X <$ 2.5 mm; -2.5 mm $< Y <$ 2.5 mm;

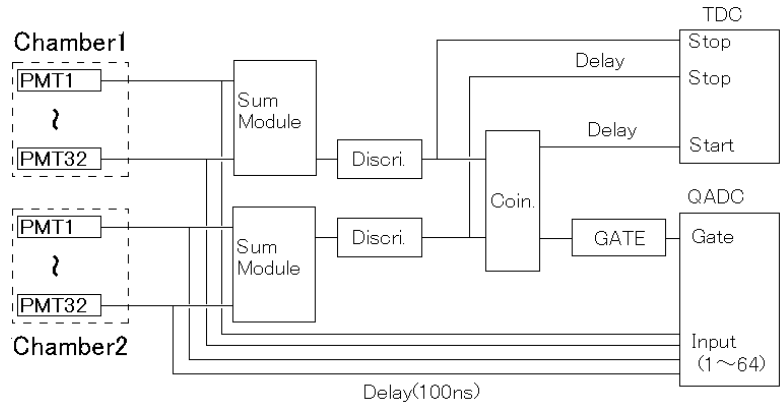

Fig. 4.24 Block diagram of data acquisition system used in the LXe TOF-PET chamber [259].

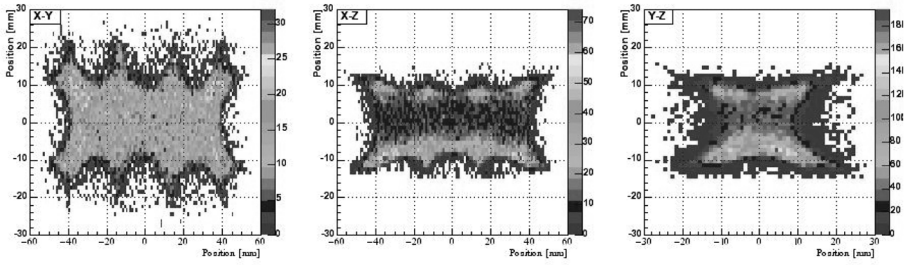

Fig. 4.25 Position distributions of the interaction points for annihilation gamma rays in XY, XZ and YZ planes inside the sensitive volume of the LXe TOF-PET chamber [259].

-2.5 mm $< Z <$ 2.5 mm) was measured to be 15.9% FWHM. The average value of energy resolution in the volumes of $5\times5\times5$ mm^3 over the effective volume was 20.5% FWHM.

The position resolution in each liquid xenon chamber was estimated by the following method. The PMTs are divided into two groups by the YZ plane at $X = 0$, and an interaction position is decided by calculating the center of gravity of PMT output signals in each group (Z_L, Z_R). The difference in Z_L and Z_R is expressed as $Z_{\Delta Z} = Z_L - Z_R$. Assuming Z_L and Z_R are independent, the width of the $Z_{\Delta Z}$ spectrum is expressed as

$$\sigma_{Z^2} = \sigma_{ZL^2} + \sigma_{ZR^2} \tag{4.2}$$

where σ_{ZL} and σ_{ZR} are position resolution of Z_L and Z_R, respectively. In the central volume (-2.5 mm $< X <$ 2.5 mm; -2.5 mm $< Y <$ 2.5 mm; -2.5 mm $< Z <$ 2.5 mm), $\sigma_{\Delta Z}$ was 2.9 mm (FWHM). Assuming $\sigma_{ZL} = \sigma_{ZR}$, a position resolution of 2.1 mm (FWHM) is obtained by dividing by $\sqrt{2}$. Similarly, the

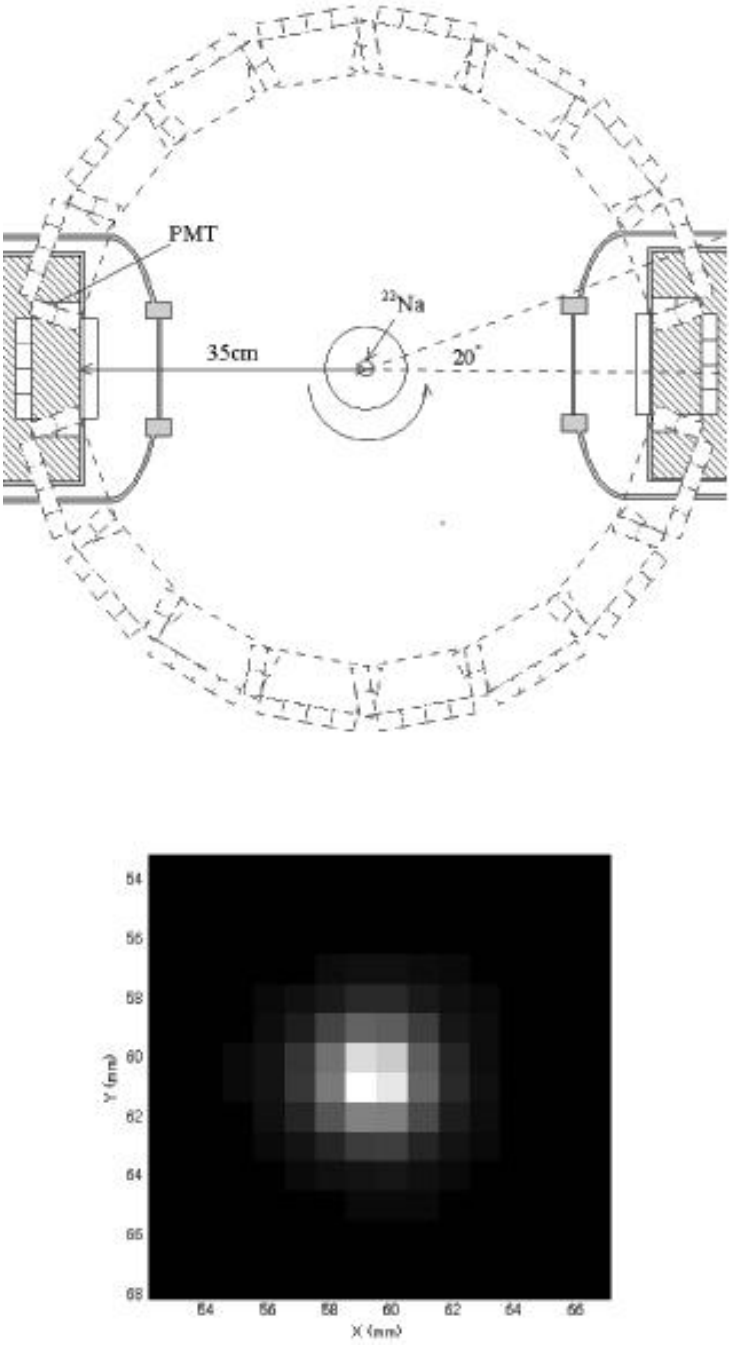

Fig. 4.26 Conceptual design of LXe TOF-PET composed with a schematic drawing of the imaging test (top) and reconstructed image of the ^{22}Na point sources (bottom) as reported by Nishikido et al. [259].

position resolutions of the X and Y-axes for the liquid xenon chamber 1 were 3.3 mm and 3.5 mm (FWHM).

A time resolution of 552 ps was obtained. This value is affected by the time difference between interaction positions and PMTs at each interaction point. However, if only the events in the central volume (-2.5 mm $< X <$ 2.5 mm; -2.5 mm $< Y <$ 2.5 mm; -2.5 mm $< Z <$ 2.5 mm) are selected, a time resolution of 260 ps is obtained. The average value of timing resolution in the volumes of $5\times5\times5$ mm^3 over the effective volume is 312 ps.

The following experiment was performed to estimate the position resolution of a reconstructed image. Because there were only two liquid xenon chambers in this experiment and the chambers cannot rotate around the center of the field of view, a ^{22}Na point source was put on the center of a turntable in the center of both chambers and measured with the prototype liquid xenon PET chambers by rotating the turntable every 20° (that is, at nine angles). The conceptual scheme for imaging test an image of the point source reconstructed by the maximum likelihood expectation maximization (ML-EM) algorithm are shown in Fig. 4.26. The locations of an array of photomultipliers drawn by the dotted line represent position relationships at each table angle. The position resolution of the reconstructed image at the center of the field of view is 3.3 mm (FWHM).

5
Ionization Detectors

Since ionizing particles interacting with noble gases generate both free carriers and fluorescent photons, ionization detectors can operate in charge and/or light collection modes. In the charge collection mode the output signals are generated by charge carriers drifting under influence of the electric field in the sensitive (active) area of the device. Only electrons are actually collected because the mobility of the positive ions is very low and their transport can be completely neglected. This means that a noble gas detector is a single-carrier device. The light generated during the primary ionization process is called the primary scintillation and can be also used to generate output signals in the noble gas ionization detectors. In some cases, it is very beneficial to measure signals generated by both electrons and UV photons. And finally, scintillation light can be generated by the electron cloud drifting in a strong electric field. This light is called electroluminescence or secondary scintillation. In the previous Chapter 4 we considered operation of noble gas scintillation detectors. In this chapter we focus our attention to detectors with readout systems based on charge measurements.

5.1
Generation of Induction Charge

The ionization detector consists at least of two electrodes (anode and cathode) immersed in the noble gas or liquid or two-phase system with electrical field $\boldsymbol{E}$ applied between them. Ionization radiation, interacting with the working medium, generates free charge Q. The charge drifting under influence of the electric field induces the charge q on the electrodes. The induced charge is converted to electrical signal with external electronic circuitry. Generally, the induced charge can be calculated by integrating the normal component of the electric field, $\boldsymbol{E}$, over S, the closed surface surrounding the electrode

$$q = \oint_S \varepsilon \vec{E} \cdot d\vec{s} \tag{5.1}$$

where ε is the dielectric constant of the medium. A simplified method for calculation of the induced charge was originally proposed for vacuum devices [266,267] and later considered for single-carrier ionization detectors (see for example, [268] and [269]).

The Shockley–Ramo theorem states that the induced charge, q, and current, are defined by the distance displacement by the moving charge carriers, regardless of the presence of space charge, for example, from low mobile positive carriers

$$q = -Q\varphi_0(\vec{x}) \tag{5.2}$$

$$i = Q\vec{v} \cdot \vec{E}_0(\vec{x}) \tag{5.3}$$

where $\varphi_0(\vec{x})$ and $\vec{E}_0(\vec{x})$ are the electric (weighting) potential and field calculated in suggestion that the selected electrode is under unit potential and all other electrodes are under zero potential and free charges are absent, and $\vec{v}$ is a drift velocity of the point-like charge Q.

Let us consider a parallel plate ionization chamber filled with a noble gas ionized by alpha particles with the energy of E_0 as a simple example. The number of electron–ion pairs produced by alpha particle, N_0, is given as

$$N_0 = E_0/W \tag{5.4}$$

where W is the average energy required to produce one electron–ion pair in the rare gas and is usually expressed in units of eV. This W value is almost constant except for the low-energy region.

We will now consider a parallel plate ionization chamber. A track consisting of N_0 electrons and N_0 positive ions is formed in the rare gas if an α-particle is emitted from an alpha source placed at the center of the cathode (Fig. 5.1). The electrons separate from positive ions under the electric field between the parallel plates and the charges drift in opposite directions.

A general electrostatic field consisting of three conductors, A, B, and C, as depicted in Fig. 5.2a, can be used to explain the induction charge. Charge Q_0 is given to conductor C, which corresponds to the drifting electrons; the other conductors (A, corresponding to the anode, and B, corresponding to the ground) have no charge, as indicated in Fig. 5.2b. Electric field lines of $4\pi Q_0$ are emitted from conductor C and divided into lines that reach conductor A and those that reach conductor B. If conductor C gradually moves close to conductor A, and separates from conductor B, then the number of electric lines between C and A increases and that between C and B decreases. The terminal of the electric lines to conductors A and B corresponds to the induced charge on conductors A and B. This appearance of an induced charge is the result of the polarization of both conductors caused by the electric field from the electron cloud. This is known as electrostatic induction. Let us now consider

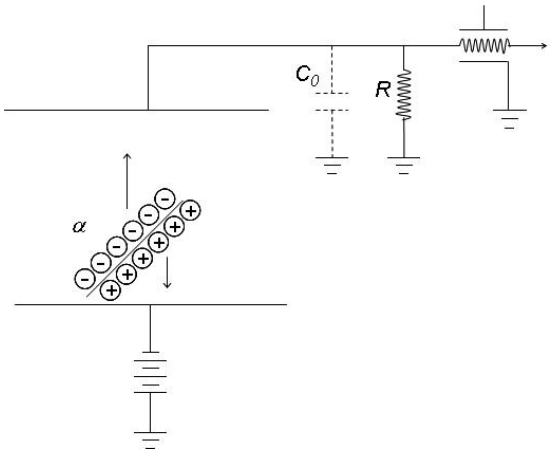

Fig. 5.1 A typical diode ionization chamber.

an example in which the conductor C with Q_0 approaches the conductor A. There are two induced charges of q and $-q$ in conductor A due to polarization. The sum of $-q'$ and $-q$ in conductor B should be equal to Q_0. If the electrostatic capacities between the conductors are C_{AB}, C_{BC}, and C_{CA}, then the electric potential of A, $V(t)$, is given as q/C_{AB}. The Q_0 is divided by the ratio of C_{BC} to C_{CA}, since it is the ratio of the number of electric lines emitted from C to A and those from C to B, if $C_{AB} \gg C_{AC}$ or C_{BC}.

The position of C is given by x, the distance from the cathode in a parallel plate chamber, and thus we can assume that C_{CA} is proportional to $1/(d-x)$ and C_{CB} is proportional to $1/x$ in the chamber. The number of electric lines between the electron plane and the anode, that is, the charge q induced at

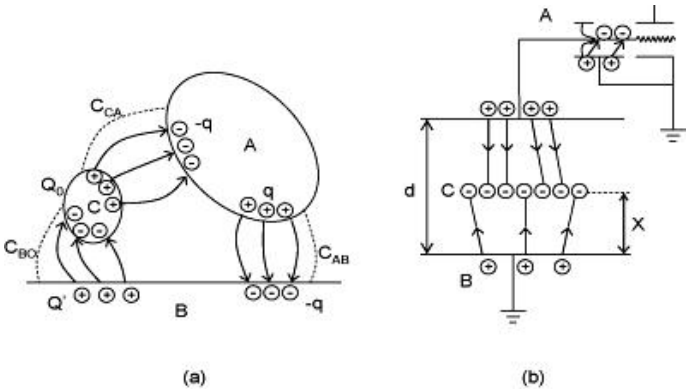

Fig. 5.2 Principle of generation of the induction charge (a) and correspondence with a diode ionization chamber (b).

the anode, is expressed as $\frac{C_{AC}}{C_{AC}+C_{BC}} \cdot Q_0$, using the above assumption on the position dependence of the capacities C_{CA} and C_{CB}. The induced voltage $V(t)$ at the anode is as follows if the capacity for the anode to the earth, C_{AB}, is given as C_0

$$V(t) = (Q_0 \times x/d) \cdot C_0 \tag{5.5}$$

where $Q_0 = eN_0$, x is the distance between the track and the cathode, and d is the distance between the anode and the cathode. Equation (5.5) can be correctly obtained if the individual tracks of electrons and positive ions are assumed to be planes. Thus, this method can be applied to derive the pulse height distribution due to alpha particles. The term $V(t)$ is a function of the charge position as indicated by Eq. (5.5). Therefore, if the initial positions of both charges are x_0, the current position at the moment t is $x = x_0 + \nu t$, where ν is the drift velocity of each charge and depends on the charge, i.e., the drift velocity of electron ν^- is much greater than that of the positive ion, ν^+. The induction voltage at the anode $V(t)$ is given as the sum of the induction voltage due to the electrons at the anode $V^-(t)$ and that due to positive ions $V^+(t)$

$$V(t) = V^-(t) + V^+(t) = -(Q_0/C_0)\{(x_0 + \nu^- t)/d - (x_0 - \nu^+ t)/d\}$$
$$or \quad V(t) = -(Q_0/C_0)\{(\nu^- t + \nu^+ t)/d\} \tag{5.6}$$

where ν^- and ν^+ are the drift velocities of the electrons and that of ions. The drift velocity of the electrons is about 1000 times faster than that of the ions. Therefore, the electrons can reach the anode faster than the ions. Accordingly, time variation of $V(t)$ after the arrival time of the electrons, t = (d - x)/ν, is expressed by the following equation:

$$V(t) = -(Q_0/C_0)\{(d - x_0)/d - (\nu^+/d)t\} \tag{5.7}$$

These variation patterns are shown in Fig. 5.3. The above equation becomes the following after the positive ions reach the cathode, i.e., after $t = x_0/\nu^+$

$$V_0 = -Q_0/C_0 \tag{5.8}$$

Therefore, we can determine the number of electron–ion pairs from Eq. (5.8) if the input capacity of the anode is known, however, we need the time in $\sim 10^{-3}$ s to do so. This chamber is known as a "slow chamber". We can measure the total charge as Q_0/C_0 with a good energy resolution in this situation, but its resolving time is on the order of milliseconds because of the slow drift velocity of ions. As a result, this type of chamber is very sensitive to acoustic noise. One can use a diode chamber as a fast chamber by using only the induction charge of electrons. Then, an effect of acoustic noise may be reduced.

To prove this statement, let us consider a fast diode chamber with an alpha source placed at the center of the cathode, as shown in Fig. 5.4. We will also

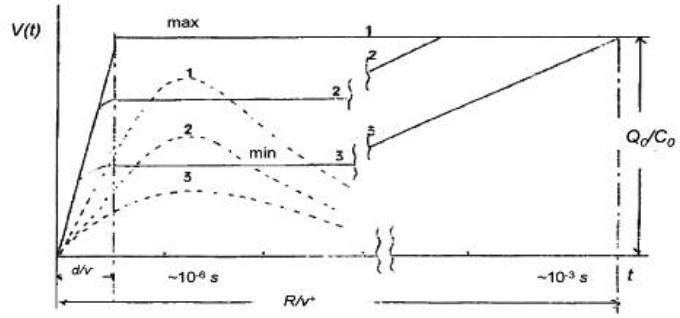

Fig. 5.3 Time variation of voltage pulse heights due to drifting electrons and ions.

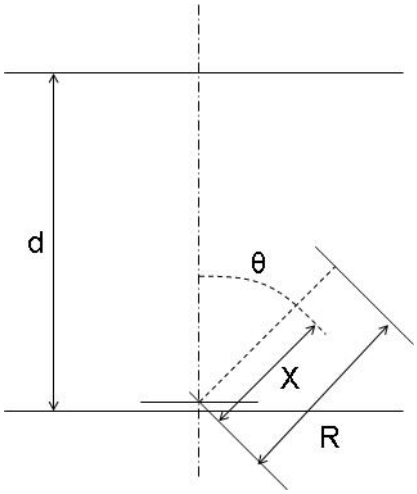

Fig. 5.4 Diode ionization chamber with an alpha source placed on the center of the cathode.

consider an alpha particle with a range of R emitted under angle θ out of the vertical axis at the center of the cathode with the center of gravity of the charge distribution located at the distance X along the alpha particle track. Assuming that Q_0 is concentrated at X and neglecting the second term in Eq. (5.6) the amplitude of the induction voltage

$$V_0 = (Q_0/C_0)\{1 - (X/d)\cos\theta\} \tag{5.9}$$

Since the number of alpha particles emitted between θ and $\theta + \mathrm{d}\theta$, dn, is proportional to its solid angle

$$\mathrm{d}n = n_0(\sin\theta/2)\mathrm{d}\theta \tag{5.10}$$

where n_0 is the number of alpha particles emitted per unit time. Equations (5.9) and (5.10) indicate that the pulse height distribution, dn/dp, can be obtained by the following equation:

$$dn/dp = (dn/d\theta)(d\theta/dp) = n/2(C_0/Q_0)(d/X) = const \tag{5.11}$$

This result reveals a rectangular shape of the pulse distribution with a width of $(C_0/Q_0)(d/X)$, as illustrated in Fig. 5.5.

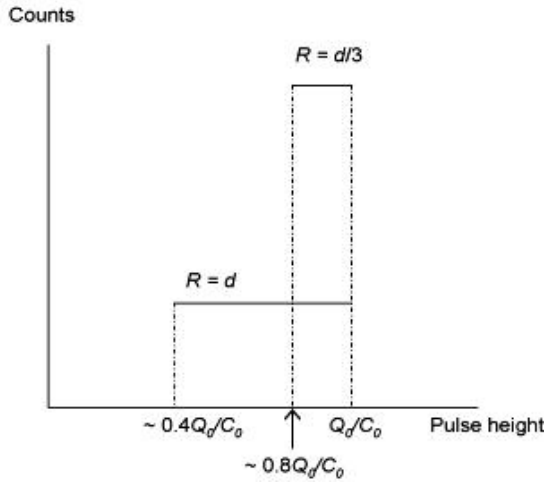

Fig. 5.5 Pulse height distributions calculated for the diode ionization chambers as shown in Fig. 5.4.

If $R = d$, the width of the rectangular shape becomes $0.6 \times$ (the highest pulse height), Q_0/C_0, since X is approximately given as $\sim 0.6R$ for a 5 MeV alpha particle. Thus the obtained energy resolution is very poor. Of course, this width is reduced as the gas pressure increases. Therefore, usually we use a high-pressure gas chamber to obtain a good energy resolution. This type of ionization chamber is known as a diode ionization chamber. Helium or molecular dopants to noble gases are used in order to increase the electron drift velocity (see Chapter 3).

5.2 Diode Ionization Chamber

We must use a high-pressure gas chamber to achieve satisfactory energy resolution as well as the fast time response obtained using a diode ionization chamber, as described above. A parallel plate chamber is not suitable for the use of high-pressure gas, due to the weak structure of this chamber under high-pressure gas. The structures of cylindrical and spherical chambers are

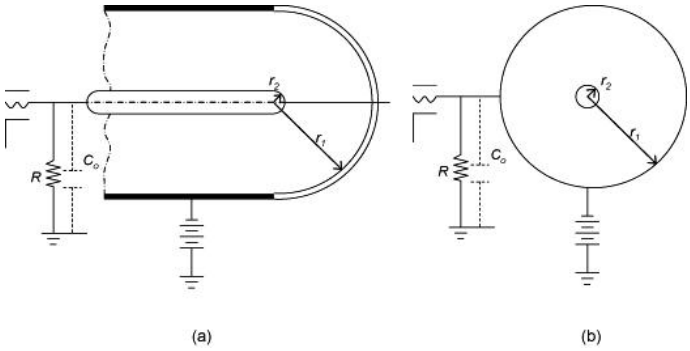

Fig. 5.6 Schematic drawings of a cylindrical ionization chamber (a) and a spherical ionization chamber (b).

much more robust against high-pressure gas. Use of a diode high-pressure cylindrical chamber is very popular, while spherical chambers are not in favor since they are difficult to fabricate. Figure 5.6 presents schematic drawings of cylindrical and spherical ionization chambers.

The central electrode is used as the anode in both types of ionization chambers, as illustrated in Fig. 5.6. This indicates that large signals can be used, since the input capacity of the anode is very small compared with that in a parallel plate chamber. Let us consider capacity C_a between the ionization track produced by ionizing radiation and the anode and that C_c between the track and the cathode. C_a is much less than C_c inside both cylindrical and spherical chambers, except for the region of the center wire or the center ball, since these capacities are proportional to the surface area of the anode and cathode. Therefore, the number of electric lines from the track to the anode becomes much smaller than in a parallel plate chamber. This indicates a reduction of the effect of positive ions compared with a parallel plate chamber when the chamber is used as a fast chamber.

Figure 5.7 shows the reduction of the effect of positive ions in the induction signals at the anode in cylindrical and spherical chambers. The energy spectra in the figure were obtained for uniformly distributed α-particles inside the chamber for a cylindrical chamber of $r_1/r_2 = 500$ and 10^4 and a spherical chamber of $r_1/r_2 = 10$ and 50. Figure 5.7 reveals that the energy resolution (FWHM) of the cylindrical chamber is about 10% and that of the spherical chamber is 2% to 5%. A better energy resolution than that depicted in the figure would be obtained if the α-particle source were coated on the cathode surface. However, construction of a spherical chamber is difficult. That type of chamber is therefore seldom used; a cylindrical chamber is more practical. Its structure is very simple; the area of the cathode surface is very wide and it can be used as a sample holder of alpha emitters with low activity. As a result, cylindrical ionization chambers are often used as low-activity alpha spectrometers.

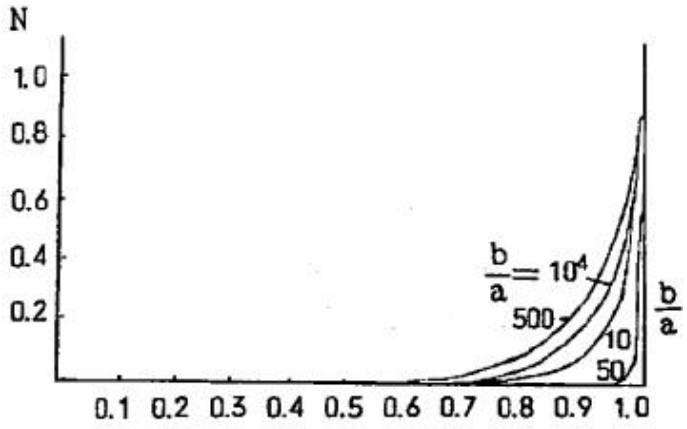

Fig. 5.7 Pulse height distributions in a cylindrical ionization chamber and a spherical ionization chamber for different parameters b/a [270].

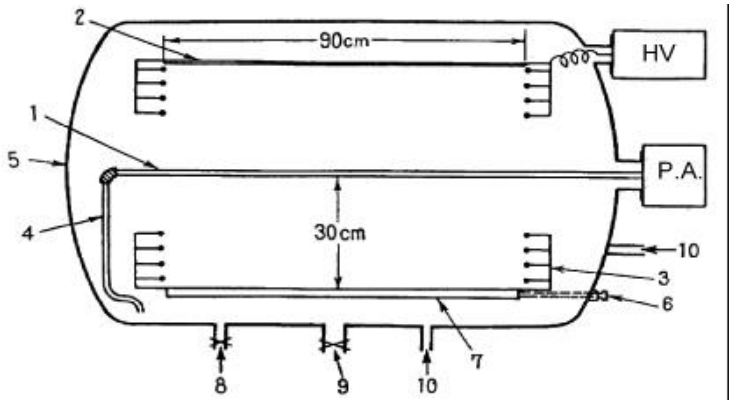

Fig. 5.8 Cylindrical ionization chamber with a large sample area: 1 - anode of 0.45 cm in diameter; 2 - sample base on the cathode; 3 - guard rings; 4 - supporting insulator for the anode; 5 - end cap; 6 - axis for rotating of a standard source; 7 - rectangular bar that a standard source is coated on one side of the bar; 8 - gas inlet; 9 - gas outlet; 10 - circulation of the gas [270].

Figure 5.8 contains a cross sectional view of a cylindrical ionization chamber constructed to measure low-alpha activities from human specimens [270]. The gas filling of argon plus 2% methane is continuously purified by cycling through hot calcium at 570 K and then through a column of charcoal cooled to 195 K to remove electronegative impurities. Up to 1.5 g of source material can be mounted on the 15 000 cm^2 cathode surface area. Thin alpha sources of ^{241}Am (5.48 MeV) have been measured with the energy resolution of 2%.

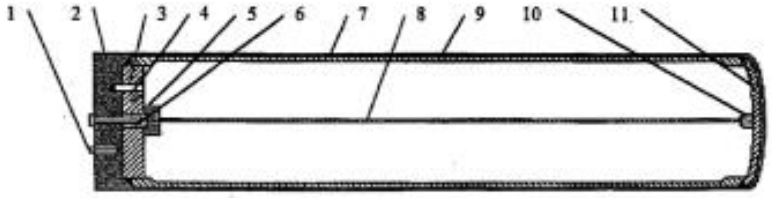

Fig. 5.9 Cross sectional view of a cylindrical diode chamber: 1 - HV connector; 2,9 - Teflon insulation; 3 - gas inlet; 4 - flange; 5 - ceramic feedthrough; 6 - signal output; 7 - high-pressure vessel; 8 - anode; 10 - ceramic insulator; 11 - elliptical cover of the high-pressure vessel [271].

A cylindrical structure is very robust for use with high-pressure gas, and thus it is also used as a high-pressure gas chamber. Figure 5.9 presents a cross sectional view of a cylindrical diode chamber. The density of xenon gas is 0.6 g cm^{-3}, the sensitive volume is 900 cm^3 and the energy resolution for 1 MeV gamma rays is 2.7%, which is slightly inferior to the triode chambers as described in the following section.

5.3 Triode Ionization Chamber

The single-carrier ionization chamber, requires that a grid electrode be placed in front of the anode to shield the electric field from ion charges, as illustrated in Fig. 5.10.

The potential of the grid electrode is generally kept constant. The leakage factor of the electric lines from the positive ions is given as the shielding inefficiency, η, as follows [272]:

$$\begin{aligned} \eta &= \{s/(2\pi d_2)\}\log(1/\rho) \\ \rho &= 2\pi r/s, \end{aligned} \tag{5.12}$$

where d_2 is the distance from the grid to the anode, s is the spacing between adjacent wires, and r is the radius of the wire. If the chamber has a grid electrode, as described above, then the effect of positive ions is reduced to $\eta \times (Q_0/C_0)(X/d)$. For example, if $r = 0.005$ cm, $s = 0.1$ cm, $d = 3$ cm, and $\eta = 0.36\%$. Thus, even if the range of alpha particle R is equal to d, the width given for the diode is reduced to $\eta \times 0.6(Q_0/C_0)$.

The electrons produced by an alpha particle must pass through the grid without being captured by the grid. To do so, the electric lines must pass through the grid without interruption except for each center line of the wire as illustrated in Fig. 5.11, since electrons move along the electric lines. The

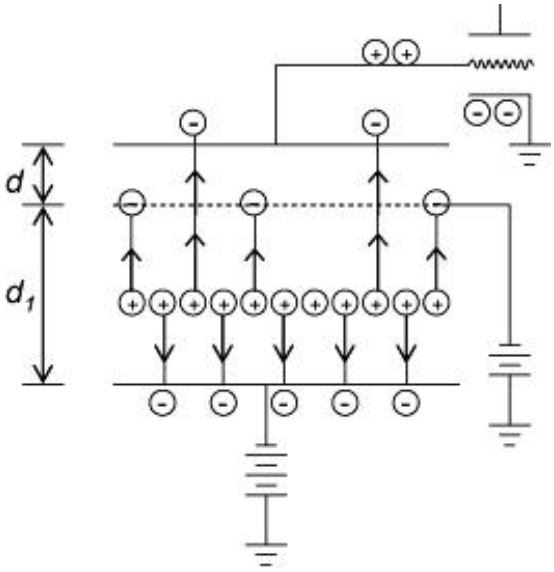

Fig. 5.10 Parallel plate gridded ionization chamber.

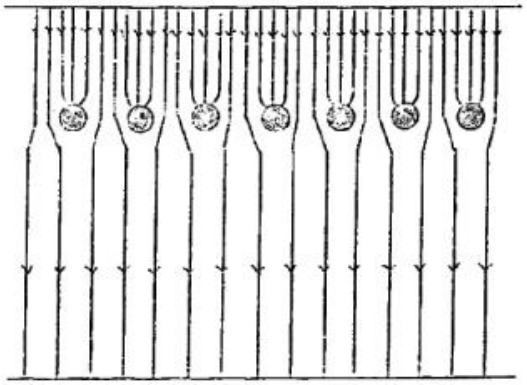

Fig. 5.11 Map of electric field lines in the vicinity of grid wires.

following formula is the condition for realizing the above pattern [272]:

$$Z > (1+\rho)/(1-\rho), \tag{5.13}$$

where Z is the ratio of the electric field between the anode and grid to that between the grid and cathode. This type of chamber is usually referred to as a gridded ionization chamber or a Frisch grid chamber.

The intrinsic energy resolution, σ_{i}, obtained by the gridded ionization chamber is given as follows [63]:

$$\sigma_{\mathrm{i}} = 2.35(FWE_0)^{1/2} \tag{5.14}$$

where F is the Fano factor. There are many contributing factors aside from this intrinsic energy resolution, including the positive ion effect, the effect of the rise time effect due to amplifiers and the electronic noise, the effect of sample thickness, the effect of microphonics, etc. However, we can suppress the effects other than the effect of electronic noise. Finally, the achievable total resolution is approximately given as

$$\sigma^2_{\text{total}} = \sigma^2_{\text{i}} + \sigma^2_{\text{en}} \tag{5.15}$$

where σ_{en} is the electronics noise. Equation (5.15) enables us to estimate the value of the Fano factor from the noise-subtracted resolution. The Fano factor was estimated for pure argon by precisely measuring the energy spectrum of a 5.3 MeV alpha particle using a typical gridded ionization chamber filled with pure argon and then estimated the contributions of the above factors [274].

Tab. 5.1 Experimental conditions and results of measurement of the Fano factor [274].

Pressure, Torr	1.10×10^3	1.37×10^3
Range, mm	26.9	21.7
E_1/p, V cm^{-1} Torr^{-1}	0.19	0.19
E_2/E_1	3.37	3.37
Δe_l, keV	16.4±0.1	16.5±0.1
Δe_n, keV	10.5±0.02	10.7±0.02
Δe_{pi}, keV	3.6	1.8
Δe^a_r, keV	0	0
Δe^a_s, keV	2	2
Δe_i, keV	12.1±0.1	12.1±0.1
Fano factor	$0.19\pm^{0.01}_{0.02}$	$0.20\pm^{0.01}_{0.02}$

Note: [a]Δe_r and Δe_s are the estimated contributions of the rise time effect and the source effect to Δe_l. All energy spreads are shown in FWHM.

The results are listed in Table 5.1. They estimated the Fano factor to be $0.2^{+0.01}_{-0.02}$. The value of the Fano factor for pure xenon has been estimated to be 0.29±0.01 by using a similar gridded ionization chamber [52]. This value for xenon is slightly greater than that (0.13 to 0.17) measured for electrons by the proportional scintillation method [49, 275]. It was suggested that this difference can be attributed to the energy loss fluctuation due to nuclear elastic collision [276].

The MEPhI group is developing high-pressure xenon gamma ray detectors as one approach to creating new gamma ray detectors with an energy resolution at room temperature close to that of germanium detectors. They have constructed three types of high pressure xenon chambers, since 1990, a triode parallel plate chamber, a diode cylindrical chamber, and a triode cylindrical

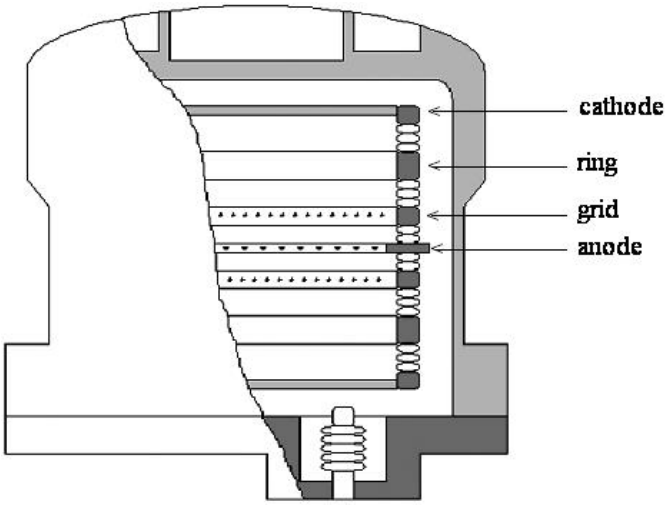

Fig. 5.12 Gamma spectrometer KSENIA with parallel plate electrode structure with internal dimensions 18-cm diameter and 25-cm height filled with Xe+0.26%H_2 gas mixture at density of 0.6 g cm^{-2} operated at the MIR space orbital station from 1990 to 1996 [277].

chamber. The second chamber was described in the previous section. The other two will be explained here. Figure 5.12 presents a cross sectional view of a parallel plate HPXe chamber, consisting of a wire anode, two shielding grids and two cathodes.

Figure 5.13 is a cross sectional view of an HPXe cylindrical chamber with a grid. The density of xenon gas under operation is 0.6 g cm^{-1} and the energy

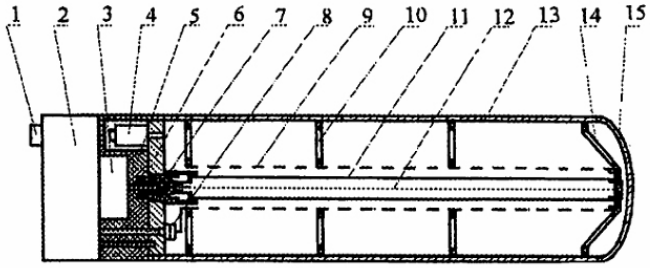

Fig. 5.13 Cylindrical gridded ionization chamber: 1 - HV connector; 2 - HV power supply; 3 - charge-sensitive amplifier; 4 - gas valve; 5 - Teflon insulator; 6 - flange; 7 - feedthrough; 8 - high voltage input for a shielding grid; 9 - shielding grid; 10 - gird supporting ceramic insulators; 11 - anode; 12 - grounded metal wire; 13 - high-pressure vessel; 14 - cover ceramic insulator; 15 - elliptical cover of the high-pressure cylinder [271].

Tab. 5.2 Primary characteristics of various configurations of HPXe gamma spectrometers [271].

	Chamber type		
	Parallel plate	Cylind. w/o grid	Cylind. w/ grid
Xenon density, g cm^{-3}	0.6	0.6	0.4–0.6
Concentr. of hydrogen, %H_2	0.26	0.28	0.27
El. field strength in the cham., kV cm^{-1}	2.6	2–15	2–10
Max. time of drift, μs	10	5	10
En. range of meas. γ-quanta, MeV	0.1–10	0.1–5	0.1–10
Sens. volume, cm^3	1000	900	5000
Ratio of work. vol. to general	0.33	0.95	0.95
Sens. surface, cm^2	100	225	565 and 100
Full en. res. at 662 keV, %	3.5	4.0	2.1
Full en. res. at 1 MeV, %	2.0	2.7	1.5
Detect. effic. at 662 keV, %	6	2	15
Detect. effic. at 1.33 MeV, %	1.5	1	7
Mass, kg	10	2.3	9.5

resolution for 1 MeV gamma rays is 2% to 1.5% [271]. The characteristics are listed in Table 5.2.

A cylindrical chamber with a grid can be used as an energy spectrometer for low-level alpha activity since its cathode can be used for a wide sampling area, similar to a diode cylindrical chamber.

Figure 5.14 presents a schematic cross sectional view of a typical cylindrical gridded chamber for measuring very low alpha activity [278]. The authors derived a shielding inefficiency of η, and the ratio of the electric fields to pass the electrons through the grid, Z, if $r_g \gg r$, as follows:

$$\eta = \log(R_Z/S_g)/[2\pi r_g s^{-1}\log(r_a/r_g) + \log(S_g - 1/S_Z)] \tag{5.16}$$

$$Z_C = (1 + \rho + (1/2)\rho^2)(\rho + \rho^2 + (1/2)\rho^3)/(\rho - (1/24)\rho^4) \tag{5.17}$$

where $S_Z = \exp(\rho)$, $S_g = \cosh(\rho)$, $R_Z = \sinh(\rho)$, $\rho = 2\pi r/s$, r is the radius of the grid wire, s is the wire spacing, r_a is the radius of the collector (anode), and r_b is the radius of the grid (see Fig. 5.14).

This chamber was typically filled with a mixture of 90% argon and 10% methane and operated at about 0.2 MPa pressure. The source area on the cathode side was 5000 cm^2 and a very low background of under the operation condition shown analytically, the very low background of 0.17 counts per hour over a spectral line width of 45 keV (FWHM) at 5 MeV was achieved for Mylar

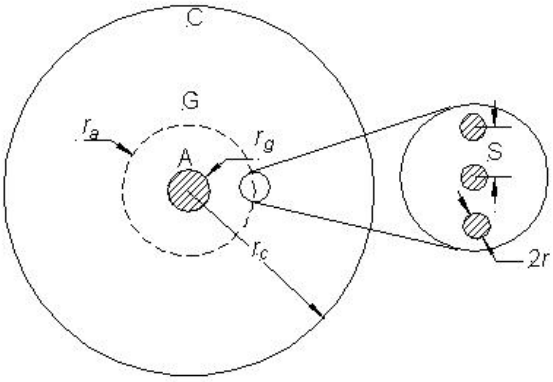

Fig. 5.14 Cylindrical gridded ionization chamber for measurement of very low alpha activity (cross section view): A - anode; G - grid; C - cathode.

sheet backing under operational conditions described analytically. Figure 5.15 shows the energy spectrum of the solution of 0.5 g marine sediment nitric acid.

The use of liquid xenon better increases the sensitivity of gamma rays. A liquid xenon dual type gridded ionization chamber was constructed as a gamma ray spectrometer to realize increased sensitivity [279]. Figure 5.16 shows a schematic cross section of the chamber and a portion of the cryostat.

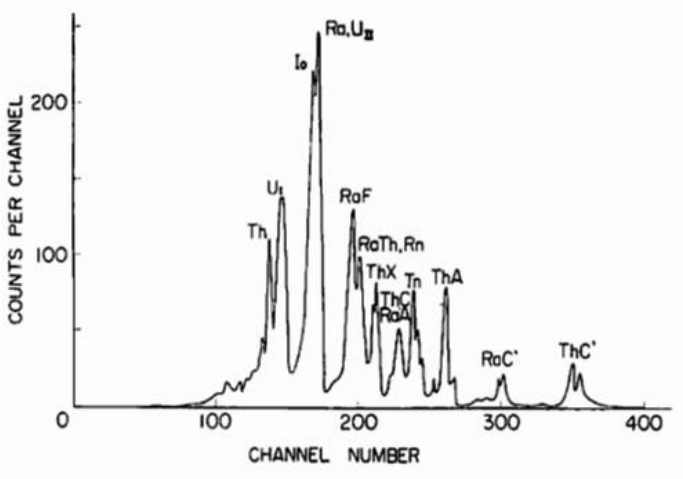

Fig. 5.15 Energy spectrum of a solution of 0.5 g marine sediment nitric acid [278].

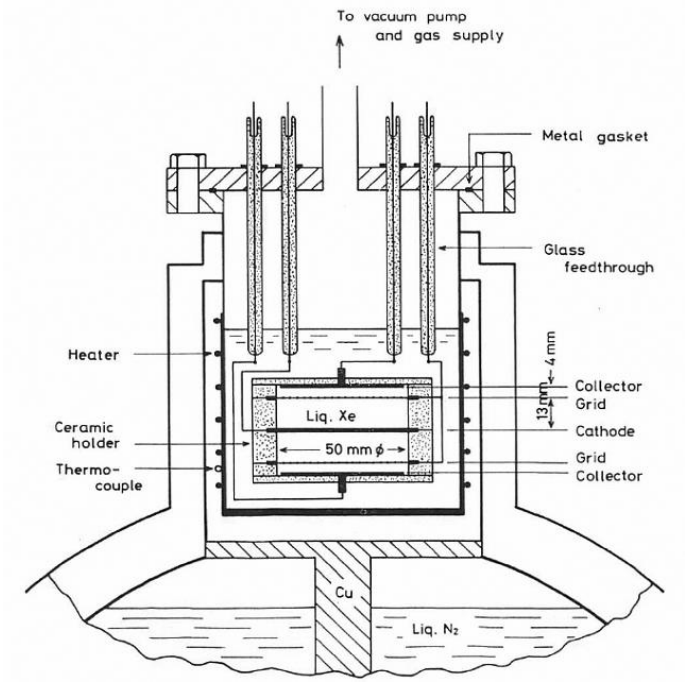

Fig. 5.16 Dual parallel plate liquid xenon gridded ionization chamber for measurement of gamma rays [279].

This chamber has an active volume of $2\times(2.5)^2\times1.3\ \text{cm}^3 = 50\ \text{cm}^3$. The energy resolution for collimated gamma rays of 662 keV was 8.6% (FWHM) and those for noncollimated gamma rays were 9.6% at 662 keV, 6.5% at 1332 keV and 4.5% at 2614 keV. An energy resolution of 4% for 662 keV gamma rays was recently obtained by using the sum signals of ionization and scintillation simultaneously produced by a gamma ray, as described later. By such a method, the energy resolution obtained by a liquid xenon chamber may be improved over that of NaI(Tl) in the near future.

5.4
Multilayer Ionization Chamber

High-energy gamma rays or electrons produce electromagnetic showers. High-energy hadrons also produce a nucleon cascade. A detector must deposit all the energies within the sensitive volume of the detector to measure them. As a result, the detector must be massive. A detector in which all the energy of incident gamma rays, electrons or hadrons can be absorbed is a calorimeter. The use of triode chamber, such as a gridded ionization chamber,

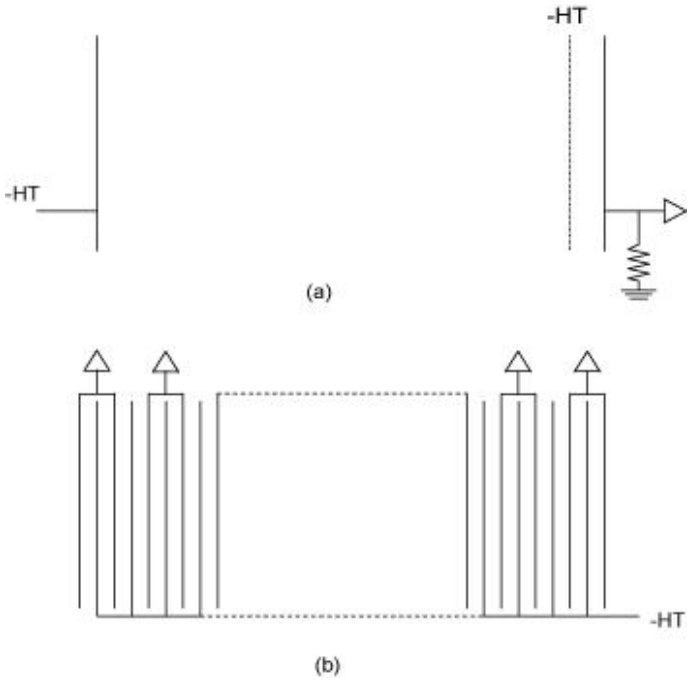

Fig. 5.17 Gridded ionization chamber with a single drift region (a) and multilayer electrode system (b).

becomes difficult in this case, since it must have a long sensitive region as indicated in Fig. 5.17a, and accordingly requires a very high applied voltage to apply the same electric field as that used in a small chamber. An electrode system consisting of many parallel plates as illustrated in Fig. 5.17b is usually used for calorimeters.

The high-energy electrons generated in an electromagnetic shower penetrate the thin electrodes and allot a portion of their energies to the sensitive medium. In that case, the positive ions are left in the sensitive medium, i.e., gap between electrodes, if only the electron signals are used. Therefore, the contribution to the induced charge from positive ions remains. Only half of the fully-induced charge is induced at the anode if they are uniform tracks. Thus, the effective number of electron–ions to be measured at the anode may be expressed as

$$N_0 = E_0/2W \tag{5.18}$$

where E_0 is the energy deposited in the sensitive medium and W can be considered to increase to $2W$, based on the above equation. The calorimeter approaches homogeneity if the nonsensitive region becomes very thin, and the energy resolution becomes better than that of a calorimeter with a thick non-

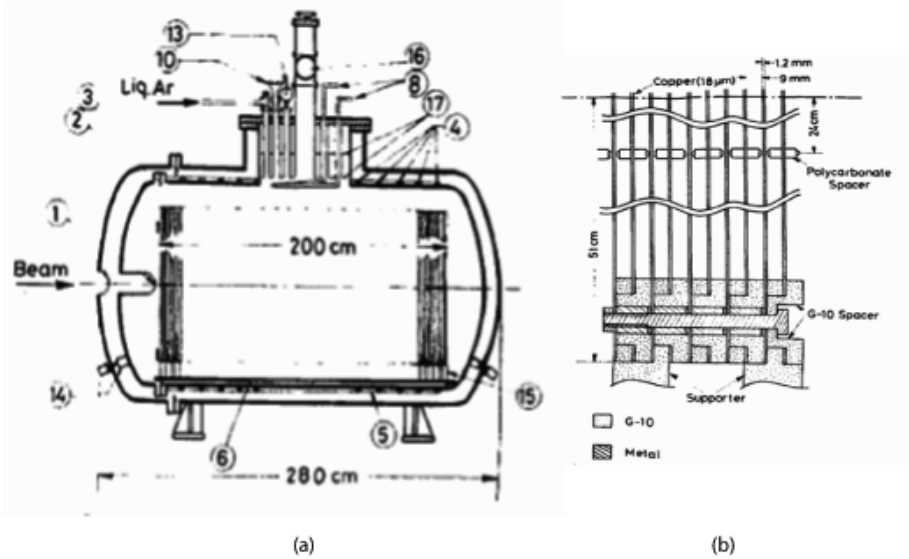

Fig. 5.18 Liquid argon homogeneous electromagnetic calorimeter (a) and a cross sectional view of a typical module of the electrode system (b) [280]: 1 - beam entrance window; 2 - indium gasket; 3 - O-ring gasket; 4 - precooling tube; 5 - aluminized Mylar sheet; 6 - rails; 7 - thermocouples; 8 - cooling tube; 9,10 - safety valves; 11 - feedthrough for thermocouples; 12 - feedthrough for high voltage; 13 - pressure gauge; 14 - support for inner vessel; 15 - support for electrodes; 16 - signal feedthroughs; 17 - copper plate.

sensitive region, i.e., thick electrodes. This type of calorimeter is referred to as a quasihomogeneous or a homogeneous calorimeter. On the other hand, the calorimeter consisting of thick electrodes becomes shorter but the energy resolution deteriorates, if electrode material with a short radiation length is used. This type of calorimeter is referred to as a sampling calorimeter.

In such a multilayer ionization chamber, it is easy to determine the positional distribution of energy deposition given by an incident beam in such a multilayer ionization chamber by using thin multistrip electrodes coated on the insulator plate (such as a G10 plate). Furthermore, two-dimensional position information can be obtained from this electrode system if other multistrip electrodes are coated orthogonally on the back surface of the insulator plate.

Descriptions of many full-size homogeneous and sampling calorimeters are provided in Chapter 9. Therefore, we will describe three prototype models of homogeneous liquid rare gas calorimeters here. A prototype model of a liquid argon homogeneous calorimeter was constructed in 1985, the first attempt in this field [280].

Figure 5.18 shows a cross sectional view of the prototype model. The parameters of the calorimeter are listed in Table 5.3, as well as those of a prototype of liquid xenon homogeneous calorimeter constructed by the Russian

Tab. 5.3 Parameters of prototype models of homogeneous calorimeters and their energy resolutions.

	Japan group (1985) [280]: LAr calorimeter	Russia group (1990) [281]: LXe calorimeter
Gap, mm	9	12
Thickness of electrode	1.2mm (G-10) + 2×18μm Cu	50 μm Al
Energy loss at electrode	18.6	0.48
Length of calorimeter, cm	196.5 (13.8 X_0)	50 (17.7 X_0)
Diameter of calorimeter, cm	102 (7.2 X_0)	25 (9.0 X_0)
Number of readouts	20	1
En. res. (rms), %	2.4 (for 1 GeV)	$3\sqrt{E}$ (GeV)

group [281]. The energy resolutions reported from the tests of these prototypes were much better than those of sampling calorimeters.

Interesting results were also recently obtained for another liquid xenon homogeneous calorimeter prototype [273]. Figure 5.19 shows the electrode configuration of the liquid xenon calorimeter. The electrodes are 108 μm thick G10 plates, the front and back surfaces of which are coated with 14-μm thick copper foil. The gap between the electrode plates is 4.1 mm. This electrode system consists of 169 cells, as indicated in the figure; eight cells are connected

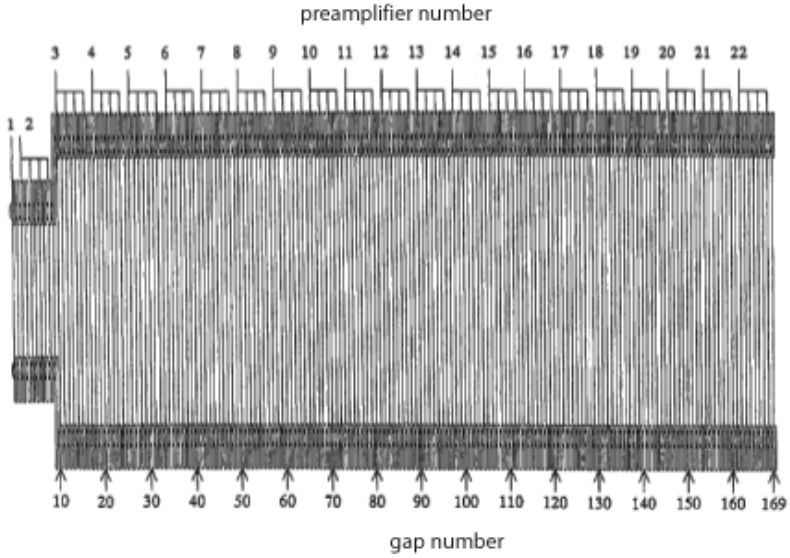

Fig. 5.19 Liquid xenon homogeneous electromagnetic calorimeter [273].

together and make one readout channel, except for the first readout channel, which consists of a unit cell. Shower leakage from the side of the calorimeter was estimated to be about 3% and was almost constant for incident energy from 10 to 70 GeV. The beam test was conducted at CERN in 1996. The measurements were made without signals from a readout channel at about 4 radiation lengths that was lost by failure. An energy resolution of 2% rms, which includes the beam momentum spread of 0.65%, was obtained for 70 GeV electrons by a simple summing of the other signals. The signal from the lost channel can be estimated by fitting a build-up curve to the obtained signals for each event. The energy resolution was 0.9%, when a correction for the contribution from the lost channel was made using the fitting method, which is close to the resolution of 0.7 % obtained by the simulation.

5.5 Ionization Chamber with Virtual Frisch Grid

A Frisch grid is usually used between cathode and anode to achieve satisfactory energy resolution. However, a Frisch grid is sensitive to acoustic noise. As a result, this noise makes the Frisch grid chamber useless in any application in which the vibration level is high. This is a significant weakness in the grid. This weakness makes it difficult to use a Frisch grid chamber for industrial applications. A coplanar grid detection technique was recently proposed to overcome the incomplete collection of positive holes in semiconductor detectors like CdZnTe, CdTe and HgI_2 [282].

The coplanar anode consists of two series of narrow strip electrodes (A, B) that are connected in an alternate manner, as illustrated in Fig. 5.20a. The potential of each electrode is adjusted so that the electrons produced by ionizing radiation can be collected in only one electrode (A). As a result, the signal of electron collection in the electrode A, q_A, and the signal in the electrode B, q_B, produced by induction due to positive ions are given as indicated in Fig. 5.20b. Thus, the difference, $q_A - q_B$, is the charge given only by electrons. This technique was directly applied to high-pressure xenon (HPXe) detectors by two or three groups [283, 284]. The MEPhI group attempted to remove the contribution to pulse height due to movement of ions by mathematical correction based on the correlation between the pulse rise time and amplitude [285]. However, this attempt did not yield satisfactory results. Therefore, scientists developing HPXe detectors concentrated on the use of a coplanar anode configuration. The dual-anode HPXe cylindrical ionization chamber developed by Bolotnikov et al. [284] will be introduced here since it is a more practical HPXe detector. They constructed a dual-anode cylindrical ionization chamber with 30-cm long and 0.75-mm diameter central two wires whose spacing is 3 mm.

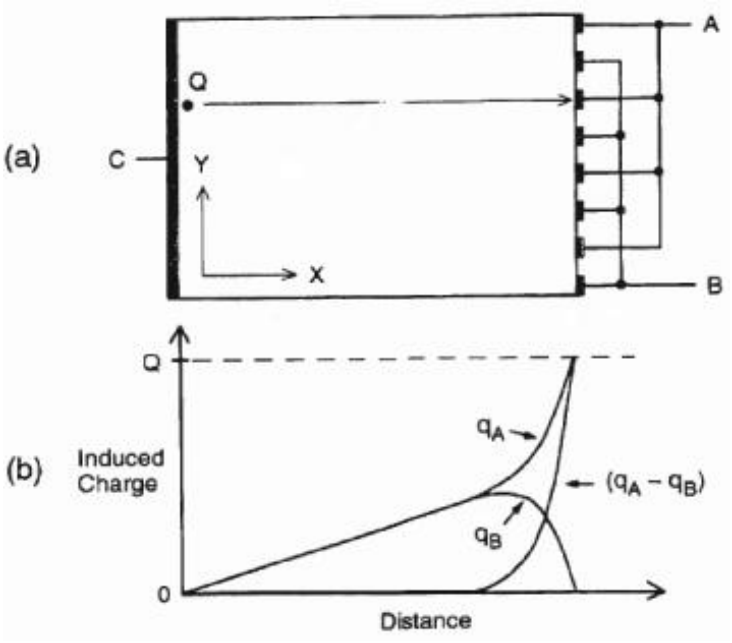

Fig. 5.20 Parallel plate ionization detector with coplanar anode configuration (a) and time variations of the induced charge charge (b) [282].

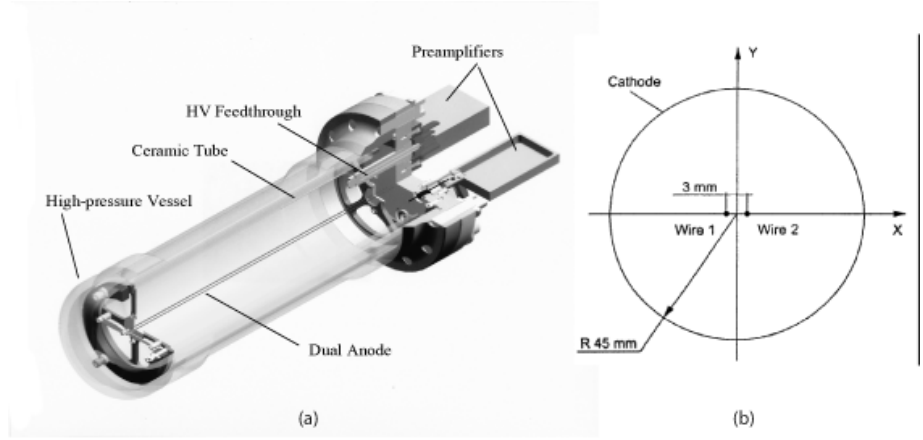

Fig. 5.21 Cross sectional view of a dual-anode HPXe cylindrical ionization chamber [284].

The cross section of the chamber is shown in Fig. 5.21. The electric field distribution in the chamber is shown in Fig. 5.22a as well as its expanded electric field in the vicinity of the anode Fig. 5.22b. The distribution is symmetrical on a large scale and is similar to the field distribution inside a single-anode

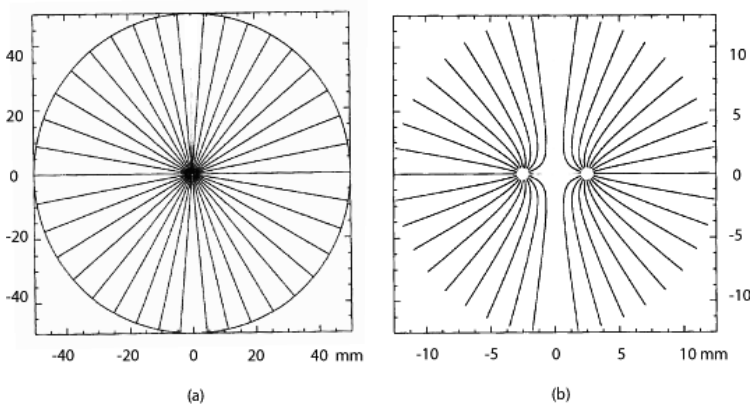

Fig. 5.22 Electric field distribution in the dual-anode ionization chamber at large distance from the anodes (a) and electric field distribution near the anodes (b) [284].

cylindrical chamber. The symmetry is broken only in the vicinity of the wires, where the field lines split between the two wires.

Figure 5.23 shows several representative examples of pulse shapes induced by 662 keV photons from a Cs gamma ray source. The measured pulse shapes are very similar to theoretically calculated ones. Each of the panels in Fig. 5.23 shows a pair of waveforms of which the top one represents the collected signal readout from the wire that actually collects the electrons, while the bottom one represents the induced signal read from the second wire. In each panel, the waveforms rise similarly until the ionization cloud approaches the wires. In the vicinity of wires, the magnitude of collected signal increases rapidly while the magnitude of the induced signal drops sharply and changes polarity due to the influence of the positive ions. This is easy to observe when the ionization cloud originates near the wires (a) and in the vicinity of the cathode (b). Also, we can observe when two interaction points occurred such way that electrons from two electron clouds collected on the same anode (c) and on different anodes (d). By using digital pulse processing all these events can be identified. Multipoint interactions are common for high-energy gamma rays.

Figure 5.24 shows the pulse height spectra from a ^{137}Cs gamma ray source measured for two modes (a) dual anodes and (b) a single anode. An energy resolution of 26 keV(4%) FWHM was achieved at 662 keV in dual-anode mode with a 20 keV electronic noise level. This compares favorably with the resolution of 8.0% FWHM (13 keV electric noise) in single-anode mode. Furthermore, the simulation demonstrated that an energy resolution better than 2% FWHM can be achieved by merely decreasing the spacing between the wire anodes below 2 mm at the typical electronic noise of $\sim$ 10 keV.

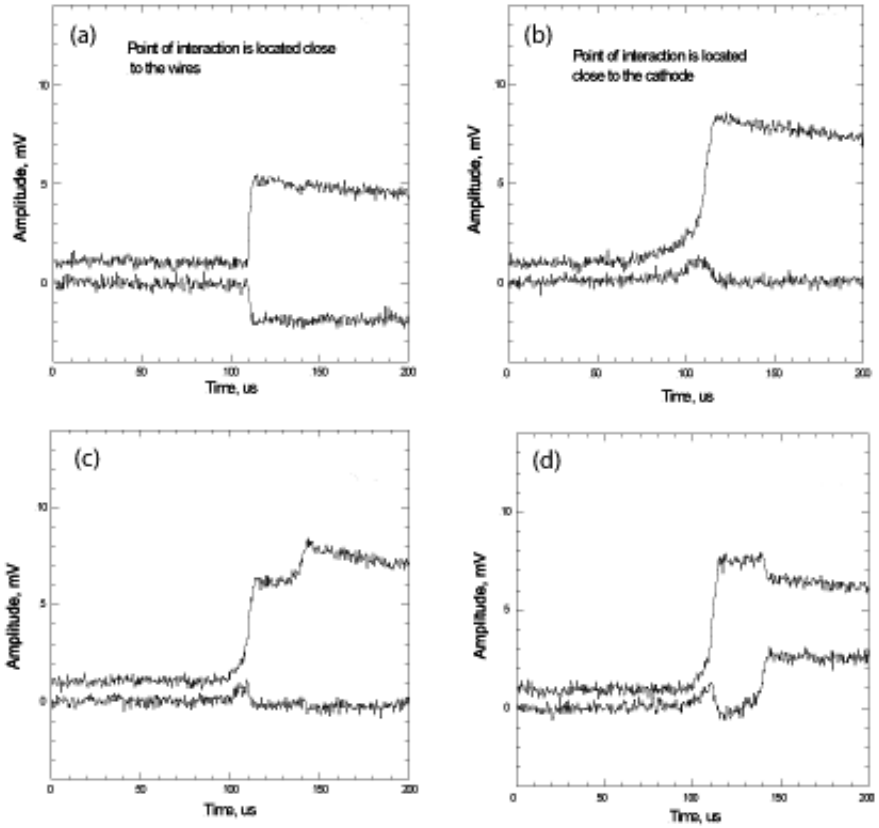

Fig. 5.23 Examples of waveforms induced by 662 keV (^{137}Cs) photons on anodes of the dual-anode ionization chambers when photoabsorption occurred in vicinity of the anodes (a), in vicinity of the cathode (b), or two-point interactions occurred such way that electrons from two clouds collected on the same anode (c) and on different anodes (d) [284].

5.6 Time Projection Chamber with Scintillation Trigger

Rare gases generate both signals of ionization and scintillation by ionizing radiation independently of their phase. No such characteristic exists in the other detector media. However, the energy resolution obtained by scintillation signals was very poor compared with that obtained by ionization signals, since only a small part of emitted photons is usually observable. Therefore, the use of scintillation signals has been recently limited to a few cases. One is its use as a trigger signal because of its fast decay. A typical example is a time projection chamber (TPC), which is primarily operated by ionization signals. A construc-

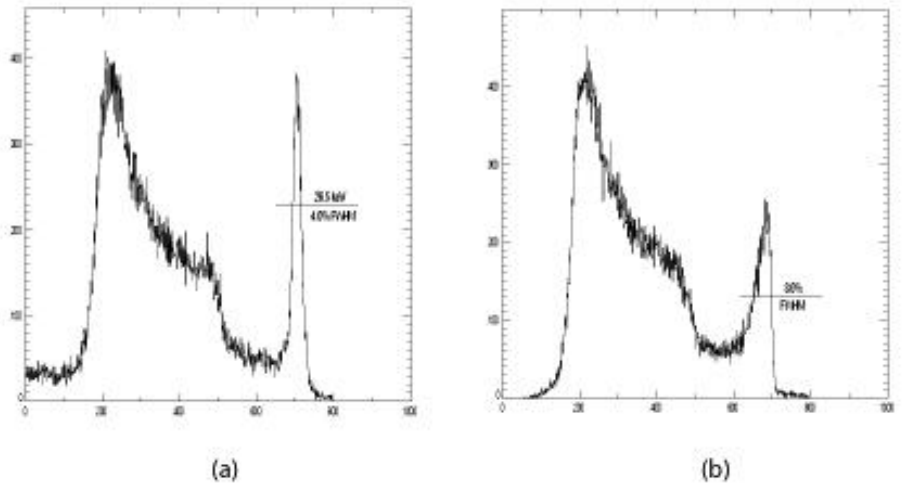

Fig. 5.24 (a) Pulse height spectrum measured with the dual-anode mode, for ^{137}Cs gamma rays, and (b) that measured with the single anode mode for ^{137}Cs gamma rays [284].

tion concept of a large scale liquid argon TPC for low background elementary particle physics experiment was proposed by Rubbia in 1977 [286]. There are two applications of TPC using liquid xenon other than that plan; one is the application to elementary particle physics experiments [287] and the other to MeV gamma ray spectrometers used, for example, in astrophysics [288]. We will address the latter as a good example on a medium scale.

The Liquid Xenon Gamma Ray Imaging Telescope (LXeGRIT) constructed by the Columbia University group is a liquid xenon TPC for imaging cosmic gamma rays in the energy band of 0.2 to 20 MeV. A schematic drawing of it is provided in Fig. 5.25. It is a typical gridded ionization chamber consisting of a cathode, a wire electrode system for two-dimensionally determining the gamma ray interaction points, and an anode. The wire electrode system consists of three wire grids. The first is a Frisch grid to shield the electric lines from positive ions. The second and the third wire grids can pick up the signals induced when drifting electrons pass through the wire intervals of the grid without loss of electrons. Individual pulse shapes are shown in the figure. These signals enable us to identify the X and Y-coordinates of the interaction points of the gamma rays. Finally, the drifting electrons are collected by the anode, and the anode signal provides the energy information. Scintillation from photomultipliers is used as triggering signals. The Z-coordinate can be obtained as a product of the electron drift velocity and the time difference between the triggering time and the time of induced signals in the wire grids. Thus, the three-dimensional coordinates of the interaction points are obtained and the track of the liberated electrons can be reconstructed.

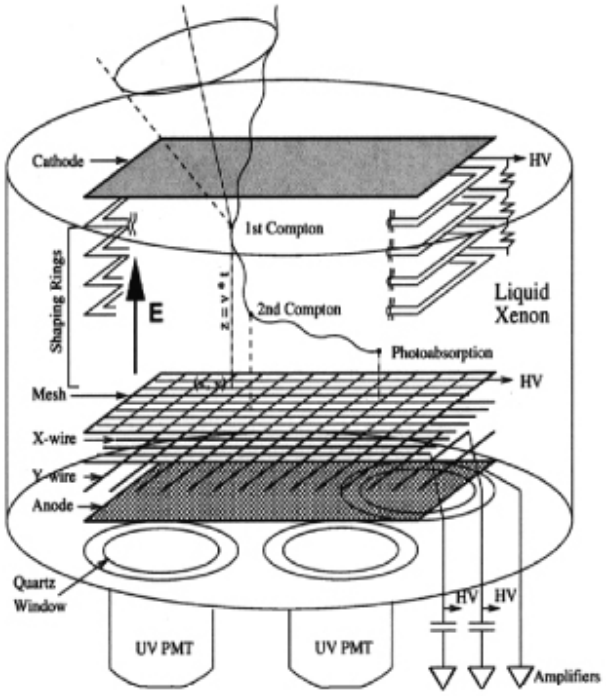

(a)

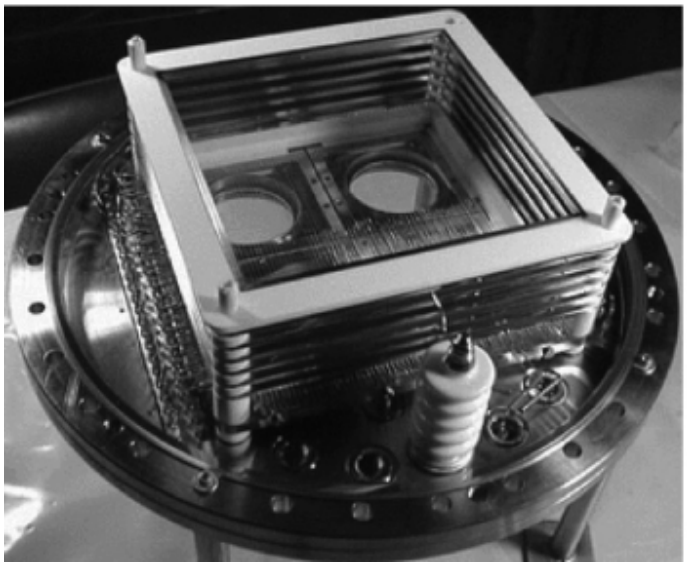

(b)

Fig. 5.25 Schematic drawing of a LXeGRIT time projection chamber (a) and photopicture of the internal structure (b) [289].

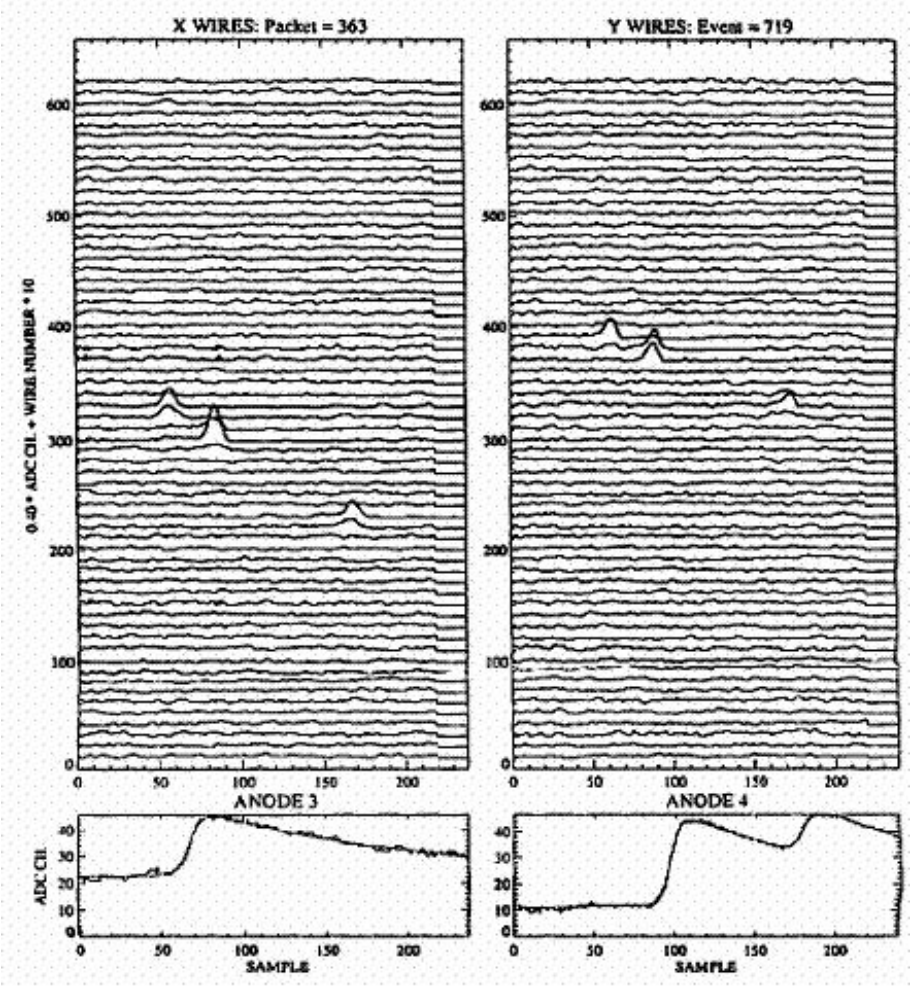

Fig. 5.26 LXeGRIT on-line display of a 1.8 MeV γ-ray event with multiple Compton interactions.

Figure 5.26 shows the LXeGRIT on a line display of a 1.8 MeV γ-ray event with multiple Compton interactions. The digitalized pulses on the wires and anodes are plotted as a function of the drift time (0.2 μs per sample). The incoming photon makes two Compton scatterings before being photoabsorbed. The photomultipliers in this LXeGRIT were placed outside of the chamber vessel, however, we can now place these photomultipliers inside of the chamber vessel since new photomultipliers that can operate at liquid xenon temperatures were recently developed [290].

5.7 Use of Both Ionization and Scintillation Signals

Simultaneous measurements of both ionization and scintillation signals in liquid rare gases improves the energy resolution. This improved energy resolution was first demonstrated in measurements of energy loss for relativistic La ions in liquid argon [200]. The energy resolution of the sum signals of ionization and scintillation was compared with those obtained for individual signals. They found that the energy resolution of the sum signals was much better than those obtained by individual signals. The same method was recently applied for relativistic electrons using a liquid xenon gridded chamber and discovered that the use of sum signals improved the energy resolution [506]. These improvements of energy resolution are caused by an anticorrelation pattern between the ionization and scintillation signals.

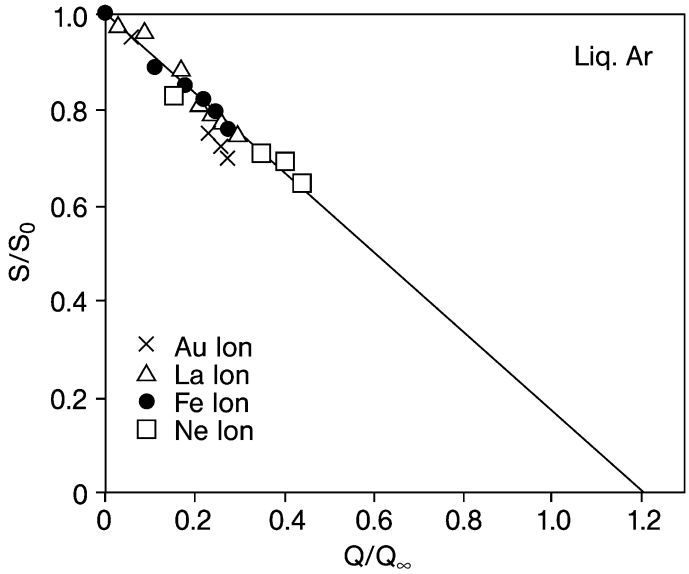

Fig. 5.27 Anticorrelation between scintillation and ionization yields in liquid argon for relativistic heavy ions; the solid line indicates the theoretical relation [506].

Figure 5.27 illustrates a typical relation between the scintillation intensity and the collected charge in liquid argon for relativistic Ne, Fe, La and Au ions. All data except that for Au ions were on a theoretically posited line. The deviation of the data points of Au ions from the straight line was caused by the quenching effect [506]. The anticorrelation pattern for 1 MeV electrons differs from that for relativistic heavy particles, as shown in Fig. 5.28 for liquid argon and xenon, in which the data points for the low electric field are not

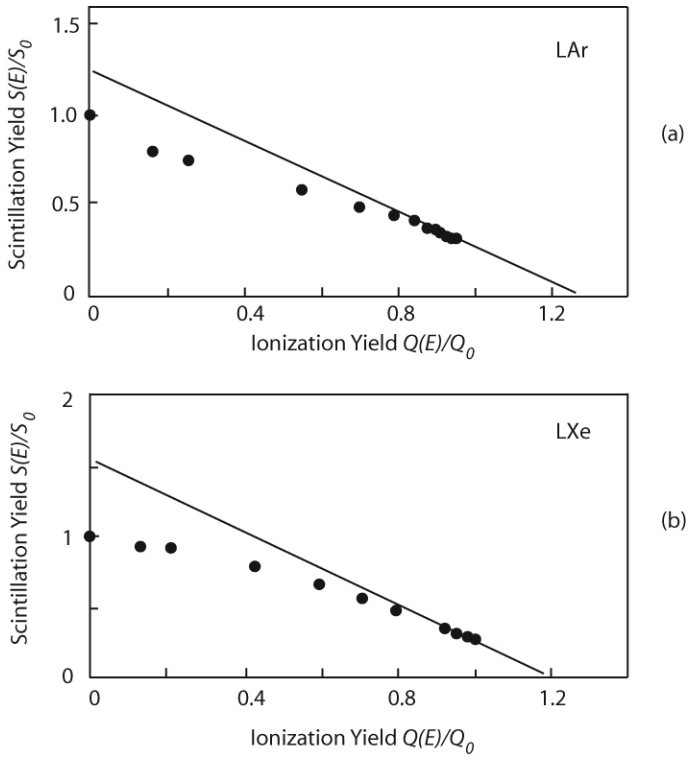

Fig. 5.28 Anticorrelation between scintillation and ionization yields in liquid argon (a) and liquid xenon (b) excited with 1 MeV electrons. The solid lines represent the theoretical predictions. Redrawn from [32].

on the anticorrelation line. This is caused by the electron attachment to the electronegative gas and a modest recombination rate.

The data points in the high electric fields are on the anticorrelation line [32]. The sum signals still provide an energy resolution better than those by the individual signals obtained by Conti et al. [291], despite the slightly weak anticorrelation. A Columbia group recently presented the best energy resolution for ^{137}Cs gamma rays using sum signals. A schematic drawing of the gridded ionization chamber, with two Hamamatsu R9288 PMTs (one on each side), that was used for their experiment is described in Section 4.2.2.2 and is shown in Fig. 4.9.

The results are provided in Fig. 5.29 with the correlation pattern between scintillation and ionization. The best energy resolution (σ) was 1.7% at a low electric field of 1 kV cm^{-1}. An energy resolution better than that of NaI(Tl) was achieved by this method despite the low electric field.

We will now describe another method using sum signals. We observed a significant increase in the collected electronic charge when we doped photo-

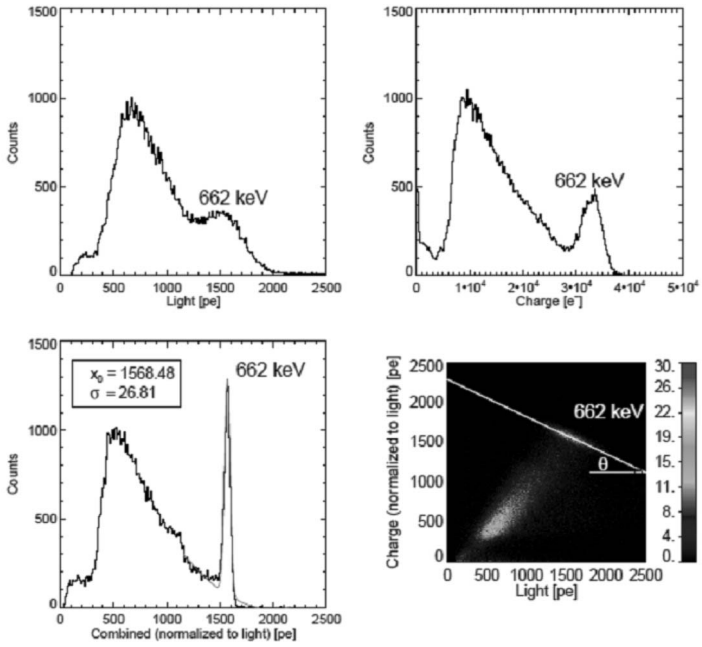

Fig. 5.29 Energy spectra of ^{137}Cs 662 keV γ-rays at a 1 keV cm^{-1} drift field in liquid xenon. The top two plots were obtained separately from scintillation and ionization. The straight line in the bottom right indicates the charge-light correlation angle θ. The bottom left presents the result obtained by the sum signals of scintillation and ionization [292].

sensitive organic materials into liquid argon or xenon. We can obtain signals near the ideal sum signals, since the quantum efficiencies of trimethylamine (TMA) or triethylamine (TEA)-doped in liquid xenon for photoionization are very high ($\sim$80%) [293].

Figure 5.30a shows the energy spectra of ^{207}Bi obtained by a pure liquid xenon and Fig. 5.30b represents that obtained by TEA-doped ($\sim$ 80 ppm) liquid xenon [294]. The energy resolution of 30 keV for 570 keV γ-rays in Fig. 5.30b was obtained at an electric field of 9.1 kV cm^{-1}. This is very close to the best value obtained thus far. In addition, the highest peak clearly splits to two peaks at 4.56 kV cm^{-1}. This splitting to two peaks has been observed in pure liquid xenon only at a very high electric field, above 10 kV cm^{-1}. The best energy resolution has thus far obtained only for such a high electric field. We can easily achieve this energy resolution in TEA-doped liquid xenon at an electric field of 4 or 5 kV cm^{-1}, which is close to the best value in pure liquid xenon. Doke recently estimated the Fano factor for the sum signals [295].

Properties of the most original high-pressure xenon ionization chambers are compared in Table 5.4.

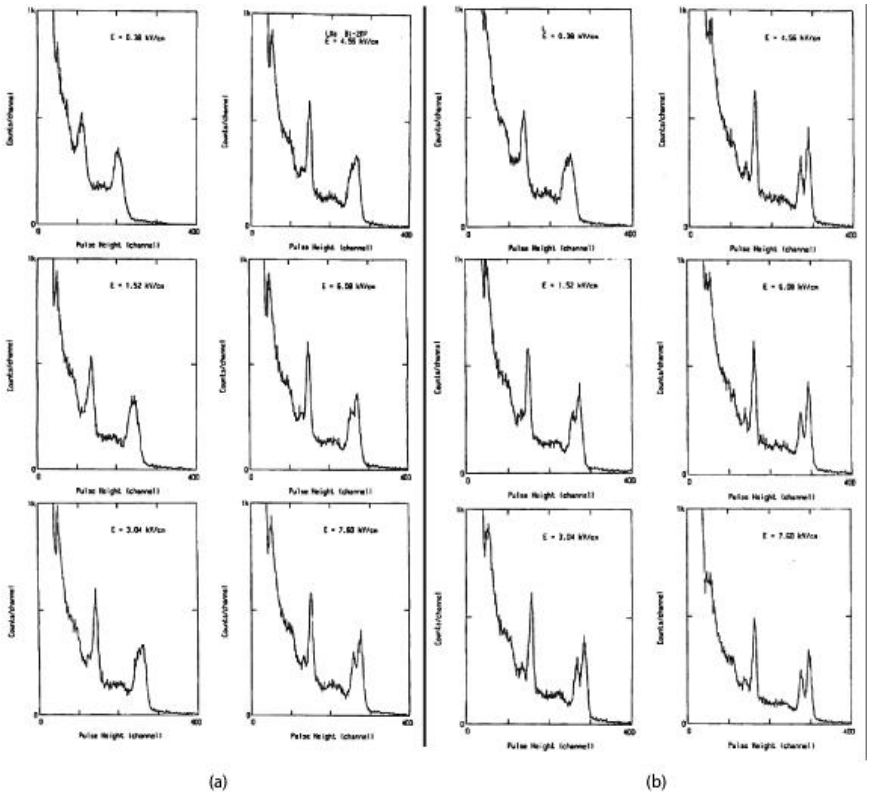

Fig. 5.30 Comparison between the energy spectra for internal conversion electrons and γ-rays emitted from ^{137}Cs obtained by pure liquid (a) and by TEA-doped liquid xenon (b) [294].

Tab. 5.4 High-pressure xenon ionization chambers.

Task	Detector type	Shield. grid	Active vol, L	Max Xe density, g cm^{-3}	En. res. at 662 keV, %	Ref.	Year
Prototype	Cylind.	Yes	~ 1	0.4	3–4	[296]	1981
TPC--prototype	Drift ioniz. chamber	No	0.2	0.3	3–4	[297]	1982
Prototype	*P-plate	Yes	0.4	1.6	2–7	[298]	1986
Prototype	TPC	Yes	~ 10	<0.1		[299]	1987
2β decay experiment	P-plate	Yes	3.7	0.3	5	[300]	1990
Xenia space stat. MIR 1991-98	P-plate	Yes	1.1	0.5	2.7	[277]	1991

Tab. 5.4 High-pressure xenon ionization chambers. (Continued)

Task	Detector type	Shield. grid	Active vol, L	Max Xe density, g cm^{-3}	En. res. at 662 keV, %	Ref.	Year
Prototype	Cylind.	No	2	0.6	3.5	[301]	1991
Prototype	P-plate	Yes	1	0.6	2.2	[68]	1993
Prototype	P-plate	Yes	0.9	0.5	2.4	[302]	1995
Prototype	P-plate w/scint. sig. readout	Yes	0.9	0.5	2.4	[303]	1995
Industr. high-temp appl-s	Cylind.	No	5	0.4	3	[271]	1996
Medical appl-s	*t* project. scintil. chamber		10	0.2	3	[304]	1996
Prototype	P-plate	Yes	1.5	0.55	2.0	[305]	1997
Prototype	Cylind.	Yes	1.5	0.5	2.2	[306]	1996
Prototype	Hemi-spherical	No	1	0.3	6	[307]	2002
Prototype	Cylind. 2-wire chamber	No	2	0.5	3	[284]	2003
Prototype	Virtual Frisch-grid chamber	No	0.2	0.5	2.2	[308]	2003
Dual γ/neutron Xe+^{4}He ion. chamb.	Cylind. 2-wire chamb. w/	No	2	0.5	3	[70]	2003
Prototype	Coplanar--grid config.	No	0.8			[283]	2003
Prototype	Cylind. coplanar--grid config.	No	1	0.3	7	[309]	2005
Prototype	Cylind. w/scint. sig. readout	No	0.2	0.2	2	[310]	2004

* Note: P-plate implies a parallel plate configuration.

6
Proportional Scintillation Detectors

In the past decade, significant progress has been achieved in the development of high-pressure xenon (HPXe) ionization chambers. These detectors have demonstrated that good energy resolution is achievable with kilograms of compressed Xe operating at room temperature. The most common method of acquiring data from HPXe detectors is to measure the charge induced on electrodes by drifting ionization electrons. To eliminate the dependence of the pulse amplitude on interaction position, the ionization chamber is often divided into two parts by a screening Frisch grid (see Chapter 5). The grid is maintained at an intermediate potential between the cathode and the anode, making it electrically transparent to drifting ionization electrons. The maximum voltage pulse amplitude induced at electrodes from collection of n_0 electrons is given by $V_{max} = en_0/C_D$, where C_D is mainly given as a capacitance of the grid relative to the anode. Thus, signal values and the electronics noise [311] of the readout system of an ionization detector is sensitive to variations of the capacitance occurring for example due, for example, to microvibrations of the grid and the anode. Since the grid is usually biased at several kilovolts and the gap between the grid and the anode is about 1 cm, vibrations causing displacements in the 1-μm range generate signals of ~ 1 V magnitude. The microphonic effect is the most important factor limiting performance of HPXe detectors.

Another method to acquire information from high-pressure noble gas ionization chambers is to detect excitation light generated by ionization electrons drifting along the electric field through the gas. In the presence of a sufficiently high electric field, ionization electrons can gain sufficient energy between successive collisions to cause excitation of atoms or secondary ionization. If the energy of drifting electrons is slightly below the ionization threshold, they do not initiate charge multiplication avalanches but rather excite noble gas atoms, A, and generate intensive electroluminescence light (EL), as described in Section 3.2.

The electroluminescence photon emission is generated as a result of radiation decay of excitons or dimers (Eq. (3.22) and (3.23)) similar to the scintillation when ionization electrons are energized by the absorbing energy of

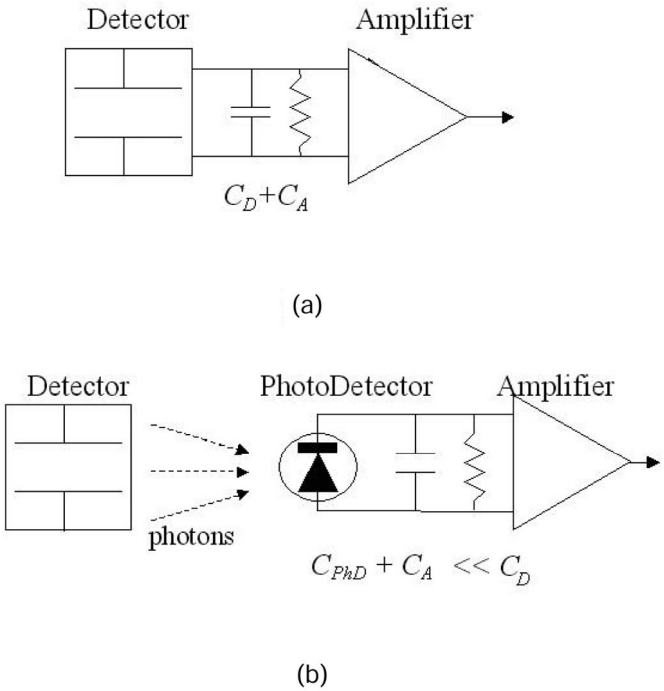

Fig. 6.1 Readout of ionization (a) and electroluminescence (b) signals from HPXe detectors. Note: C_D - capacitance of detector; C_A - capacitance of amplifier; C_{PHD} - capacitance of photodetector [312].

ionization particle. That is why spectra of electroluminescence and scintillation are similar and the EL process is often called proportional scintillation.

EL has been observed in all noble gases and their mixtures. In gas mixtures containing $> 0.1\%$ Xe, the light output and spectrum of electroluminescence is very similar to that of pure xenon. The EL process is not something specific only for noble gases. The effect is widely used in solid semiconductor devices such as LEDs.

Most importantly, as one can see from Eq. (3.24), the electroluminescence signal is not sensitive to the capacitance of the electrode system, and in a uniform electric field at sufficiently high electric field strength, the signal is proportional to the voltage drop between electrodes rather than the electric field strength. With optical readout, the capacitance of the detector electrode system is decoupled from the amplification circuitry (Fig. 6.1). This means that the principal factor limiting the performance of ionization detectors can be eliminated in electroluminescence detectors.

Soon after the first R&D efforts it was understood that EL detectors promise very good energy resolution [313]. Since that time, the performance of noble

Tab. 6.1 Parameters of some gas and solid state detector media affecting intrinsic energy resolution.

	F	W, eV	$(FW)^{1/2}$, $eV^{1/2}$
Si (77 K)	0.08–0.13	3.57	0.5–0.7
Ge (77 K)	0.06–0.13	3.0	0.4–0.6
CdZnTe (-40 °C)	0.14	5.0	0.7
HgI_2	0.30	4.2	1.1
Ne + 0.5%Ar	0.050	26.2 (Ar)	1.1
Xe	0.13	22.0	1.7

gas electroluminescence detectors has been explored in great detail. It is commonly accepted that the energy resolution of an electroluminescence detector operating just below the charge multiplication threshold at energy E, is determined by the statistical variation in the production of primary electrons, the conversion of ionization electrons to photoelectrons in the photodetector, and the photoelectron counting statistics. The expression for energy resolution may be given in the following form:

$$\Delta E_{\mathrm{exp}}/E = 2.35[FW/E + W/\varepsilon YE + \sigma^2/(\varepsilon YE/WG^2)]^{1/2} \tag{6.1}$$

where F is the Fano factor, W is the energy required to produce an electron–ion pair (21.5 eV for xenon), σ^2 is the variance of the photodetector single electron pulse height distribution, G is the mean gain in the photodetector, ε is the efficiency of light collection and photon-electron conversion in the photodetector, and Y is the total light yield of electroluminescence measured in photons per drifting electron

$$Y = \int_0^V (\mathrm{d}N_{ph}/\mathrm{d}\overrightarrow{r})\mathrm{d}\overrightarrow{r} \tag{6.2}$$

In an ideal detector, the energy resolution is limited by statistical fluctuations in the number of ionization electrons

$$\Delta E_{\mathrm{i}} = 2.35[FWE]^{1/2} \tag{6.3}$$

One can see that the best achievable energy resolution is proportional to $(FW)^{1/2}$. For noble gases of moderate density ($< 0.55\ \mathrm{g\,cm^{-3}}$ for xenon), this factor has a relatively low value, comparable to that of semiconductors (Table 6.1). The lowest Fano factor could be achieved with mixed noble gases such as Ar+0.5%Xe, Ne+0.5%Xe, and Xe+5%He [64]. The theoretical limit for the energy resolution of xenon-filled detectors may be estimated to be 0.3–0.4% FWHM at 662 keV.

In the low-energy range, the energy resolution of pulse ionization chambers is determined by the electronics noise, i.e., Johnson (thermal) noise in the input circuit of the amplifier that includes the capacitance between the grid and

the anode. Since in electroluminescence detectors the detector capacitance is decoupled from the amplifier, electronic noise of the amplification circuitry may be negligible. However, EL detectors have an additional noise source associated with light production, light collection, and light detection in photodetectors. In an ideal ELD using an ideal photodetector (the third term in Eq. (6.1) is negligible), the second term in Eq. (6.1) should introduce less fluctuation than the statistical term. From this requirement we have the following condition (in order of value) for realization of the ideal ELD:

$$\varepsilon Y > 1/F, \tag{6.4}$$

or assuming $F \sim 0.1$,

$$\varepsilon Y > 10. \tag{6.5}$$

It means that the conversion efficiency of the wavelength shifting and light collection system is a crucial factor along with sufficient Y integral light output of the EL process. If in the proposed EL detectors the total light yield of electroluminescence Y can reach ~ 400 photons per electron, the theoretical limit on the energy resolution in the electroluminescence detector will be achievable at the electron-photoelectron conversion efficiency

$$\varepsilon > 5\% \tag{6.6}$$

We have to note that such high efficiency of electron-photoelectron conversion has never been achieved in high-pressure EL detectors. For example, the total conversion efficiency of the imaging EL detector with fiberoptic readout has been measured by Parsons et al. [314] to be $\sim 0.6\%$; the total conversion efficiency of the imaging EL detector SDC-19, using nineteen PMT array readout, was estimated to be $\sim 0.4\%$ [304]; 1.1% of the photons produced in a gas scintillation proportional counter (GSPC) with a spherical electrical field and PMT placed outside the detector filled with 0.1 MPa xenon have been detected [49]. Using a windowless solid state photodiode with high quantum efficiency installed directly inside EL detectors is one way to enhance the conversion efficiency.

The most interesting approaches in the design of EL detectors excluding two-phase detectors, which are subject of a special discussion in the Chapter 7, will be considered in this chapter.

6.1 Gaseous EL Detectors with Parallel Plate Electrode Structure

The most popular modern gas detectors utilize effect of gas gain (e.g., see [315]). The electron multiplication process in detectors with gas gain

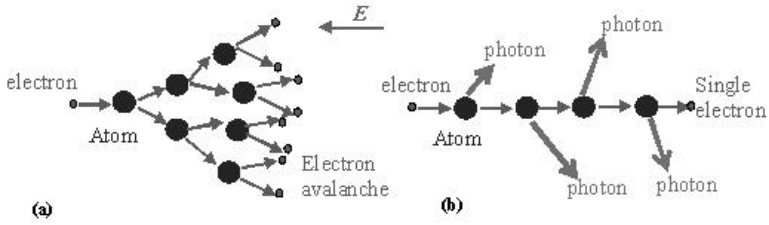

Fig. 6.2 Amplification process in gas detectors with gas gain (a) and electroluminescence (b) or proportional scintillation.

is an exponential process (Eq. (3.20), even at a uniform electric field. In contrast, electroluminescence is a linear amplification process since the number of produced photons is practically linearly dependent of the electric field (Fig. 6.2).

Moreover, as it follows from Eq. (6.1), in detectors with uniform electric field, at sufficiently high electric fields, the number of produced photons is proportional to the voltage drop over the light production gap rather than to the electric field strength: $N_{\mathrm{ph}} \sim V$. This means that detectors with a parallel plate electrode structure are relatively insensitive to variations in the electric field due to relative motion of the electrodes. As a result of this weak dependence of gain on the electric field, the microphonic effect may be essentially suppressed and spectrometric performance further enhanced as demonstrated in Fig. 6.3.

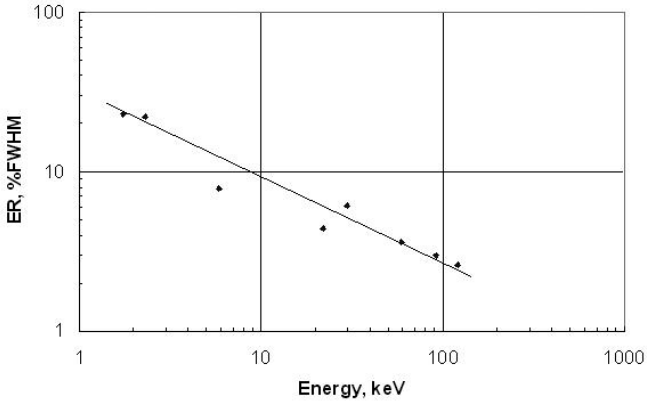

Fig. 6.3 Dependence of energy resolution of the spectrometric electroluminescence detectors on energy of measured X-ray and gamma radiation. Points represent experimental data by Lopes et al. [316], Veloso et al. [317] and Bolozdynya et al. [304]. The line is drawn for better reading of the graph.

Note, that the best results have been achieved with detectors using different photosensors.

6.1.1 Gas Proportional Scintillation Counters

Since their introduction by Conde and Policarpo [318], low-pressure electroluminescence detectors with uniform electric field (also called gas proportional scintillation counters: GPSC) have been successfully used for precision spectrometry of X-rays and soft gamma rays.

6.1.1.1 GPSCs with PMT Readout

A photomultiplier (PMT) is the most used photodetector in GPSCs. The straightforward design of a GPSC is similar to a scintillating crystal detector design: a light-generating medium encapsulated in a can with a thin Be window for input radiation and an optical output window coupled to an externally mounted photomultiplier [313]. This design is ideal for low energy X-ray spectrometry, providing good efficiency and energy resolution (Fig. 6.4).

One of the first EL detectors to become commercially available was the BDELG-3DM model from Bourevestnic, Inc. (St. Petersburg, Russia) shown in Fig. 6.5.

The detector is designed to be used in the X-ray energy range of 2 to 30 keV with X-ray diffractometer for light gathering registration of thin film X-ray diffraction patterns. The input window has a diameter of 20 mm. The energy resolution on MnKa line at quasiparallel radiation beam of 10 mm in diameter does not exceed 9% FWHM at 1 kHz counting rate and 9.5% FWHM at 2 kHz counting rate. The GPSC designed by Borges et al. [320] has been used to investigate the influence of gas gain accompanying electroluminescence (Fig. 6.6).

With this detector it was clearly demonstrated that electroluminescence detectors lose energy resolution as soon as the gas gain begins to play an important role and the electroluminescence yield is increasing nonlinearly. The study of this phenomenon allowed calculation of the first Townsend coefficient dependent on the reduced electric field in xenon gas of low density.

While PMTs provide the lowest noise, they are bulky, fragile, and their use becomes awkward at elevated pressures and increased detector acceptances. Using optical windows with significantly reduced transparency in the VUV region severely limits the quantum efficiency of the detection system. In low counting rate experiments, the glass envelopes of standard PMTs introduce significant background due to presence of radioactive isotopes of potassium in the glass. In the following sections, we consider alternative solutions based on large silicon avalanche photodiodes (LAAPD) and microstrip chambers with

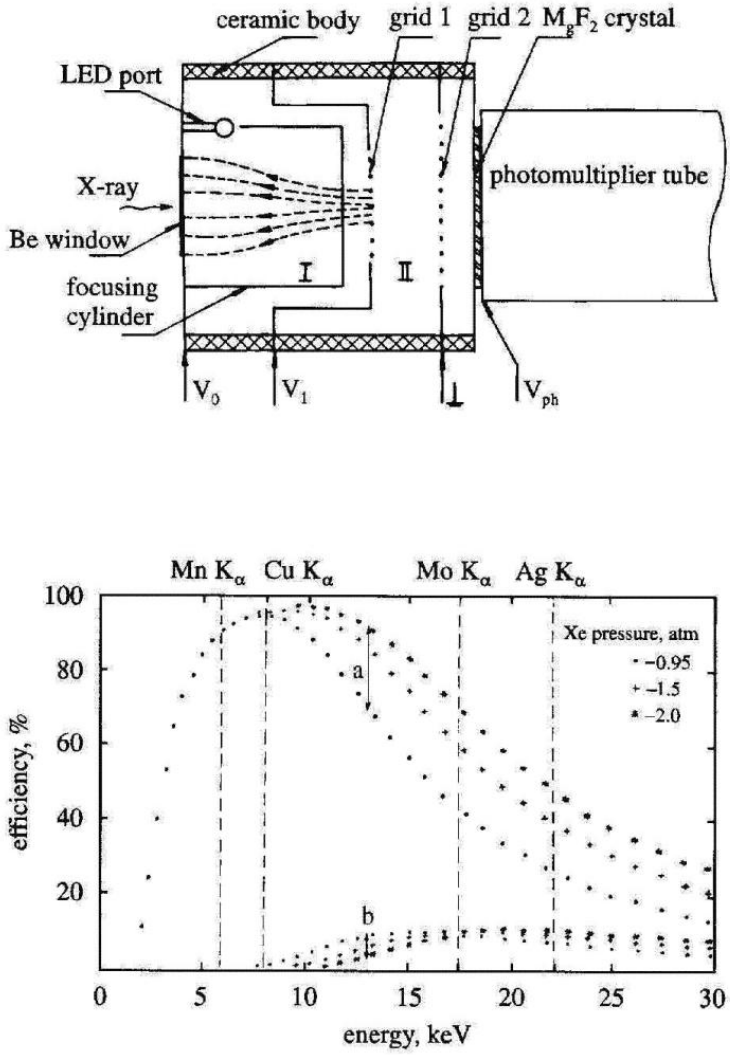

Fig. 6.4 A diagram of a compact electroluminescence X-ray spectrometer developed by Goganov and Schultz [319] and data showing the dependence on the detection efficiency of the detector on the energy of X-rays in xenon at different pressures.

CsI photocathodes, which have been successfully tested and have demonstrated the effectiveness of replacing PMTs with alternative photosensors.

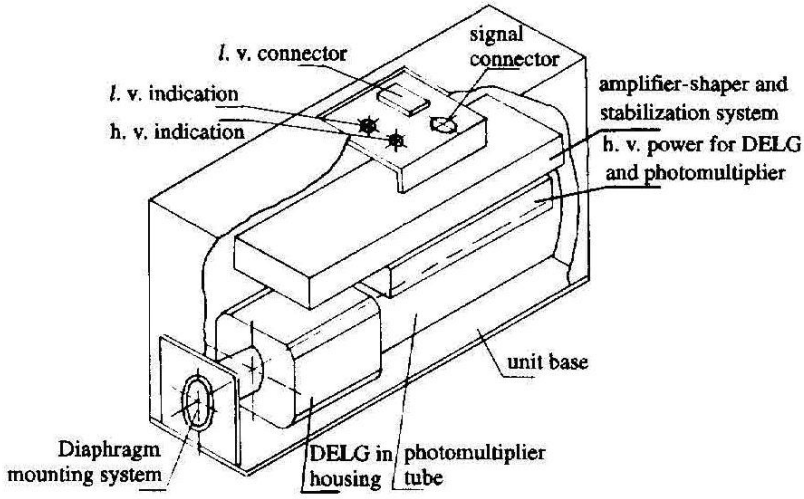

Fig. 6.5 Schematic drawing of BDELG-3DM electroluminescence X-ray spectrometer commercially produced by Bourevestinic, Inc., adopted from [319].

6.1.1.2 **GPSC with Photodiode Readout**

Photodiodes of vacuum type [321] and solid state [322] have been considered as alternative photosensors for GPSCs. However, these detectors were too noisy for low energy X-ray detection and were too fragile to be used at elevated pressures for detection of higher energy gamma rays, and as a consequence, they did not find broad recognition. The recent successful development of avalanche photodiodes with large sensitive area and intrinsic gain presents an alternative technology to employ for development of high performance GPSCs.

Lopes et al. [316] constructed a GPSC detector equipped with a large (16-mm diameter) avalanche photodiode (LAAPD) by Photonix (Fig. 6.7a). The detector had a 2.5-cm deep drift region, a 0.8-cm deep electroluminescence gap and filled with 110 KPa Xe purified by passing through hot metal getters. Grids were made of 80 μm stainless steel wire on a 900-μm pitch. The detector radiation window is made of 6-μm thick Mylar of 2-mm diameter. A low vapor pressure epoxy was used to seal the Macor insulators, Mylar window and feedthroughs. The LAAPD had demonstrated 105% quantum efficiency at 170 nm. With this detector they have achieved the best energy resolution measured with low-pressure xenon electroluminescence detectors for ^{55}Fe 5.9 keV (7.9% FWHM) and ^{109}Cd 22.1 keV (4.4% FWHM) X-ray lines (Fig. 6.7b).

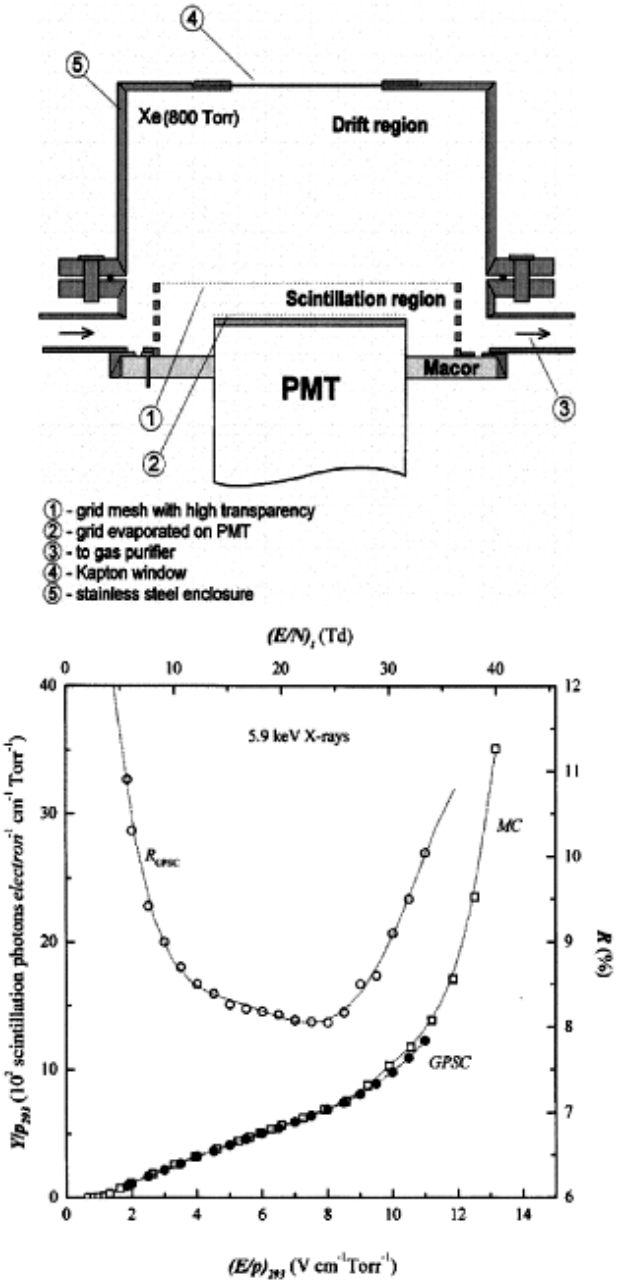

Fig. 6.6 Schematic drawing of the GPSC (top) used by Borges et al. [320] to measure the reduced electroluminescence yield (experimental data - closed circles, computer simulations - open squares) and the detector energy resolution (open circles) as a function of the reduced electric field in the light production region for 5.9 keV X-rays stopped in 106 KPa Xe gas (bottom).

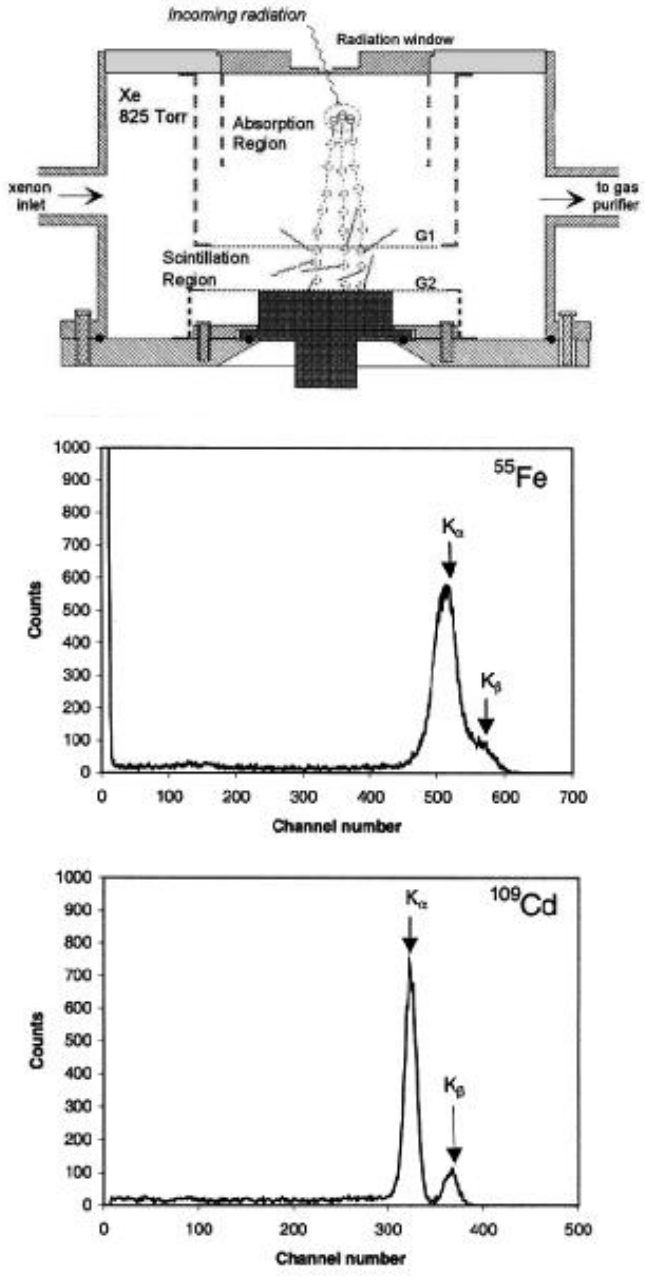

Fig. 6.7 Schematic diagram of GPSC (Xe pressure = 110 KPa) and pulse height distributions for ^{55}Fe and ^{109}Cd X-ray sources [316].

6.1.1.3 GPSC with Open Photocathode Readout

The use of bare photocathodes allows the construction of GPSCs not requiring an optical window to convey electroluminescence light to the photodetector. Among the possible photocathodes are CsI, Cs_2Te, and semiconductors with a surface with negative affinity to electrons that have been considered for application in Cherenkov detectors (see, for example, review by Mine [323]). The idea of using open photocathodes to detect electroluminescence from xenon for the first time was realized by Bagryanskii et al. [324] in 1985. A detector was designed for detection of X-rays with a parallel plate electrode structure enclosed in a glass envelope as shown in Fig. 6.8.

X-ray radiation passed through a 30-mm diameter and 0.15-mm thick Be window (1) diffusion bonded to the flange (2), into the drift region, which is formed by the cup-shaped electrode with the flat grid (4) and the flange (2). The electric field of 500–700 $V\,cm^{-1}$ was applied between grids (4) and (5) with 12-mm gap in order to generate electroluminescence from xenon at a pressure of 1.3 atm pressure. The grids are made of 0.1-mm diameter nickel wires welded with pitch of 2 mm. UV photons generated during electroluminescence cause electron emission from the photocathode (6) placed behind the double gridded screen (5) at a distance of 3 mm. The cathode is installed onto the flange (9) with glass tube (7), and connected to the charge-sensitive preamplifier via a glass feedthrough (10). The removable flange (9) is sealed to the flange of the detector body (8) with a copper gasket. The cathode was coated with vacuum deposited 200-μm thick CsI. The detector was backed at > 520 K before filling with xenon and installation of the photocathode. This device achieved the best energy resolution for ^{55}Fe up to that time with a value of 20.4% FWHM at 5.9 keV.

Open photocathodes provide additional advantages when deposited onto microstrip electrode structures as proposed by Akimov et al. [325] in 1994. The strong electric field localized between microstrip anodes and cathodes may be used to generate short electroluminescence signals generated by electrons collected from the drift region and from photoelectrons liberated by UV photons impinging on the CsI coating of cathode strips. The second process enhances the light gain and is used to amplify the charge signal. Placing the MSP/CsI structure in condensed (liquid) xenon may further enhance the gain due to the reduced work function of CsI. Electroluminescence of xenon between microstrips has been generated using a 2×2 mm^2 microstrip plate (MSP) consisting of 7-μm wide anodes, 80-μm wide cathodes on a 200-μm pitch made of vacuum deposited aluminum onto 0.35 mm thick sapphire and vacuum coated with a 500-nm thick layer of CsI; the backside of the MSP has been continuously coated with aluminum. Electroluminescence signals were detected by a glass photomultiplier coated with *para*-terphenyl, to shift the UV electroluminescence light into the visible region of the spectrum, and placed

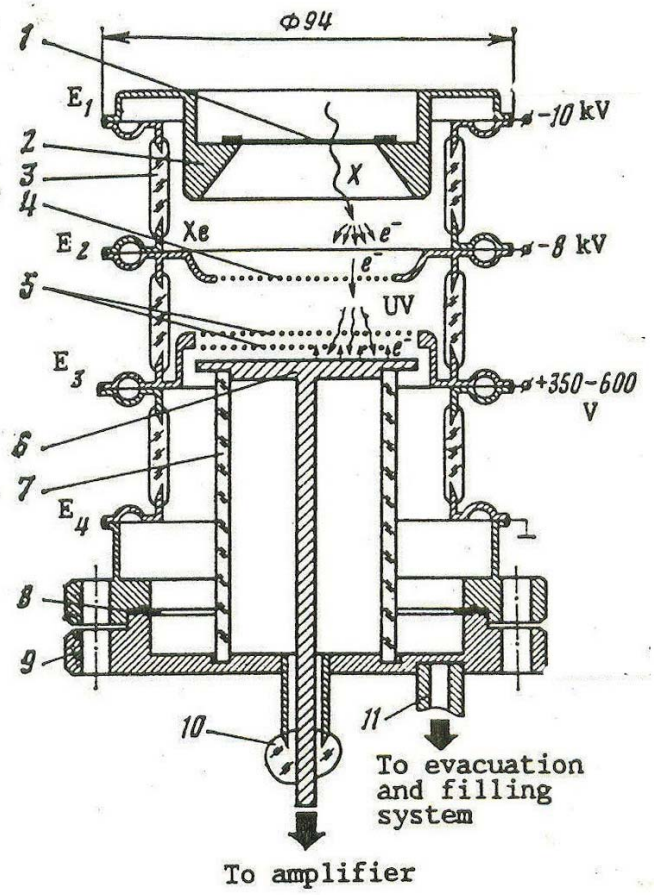

Fig. 6.8 A schematic diagram of GSPC with a bare CsI open photocathode designed by Bagryanskii et al. [324]. Note: 1 - 30-mm diameter 0.15-mm thick Be window; 2 - flange with 94 mm outside diameter biased at E1 voltage; 3 - glass vessel; 4 - the cup-shaped flange equipped with a flat grid and biased at E2 voltage; 5 - double grid screening electrode biased at E3 voltage; 6 - the photocathode coated with CsI; 7 - glass insulating tube supporting the cathode; 8 - copper gasket; 9 - removable flange supporting the cathode and biased at E4 voltage or grounded; 10 - glass insulator; 11 - gas input/output.

above the MSP. With this MSP a light gain of 35 times the original scintillation light was measured in a 0.9 MPa Xe using alpha particles.

Conde's group has developed this approach through a series of investigations [143]. One typical detector of this class is presented in Fig. 6.9 along with schematic drawing illustrating the principle of conversion of the electroluminescence light to the charge. Veloso et al. [317] used a microstrip plate vacuum coated with a 500-nm thick layer of CsI, acting as a photocathode to detect very soft X-rays in low-pressure xenon. The microstrip plate was a

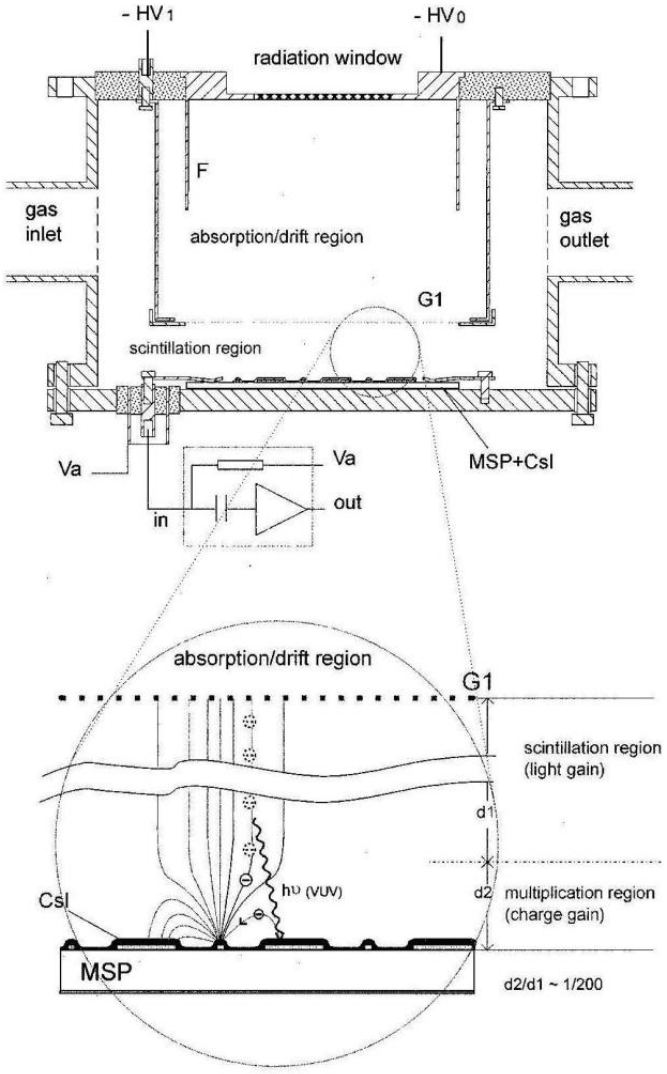

Fig. 6.9 Schematic diagram of GSPC with CsI-coated multistrip chamber and illustration of the principle of operation [317].

CERN MS-4 model MSP consisting of 10-μm wide anodes, 80-μm wide cathodes deposited on a 200-μm pitch onto 0.5-mm Desag D263 glass substrate with a backplane coated with 0.1 μm chromium. The active area was 30 by 30 mm^2. The backplane and cathodes were maintained at ground potential while a positive voltage of a few hundred volts was applied to the anodes. Energy resolutions of 23% and 22% FWHM were obtained for 1.74 and 2.3 keV X-rays, respectively (Fig. 6.10).

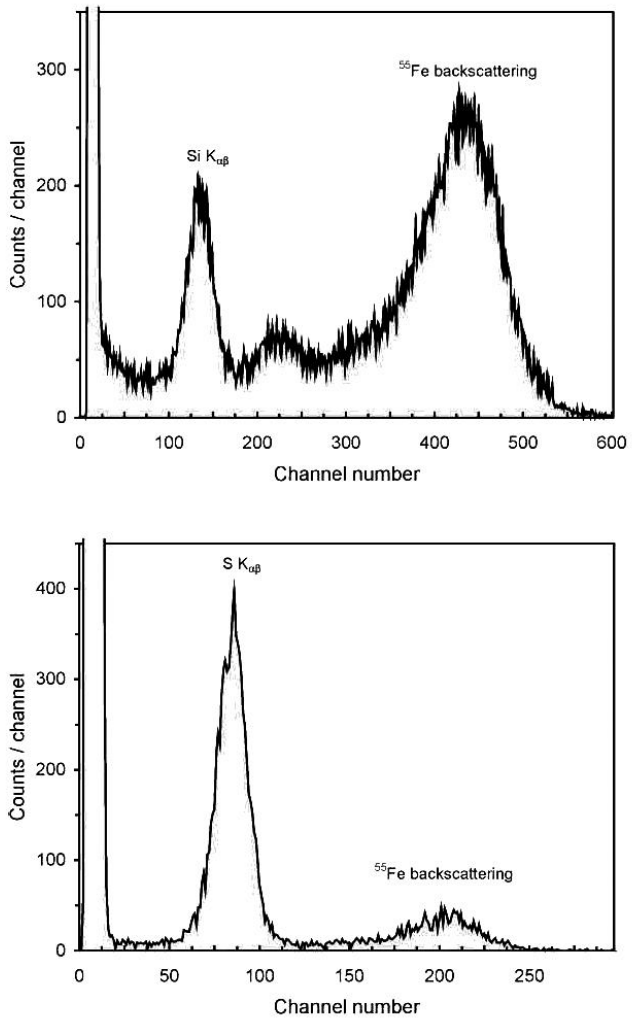

Fig. 6.10 Pulse height distributions of signals generated by fluorescence photons from pure silicon and sulfur targets activated with a ^{55}Fe X-ray source by Veloso et al. [317].

The detector has demonstrated 300 eV detection thresholds and a unique ability to operate in strong magnetic fields. At a magnetic field of 5 T, amplitudes of signals acquired from the detector were reduced by less than 25%, while the detector energy resolution and pulse rise time increased by less than 10% (Fig. 6.11).

The detector was developed for muonic hydrogen spectroscopy. Montiero et al. [326] investigated Xe+Ar gas mixtures in the detector shown in Fig. 6.9

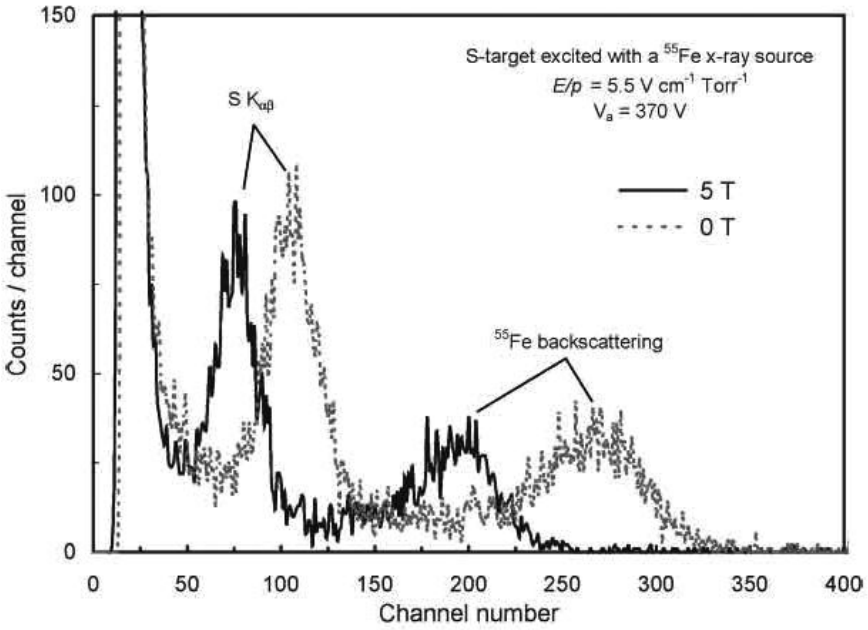

Fig. 6.11 Influence of a strong magnetic field on pulse height distribution signals acquired from the detector irradiated by fluorescence X-rays from the sulfur target excited with a ^{55}Fe X-ray source by Veloso et al. [317].

They found that a Xe+30%Ar mixture provides the best charge amplification and the energy resolution (Fig. 6.12).

Implementation of charge gain with open photocathodes has a serious drawback [143]: intensive electroluminescence accompanying charge multiplication in pure noble gases releases secondary electrons from the open photocathode, leading to a positive feedback process, which limits the maximum allowable charge gain. To avoid this effect, the charge multiplication structure (MSP or wire chamber) with a solid photocathode can be separated from the light-generating region by a thin CaF_2 or quartz window and filled with non-scintillating mixture for proportional chambers such as methane [327] or P-10 gas mixture [317]. At 2.7 kPa CH_4 the quantum efficiency of CsI is reported to be 9%. The combination of a two-stage low-pressure proportional chamber with a CsI cathode yields the energy resolution of 6.4 and 4.1% FWHM for 30 and 60 keV X-rays, respectively. Dangendorf reported on the development of such a detector having a sensitive area of 300 cm^2, and filled with 2.5 MPa Xe to detect X-rays emitted in high-energy ion-atom collisions [327].

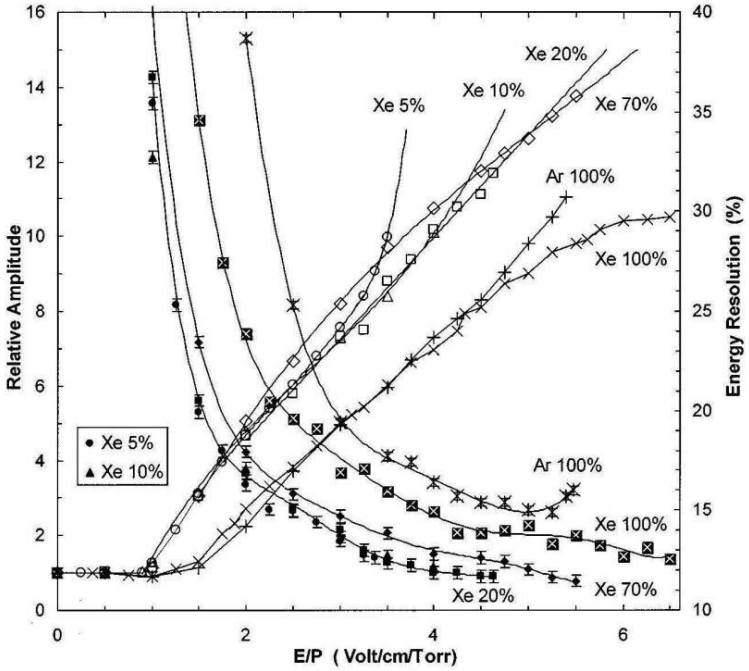

Fig. 6.12 Shown are the relative charge signal amplitude in a GSPC of electroluminescence photons and the energy resolution versus the reduced electrical field, E/p, of the light production (electroluminescence) region. The device used for these measurements utilized a CsI-coated microstrip chamber described in [326] and filled with Xe+Ar gas mixed in various ratios.

6.1.2 High-Pressure Electroluminescence Detectors

The attractive properties of electroluminescence detectors stimulated a few attempts that were undertaken to develop a high-pressure xenon ELD capable of spectrometry and position identification of relatively high-energy gamma rays. In one study, Bolozdynya and DeVito [312] demonstrated extremely low sensitivity of a high-pressure xenon electroluminescence detector with uniform electric field to vibrations. A schematic design of the EL detector used in this study is presented in Fig. 6.13.

The cathode (2), drift electrodes (3), and the grid (4) define a sensitive volume of 5 cm in diameter and 5 cm in depth. A parallel plate electrode arrangement consisting of photolithography-made mesh grids (4, 5) was used to generate electroluminescence that was detected by a photomultiplier (9) optically coupled to a window placed behind the lower, grounded, grid.

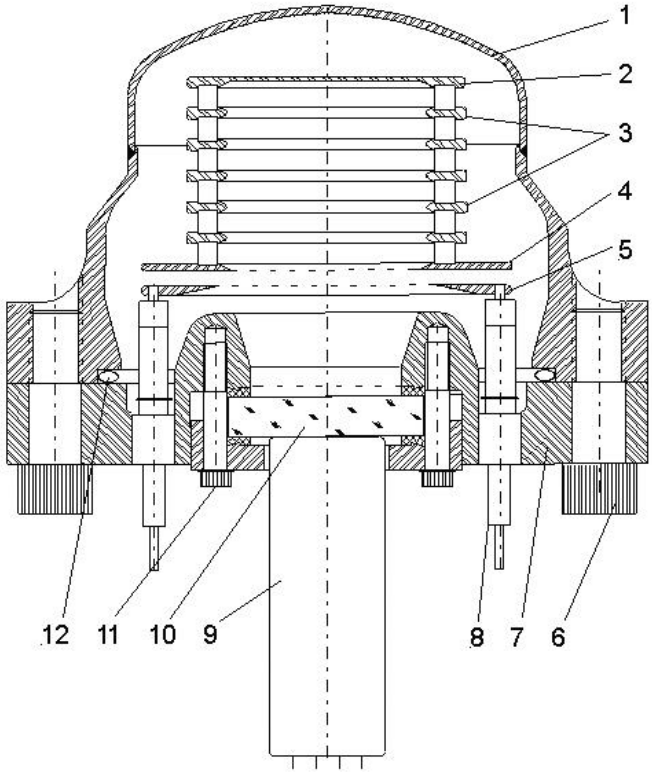

Fig. 6.13 Electroluminescence high-pressure xenon detector with parallel plate electrode system and photomultiplier readout. Note: 1 - high-pressure vessel; 2 - aluminum cathode; 3 - drift electrodes separated by stand-off ceramic insulators; 4 and 5 - grid electrodes forming electroluminescence region; 6 - bolt; 7 - flange; 8 - HV feedthroughs; 9 - photomultiplier; 10 - optical window coated with p-terphenyl wave-length shifter; 11 - bolt; 12 - Helicoflex gasket in aluminum jacket. Sensitive volume of the detector enclosed into the electrode system of 2–4 has a 5-cm diameter and 5-cm depth [312].

A 0.5 mg cm^{-2} layer of p-terphenyl ($C_{14}H_{18}$), serving as a wave shifter, was vacuum-deposited on the input surface of the optical window, enabling the photomultiplier to *see* the 170 nm UV light generated during the electroluminescence process. The quantum efficiency of the p-terphenyl wave shifter has been measured to be $> 90\%$ in pressurized xenon [144]. The emission spectrum of p-terphenyl has 2 peaks: one at 350 and another at 450 nm. An important property of this well-known scintillating dye is that it does not contaminate xenon. High voltage feedthroughs (8) were installed in the flange (7) to supply voltage to the electrodes. The flange is equipped with a knife-edge groove for 2-3/4″ CF gaskets, which were used to install a 10-mm thick UV-grade optical window (KU-8) coated with p-terphenyl wavelength shifter.

A blue-sensitive EMI THORN 9125B photomultiplier with 30-mm diameter input window was optically coupled to the external face of the window.

Before assembly, all metal and ceramic-made detector parts were baked at 500 K under a vacuum of $< 10^{-4}$ Pa. The assembled detector was pumped down to 10^{-6} Pa for a week before filling with xenon. Pure Xe or Xe+0.2%H_2 gas mixture used to fill the detector. A spark purification technique was used to remove electronegative impurities from the gas. The ultimate purity of the gases used in these investigations corresponded to several milliseconds of electron lifetime.

The detector operates in the following manner. Ionization radiation absorbed in the sensitive volume generates electrons, which drift into the EL region and generate an EL flash. UV light is shifted into the 350–450 nm range by p-terphenyl deposited on the inside surface of the window viewed by the PMT.

The EL detector was tested with pure Xe and Xe+0.2%H_2 gas mixtures pressurized up to 3.1 MPa. The best energy resolution was achieved at pressures of about 2 MPa. In order to prove the statement about vibration insensitivity, an electric engraver (10 W, 60 Hz) was used to disturb the ELD. The writing pin of the engraver was installed onto the flange of the ELD. Pulse height spectra of ^{241}Am gamma source were taken for the same acquisition time while the engraver was working and when it was turned off. No significant difference between spectra in the range of >10 keV was found (Fig. 6.14).

When repeated with HPXe ionization chambers, the test demonstrated that the working engraver generated enormous signals exceeding the ionization signals from the gamma sources by two orders of magnitude, i.e., the microphonic effect introduces the risk of damage to preamplifiers and prohibits any spectral measurements with HPXe detectors under these conditions.

In attempt to construct a more robust HP ELD, the fragile optical window and PMT in the detector described above detector were replaced with a large avalanche photodiode installed directly inside the detector [328]. The input surface of the LAAPD was coated with p-terphenyl wavelength shifter. The detector demonstrated about the same energy resolution as it did using a PMT readout, however, it was found to be more sensitive to vibrations because of vibrosensitivity of the used charge-sensitive preamplifier that was installed directly onto the flange of the detector. The authors planned potting preamplifier with GE RTV in order to reduce the vibration of the wiring.

6.1.3
Imaging Electroluminescence Detectors

Emission of light generated by electrons drifting through noble gases at high electric fields have been used for imaging trajectories of high-energy particles

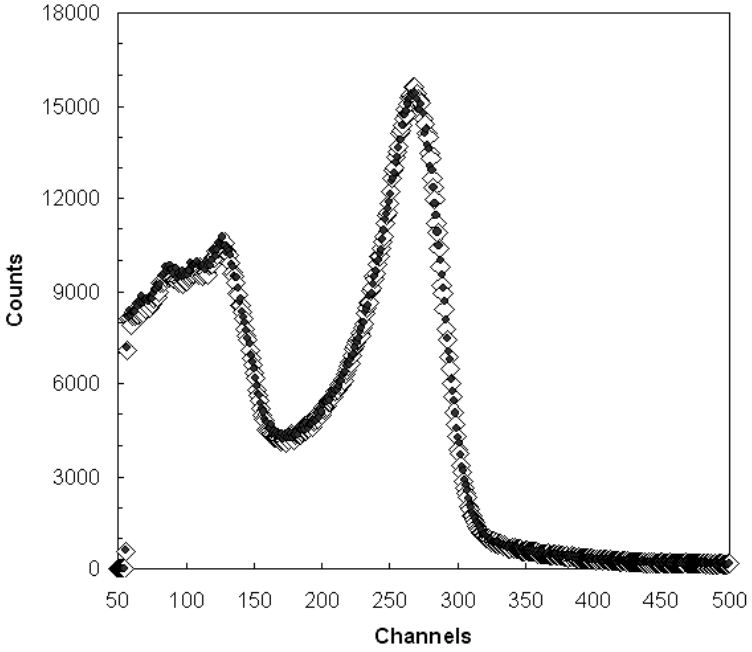

Fig. 6.14 Spectra of ^{241}Am gamma ray source measured in absence (open diamonds) and presence (closed circles) of mechanical vibrations generated by an electric engraver in HP ELD filled with 2 MPa Xe [312].

in spark chambers, popular devices of high-energy physics in the 1960s and 1970s [329]. In a spark discharge, the number of generated photons is so high (10^{11}–10^{12}) that a photofilm technique can be successfully applied. However, spark chambers have a large dead time needed to clear ions from the electrode gap and accumulate sufficient energy for the next discharge and they cannot provide accurate measurements of ionization. Since Policarpo's pioneering work on the development of gas scintillating proportional counters, the electroluminescence (EL) detectors have been considered as a promising alternative in the development of instrumentation for imaging radiation fields. Electroluminescence allows the transformation of ionization signals into photon signals and gains the last ones.

6.1.3.1 **Analog Imaging Electroluminescence Detectors**

The principal advantage of analog imaging is that complex images and unexpected events can be detected. Historically, this method was the first available. Becquerel discovered radioactivity in 1895 when he noticed the accidental projection imaging of uranyl sulphate crystals that were wrapped in black paper and placed on photographic plates.

Oscillating Field

The electroluminescence of noble gases in a DC electric field is normally too weak to be detected by photographic techniques. To increase the light output, Cavalleri et al. [330] applied an oscillating electric field to Ne+2%Ar gas mixture at a pressure of about 0.1 MPa. They succeeded by photographing tracks of individual alpha particles. The light chamber consisted of a Pyrex glass cylinder (12-mm height, 80-mm internal diameter, 3 to 4-mm wall thickness) closed with two flat glass disks covered with a semitransparent conductive layer of SnO_2. The chamber was sealed with enamel or Araldite Type 101 compound. The external electrodes allowed a high degree of field uniformity inside the chamber. The damped oscillating HV pulse was triggered with a photomultiplier detecting scintillation of the gas.

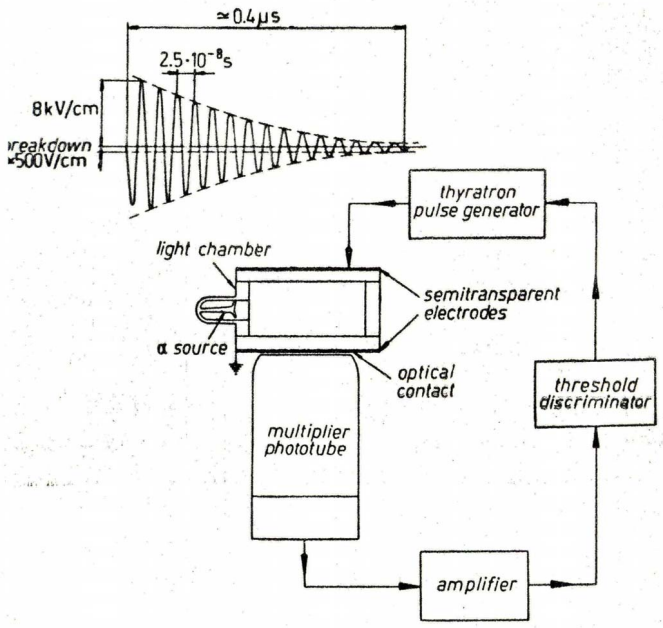

Fig. 6.15 Operational principle of the light chamber developed by Cavalleri et al. [330] for imaging individual charged particle tracks in an oscillating electric field and triggered from scintillation of the gas.

Figure 6.15 shows the block diagram of the electronics and the characteristics of the HV pulse used for light amplification. Electroluminescence tracks were photographed with a photo camera using 32 DIN film. From the photographs, the spatial resolution of 2 mm has been defined in perpendicular direction to the field and about 3 mm along the field. The spatial resolution was limited by diffusion of electrons during the HV oscillating pulse. A light gain exceeding 10^7 was measured with a photomultiplier as shown in Fig. 6.16.

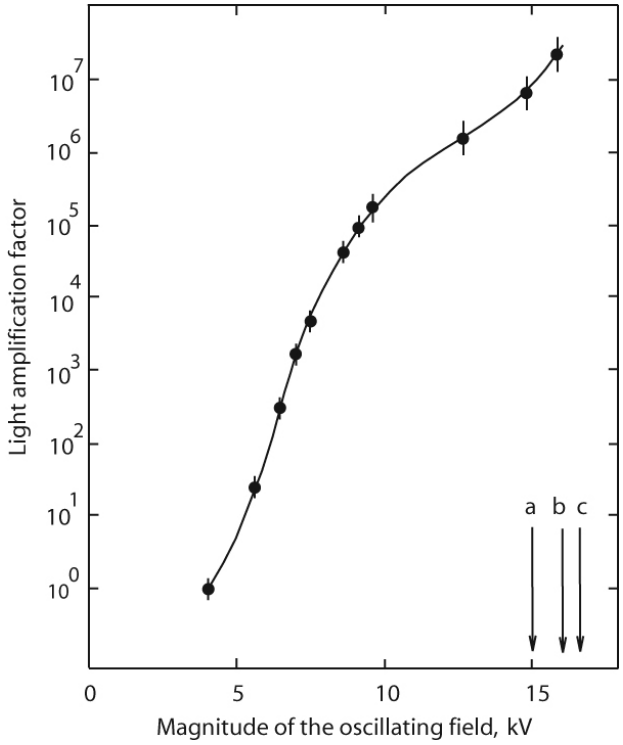

Fig. 6.16 Dependence of the light amplification factor on the magnitude of the oscillating electric field in the light chamber by Cavalleri et al. [330]: a - threshold of eye sensitivity ; b - field used for photographing; c - threshold for streamer production. Redrawn from [330].

This value probably included a factor due to electron multiplication that could not be separated in these measurements.

Image Intensifier

Gorenstein and Topka [331] considered an image intensifier for imaging electroluminescence photons from noble gases. They developed an imaging detector placed in the focal plane of an X-ray imaging telescope. Each image point in the focal plane is the convergence of a cone of X-rays. In order to achieve good angular resolution X-rays must be absorbed in a narrow depth. This means that the gas must be strongly absorbing such as xenon at a pressure of 0.22 MPa for 6 keV X-rays.

The detector is shown in Fig. 6.17. X-rays enter the detector through a thin window supported by a tungsten mesh and absorbed in a 4.5-mm region A. Ionization electrons drift into a 3-mm region B. The light production region B is imaged by a reflecting Cassegrain telescope onto a readout system consist-

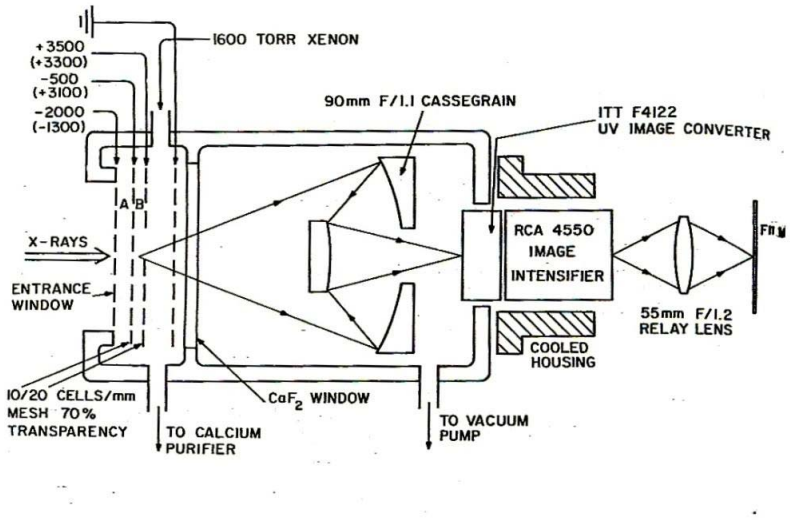

Fig. 6.17 A schematic diagram of the scintillating imaging proportional counter. The number assigned to the entrance window, cathode, and anode are voltages; the upper values are typical operating values, the lower values (in parenthesis) refer to the situation where the spatial resolution is better [331].

ing of a UV-to-visible image converter ITT F4122 and RCA 4550 image intensifier coupled to the converter via fiber optics. It is estimated that about 50 UV photons are imaged onto the converter for each 5.9 keV X-ray. The light production chamber is insulated from the optics by a CaF_2 window. The device allowed photographic capture of a single 5.9 keV point with film such as Kodak 2475. The sensitive area of the detector is 5×5 cm^2. The performance of the detector was studied with a masked ^{55}Fe source and 0.5 mm special resolution of the integrated flux was measured.

With the development of sensitive CCD cameras, similar detectors have been constructed for computerized, digital X-ray imaging [332].

GEM

One of the latest developments in the analog imaging technology has been ignited by rapid progress in the development of gas electron multipliers (GEMs) [333] and sensitive CCD cameras (>10% QE between 400 and 1000 nm). In 2003 Fraga et al. [334] reported imaging of single alpha particle track in Ar+5%CF4 gas with a CCD camera using light emission from a GEM. The gas mixture provided adequate emission spectra with relatively high light output ($\sim$ 0.7 photons per electron). Advantages of GEMs include high gain using up to four stages, suppressed ion and photon feedbacks; yet, GEMs can

be manufactured in large areas ($\sim 30\times30\text{cm}^2$) with high granularity (90-μm pitch). Using two cascaded GEMs filled with 0.3 MPa Xe+2.5TMA and viewed with a PMT, energy resolution better than 20% has been achieved at 22.1 keV (^{109}Cd). Further development of this approach may result in construction of a high-performance X-ray and gamma ray imaging system.

6.1.3.2 Digital Imaging

Digital imaging techniques were implemented in the 1970s when analog to digital converters and powerful computers became available. The principal advantages of the digital imaging over film technology include the following:

- Less ionization can often be used to achieve the same high quality picture.
- Digital images can be enhanced and manipulated with computers.
- Digital images can be sent via network to other workstations and computer monitors so that many people in remote locations can be involved in data analysis.
- Digital images can be archived onto compact optical disk or digital tape drives saving tremendously on storage space and manpower.
- Digital images can be retrieved from an archive at any point in the future for reference.

GSPC with Wire Chamber Readout

Multiwire proportional chambers (MWPC) permit position determination in digital form. The intrinsic position resolution (FWHM) can be about 1 mm and the time resolution can be about 10 ns. There have been many attempts to combine the technology of multiwire chambers with electroluminescence light amplification in pure noble gases. Since the quenching admixtures used in wire chambers allow stable operation at high gas gain, the light-generating region can be used to be separated from the wire chamber with a UV transparent window. Only low-pressure GSPCs may be constructed in this configuration. In order to make the wire chamber sensitive to UV light, photoionizing admixtures such as vapors of triethylamine (TEA) and tetrakis-(dimethylamino)-ethylene (TMAE) at room temperature are required. A compilation of photoionization potentials of various photosensitive compounds and their photocurrent thresholds may be found in review paper of Policarpo [335]. Full advantage of multiwire proportional chamber readout was realized by using the center-of-gravity technique to determine the position of highly collimated beams of X-rays: in the direction orthogonal to the anode wires, the position

resolution of $\sigma \sim 150$ μm was achieved [336]. The energy resolution associated with the detection of electroluminescence is below 1% for energies larger than about 0.6 MeV and $\sim 2\%$ for 150 keV.

In 1982 Ku et al. [337] described one of the first examples of a xenon-filled GSPC coupled to a multiwire proportional chamber (MWPC). The device was filled with a TMAE + P20 gas mixture described by Ku et al. [337] in 1982. They reported 9% FWHM energy resolution and 0.9 mm FWHM spatial resolution for 5.9 keV. Later developments such as improved xenon purification achieved by continuously circulating xenon through a purifier [338], improvements of the detector ceramic design, and enlarged sensitive area up to 17.8-cm diameter [339] did not bring significant improvements in the performance of these detectors. A GSPC coupled to a MWPC has been successfully used for X-ray imaging in astrophysics research (see Chapter 9).

Avalanche Cameras with Gas Wavelength Shifter

Charpak was one of the first who considered the idea of using the light pulses produced by electron avalanches in proportional counters (see, for example, Ref. [340]). Photons emitted by avalanches in gases can be detected with an image intensifier coupled to a solid state camera [341]. The problem is that noble gases, which are the most effective light-emitting media, radiate in UV and VUV range. Several gaseous wavelength shifters such as TEA, N_2, and TMAE have been investigated in order to shift the light emission toward or into the optical range. It was found, that the emission spectrum of TMAE-based mixtures peaked at 480 nm in comparison with 280 nm for TEA and 340 nm for N_2. The shape of the spectra is almost independent from the other components of the gas mixture, if they are transparent in the region of emission. However, TMAE is not easy to handle and the conversion UV light by TEA or gas mixture containing TEA and TMAE have been used more often. Photon gain is simply related to charge gain: the highest photon gain (up to 10^3 for Ar+2%TEA) has been achieved with charge gain of less than 10.

The imaging chamber usually consists of a multistep parallel plate conversion and light-generating chamber separated from an imaging optical camera with a CaF_2 optical window (see, for example, Fig. 6.18). Such detectors with sensitive areas up to 20×20 cm^2 have been proposed for imaging Cherenkov rings, electromagnetic showers, and tracks of individual high-energy particles [343], and photoelectrons in X-ray polarimetry [344]. Note that the avalanche chamber does not require a trigger and may be operated in continuously sensitive mode.

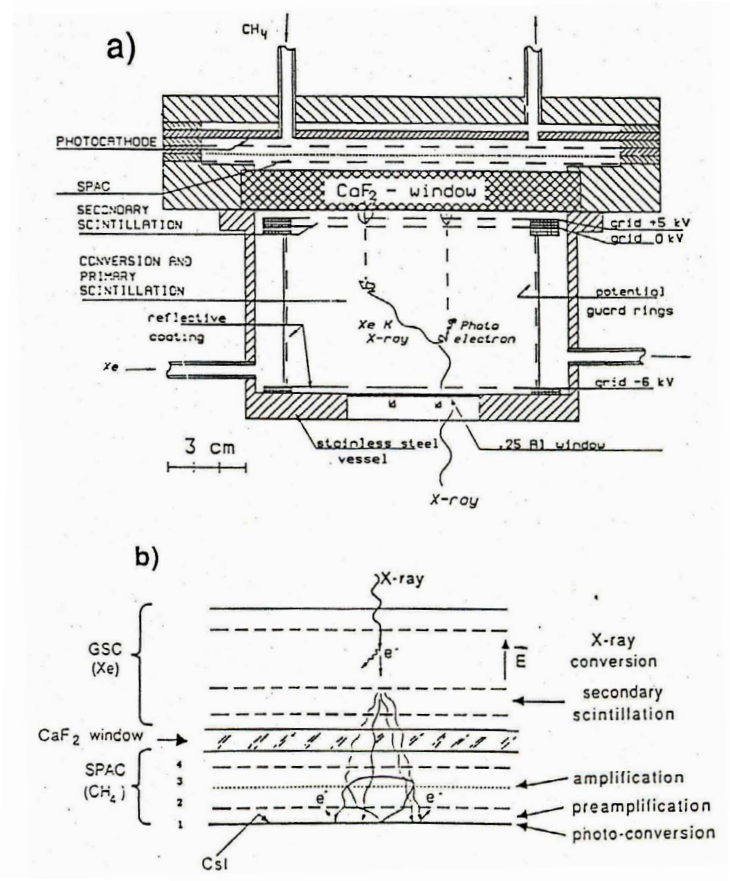

Fig. 6.18 Gas scintillation proportional chamber coupled to the solid photocathode avalanche chamber: (a) general layout of the detector and (b) a schematic view of the electrode structure and the operating principle [342].

Scintillation Drift Chambers

Drift chambers are position-sensitive detectors in which spatial resolution is achieved by measuring the time electrons need to reach the anode wire, measured from the moment that the ionizing particle traversed the detector. This results in higher resolution and wider wire spacing than is possible with simple multichannel detectors. Fewer channels have to be equipped with electronics, although the cost per channel is increased. Drift chambers use longer drift distances, hence are slower than multiwire chambers; therefore, they are typically not used in the primary beam, in high-rate colliders, or for triggering purposes. Drift chambers have been built in many different forms and sizes, and they are standard tracking detectors in more or less all high-energy

physics experiments; this is true even in high-rate colliders, where the collision rate can be shorter than the maximum drift time. Planar (or cylindrical) chambers, with the drift in the same plane as the wires, have been operated with anode wires up to 50 cm apart, but more typically distances of around 5 cm are used.

Scintillation drift chambers can be triggered with scintillation of the working medium produced at the time of the initial interaction of detected radiation with the detector medium; after drifting through the gas, ionization electrons passing through the high electric field region generate electroluminescence or secondary scintillation light, which has intensity proportional to the energy initially deposited by the radiation. Detection of the electroluminescence allows two dimensions of spatial imaging perpendicular to the drift direction, and the comparison of the times of the scintillation and beginning of the electroluminescence gives the drift time of the electrons and, therefore, the position of the initial interaction in the drift direction.

The scintillation drift chamber (SDC) was invented by Charpak, Ngoc, and Policarpo at the end of the 1970s and registered in the US Patent Office in 1981 [345]. Generally, SDCs consist of a pressure vessel that contains a low field drift region, followed by a high field light-generating gap, defined by two transparent wire electrodes. Sometimes, shaping rings are used to provide a more uniform electric field in the drift region. The light gap is viewed by an array of photodetectors. In many SDCs, photomultipliers placed outside the high-pressure vessel have been used (Table 6.2). An array of seven small size (1/2″-diameter) PMTs have been successfully tested inside 50 mm FOV SDC filled with 2 MPa xenon [144]. Other photosensors that have successfully been employed include wave-shifting fiber arrays coupled to PMTs [314], avalanche chambers with a CsI open photocathode [346], and microstrip chambers [325]. Detectors of this type have been successfully used at BeppoSAX satellite-born X-ray laboratory in 1996 [347]; another one tested in balloon flight in 2001 as a focal plane array of a hard X-ray telescope at Marshall Space Flight Center [348].

One of the most successful SDCs (Fig. 6.19) consists of a stainless steel pressure vessel and an electrode structure, supporting a 37-mm deep drift region followed by a 6-mm deep light-generating gap defined by two wire electrodes. Scintillations in the drift region and electroluminescence in the light-generating gap were both detected by nineteen 80-mm diameter glass photomultipliers (PMTs). Each PMT was optically coupled to a separate glass window, the inside surface of which was covered by a p-terphenyl wave shifter. A 3-mm thick spherical aluminum entrance window allows gas pressure of up to 2 MPa. An additional grounded thin aluminum electrode is installed to maintain a uniform electric field in the drift region. Radiation absorbed in the drift region produces primary scintillations in addition to ionization clus-

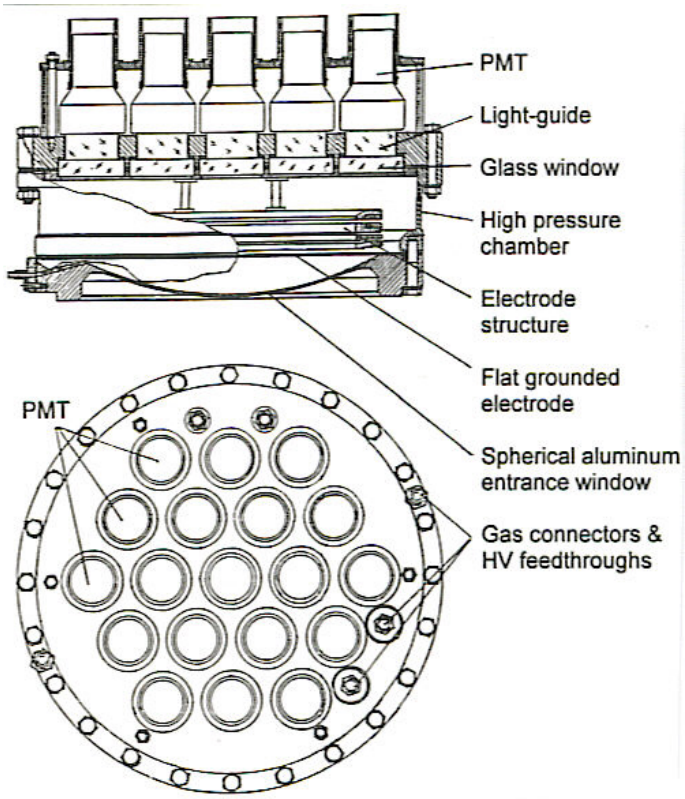

Fig. 6.19 Schematic diagram of the scintillation drift chamber SDC-19.

ters. In the low reduced electric field ($\sim 0.1\ \mathrm{kV\,cm^{-1}\,bar}$) applied to the drift region, the electron clusters drift to the light-generating gap, where the high reduced electric field (2–3 $\mathrm{kV\,cm^{-1}\,bar}$) is applied to generate electroluminescence of the gas. The two-dimensional position of the point-like ionization clusters projected on the light-generating gap is measured from the distribution of the electroluminescent signals over the PMT array. The coordinates and deposited energy, E, of point-like ionization clusters projected on the plane of the PMT matrix entrance windows and energy deposited E are determined by the following weighting procedure:

$$E = \sum k_i A_i, \quad x = \sum x_i A_i / \sum A_i, \quad y = \sum y_i A_i / \sum A_i$$

where $i = 1, \ldots, 19$, A_i is the response signal from the ith PMT, centered in the point with coordinates of $\{x_i, y_i\}$. The primary coefficients, k_i, are calculated, assuming amplification coefficients of nineteen PMTs to be equal and using specially measured response function for single PMT of FEU-139 type. Measurements with a multihole lead mask with regular holes of 4-mm diameter

and of 8-mm pitch, placed just before the entrance window of the SDC and irradiated with a ^{57}Co point source located at the distance of 1.5 m from the detector, demonstrated up to 10% nonuniformity in the energy response and up to 3 mm coordinate nonlinearity at the edges of the field of view. After that, k_i, x_i and y_i coefficients were corrected in some number of linear iterations, less than 1% nonuniformity and less than 1 mm nonlinearity were achieved. The intrinsic spatial resolution of the SDC filled with xenon at a pressure of 0.9 MPa was estimated by measuring the point spread function using collimated ^{57}Co and ^{241}Am γ-sources.

When the camera is triggered by the primary scintillation, the position of the original ionization cluster along the length of the drift region is determined from the time delay between the primary scintillation signal and the electroluminescence signal. The readout system of the camera allows recognition of 1, 2, 3 or more ionization clusters in the drift region. The data acquisition system is CAMAC-based and uses a Pentium PC as the host computer. The detection efficiency of the camera triggered by the primary scintillation was measured to be 60% for 60 keV (^{241}Am) γ-rays in xenon at 0.9 MPa (density 0.054 g cm^{-3}). Under the same conditions the detection efficiency of the camera triggered by electroluminescence signals is about 80%. At this pressure, the energy resolution of this detector for 122 keV (^{57}Co) γ-rays was an average of 2.7% FWHM over the 22 cm field of view. Three-dimensional position was measured with a resolution of 3.5 mm FWHM in the plane of the PMT array and 0.6 mm FWHM in the depth of the drift region for the 60 keV photoabsorption peak of ^{241}Am. The count rate capability of the camera depends on the mode of operation. When the camera is triggered by electroluminescent signals, $\sim$ 100 kHz count rate is achievable, which is comparable to the count rate of usual scintillation gamma cameras. When the camera is triggered by primary scintillation signals and measures the 3D positions of several ionization clusters distributed over the drift region, only $\sim$ 20 kHz count rate can be achieved.

For two-dimensional imaging the camera can either work only with electroluminescent signals or be triggered with fast scintillation signals to measure the 3D positions of ionization clusters (vertices). The knowledge of the Z-coordinate of the interactions can be used to improve the two-dimensional imaging. For example, the effect of electron capture of drifting electrons by electronegative impurities in the gas can be taken into account to achieve better energy resolution. The photoabsorption vertices that occur in the vicinity of the entrance window can be selected. Such selection could be used to improve the position resolution of the camera working in the Anger camera mode.

Figure 6.20 shows an image of a lead mask with regular holes of 4-mm diameter and 8-mm pitch placed just before the entrance window of the SDC-19

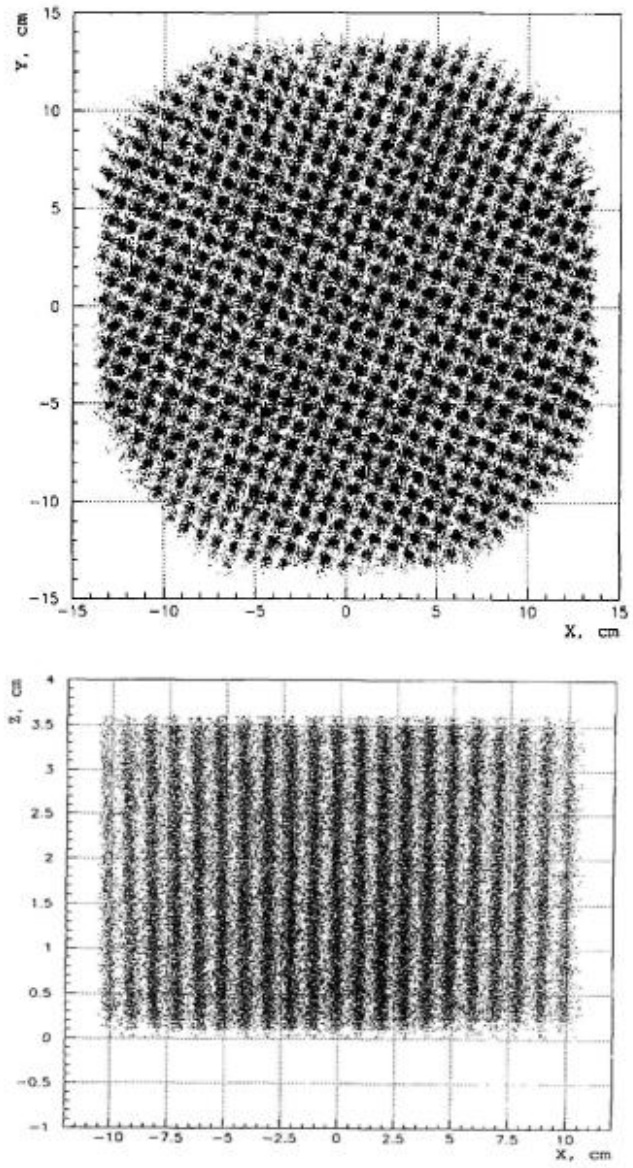

Fig. 6.20 Image of a lead mask with regular holes of 4 mm in diameter and 8-mm pitch placed just before the entrance window of the SDC-19 and exposed with a point-like ^{57}Co gamma source, located at a distance of 1.5 m from the SDC-19, in the plane of the photomultiplier windows (top) and over the depth of the drift region in xz projection [304].

and exposed with a point-like ^{57}Co gamma source, located at a distance of 1.5 m from the SDC-19, in the XY-plane of the photomultiplier windows (top) and over the depth of the drift region in XZ projection [304]. The ability to measure 3D positions of low energy ionization clusters allowed testing the camera in the Compton camera mode.

At a xenon fill pressure of 0.9 MPa, the best energy resolution that detectors of this type can obtain for collimated 122 keV (^{57}Co) γ-rays was found to be 2.4% FWHM (Fig. 6.21). About 70% of interacting 122 keV γ-rays generate two-vertex events. Figure 6.22 shows a a two-dimensional plot of energies deposited in two simultaneous ionization clusters for the three-vertex events when one vertex was identified as a fluorescent photon and the detector was exposed with a 99 mTc (140 keV) gamma ray source. The events containing 92 keV vertex from photoabsorbed primary γ-ray and those containing 30 keV photoabsorbed fluorescent photons form the most intense spots; events containing one 30 keV photoabsorbed fluorescent photon and a Compton vertex of the primary γ-ray form the horizontal and vertical bands; events containing a Compton vertex followed by photoabsorption vertex form a 60 keV photoabsorption, a position resolution of 3.5 mm FWHM in the XY-plane and 0.6 mm FWHM in the Z-direction has been measured. Knowledge of the position in three dimensions along with accurate measurement of energy for each vertex allows one to correct for the effect of electron capture by electronegative impurities that occurs as electron clouds traverse the drift region.

A small high-pressure scintillation drift chamber having a field of view approximately 5 cm in diameter was developed by Belogurov et al. [144]. The body of the chamber is capable of withstanding up to 4 MPa internal pressure. The electrode system of the chamber consists of two grid electrodes (50-μm diameter stainless steel wires point-welded to a ring-frame on a 0.5 mm pitch with a 4-mm gap between them. They lie 17 mm behind an entrance window, which is coupled to the collimator. Electrodes are separately installed on the top flange through Teflon isolators. PMTs are placed above the 17-mm light production gap and screened with a grounded grid made from 70 μm stainless steel wires on a 2-mm pitch to assure the electric field in the chamber does not influence on the PMT photocathode; 30 kV rated alumina feedthroughs and 2 gas inputs are placed on the top flange. Voltage dividers for the PMTs are placed outside of the chamber and connected to PMT pins via a multipin feedthrough. Seven of the 1/2" diameter FEU-60 type PMTs that lie within the chamber are arranged in a hexagonal pattern, 2 mm apart from each other, and they are fed from the same voltage divider placed outside the chamber. PMT anodes are connected separately to individual Fera ADC inputs. The readout system is triggered by electroluminescence signals. Spectrometric properties of the detector are listed in Table 6.2. A detection threshold of about 1 keV was measured with this detector. The image of a 1-mm diameter pinhole collima-

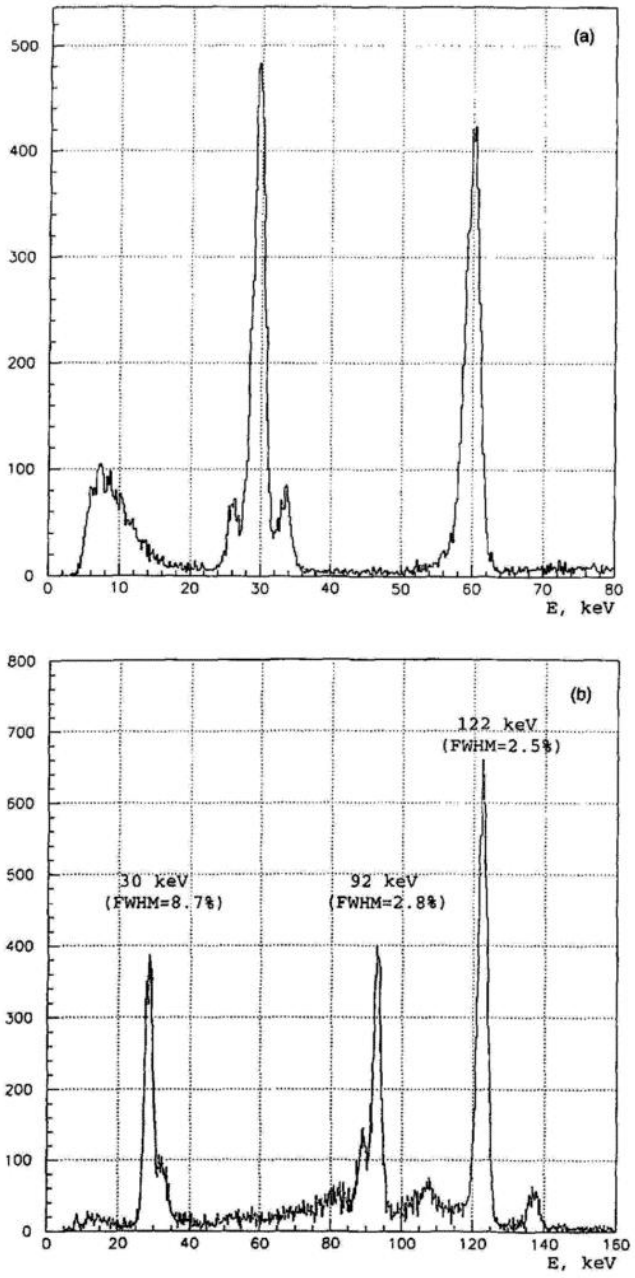

Fig. 6.21 Pulse height distributions measured: (a) for ^{241}Am and (b) ^{57}Co gamma rays sources from the scintillation drift chamber SDC-19 [304].

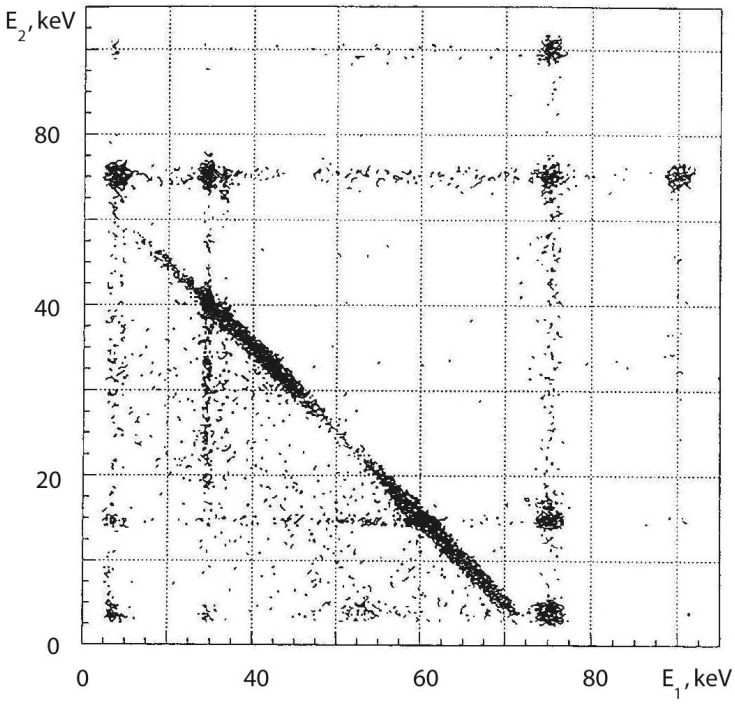

Fig. 6.22 Two-dimensional plot of energies deposited in two detected in row ionization clusters measured with SDC-19 exposed to a 99 mTc point source located 1.5 m from the entrance window at 0.9 MPa Xe filling [304].

tor was taken with 59.6 keV γ-rays. The FWHM of the distribution was found to be 1.7 mm. Taking into account diameter of collimator (1 mm) and geometrical factor, one can estimate the intrinsic spatial resolution of the 7×FEU-60 SDC as 1.2 mm FWHM.

Tab. 6.2 Summary of the characteristics of high-pressure xenon imaging scintillation drift chambers.

Gas and pressure in bar	Photosensor	Sens. vol.	Energy resolution, % FWHM, (energy in keV)	*XY* Position resolution, mm FWHM (energy in keV)	Ref.
Xe, 5	5 PMTs O	(10/10)	5.4(30); 3.2(60); 4.9(122)	$\sim$ 5(60), 2.7(25)	[349] [350]
Xe+0.6%^{3}He, 4	5 PMTs O	(10/10)	2.5(760)	1.8(760)	[351]
Xe, 1	7 PMTs O	(7/1)	10(6)	0.9(6)	[352]
Xe+15%He, 4	7 PMTs O	(25/10)	10.6(30); 7.6(51) 5.8(81)	3–4(60)	[93]
Xe , 8	19 PMTs O	(30/6)	4.3(60)	3.3(60)	[353]
Xe+10%He, 15	15$\times$30Fibers/ /2 PMTs	(6/7)	33(30); 11(90); 5.8(122)	0.4(60)	[314]
Xe, 4.5	MWPC/CsI O	(10/6)	4.1(60)	1.8(60)	[346]
Xe, 20	7 PMTs In	(5/1)			[144]
Xe+4%He, 1.2	16X$\times$16Y maPMT O	(5/1)	7.63(5.9)	0.5(5.9)	[354]
Xe, 9	19 PMTs O	(22/3.8)	3.6(60); 2.6(60)	3.7(60), *Z* 0.6	[304]
Xe+10%He, 5	7 PMTs O	(24/10)	8.3(30);5.2FGM(30); 3.3(60); 2.4FGM(60)		[347]
Xe+4%He, 10	32-channel maPMT O	(4.5/5.5)	5.5(32); 5.1(60)	0.4 ($>$ 25)	[348]

Note: Photosensors position shown relatively sensitive volume (O - outside, In - inside): sensitive volume (Dia/Depth) given in centimeters, PMT - photomultiplier, maPMT - multianode PMT, MWPC - multiwire proportional chamber, FGM - fluorescence gated mode.

6.2 High-Pressure Xenon Electroluminescence Detectors with Nonuniform Electric Field

6.2.1 Cylindrical Proportional Scintillation Counters and Drift Chambers

Cylindrical electroluminescence detectors with wire anodes were the first of this detector type to be studied (see, for example, Policarpo et al. [355]). Drift chambers with EL around wires appeared to be a natural extension of the well-developed technology of ionization drift chambers with charge collection and gas gain. The first detectors used an argon-nitrogen gas mixture at a pressure of about 0.1 MPa. Nitrogen in this mixture played the role of a wavelength shifter, shifting light from UV range to the visible blue light (330 nm). Later, many different gases were investigated, including all noble gases and simple molecular gases and their mixtures.

Figure 6.23 shows data on the light output from different gases versus the anode voltage measured with a proportional counter developed by Keirim-Markus et al. [356]. This proportional counter consisted of a 0.1-mm diameter tungsten anode stretched down the middle of a 50-mm diameter cylindrical cathode coated with an aluminum reflector. Photons were detected with a 1″ diameter FEU-39 photomultiplier with a quartz window mounted on the side of the cathode. The gases were ionized by a collimated beam of alpha particles, emitted from a ^{237}Np source, installed on inside surface of the cathode. The strongest light output in the range of greatest response for the photomultiplier (> 200 nm) was found to be ~ 200 times that of a NaI(Tl) crystal with a gas mixture of He+10%Xe; the most moderate result has been achieved with pure methane. The best light outputs exceeded the poorest by 5 orders of the magnitude. A similar experimental setup has been used in a number of experiments investigating electroluminescence spectra and kinetics in pure noble gases (see, for example, Suzuki and Kubota [357]). The conclusion was that xenon gas at pressures of more than 0.1 MPa is the most promising gas for proportional scintillation counters for handling high rate events, because it has the shortest decay times and the range of incident particles, which controls the rise time, is also shorter in xenon. After initial attempts to develop an electroluminescence drift chamber for high-energy experiments with a low-pressure xenon/nitrogen mixture [358], the best results for position resolution have been achieved with a drift chamber filled with 2 MPa pure xenon [359]. In this work, the electroluminescence signal produced by electrons near the 50 μm anode wire was used as a stop signal. Since electroluminescence intensity is proportional to pressure, the high-pressure gas enables utilization of a very small light-producing region around the anode wire. Yet, high pressure

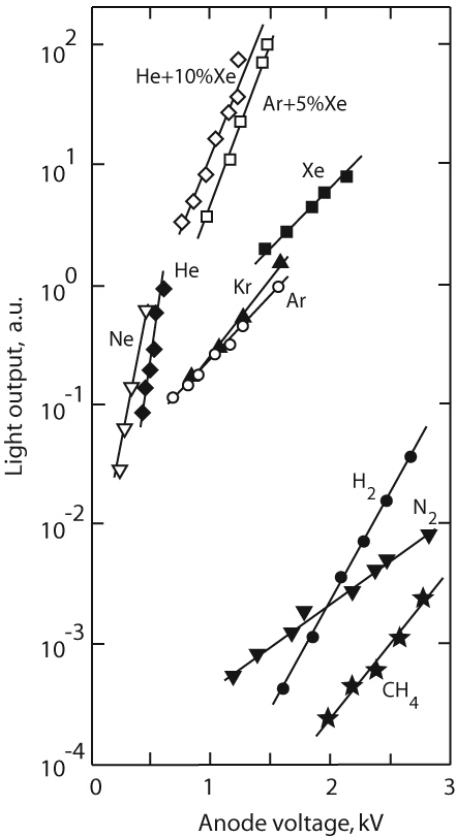

Fig. 6.23 Light output versus anode voltage for scintillation proportional counter filled to a pressure of 79 kPa with a 50-μm anode and irradiated with 661 keV gamma rays. Redrawn from [356].

reduces diffusion of the drifting electron cloud, producing a short electroluminescence signal rise time. The record for best spatial resolution using this type of drift chamber was demonstrated with a double drift chamber as shown in Fig. 6.24.

The drift space in each chamber is formed by two sets of parallel wires (0.1 mm in diameter and 1 mm apart) with the potential divided in a way to provide a homogeneous field in the drift space. The sensitive area is 40×40 mm^2. The gap between the planes of cathode wires is 5 mm. Each of the two anode wires was placed at the end of the drift space. The thickness of the aluminum window was 1 mm to allow admission of a particle beam. A pair FEU-85 glass photomultipliers detected the electroluminescence flash around the anode wires. The two chambers were optically isolated from each other in such a way that electroluminescence light in a particular chamber could only be observed by a single PMT, associated with that chamber. A layer of 0.1 mg cm^{-2} p-terphenyl was deposited onto the inner side of Mylar

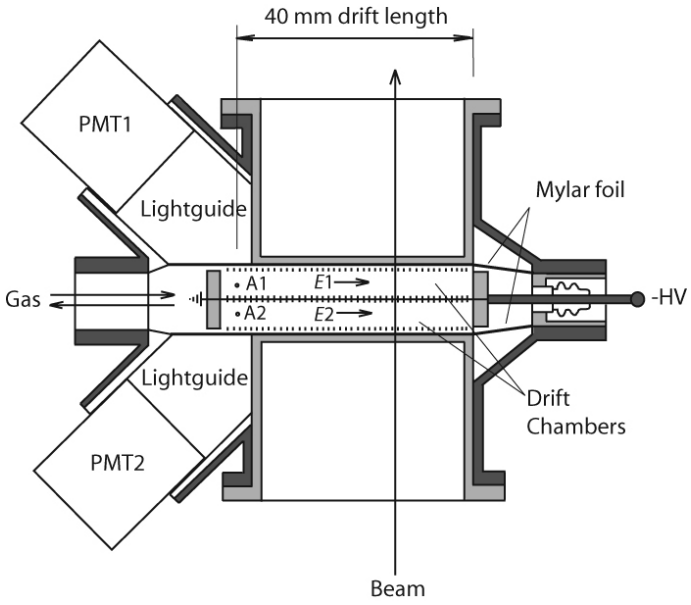

Fig. 6.24 High-pressure xenon double drift chamber: PMT1 and PMT2 photomultipliers viewing wire anodes A1 and A2, respectively; E1 and E2 drift electric fields in the drift chambers; -HV is a cathode high voltage. Redrawn from [359].

optical windows to serve as a wave shifter. The position of anode wires was adjusted under an optical microscope with accuracy of better than 5 μm. The detector was exposed to a beam of relativistic particles with momentum between 1 and 5 GeV c^{-1} at the Serpukhov (Protvino) accelerator. The beam of particles entered the chamber in a direction perpendicular to the drift field. The detector was triggered with an array of scintillation counters providing determination of the track position to an accuracy of $\pm$ 0.5 mm and divergence down to $\pm$ 1.8 mrad. The detector demonstrated an energy resolution of 22% FWHM for a 17.3 keV monochromatic X-ray line (Mo K_α). In order to determine the spatial resolution, analyses of electron arrival time differences in the two chambers were used. For the arrival time analyses, amplifiers with a time constant of 0.5 μs were used to generate bipolar pulses whose zero crossings were detected and used to produce an output of logic pulses that was fed into a time-to-pulse height converter. The distribution of time differences was close to Gaussian and the spatial resolution for relativistic charged particles was measured to be 16 μm along the drift direction. The contribution of the diffusion to the resolution at this pressure amounts to 12 μm. The double drift chamber has been considered for registration of transition radiation and rejection of the background of relativistic particles.

Another original design of a high-pressure xenon electroluminescence drift chamber was proposed by Rodionov and Chepel [360]. They have considered a system of three flat multiwire electrodes (grids) inclined by a few degrees relative to each other. Electrical fields between electrodes were selected such that the two lower electrodes had 50–77% transparency to drifting electrons. The drifting electron cloud is split twice: some of the electrons pass through the grids and some end their paths on the wires, exciting flashes of electroluminescence. Thus, each gamma ray interaction in the detector is accompanied by three electroluminescence flashes that are separated in time by intervals that are proportional to the projected X and Y-coordinates of the electron cloud. Detection of the primary scintillation allows determination of the third coordinate Z.

The detector design (Fig. 6.25) was tested with up to 4.5 MPa of pure xenon, achieving a spatial resolution of 3 mm FWHM for 60 keV gamma radiation [142]. The detector has been used to measure the transparency of pressurized xenon to its own electroluminescence radiation. It was shown that xenon begins to loose transparency to the own emission light at a density of about 10^{21} cm^{-3} (Fig. 6.26). This data confirmed measurements by Koehler et al. [177] published in 1974. One of possible explanations of the effect is clusterization of xenon (see Chapter 2 for details).

With the purpose of designing a robust and compact high-pressure electroluminescence detector capable of detecting high-energy gamma rays, a cylindrical detector using scintillating fibers coupled to a single photodetector has been considered. Akimov et al. [361] constructed such a cylindrical detector with 6 cathode wires of 60 μm diameter surrounding the 50-μm diameter anode wire at a distance of 1 cm. A set of 72 1-mm diameter wavelength shifting fibers coated with p-terphenyl and coupled to a single photomultiplier via a sapphire optical window was used for readout optical signal. They tried to combine the effects of gas gain and of electroluminescence in pure xenon at 2, 4, and 8 bar pressures in order to reduce the detection threshold and achieve good energy resolution. At the lower pressure, an energy resolution of 13% FWHM at 13.9 keV was measured. At the higher pressures, the detection threshold of 0.2 keV mostly associated with PMT noise was demonstrated with an ^{241}Am radioactive source placed inside the detector. The authors concluded that gas gain degrades energy resolution. It is true that the best energy resolution has been achieved with electroluminescence detectors having parallel plate electrode geometry whose uniform electric fields are favorable for reducing the probability of the electron multiplication (see Section 6.1).

In an attempt to reduce the effect of electron multiplication while maintaining the advantages of a cylindrical geometry and fiber optics readout, a larger HPXe cylindrical ELD was constructed by Bolozdynya and Austin [328]. A 4 mm diameter electropolished stainless steel rod served as the anode.

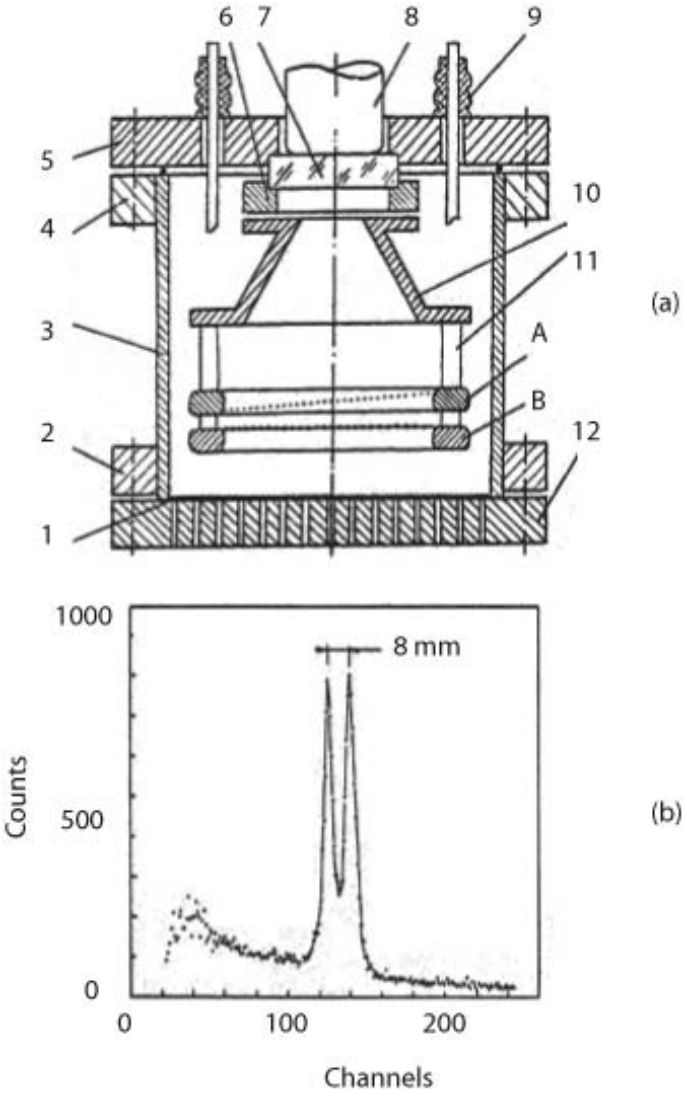

Fig. 6.25 Schematic drawing of a high-pressure xenon TPC with coding grids (a) and position sensitivity of the detector for two 8 mm apart located 60 keV gamma sources (b): 1 - 1.5-mm thick aluminum input window; 2,4 - rotating flanges; 3 - vessel; 5 - indium sealed lid; 6 - inner flange supporting a glass window; 7 - coated with p-terphenyl wavelength shifter; 8 - glass photomultiplier; 9 - electrical feedthrough; 10 - aluminum reflector coated with p-terphenyl wavelength shifter; 11 - ceramic insulator; 12 - collimator supporting the input window; A and B - flat grids of 110-mm diameter made of nichrom wires of 30 mm in diameter with pitch of 2.4 mm; grid A inclined at 4° relative to grid B and the input window [142].

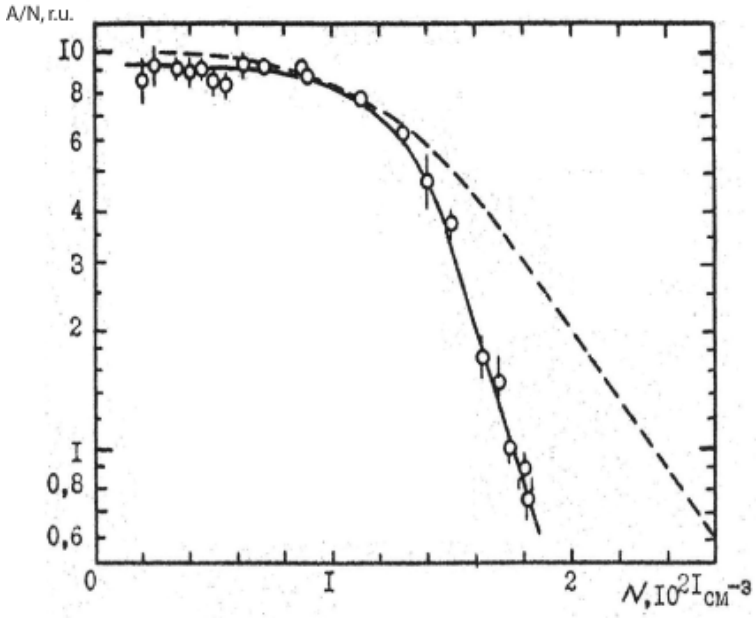

Fig. 6.26 Transmission of pressurized xenon to electroluminescence light measured by Goleminov et al. [142] in comparison with data of Koehler et al. [177], shown as a dashed line.

A monolayer of 1-mm diameter Bicron BCF-12 scintillating fibers without cladding covered the internal surface of the cylindrical, 72-mm diameter cathode. A grounded grid (4×5 mm^2 openings between 0.1 mm wires) covered the fiber array to protect it from the influence of the applied electric field. The cylindrical fiber array serves as a light collection and wave-shifting optical system transmitting the trapped light to a photodetector. Two configurations were tested: an externally mounted photomultiplier coupled to a UV transmitting window and a LAAPD installed directly inside the chamber. The LAAPD configuration demonstrated exceptional vibroinsensitivity, while being vibrated by an engraver directly installed into the flange of the detector. An alpha particle spectrum measured at an rms acceleration of about $4g$, was not found to differ from that measured from the undisturbed detector. Unfortunately, Bicron BCF-12 p-terphenyl activated fiber selected for the light collection system has demonstrated relatively poor conversion efficiency for UV photons, about 10^{-4}, which is mostly associated with the collection of the visible part of xenon electroluminescence emission spectrum. This means that the absorption length of the emission light in an acrylic fiber is much smaller than conversion range of p-terphenyl dissolved in it. That is why this detector demonstrated poor energy resolution. In order to improve the light collection efficiency the authors planned to return to coating fibers with p-terphenyl.

6.2.2 Gas Scintillation Proportional Counters with Spherical Electrical Field

A GSPC having a spherical electrical field may be considered as a natural modification of the parallel plate geometry necessary for increasing the acceptance for a single photodetector channel (i.e., a PMT) and operation at increased pressure. For low energy X-rays, the drift lengths of the primary electrons from creation to light multiplication are approximately equal. The last property minimizes the spread in rise times, which is crucial for rise time discrimination of events that are not X-rays. The first GSPC having a spherical electrical field used a ball anode [275,362]. The introduction of the curved grid GSPC allowed the construction of GSPCs with spherical geometry and larger sensitive areas. Anderson et al. [49] developed a spherical GSPC with a 285 cm^2 acceptance area.

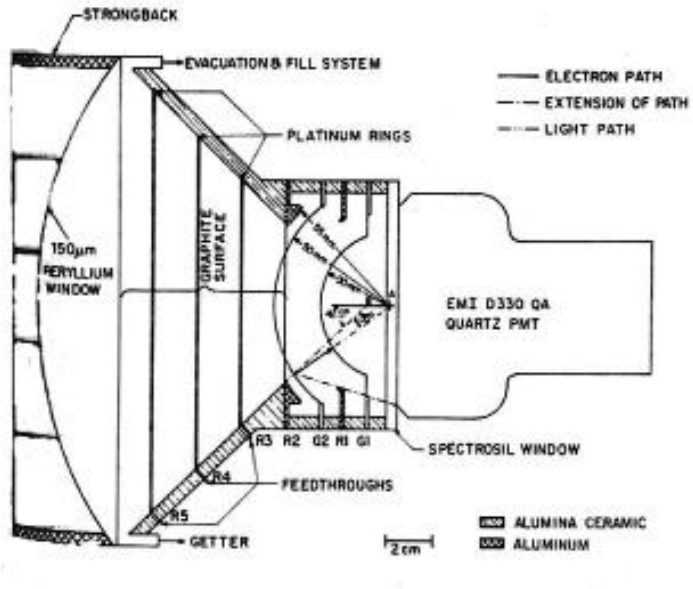

Fig. 6.27 Large-area GSPC with curved grids forming spherical electric field (a) and (b) pulse height spectrum measured using a noncollimated ^{241}Am gamma ray source placed at 40 cm in front of the input widow of the detector filled with 0.1 MPa Xe [49].

A schematic diagram of the GSPC with curved grids forming a spherical electric field is shown in Fig. 6.27. The detector has been equipped with a 150 μm beryllium window supported by a 93% open-area aluminum strong back. The detector body was made of alumina ceramic. To maintain a correct potential distribution, the conic (42.5° opening angle) part of the body was

coated with platinum rings; graphite coatings between them provided a total resistance between ring R2 and the Be window of a few gigaohms. The optical window was made of 4.8-mm thick Spectrasil coupled to EMI D330 QA PMT of 89-mm diameter with a Spectrasil window and bialkali cathode. Epibond 8519 epoxy was used to assemble the detectors because of its low outgassing characteristics. Research grade xenon was used to fill the detector to a pressure of 0.1 MPa. Gas purity was provided by ST177 SAES getters. Because the geometry of the focusing cone is not strictly radial, the ring potentials were optimized using experimental data.

An overall energy resolution of 9.3% FWHM at 5.9 keV was measured at potentials slightly lower than the optimum when frequent discharges were observed. When a collimated ^{55}Fe X-ray source was used, a resolution of 8.6% FWHM was measured. The energy resolution of 5.8% FWHM extrapolated to large pulse heights could not be achieved because of charge multiplication which began at about 4000 V cm^{-1} at 0.1 MPa pressure. An energy resolution of 3.2% FWHM was measured for the 59.5 keV line from ^{241}Am noncollimated source placed 40 cm away from the detector input window.

The detector has been used to determine the Fano factor in the following procedure. With all other voltages held constant, the voltage on G1 was varied, and both the resolution and the pulse height were recorded for each setting with collimated ^{55}Fe X-ray source. Linear extrapolation of the resolution squared versus the reciprocal of the pulse height to infinite pulse heights lead to 5.2% FWHM theoretical limit of the energy resolution for 5.9 keV X-rays. The best fit to the data gives a value of the Fano factor of $F = 0.13 \pm 0.01$ using a value of 21.9 eV per ion pair production in xenon.

While the spherical field GSPCs have good energy resolution and can utilize rise time discrimination to reject background at energies below ~ 20 keV, their performance degrades at energies due to the physics of photoabsorption of X-rays whose energy is greater than the K-shell binding energy [25].

6.3 Multilayer Electroluminescence Chamber

The development of effective fiber array readout systems has opened up a new interesting possibility that may be considered as an electroluminescence camera in which the light-generating gap and electron drift region are superposed [24]. A working layer of the camera is formed by two electrodes with ~ 1 cm distance between them. The electrodes are made of a thin foil covered by thin photodetector arrays, for example, orthogonal arrays of wave-shifting fibers coupled to remote photomultipliers. As soon as ionization occurs between electrodes, the ionization electrons drift to the anode and excite elec-

troluminescence of the gas. Two-dimensional coordinates of the point of primary γ-interaction are determined by the centroid of electroluminescent signals distributed over the photodetector arrays. The z-coordinate of the point of energy deposition in the direction of the drift electric field is determined from duration of electroluminescent signal, Δt, and the well-known electron drift velocity, v_d

$$z = v_d \cdot \Delta t \tag{6.7}$$

The total charge of photoelectrons measured from illuminated photodetectors is proportional to the z-coordinate and the energy deposited. The total charge of electrons and ions collected on the readout fibers is negligible because there should be no gas gain during the electroluminescence process. An important feature of electroluminescent signals in the fiber arrays is that the magnitude of the total electroluminescent signal, summing all x and y array signals, does not depend on the drift time. The magnitude of the total electroluminescent signal is proportional to the number of drifting electrons, i.e., to E_γ/W. Thus, the deposited energy can be obtained from the magnitude of the total electroluminescent signal measured from all fibers of the same layer. The total time-integrated charge of photoelectrons measured from all fibers is proportional to $E_\gamma \cdot z$.

One of the advantages of this design is a high efficiency of electroluminescent light capture and conversion of light signals into electrical signals. The total efficiency of conversion of electroluminescence photons into photoelectrons in photodetectors coupled to fibers can be estimated as $\varepsilon > 1.5\%$ for photodetectors with quantum efficiency of $QE_{PD} > 60\%$. Thus the condition of Eq. (6.5) could be satisfied and the energy resolution of the camera may be limited only by fluctuations of primary ionization. Note, that even using photomultipliers ($QE_{PD} \sim 20$–30%), this kind of electroluminescence camera will allow much better energy resolution than that of any existing SDC design. Simulations have shown that the new detector can achieve position resolution approaching the primary ionization cluster size. To provide high detection efficiency, electrodes covered with scintillating fibers can be stacked into a multilayer structure called a multilayer electroluminescent camera (MELC). The major gas (He, Ne, Ar or Xe), gas pressure, number of layers and total thickness of the detector can be chosen to achieve a required detection efficiency for different interactions. Light noble gases (He, Ne, and Ar) have a dominant Compton cross section for 140 keV γ-rays. Xenon provides the most effective photoabsorption of γ-rays and a high light output of electroluminescence in noble gas mixtures. For example, a 20-cm thick MELC consisting of 20 layers of 1 cm depth and filled with 2 MPa Xe will have 85% photoabsorption efficiency for 140 keV γ-rays. This is comparable to the detection efficiency of 3/8″ thick NaI(Tl) scintillators usually used in gamma cameras.

The MELC filled with 2 MPa Ar will be 8% effective for Compton scattering 140 keV gamma rays and practically transparent for photoabsorbing 140 keV γ-rays. The same efficiency for Compton scattering is achievable with a 3-mm thick Si scatter detector.

In the range of electric fields that generate electroluminescence, the electron drift velocities in noble gases are about 10^6 cm s^{-1}. Then, a MELC with N_l layers can achieve a counting rate of $\sim N_l$ MHz. Filled with 2 MPa Xe, the MELC can operate as an Anger gamma camera with a collimator for two-dimensional γ-imaging. A MELC filled with high-pressure Ar or Ne can be used as a fast and precise 140 keV γ-ray Compton scatter detector. A MELC filled with high-pressure Xe can be used as an absorption detector of scattered γ-rays. Together they may comprise a complete Compton SPECT system [363].

6.4 Liquid Electroluminescence Detectors

Electroluminescence of liquid xenon in the high electric fields near anode wires was first reported by Lansiart et al. [364]. This first observation stimulated investigation of the possibility of constructing scintillation proportional and drift wire chambers with liquid noble gases.

Similar to Baskakov et al. [359] who achieved 16 μm position resolution in a high-pressure Xe electroluminescence chamber (see Section 6.2), Miyajima et al. [365] used electroluminescence around wire anodes as a stop signal but in liquid xenon. They have used primary scintillation from alpha particles as a start signal for a time-to-pulse height converter and have achieved 20 μm rms position resolution at 13 mm drift pass in the detector configuration shown in Fig. 6.28.

The position resolution was limited with ranges of alpha particles in liquid xenon. The energy resolution measured with electroluminescence signal was about 15% FWHM versus 8% FWHM measured in ionization mode with the same detector. Using similar detector and conversion electrons from ^{207}Bi for ionization of LXe, Masuda et al. [366] explored a possibility to construct a LXe scintillation proportional counter for spectrometry of high-energy gamma rays. The best resolution of 18% FWHM for 1 MeV electrons, which is almost the same as measured with charge collection in the ionization mode of operation, has been achieved. The anode diameters between 4 and 20 μm have been investigated. The best resolutions for the various anode wire diameters were almost the same though the optimum voltages were different. This suggests that the energy resolution is limited by fluctuations associated with the accompanying charge gain.

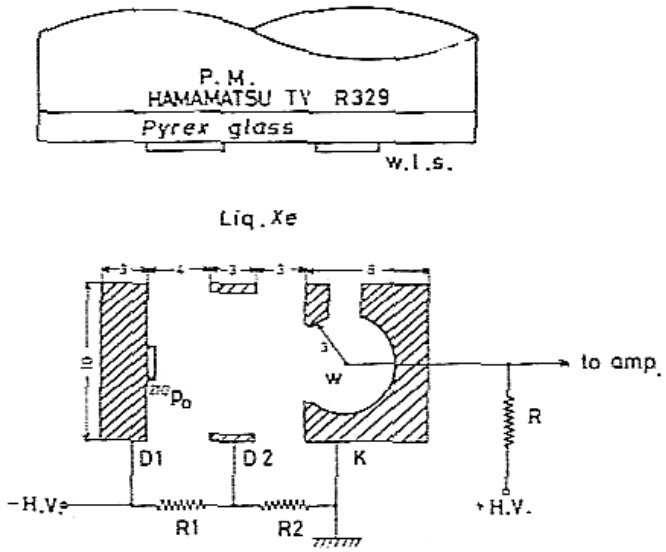

Fig. 6.28 Schematic drawing of a miniature LXe drift chamber [365]: D1 is a cathode with deposited ^{210}Po alpha source; D2 is a drift ring; W is the anode wire of 4-μm diameter (sizes are shown in millimeters).

Therefore, no clear advantage has been found for the electroluminescence mode over the ionization mode. But triggering on the scintillation signal looked like the most direct way to achieved three-dimensional position sensitivity.

7
Two-Phase Electron Emission Detectors

Physical amplification of primary ionization signals improves performance of the ionization detectors. Earlier attempts to achieve effective charge or light multiplication in the vicinity of thin wires in condensed noble gases have not been very successful [108,368]. For this purpose, microstrip boards [138,325] and chemically etched needles [139] were investigated with only a low amplification factor (of about 10–100) and poor energy resolution achieved. In rarefied phases, however, electronic signals can be easier amplified. In some cases, ionization electrons can be extracted from condensed dielectrics into the gas phase where effective amplification processes are then used.

Two-phase emission detectors employ condensed (liquid or solid) phases of nonpolar dielectrics (in particularly, noble gases) as active media interacting with detected radiation. Ionization electrons extracted from the condensed phase are relatively easy to detect within the gas (or vacuum as a particular case of gas of low density) using amplification procedures such as electroluminescence or gas discharge. Basic physics of electron emission from nonpolar dielectrics is considered in Chapter 3. Emission detectors combine the high radiation detection efficiency of massive and dense working media with the effective amplification of electron signals possible only in the rarefied phases. Emission detectors are considered as the most promising detector technology to be employed in the search for exotic particles and rare events in experiments having fundamental significance (see Chapter 9).

The first two-phase (solid/gas Ar) emission detector was constructed by Hutchinson [10] in 1948. Electron emission of quasifree electrons from condensed argon has been rediscovered and advantages of the emission detector combining condensed working medium and gas amplification was understood in 1970 [369]. Since that time a variety of different emission detectors developed as it is reviewed in this chapter.

7.1 Emission Ionization Chambers

The first emission detector built by Hutchinson was a three-electrode parallel plate ionization chamber with a few millimeters of gas between electrodes and a screening grid placed in the gas above the solid argon [10]. Electrical pulses have been observed when solid argon irradiated with gamma radiation and electrical field exceeded 500 V cm^{-1}. Hutchinson claimed observation of effective emission of fast negatively charged carriers, which he identified as electrons.

Later, emission ionization chambers were used for investigation of emission properties of nonpolar dielectrics including condensed noble gases, liquid at room temperature saturated hydrocarbons, and superfluid helium [102, 152, 153, 370, 371].

One of these devices was a miniature two-electrode ionization chamber [371] with 25-mm diameter electrodes, 4-mm gap between them and 8-mm diameter and 0.4-mm thick aluminum window for introduction of X-ray radiation through the bottom electrode as shown in Fig. 7.1.

A controlled X-ray tube of BSV-7 has been used to generate μs pulses of X-ray radiation with maximum energy of 35 keV at 100 Hz repetition. X-ray radiation absorbed in less than a 0.1-mm thick layer of the condensed krypton has generated a compact (in the direction of the electric field) cloud of electrons. In Fig. 7.1 typical emission curves of induced voltage pulse $U(E)$ measured with a charge-sensitive preamplifier or emission current $I(E)$ measured with electrometer dependent on the electric field in the condensed krypton are presented. The threshold field of emission has been defined by linear extrapolating branches of the curves as shown with dashed lines. This emission detector has been used for observation of electron drift through and along the free surface of liquid and solid krypton and investigation of influence of methane dope on emission of hot electrons. Cryogenic system of this device served as a prototype for many following developments of condensed noble gas scintillation and emission detectors (see Chapters 4 and 7).

A large (41-cm diameter and 6-cm gap) two-electrode ionization chamber was used for measurements of concentration of the ^{85}Kr isotope in the natural mixture of krypton isotopes separated from air [372]. This experimental study happened around the year of the Chernobyl catastrophe and allowed for the observation of elevated concentrations of ^{85}Kr in the product of the Lisichansk Plant of rare gases in the Ukraine after the accident. The observation made with the large liquid krypton ionization chamber by one of the authors of this book (AIB) but, unfortunately, has never been published. This large ionization chamber has been tested as an emission detector, monitoring purity of the liquid krypton. With this detector, large fluctuations of the emission current have been observed in the range of the extraction fields ap-

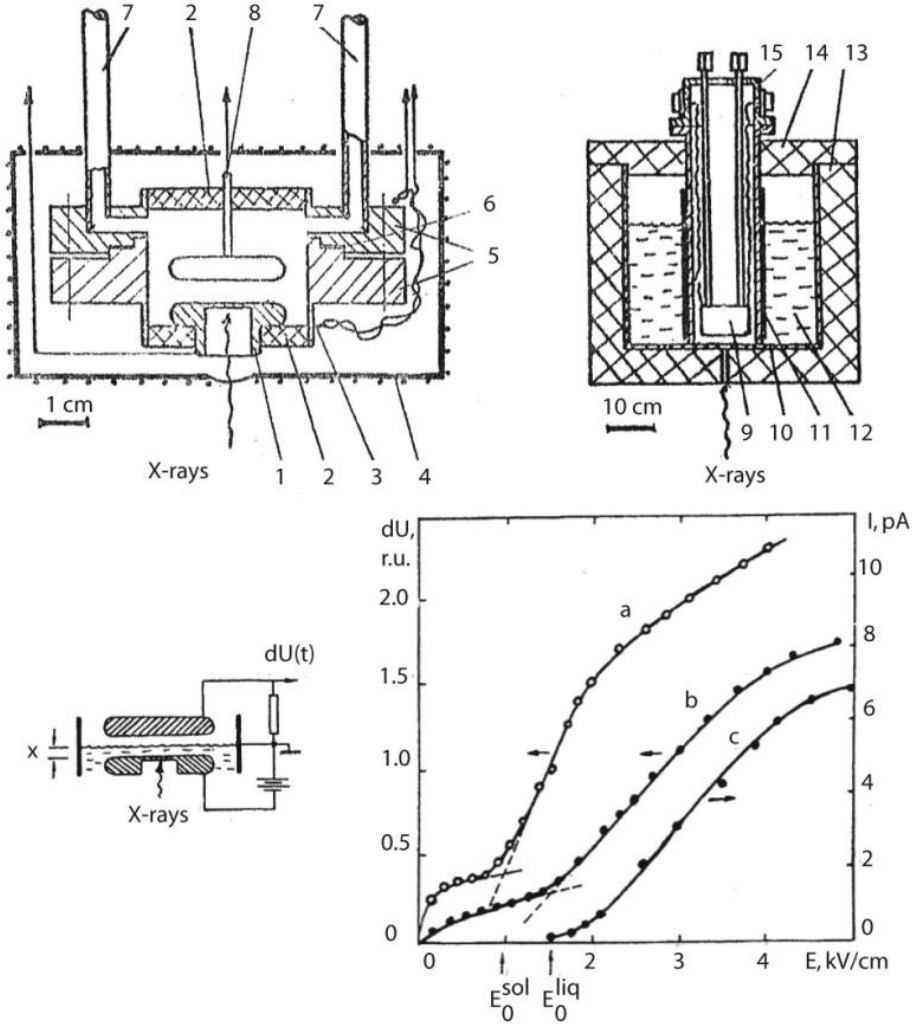

Fig. 7.1 Two-electrode emission ionization detector for investigation of emission properties of condensed noble gases, electrical circuitry for measurement of ionization signals from the detector with two-phase fillings, and typical emission curves measured with this detector from solid (a) and liquid (b, c) krypton in pulsed (b) and current (c) mode: 1 - cathode with aluminum window; 2 - ceramic insulator; 3 - thermocouple; 4 - copper screen with electrical heater; 5 - flanges; 6 - indium seal; 7 - gas inlet/outlet pipes; 8 - anode; 9 - the detector in cryostat; 10 - cryostat; 11 - copper screen with heater; 12 - liquid nitrogen bath; 13 - foam thermoinsulation; 14 - lid; 15 - top flange with connectors [149, 371].

proaching the threshold electric field. The effect was not observed before with smaller emission detectors. The effect is probably associated with instability of the liquid surface charge with nonemitted charge carriers. Later, similar observation were reported in publication [265].

7.2
Emission Proportional Chambers

Either saturated vapor of condensed phase or a ballast gas placed above the solid detection medium or a mixture of gases may be used in emission detectors for effective electron multiplication.

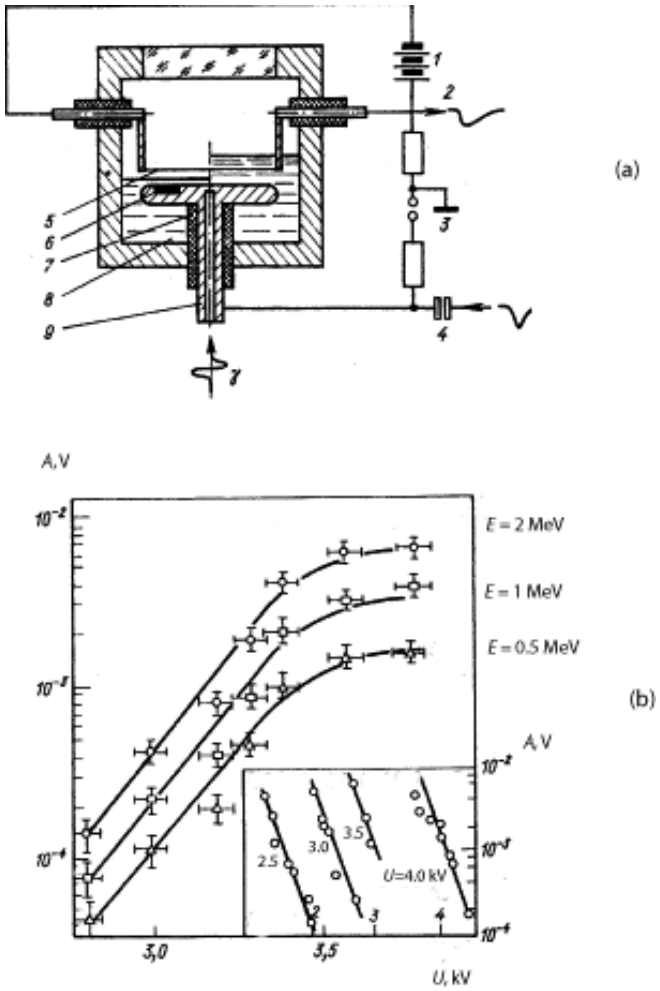

Fig. 7.2 Emission wire proportional chamber with multiwire anode operating under or above the free surface of liquid argon (a) and dependence of amplitude of anode signal on applied voltage at 0.35 MPa pressure, and on pressure of the vapor as shown at the insert at a few applied fields (b): 1 - battery heating wires with 0.3 A current; 2 - output anode signal; 3 - DC high voltage; 4 - pulsed high voltage; 5 - anode composed of 100-μm wires; 6 - alpha particle source; 7 - HV feedthrough; 8 - liquid argon; 9 - collimator [373].

One of the first such emission detectors was a two-electrode liquid argon ionization chamber with multiwire anode [373]. The operation principle of this detector is illustrated in Fig. 7.2a. As seen, the anode consisting of 50 to 200-μm diameter wires may be placed above or below the liquid surface. Unstable electron multiplication with a gas gain of less than 500 has been observed in the first case. In liquid argon, the anode wires have been heated by 0.1–1 A electrical current in order to boil the liquid and to form a vapor jacket around the wires. In this case, electrons have been emitted inside the vapor jacket and avalanched in the vicinity of the wires. The avalanche length was limited with the size of bubbles forming the gas jacket. The gas gain of 10^4 has been achieved (Fig. 7.2b) by the cost of increased dead time (10 ms against 0.1 ms in the vapor). The elevated dead time was probably associated with localization of positive ions inside bubbles. With pulsed HV supply, the gain around heated wires in liquid argon increased up to 10^6. However, this approach required too much electrical power to be considered for practical use.

Another important example of the emission chamber utilizing gas gain is a wire proportional chamber with liquid isooctane (2,2,4-trimethylpentane) working at room temperature. Emitted electrons multiplied around anode wires in saturated isooctane vapor at $\sim$ 13 KPa pressure [374]. The design of the sealed-off glass chamber used in this study is shown in Fig. 7.3a. The isooctane has been ionized with a 30-mm diameter alpha source installed on the cathode immersed in the liquid. The anode was made of planar 30 μm nichrome wire grid with pitch of 3.5 mm. At a distance of 4 mm, the anode was surrounded with two flat screening grids made of 200-μm diameter nickel wires with a pitch of 0.8 mm. The wire chamber formed by the anode and two screening grids has been installed above the liquid. The isooctane was purified with molecular sieves and sodium thin film getter. In addition, a sodium getter mirror was deposited on the walls of the storage reservoir attached to the detector. A brightness of the sodium mirror served as an indicator of purity of the liquid. A thickness of the liquid inside the detector was controlled by removing or adding the liquid from the reservoir. During six months of the detector operation no aging effect was observed; a lifetime of quasifree electrons in the liquid stayed without changing at the level of 7 μs. A stable proportional electron multiplication has been achieved with a gain of 30 000 (Fig. 7.3b).

A gas gain of over 10^3 has been observed in the parallel plate two-electrode emission chamber filled with 2,2,4,4-tetramethylpentane (TMP) at room temperature [375]. A design of the glass sealed-off detector was similar to the one shown in Fig. 7.3a. A ballast gas of 10.6 kPa argon has been added to the TMP vapor (1.8 kPa at 20 °C) in order to increase the gas pressure above the liquid and to improve the electron multiplication. The electron lifetime in TMP has been measured to be 7 μs not degraded by adding argon.

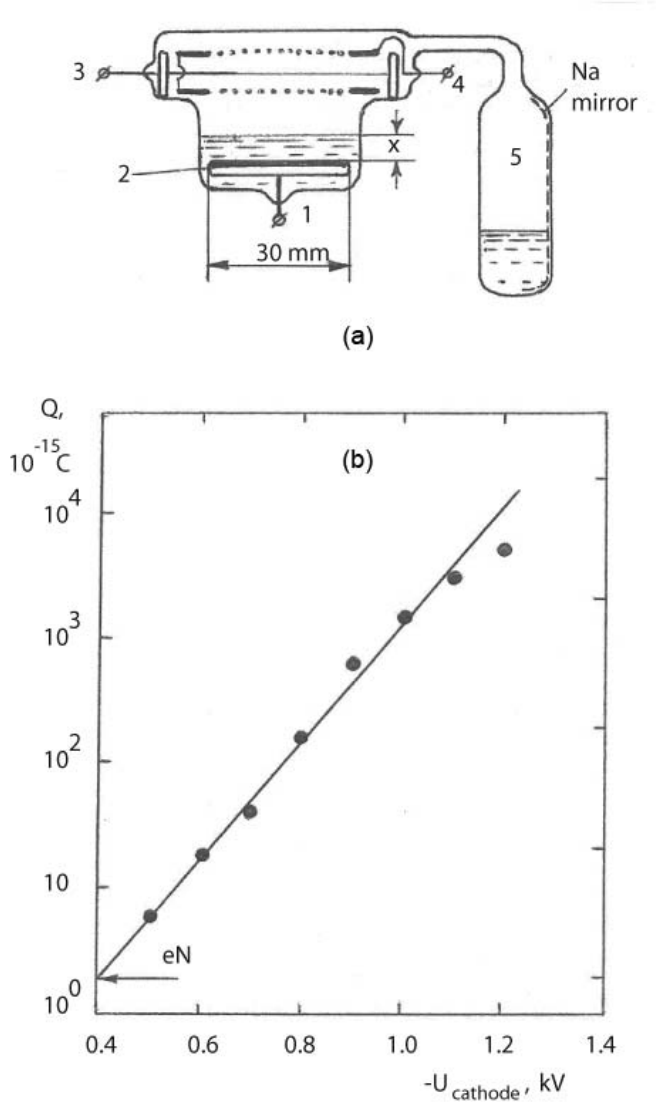

Fig. 7.3 Emission wire proportional chamber with liquid isooctane working medium operated at room temperature (a), and gas gain curve (b): 1 - cathode; 2 - alpha particle source; 3 - multiwire anode; 4 - grid; 5 - storage reservoir with sodium getter (mirror) deposited onto the inside surface of the reservoir [374].

Electron multiplication in krypton vapor has been studied for detection of radiation in the model of emission detector as described above (Fig. 7.1). In this experiment, 13-mm diameter central part of the anode was equipped with a grid consisting of 20 μm tungsten gold-plated wires with pitch of 1 mm [376].

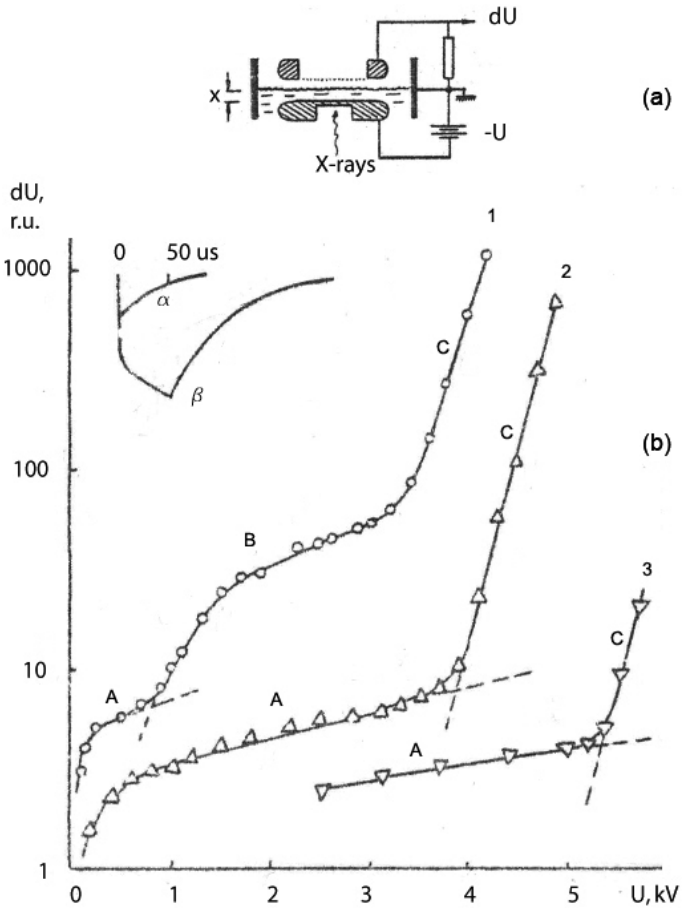

Fig. 7.4 Schematic drawing of the emission ionization chamber as shown in Fig. 7.1a but equipped with a multiwire anode (a) and emission curves (b) measured with this detector filled with pure liquid krypton (1), liquid mixture of Kr+4.4%molCH_4 (2), and liquid mixture of Kr+12%molCH_4 (3). A thickness of the liquid is 1 mm; a calculated methane concentration in the gas phase is 2% (2) and 5.8% (3); inserted oscillograms represent the shape of anode voltage pulses without gain effect (α) and with gain effect (β) [376].

Pure krypton or a krypton-methane mixture has been used to fill the detector. In pure krypton vapor, only gas gain of 60 has been observed above the liquid krypton; in the mixture of Kr+5mol%CH_4, a gas gain of 200 has been achieved; in the mixture of Kr+39mol%CH_4, the gas gain of 500 has been observed. Evolution of emission curves (amplitude of the induced pulse voltage ΔV measured from anode versus the applied voltage V or electric field in the liquid E_1) is presented in Fig. 7.4b. The thickness of the liquid was 1 mm in all cases. X-ray radiation with maximum energy of 35 keV has been used for irradiation of the liquid. In Fig. 7.4, branches of types A and B represent tradi-

tional branches of emission curves (compare to Fig. 7.1b); the branch of type C is associated with gas gain above the liquid. Anode signals had a simple triangle shape (α) in the branches of A and B type. The shape of the signal changed to a trapezoid (β) in branches of type C. Changing shape of signals is associated with appearance of the ion current when electron multiplication occurred around wires. One can see from Fig. 7.4 that the threshold of the emission is increasing with increased concentration of methane due to effect of cooling electrons in collisions with methane molecules. A saturation effect observed in the threshold value at increased concentrations of methane is probably associated with evolution of the ground state of electrons from -0.45 eV in pure krypton to ~ 0 eV in pure methane, which compensates for the electron cooling effect.

Gas gain in pure noble gases is unstable and limited with relatively low values due to effective developing of secondary effects such as generation of UV photons, photoemission of electrons from electrodes, and as a result of these processes easily developed discharge. In an attempt to suppress the photon feedback, gas electron multipliers (GEM) have been tested with the emission detector [377]. A principle operation of emission detector with GEM readout is shown in Fig. 7.5a.

The three-layer GEM of 28×28 mm^2 sensitive area is made of 50-μm thick Kapton with 70 and 55-μm hole diameters on the copper coating and the insulating foil respectively at 140-μm pitch. The distance between the GEM1 and the chamber bottom is 5 mm; the distances between GEM1, GEM2, and GEM3 are 2 mm. Electrical connections and the readout scheme are shown in Fig. 7.5b. The signals were recorded from the last layer, GEM3, in a current or pulse-counting mode. In the latter case, a charge-sensitive amplifier has been used with 10 ns rise time, 8 μs decay time and sensitivity of 0.5 V pC^{-1}. The detector was operated as an emission device filled with liquid krypton and irradiated with particles from a ^{90}Sr source. Gain-gain characteristics at room and low temperatures are shown in Fig. 7.5c. The gas gain of 10^4 has been achieved in the two-phase mode in pure krypton.

7.3 Emission Spark Chambers

At elevated voltages, it is relatively easy to develop sparks in pure noble gases. Sparks in the argon vapor have been used to perform imaging of the alpha source placed in the liquid in one of the first emission detectors shown in Fig. 7.2. The spark discharges have been pictured with a photo camera placed above the wire anode [369]. The next modification of the spark emission chamber was an emission streamer chamber tested at beam of high-energy pions at

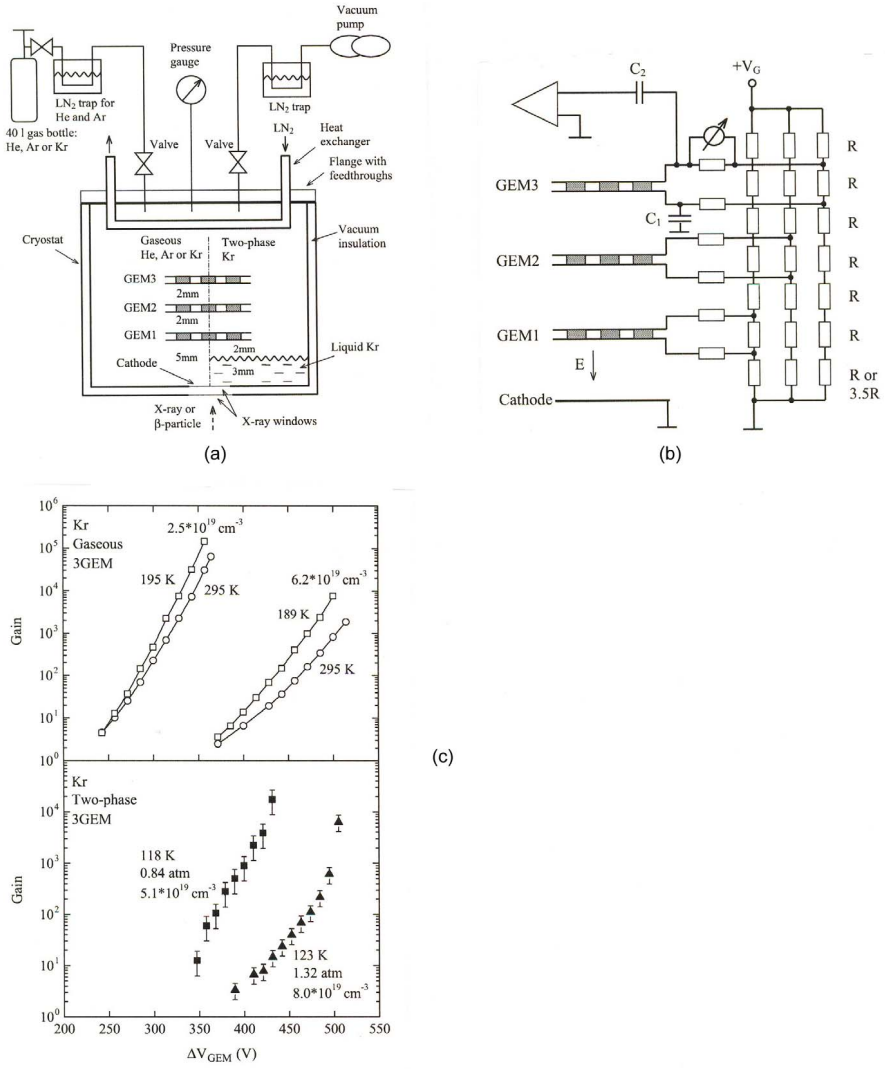

Fig. 7.5 Schematic drawing of the LKr emission detector with triple-GEM readout system (a), electrical connections of the triple-GEM and readout scheme (b), gas gain characteristics of the detector operated with room temperature and cold gas and two-phase filling (c), as reported in Ref. [377].

the ITEP (Moscow) synchrotron from 1977 to 1978 [378, 379]. The emission streamer chamber (Fig. 7.6) utilized a 1-cm thick layer of the solid krypton as working medium and 1 cm gas gap filled with neon as an amplification medium. The anode had 12.5-cm diameter gridded central part allowing picturing of the gap between the anode and the layer of the solid krypton through

the glass window installed above the anode. The window has been used as a high voltage insulator supporting the anode. The bottom of the detector vessel served as a cathode shaped in such a form that it provides a uniform electric field between the gridded part of the anode and the cathode. A positive DC voltage has been applied to the anode to provide the emission of electrons, and a 100 kV pulse at a duration of 60 ns has been applied to generate the streamer discharge along the electron image of particle tracks extracted from the solid krypton. The detector was triggered by a telescope of scintillation counters. Tracks of 3 GeV c^{-1} pions formed by chains of streamers have been pictured by the photo camera or two photo cameras for stereoimaging. The tracks obtained in emission mode consisted of 2-mm long and about 0.5 mm in diameter streamers packed with density of about 1 streamer per 1 mm of the track length. Observation of such dense streamer tracks guided the authors to the consideration that such kind of detectors could be used for detection of hypothetic abnormal low-ionizing particles [380].

An attempt was made to develop a large emission chamber with a 0.5-m diameter and 20-cm deep condensed krypton working medium and a 1.5-m diameter cryogenic streamer chamber placed above the condensed krypton for investigating antiproton annihilation in heavy atoms [18]. The detector was constructed at ITEP (Moscow) in the early 1980s and tested in parts: a whole-metal streamer chamber detecting tracks imitated with a UV laser and, independently, a 0.5-m diameter emission section of the detector used as an ionization chamber for measurement of krypton radioactivity, and an electron emission purity monitor for large amounts of liquid krypton [372, 381].

7.4 Emission Electroluminescence Detectors

Emission detectors with proportional scintillation or electroluminescence of the gas phase used for signal amplification are today the most often used two-phase detectors. First, such detectors have been used to detect alpha particles in liquid argon [382] and in liquid xenon [364] with electroluminescence of vapors measured with a single photomultiplier placed outside detectors. Similar simple devices have been used in the first observations of electron emission from solid xenon into the gas phase of neon [383] and to study threshold field effects of electron emission from solid argon [384], liquid and solid krypton, methane (with neon as a ballast gas), and their mixtures [371], as well as for comparison scintillation properties of different condensed noble gases (see Section 3.4).

Operating in the mode of time projection chamber, emission detectors may be used for precise measurements of the coordinate in the direction of the extracting electric field. Obodovsky with colleagues constructed this time pro-

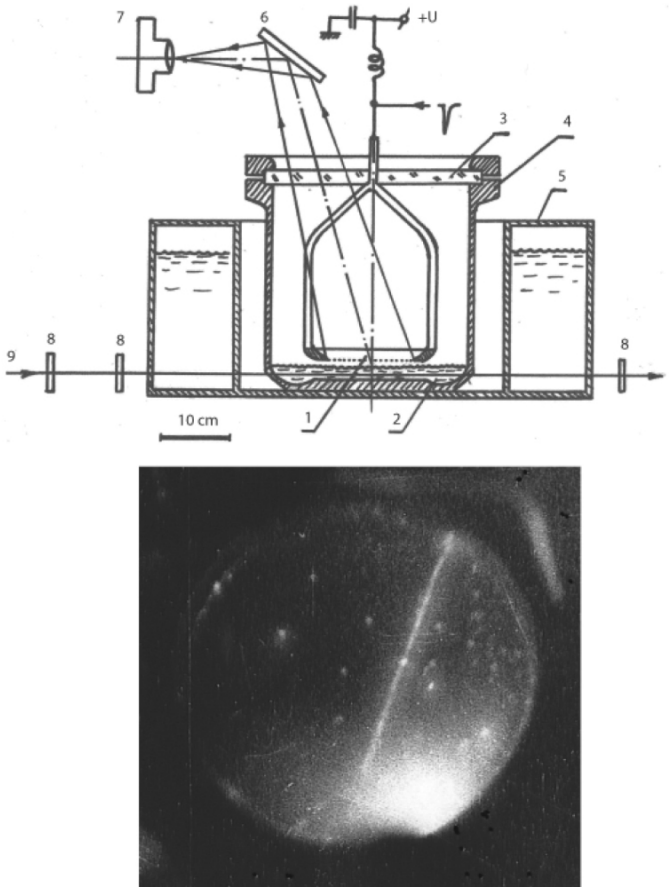

Fig. 7.6 Emission streamer chamber and photo of a typical 3 GeV c^{-1} pion track. Note: 1 - wired anode; 2 - solid krypton; 3 - HV electrode installed through the optical window; 4 - detector vessel; 5 - liquid nitrogen tank; 6 - mirror; 7 - photo camera; 8 - telescope of scintillation counters.

jection liquid Xe emission drift chamber (Fig. 7.7) used in studies of the angular distributions of positron annihilation gamma quanta [385]. At a drift path of 2 cm, the detector demonstrated 0.5-mm spatial resolution in the direction of the electron drift. The resolution was mostly limited by the size of diffused electron clouds.

An emission electroluminescence camera with array of nineteen 3″-diameter photomultipliers (Fig. 7.8) was developed for two-dimensional gamma ray imaging in nuclear medicine in the 1980s [386, 387]. The stainless steel vessel of the detector enclosed a 30-cm diameter anode with a 24.5-cm diameter gridded central part. The flat grid consisted of nichrome wires of 50-μm diameter parallel-stretched with 1-mm pitch. Nineteen 7-cm diameter

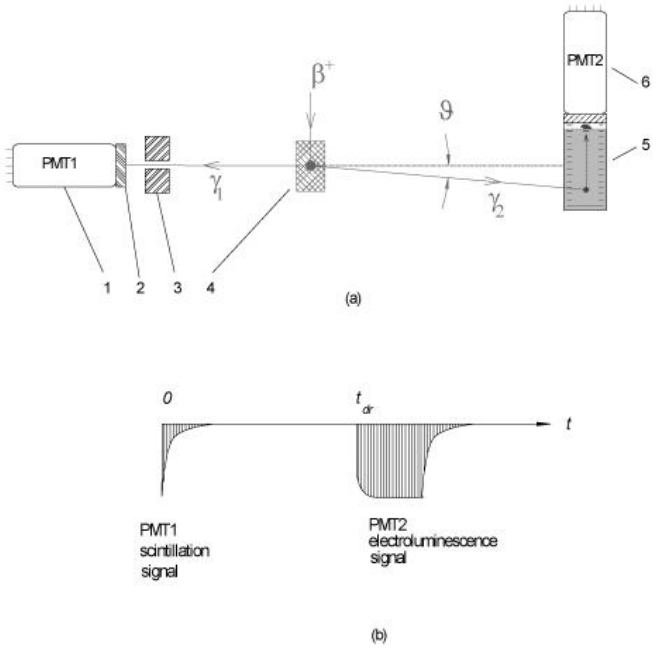

Fig. 7.7 Schematic drawing of experimental setup with single-channel time projection LXe emission electroluminescence drift chamber used in study of angular distributions of positron annihilation gamma quanta (a) and principle of readout (b): 1 - photomultiplier for detection of scintillation signal used as a trigger; 2 - plastic scintillator; 3 - collimator; 4 - sample, where positrons annihilate; 5 - LXe emission electroluminescence TPC; 6 - photomultiplier detecting electroluminescence flash in the TPC.

glass windows coated with 0.5 mg cm^{-2} p-terphenyl wavelength shifter were installed in the lid of the vessel in hexagonal order. Every window has been viewed with an 8-cm diameter glass photomultiplier of FEU-110. Xenon was purified by passing through a hot (920 K) calcium absorber. The gas was stored in a stainless steel tank, whose inside surface was sputtered by a titanium getter from the head of an evaporation pump installed on the top of the tank. In addition, xenon was purified with chromosilicate oxygen adsorbent similar to the Oxisorb. The detector was cooled down with nitrogen vapor circulating in the jacket surrounding the vessel. The gas condensed in the layer of up to 1-cm thick at the thin bottom of the vessel serving as a cathode. Coordinated electroluminescence flashes were determined as the position of the center-of-gravity of the signals acquired from all PMTs (Anger camera mode). A storage oscilloscope was used to collect all data and display images of the alpha source placed on the cathode and lead multihole collimator illuminated with gamma radiation of ^{241}Am or ^{57}Co gamma sources placed outside the detector. Internal position resolution measured with the alpha source was measured to be 3.5 mm. The energy resolution of 15% FWHM was

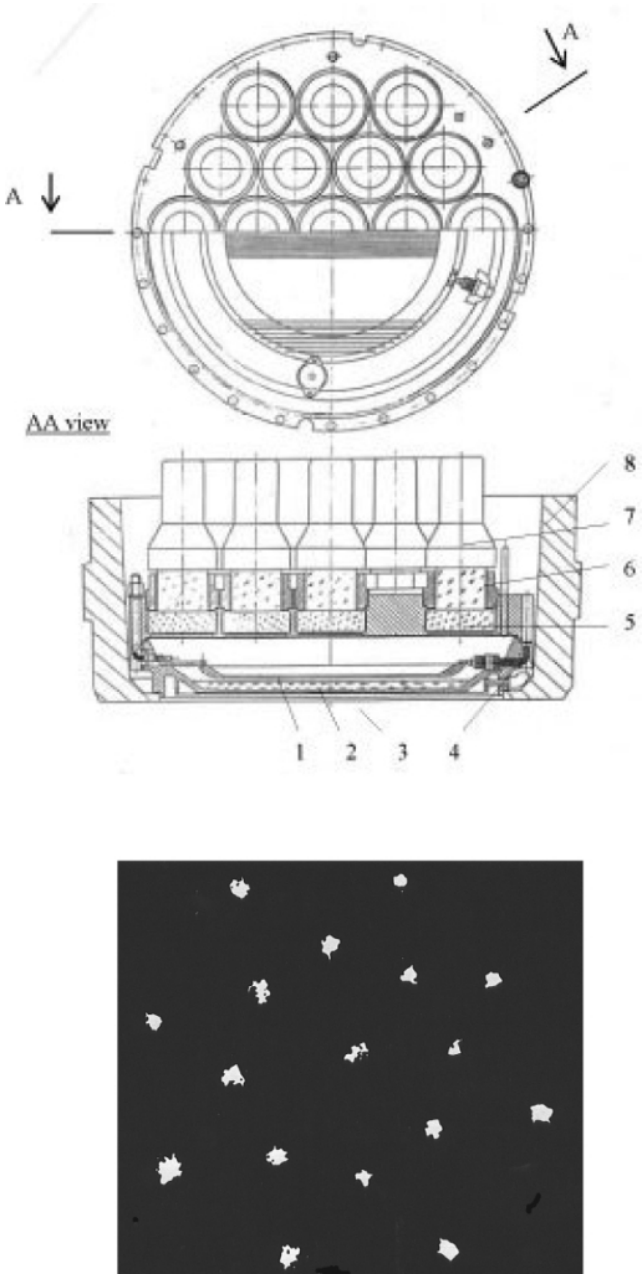

Fig. 7.8 Emission electroluminescence imaging gamma camera (top) and image of the lead mask in 122 keV ^{57}Co gamma rays at 22-cm field of view (bottom): 1 - multiwire anode; 2 - solid xenon; 3 - thin foil (0.1 mm) radiation input window insulated with cold nitrogen jacket; 4 - HV ceramic feedthrough; 5 - glass window with p-TP wave shifter deposited on the inside surface; 6 - gas filled light guides; 7 - glass window 3”-diameter FEU-110 PMT; 8 - lead shielding of the camera [386, 387].

measured with the ^{57}Co gamma source. The relatively poor energy resolution was associated with the relatively low purity of xenon and, in part, the inadequate readout system developed for short scintillation signals of the NaI(Tl) scintillator. The detector was tested with krypton and xenon fillings. Note that with this detector electroluminescence of liquid xenon has been observed in a uniform electric field of about 10 kV cm^{-1} (see Section 3.4).

Due to the high sensitivity of photomultipliers, the emission detectors allow detection of both the primary scintillation and electroluminescence in order to achieve three-dimensional position sensitivity. Such a 3D position-sensitive electroluminescence detector triggered with primary scintillation was demonstrated with a high-pressure xenon scintillation drift chamber as described in Section 6.1. This development allowed for formulating a concept of a wall-less emission detector for low background experiments [146]. Another important advantage of emission detectors used like this application (for details, see Section 9.1) is that multimode readout helps distinguish events of different origin and effectively suppress the background of gamma rays [263, 388, 389]. For example, in condensed noble gas ionization, scintillation and electroluminescence can be generated. In superfluid helium, in addition to photons and electrons, such quasiparticles as rotons can be generated. In solid noble gases, phonons may be observed at low temperatures. These features along with availability of superpure noble gases in large amounts, make them a most attractive medium for emission detectors.

The advantage of two-mode readout from LXe emission detectors has been investigated with a dual-phase and three-grid emission detector [246] equipped with metal body quartz window Hamamatsu R6041 PMT (20% quantum efficiency at 178 nm) as shown in Fig. 7.9a. A 6-cm diameter stainless steel disk with ^{207}Bi beta source placed in the center served as a cathode. The grid structure was mounted at 10 mm above the cathode and consisted of 0.1-mm wires at 1-mm pitch. A typical waveform measured from the PMT is presented in Fig. 7.9b: the first signal S1 is associated with a scintillation of the liquid xenon, the second signal S2 is an electroluminescence flash of the Xe vapor when the cloud of ionization electrons drift through the gas. Energy spectra from S2 signals (Fig. 7.9c) are compared with the charge spectrum when the detector was working in the mode of the LXe ionization chamber with a grid (Fig. 7.9d). There is a peak at about 80 keV in the S2 spectrum while the low-energy section of the charge spectrum is dominated by noise. This is a clear demonstration of the advantage of emission detectors against ionization chambers. The detector served as a prototype of a large emission detector, which is under development by XENON collaboration for the search of cold dark matter.

Two photomultipliers working in coincidence have been used in a similar study with a 0.3-L active volume emission LXe detector XMASS-II [265]. The detector has improved light collection efficiency due to focusing Teflon reflec-

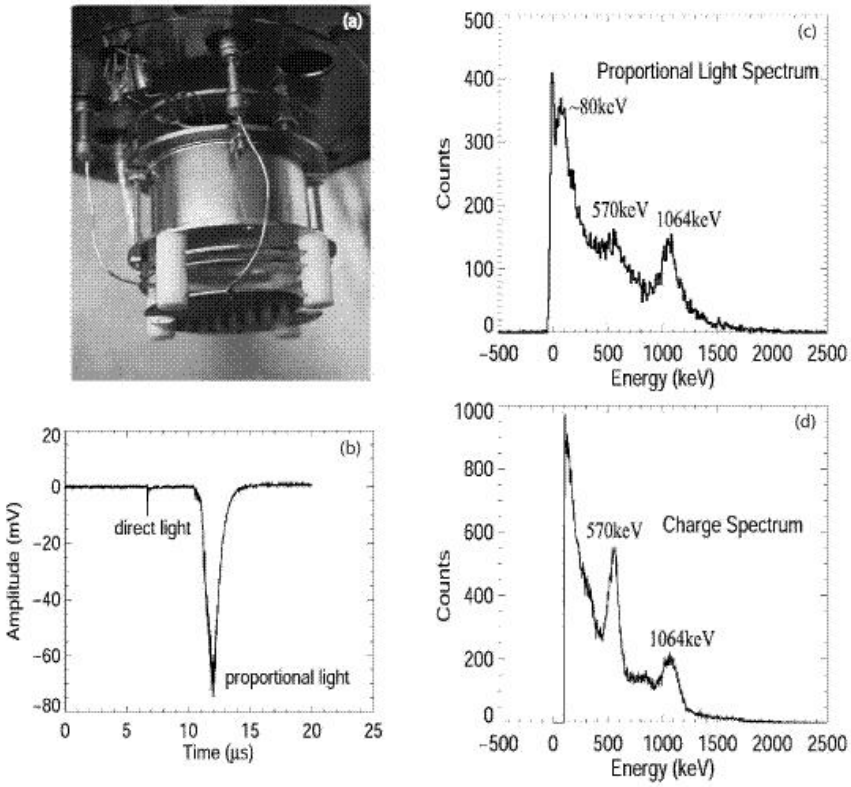

Fig. 7.9 Picture of dual-phase xenon chamber for investigation of correlations between scintillation and electroluminescence signals (a), waveform of typical signal from the detector including original scintillation flash (direct light) in LXe and electroluminescence (proportional light) (b), energy spectra from the proportional light in dual-phase operation mode (c), and from induced electron collection charge measured in single-phase operation mode (d) reported by Aprile et al. [246].

tors installed as shown in Fig. 7.10a. The anode and the cathode diameters and distance between them are 84, 46, and 85 mm, respectively. The anode structure consists of two grids placed 5 and 15 mm apart as shown in the figure. The grids are made of 30-μm diameter wires with 2-mm pitches. Grounded cathode meshes with 90% optical transmittance are evaporated on the inner surface of the MgF2 windows. Two UV sensitive PMTs (9426B by Electron Tubes, 32% QE at 174 nm and room temperature) are mounted outside the windows. The detector has been evacuated at 10^{-5} Pa and backed out for about 3 weeks at 120 °C. Xenon was purified by passing through 3.3l Messer Grieshein Oxisorb. A 40-L liquid nitrogen bath was installed above the detector and used to cool down the detector via cold finger system, adjusting the temperature at 180 K with heaters as shown in Fig. 7.10b. Typical spectra

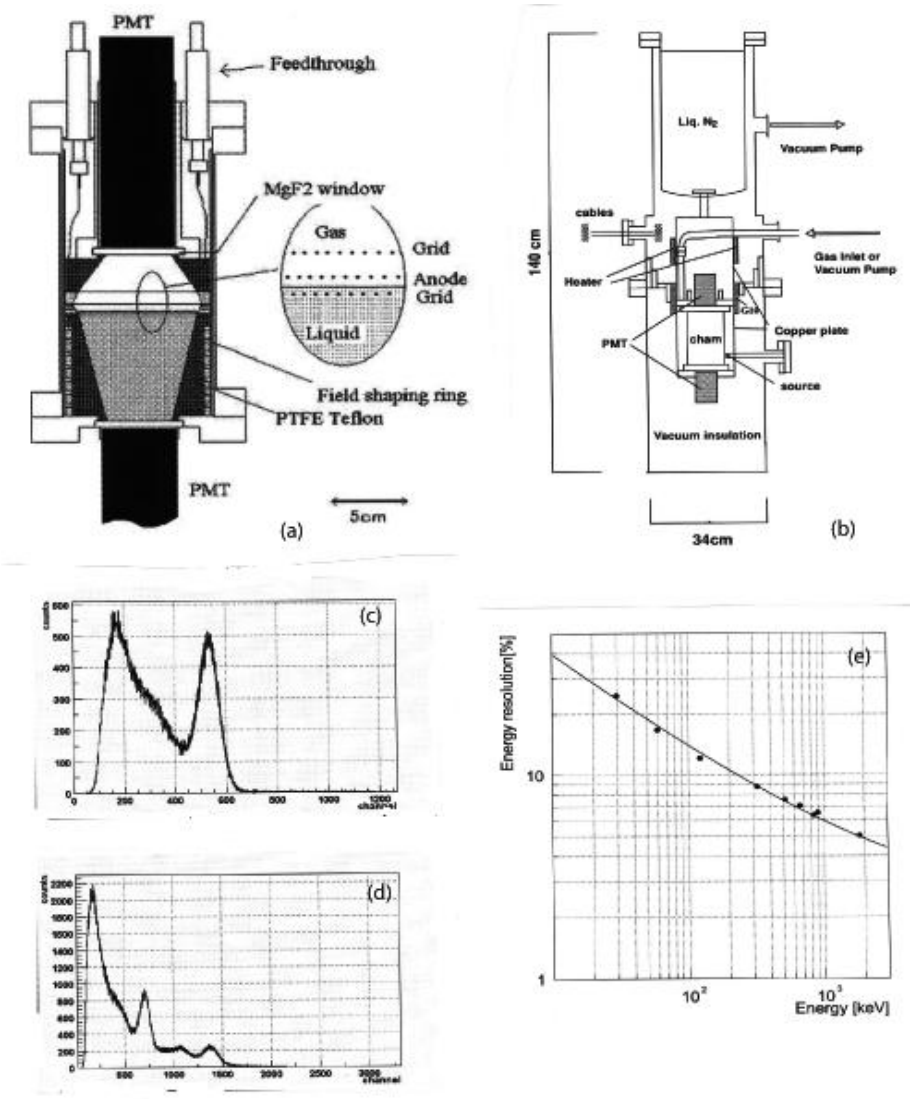

Fig. 7.10 Schematic drawing of the double phase emission detector XMASS-II with two-channel PMT readout (a), its cryogenic system (b), energy spectra acquired with this detector from ^{137}Cs (c) and ^{88}Y (d) gamma sources, and the dependence of energy resolution on the gamma ray energy (e), as reported by Yamashita et al. [390].

of the summed signal from two PMTs acquired with ^{137}Cs (662 keV) and ^{88}Y (898 and 1836 keV) in two-phase mode are shown in Figs. 7.10c,d, respectively. A dependence of the measured energy resolution of the detector on energy of gamma rays is shown in Fig. 7.10e, along with the fitted function of σ/E

= $118/\sqrt{E}$ + 2.2% where E is measured in keV. The authors concluded that analyses of correlation between S1 direct (scintillation) and S2 proportional (electroluminescence) signals allows for distinguishing between neutron recoils and gamma rays better than 99% in the range of 10–100 keV.

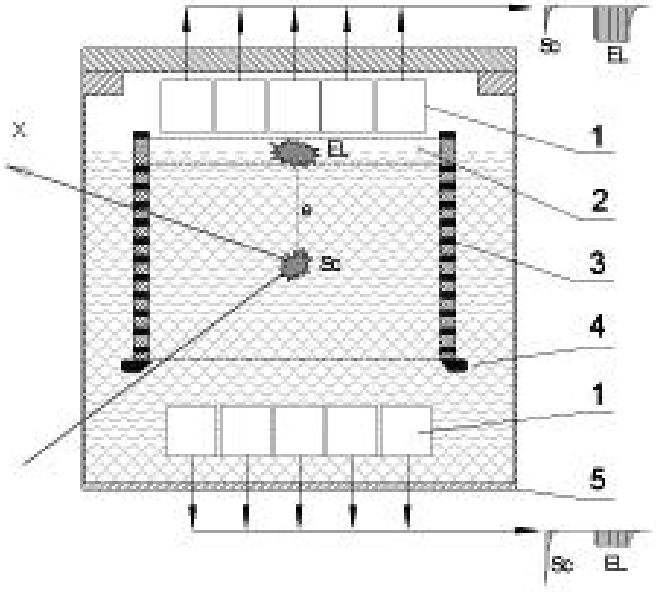

Fig. 7.11 Principle operation of contemporary emission electroluminescence detector: (a) measured radiation generates the fast scintillation signal triggering the detector at $t = 0$; (b) emitted electrons excite the gas and generate the second signal, amplified due to electroluminescence at $t = Z/v_{dr}$ [160].

As of today, there are a few experiments planning to use condensed noble gas emission detectors with electroluminescence readout (for details, see Chapter 9). All these detectors work as follows (Fig. 7.11):

- Measured radiation interacts with a condensed working medium, excites and ionizes atoms, and generates the first signal via emission of photons or quasiparticles (scintillation in noble liquids and solids, phonons in crystals, rotons in superfluid helium).
- In an external electric field applied to the working medium, ionization electrons drift to interphase, escape into equilibrium gas phase, excite and ionize atoms of the gas and generate the second (amplified) signal; the signal is delayed relative to the first signal and used for two-coordinate and energy measurements; the third coordinate is defined by the delay time between the first and the second signals.

7.5 Vacuum Emission Detectors

Electron emission from metals in a vacuum were discovered by Hertz in 1887 and since that time, the effect has been successfully used in many vacuum devices such as kinescopes, radio bulbs, photomultipliers, electron guns, etc. The advantage of electron collection in a vacuum is the possibility to supply it with high energy from an external electrical field that allows detection of single electrons. The effect of secondary electron emission from metals was used for the development of parallel plate vacuum ionization chambers for detection of high-intensity beams of high-energy particles [391]. Solid state electron emitters include ionic crystals such as MgO and CsI [392, 393] and semiconductors with negative surface electron affinity (NEA) [394]. Attempts to extract electrons from bulk semiconductors were not so successful.

Since the electrical field cannot penetrate deeply inside metals and highly doped NEA, the escape depth of electrons from these materials is limited by the thermalization length of electrons. In metals, this value is about the wavelength of the visible light. For this reason metals can be used as very thin detection media, which are effective only for short-range light photons. In a p-type silicon, the thermalization length may achieve 10 μm. For this reason NEA have been used as thick photocathodes for detection of relatively long-wave (infrared) photons. However, metals and NEA semiconductors are ineffective for detection of more penetrating radiation.

Porous ionic crystals such as microcrystallic MgO with thickness up to 10 μm and density consisting of only 0.7% of the density of the bulk crystal can operate as an emission detector at sufficiently high electron extraction fields (10–100 kV cm^{-1}); at electric fields >100 kV cm^{-1}, secondary multiplication of emitted electrons occurs in pores [395]. Such emission detectors were proposed to be used as fast, highly sensitive detectors of high-energy particles in accelerator experiments.

The absence of diffusion in a vacuum, the high rate of transition of electrons, and the possibility of easy transformation of electronic images makes the idea of emission detectors with solid noble gas working media attractive. A necessary condition like this detector is a low density of vapors ($<10^{10}$ cm^{-3} or pressure $<10^{-4}$ Pa). The attempt to construct a fast solid argon emission detector as a vertex detector for accelerator experiments was made by Guschin, Somov, and Dolgoshein at the end of the 1970s [396]. An operating principle of the time projection emission detector is illustrated in Fig. 7.12.

Electrons extracted from tracks of short-living particles are shown to be extracted from the solid argon, to be accelerated in the vacuum, and to bombard the plastic scintillator viewed with a fast photomultiplier. Analysis of a waveform of signals acquired from the PMT allows to reconstruct the range of the short-living particle. For example, if the lifetime of the short-ranged neutral particle is 10^{-13} s, it travels 30 μm in solid argon before being de-

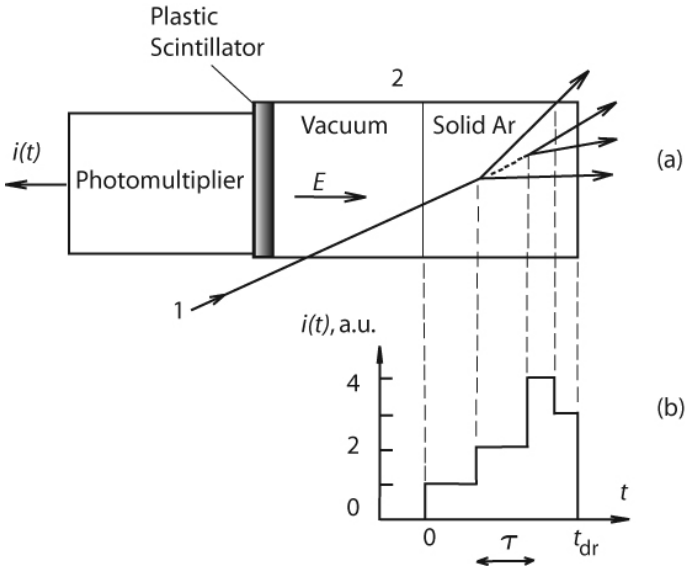

Fig. 7.12 Schematic drawing of time projection solid argon/vacuum emission detector (a) and waveform of scintillation pulse (b) measured with photomultiplier: 1 - incoming high energy particle decaying in short-living neutral particle with life-time τ; 2 - detector chamber; t_{dr} - drift time of electrons in the solid argon body; E - electric field extracting electrons from the solid argon and accelerating them in vacuum. Redrawn from [396].

cayed into charged particles. This feature in distribution of ionization electrons transforms into the current pulse of 3 ns, which can be measured with the PMT. In this calculation, it is suggested that the electron drift velocity is about 10^6 cm s^{-1} in the solid argon. Unfortunately, a performance of the device was not very good because of the low mobility of ions in the solid argon, leading to fast polarization of it in the intensive beam of high-energy particles and discharges in a vacuum, paralyzing PMT operation.

We believe that this approach may be more fruitful in the future for low rate applications such as the search for exotic particles. Another intriguing possibility is a development of an emission microscope or telescope using relatively easy transformations of electron images in a vacuum. This kind of emission detector may be used for example, for detail investigation of track structures (with purpose of background rejection, for example) or for the collection of data from a large area detector to relatively small readout devices, such as arrays of charge-coupling devices (CCD).

7.6 Further Developments of Two-Phase Detectors

Emission detectors is a fast-growing area of radiation detector technology. Most of their modern applications are associated with fundamental physics experiments searching for rare events and exotic particles. These applications require detectors with good spectrometric properties, low detection thresholds, and three-dimensional position sensitivity. Parameters of several tested emission detectors are compared in Table 7.1. One can see that the position resolution is measured to be good in comparison with liquid ionization chambers, parameters of which are reviewed, for example, by Lopes and Chepel [238]. At the same time, the energy resolution of the emission detectors is about twice as bad as that of single-phase ionization chambers and single-phase electroluminescence detectors. That is a result of fluctuations of the collected charge associated with transition of charge carriers through the interphase surface. Note that macroscopic fluctuations of the electron emission current at electric fields close to the emission threshold E_0 have been observed in the large (41-cm diameter) LKr emission detector [381]. Thermoactivated emission of charge carriers accumulated under the interphase surface introduces additional uncertainty in the measured electron signal. It has been shown [149] that the Richardson–Dashman equation for thermoemission of an ideal electron gas can be applied to the electron emission from such nonpolar dielectrics as liquid Kr, and therefore, the probability of thermoelectron emission is sensitive to the temperature as $\sim T^2\exp(-V_0/kT)$. Therefore, reducing the temperature should significantly reduce the probability of thermoelectron emission, reduce electron signal fluctuations, and improve the energy resolution of emission detectors. Otherwise, the effect of microwave instability of the charge interphase surface should be suppressed for the solid interphase surfaces. This may explain why the energy resolution of the old S/G Xe emission detector was observed to be twice as good as that of the modern L/G Xe emission detector (Table 7.1).

The detection threshold is normally limited by electronics noise which, for all aforementioned emission detectors, exceeds 10 keV. According to Radeka [311], only thermal fluctuations in dielectrics (for example, in printed circuit boards) generates noise

$$ENC_{\mathrm{d}} \cong (2.4kTDC_{\mathrm{d}})^{1/2} \tag{7.1}$$

The dissipation factor for the best dielectrics $D \cong (5\text{–}10)\times 10^{-5}$, which results in $ENC_{\mathrm{d}} \cong 50\text{–}100$ rms es at $C_{\mathrm{d}} = 10$ pF. Also, this noise cannot be eliminated for devices working at room temperature. The only way to reduce the electronics noise and associated detection threshold is development of emission detectors working at cryogenic temperatures. As follows from the above consideration, cryogenic emission detectors coupled to transition edge sen-

Tab. 7.1 Properties of noble gas emission detectors.

Media	Size, cm	En. Res. (E)	Δx,Δy, mm	Δz, mm	Readout	Ref.
S/G Xe	Ø 22×0.5	15(122)	1.5		19 PMTs	[353]
L/G Ar	Ø 2.5×0.4	25(5486)			1 CSA	[375]
L/G Xe	Ø 2×2			0.5	1 PMT	[385]
L/G Xe	Ø 5×1.5	24(122)			1 PMT	T. Shutt, (private communication, 2006)
L/G Xe	Ø 5×1.5	18(50ee)		0.4	1 PMT	[397]

Note: PMT - photomultiplier; CSA - charge-sensitive amplifier; Energy resolution given in % FWHM; E - deposited energy (in keV); L - liquid; G - gas; S - solid; ee - electron-equivalent.

sors may have a detection threshold < 10 eV. The detector architecture may be similar to that used in the CDMS-II and proposed for the SuperCDMS experiment [398] utilizing arrays of cryogenic germanium and silicon detectors. The detector may consist of a solid xenon time projection chamber where ionization electrons are collected from the bulk solid xenon into superconductive aluminum anodes coupled to the transition edge sensors [160]. Since the drift length of quasifree electrons in solid xenon already have been observed to be more than 1 meter, the mass of the working medium can be equal to a few tons. The detector should be surrounded with several heat screens connected to the dilution refrigerator cooling the detector below 100 mK.

Thus, we believe that further enhancements of the emission detector technology may be associated with exploration of solid working media such as solid xenon operating at reduced or even cryogenic temperatures.

8
Technology of Noble Gas Detectors

The technology of noble fluid detectors has been rapidly developing in the last two decades. The subject area attracted attention of researchers and detector technologists at many universities and national laboratories. A valuable progress in the development of this technology has been achieved mostly due to the discovery of effective methods of purification of large amounts of noble gases, the introduction of low-noise electronics, and the development of new VUV sensitive photosensors such as UV photodiodes and compact photomultiplier tubes capable of working at low temperatures and at elevated pressures. In this chapter, we describe specific technical solutions and methods supporting operation of noble fluid detectors. The chapter includes recommendations on construction materials, requirements of mechanical design, references to proven electrical and optical parts, most applicable insulators, feedthroughs, safety devices, photosensors, etc. Significant emphasis will be placed upon the description of purification methods, systems monitoring purity and other important properties of the media. The chapter cannot cover all aspects of the technology but it may serve as an introduction to the technology for beginners.

8.1
Selection of Materials and Mechanical Design

The materials of choice for pure noble gas detectors are very similar to materials used in ultrahigh vacuum systems. The major requirement is to reduce the outgassing rate to a value that the desired purity of working media can be provided.

8.1.1
Metals

8.1.1.1 Construction Metals

Austenitic stainless steel is the most commonly used metal for manufacturing vessels of noble gas detectors. Russian 12X18H10T and US 304 stainless steel

(T304 Alloy; density 8.03 g cm^{-3}; composition: 9.25%Ni, 19.00%Cr, 1.00%Si, 2.00%Mn, 0.080%C, 0.045%P, 0.030%S, the rest is Fe) are chosen most frequently for their satisfactory argon-arc welding, good mechanical properties, and acceptable outgassing rates. Usually this kind of steel is not used at temperatures above 1200 K. The radioactivity of the stainless steel is ranged between 0.02 and 0.1 Bq kg^{-1}.

Aluminum and aluminum alloys are very cheap, easy to machine, and have a low outgassing rate as long as the alloy does not have a high zinc content. They have the disadvantage of low strength at high temperatures and high distortion when welding. Alloys with a copper content also present welding problems. Aluminum that will be exposed to a vacuum should never be anodized due to serious outgassing problems. There are also some potentially violent chemical reactions that can develop when cleaning freshly machined aluminum with trichloroethane or trichloroethylene-based vapor degreasers. The high vacuum sealing between two aluminum flanges may constitute a problem, however.

Oxygen-free high conductivity (OFHC) copper is easily machined with good corrosion resistance and is widely used in detectors. It is not generally used for vessels that require baking due to possible heavy oxidation. The low radioactivity of OFHC copper is an important property for some applications.

Titanium alloys are sometimes used for fabrication of special low-mass and low-radioactive (for selected alloys) vessels. Titanium requires special techniques for arc welding to protect it from intensive oxidation at elevated temperatures.

Brass has good corrosion resistance and in the past often used as a major construction metal. In modern pure systems, brass components are usually nickel-plated to reduce outgassing due to the zinc content.

8.1.1.2 **Sealings**

Metal sealings are most often used in the constructions of noble gas detectors that require periodic openings as well as in gas fittings of associated vacuum and purification systems.

Copper rings are commonly used for systems with ConFlat-type flanges that use a copper ring compressed between two knife edges. The seals are bakeable up to 720 K, and are widely used because of relatively low cost and because the thermal expansion coefficient of copper is very close to that of stainless steel.

Aluminum wire rings are very cheap and bakeable up to 500 K.

Indium wire can be used between flat flanges. It is very soft and continues to flow after initial tightening (needs special groves for good sealing). Combined indium-coated copper gaskets can be used for sealing very different materials such as optical windows between steel flanges, for example. It can be heated up to 400 K.

Gold wire is often used for ultrahigh vacuum seals between flat surfaces and can be baked to 720 K.

Swagelok, Tylok, VCR, and other whole-metal brand seals are now widely used. The best practical results were achieved with VCR-type sealings capable of operating at elevated and cryogenic temperatures, at high-vacuum and high-pressure conditions.

Helicoflex spring energized seals consist of a jacket tube and helical spring inserted inside. The sealing principle is based upon the plastic deformation of a jacket (most often made of aluminum) and the compression resistance provided by the spring. Each coil of the helical spring acts independently and allows the seal to conform to imperfections on the sealed flange surfaces. The seal perfectly performs in the temperature range from cryogenic to 1255 K and the pressure range from ultrahigh vacuum to 340 MPa. Special designed Helicoflex seals can be used with the ConFlat flanges. The main disadvantages are that Helicoflex seals are relatively expensive and can be used only once.

8.1.2 Insulators

Generally, the use of plastics should be kept to a minimum due to their high gas permeability and high desorption rates compared with metals, glass and ceramics. In spite of this, plastics are often used in vacuum systems because of their insulating properties, elasticity, low radioactivity, and affordable price.

PTFE (Teflon DuPont) has self-lubricating properties, a relatively low outgassing rate, is a good electrical insulator, and can be used at higher temperatures than other plastics. High permeability makes PTFE unsuitable as a part of the vacuum envelope.

Nylon has self-lubricating properties but a high outgassing rate and a high adsorption rate for water is a drawback.

PVC has a high outgassing rate but does find application for rough vacuum lines and temporary connections such as to a leak detector.

Polyethylene may be usable if well outgassed. It is inherently low-background material with high electric strength. In the UK the polymer is called *polythene*. The main disadvantage is its relatively low melting temperature.

Vespel polyimide is ultrahigh vacuum compatible, easily machined, and an excellent insulator from DuPont. Vespel tends to be very expensive.

G10 Glass Epoxy is available in blocks and sheets, difficult to machine, and has a high initial outgassing rate. It is often used for printing circuits in, for example, liquid argon and liquid krypton ionization calorimeters.

Fluoroplastics include Kel-F, PVDF (Kynar), TFE, etc. Kel F has a fairly tolerable outgassing rate and while expensive it is much cheaper than Vespel for some applications.

Kapton is a DuPont polyimide film that has more than 35 years of proven performance as the flexible material of choice in applications involving very high (673 K) or very low (4 K) temperature extremes. Kapton is used in a wide variety of applications such as substrates for flexible printed circuits, transformer and capacitor insulation and perfectly performed as a construction material of electrode systems of noble liquid ionization calorimeters.

Cirlex is an all-polyimide sheet material made of Kapton films. With a thickness of 3–4 mm and plated with copper, it has demonstrated a good performance for fabrication of printed circuit boards for LXe detectors. It has a temperature range of 4 to 624 K; electrical strength for breakdown 2790 V mil^{-1} at thickness of .009″ (.23 mm).

Ceramics are widely used, with alumina ceramic (92–99.8% Al_2O_3) being the most widely used material out of a variety of fine ceramics. It features the same crystal structure as sapphire and ruby. Alumina ceramic demonstrates a low leakage current, low outgassing rate, low gas permeability, and can be used from cryogenic temperatures up to 1800 K. The ceramic is most often used for manufacturing electrical feedthroughs due to highly developed technology of the ceramic to metal brazing. There are also some machinable ceramics available such as Macor, which includes mica and because of that cannot be used for low-background applications. All ceramics are brittle and must be handled with care but mechanically perform much better than any glass.

8.1.3 Feedthroughs

Types of feedthroughs used in noble gas detectors include single-channel, multipin and high voltage electrical feedthroughs, fiber optic feedthroughs, and motion feedthroughs. The following basic principles have to be taken into consideration when selecting the feedthroughs:

- Construction material should be clean and do not impose a risk of contamination of noble gas with electronegative and molecular impurities.
- Construction should be helium-leak tight at least at a level of 10^{-9} mbar L s^{-1}.
- Radioactive or Rn-emitting (porous) materials are not permitted or should be shielded for low-background applications.

8.1.3.1 Electrical Feedthroughs

Glass-to-metal sealed electrical feedthroughs have often been used in the past. Ceramic-to-metal seals, bonding metals to ceramics, are fundamental to the electrical feedthroughs used in contemporary devices. This kind of ceramic

feedthrough can operate from cryogenic to 723 K and from ultrahigh vacuum to 24 MPa pressure. Multipin instrumentation feedthroughs contain more than one conductor path or pin and are also fitted with a fastening air-side connector. These feedthroughs are used for the transmission of voltage and current signals. Among many manufacturing companies the authors prefer products of CeramTec and Kyocera.

There are a few designs of HV feedthroughs discussed in the literature. In fact, all those designs are based on the idea of HV cable connectors:

1. Ground shielding of HV cable is firmly connected to the body of the device with a nut or flange.

2. At this point, the cable has no shielding (open cable), consisting of a conductor surrounded with a thick enough insulator, and introduces HV to the point of application; it is important that the length of the open cable is selected long enough to withstand surface breakdown between the point of HV application and grounded point of the shielding connection.

ICARUS design [399] follows the design of the detachable HV cable. This is a solid HV cable with tube conductor installed inside a long high-density polyethylene (HDPE) rod, which is sealed to the detector body with Viton O-rings. The O-rings are continuously flushed with dry nitrogen to prevent oxygen diffusion along the conductor but still oxygen diffusion cannot be excluded. This design is acceptable for LAr detectors with relatively liberal requirements to the gas purity but cannot be accepted for LXe detectors.

For low-background installations, the well-proven ceramic feedthrough (for example, 90 kV Ceramaseal p/n 17057-02-CF) can be mounted outside of the passive shielding to the top of the long metal pipe connected to the detector as shown in Fig. 8.1. HV insulation inside the pipe provided with two (or more) insulating tubes, which are open at both sides. The tubes could be made of Teflon or quartz. The design of this kind of HV feedthroughs with quartz insulating tubes has been proven in a LAr ionization chamber used in the experiment searching for double beta decay of ^{100}Mo [400], in the high-pressure xenon ionization chamber used in the experiment searching for double beta decay of ^{136}Xe [401], and in the large LKr/LXe spark purifier [402].

8.1.3.2 **Optical Fiber Feedthroughs**

The use of epoxy is undesirable as outgassing can occur. As an example of clean design, we mention the Oxford Electronics optical fiber vacuum feedthroughs using *CuBall* metal-coated optical fibers which are brazed to a stainless steel tube to make a vacuum tight seal and then brazed to an SMA connector on the vacuum side. The optical fiber feedthrough allows

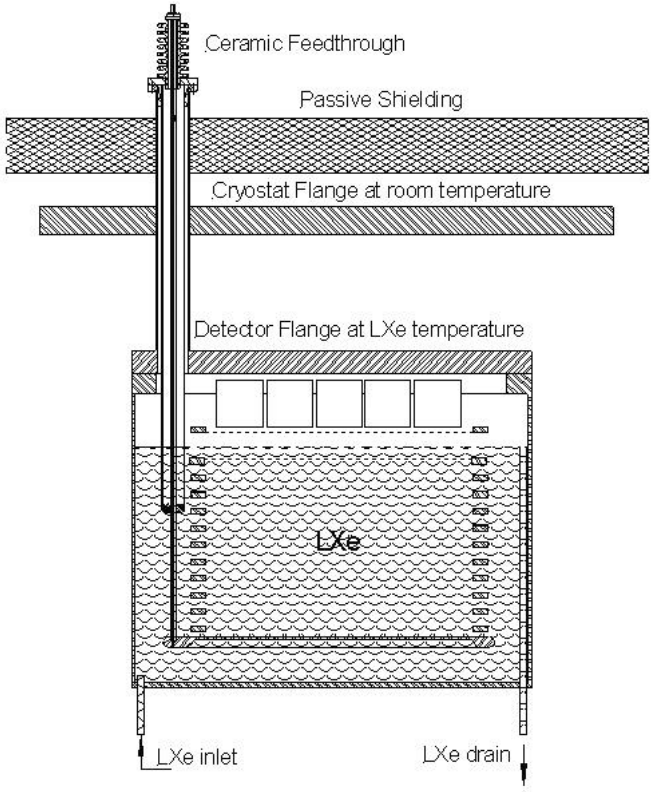

Fig. 8.1 Installation of alumina HV feedthrough in LXe detector working for a low-background experiment.

for unfastening the optical connection easily at either side of the detector vessel or vacuum chamber. This feedthrough is weldable into a variety of standard vacuum flanges to provide an optical fiber UHV system. Vacuum feedthroughs and compatible optical fiber vacuum cable, and external cables are available in core diameters of 400 µm, 600 µm and 1000 µm. The cables are SILICA/SILICA construction and are available in UV-visible range of 180–1200 nm or the visible-IR range of 500–2400 nm.

8.1.3.3 **Motion Feedthroughs**

Motion feedthroughs are used in whole-metal pumps, level meters, and movable radioactive sources. The most popular motion feedthroughs are based on a magnetically-coupled drive. The rare-earth magnetic drivers are an excellent option to conventional bellows and diaphragm-sealed motion devices. There are no sliding seals inside the detector or gas purification system and

stray magnetic fields are virtually nonexistent. The in-gas armature is made of paramagnetic materials with stainless steel and silicon nitride bearings and is capable of repeated bake-out to 473 K (with magnets removed). There are commercially available magnetic actuators such as the *MagiDrive* series of UHV rotary feedthroughs (UHV Design Ltd., England). Their high flux magnetic coupling removes the need for bellows or dynamic seals, resulting in an extremely robust design, fully compatible with the UHV environments; it is compact, bakeable to 523 K and offers true UHV performance.

8.1.4 Electrodes

While electrodes of few-channel ionization detectors are relatively simple and repeat the design of traditional ion ionization chambers, vacuum tubes, etc., there are some specific electrode systems developed specially for use in pure noble fluid detectors. In this section we mention namely this kind of device.

8.1.4.1 Active Cathodes

Active cathodes can be used as a source of electrons in applications where only electron charge carriers are desirable. Photocathodes coated with Au, Zn and illuminated with a laser beam or an UV flash lamp were used for investigation of quasifree electron transport properties of noble liquids and solids and for measurements of electron attenuation drift length in purity monitors. Aluminum or stainless steel cathodes coated with CsI or CdTe placed in gas or liquid phase (to reduce the work function) were used for detection of VUV photons generated in scintillation or electroluminescence of noble gases.

The thermoelectron emission cathode (tungsten wire of 0.2 mm diameter) placed in the gas phase of the two-phase xenon ionization chamber were used to generate electron current up to 6 mA to pass through the liquid with purification purposes [166].

Autoelectron emission cathodes are used in several noble liquid ionization chambers for purification from electronegative impurities by means of passing the electron current through the liquid (see Section 8.3.3) or for spattering titanium getter for purification of noble liquids or dense gases (Section 8.3.4).

8.1.4.2 Grids

In order to screen the electrical field of drifting charge carriers in ionization chambers or to make electrodes transparent to light signals or amplify signals in nonuniform electrical fields, wired electrodes or grids are often used in noble gas detectors. The technology of wire chambers is greatly developed for various applications in high-energy physics and X-ray medical imaging. However, in detectors using pure noble gas working media, the purity is the

main concern and the technology of the wire chambers, including a broad variety of epoxies, plastics, and composite materials, cannot be directly copied. Below we mention only *pure* techniques, well-proven in experimental practice of noble gas detectors.

Wired electrodes, at earlier stages of the development of noble liquid detectors, were made of stainless steel or CuBe wires stretched on springing metal frames (see, for example Refs. [369, 373, 378]). Later, stainless steel wires spot-welded to stainless steel rings with diameters of up to 0.5 m were used [304, 353, 386]. They were probably the cleanest grids ever used but their production required a lot of man power. The similar technique was used by Chepel et al. [195] in design of a PET LXe chamber where stainless steel wires supported by two MACOR frames were kept under tension with individual springs made of Be-bronze. With the development of new clean insulating materials such as G10, Kapton and Cirlex, the technology of wire chambers became more acceptable. For example, the wired (aluminum copper-clad and gold-plated wire of 0.12-mm diameter produced by California Fine Wire Corp.) electrodes soldered to the Cirlex-based printed board have been successfully used in the two-phase xenon emission detector (T. Shutt, private communication, 2006).

Electrochemically etched fine grids can be produced in large sizes and high quality provided by electropolishing and gold plating. A process of photochemical machining (often abbreviated as PCM, and sometimes referred to as chemical milling or chemical etching) is a technique for manufacturing high-precision flat metal parts. In the process of etching away the unwanted material, a photographically prepared mask is used to protect the metal that is to remain after the etching process. For example, the Fotofab Corp. (Chicago) offers unusual configurations with tolerances within 0.0005", including the capability of producing small holes and bars that are not possible with mechanical machining. The technique was applied to the construction of high pressure xenon ionization chambers [33, 403], high-pressure xenon electroluminescence detectors [328], and LXe detectors [243].

Microstrip electrodes with fine aluminum or gold multistrip structure deposited on a sapphire or glass substrate have been used in high-precision electrode systems of many noble gas and liquid detectors (Akimov et al. [325], Veloso et al. [317]). Solovov et al. [404] reported on the development of a 5×5 cm^2 ministrip ionization chamber, which used a thin glass plate with two sets of strips deposited on both sides in perpendicular directions. The front strips are thin and widely spaced while the back strips are wide. The electrons collected at the thin strips induce charge on the back side of the plate and the two set of signals are used for two-dimensional readout with resolution < 1 mm for gamma radiation in the range of energies of 110–220 keV absorbed in liquid xenon.

8.1.4.3 Multilayer Structures

Noble liquid ionization calorimeters use sophisticated electrode structures [81]. The electrodes can be arranged to form a single gap ionization chamber or interleaving two absorber plates with a thin readout electrode, to form a double gap chamber. Multilayer electrode structure could be perpendicular to the incoming particles, as in earlier designs of the liquid argon calorimeters MARS, BARS, liquid krypton calorimeter KEDR, liquid xenon calorimeter SDM-2M, or they may have strong longitudinal zigzag structures like the accordion-shaped electrode structure of the ATLAS LAr calorimeter, or slightly zigzagging thin strip electrodes of the NA48 LKr calorimeter (for more details see Chapter 9). Electrodes arranged in the beam direction are easy to group in towers or modules of several meter sized detectors. For example in the NA48 liquid krypton ionization calorimeter filled with 8 m^3 of liquid krypton, the active volume has a transverse octagonal shape 2.4 m across and is 1.25 m deep (26 radiation lengths); 13 500 cells of 2×2 cm^2 are formed by 1.8-cm wide and 40-μm thick copper beryllium (CuBe) strips individually tensioned and stretched along the particle direction in a projective geometry, with small alternating left-right tilts as shown in Fig. 8.2.

The CuBe ribbons are guided by five spacer plates to perform a longitudinal zigzag. The ribbons are stretched between base plates made of Stesalit epoxy-fiberglass composite. This design provides minimal thickness of the dead material for incoming particles and makes the calorimeter quasihomogeneous. For sampling calorimeters like that used in ATLAS, the electrode structure includes absorber electrodes made of stainless steel-clad lead. Two such electrodes are interleaved by one three-layer copper-clad Kapton readout electrode (Fig. 8.2).

8.1.4.4 Amplifying Electrode Structures

Recently, it was shown that technology of gas electron multipliers (GEM) can be used in pure noble gas detectors. The GEMs, supplied by the CERN Gas Detector Development (GDD) Group, are manufactured from a 50-μm thick copper-plated Kapton foil by a chemical etching process that produces holes with a conical shape; the typical diameters of the holes are 50–80 μm with pitch of 100–200 μm. GEM structures have been used in two-phase emission detectors for electron signal amplification [406]; they may be used for generation of electroluminescence signals especially being coated with p-terphenyl wavelength shifter [407]. However, stability of the gas gain and noise, associated with direct photoeffect and spontaneous thermoactivated electron emission, are still issues for the use of GEM structures in pure noble gases. For example, the maximum gain achieved in the triple-GEM did not exceed 1000 in krypton saturated vapor and 100 in xenon saturated vapor above suit-

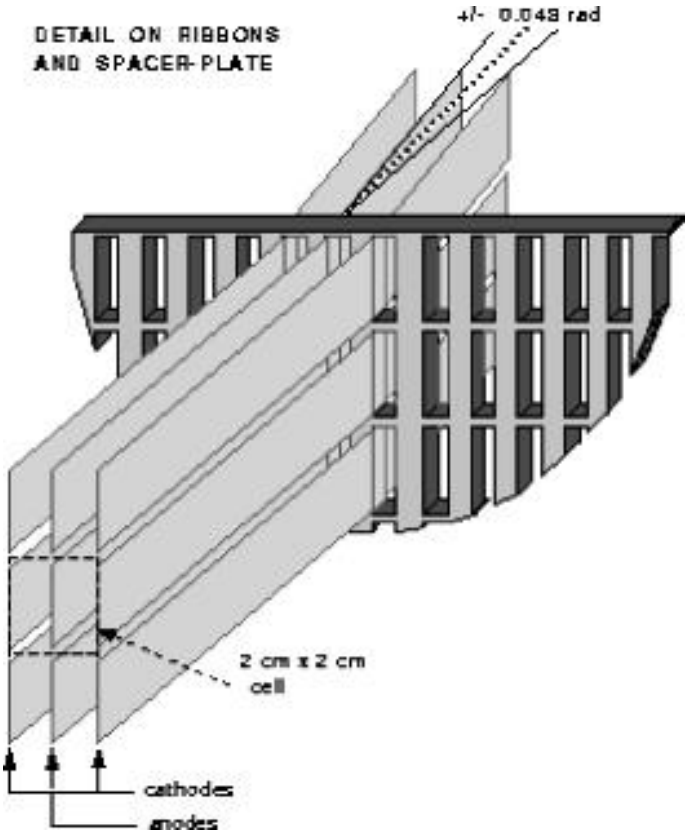

Fig. 8.2 Schematic drawing of NA48 liquid krypton calorimeter electrode structure [405].

able liquids [406, 408]. New microstructures such as microhole and strip plate (MHSP) chambers [409] may be useful for further reduction of the positive ion feedback and allow to increase gas gain and stability of the gas multipliers. However, it is pretty clear a priori that the devices using electron avalanche amplification effect cannot achieve the best performance in pure noble gases without quenching admixtures.

8.1.5 Viewports and Windows

At earlier stages of the noble gas detector development, glass-made chambers were often used. This allowed observing the level of the liquid media and detecting light signals through the detector walls. Such detectors were very fragile and did not allow overpressure above the atmospheric pressure. With the development of the technology, the detectors manufactured out of metal

require special devices for visual access to the interior part of the detector or detection of light signals. Optical windows are usually used in scintillation and electroluminescence detectors including high-pressure xenon, noble liquid scintillation, and two-phase emission detectors for delivery of light signals to photosensors. Small viewports can be used to monitor the liquid level and for inspection of the detector interior.

8.1.5.1 **Materials**

Optical silicon of monocrystalline and polycrystalline grade is most often used in infrared (IR) systems operating in the 3–5 μm wavelength range. Silicon's low density gives it an advantage over other infrared materials with optical transmission greater than 52%. Silicon windows can be mechanically polished to optical quality with diamond powder or chemically polished.

Fused silica is a synthetic silica glass material, which has low optical absorption in the UV range. Fused silica has an excellent homogeneity and resistance to high-power laser energy, with the ability to withstand temperatures over 1000 °C. UV fused silica has low thermal expansion allowing for rapid changes in temperature without the risk of breakage due to thermal shock. Fused silica polished windows have high transmission from deep UV at 180 to 2000 nm. There are several grades of fused silica which are free of UV fluorescence, and have improved refractive index homogeneity, as well as excimer laser grades tuned for maximum transmission and prolonged life such as Spectrosil and Heraeus.

Fused quartz is produced by fusion at very high temperatures of naturally occurring high purity quartz rock crystal. Flame fused quartz has very good transmission at near ultraviolet and visible wavelengths with useful transmission range from 260 to above 2000 nm. Fused quartz polished windows are manufactured from a range of grades of materials by major quartz processors from around the world: Vitrosil, Heraeus, GE fused quartz is a low-background material used in electrical insulators and feedthroughs of liquid noble gas detectors searching for double beta decay [245, 400, 401]. Optical sapphire windows, which are extremely hard and scratch resistant, are useful for the visible and IR spectrum.

Optical sapphire is made to have a random orientation or cut to a specified orientation. It has an excellent thermal conductivity at low temperatures allowing single crystal sapphire to be used in many diverse fields requiring high thermal conductivity. Sapphire has a high dielectric constant and is resistant to common chemical acids and alkaline. Optical sapphire has no color; its transmission ranges from 170 nm to 6 μm. It was used in high-pressure (3.5 MPa) ^{3}He scintillation detectors with wavelength shifter deposited on the entrance surface.

UV optical windows provide high light transmission from 150 to 400 nm. UV windows are fabricated in a range of optical and crystal materials. There are grades of UV optical glasses that transmit at the higher end of the UV, close to 400 nm. For example, Schott 8337B optical glass has 80% transmission at 220 nm and has good transmission from 205 nm into the visible region. UV grade fused silica has excellent thermal properties. Fused silica windows are chemically inert with excellent resistance to most chemicals. Other UV optical and crystal windows for ultraviolet transmission include UV grade calcium fluoride (CaF_2), zinc selenide (ZnSe), lithium fluoride (LiF) and magnesium fluoride (MgF_2).

8.1.5.2 **Optical Windows for High-Pressure Detectors**

Pressure windows are often made of glass or quartz. There are formulas available for calculating the strength and thickness of the window when it is under a vacuum or high pressure for circular, square or rectangular windows. Among the factors to be considered in determining the thickness are:

- operation temperature
- pressures to each side of the window
- supported area
- usable clear aperture
- safety factor.

The mechanical strength of the window must be calculated to a large safety factor (one of the authors used factor 10) and a good inspection should be given to the window. Great care and attention to all surfaces and edges of the window must be paid at both the fabrication and inspection stages. In some situations, a defect on the edge or surface can cause a failure sometimes delayed by hours after assembling. When mounting, the usual method is to clamp the joint area between semirigid gaskets such as annealed copper flat gaskets with indium or Teflon wire implanted. A symmetric from both sides sealing design is preferred more. Irregularities of the gasket surface can cause high local stress resulting in breakage of the window. If the temperature is likely to vary during the operation, both the clamping pressure and gasket material must be such as to permit the window to slide relative to the metal frame to allow compensation for the difference in thermal expansion.

8.1.5.3 **Glass Machining**

Diamond drilling uses hollow diamond impregnated drills. This process can achieve a good finishing quality with a tolerance for 0.05 mm of holes over a 2-mm diameter. It is ideal for making holes and glass rings.

Ultrasonic drilling is suitable for drilling holes less than 2 mm in diameter. Using a hardened steel point and an abrasive, the pulsation of the point grinds through the glass with little stress producing a precise clean-cut hole.

Milling is possible using CNC machine technology with diamond impregnated tools and cutters.

Beveling is a process for machining sharp edges using diamond wheels and various grades of abrasives. The processing increases the window strength, and is particularly important when pressure is applied. With some optical materials it is standard practice to chamfer the edge for protecting the optical window through polishing.

8.1.6 High-Pressure Vessels

A pressure vessel is a container that holds liquid, vapor, or gas at a pressure other than the atmospheric pressure; even a vacuum vessel is classified as a pressure vessel. Pressure devices should be provided with at least one or more safety valves and other monitoring and control equipment that ensure safe operation. In some states in the US, for example, it is required by law that the tank with a volumetric capacity more than 2000 gallons is equipped with at least two safety valves, the smallest of which must have a relieving capacity of at least 50% of that of the largest valve. There are standard regulations and formulas to which pressure vessel designs adhere in order to avoid potential hazards associated with pressure containment. The American Society of Mechanical Engineers (ASME) provides a boiler and pressure vessel code on which the engineers should base their design of pressure vessels. Materials suitable for pressure devices include stainless steel (US 304 stainless steel is most often used), aluminum, titanium, and composites. Because of purity considerations, composite vessels should use aluminum or stainless steel liners and a composite material overwrapping in an epoxy resin. The composite materials include fiberglass or carbon-fiber reinforced plastics, aramid or Kevlar by DuPont. Composite fiberglass wrapped high-pressure vessels are up to 60% lighter than steel or 25% lighter than aluminum-made vessels and provide a good transparency for gamma rays that is important, for example, for application of high-pressure xenon ionization chambers in gamma spectrometry.

Overpressure can lead to a variety of disasters - injuries, damaged equipment, lost pure and expensive gas. There are a few types of protection devices that can be used to release the overpressure and to direct the pollution to a safe place: rupture disks, relief valves, safety relief valves, and safety valves. Rupture disks are the cleanest and cheapest devices and they are most often used in noble gas detectors. A relative disadvantage is that they can only be

used once. They are the only device that can be used in conjunction with other overpressurization devices, for example to be installed between liquid noble detectors and cold storage reservoirs. In the US, the safety relief valves should be designed and installed in accordance with the ASME Boiler and Pressure Vessel Code, Section VIII. The discharge pipes connected to safety valves and rupture discs installed must satisfy the following requirements:

- have a cross section area at least equal to the combined outlet areas of all valves discharging into them;
- be designed and installed so that there can be no interference with the proper operation or discharge capacity of the safety valve or rupture disc;
- have no valve of any description;
- be fitted with open drains which prevent accumulation of liquid above the safety valve or rupture disc;
- be installed and supported in a manner that prevents undue stresses on the safety valve or rupture disc;
- be led to a safe place of discharge.

8.1.7 Cryogenics

Cryogenic devices are used to support the operation of noble liquid detectors, purifiers and storage tanks. There are three basic types of cryostats used to support filling, operation and discharge of noble liquid detectors:

1. Cold bath used to immerse the detector into the coolant;
2. Cold screen or finger used as a heat sink from the detector;
3. Local heat exchanger installed into thermoinsulated detector vessel.

The first two types of cryostats are used for small to medium size (< 1 m^3 detector volume) detectors. They employ electrical heaters for precision regulation of the temperature. The first type provides low and well-controllable temperature gradients that are important for applications requiring uniform light collection. The second type is technically more simple and works perfectly for very small detectors of $< 10^3$ cm^3 working volume. The third type of calorimeters is most often used for large detectors, when the first two types are difficult to implement. The dynamic cooling scheme with the recirculation of the working medium via constant condensation of the returning gas may

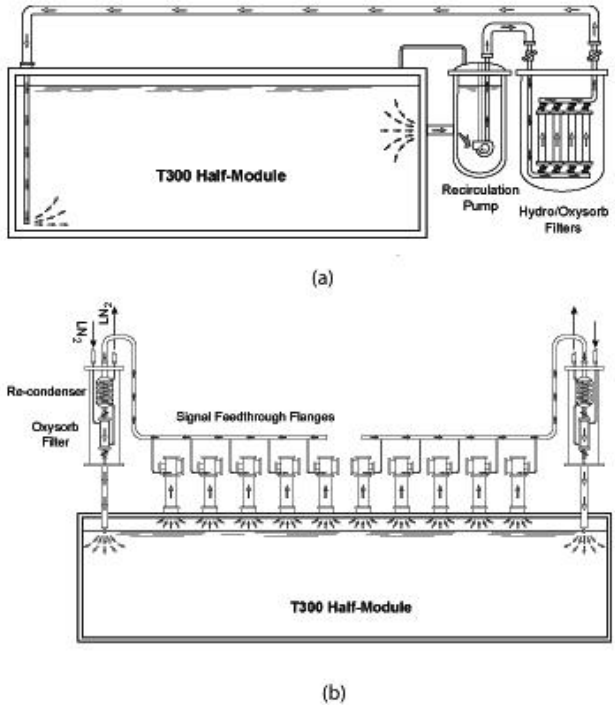

Fig. 8.3 Circulation systems used in ICARUS-T600 LAr detector: (a) for purification of liquid argon and (b) for cooling and recondensation of the evaporated argon [399].

require special precautions in order to minimize the convection motion of the liquid.

As an example of the third type of cryostats we can consider the cryostat for ICARUS-600 [399]. The detector vessel is of parallelepiped shape with external dimensions of $4.2 \times 3.9 \times 19.9$ m^3 (Fig. 8.3). The basic elements of the cold vessels are panels with a thickness of 150 mm and a surface of about 2×4 m^2. They are made of aluminum honeycomb, surrounded by frames of aluminum profiles and sandwiched between two aluminum skins. Cooling pipes for LN_2 circulation are directly inserted in the middle of the panel honeycomb structure. Aluminum honeycomb is perforated to allow the circulation of nitrogen gas or evacuation of the whole panel. Maximum overpressure inside the cold vessels is limited to less than 0.15 MPa abs. Holes for cables, wires, vacuum and gas ports are equipped with the inner aluminum part welded to the container body and the outer stainless steel part machined as a standard ConFlat flange, using bimetal (aluminum to stainless steel) joints. Feedthrough flanges are mounted outside the insulation, at room temperature.

Thermal insulation based on panels of $4.5 \times 2 \times 0.465$ m^3 made of Nomex honeycomb sandwiched between 2-mm thick aluminum skin at room temperature, an internal layer made of Kevlar crossed fibers in epoxy resin at LAr temperature, and installed in the middle of two 20-cm thick Nomex honeycomb panels the perforated aluminum panel. The 40-mm gap between the LAr containers and the insulation was filled with polyurethane foam.

Cooling of the cryostat is performed by circulating pressurized LN_2 at 0.27 MPa pressure and nominal temperature of 89 K. The temperature of LAr is uniform and stable within 1 K that is needed to avoid changes of the electron drift velocity and prevent large convection motions inside the LAr volume.

8.2 Processing High Purity Noble Gases

Three sources of noble gas contamination can be distinguished: gas absorbed on surfaces of construction elements, the residue gas after pumping the detector, and impurities dissolved in the bulk detector medium.

8.2.1 Pretreatment

Mechanical, chemical and electrochemical methods have been widely used for the pretreatment of detector components to reduce outgassing. Dirty parts should be ultrasonic cleaned in Liquinax for 10 minutes, rinsed with distilled (deionized) water, and ultrasonic cleaned in alcohol for 10 minutes. The last procedure is recommended as final for all parts before assembly. For all small metal parts all surfaces should be machined. Stainless steel brushes and pads could be used to clean metal parts. Cotton swabs wet with alcohol must be used to clean blind holes and test their cleanness. The outgassing rate of Duralumin could be reduced by a factor of ten by mechanical scouring and washing in benzol and acetone. Washing aluminum in detergent reduced the outgassing by a factor of ten. Sandblasting of steel decreases the rate by a factor of four [410]. Brass parts should be first cleaned with clean room cloth and a bottle brush or stainless steel or brass wire over threaded areas, ultrasonic cleaned for 10 minutes in alcohol at room temperature in a fume hood, the parts blown with dry nitrogen (recommended for other parts as well), and wrapped in UHV aluminum foil. Water or water-based cleaners should not be used with brass since this will cause an oxide layer on the brass part.

Vacuum backing of the metal and ceramic components is a simple and effective method of reducing the amount of gas absorbed in the bulk of the material. Baking is not recommended for brass since it may contaminate the vacuum oven with lead, beryllium or zinc.

8.2.2 Pumping

An important step in preparation of the noble gas detector to operation is removing the air after it is sealed off and before it is filled with the working medium. A vacuum system should provide oil-free pumping to the lowest possible residue pressure. It is highly recommended that before pumping the detector interior should be washed with argon of technical grade purity; the pumping station should provide high pumping speed for washing gas.

An *ideal* UHV work station should consist of at least two (roughing and high-vacuum) pumps from the following modern types of pumps:

- a cryosorption (molecular sieve trap cooled with liquid nitrogen) pump or trapped rotary pump for initial pump-down from atmosphere;
- a turbomolecular pump to pump rare gases, assist in initial pump-down, and to pump load-locks;
- an ultrahigh vacuum pump such as ion pump/Ti sublimation pump, diffusion pump with a cold trap, or cryopump.

All mentioned high-vacuum pumps are capable of achieving very good high-vacuum scales as low as 1×10^{-6} Pa, which is excellent for our purposes. Pumping beyond that is impractical because below 10^{-7} Pa the pump actually is pumping light gases such as hydrogen that permeate through the wall of the detector.

8.2.3 Baking

Baking procedure is a reduction of the amount of gas (water, hydrocarbons, etc.) in an absorbed layer by heat treatment. Water is particularly troublesome because the activation energy of desorption on most solids is about 20 kcal mol^{-1}. Rigorous baking is particularly important for glass parts because glass contains large quantities of dissolved water. Baking of metal parts not only removes the absorbed water, as with glass parts, but also assists in the removal of hydrogen that is the predominant gas in solution in most metals. Most of chemically active gases in noble gas detectors (H_2, N_2, O_2) are dissociatively absorbed on metals. Rate of desorption $\sim \exp(-E_d/kT)$ in the event that no molecules is returning where E_d is the activation energy for desorption. Obviously, stainless steel, ceramic parts, wires with Kapton insulation should be baked in a vacuum at 200 $^\circ$ at least 48 hours; aluminum, ceramic, glass, and Teflon parts should be baked in a vacuum at 400 K at least 48 hours. Heating for degassing purposes can be done by resistive heating, RF heating, radiant heating or ion bombardment. The first and last methods are the most

convenient and often used. It is important to degas all surfaces simultaneously so that gas does not transfer from one surface to another. The degassing of electron-bombarded electrodes in gauges and mass spectrometers is particularly important since the bombarding electrons can desorb gases such as oxygen by electron impact, which cannot be easily removed by heating. Low melting point materials (wavelength shifters or plastic fibers) can be degassed by ion bombardment.

8.2.4 Handling

Clean facilities should be used for assembling detectors. Usual practice includes using gloves, dust-free laminar flow benches, and storing clean parts in warm and dry cabinets. Small parts may be stored in stainless steel or glass containers or desiccators which are cleaned and prepared in the same way as vacuum equipment. Tables and work areas for cleaning, assembly, testing clean parts are to be lined or covered with fresh aluminum foil. Assemblies too large to be processed on clean benches should be processed in portable clean rooms.

In practical systems, being used for the first time, the largest source of contamination of the working medium is from the residue gas. Recommendation is to wash the detector with pure inert gas (for example, argon of technical purity) before final pumping and filling the detector with pure working gas.

A thin film coating would provide reduced degassing and surface pumping without requiring any additional space. Some materials provide good gettering properties and are used to support purity of the medium for a long time. Coatings with Ti, Zr, Hf can be produced by sputtering. There is a positive experience in evaporation of Ti on the inside surface of stainless steel storage tanks for pure Kr [378]. These films may be activated during vacuum baking or electron bombardment. During activation under UHV conditions, the oxygen surface content is progressively reduced. Among the coatings of pure Ti, Zr, Hf and their equiatomic combinations, the lowest activation temperature was found for TiZr [411]. Na and Ba mirrors vacuum deposited onto glass containers have been used for a while for support purity of saturated organic liquids in room temperature ionization detectors [18]. Getter coatings reduce both static and radiation-induced degassing, provide pumping of residual gases, and support high purity of pure materials during storage in coated reservoirs. Coating with active metals should be recommended for large detector systems dedicated to long running experiments such as searching for WIMPs.

8.3 Purification

Both charge and light signals produced by an ionizing particle inside condensed noble gases can be employed to identify an interaction event and to measure the energy deposited by rare particles. However, the amount of charge or light actually collected can be significantly affected by impurities contaminating the noble gas. To fully exploit the excellent detection properties of condensed noble gases, the attenuation length of ionization electrons and UV photons produced as a result of particle interactions should be longer than the size of the active detector volume. The purity of working media remains the most crucial factor limiting a sensitivity of detectors for rare particles.

8.3.1 Impurities

The most dangerous contaminants of commercially available noble gases are so-called electronegative molecules that trap electrons (see Section 3.1.3). The absolute concentrations of these impurities, which are typically on a scale of less than 1 ppm, are very difficult to measure. Moreover, the absolute concentration does not represent the purity of gas from the point of view of electron collection efficiency. Thus, the purity is normally referred to in terms of the electron lifetime, and this depends not only on the concentration of impurities but also on the density and the aggregate phase.

8.3.2 Chemical Methods of Purification

Commercially available noble gas purification systems are based on impurity absorption devices such as Oxisorb purifiers, molecular sieves, and high-temperature getters such as MonoTorr by SAES. The latest alone is very effective for argon. For example, Barabash and Stekhanov [412] reported purification of the commercially available argon with hot titanium sponge at a rate 0.6 m^3 per hour in order to achieve the gas purity of about 1.9 ppb *equiv.* O_2.

In the past, hot metal getters used alone seemed to contaminate xenon [132, 166] and krypton [130] with N_2O-type impurities capturing electrons at relatively high drift electric fields [128]. In recent experiments, Ba-Ti getters operated at a temperature of 873 K were successfully used to support 1 to 2-m electron drift lengths in liquid argon and xenon [368, 413].

The low-pressure ($\sim$ 0.27 MPa) Xe gas can be effectively purified by normally cycling through the combinations of two components connected in series: Oxisorb + getter. In principle, such systems can be used to purify large amounts of gas. However, Oxisorb and molecular sieves contaminate noble gases with the radioactive noble gas radon (Rn), which cannot be acceptable for low-background experiments.

Cold metal getter such as SAES ST 172 can be used to support purity of the noble gas (xenon) in sealed detectors [317, 414].

8.3.3 Electron Drift Purification Method

Noble liquids may be purified from electronegative impurities by electrical current. Schnyders et al. [105] were the first who demonstrated efficiency in this approach. They purified argon and krypton first by chemical adsorption methods and, at the final stage, using a 10^{-12} A current, generated by alpha particles or field electron emission from a tip cathode, collected for about 2 h to electrolytically remove trace amounts of electron-trapping impurities from the liquids. At the end of this 2-h period, the collector current had usually increased by an order of magnitude or more, indicating the appearance of charge carriers of large mobility, i.e., quasifree electrons rather than relatively slow ions. Using very intensive radioactive sources the effectiveness of the method may be increased [415].

Zaklad et al. [416] and Derenzo et al. [108] used autoelectron emission from thin tungsten wires (2.9 to 5.0-μm diameter) as a source of electrical current of 5–50 μA when a negative potential of up to 5 kV applied. After 10 to 60 min of this electronegative ion pumping the pulse height reached a level that is not increased by further processing. The authors stated that these techniques are capable of reducing the impurity level to the point where electrons have a capture mean free path > 20 cm. Bressi et al. [417] used 148 sharp tips to generate 400 μA current in liquid argon; after 6 h of the *current* purification of about 1.5 L of LAr, the lifetime was changed from about 60 μs to more than 3 ms manifesting the final concentration of the electronegative impurities to be < 0.09 ppb in oxygen equivalent.

Barabash et al. [166] used thermocathode (tungsten wire of 0.2-mm diameter, 10-mm length, and a heat current of 5 A) placed in a gas phase above the liquid xenon or argon to generated up to 6 mA current through the liquid. After 100 h of operation the cathode was still active and no decrease in the emission (from the gas into the liquid) current was observed. Attachment of electrons to electronegative impurities occurred mostly in the liquid phase as the absolute concentration of impurities in the liquid is higher than that in the gas by a few hundred factors according to Henry's law. In result of this procedure, the author had achieved electron attenuation drift length in liquid xenon and liquid argon of about 10^3 cm^3 volume to be $L_e > 150$ cm at electric field strength of $E = 1.5$–3 kV cm^{-1}. In liquid argon at $E = 50$ V cm^{-1}, $L_e > 66$ cm was measured, which responds to relative concentration of oxygen to be < 0.1 ppb. The purity was not changed for 5 h in operation cycle of the detectors.

8.3.4 Spark Purification

There is another technique based on the use of a spark discharge to spatter metal from electrodes placed inside the noble liquid [418,419] or high density gas [91]. The operating principle of the spark discharge purification process can be described as follows. A continuous spark discharge between metal electrodes placed in a dense noble gas (Fig. 8.4) creates a large amount of metal dust, which is chemically clean and has a large extremely reactive surface area. The metal dust absorbs many chemically active impurities such as oxygen in the same manner as a high-temperature getter. In addition, UV light generated in the process breaks down complex organic molecules, enhancing the purification process. Dust covering the walls of the purifier works as a getter with a large active surface. The best results have been achieved with electrodes made from titanium. Titanium dust continues to absorb impurities for a long time after the discharge is terminated.

This technology has been proven in high-pressure xenon ionization chambers [420,421]. The largest spark purifier for liquids served in achieving > 1 m electron attenuation length in liquid xenon and liquid krypton samples of up to 0.1-m^3 volume [402].

8.3.5 Separation of Noble Gases

In low-background experiments (see Chapter 9), it is required that the detector material contains extremely low levels of radioactive impurities. The sensitivity of these experiments is ultimately limited by the detector volume (which sets the signal rate) and the detector background. Among radioactive contaminants there are a few isotopes of noble gases (^{85}Kr, ^{222}Rn, ^{226}Rn, ^{39}Ar, etc.) that may play an important role forming the majority of the background in the noble gas detectors. Separation of these chemically inert impurities from the inert working medium is a difficult task.

Separation can be achieved using different physical properties of the substances. For example, noble gases argon, krypton, and xenon are commercially obtained by the fractional distillation of liquid air using the difference in their boiling temperatures,and a trace amount of neon separated from the heavier noble gases using their different absorption properties. The adsorptive separation may be achieved by different effects. The *steric* effect derives from the molecular sieving property of *zeolites*. In this case only small and properly shaped molecules can diffuse into the adsorbent, whereas other molecules are totally excluded. Kinetic separation is achieved by virtue of the difference in diffusion rates of different molecules or atoms.

One of the challenging tasks of this sort is separation of xenon from the trace content of krypton. The best commercial grade of xenon appears to have

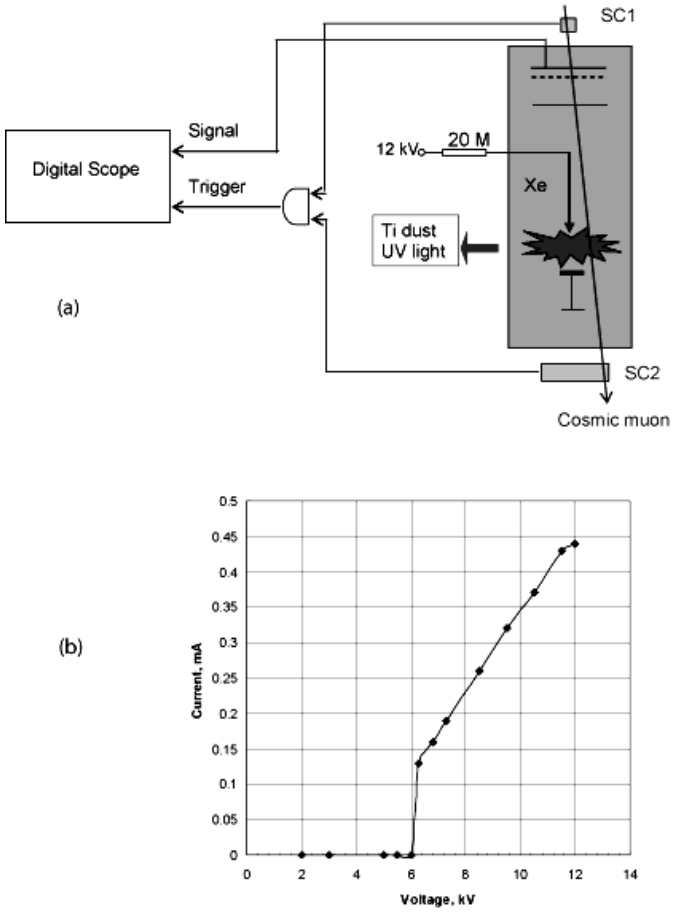

Fig. 8.4 (a) Schematic drawing of the spark purifier and (b) an example of IV curve for single gap spark purifier working at 800 psi Xe gas.

Kr contamination at about 1–5 ppm. The radioactive isotope of ^{85}Kr is 10.756 years half-life beta emitter with a maximum energy of the beta spectrum of 687 keV. It is present in the air at $\approx$ 1.16 Bq m^{-3} from nuclear fuel reprocessing (Kr is 1.14 ppm mole fraction in air, and ^{85}Kr has 2×10^{-11} isotopic abundance). The goals for 100 kg and 1 ton dark matter detectors are to reduce concentration of krypton below 300 ppt and 30 ppt, respectively. The Japanese XMASS project has developed a distillation system for Kr removal, and has succeeded in reaching $\approx$ ppt levels [422]. The kinetic adsorption separation has been developed at Case Western Reserve University for XENON dark matter search experiment. There are certain advantages of this approach for processing large amounts of xenon in an underground laboratory. First, the method does not require noisy and expensive cryogenic equipment to be

installed underground. Second, the method could be applied for removing radon content as well. In this approach, xenon has to be mixed with a helium carrier gas and passed through a charcoal absorbent column. The time it takes for each gas species to flow through the column, τ, is determined by the strength of its adsorption via $\tau = kM\Phi$, where k is the adsorption constant (experimentally obtained $k_{Xe} = 0.95 \pm 0.6\ \mathrm{L\,g^{-1}}$, and $k_{Kr} = 0.055 \pm 0.007\ \mathrm{L\,g^{-1}}$), M is the charcoal mass, and Φ is the carrier gas volume flow rate. The process consists of the following three stages, which are cyclically repeated under computer control:

1. Feed: Xe, initially contaminated with Kr, is fed in along with a He carrier gas.
2. Purge: He carrier gas alone is fed until the faster moving Kr is removed from the column while the Xe is still fully contained. A 77 K charcoal canister traps the Kr.
3. Recovery: He carrier gas continues to be fed, at a higher rate than previously, to sweep out the Xe gas, which is collected in a 77 K condenser.

When the condenser is full, the cycle is paused and He is fully removed from the condenser by pumping. The concentrated Kr in the charcoal trap is recovered by warming and sampled in a mass spectrometer with estimated sensitivity at the level of $\approx$ ppt for a few kg Xe sample.

8.3.6 Circulation

Circulation of noble gas or liquid in a closed cycle through a purification system and detector is a powerful tool in achieving high purity of a large mass of working medium and purification of the detector itself, especially in the case when the detector has a complicated structure and cannot be baked before operation. For example, this method was used to achieve, for the first time, the macroscopic (34 cm) attenuation light length in 26 kg of krypton using relatively weak calcium getter [188] and purify a high-pressure xenon scintillation drift chamber with nineteen 3-inch diameter windows coated with p-terphenyl wavelength shifter in order to keep the detector operating for a week without degradation of the energy resolution when the circulation is stopped [304]. In these two experiments a custom-made whole-metal diaphragm circulation pump with magnetic actuation was used. Xenon gas recirculation systems are used for continuous purification of the liquid xenon in experiments MEG and XENON.

The most effective and energy consuming method is circulation of the noble liquid. Such an approach is used in the installation of ICARUS-T600, which

keeps purity of 600 tons of LAr at the level of < 0.1 ppb O_2 [399] for a period of several years. The production rate of this circulation system is 2 m^3 LAr per hour in order to restore the operating conditions in less than 1 month, starting from contamination of 10 ppb O_2 equivalent. Active elements of the system is two sets of Oxysorb/Hydrosorb filters in series. Each unit is made of four identical cartridges in parallel and filled 1/3 with molecular sieves 5 A (Hydrosorb) and 2/3 with Oxysorb. A schematic drawing of the recirculation systems is shown in Fig. 8.3. Since the installation ICARUS-T600 includes two similar units, each of them is equipped with the similar recirculation systems with 1/2 rate from that mentioned above.

Two standard LN_2 cryogenic circulation pumps are installed with a nominal maximum speed of 24 m^3 per hour and 0.5 MPa maximum pressure. The circulation pumps are fed in by a small buffer dewar of 0.8 m^3 which in turn is filled by the primary LN_2 storage tanks, two of 20 m^3 each. The pressure in the buffer dewar is regulated to the desired value in order to set the temperature of the circulating LN_2 (89 K for the normal working conditions).

8.4 Monitoring the Working Media

8.4.1 Electron Lifetime

A commonly used technique to determine electron lifetime is to measure the voltage or charge pulse induced by an electron cloud as it drifts under an electric field between two electrodes of an ionization chamber. In the simplest case, when the electrons drift at uniform electric field between electrodes of the parallel plate ionization chamber and the drifting electron cloud is much smaller than the drifting path, the induced electric charge, $Q(t)$, depends on the electron lifetime, τ_e, and the drift time over the between-electrode gap, t_d, as

$$Q(t) = Q_0(\tau_e/t_d)[1 - \exp(-t/\tau_e)] \tag{8.1}$$

where Q_0 is the charge induced in the vicinity of the cathode by ionizing radiation. If the medium is relatively pure, $\tau_e \gg t_d$ and the induced charge will be characterized by the linear rising time

$$Q(t) \approx Q_0(\tau_e/t_d) \tag{8.2}$$

Therefore, the shape of the pulse can be used to estimate the electron lifetime and a fraction of electrons lost due to attachment to electronegative molecules of impurities. Many R&D groups used techniques like this but with different ionization sources. For example, Bolotnikov and Ramsey [33] used cosmic

muons to produce electrons inside a high-pressure xenon parallel plate ionization chamber with a grid. The chamber had a 5 cm drift region between the cathode and the grid, and a 1 cm induction region between the grid and the anode. The optimal magnitude of the electric field strength in the drift region was 10 $\mathrm{V\,cm^{-1}}$. The current signals from the anode were integrated with a charge-sensitive preamplifier and sent to a digital oscilloscope. Typical shapes of the output signals are shown in Fig. 8.5.

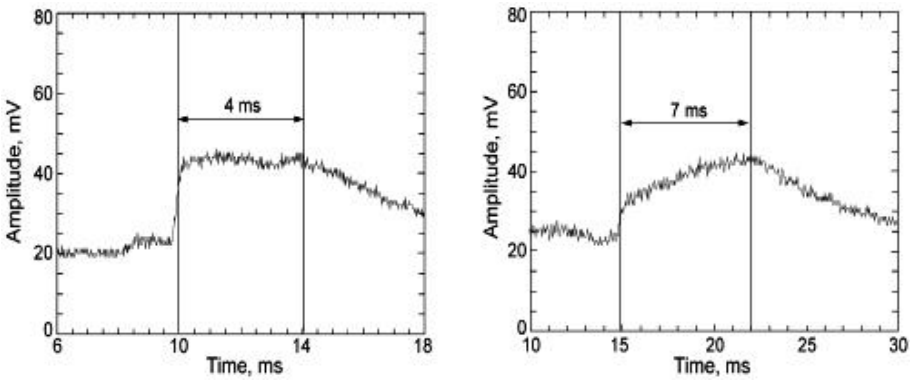

Fig. 8.5 Typical waveforms generated by single cosmic muons in the parallel plate gridded ionization chamber used for electron lifetime measurements by Bolotnikov and Ramsey [33].

A fast-rise part of the pulse is induced by electrons produced between the grid and the anode, while the slow-rise part corresponds to electrons passing through the mesh from the drifting region. The duration of the fast-rise part ($\sim$ 200 μs) is fixed and equal to the drift time between the grid and the anode. The duration of the slow-rise part (0.5–10 ms) depends on the purity of the Xe. The lifetime was measured as the longest duration time of the slow-rise part of the pulse.

The liquid argon purity monitoring system described by Barrelet et al. [423] has been successfully operating at the H1 liquid argon calorimeter operated at the HERA ep-collider since 1992. The design of the purity probes and their location in the calorimeter are shown in Fig. 8.6. The individual probe is a small two-electrode ionization chamber made of aluminum and Teflon. A radioactive source emitting alpha particles (^{241}Am, 7.4 kBq) or the internal conversion electrons (^{207}Bi, 34 kBq) is used to ionize the LAr filling between the electrode gap (2 mm for alpha source and 4–6 mm for beta source). The whole assembly including preamplifier (used by the experiment NA34 at CERN) and a 10 pF glass calibration capacitor is housed in the brass case with holes that allow the liquid argon to circulate through the housing. A purity of the liquid argon was derived from analyses of pulse height spectra recorded with MCA from the probes. The measured electron attenuation length was measured up

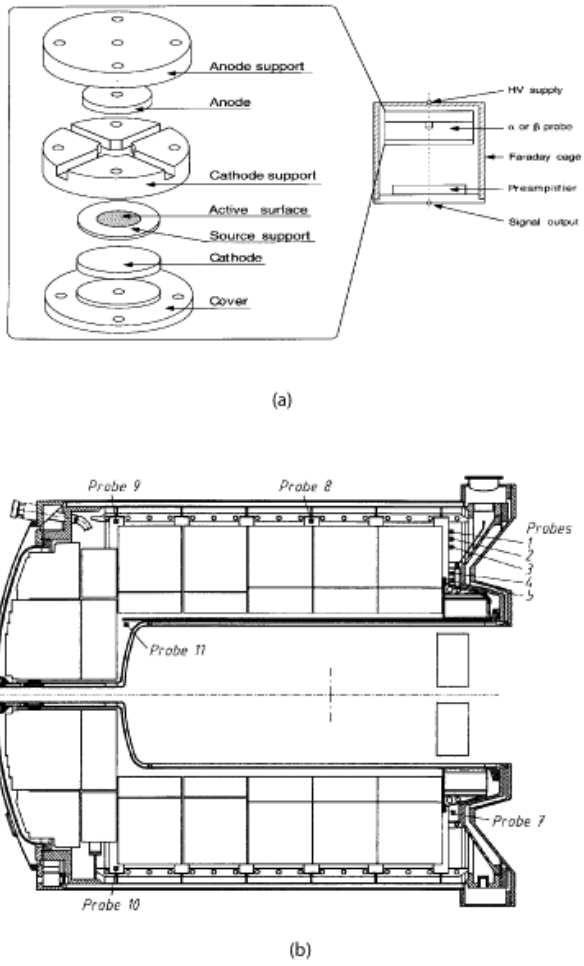

Fig. 8.6 (a) Schematic view of the LAr purity probe and (b) location of the purity probes inside the H1 LAr calorimeter [423].

to 7.5 cm at 15 kV cm^{-1}. The monitoring system allowed for observing air leakages in minutes.

Dmitrenko et al. [91] used an X-ray tube to produce an electron cloud inside a high-pressure Xe ionization chamber with a drift region of 1 cm. An X-ray pulsed source can provide a large ionization signal. However, it is difficult to use in cryogenic liquids and to ionize relatively low-density and low-Z materials such as argon. A cold photocathode was used by Benetti et al. [424] to create electrons inside a liquid Xe ionization chamber with a drift region of 5 cm. Fiber optic cable has been used to deliver light to the photocathode. This approach requires the use of a power pulsed laser to generate a large enough

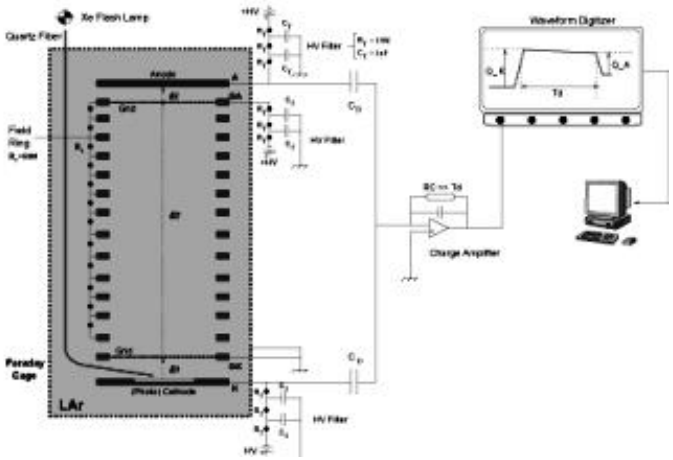

Fig. 8.7 Liquid argon purity monitor used in ICARUS-T600 detector [399].

amount of electrons, due to the fact that a small acceptance angle of the fiber cable dramatically reduces efficiency of the light collection system. It is also possible to employ high-energy cosmic ray particles (muons) to produce an electron cloud inside the chamber triggered by the external scintillation telescope [421]. However, cosmic muons provide very rare events and relatively weak ionization signals that are difficult to measure accurately in a noisy industrial environment.

A dedicated purity monitor was developed by the ICARUS Collaboration (see, for example, Amerio et al. [399] and references therein). The basic element is a double-gridded drift chamber (Fig. 8.7). The electrode system includes the photocathode K, a first grid GK, a second grid GA and the anode A, and 15 coaxial field-shaping rings. The diameter of the electrodes is 80 mm, the drift distance is 160 mm. The grids are electroformed nickel meshes with 1.9-mm pitch, 100 μm thickness, and 89.7% optical transparency. The electric fields of $E_3 > 2E_2 > 2E_1$ are ranged between few tens $\mathrm{V\,cm^{-1}}$ in the first gap and hundreds $\mathrm{V\ cm^{-1}}$ in the others. A quartz optical fiber of 0.94 or 1.55 mm core diameter made of silica are used to deliver light from the source (Xe flash lamp, the emission peak centered at 240 nm or 4.9 eV) to the photocathode coated with Au or semiconductors (GaAs or CZT). Bunches of electrons can be extracted from the cathode via the photoeffect. The electron cloud moves towards the anode crossing a drift region between two parallel electron-transparent grids. The system is designed to compare the charge of the electron cloud before and after passing the drift region and define the electron lifetime according to Eq. (8.2).

A typical waveform of the ionization signal is shown in Fig. 8.8.

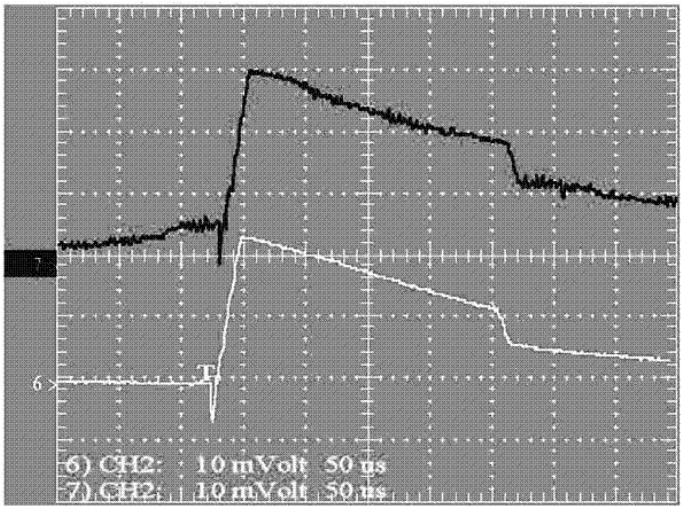

Fig. 8.8 Waveform of signal readout from the liquid argon purity monitor used in ICARUS-T600 detector [399].

8.4.2 Optical Transparency

Transparency of noble liquids to luminescence may be monitored by simple measurement of position of the peak in the scintillation pulse height distribution, for example, from an alpha source. The accuracy of the relative measurements depends on stability of photodetector and the light collection conditions. For example, in the scintillation calorimeter LIDER several alpha sources have been used for monitoring the transparency of liquid krypton; stability of the PMTs was controlled with a single LED illuminating a gang of optical fibers delivering the reference signal to each PMT [190].

The task is more complicated if the attenuation length of the luminescence light needs to be measured. Akimov et al. [190, 224] used a beam of accelerated particles to scan a long liquid cell or two alpha sources placed in the liquid at different distances from the PMT. Comparing the signals from differently located light sources allowed to determine the attenuation length of the liquid. The accuracy of the method depends on correct knowledge of the reflecting properties of the cell, geometry of the light collection, and sometimes the refractive index of the liquid if the two-phase system is involved. The reflectance of the light collection structure can be minimized using a set of diaphragms or special darkened surfaces. For example, Ishida et al. [413] used an Alumilite-coated black aluminum cell to avoid light reflection from the walls. They moved the alpha source placing it at different distances from the window coated with sodium salicylate wavelength shifter and viewed by

a PMT. With this approach, the attenuation length in LXe purified with Ti-Ba hot getter was measured to be $2.9^{+6.3}_{-1.2}$ m, 29±3 cm, and 35±3 cm in different measurements [192, 413].

Solovov et al. [425] used a floating alpha source, which could be kept by a magnet at the bottom of a long vertical chamber or released to occupy a different position in the liquid. A set of diaphragms was used to suppress the reflections. Comparing the responses from a PMT, placed above the liquid, obtained at different liquid levels, the accurate measurement of the attenuation length may be provided. The authors have measured the attenuation length to be 36.4±1.8 cm.

8.4.3
Mass and Position of Free Surface

The very first detectors were built of glass or had large viewports so that the level of the liquid could be easy monitored by the naked eye. With development of modern detector technology, it becomes obvious to use remote controlled devices for measurements of the noble gas mass condensed into closed vessels and position of the free surface of the condensed phase. The latest is important for two-phase emission detectors. In the XENON project, both measurements are used. The mass of xenon stored in high-pressure storage cylinders is measured with OMEGADYNE^{TM} industrial load cells. High-pressure cylinders hooked to a rack are connected to the gas system with flexible helicoid tubing adjusted in such a way that minimizes the force applied in the vertical direction. The level of liquid xenon is measured with cylindrical and parallel plate capacitors. Since the purity issue, capacitors are custom made of stainless steel and Teflon. The cylindrical capacitor vertically installed in two-phase detectors is used to control a filling process. A few parallel plate capacitors are installed in the vicinity of the horizontal plate, where the free surface of LXe should be located. The sensitivity of the measurement allows for controlling the position of the liquid surface with an accuracy of about 0.1 mm. Comparison of readings from three or four capacitors located on the periphery of the field of view allows leveling of the detector installation in such a way that the surface becomes parallel to the planes of gridded electrodes.

8.4.4
Temperature, Pressure, and Density

There is a broad variety of temperature and pressure metering devices commercially available that can be used in noble gas detectors. The preference should be given to those instruments that do not contaminate the detector medium. Among temperature sensors the most popular are platinum resis-

tors and thermocouples. Copper-constantan thermocouples are cheap and easy to make in the lab with spot-welding machines but they require using microvoltmeters. Among pressure sensors the most popular are diaphragm digital transducers. Pressure applied to the pressure transducer produces a deflection of the diaphragm, which introduces strain to the gauges; the strain produces an electrical resistance change proportional to the pressure. This kind of pressure transducer is totally sealed with a stainless steel diaphragm from the detector medium; it is often connected to the detector via VCR fittings.

Density of the condensed phase is well-defined by the temperature. Density of the high-pressure xenon can be defined via measurements of the capacitance between the detector electrodes when the detector is empty and when it is filled using the fact that the dielectric constant of gases depends on density. For example, if the detector is an ionization chamber with screening grid, the pulses from a precision pulse generator may be applied to the mesh and the amplitudes of the induced signals are measured from the anode using a charge-sensitive preamplifier, shaping amplifier, and multichannel analyzer [421].

Measuring the signals when the detector is under vacuum A_0 and when it is filled with the dense gas A, one can obtain the density of the gas. For pressurized xenon, the density is defined by the ratio A/A_0 as shown in Fig. 8.9.

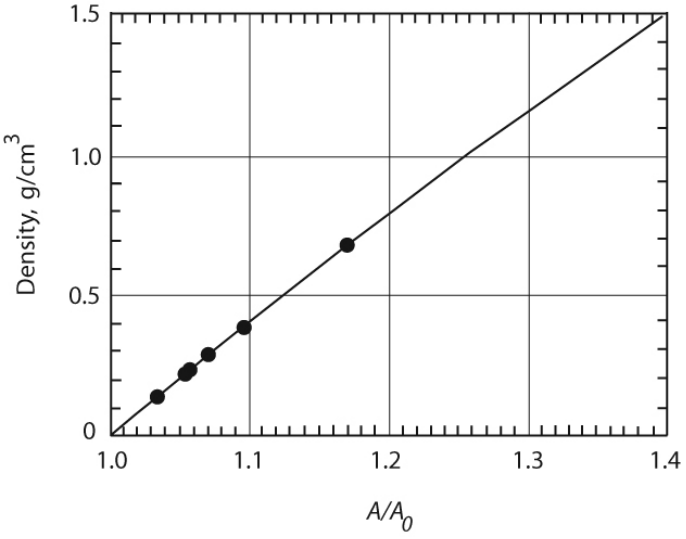

Fig. 8.9 Dependence of the density of pressurized xenon on the ratio of A/A_0. Redrawn from [421].

8.5
UV Light Collection

8.5.1
Reflectors

The best broad band reflectance properties in the extreme UV range have been demonstrated with metal (aluminum, iridium, gold, rhodium, platinum) coatings *enforced* with MgF_2. The reflectance of such mirrors may achieve 90% in the range from 400 nm down to $\sim$ 160 nm. There are many different base materials used for metal reflectors and ranged from optical glasses to polymer films such as Mylar. For example, aluminized Mylar has been used for production of multicell reflecting structures of LKr and LXe scintillation calorimeters [190, 361]. Specially designed multilayer dielectric coatings, consisting of alternating quarter-wavelength layers of high and low refractive index media on high-quality optical substrate, offer up to 99% reflectance for certain wavelengths such as 157 nm and 193 nm in the narrow ($\pm$5 nm) band used in optical systems of excimer lasers. There are commercially available polymer films with multilayer dielectric coating that provides high reflectivity in a broad band of visible range. For example, Vikuiti^{TM} Enhanced Specular Reflector (ESR) is used as a highly efficient light guide or bulb cavity reflector with a reflectivity of 98.5% across the visible spectrum.

The diffuse reflectance of pressed PTFE (polytetrafluoroethylene) powder is very high over the spectral range of 220–2500 nm [426, 427]. The reflectance of PTFE powder is influenced by the density to which the powder is pressed. The highest reflectance in the range 300–1800 nm is achieved at 1.0 g cm^{-3} density and it drops for 2% at density of 2 g cm^{-3}, which is standard for bulk construction Teflon. Similar diffuse reflectance properties have been demonstrated with *Spectralon* by Labsphere. Spectralon is a thermoplastic resin that can be machined in a variety of shapes for the construction of optical components. The material has a hardness roughly equal to that of high-density polyethylene and is thermally stable up to 623 K. The manufacturer states that Spectralon gives the highest diffusive reflectance of any known material or coating over the UV-VIS-NIR region. Space-grade Spectralon is extremely pure and low outgassing.

Optical properties of selected diffuse reflective materials have been studied in the 120–220 nm range by Kadkhoda et al. [428]. They found that Spectralon and PTEF exhibit a high reflectance ($>$ 70% and $>$ 55%, respectively) and Lambertian scatter behavior for the spectral region above 175 nm, but no significant reflectance is observed for these materials below 170 nm. With respect to the stability of its optical properties, PTEF is not recommended for applications below 220 nm. Microroughened SiC ceramic shows a Lambertian scatter behavior for the entire spectral region from 120 nm to 220 nm with

reflectance about 20% above 160 nm. The reflectance factor of SiC can be enhanced with the help of a high reflective thin metal coating. Similar properties are demonstrated by $BaSO_4$.

It is interesting to note that there is data demonstrating that PTFE works as a weak wavelength shifter with excitation band in the range of < 290 nm and emission band in the wavelength range of 310–350 nm [426]. This observation may explain why PTFE reflectors have been successfully used in LXe scintillation detectors equipped with photomultipliers with low quantum efficiency below 180 nm [245].

8.5.2 Wavelength Shifters

There are three advantages using wavelength shifters in large detectors:

1. Light collection reflectors such as PTFE can be enhanced.
2. Less expensive glass window photomultipliers may be used in large arrays.
3. Rayleigh scattering for shifted wavelength is essentially less than that for the original emission light since the attenuation length $\sim \lambda^4$ (see, for example, the recent publication of Seidel et al. [193]).

8.5.2.1 Wavelength Shifters Dissolved in Noble Gases

One of the first wavelength shifters used with noble gas scintillators was a gas admixture of nitrogen. For example, Grün and Schopper [228] used argon in mixture with 2% of nitrogen in their development of a detector for triggering of cloud chambers. The addition of a small amount of nitrogen to noble gases enhances the light emission in the blue range. At earlier studies it was concluded that nitrogen acts as a simple fluorescent converter. However, the nitrogen also acts as the quenching agent: its addition to the noble gas results in decreasing the absolute scintillation efficiency. For example, Northrop and Nobles [13] observed that there is a reduction in the practical light output of a xenon gas scintillator, used with solid wavelength shifter, when nitrogen is added. The efficiency is reduced by about 1/3 by addition of 10% of nitrogen or hydrogen. The latter is often used in high-pressure xenon detectors to increase the drift velocity of electrons. Another undesirable feature of nitrogen is the introduction of a slower component of decay time. For example, the addition of 10^{-4} N_2 introduces in argon scintillator a component with decay time of 0.5 μs, which accounts for 75% of the total photon emission [170]; the decay time reduces with an increase in the concentration of nitrogen, however, this reduces the total light yield. From all these facts, one can conclude

that nitrogen as a wavelength shifting agent has limited application and preference should be given to solid fluorescent converters and/or photodetectors sensitive to UV photons.

8.5.2.2 **Solid Wavelength Shifters**

A number of solid wavelength shifters deposited onto optical elements such as windows and mirrors have been considered including *trans*-stilbene, tetraphenylbutadiene (TPB), sodium salicylate, p-quaterphenyl, diphenylstilbene, and p-terphenyl (see, for example, McKinsey et al. [429] and references therein). The last one was found to be the best one to be used with xenon and xenon-containing gas mixtures from the point of view of high quantum efficiency ($> 90\%$ according to Belogurov et al. [144]), low hydroscopic, chemical inertness, and exclusive radiation hardness. Emission and absorption spectra of p-terphenyl are presented in Fig. 8.10.

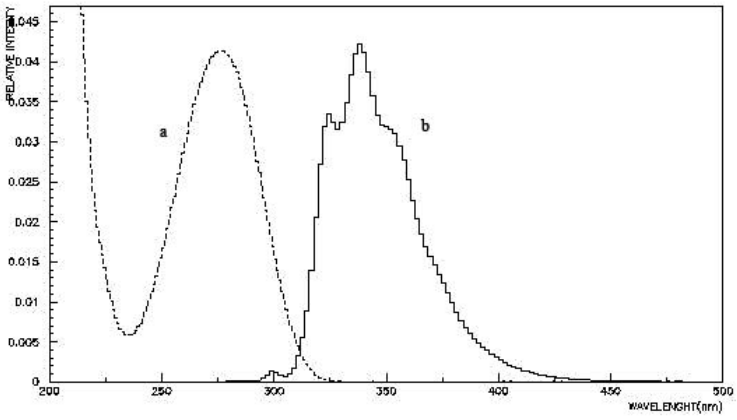

Fig. 8.10 (a) Absorption and (b) emission spectra of p-terphenyl [407].

The p-terphenyl is reported to have a short decay time of 2–5 ns and widely used as a scintillating dye in plastic scintillators. Kumar and Datta [430] compared properties of p-terphenyl (vacuum evaporated) and sodium salicylate (solvent spray deposited) wavelength shifters excited with 253.7 nm light. They demonstrated that quantum efficiency of p-terphenyl is peaked at 0.4–0.5 mg cm^{-2} coating thickness and normally much higher than that of sodium salicylate. Fluorescence efficiencies of evaporated, sprayed, and doped plastic films at incident wavelengths of 58.4 and 74.0 nm were measured by McKinsey et al. [429]. They found that relatively thick evaporated films are nec-

essary for efficient soft UV detection; thinner and less opaque films may be used for detection of XUV radiation. Evaporated films of TPB, PTP, and DPS were found to yield the best efficiencies (Table 8.1). Scintillation efficiencies of doped plastic films are 3 to 5 times less than that of evaporated films. However, the doped plastic films may be a useful alternative to evaporated films since they can be index matches to plastic light guides, avoiding the need for a secondary wave shifter for light guide coupling. Phototubes coated with transparent plastic film doped with p-terphenyl show significant increase in sensitivity to detection of Cherenkov light [431]. Aluminized Mylar reflectors coated with vacuum deposited p-TP have been used in construction of a 45-channel scintillation LXe/LKr electromagnetic calorimeter (see Chapter 4). In order to detect the scintillation light in high-pressure helium scintillators, a two-step wavelength shifting process has been used: (a) the admixture of Xe into the gas and (b) coating of internal surfaces and optical windows with p-terphenyl [171, 234, 235].

Tab. 8.1 Fluorescent efficiency of vacuum evaporated films relatively to sodium salicylate [429].

Wavelength shifter	Emission peak/ /width, nm	Thickness, mg cm^{-2}	Efficiency at 58.4 nm	Efficiency at 74.0 nm
Sodium salicylate	420/80		1.0	1.0
Tetraphenyl butadiene	440	0.2	3.9	3.7
p-terphenyl	335	0.1	3.4	3.0
Diphenyl stilbene	409	0.2	3.4	3.3

8.6 Photosensors

8.6.1 Photomultipliers

8.6.1.1 Low Temperature

Araujo et al. [432] observed no degradation of quantum efficiency (QE) of Hamamatsu R1668 (bialkali photocathode of 1–1/3″-diameter in VUV down to 143 K and even saw an improving of QE by 25–30% when the temperature decreases. However, photomultipliers with large size (2″-diameter) bialkali photocathodes are known to exhibit significant loss of sensitivity at 173 K and below because of the rapidly increasing photocathode resistivity [433]. To reduce this effect, the photocathodes of some recently developed PMTs are provided with metal strips, disposed radially. Using this approach, the Hama-

matsu Photonics Co. developed a 2″-diameter photomultiplier [434], and the Electron Tubes Ltd. developed 2″-diameter D730 PMTs based on the parent model ETL 9829Q [435]. The temperature dependence of the parameters of the D730 PMT is the following: the signal increases by about 35%, while the quantum efficiency at 175 nm increases linearly by 20% from room temperature down to -100 °. Cooling did not affect significantly the timing properties or the dark current.

Fig. 8.11 Picture of 1″-square photomultiplier Hamamatsu R5900-06AL12S-ASSY [260].

Recently, the Hamamatsu Photonics Co. developed a 1″-square R5900-06AL12S-ASSY PMT with metal envelope (Fig. 8.11). The PMT has K-Cs-Sb photocathode, 12 dynodes and demonstrated gain more than 10^6 and quantum efficiency about 25% at 175 nm. A comparison of the properties of some PMTs is shown in Table 8.2. A similar design was used by Hamamatsu for development of PMTs for XENON collaboration, 1″-square R8520-06-Al single-channel PMT with metal envelope based on the parent model of the multianode photomultiplier tube.

Tab. 8.2 Properties of cryogenic UV sensitive photomultipliers produced by Hamamatsu Photonics [259].

	R5900-06AL12S-ASSY	R5900-06MOD
Quantum efficiency in liquid Xe	25%	5%
Gain (HV = 800 V)	10^6	10^5
Number of dynodes	12 stages	10 stages
Material of photocathode	K-Cs-Sb	Rb-Cs-Sb
Size of photocathode		
Material of window		

8.6.1.2 PMTs for High Pressure

Usual glass envelope PMTs are not designed to operate at high environmental pressures and special high-pressure envelopes are used to protect PMTs in such cases. However, as reported by Belogurov et al. [144] some glass PMTs with unpolished entrance windows demonstrate exceptional stability at elevated pressures and have been used in pressurized noble gas detectors (Table 8.3).

8.6.2 Semiconductor Photodiodes

In the past a few experiments using ultraviolet silicon photodiodes [42, 436, 437] and infrared InGaAs photodiodes [438] immersed into noble liquid or gas have been conducted. The silicon photodiodes have demonstrated very high quantum efficiency at 175 nm and a large sensitive area ($\sim$ 70% and $\sim$ 11 cm^2, respectively, as reported by Kashiwagi et al. [437]). However, since the photodiodes are based on direct detection of the photocurrent they are too

Tab. 8.3 Parameters of glass tube photomultipliers with SbCs semitransparent photocathodes (MELZ, Moscow) tested in pressurized noble gases [144].

	$FEU-85$	$FEU-60$
Diam. of photocathode, mm	25	10
Spectral sensitivity , nm	300–600	300–600
Maximum sensitivity, nm	340–440	380–490
Luminous sensitivity, μA lm^{-1}	78	50
Number of stages	11	10
Tube diameter, mm	30	15
Tube length, mm	110	70
Mass, g	50	12
Max. outside press., MPa	0.8	4.5

noisy and too slow in comparison with PMTs. Practically, their applications are limited to spectrometry of relatively intense luminescence such as scintillation produced by heavy ions or alpha particles in LXe. Recently, silicon large area avalanche photodiodes (LAAPD) by Advanced Photonics were successfully used in several noble gas detectors. It was shown that these LAAPD can operate in pressures up to 3.5 MPa ^{3}He [171] and in liquid xenon at temperatures below 173 K without degradation of their performance [242]. Figure 8.12 shows the LAAPD gain as a function of voltage measured at 173 K.

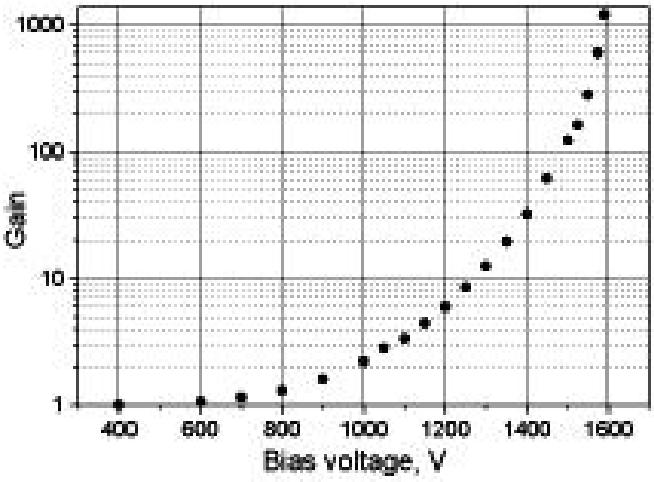

Fig. 8.12 LAAPD gas as a function of bias voltage measured at 173 K [242].

The 10% FWHM energy resolution was demonstrated in LXe with ^{241}Am alpha scintillations; later, Ni et al. [243] measured 6.1% FWHM energy resolution for ^{210}Po alpha scintillations with LAAPD operated at $G = 57$. Solovov et al. [242] have shown, that for gains lower than 10, the resolution is degraded by the preamplifier noise; for gains more than 200, the resolution becomes worse as the excess noise factor increases with gain. However, at higher gains a good time resolution has been demonstrated (0.9 ns FWHM at gain $G = 605$) with a pair of 511 keV gamma rays in coincidence. Note, this result is similar to time resolution reported for such popular solid state scintillators as LSO and YAP. Good performance of LXe scintillators with LAAPD readout results from about 100% quantum efficiency for 178 nm photons. Inherently low radioactivity of LAAPD can be an additional benefit for applications in low-background experiments such as search for cold dark matter in the form of WIMPs.

8.6.3 Open Photocathodes

Due to a high quantum efficiency of CsI open photocathode in the range of 120–200 nm (between 20 and 30% as measured by Rabus et al. [439], the efficient and fast single-photon detection can be achieved in pure noble gases. Recently, Meinschad et al. [440] have shown that a CsI-coated GEM detector can effectively detect scintillation and electroluminescence signals in pure xenon gas at normal conditions. Scintillations generated by 5.9 keV and 22 keV X-rays have been detected with 2 and 10% efficiency, respectively; electroluminescence signals generated at 2.5 $\mathrm{kV\,cm^{-1}}$ field through 5-mm deep drift region have been detected with efficiency of 76%. It was shown that placing a CsI photocathode in noble liquids decreases the electron escape work function and increases quantum efficiency up to 100% [441].

9
Applications

In this chapter we describe the most important applications of noble fluid detectors. Preference is given to those instruments that have already demonstrated their advanced performance and detectors which are being developed to study fundamental science.

9.1
Astronomy

9.1.1
Instrumentation for X-ray Astronomy

9.1.1.1 Gas Imaging Spectrometers On-Board ASCA

Two Gas Imaging Spectrometers (GIS) were built by scientists and engineers of Tokyo University for the X-ray astronomy observatory ASCA. ASCA carries four identical grazing-incidence X-ray telescopes (XRT) each equipped with an imaging spectrometer at its focal plane [414]. The telescope utilizes multinested (119 layers) thin foil conical optics for X-rays in the energy range 0.7–10 keV. The focal plane detectors are two CCD cameras (Solid state Imaging Spectrometer, or SIS) and two gas scintillation imaging proportional counters (Gas Imaging Spectrometer, or GIS). The SIS has superior energy resolution and is sensitive down to 0.5 keV. The GIS is practically insensitive below 1 keV because of its 10-μm beryllium entrance window, but has higher detection efficiency than the SIS above 3 keV.

The ASCA instruments cover the most important energy band for plasma diagnostics. The K-lines and the K-absorption edges from the elements oxygen through iron at various ionization stages lie within this band. Motion of plasma of the order 1000 km s^{-1} can be measured from the Doppler shift of these lines. Spatially resolved spectroscopy with ASCA provides a powerful tool for the investigation of spatially extended plasmas in supernova remnants, galaxies, and clusters of galaxies.

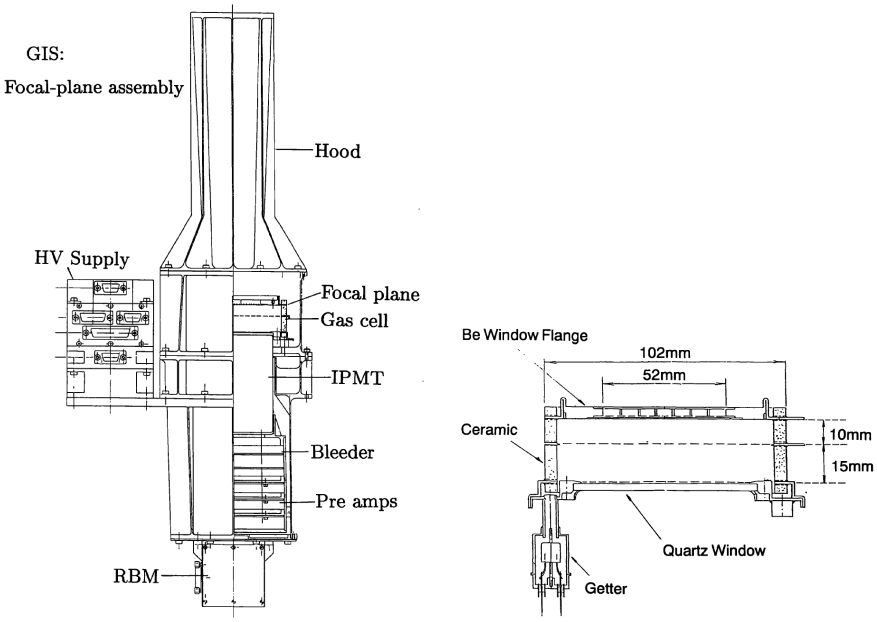

Fig. 9.1 Gas Imaging Spectrometer for ASCA experiment: (a) focal plane assembly and (b) gas cell. Redrawn from [354].

The GIS operates according to the principle of the gas scintillation proportional counter, originally flown on-board the Tenma mission [442]. It has two main components: the gas cell, and the light position sensitive photomultiplier, a Hamamatsu R4268, as shown in Fig. 9.1. The gas is 25 mm deep. It is filled with 96% xenon and 4% helium with a pressure of 0.12 MPa at 273K. The high-energy efficiency is 94% at 7 keV and 67% at 10 keV. The low-energy efficiency is strongly affected by the entrance window. By using a very thin 10 μm beryllium foil an efficiency of 14% at 0.8 keV could still be reached. At 1 and 2 keV the efficiencies are 32% and 80%, respectively. The large window diameter of 52 mm ensures a 50 arcmin diameter field of view. Negative high voltage in the range 6–8 kV is applied to the window. For details we refer to Ref. [354].

The GIS readout consists of two sensors (GIS-S2 and GIS-S3) and an analog/digital electronics unit (GIS-E). Pulse height analysis is provided in the GIS-E unit. At 5.9 keV the energy resolution is 8.0% FWHM. This value scales as the inverse square root of the energy. Additionally the X and Y positions of a detected photon are calculated by a processor in the GIS-E using the outputs from the 32 multiwire anodes (16X and 16Y) of the phototube. The position resolution is about 0.5 mm FWHM at 5.9 keV. The position resolution

also scales as the inverse square root of the energy. Background rejection is performed through hard-wired rise time discrimination (RTD), augmented by spread discrimination (SPD).

The GIS also provides the radiation belt monitor (RBM) function. Compared with the SIS, the GIS has a better hard X-ray efficiency (a factor of 2 at 7 keV), better time resolution, higher signal saturation flux, and a four times wider field of view than the SIS. However, the GIS has a lower soft X-ray efficiency, a somewhat worse position resolution, and a factor of 2–4 poorer energy resolution than the SIS. It has been developed mainly by University of Tokyo, ISAS, and Meisei Electric Co., Ltd.

The ASCA Large Sky Survey covered a continuous area of 7 square degrees around the north galactic pole region. It was used for the identification of 107 sources and the investigation of the origin of the cosmic X-ray background [443].

9.1.1.2 High-Pressure Gas Scintillation Proportional Counter at BeppoSAX

The Italian-Dutch Satellite for X-ray Astronomy SAX (Satellite Astronomia X) was renamed BeppoSAX in honor of the famous Italian physicist Giuseppe Occhialini, who contributed to the discovery of the pion and aided the development of the photoemulsion chamber. BeppoSAX was delivered into a 600-km high orbit by an Atlas Centaurus rocket on April 30, 1996 and operated for six years. This was the first X-ray mission with a scientific payload covering more than three decades of energy, namely from 0.1 to 300 keV. It had a relatively large effective area, medium energy resolution, and imaging capabilities in the range of 0.1–10 keV. Science highlights of BeppoSAX include the first arcminutes localization of gamma ray bursts (GRBs) and first X-ray follow-up observations and monitoring of GRBs, as well as a broad band spectroscopy of different classes of X-ray sources.

The BeppoSAX payload included the High-Pressure Gas Scintillation Proportional Counter (HPGSPC) filled with 0.5 MPa xenon gas. This imaging detector operates in the 4–120 keV energy range with an effective area of 240 cm^2 at 30 keV. The primary scientific goal of the HPGSPC was the investigation of radiative transport in highly magnetic plasmas through observation of cyclotron features in X-ray spectra of celestial sources [347].

The cross section of the sealed cylindrical gas cell, whose cross section is shown in Fig. 9.2. Its construction was carried out by AEG, Ulm, Germany following ultrahigh vacuum standards to avoid deterioration of the gas purity over many years of service. The beryllium window was one of the technically most challenging parts of the instrument. The design had to meet two contradictory requirements: transparency to X-rays down to 3 keV and mechanical stiffness required to withstand the 0.5 MPa differential pressure on a diam-

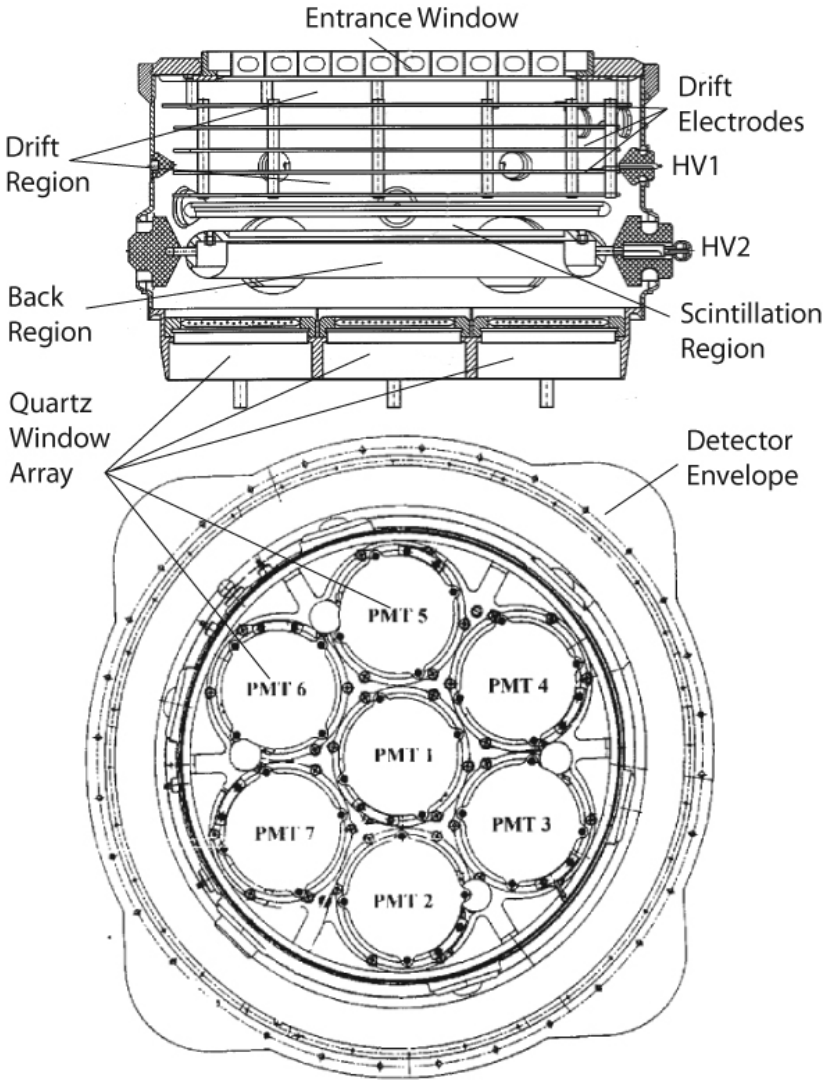

Fig. 9.2 High-Pressure Gas Scintillation Proportional Counter of BeppoSax satellite mission. Redrawn from [347].

eter of 30 cm. The window is made of two beryllium foils, 0.5 and 0.8-mm thick, supported by an egg crate like structure of orthogonal beryllium ribs. The core of the self supporting structure is welded to the titanium body via an aluminum/titanium transition ring aimed at compensating for mechanical stresses generated during the bake-out at 300 °C.

The HPGSPC absorption gap (drift region) of 10 cm and the scintillation gap (scintillation region) of 1 cm are defined by two circular grids with a diame-

ter of 300 mm made of orthogonal titanium wires of 150-μm diameter, spaced by 3 mm. To maintain the uniformity of the electric field in the drift region five field shaping rings placed every 16 mm. The two grids can be biased to a nominal value of 10 kV and 25 kV. In the flight model, however, because of microdischarges localized in one of the high voltage feedthroughs, the reduced field applied in the scintillation region was only 2 kV per cm per atm, which implied a reduction of VUV light production.

At the bottom of the detector seven rugged EMI D319Q photomultipliers in an Anger camera configuration, detect the VUV light produced in the scintillation region. The interface between the PMTs and the pressurized gas cell is formed by a titanium flange, welded to the titanium body, which supports seven *Suprasil 1* quartz windows each 5 mm thick. The 6.3 cm between the scintillation grid and the quartz windows define the so-called back region. On top of the detector a 10-cm high collimator (manufactured by Officine Galileo, Florence, Italy) limits the field of view to $1^\circ \times 1^\circ$ FWHM. The collimator consists of hexagonal cells made of 50-μm thick aluminum plate coated with 10 μm lead. Four highly collimated calibration sources are mounted in the collimator. Each calibration source consists of a mixture of ^{55}Fe and ^{109}Cd radioactive sources, providing calibration lines at 6, 22, 25, and 88 keV. The sources are used for continuous monitoring of the gain and for a real time equalization of the relative gain of the photomultipliers. The equalization is performed by the automatic gain control (AGC) chain. To reduce the residual background, the detector unit is shielded with 1 mm of lead and 2 mm of tin around the sides and bottom.

The seven signals from the PMTs are preamplified, shaped and then transmitted to the electronic unit (EU). In the EU, the PMT signals are processed by gated integrators, digitized, and formatted for transmission to the on-board data handling (OBDH) bus. In addition, housekeeping signals for high voltage and temperature monitoring are converted and formatted, together with other digital housekeeping data for transmission to the OBDH. The pulse duration of analog sum of the seven PMTs signals, each integrated with 8 μs is also measured by the burst length chain. This device measures the time interval between 20% and 80% of the integrated sum signal. Information on burst length is used to discriminate genuine X-rays against background events or anomalous events, e.g., events absorbed in the scintillation region and/or back region.

9.1.1.3 High-Pressure Gas Scintillation Proportional Counter On-Board HERO

The balloon-borne hard X-ray telescope HERO (High-Energy Replicated Optics) was designed for imaging in the hard X-ray region. HERO will achieve millicrab-level sensitivity in a typical 3 hour balloon flight and 50 μcrab sensi-

tivity on ultralong flights. A recent *proof-of-concept* flight with a small number of mirror shells captured the first focused hard X-ray images of galactic X-ray sources [444]. The HERO hard X-ray optics includes 16 full-shell electroformed nickel-replicated mirrors coated with iridium to enhance reflectivity. The mirrors are mounted on a carbon-fiber optical bench 6 m above a focal plane detector. The use of high-resolution X-ray mirrors places stringent requirements on the imaging detectors used in the focal plane. The detectors must have good response over the mirror's operational energy band (from 15 keV set by the atmospheric attenuation to 75 keV cutoff energy for iridium-coated mirrors), good spatial resolution to accurately resolve the mirror's focal spot, good energy resolution to resolve features in a sources spectrum. The current focal plane detector for the HERO payload is a high-pressure gas scintillation proportional counter (HPGSPC) with sensitive area of approximately 20 cm^2. A schematic drawing of the detector is shown in Fig. 9.3.

It is a scintillation drift chamber similar to two-dimensional electroluminescence imaging devices described in Chapter 6. It uses a 96%Xe+4%He gas mixture at a total pressure of 1 MPa [445]. A collimation tube, used to prevent a detection of atmospheric gamma rays, is followed by a low-pressure beryllium window installed to seal off a main beryllium window by ceramic and the space between the windows filled with 1 MPa of air. The stainless steel chamber is equipped with two windows: a 3.2-mm thick main beryllium window for incoming X-rays and a 9-mm thick fused quartz window through which the scintillation light exits. The depth of the absorption and drift region is 55 mm. A 4-mm light-emitting region is formed from a pair of nickel grids. The lower grid is 4 mm above the UV transmitting exit window brazed into a stainless frame. Bias voltage is split so that such a negative voltage is applied to the entrance beryllium window, the upper grid is grounded and the lower grid is run at positive high voltage. The performance of the detector is summarized in Table 9.2.

The use of only stainless steel and ceramic materials and an electrically activated SAES getter ensures that the detector will operate stably for long periods. The current units have been operated for over a year without degradation of the performance. The readout system is based on 16×16 position-sensitive Hamamatsu H2486 imaging PMTs. In order to reduce the number of readout channels, however, successive groups of four PMT anodes were ganged together. The output signals from the PMT are digitized by an analog-digital converter (ADC) over a 20 μs interval at sample rate of 5 MHz. The data obtained from the ADC are stored in the flight data recorder. A portion of the data are sent to the ground, at a 600 kb rate, and used to monitor the health of the detectors during flight.

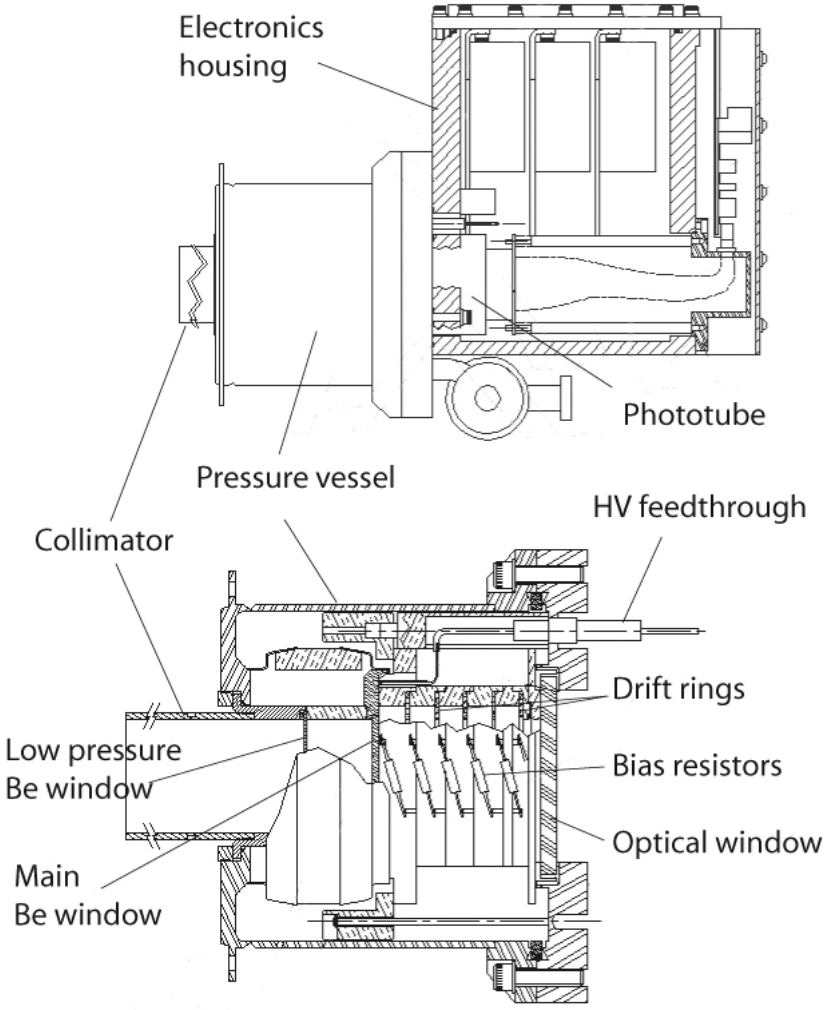

Fig. 9.3 Overall view (top) of HPGSPC focal plane detector of HERO X-ray telescope and cross section of the high-pressure vessel (bottom). Redrawn from [445].

9.1.2 Instrumentation for Gamma Ray Astronomy

9.1.2.1 KSENIA On-Board MIR Orbital Station

A high-pressure xenon parallel plate ionization chamber KSENIA (Fig. 5.12) was designed for measurements of cosmic gamma ray lines in the range 0.1–8.0 MeV. The chamber volume was 3×10^3 cm^3, out of which, about 10^3 cm^3 is active. The chamber was filled with 0.6 g cm^{-3} of xenon (5.5 MPa at 296 K)

mixed with 0.26% hydrogen to increase the electron drift velocity. The sensitive area is 100 cm^2. The noise-subtracted energy resolution was 1.3% FWHM at 1 MeV [277]. The observed FWHM energy resolution was 3.5±0.25% at 662 keV and 2.0±0.2% at 1 MeV [446]. A disadvantage of this detector was the relatively low detection efficiency of 4.5±0.2% at 662 keV and 1.5±0.1% at 1.33 MeV.

In 1990, Ksenia was installed on-board the orbital space station MIR, in a practically circular orbit with a height of 350–400 km and $\sim 51^\circ$ inclination. The high-pressure xenon gamma spectrometer was enclosed in a compartment with 2-mm thick aluminum walls. The influence of proton and neutron space radiation fluxes on the spectrometric characteristics performance of the high pressure xenon gamma spectrometer was studied over the six year period on-board MIR. The gamma spectrometer was exposed to an albedo neutron flux of about 1 neutron cm^{-2} s^{-1}, for a total of 2×10^{10} neutrons over six years.

Twice a day the MIR station crossed the radiation belt of the Earth over the region of the Brazilian anomaly. Each crossing lasted 10–15 minutes. The total number of protons with $E_p > 30$ MeV and electrons with $E_p > 30$ MeV through the detector over six years was about 5×10^9. The 511 keV annihilation line was observed during each passage of MIR over the South Atlantic anomaly (SAA). This line occurs due to interaction of space radiation with the massive (100 ton) metal body of the MIR station.

The results show that the energy resolution and the position of the 511 keV line were practically unchanged during the six year period, a testimony to the radiation hardness of xenon [446].

9.1.2.2 LXeGRIT Balloon-Borne Compton Telescope

Observation of gamma rays in the MeV energy band has a great scientific potential for astrophysics since emission in this range witnesses nucleosynthesis processes, supernova explosion mechanisms, star formation, distribution of massive stars, and the physics of accreting black holes. Imaging of cosmic gamma rays in this range cannot be done by focusing optics. The Compton scattering is the dominant interaction of photons with matter in this energy band, providing a direct determination of the photon incoming direction through the observation of consecutive scatterings in two separate, massive and position sensitive detectors (double scatter Compton telescope). Compton imaging of cosmic sources is complicated by the atmosphere's opaqueness to MeV gamma rays, which requires deployment of instruments on high-altitude balloon-borne platforms or satellites, where intense radiation fields generate high background levels [289, 447].

The Liquid Xenon gamma ray Imaging Telescope (LXeGRIT) is a balloon-borne experiment which uses a liquid xenon time projection chamber (LX-

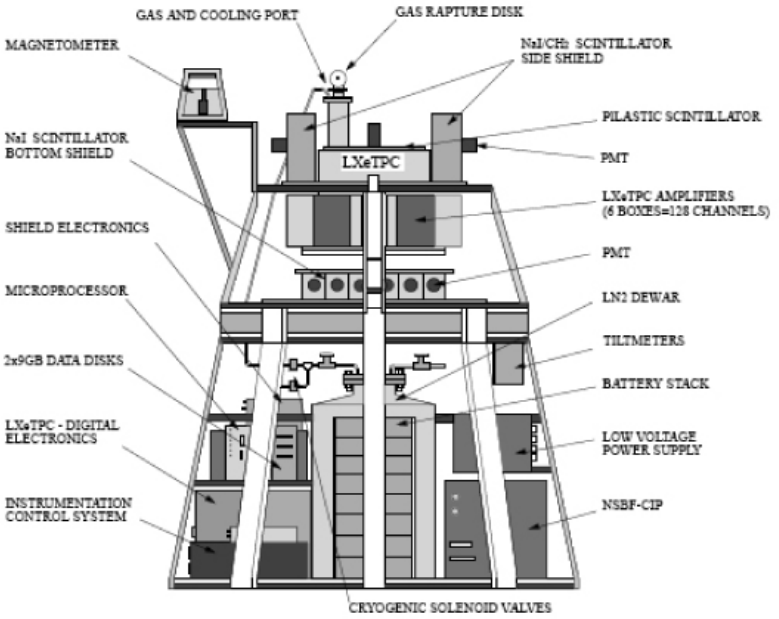

Fig. 9.4 Schematic drawing of LXeGRIT payload in 1999 flight configuration [448].

eTPC) to image gamma ray emission from cosmic sources in the 0.15–10 MeV energy band (Table 9.1). The detector is the original prototype developed by Columbia University in collaboration with Waseda University to demonstrate gamma ray spectroscopy and imaging in a homogeneous, 3*D* position-sensitive LXeTPC with combined charge and light readout. To verify the application of this technology in space, the TPC was turned into a balloon-borne instrument, and tested in three flight campaigns, from the Northern Hemisphere. Following the first engineering flight, of short duration, in 1997, LXeGRIT was successfully operated as gamma ray telescope on two longer duration flights in 1999 and 2000, at an average altitude of 40 km. A schematic of the LXeGRIT payload in 1999 flight is shown in Fig. 9.4.

During this flight, the LXeTPC was heavily shielded on the bottom and the sides by scintillators. The performance of the detector during this flight is reported in [449]. For the 2000 flight, the shield was removed and the data acquisition system upgraded, to handle 300 triggers per second out of a total of about 600 Hz, including charged particles [450]. A total of about 36 hours of data, were accumulated during this flight. Single-site events from the dominating low-energy gamma ray background and charged particles were mostly rejected on-line at the first and second trigger level. The remaining

count rate of single-site gamma ray events, at an average atmospheric depth of 3.2 g cm^{-2}, is consistent with that expected from atmospheric and diffuse gamma ray background [451]. Table 9.1 lists the LXeGRIT characteristics during the 2000 flight campaign.

The TPC has worked well during both flights, validating the first time application of a TPC for MeV gamma rays detection in near space conditions. The background rate measured in flight is consistent with that expected from the dominant flux of atmospheric gamma rays, confirming the radiation hardness of Xe as detector material [452]. Imaging of MeV emission from the strongest source in the sky, the Crab Nebula/Pulsar, in the 1 steradian field of view of LXeGRIT for 6 hours during the 2000 flight, has been carried out, using Compton reconstruction of events with two and three interactions in the liquid.

A simplified mechanical drawing of the LXeGRIT detector and its vacuum cryostat and a picture of the internal TPC structure are shown in Fig. 5.25. The liquid ionization chamber is triggered with the primary scintillation light. The sensitive area is 19×19 cm^2 and the drift region in the liquid is 7 cm.

The sensing electrodes consist of two arrays of orthogonal $X-$ and $Y-$ wires in each direction with a 3-mm pitch and 3-mm distance between electrode planes. The ionization electron clouds produced by gamma ray interactions in liquid xenon, drift in an electric field of 1 kV cm^{-1}. After passing the grid, the drifting charges induce signals on the wires, providing the two-dimensional localization of the interactions. The depth of the interaction (Z-coordinate) is inferred from the drift time measurement triggered with the primary scintillation. The light is detected by four UV sensitive 2″-diameter photomultipliers EMI 9813, viewing the liquid xenon vessel through quartz windows [451]. The energy deposited in each interaction is measured from the collected charge

Tab. 9.1 LXeGRIT payload characteristics [448].

Energy range	0.2–20 MeV
Energy resolution (FWHM)	$8.8\% \times (1\ \text{MeV}\ E^{-1})^{1/2}$
Position resolution (1σ)	1 mm (3 dimensions)
Angular resolution (1σ)	3° at 1.8 MeV
Field of view (FWHM)	1 sr
Effective area (Imaging)	16 cm^2 at 1 MeV
LXeTPC active volume	20 cm × 20 cm × 7 cm
Active back shield	2730 cm^2, 10-cm thick NaI(Tl)
Active side shield	4750 cm^2, 10-cm thick NaI(Tl)&CH_2
Active top shield	1600 cm^2, 1.2-cm thick plastic
LN_2 dewar	0.1 m^3
Instrument mass, power	1100 kg, 450 W
Telemetry, on-board storage	2 × 500 kbps, 2 × 9 GB

signals on the four anodes. The induction and collection signals are digitized by flash analog-to-digital converters with a 5 MHz sampling rate and a resolution of 8 bits for X and Y, and 10 bits for the anodes [453]. The detector vessel contains 8 L of high-purity liquid xenon.

As follow-up to LXeGRIT, the LXeTPC technology was proposed for a larger, more sensitive, Compton telescope instrument (XENA) on an ultralong duration balloon-borne mission. Many important scientific observations in fields such as hard X-ray/gamma ray and infrared astronomy, cosmic rays and atmospheric studies have been made from balloons. XENA was designed to image about 50% of the gamma ray sky within a 2 weeks flight from the Southern Hemisphere. The telescope, optimized for the energy range 0.3–10 MeV, combined high efficiency within a 3 sr field of view with about 1° angular resolution and excellent background reduction capability. The XENA mission had as primary scientific goal the discovery and mapping of ^{60}Fe radioactivity from the Galaxy, which is pivotal for understanding nucleosynthesis. XENA's sensitivity for the 1.8 MeV line from ^{26}Al was estimated at 6×10^{-6} cm^{-2}s^{-1}, a significant improvement over previous missions. The telescope consisted of two large area (2500 cm^2) Liquid Xenon Time Projection Chambers (LXeTPCs) at a distance of 10 cm. Each detector layer is made up of four modules, of 25×25 cm^2 in area. For efficient detection of the primary scintillation light, the sensitive LXe volume of each module is viewed by compact VUV sensitive PMTs from the side. The upper LXeTPC is 3 cm thick. Its role is to Compton scatter the incoming gamma ray only once and to accurately measure the energy of the Compton electron and its location with millimeter precision. The energy of the scattered gamma ray is deposited in the lower LXeTPC, through a photoabsorption, one or multiple Compton scatterings and/or pair production. The thickness of the lower TPC is 20 cm of LXe, divided in four TPC layers with 5 cm drift gap each. This provides high stopping power for gamma rays well above 10 MeV while the size of the drift gap and therefore the required voltages and maximum drift times remain practical. The coordinates and energy depositions of all interactions taking place in the lower TPC are measured with the same accuracy as in the upper TPC. The millimeter position accuracy together with the modest separation between the detectors provides a high angular resolution but also conserve a good detection efficiency.

Tab. 9.2 Characteristics of noble gas detectors used in X-ray and gamma ray astronomy.

Apparatus/ Mission: years	Working medium dimensions, cm	Sensor	Energy range, MeV	Energy resolution, % FWHM (E, keV)	Position resolution, mmFWHM (E, keV)	Efficiency, % (E, keV)	Ref.
KSENIA/ MIR: 1990–1996	0.6 g cm^{-3} Xe+0.26%He	Ioniz. chamb.	0.1–8.0	3.5(662) 2.0(1000)	2(1000) 3.5(662)	1.5(1000) 4.5(662)	[277]
GIS/ ASCA	0.12 MPa Xe+4%He Ø 5×1	32 ch maPMT	0.0007–0.010	7.63(5.9)	0.5(5.9)		[354]
HPGSPC/ BeppoSAX	0.5 MPa Xe+10%He Ø 24×10	7 PMTs array	0.004–0.12	8.3(30) 5.2FGM(30) 3.3(60) 2.4FGM(60)			[347]
HPIGSPC/ HERO	1 MPa Xe+4%He 4.5×4.5×5.5	32 ch maPMT		5.2(32) 3.8(60)	0.5 (30–50)	99(40) 73(70)	[348]
LXeGRIT: 1999–2000	LXe	Ioniz. chamb.	0.15–10	8(662)	2.5(662)	20(662)	[450]

Note: PMT - photomultiplier; maPMT - multianode PMT; MWPC - multiwire proportional chamber; FGM - fluorescence gated mode; GIS - Gas Imaging Spectrometer; HPGSPC - High Pressure Gas Scintillation Proportional Counter.

9.2
Low-Background Experiments

As new physics can be learned at charged particle accelerators with high collision energies, new phenomena in elementary particle physics can also be learned in low-background installations with experiments highly sensitive to rare events such as neutrino interactions, scattering of dark matter particles, and double beta decay. Recently, underground high-energy neutrino detectors of the Super-Kamiokande, SNO, and KamLAND have proved that neutrinos have mass. This became the first substantial change in the standard model of particle physics in the last 20 years [454]. In addition, new highly sensitive dark matter detectors CDMS, EDELWEISS, and ZEPLIN have driven down the limits on cold dark matter scattering cross sections. There are a few more new experiments proposed recently and some of them are based on properties of noble gas detectors, which is the subject in this chapter.

9.2.1
Direct Detection of Particle Dark Matter

One of the fundamental problems in astrophysics is the missing mass (dark matter) in the Universe. This dark matter indicates its presence only via gravitational forces [455]. The nature and quantity of the dark matter in the Universe remain unknown, providing a central problem for astronomy and cosmology since more than two decades. One popular explanation of the invisible mass is that it consists of weakly-interacting massive particles (WIMPs) predicted in the super symmetry model. One of the earliest ideas was to use a massive ($\sim$ 100 kg) saturated hydrocarbon liquid as working media of a light emission detector for detection of WIMPs with mass around 1 GeV c^{-2} [456]. Recent experimental bounds from the CERN e^+e^--collider LEP give a lower limit for the WIMP mass of 46 GeV c^{-2} (see, for example, Ref. [263], and references therein). The modern technology of purification of noble gases provides more than 1 m drift length of quasifree electrons and $\sim$1 m attenuation length for scintillation photons in condensed xenon. It means that detectors with working mass in the tons range could be constructed. That makes liquid/gas xenon emission detectors to be considered the most promising candidates for the next generation of WIMP search experiments.

The XENON collaboration is developing a liquid xenon emission detector for dark matter detection. Using a xenon mass of 1 ton (about 70 cm linear size of the sensitive volume), such a detector can reach a sensitivity of 10^{-46} cm^2 for spin-independent cross sections, which is several orders of magnitude below the current limit of 1.6×10^{-43} cm^2 [457].

A prototype module, XENON10, contains an active xenon target of 15 kg. The active volume is delineated by a Teflon cylinder with 20-cm inside diam-

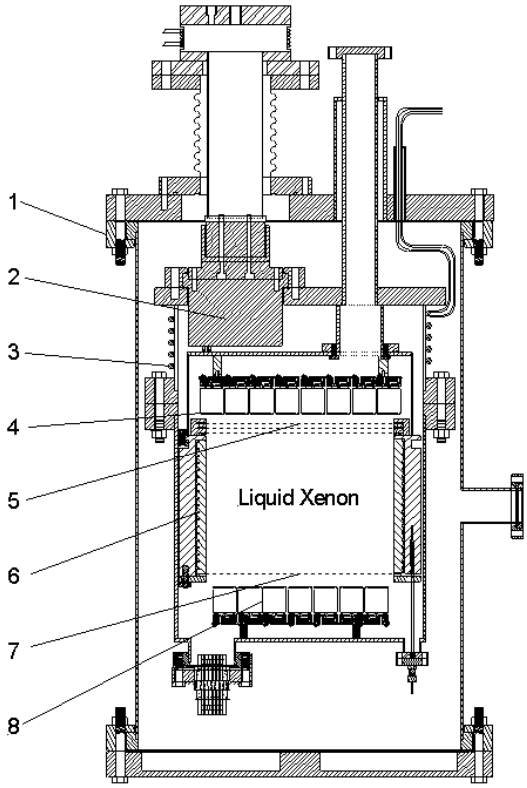

Fig. 9.5 XENON10 liquid xenon two-phase TPC for WIMP search experiment: 1 - vacuum vessel; 2 - pulse tube refrigerator; 3 - cooling coil; 4 - top array of 48 photomultipliers; 5 - grids; 6 - drift field shaping rings and Teflon reflector; 7 - cathode mesh; 8 - bottom array of 41 photomultipliers [457].

eter and 15-cm height (Fig. 9.5). A mesh on the bottom of the cylinder serves as cathode. A set of 3 meshes defines the electric fields for extraction of the drifting electrons from the liquid into the gas phase, and to accelerate the free electrons to produce proportional scintillation. An array of 41 PMTs immersed in the liquid below the cathode mesh mostly observes the prompt direct scintillation light. A second array of 48 PMTs above the top grids observes the proportional light, and also provides position resolution. The PMTs are 1″ square metal channel photomultipliers Hamamatsu R8520-AL. These PMTs are designed to withstand the low temperature (173K) and the operating pressure ($<$0.35 MPa) of the liquid xenon detector. They are optimized in sensi-

tivity for the wavelength of xenon scintillation light (178 nm). The detector is enclosed in the cryostat, which is 41 cm in diameter and 65 cm high.

The elastic scattering of a WIMP within liquid xenon results in a low-energy Xe recoil. The moving recoil produces both ionization electrons and fast UV scintillation photons from the deexcitation to the ground state of excited diatomic Xe molecules (Xe_2). Under a high electric field, the nuclear recoil will yield a very small charge signal and a much larger light signal, compared to the electron recoil of the same energy. The distinct charge/light ratio is the basis for nuclear recoil discrimination in a LXe detector. To detect the small charge signals, the process of electroluminescence is used. The free ionization electrons are extracted from the liquid to the gas phase where in a strong electric field they induce proportional scintillation light. The number of photons generated by one drifting electron is sufficient to be detected by PMTs.

In addition to the background discrimination based on the different ratio of ionization and scintillation, the 3D-position sensitivity of the XENON TPC offers another powerful method for rejecting surface background events. The background will be further suppressed by a passive gamma and neutron shield surrounding the detector from all sides.

The XMASS experiment is a multipurpose low-background search based on a large volume of liquid xenon scintillator [422]. The science goals are solar neutrinos and WIMP dark matter detection, as well as detection of ^{136}Xe neutrino-less double beta decay. The experiment has three stages in the scale up of the detector. A 100-kg detector with PMTs coupled to the LXe scintillator via quartz window, has been built and is operating underground, at Kamioka Laboratory, in Japan. Much effort is being placed in the development of PMTs with low radioactive content. XMASS has also demonstrated the effective reduction of radioactive ^{85}Kr in the liquid xenon to a level of 3 ppt, using a gas distillation column [458]. The 100 kg XMASS prototype is a cube with 31 cm side, made of copper. Each side is viewed by 9 PMTs (Hamamatsu R8778) via quartz windows and light guides. The detector is enclosed in a passive gamma and neutron shield of $\sim$ 2 m outer dimension. Two recently obtained important results from the experiment with the 100 kg detector are a demonstration of expected performance of self-shielding and the fact that a purification system utilizing distillation allowed to reduce krypton contamination of liquid xenon by a factor of a thousand [458].

The next step is an 800-kg detector, to be followed by a 10-ton fiducial mass detector, with a large number of PMTs directly immersed in the liquid. In its final 10-ton configuration, XMASS expectation is 3.3×10^{26} y half-life sensitivity for $0\nu\beta\beta$ (^{136}Xe) decay, 30 dark matter events per day; 10 pp-neutrino and 5 ^{7}Be-neutrino per day. XMASS II is an alternative liquid xenon emission detector. A 1-kg detector (see Section 7.4, Fig. 7.10a) was tested recently. The second version of the detector containing 15-kg Xe and using 14 PMTs will start dark matter search in the Kamioka mine beginning in the middle of 2006.

The UK Dark Matter Collaboration in cooperation with US, EU and Russian collaborators is developing a series of detectors based on liquid xenon [389]. The first, ZEPLIN I, has a fiducial mass of 3.1 kg and is based on LXe scintillation only.

The target mass is housed in a copper vessel of specific shape and lined with Teflon reflector, for maximum light collection. The LXe is coupled via quartz windows to three PMTs (EMI9265QA) through optically isolated "turrets" of liquid xenon, which act both as light guides and passive shielding for the gamma background from the PMTs. A 1 ton liquid scintillator and an outer passive lead shield enclose this small LXe target.

The second generation of detectors use simultaneous detection of ionization and scintillation, in a similar fashion as the XENON experiment. ZEPLIN II (30 kg LXe) and ZEPLIN III (6 kg LXe) are currently being operated underground, at the Boulby Laboratory, in England, and above ground, respectively.

Figure 9.6 shows a schematic drawing of the ZEPLIN II detector. A target mass of 30 kg is viewed by an array of 7 PMTs. A Compton veto system will be also provided as for ZEPLIN I. The ZEPLIN III detector will operate with elevated up to 8 kV cm^{-1} electric field in the liquid in order to record a small ionization signals from the nuclear recoils as well as from the electron background. The active volume comprises a cylinder of 3.5 cm height and 40-cm diameter and viewed by 31 PMTs. The PMTs record both scintillation and electroluminescence signals. As expected, the improved light collection will allow to reduce the detection threshold compared to that predicted for ZEPLIN II.

The WARP (WIMP Argon Programme) experiment aims to the detection of WIMP elastic scattering interactions occurring in a target of liquid Argon [460]. The simultaneous detection of the prompt scintillation light in liquid argon and of the delayed signals coming form the extraction of ionization electrons in the gas phase provides a clean identification of recoil events in the range 10–100 keV. The WARP experiment has been conceived profiting from the experience achieved by the ICARUS collaboration (see, for example, [399]) in the use of large amounts of liquid argon. The rejection of the background will be based on two techniques: analyzing ratio of scintillation (S1) and ionization (S2) signals and analyzing the rise time of the primary scintillation signal. The first technique is similar to that used in XENON, ZEPLIN II and III. The second one is based on the fact that the argon scintillation light is mainly produced by the deexcitation of the Ar_2 dimer singlet and triplet excited states (See Chapter 3 for details). The two states have very different lifetimes (7 ns and 1.8 μs) and are populated in a different way by recoil-induced and electron-induced interactions. The two selection criteria are largely uncorrelated and a total background rejection factor of 10^7 is expected for the WARP experiment.

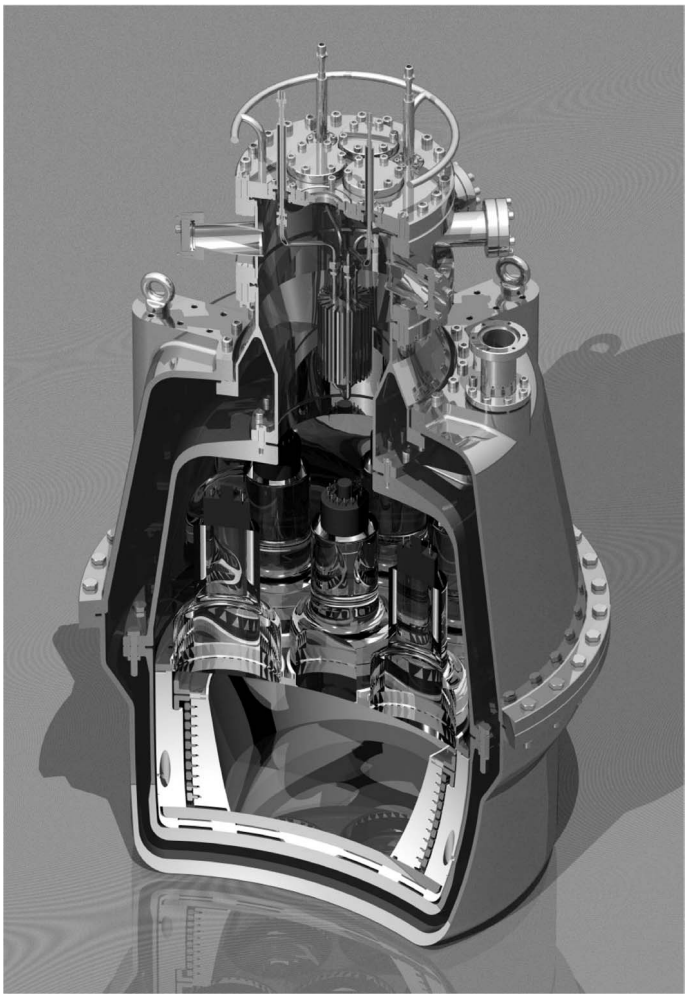

Fig. 9.6 Cut-away view of the ZEPLIN II detector [459].

The 100-L detector is currently under construction at the Gran Sasso Laboratory, to achieve a sensitivity of a few 10^{-8} pbarn. An array of 61 2″-diameter PMTs are used in the gas phase to record both primary and secondary scintillation. The detector is surrounded with an active shield of about 200 kg of LAr. A total of 436 3″-diameter PMTs will be installed to read scintillation light from the active LAr shield. Externally to the active shield there is a passive shield composed of layers of polyethylene, lead, and OHFC copper. The overall external dimensions of the shield are $7\times7\times6.9$ m^3 and its total weight is about 200 tons.

In the same underground site a 2.3-L prototype (10-cm radius, 7.5-cm drift distance) has been operated for one year collecting more than 5×10^6 events.

Two different setups have been tested: in the first setup seven 2″-diameter photomultipliers have been used while in the second four 3″-diameter photomultipliers were arranged on the top of the gas phase. In both cases a light yield of 1.0 photoelectron per keV was obtained. The background activity associated with cosmic rays and the beta decay of ^{39}Ar isotope was analyzed. A total amount of 3.3 events per second induced by ^{39}Ar beta decay is expected in the WARP 100 L detector in the energy range 30–100 keV. With the rejection factor 10^7, this background will be reduced to a level of <1 event per 100 days.

Characteristics of the noble liquid WIMP detectors are compared in Table 9.3.

9.2.2 Neutrino Detectors

One of the fundamental but never measured parameters of neutrino is a magnetic moment. The magnetic moment may help to explain the solar neutrino deficit and the anticorrelation of the measured neutrino flux with solar magnetic activity. Presence of the magnetic momentum can essentially influence calculations of neutrino interactions in nuclear reactors, stars and affect many theoretic predictions in evolution of the Universe. The lowest limits on the neutrino magnetic moments come from both solar neutrino experiments and reactor experiments. Data from Super-Kamiokande experiment set the tightest limit to date $\mu_\nu < 1.5\times10^{-10}\mu_B$ at 90%CL that is comparable to the best reactor limits [461]. Since 1992 a liquid xenon detector has been considered to probe antineutrino/electron scattering cross sections in the range of < 100 keV deposited energy where a neutrino magnetic moment of $10^{-12}\mu_B$ may exceed the electroweak cross section of additional magnetic dipole-dipole scattering [462].

LXe emission detector for neutrino magnetic momentum measurement was constructed at ITEP (Moscow) in 1994 to 1998. The detector was designed as emission camera with seven 2″-diameter photomultiplier array placed in the gas phase above the liquid xenon. The array is viewing $\sim$ 1-cm gap between two grids. The top (anode) grid is placed in the gas phase, the bottom one is placed just below the liquid surface. The electrode system includes the anode and the bottom grid, drift ring electrodes, and thin aluminum cathode placed in the liquid. The liquid is contained in the 30-L vessel made of low-background titanium alloy.

A schematic drawing of the detector and a photograph of the electrode structure during installation inside the vessel are shown in Fig. 9.7. For purification of xenon a large (0.1 m^3) spark purification system was developed.

Another never observed prediction of the standard model is the coherent neutrino-nucleus scattering, which cross section depends on the nucleus num-

Tab. 9.3 Parameters of the energy balance equation for condensed heavy noble gases [23].

Experiment/ Detector start of operation	Working medium: tot. mass/ volume	Location: underground laboratory, depth	Sensitivity, pbarn	Background rejection factor	Ref.
XENON	LXe: Two phase	Gran Sasso (Italy),			[457]
XENON10: March 2006	15 kg	3800 m.w.e		10^2	
XENON100	100 kg				
XENON1000	1000 kg		10^{-10}		
XMASS	LXe Single phase	Kamioka Mine (Japan),			[422]
	100 kg	2700 m.w.e			
	800 kg (100 kg fiduc.)		10^{-8}		
	27t(10t fiduc.)				
XMASS II 2006	14 kg			10^2	[265]
ZEPLIN:	LXe Single phase	Boulby Mine (UK),			[389]
ZEPLIN I	3.1 kg	2800 m.w.e			
			10^{-6}	10	
	Two phase				
ZEPLIN II	30 kg		10^{-7}	10^2	
ZEPLIN III	6 kg		10^{-7}	10^3	
ZEPLIN MAX	1000 kg		10^{-9}		
WARP	LAr:	Gran Sasso (Italy),			[460]
2006	100 L	3800 m.w.e	10^{-8}	10^7	

Notes: Sensitivity is defined as a top limit for a cross section of WIMP-nucleon spin-independent interaction after 1 year of operation; m.w.e. - meters water equivalent (depth of underground location).

ber N, and the neutrino energy E_ν [463], as

$$\sigma \sim 0.4 \times 10^{-44} N^2 (E_\nu/\mathrm{MeV})^2 \; cm^2$$

This formula is valid for neutrino energies up to about 50 MeV, and thus applies to reactor, solar, and supernova neutrinos. The magnification factor N^2 gives a significant count rate from nuclear reactors and natural sources in rel-

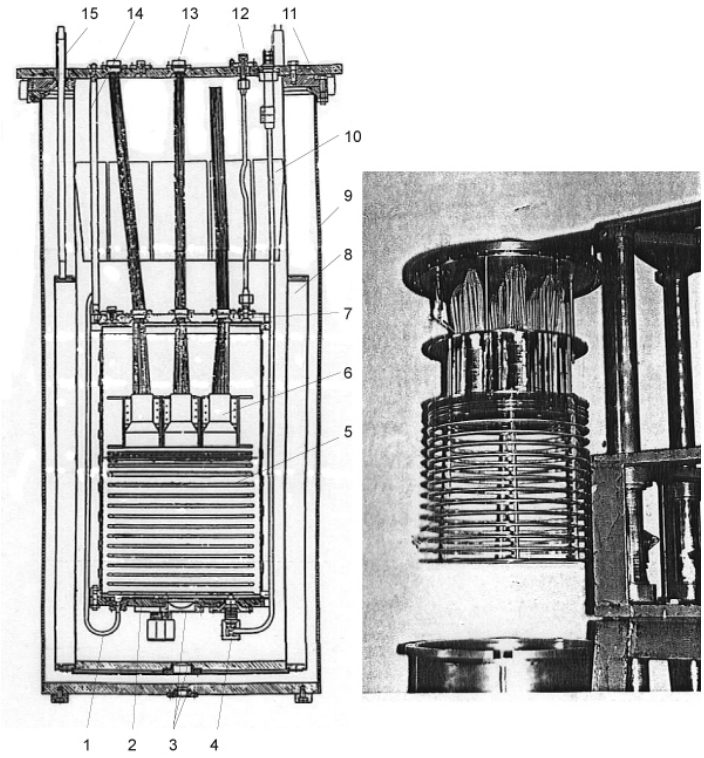

Fig. 9.7 ITEP LXe emission detector for neutrino magnetic momentum measurement (a) and photopicture of the electrode system at moment of installation inside the vessel (b): 1 - bottom gas inlet; 2 - cathode; 3 - X-ray windows; 4 - high voltage feedthrough; 5 - drift electrodes; 6 - array of 7 photomultipliers; 7 - top flange of the detector chamber with glass-metal feedthroughs; 8 - liquid nitrogen tank; 9 - vacuum vessel; 10 - foam thermo-insulation; 11 - top flange supporting the detector chamber and the liquid nitrogen tank; 12 - top gas inlet; 13 - room temperature multipin feedthrough; 14 - support rod for the detector; 15 - inlet/outlet line for liquid nitrogen.

atively small detectors that may have a great impact on nuclear reactor monitoring technique. However, a signal consisting of only a few electrons is below a threshold of conventional solid or liquid state detectors without internal amplification. There is proposed a compact (kg scale) two-phase (liquid/gas Ar) emission detector to measure coherent neutrino scattering [464]. Argon has been chosen as a working medium because of its more favorable kinematics of nuclei recoils against xenon. For a neutrino flux at 25 m distance from a 3 GWt reactor, the expected event rates before detection efficiencies are $56\,\mathrm{kg}^{-1}\mathrm{day}^{-1}$ for coherent scattering off argon compared to $2.8\,\mathrm{kg}^{-1}\mathrm{day}^{-1}$ for the inverse beta decay reaction in $(\mathrm{CH})_n$.

It was suggested that the detector is surrounded with 20 cm low-background concrete. A reduction of the external background by factor ~ 100 is achieved with a shield consisting of 2 cm lead (inner) and 10 cm of borated polyethylene (outer).

9.2.3 Double Beta and Double Positron Decay Search

Extreme interest to search for neutrino-less double beta decay is due to its connection with fundamental aspects of particle physics. The neutrino oscillation experiments indicate that neutrinos do have mass and, in particularly, at least one neutrino has a mass greater than 50 meV. The upcoming $\beta\beta(0\nu)$ experiments in particularly with large noble gas detectors will have good enough sensitivity to check below this critical mass scale. It is expected that a positive result will be achieved within the coming decade [465].

9.2.3.1 Experiments with Active Targets

LXe Scintillation Detector

The scintillation LXe detector [244] has been used in one of the first experiments searching for double beta decay of ^{136}Xe [245]. The detector construction is described in the Section 4.2.2. The experiment was carried out in the Baksan Underground Laboratory (859 m.w.e.). The result of the experiment is presented in Table 9.4.

The XMASS 10-ton scintillation LXe detector designed for solar neutrino studies and dark matter search (see description in Chapter 4) will have sensitivity to the $0\nu\beta\beta(^{36}\text{Xe})$ decay; its performance will depend on practically achieved detection threshold.

High-Pressure Gas Xenon TPC

There are two possibilities here, a high or low pressure time projection chambers (TPC). The low pressure TPC yields momentum measurements with a magnetic field and capability for beta particle track imaging. This technology is implemented in the installation DEVIS running at ITEP (Moscow) for ITEP-832 Experiment from 1988 [466, 467]. Since for this publication we have to limit the area of our interest to just high-density noble gas detectors, in this section we will not discuss multiwire drift chambers, working at atmospheric pressure, but rather focus our attention on experiments with relatively dense pure noble gases. We believe that the detectors with dense working media have the most perspective for achieving the highest sensitivity in experiments of the next generation.

The limits on different $2\beta^-$-decay modes of ^{136}Xe and ^{134}Xe and also $2\beta^+$ and Kβ^+ decay modes of ^{124}Xe are obtained using a high pressure xenon gas TPC installed at the Baksan Underground Laboratory (850 m.w.e.); in particular, for the $2\beta(2\nu)$-decay of ^{136}Xe it was found that $T_{\frac{1}{2}} > 8.4\times10^{19}$ y [401]. The detector had working volume 3.66 L (fiducial volume is 3.14 L) filled with Xe (natural or 93% enriched with ^{136}Xe)+0.8%H_2 gas mixture under 2.94 MPa pressure. The electrode system consisted of a multiwire flat anode (0.1-m diameter wire with 10-mm step) both sides surrounded by grids (0.1-mm diameter beryllium bronze wire with 2-mm step). The anode-grid gap is 1.3 cm; both grid-cathode drift regions are 8 cm deep. The vessel is made of low-background titanium alloy; all insulators are made of quartz. The passive shielding included 10-cm thick internal layer made of oxygen-free copper alloy and 15-cm thick outer layer made of lead. The results presented in Table 9.4 acquired after 685.4 hours exposition with enriched xenon gas mixture and 710 hours exposition with natural mixture of xenon isotopes containing 8.8%^{136}Xe. It was suggested to improve the results after modification of the detector in order to improve the energy resolution, to increase the density of xenon, and to purify xenon from possible contamination with ^{226}Rn.

The best record as of today on $0\nu\beta\beta(^{36}\text{Xe})$ decay lifetime has been achieved with a 5-bar pressure gas xenon electroluminescence time projection chamber with 3.3 kg of 62.5% enriched ^{136}Xe placed in the Gotthard Tunnel [468]. The tracking features of the detector permitted the identification of two-electron tracks as a signature for double beta decay. The detector demonstrated the energy resolution of about 6.6% FWHM at the endpoint (2.481 MeV) of the $0\nu\beta\beta(^{36}\text{Xe})$ decay. The sensitivity of the experiment was limited with Compton-scattered electrons from natural gamma background. These electrons sometimes imitated the double beta events. From this point of view, experiments with liquid targets have a certain advantage, since the fiducial volume is shielded very well from outer layers of the liquid xenon.

The Enriched Xenon Observatory (EXO) experiment has been proposed to search for $0\nu\beta\beta(^{136}\text{Xe})$ decay with massive (up to 10 ton) xenon detector and a system for laser tagging the daughter nucleus, ^{136}Ba [469].

9.2.3.2 Experiment with a Passive Target

Liquid ionization chambers with light media such as liquid argon and methane have been proposed for searching double beta decay of metal isotopes, which can be used for manufacturing thin foil electrodes [470]. Advantages of such an approach include:

- good energy resolution of ionization chambers in comparison with scintillation detectors;
- possibility to measure angle correlations, for example, using analyses of the signal waveforms;

- good position resolution;
- possibility to use exclusively low-background materials;
- possibility to use a few targets in the same detector.

A multisection liquid argon ionization chamber has been constructed for search of double beta decay of ^{100}Mo [471]. The sensitive volume of the detector has a 30-cm inside diameter and height of 56 cm (Fig. 9.8). The electrode system consists of 14 foil cathodes, 15 anodes and 28 screening grids. The grid-anode distance is 5.5 mm and grid-cathode distance is 14.5 mm. The cathodes are made of molybdenum foil of ~ 50 mg cm^{-2} thick. The energy resolution is 6% FWHM at 3 MeV. The trigger requires that at least one anode signal ex-

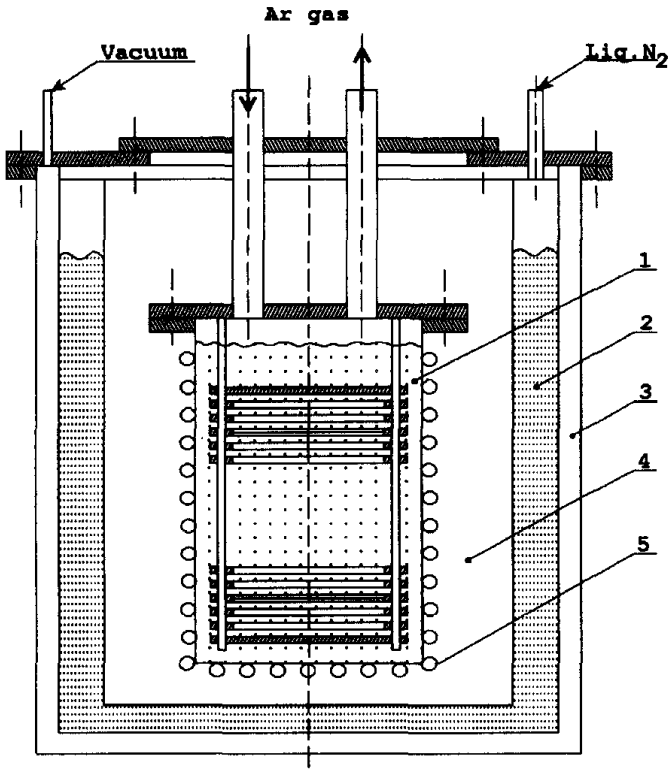

Fig. 9.8 Multisection LAr ionization chamber searching for double beta decay of ^{100}Mo: 1 - detector vessel made of low-background titanium alloy with inner dimensions of 40-cm diameter and 70-cm height; 2 - liquid nitrogen jacket; 3 - vacuum cryostat; 4 - heat-exchanging jacket filled with nitrogen gas; 5 - electrical heater for thermostabilization of the detector [400].

ceeds the 0.8 MeV threshold. The trigger causes digitizing signals from all anodes. Two-electron events generated in neighboring sections with time difference of less than 0.6 μs were selected. Cathodes made of natural molybdenum have been used for background evaluation. Data have been processed off-line. The electrode system is placed inside the vessel of 40-cm diameter and 70-cm height made of low-background titanium. Insulators made of Teflon. Passive shielding is made of 15-cm thick lead. In order to reduce a radon background, the detector setup was enclosed in a plastic bag filled with nitrogen evaporated from the detector during the experimental run. This measure allowed reduction of the count rate associated with ^{222}Rn from $\sim$ 200 Bq m^{-3} outside the lead shielding down to $\sim$ 2 Bq m^{-3} inside the shielding.

The experiment was located in the Gran Sasso Underground Laboratory at 3500 m.w.e. The energy range of 2.8–3.1 MeV and threshold 1 MeV used for study of the 0ν-decay. The energy range of 2.3–3.0 MeV has been investigated for $0\nu\chi^0$-decays. For 2ν-decay, the energy range 1.4–2.3 MeV was analyzed. In result of 313 hours of data taking with 138.7 g ^{100}Mo and 2063 hours data taking with enriched molybdenum, the limits on half-lives for 0ν and $0\nu\chi^0$-decays of ^{100}Mo were obtained: $> 5.0\times10^{21}$ y and $>2.7\times10^{20}$ y, respectively at 90%CL; $2\nu\beta\beta$ decay of ^{100}Mo was detected with its half-life $(7.5\pm1.1(\text{stat.})\pm1.5(\text{syst.}))\times10^{18}$ y [471]. The systematic error is mainly associated with possible contamination of the cathode foil with radioactive impurities.

9.2.3.3 Double Positron Decay Experiments

Searching for neutrino-less transitions in positron decays gives a unique signature because of the possibility to select these very rare events in coincidence with annihilation photons [472]. The clear signature is competing with very long lifetimes predicted for double positron decays, which are several orders of magnitude larger than those for $\beta^-\beta^-$ decays [472]. Two from 7 famous isotopes enabling neutrino-less positron decay are noble gas isotopes of ^{124}Xe and ^{78}Kr. The best limits for lifetimes of ^{136}Xe and ^{134}Xe $2\beta^-$-decays are measured with high-pressure xenon gas ionization chambers and TPC, demonstrating good energy resolution in the MeV range.

Experiment with High-Pressure Gas Ionization Chamber

Positron emission from the ^{78}Kr isotope was studied with a high-pressure krypton ionization chamber [473]. The installation for this experiment is shown in Fig. 9.9 and technical details of the detector construction are described by Saenz et al. [474].

The ^{78}Kr transition to ^{78}Se leads to deposition 2.881 MeV in the detector medium that is the largest value among the potential $2\beta^+$ emitters. There are

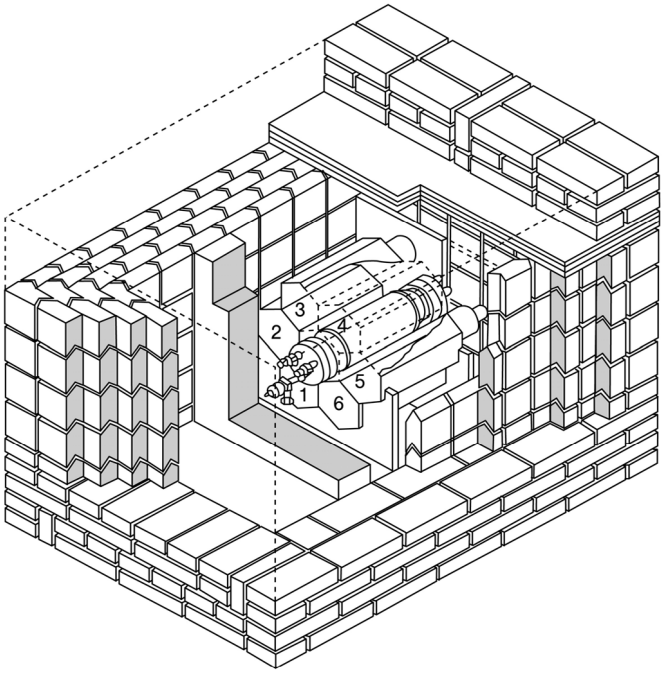

Fig. 9.9 Experimental installation for double positron decay of ^{78}Kr search with high-pressure krypton ionization chamber [473].

a few processes allowed for transitions to the ground state:

- double positron emission
- electron capture followed by positron emission
- double electron capture.

Yet, the transition to the excited states of ^{78}Se is possible. Experimental research is focused on exploring processes $2\beta^+$ and $K\beta^+$ (with or without neutrino), which can be detected in coincidence mode. In the described experiment, the coincidence was searching between the positron(s) ionization signal in a high pressure krypton gas ionization chamber (IC) and the 511 annihilation photons detected in a set of six sodium iodide detectors surrounding the IC. The signature of the neutrino-less electron-positron conversion would be an energy deposition of 1852 keV in the IC (positron kinetic energy plus the selenium K-shell binding energy) in coincidence with the two annihilation gamma rays detected in the NaI(Tl) scintillators. The neutrino-less $2\beta^+$-decay would show the positron-deposited ionization energy of 837 keV in the IC in coincidence with up to four annihilation gamma rays absorbed in the NaI detectors. The experimental installation for this experiment is shown in Fig. 9.9.

The instrument consists of a high-pressure krypton gas ionization chamber (IC) placed within a hexagonal array of large NaI scintillation detectors (1–6). The performance of the cylindrical gridded ionization chamber is described elsewhere [474]. The IC has a 10.6-cm inside diameter and 14-cm length enclosing the volume of 1.54 L. The cylindrical vessel of 2-mm thickness plays a role of the grounded cathode. The central anode has a 12-mm diameter and it is surrounded by a grid with a diameter of 40 mm, formed by tungsten wires of 50-μm diameter, spaced 2 mm apart. The body flanges and electrodes have been made of stainless steel; quartz was used as insulator. The chamber was filled with 35 L (fiducial volume) of isotropically enriched (94.08% ^{78}Kr) krypton with 0.2% admixture of hydrogen at 2.5 MPa pressure. The scintillation array was composed of a set of six Bicron NaI detectors based on a 13.5-cm diameter and 20.4-cm long NaI(Tl) crystals. The measured energy resolution of the IC was 1.86±0.09% FWHM at 1836.2 keV and 2.76±0.06% FWHM at 814.2 keV. The measured energy resolution of the NaI detectors was 6% FWHM at 1.33 MeV. The detectors have been made from especially chosen low-background materials and have been exposed underground for more than 4 years before the start of this experiment. The detector setup was surrounded by a passive shielding consisting of a 20 cm layer of aged (70 years) lead.

The installation was mounted in the Canfranc Underground Laboratory (675 m.w.e.). The results of a search for the $2\beta^+$ and $K\beta^+$ decay modes of ^{78}Kr are presented in Table 9.4. After 4434 hours of counting time, the half-life lower limits obtained are $T_{\frac{1}{2}}(K\beta^+)_{0\nu} \geq 5.1\times10^{21}$ y and $T_{\frac{1}{2}}(2\beta^+)_{0\nu+2\nu} \geq 2.0\times10^{21}$ y at 68% C.L.

Tab. 9.4 Performance of completed and currently running double beta decay experiments using noble gas detectors.

Isotope	Mass, kg	Process	Detector	Experimental conditions	Measurement time	$>T_{\frac{1}{2}}^{exp}$, y (67%CL)	$T_{\frac{1}{2}}^{theor}$, y	Ref.
^{136}Xe	2.1	$2\beta^-(0\,\nu)$	SDC	Gotthard Tunnel	1.47 y	4.4×10^{23}	2.2×10^{24}	[468]
^{136}Xe	0.921	$2\beta^-(0\,\nu)$	LXe Scint.	Baksan U.L.	309 h	2.36×10^{21}	2.2×10^{24}	[245]
^{136}Xe	0.921	$2\beta^-(0\,\nu)$	h.p.TCP	Baksan U.L.	931 h	3.3×10^{21}	2.2×10^{24}	[401]
^{136}Xe	7.5	$2\beta^-(0\,\nu)$	$13m^3$l.p TCP in 1 kGs m.f.	OG	running	$2\text{-}4\times10^{24}$	2.2×10^{24}	[466]
^{78}Kr	3.04	$2\beta^+(2\,\nu)$ $K\beta^+(2\,\nu)$ $K\beta^+(0\,\nu)$	h.p. Ioniz. Chamb.	Canfranc U.L.	4434 h	2.0×10^{21} 1.1×10^{20} 5.1×10^{21}	7.1×10^{27} 2.2×10^{24} 4.2×10^{27} $< m_\nu >^{-2}$	[473]

Note: * - project; OG - overground; UG - underground; CL - confident ional level; SDC - scintillation drift chamber; TPC - time projection chamber; U.L. - underground laboratory; m.f. - magnetic field; n.m. - content in natural mixture of isotopes; h.p. - high pressure; l.p. - low pressure.

9.3 High-Energy Physics: Calorimeters

Calorimetry is one of the major tools of particle physics. Calorimeters are used to measure the energy of high-energy particles by means of total absorption of their kinetic energy and transformation into a measurable amount of charge or light. Depending on preferable interactions of the measured particles (electromagnetic or strong), the calorimeters are often classified as electromagnetic or hadron calorimeters. In order to provide higher stopping power, calorimeters may consist of alternating layers of passive high-density absorber and an active detector medium that provides effective signal generation. This sort of calorimeter, called sampling calorimeters, are most often used for measuring the energy of strongly interacting particles (hadrons). In contrast, homogeneous calorimeters are built almost exclusively from the active detection materials; for this reason they provide the best energy resolution.

The requirements of an ideal calorimeter for high-energy experiments at high-luminosity accelerators have been formulated by Chen et al. [249] and considered in details by Fabian and Gianotti [80].

9.3.1 Ionization Calorimeters

Technically, an ionization calorimeter is a large multigap ionization chamber. In order to achieve the position sensitivity the electrodes are divided in segments or strips with individual readout channels. In this section we will review the most developed and charismatic designs of noble liquid ionization calorimeters. Data on the most advanced apparatuses are collected in Table 9.5. Some parameters such as position or angle resolution are difficult to be included in the table because, obviously, they are complicated functions of kinematic parameters of measured particles and geometry of installations. By compiling the data in the table, we want to form a general view on this detector technology and to direct those readers who are interested in details to cited original publications and dedicated reviews [80–82, 238].

9.3.1.1 Liquid Argon Calorimeters

Liquid argon is the most commonly employed noble liquid for sampling calorimeters because of its low cost, availability in large amounts, and relatively easy purification.

The BARS liquid argon calorimeter was originally constructed for the tagged neutrino facility at IHEP (Russia) proton synchrotron [475]. The calorimeter consists of two identical units, BARS-1 and BARS-2. Each detector contains 216 tons of liquid argon with 154 tons filling the sensitive volume (Fig. 9.10).

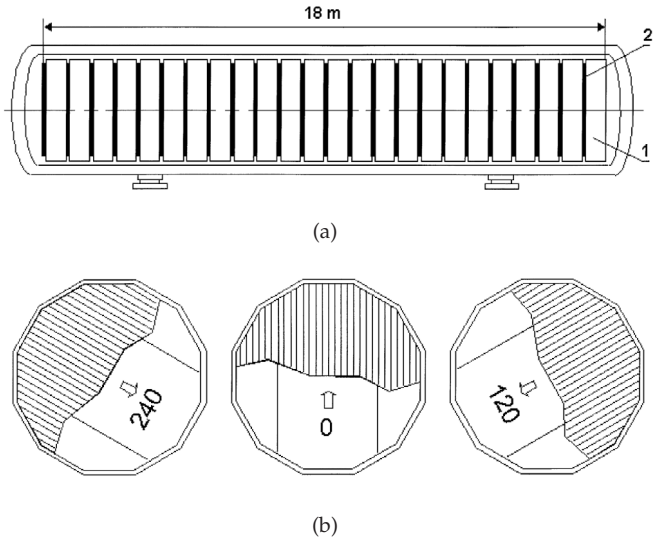

Fig. 9.10 Schematic drawing of one of the BARS detector (a) and the transversal structure of signal planes (b): 1 - section of ionization chambers; 2 - scintillation trigger plane [475].

Beyond the multilayer electrode structure, the detectors contain plastic scintillators immersed in the LAr used for generation of fast triggers. The electrode system of 3-m diameter is formed by double-gap ionization chambers formed by an interleaved signal and ground planes. Signal electrodes are made of Al strips which are 3 mm thick and 61 mm wide. The grounded Al electrodes are 6 mm thick. The active gap of 24 mm is filled with LAr. Each signal plane consists of 48 strips; the strips in adjacent planes are rotated by 120 $^\circ$ forming u, v and x-coordinates (Fig. 9.10). There are 24 sections in the calorimeter (288 signal planes) of 18-m length. The total number of spectrometric channels is 13824 in each calorimeter. The triggering system of the calorimeter consists of 24 planes of scintillation counters. Each plane consists of eight 22-mm thick and 334-mm wide plastic (PMMA) scintillators. Scintillation light is collected by the wavelength shifting bars placed between the counters and viewed from both ends by glass window fast FEU-84 PMTs immersed in LAr with their bases. The time resolution of the triggering plane is about 5 ns FWHM. The total number of scintillation counters placed in liquid argon is 384. The technology of the BARS detector has been explored first with smaller prototypes MARS [476] and MARS-2 [477]. One of those sampling calorimeters (MARS) used charge collection readout from aluminum foil strip electrodes (6288 x-strips with 62.5-mm pitch and 394 HV planes) with thin 1.9 mm active layer; another one (MARS-2) used current readout from fewer strips (315 x, u, v-strips with 101-mm pitch) and wider

active gap (28 mm). Both demonstrated similar energy resolution (about 4% at 1 GeV) but the MARS-2 readout scheme was accepted as cheapest and compatible with modest purity of liquid argon. Since 1996, BARS-2 was used for horizontal cosmic-ray muon spectrum measurements; one of tasks in this experiment was to search for muon-pair production. The task is well matched to the unique properties of the detector: a combination of large dimensions (137.4 X_0 total thicknesses) with fine segmentation in the longitudinal and the transverse dimensions, a good energy resolution for EM showers, and a high detection efficiency of detection of charged particles with minimal ionization. Recently, Anikeev et al. [478] reported the observation of the rare process of muon-pair production by cosmogenic muons.

The liquid argon calorimeter of the H1 detector was the largest ever used in accelerator experiments. The experiment employed collisions of highly energetic protons (820 GeV energy) with electrons (positrons) (27.6 GeV energy) provided by the HERA accelerator. The particles created in the collisions are detected with the H1 detector. The physics goals of this experiment are to measure the structure of the proton, to study fundamental interactions between particles, and to search for physics beyond the standard model of elementary particles. Construction of the H1 liquid argon calorimeter was completed in December 1990 and the first physics run was started in June 1992. A detailed description of the calorimeter may be found in publications of the H1 Calorimeter Group (see, for example, Ref. [479]). The calorimeter included electromagnetic (barrel) and hadronic (end cap) sections placed in the same cryostat of 120 m^3 total volume. The absorber material in the electromagnetic section is lead in plates 2.4 mm thick; the total thickness of the electromagnetic absorber varies between 20 and 30 X_0. The absorber material in the hadronic section consists of 16 mm stainless steel plates with additional 3 mm of steel in readout elements; the total amount of absorbing material varies between 4.5 and 8λ. The absorber plates are separated with LAr gaps, 2.34-mm thick, in the electromagnetic section and twice 2.4 mm in the hadronic part. In order to keep the systematic errors at the required level, the total argon thickness is constant within $\sim 1\%$ in the electromagnetic section and $\sim 2\%$ in the hadronic section. The detection parameters of the calorimeter are summarized in Table 9.5.

The liquid argon calorimeter of the ATLAS detector installed at the Large Hadron Collider (CERN) is one of the most advanced instruments. The calorimeter divided into a barrel part (pseudorapidity $|\eta| < 1.475$) and two end caps ($1.375 < |\eta| < 3.2$) and segmented into three compartments in depth. The outer radius of the calorimeter is 2 m. The barrel part consists of 32 modules assembled in two identical wheels. Each module is composed of 64 lead absorbers and an equal number of anode electrodes that are kept in the middle of the liquid argon gap by honeycomb-structured spacers. In total, the barrel

calorimeter has 54784 readout channels per half-length wheel. Each end cap part is made of eight wedge-shaped modules with η-dependent granularity. In total, there are 31104 readout channels per end cap. Thin active presampler layers (11 mm for the barrel and 4 mm for the end cap) are installed to measure and compensate for the energy lost in upstream material.

Basically, the electrode structure of the ATLAS LAr calorimeter is similar to the electrode structure of the H1 LAr calorimeter but architecture of the electrode system is very different (Fig. 9.11): the absorber and the electrode plate are shaped in accordion-like zigzag structure with a bend angle of 90° and a fold width of 40.1 mm. Such an electrode shape makes the position response function to be more uniform and independent on the direction of development of EM shower. The electrodes are assembled in longitude towers as shown in Fig. 9.11c. More details about construction of the electrode structures could be found in Ref. [482] and general properties of the installation are presented in Table 9.5.

9.3.1.2 Liquid Krypton Calorimeters

Krypton is usually preferred for homogeneous or quasihomogeneous calorimeters because of its relatively short radiation length, which allows more compact detectors than LAr-based devices; however, the natural radioactivity of about 300 Bq cm^{-3} associated with beta decay (0.7 MeV maximum energy) of ^{85}Kr isotope (11 years half-life) should be taken into account.

The $NA48$ experiment is a fixed target experiment located in the ECN3 hall of the SPS accelerator at CERN, which was aimed at measuring the direct CP violation parameter by detecting simultaneously $K^0_{S,L} \longrightarrow \pi^0\pi^0$ and $K^0_{S,L} \longrightarrow \pi^+\pi^-$ decays. A mass resolution for $\pi^0 \longrightarrow \gamma\gamma$ decay of about 1 MeV is required in order to reject the combinatorial background from $K^0_L \longrightarrow 3\pi^0$ decays when two photons are lost. This was achieved by using a quasihomogeneous liquid krypton calorimeter with tower readout structure. The active volume of 8 m^3 of liquid krypton in a cryogenic vessel has a transverse octagonal shape 2.4 m across and is 1.25 m deep (26 radiation lengths). A number of 13 500 cells of 2×2 cm^2 are formed by 1.8-cm wide and 40-μm thick copper-beryllium strips individually tensioned and stretched along the particle direction in a projective geometry, with small alternating left-right tilts. The thin electrode structure made the calorimeter to be quasihomogeneous and allowed to achieve good response uniformity and to reduce the constant terms in energy resolution down to 0.5%. The readout system included preamplifiers located in LKr, followed outside the cryostat by shapers (80 ns shaping time), 10-bit 40-MHz flash ADC. The reconstructed π^0 mass had a resolution of 1.1 MeV, and the calorimeter time resolution for the K^0 event was 230 ps. The energy resolution measured on a prototype detector [483] with the same

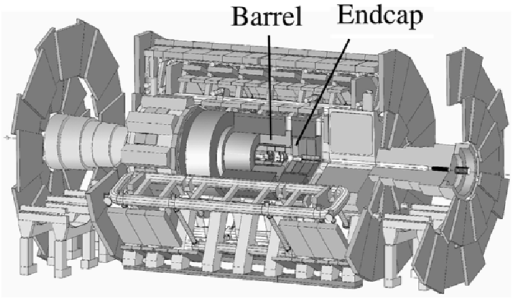

(a)

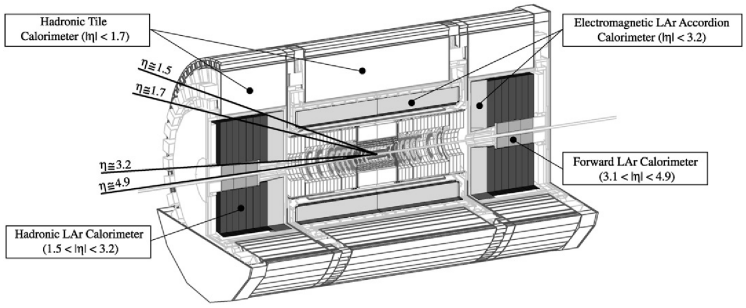

(b)

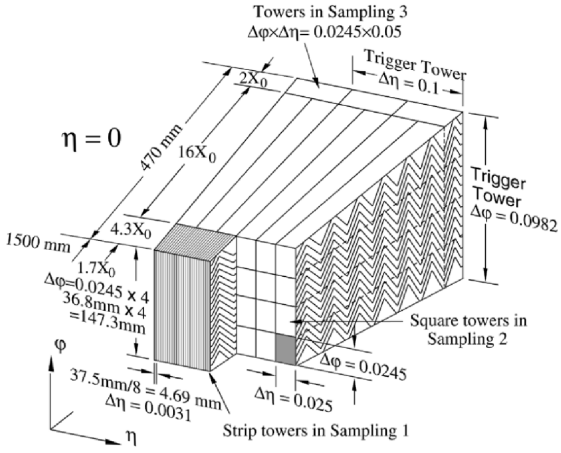

(c)

Fig. 9.11 Artistic drawing of (a) the ATLAS (CERN) detector, (b) the LAr ionization calorimeters of the ATLAS, and (c) a schematic drawing of a tower based on Accordion electrode structure, reported by Puzo [480] and Lund-Jensen [481].

structure and a reduced transverse size is

$$\sigma_E/E = 3.5\%/\sqrt{E} \oplus 0.42\% \oplus 40\ \text{MeV}/E,$$

where E is measured in GeV. A scintillating fiber hodoscope is embedded into the calorimeter structure, inside the liquid, at a longitudinal depth corresponding to 10 radiation lengths, and is used to obtain an independent time measurement with $\approx$ 250 ps time resolution.

A barrel electromagnetic calorimeter based on liquid krypton has been designed for the detector KEDR at e^+e^- collider VEPP-4M at the Budker Institute (Novosibirsk, Russia). The design luminosity of VEPP-4M is 2×10^{30} cm^{-2}s^{-1} at $2E = 3.0$ GeV and 2×10^{32} cm^{-2}s^{-1} at $2E$ = 10.0 GeV. KEDR is the only detector installed at VEPP-4M for study of two-photon processes with a resolution of 0.5–1.0%. The LKr calorimeter assembly was finished in 2001. The inner radius of the barrel is 75 cm, the thickness is 68 cm (15 X_0). The parallel plate ionization chambers have a 2 cm active gap filled with 27 tons of liquid krypton. The electrodes are made of double-sided (2×18 μm Cu) and 0.5-mm thick G10. The signal is read out from high voltage electrodes divided into rectangular pads. The electrodes are assembled in towers with the entrance size of 10×10 cm^2. The towers are oriented to the interaction point. Eight grounded electrodes of the first $6X_0$ thickness are divided into strips of about 5 mm in width for z- and φ-coordinate measurements. At electric field 0.5 kV cm^{-1}, the electron drift time is about 8 μs. The collected charge is measured with charge-sensitive preamplifiers, shaped with a simple RC-2CR filter with 1 μs time constant and recorded with 12-bit ADCs. The typical value of the equivalent noise charge is about 2000 electrons. The total number of electronics channels is 7240 (2304 are connected with the towers, 1864 with z-strips and 3072 with φ-strips). Extensive prototyping has shown that excellent energy and spatial resolution can be obtained 2.5% and 4 mrad at 1 GeV, respectively [281, 484, 485]. General parameters of the LKr calorimeter are listed in Table 9.5.

9.3.1.3 Xenon Calorimeters

Xenon is the most attractive medium among noble gases to be used in electromagnetic calorimetry because of its high photoabsorption cross section and relatively low energy for production of electron–ion pair. Disadvantages are the relatively high cost and difficult purification.

High-Pressure Gas Sampling Calorimeters

Gas sampling calorimeters have been widely employed before introduction of liquid noble gas calorimeters, mainly because of their low cost and segmentation flexibility [80]. They lost in the competition with liquid calorimeters

for the next generation of experiments because of their inherent modest energy resolution ($a \leq 20\%$). Since there is a low density of the active medium, the sampling fluctuation is small ($\ll 1\%$) by the cost of relatively weak signal. Operation in proportional mode with gain of about 10^3-10^5 is therefore required to obtain an acceptable signal-to-noise ratio. However, the stability and uniformity of the detector response is modest because the gain is sensitive composition of the gas, quality of wire surface, gas purity and therefore essentially affected by aging effects. One of the best performing gas sampling EM calorimeters was used in the ALEPH experiment at LEP (CERN).

Baskakov et al. [359] tested a model of a high-pressure (2.45 MPa) xenon sampling calorimeter with 150-mm diameter electrodes made of tungsten and copper. The thickness of the plates and the gap between them were variable in the range 1–8 mm and 2–8 mm, respectively. The number of the plates can be changed from 50 to 120. Xenon was mixed with 5% accelerating electrons admixture of methane. The gas of research grade purity was used without additional purification. The total energy resolution measured the electron beam of 31 GeV energy to be 6.2% FWHM at the gas pressure of 1.96 MPa. Time resolution was defined to be 7.1 ± 0.5 ns. Despite of relatively good performance, high-pressure calorimeters were not accepted in the experimental practice because of safety considerations and it was necessary to use massive and thick wall vessels.

LXe Ionization Calorimeters

The electromagnetic calorimeters based on heavy noble liquids open the possibility to obtain an energy resolution comparable with that in the energy range of 30–5000 MeV but with much better position resolution in measuring the photon conversion point. The fine granularity of ionization calorimeters provides information for particle identification using $\mathrm{d}E/\mathrm{d}x$ methods as well as e, μ and π identification using the shower longitudinal structure.

The first full scale prototype of LXe homogeneous ionization calorimeter has been tested at a 1–6 GeV electron beam of the Serpukhov accelerator [486]. The prototype was a cylindrical detector with operating volume of 25 cm in diameter, 45 cm in length and the electrode system consisted of a multigap parallel plate ionization chamber with aluminum electrodes of 50 μm thickness. The energy resolution of $3.4\%/\sqrt{E(\mathrm{GeV})}$ has been demonstrated.

The detector CMD-2 has been running at the VEPP-2M electron-positron collider in the Budker Institute (Novosibirsk) from 1992 to 2000 for study of the center-of-mass energy range from 0.36 to 1.4 GeV. Upgrading the accelerator to VEPP-2000 for higher luminosity and energy required updating EM calorimeter part from CsI crystals to 400-L LXe [487]. The architecture of the installation CMD-2M is very specific for center-of-mass experiments (Fig. 9.12).

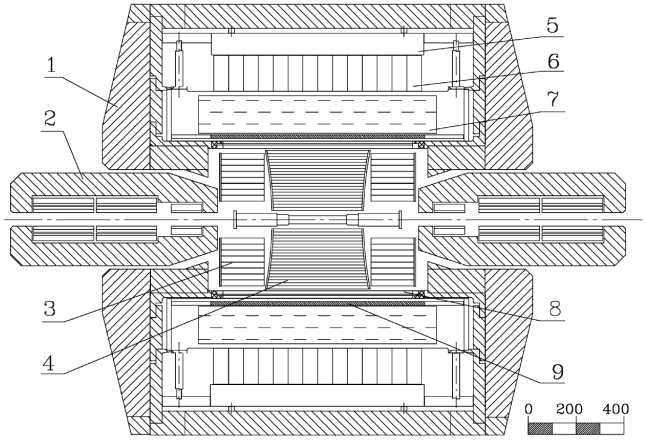

Fig. 9.12 Schematic drawing of the detector CMD-2M: 1 - magnet yoke; 2 - focusing solenoid; 3 - BGO end cap calorimeter; 4 - drift chamber; 5 - support and electronics of CsI crystals; 6 - CsI barrel calorimeter; 7 - LXe barrel calorimeter; 8 - Z-chamber; 9 - superconductive solenoid. The scale is shown in millimeters. Adopted from [487].

The barrel part of the electromagnetic calorimeter consists of the inner section (7) based on ionization chambers filled with LXe and the outer section (6) based on CsI crystals. The LXe section has a 15-cm ($5X_0$) thickness and is used to measure coordinates of the photon conversion point. The total thickness of the barrel calorimeter is 13 X_0, which is acceptable for total absorption of relatively low-energy gamma quanta absorbing in the detector. The expected energy and angle resolutions of the combined calorimeter are σ_E / E = 4.7–3% and $\sigma_{\theta,\varphi}$ = 30–20 mrad at E_γ = 0.1–0.9 GeV. The fine angle resolution is resulted from fine position resolution of the LXe section. The electrodes of the ionization chambers are made of 2-mm wide copper strips on G10. The thicknesses of the strips are 0.5 mm (anode) and 0.8 mm (cathode). An active gap size is 10.2 mm, which gives a drift time to be about 4.5 μs. The conversion point coordinates are measured by the center of gravity of induced charge.

9.3.2 Scintillation Calorimeters

In spite of expected excellent detection properties, scintillation calorimeters based on noble gas technology are not so as well developed as ionization calorimeters. A reason for this is the more difficult technology for effective collection of light (see Section 4.4). Although ionization calorimeters introduced in experimental practice in the 1970s [488] and already in ten years appeared

to be presented practically at all the most advanced accelerator experiments in the world, the most technical problems for building scintillation calorimeters have been solved only in the past decade, when funding for high-energy physics was rapidly reduced because of the changing political situation in the world. That seriously affected the introduction of this new, relatively expensive, but very promising technology into the experimental practice.

The most successful development at the moment is a barrel type LXe scintillation calorimeter developed for the MEG experiment at PSI (Switzerland) [248, 252–254]. The MEG collaboration, comprised of some 80 members from 12 institutes in Italy, Japan, Russia and Switzerland, is currently commissioning the initial part of the beam line, as well as the first detector components, which have already arrived at PSI. The ambitious goal of this experiment is to achieve a single-event sensitivity for the decay $\mu^+ \longrightarrow e^+\gamma$ that will be more than two orders of magnitude lower than the current best limit on the branching ratio BR $< 1.2 \times 10^{-11}$, achieved by the MEGA collaboration at the Los Alamos Meson Physics Facility (LAMPF) [255]. The MEG experiment is aimed to achieved BR in the range 10^{-12}–10^{-14} as predicted by supersymmetric theories of Grand Unification [256].

A schematic design of the MEG experiment is shown in Fig. 9.13 (see, for example, Baldini et al. [21]). Muons of 29 MeV c^{-1} momentum are stopped on a thin polyethylene target where they decay at rest. A set of radial drift chambers inside an inhomogeneous magnetic field measure the position momentum while the positron timing is given by plastic timing counters. The photon energy, direction, and timing are measured by a LXe scintillation calorimeter of the barrel type. The calorimeter is C-shaped and contains 900 L of LXe. The volume is viewed by 846 2″-diameter photomultipliers. Basic parameters of the calorimeter are presented in Table 9.6.

A milestone in the development of the calorimeter was recently achieved with beam tests in Japan and at PSI. A prototype detector with about one-tenth of the volume and 228 PMTs has yielded a resolution of 4.9±0.4% FWHM at 55 MeV, as well as a position-dependent spatial resolution σ_x = 2–4 mm [189].

9.4 Medical Imaging

In medicine, ionization radiation is used for imaging and diagnostics of functioning inner organs. Development of any new detection technique traditionally attempts to apply it to medicine needs. Very few of them are successful but all of them cultivate the ground for revolutionary developments in the future. The idea of using a unique combination of detecting properties of liquid xenon for medical imaging, stimulated by the significant technological progress, continues to interest physicists. With respect to γ-ray detection, LXe

Tab. 9.5 Parameters of some noble liquid calorimeters constructed for accelerator experiments.

Install. (acceler./ /instit.)	Type of device	Medium mass & volume	Segmentation & electrode struct.	En. Res. terms a b c	Readout & time res.	Ref.
ATLAS (LHC)	EM EC	LAr	Accordion	<0.4% 10% <12.5%	2×54 784(EM)+ 2×31 104(EC) ch	[480,481]
H1 (HERA/ /DESY)	a)EM b)H	LAr 53 m^3	2.4 mm LAr/ a)2.4 mm Pb b)16 mm st.st.	a)10 b)55	Pads/G10 a)30 784 b)13 568	[479]
D0 (FNAL)	a)EM b)H	LAr 2×15 m^3	2×2.3 mm LAr/ a)3 mm U b)6 mm U	15 50	Towers; 50 000 ch	[489]
EMLAC (E706/ /FNAL)	EM H	LAr,70 m^3 (40 m^3 active)	2.5 mm LAr/ a)2 mm Pb b)16 mm st.st.	15		[490]
MARKII (SPEAR/ /SLAC)	EM	LAr 15 m^3	3 mm LAr/ 2 mm Pb	12	Strips/PCB	[491]
BARS (U-70/ /IHEP)	EM	LAr 2×216 t	a)26 mm LAr/ 6 mm Al b)22×334mm^2 PMMA scint.	a)4% at 1 GeV b)5ns FWHM	a) Al strips, 2×13824 ch b) plast. scint., 2×384 ch	[475]
NA48 (SPS/ /CERN)	EM	LKr 8 m^3	2×2cm^2 cells Accordion	3.5% 0.4%	Time res 230ps	[80]
KEDR (VEPP-4M)	EM	LKr 27 t	2 cm LKr/ 0.5 mm G10+ 2×18μm Cu	2.5% at 1 GeV	Pads/G10 7200 ch	[485]
CDM-2M	EM	LXe ($5X_0$) 1.5 t	2 mm strips 10 mm LXe/0.5–0.8 mm Cu/G10	4.2% at 0.2 GeV	1.5 mm at 0.2 GeV 2124 ch	[487,492]
LXe EMC	EM	LXe ($25.4X_0$)	4.1 mm LXe / 108μm G10+ 15μm Cu	2%rms at 70 GeV	22 ch, 8 μs shaping time	[273]

Note: Energy and position resolution are presented in σ terms. Abbreviations used: PMMA - polymethylmethacrylate; EM - electromagnetic; EC - end cap; H - hadronic.

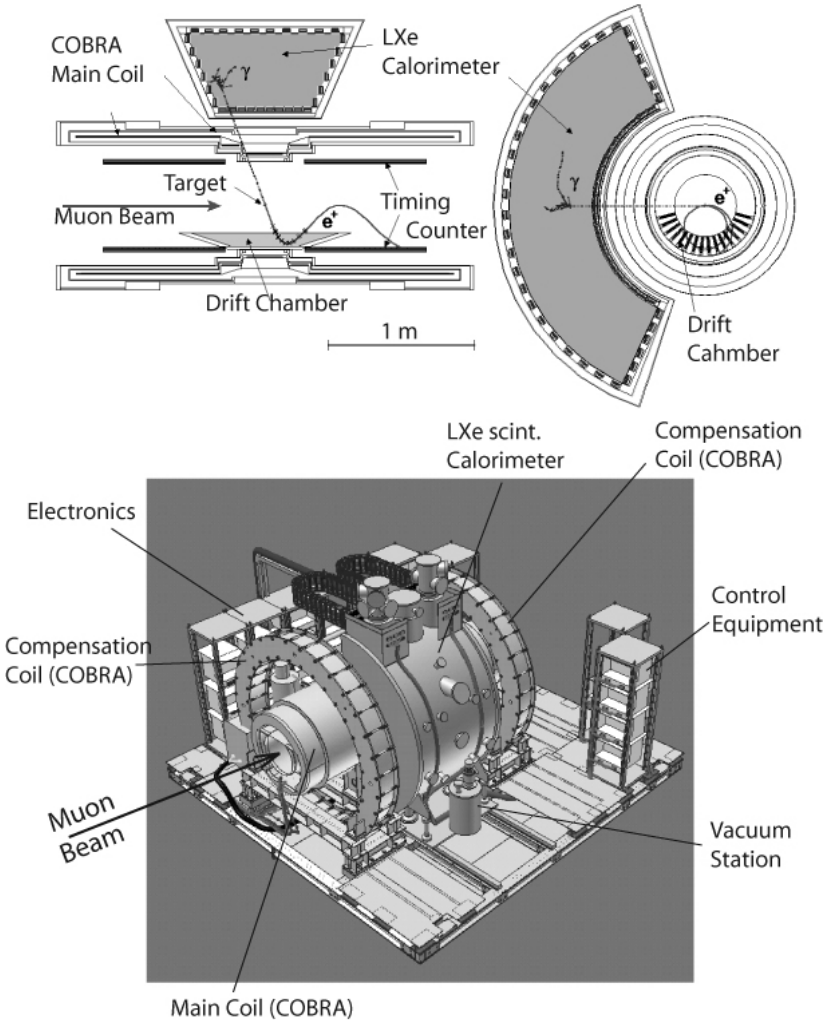

Fig. 9.13 Schematic drawing [189] and the artistic view (courtesy of S. Mihara) of the MEG experimental installation.

Tab. 9.6 Basic parameters of the LXe scintillation calorimeter for the MEG experiment (courtesy of S. Mihara).

Inner radius of the vessel	634 cm
Outer radius of the vessel	1104 cm
Acceptance angle	$\pm$ 60°
Volume of liquid xenon	0.9 m^3
Number of photomultipliers	846
Total mass of PMTs with their holders	450 kg
Weight of the vessel	2.8 tons
Total weight of the calorimeter	6 tons

is comparable with NaI(Tl): it has similar atomic number ($Z = 54$) and density ($\rho \approx 3\ \mathrm{g\,cm^{-3}}$). Its scintillation light yield is also similar to NaI(Tl) but the decay time of LXe scintillation is much shorter (for details, see Chapter 4). Another very important feature of liquid xenon, which no inorganic scintillator has, is a free behavior of electrons liberated in the ionization process that can be easily extracted from the particle track by an electric field and collected onto electrodes. The number of collected electrons produced in the liquid by γ-rays, usually used in medicine, is not very large but detectable (for instance, 511 keV photon produces about 25 000 electrons; 80% of them escape recombination in a field of $\geq 1\ \mathrm{kV\,cm^{-1}}$). Therefore, detection of the ionization signal allows precision position measurements, while the scintillation can ensure the fast timing [262].

Among the problems related to the use of liquid xenon detectors, the necessity of the high purification of xenon in order to ensure both long lifetime of free electrons in the liquid and large attenuation length for VUV photons was noticed. Free electron lifetime has to be large enough to allow an electron to cross the detector (typically, several centimeters), otherwise it would be captured by an impurity molecule, form a very low mobility negative ion and fall out the process of ionization signal formation. Large attenuation length for VUV photons is needed for better scintillation light collection. Another problem was related to the detection of a very small charge signal ($\sim$ 104–106 electrons depending on the multiplication gain) that requires a large number of expensive low-noise charge-sensitive preamplifiers. Among the drawbacks of LXe, there is also the necessity of cooling the chamber down to 163–213 K (Xe vapor pressure at such temperature is between 0.1–0.8 MPa).

Since the 1970s, a remarkable progress in solving the problems associated with the use of LXe in radiation detection has been achieved. Commercial purifiers are now available providing an attenuation length of electrons and VUV photons in liquid xenon of tens of centimeters. A wide experience of designing a *clean* environment (gas handling and purification systems, chamber materials, regeneration of the liquid in the chamber during the operation, etc.) has also been accumulated. Furthermore, a fast development of electronics allows one to think about thousands of reasonably cheap low-noise readout channels.

9.4.1 X-ray Imaging

Since xenon has a high cross section for the photoeffect in the range of 10–100 keV, it has been often considered as working medium for X-ray imaging systems.

9.4.1.1 Analog X-ray Imaging

Gas filled (0.5–1 MPa) chambers with a 1-cm gap were utilized many years ago in iconographic imaging systems. The principle of operation is the following. Charge carriers are collected on stretching an insulating Mylar foil across the appropriate electrode. The charge pattern is developed off-line using a powder or a liquid toner or read out using a guarded electrometer probe to scan the Mylar foil storing potential image. The best position resolution of 10 line pairs per millimeter has been achieved with a xenon filled chamber irradiated by 69 keV X-rays [493]. The iconographic systems did not have wide use because of the bulky method of image processing. The Fuji imaging system with phosphor image-storing screen has been found to be much more convenient, with higher photon absorption efficiency (50% for 80 keV), and better position resolution. A multiwire spark chamber with TV-camera readout has been tested for gamma ray imaging in the range of 20–150 keV [494]. It has shown a good position resolution (3–5 mm) but poor energy resolution and low count rate ($<$5 kHz).

9.4.1.2 Digital X-ray Imaging

CT Scanners

Computer tomography (CT) scanners produce thin cross sectional images of the human body for a wide variety of diagnostic procedures. CT is a noninvasive radiographic technique that involves the reconstruction of a tomographic plane of the body (a slice) from a large number of collected X-ray absorption measurements taken during a scan around the body's periphery. The result of a CT study is usually a set of transaxial slices, which can be mathematically manipulated to produce image slices. CT is clinically useful in the diagnosis of spine and head injuries, intracranial tumors, blood collections in the brain, eye trauma, soft-tissue lesions in the extremities, gastrointestinal lesions, abdominal and pelvic malignancies, and hepatic metastases. CT is also used to visualize the cerebral ventricles and the chest wall, to evaluate intestinal obstructions and deep seated abdominal organs, to examine musculoskeletal degeneration, and to examine the large blood vessels. Obviously, a CT system consists of an X-ray multichannel detection system, an X-ray tube, a gantry, a patient table, and a data-acquisition system. The gantry houses the X-ray tube, detector system, collimators, and rotational circuitry; in some scanners, it also contains a compact, high-frequency X-ray generator. During a CT scan, the table moves the patient into the gantry, and the X-ray tube rotates around the patient. As X-rays pass through the patient to the detectors, the computer acquires and processes data to form an image. The computer also controls the X-rays, gantry motions, table motions, and image display and storage.

Multichannel xenon ionization chambers pressurized up to 2.5 MPa have been developed in the 1970s and 1980s [495, 496] and used in a third generation of clinical CT scanners such as 768-channel Philips model LX CT, General Electric model CT 90000 Series II, and Siemens model Somatom CR. Xenon ionization chambers have several advantages over scintillators including relative simplicity of construction, a high signal level which simplifies the data acquisition system, and homogeneity of the detection material in the cells. The position resolution of multichannel ionization chambers has been measured to be about 2 line pairs per millimeter that is limited with diffusion of electrons and thickness of the absorption gap (parallax error). The position resolution is compromised with detection efficiency and sensitivity of the detectors. In order to achieve good efficiency (60–93%), the ionization chambers had a long path length of 5 to 10 cm in the direction of X-ray travel. With these factors, and because of the inherent collimation provided by the plate electrodes, xenon detectors are not used in the fourth generation of CT scanners, where the source-detector geometry is not constant during the scan.

Multiwire Proportional Chambers

Multiwire proportional chambers (MWPC) allow measuring coordinates in digital form. The intrinsic position resolution can be about 1 mm and the time resolution can be about 10 ns. MWPC was one of the first techniques developed for digital X-ray imaging, autoradiography and tested for SPECT and PET. One of the first high-pressure MWPC gamma camera for imaging low-energy photons was built at MIT and tested at Harvard Medical School [497]. The energy resolution was measured to be 10% FWHM for the 81 keV ^{133}Xe. The count rate was found to be 70 kHz over 10 cm FOV. The position resolution was measured to be 3.7 mm and the efficiency was 70% in the Anger camera mode at 81 keV. The lager camera was built with 25 cm FOV [498]. But, it was tested only at 0.3 MPa pressure a of xenon-methane gas mixture. The detection efficiency of 50% at 40 keV and 10% at 100 keV, the intrinsic energy resolution of 33% at 22 keV and the count rate capacity of 850 kHz for 50% dead time was measured. The intrinsic spatial resolution was about 2.5 mm FMHM but the system resolution with collimator was measured to be only 20–25 mm at 10 cm distance of a point-like gamma ray source from the object. The system resolution of MWPC suffers from the parallax effect and blurring image with fluorescent photons. Review of MWPC developments for X-ray imaging can be found in Refs. [499, 500]. The shortcomings of MWPCs used for gamma ray imaging include a low detection efficiency and poor energy resolution. Their advantages are a high position resolution, high count rate capacity, and the possibility of construction of detectors with large FOV.

9.4.2
Single-Photon Emission Computing Tomography (SPECT)

SPECT is a nuclear medicine tomographic imaging technique using radionuclide emitters of single gamma rays. The technique results in a set of image slices through a patient, showing the distribution of a radiopharmaceutical over the body and in the blood stream. SPECT is a power tool for investigation of cardiac perfusion, development of abnormal tissues and function of organs. SPECT is routinely performed in nuclear medicine clinics.

9.4.2.1 Liquid Xenon Detectors for SPECT

In the first attempt to extend technology of gas MWPC to denser working media for radioisotope medical imaging, L. Alvarez's group at the Lawrence Berkeley Laboratory developed a liquid xenon multiwire chamber [416]. The process of electron multiplication around thin wires in liquid pure xenon was discovered, however only a multiplication factor of ~ 100 was achieved [108, 501]. Large fluctuations of the amplification factor did not allow for achieving the energy resolution acceptable for medical applications. Nevertheless, the group has tested the first liquid xenon gamma ray imaging camera with $\sim 50\ \mathrm{cm}^{-2}$ FOV and 4 mm FWHM position resolution and published the first images acquired with the noble liquid detector [416]. The liquid xenon imaging multiwire proportional chamber of $70 \times 70\ \mathrm{mm}^2$ of active area and 15-mm thick, had 24 anode wires of Ø 5 μm stretched with a step of 2.8 mm perpendicular to 24 cathode strips (Fig. 9.14).

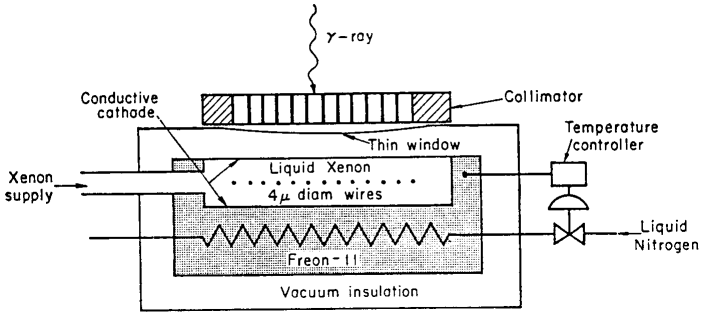

Fig. 9.14 Liquid xenon multiwire gamma ray camera [416].

All the wires were connected to a distributed RC-circuit which was read by low-noise charge-sensitive preamplifiers at both ends. The RC-circuit provided a division of the charge between two outputs proportionally to the position of the point where the charge was injected, i.e., to the position of the wire. The second coordinate was measured by the same method using the

signals induced on the cathode strips. Spatial resolution of the chamber was measured to be as good as 4 mm FWHM for 279 keV γ-rays (^{203}Hg) and some images of small animals were obtained. Energy resolution of 25% FWHM was measured and the detection efficiency for this energy was calculated to be of about 55%. The problem of electrostatic instability of the wires was noticed at a high voltage, therefore, some of the wires could not stand the tension and broke. Practically, the chamber could only work at the gain of 10 or less. A later attempt to use a microstrip plate rather than multiwire chamber in liquid xenon did not show significant advantage [138].

Another approach, using secondary scintillation of xenon gas in a dual-phase emission chamber, was also developed [386,387]. The LXe gamma camera of Ø 250 mm field of view was built (Fig. 7.8).

In this chamber, γ-rays interact also mainly with the liquid, while the measurement of the position takes place in the gas. Liberated electrons drift from the liquid to the gas phase and produce secondary scintillation of the gas while being accelerated in the uniform field between the LXe surface and multiwire electrode (3). The secondary scintillation was detected by an array of photomultiplier tubes (PMT) and position was defined by the method similar to that used in Anger gamma camera with a NaI(Tl) crystal. As the number of photons emitted in secondary scintillation is much larger than in the primary scintillation either in LXe or NaI(Tl) (by a factor of about 70, as reported), position resolution has to be better than that for a gamma ray camera. Indeed, the resolution of 2.5 mm FWHM has been achieved with 122 keV γ-rays. The reported value of energy resolution is 15% FWHM.

9.4.2.2 High-Pressure Noble Gas Detectors for SPECT

Noble gas detectors have been tested in several gamma ray imaging systems. High-pressure xenon electroluminescence detectors possess inherently better energy resolution than crystal scintillators coupled to photomultipliers, which have been used in SPECT for more than 40 years. A huge light output achievable with electroluminescence allows for the development of compact imaging systems of enhanced spatial and contrast resolution. With fiber optics readout, high efficient multilayer gas detectors could be constructed in a variety of cylindrical configurations that is difficult to get with crystal scintillators. This detector technology was reviewed above in Section 6.1.3.

9.4.3 Positron Emission Tomography (PET)

PET is a powerful diagnostic technique based on the measurement of three-dimensional distribution of a tracer labeled with positron-emitting nuclides, such as ^{11}C, ^{13}N, ^{15}O or ^{18}F. The positron is emitted into the surrounding tis-

sue, slows down and finally annihilates with one of the atomic electrons of the medium, resulting in two back-to-back annihilation photons with energy of 511 keV each. The annihilation occurs at the distance of 1–3 mm from the source. By detecting the two photons in coincidence and recording their interaction point coordinates within the detector, it is possible to define a line along which the positron-emitting nuclide is located. A set of such intersecting lines (chords) allows one to reconstruct a three dimensional distribution of the radionuclide. Therefore, the main requirements of a PET detector are: high detection efficiency ($\sim$ 80% for each photon), position resolution in the range of a few millimeters, time resolution as good as possible (it contributes to the decrease of the random coincidence rate and, moreover, if it is in a subnanosecond region, time-of-flight information can assist the image reconstruction), good energy resolution ($<$ 100 keV FWHM) in order to discriminate the photons scattered in the object, and a count rate capability on the order of 10^5–10^6 s^{-1} per 1 cm^2 of the detecting surface [502].

Modern commercially available whole-body PET scanners have an energy resolution of 15% to 25% and a spatial resolution of 4 to 6 mm after reconstruction. The average energy resolution over all events of the sensitive region is not as good as that in the center part of the sensitive region but can be improved by correction of gamma ray interaction points. Considering this, a liquid xenon scintillation PET should produce better energy and spatial resolutions than commercially available crystal scintillation detectors. The scintillation signals from liquid xenon also decay faster than those of other crystal scintillators. Table 9.7 compares the performance of a liquid xenon PET and commercially available crystal PETs. The principal advantage considered below of LXe PET systems is that they allow for the determination of in-depth (Y) coordinates of the point of gamma ray interaction with detector material.

Tab. 9.7 Physical properties of scintillation materials for common PET detectors [260].

	NaI	BGO	GSO	LSO	LXe
Effective atomic number	50	73	58	65	54
Density(g cm^{-3})	3.7	7.1	6.7	7.4	3.0
Relative light output (%)	100	15	20–40	45–70	80
Decay time (ns)	230	300	60	40	2.2, 27, 45

9.4.3.1 Liquid Xenon TPC with a Scintillation Trigger

A detector that would make use of both the excellent scintillating properties of LXe and availability of an ionization signal has been recently proposed for positron emission tomography (PET) [262] and the first results of prototype reported by Chepel et al. [196].

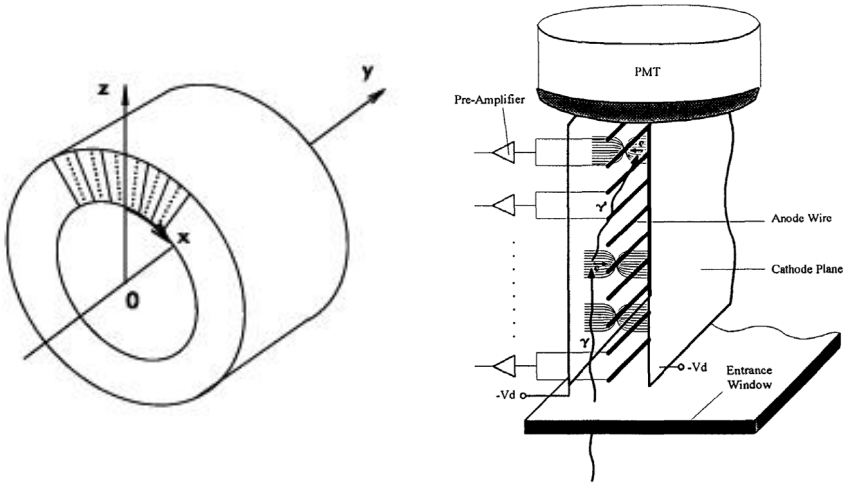

Fig. 9.15 Schematic drawing of the LXe positron tomograph ring (a) based on multiwire cells (b) [196].

The proposed liquid xenon detector is composed of about 200 cells disposed as shown in Fig. 9.15a. Each cell is a multiwire ionization chamber filled with LXe (Fig. 9.15b) with individual readout of each anode wire by a low-noise preamplifier. The cell is viewed by PMTs that detect the primary scintillation produced in the interaction of an annihilation photon within the cell (for 511 keV γ-rays photoabsorption occurs in LXe in 22% of interactions). A negative voltage is applied to cathode plates while the anode wires are kept at ground potential. Therefore, free electrons, liberated due to the ionization of the liquid by the photo or Compton electron, drift toward the wires and induce a current at the input of one of the preamplifiers. As the average energy needed to create an electron–ion pair in LXe is about 16 eV, the 511 keV γ-photon produces $\sim$ 30 000 electrons and ions at the end; nearly 80% of them escape recombination with ions and become free. Thus, a simple charge-sensitive preamplifier with the equivalent noise of 1000 electrons seems to be suitable for the detection of the ionization signal even if there is no charge multiplication near the wires (one thousand electrons is a fairly moderate noise level for modern electronics). The scintillation, detected by PMT, gives a trigger for both coincidence analysis and the measurement of the drift time of free electrons in the detector. The better the coincidence time resolution, the smaller the number of random coincidences and thus, better is the quality of the image. Since LXe is a very fast scintillator, one can expect the time resolution better than 1 ns. Measurement of the drift time of free elec-

trons, from the point where the interaction occurred to anode wire, gives the position of the interaction point relatively to the wire plane (X-coordinate in Fig. 9.15a).

As drift velocity of electrons in LXe is about 2.3×10^5 cm s^{-1}, their maximum drift time in the cell, 1 cm wide, (cathode to cathode) is 2.2 μs. In order to get spatial resolution along X of 1 mm, the accuracy of the drift time measurement should be about 0.4 μs, which is certainly available. In the present design, the position along each wire, i.e., the Y-coordinate, is supplied by comparison of the signals of the PMTs observing the same multiwire cell. Recently, the one-cell prototype of this PET system using induced signal readout from ministrip electrodes deposited on a glass substrate was tested [404]. The prototype demonstrated ≤ 1 mm FWHM position resolution for free charge depositions equivalent to those due to gamma rays with energies from 110 to 220 keV. Note, that this approach probably cannot be used for small PET systems because of the relatively low counting rate per channel ($<1/(2.2\ \mu s) = 4.5\times10^5$ s^{-1}) but it still looks feasible for full scale clinical systems.

9.4.3.2 Liquid Xenon Scintillation Time-of-Flight PET

The short decay time constants and the high scintillation yield of liquid xenon are superior to those of crystal scintillators. Potential use of the scintillation of liquid xenon in detectors imaging positron emitters has been studied by Lavoie [257]. A fast timing available with liquid xenon has been noticed, which could be applicable for time-of-flight measurements of the third coordinate in positron imaging.

The progress of this type of PET depends on the progress made in photomultipliers. Multianode photomultipliers are being considered for the development of a compact LXe PET camera dedicated for small animal tomography [261, 503, 504]. Advantage of this approach is that a relatively small and totally functional PET ring system may be constructed. However, observed technical difficulties in development of very precise and effective multichannel light collection system immersed in LXe still need to be resolved.

Another approach is based on the use of large photomultipliers, well-proven to work in LXe, in the course of development of noble liquid scintillation calorimeters and emission detectors (see Chapters 4 and 6). A principal advantage of using large PMTs is that a better signal-to-noise ratio can be achieved. Doke, Kikichi, and Nishikido [260] designed a time-of-flight (TOF) PET based on a circular ring of 630 1″×1″ Hamamatsu Photonics Corp. photomultipliers R5900-06Al12S. The internal diameter of the sensitive volume is 80 cm, the thickness is 6 cm and the axial length of the sensitive region is 9 cm. The cryostat is filled with 115 L of LXe. Because the timing resolution of the PMTs is about 300 ps, the Z-axis resolution due to time-of-flight techniques is expected to be 3.3 mm (FWHM). Figure 9.16a illustrates a cross

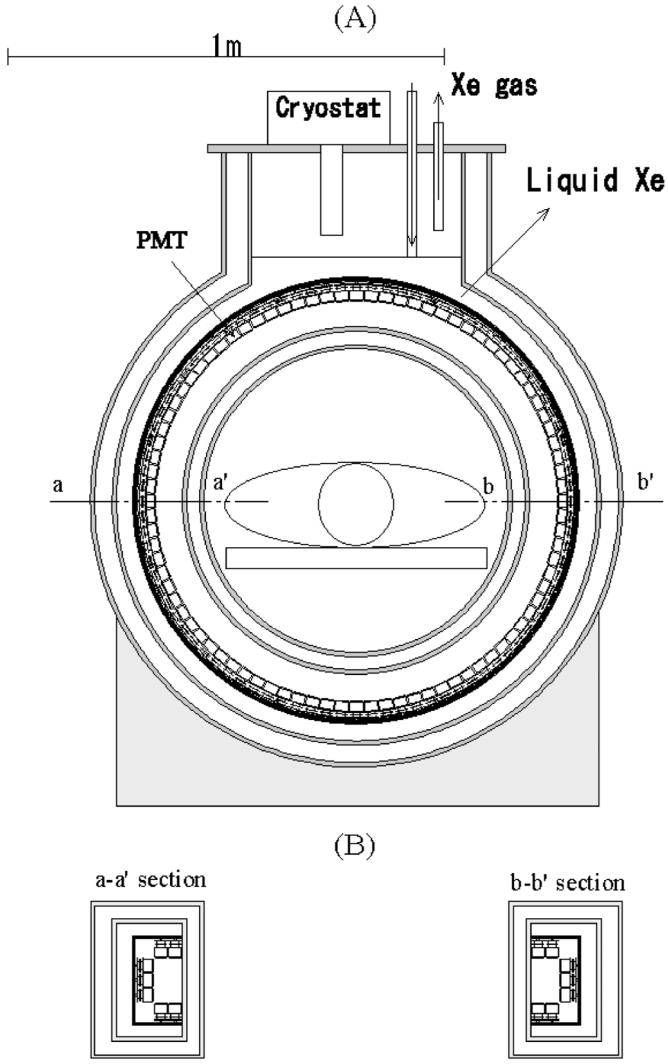

Fig. 9.16 Cross sectional view of liquid xenon scintillation TOF-PET seen from (a) the front and (b) two cross sectional views seen from the top of the TOF-PET.

sectional view of a liquid xenon scintillation TOF-PET seen from the front and Fig. 9.16b represents two cross sectional views of the TOF-PET seen from above. A mechanical cryostat system maintaining the liquid xenon has already been proven during the test of a prototype of the liquid xenon scintillation calorimeter [505]. Table 9.8 shows the main parameters of the TOF-PET.

Tab. 9.8 Comparison of performance of liquid xenon and commercially available whole-body crystal PETs [507].

	ALLEGRO (Philips--ADAC)	ECAT EXACT HR+ (CTI-Siemens)	ADVANCE/ /ADVANCE Nxi (General Electric)	LXe TOF-PET
Scintillator	GSO	BGO	BGO	Liquid Xe
Energy resolution, % FWHM	15	25	25	15.9–20.5
Spatial res. of reconstructed image at center of FOV, mm FWHM	4.8	6.0	4.8	3.3
Time resolution, ps	-	-	-	260–312

References

1 J. Thomson, Nature **55**, 606 (1897)

2 P. Curie, Acad. Sci. **134**, 420 (1902)

3 H. Geiger, Verch. D. Phys. Ges. **15**, 534 (1913)

4 H. Geiger, Phys. Zeits **14**, 1129 (1913)

5 H. Geiger and E. Rutherford, Phil. Mag. **24**, 618 (1912)

6 H. Geiger and E. W. Mueller, Phys. Zeits **29**, 839 (1928)

7 H. Geiger and E. W. Mueller, Phys. Zeits **30**, 489 (1929)

8 H. Geiger and O. Klemperer, Zeits. f. Phys. **49**, 753 (1928)

9 N. Davidson and A. E. Larsh, Phys. Rev. **74**, 220–227 (1948)

10 G. W. Hutchinson, Nature **162**, 610–611 (1948)

11 I. H. Marshall, Phys. Rev. **91**, 905–909 (1953)

12 I. H. Marshall, Rev. Sci. Instrum. **25**, 232–237 (1954)

13 J. A. Northrop and R. Nobles, IRE Trans. Nucl. Sci. **3**, 59–61 (1956)

14 J. A. Northrop, J. C. Gursky and A. E. Johnsruf, IRE Trans. Nucl. Sci. **5**, 81–87 (1958)

15 L. W. Alvarez, Lawrence Radiation Laboratory, Physics Notes **672** (1968)

16 V. G. Fastovsky, A. E. Rovinsky and Y. V. Petrovsky, *Inert Gases (in Russian)*, Atomizdat, Moscow, 1971

17 M. L. Klein and J. B. Venables, editors, *Rare Gas Solids*, vol. 1 & 2, Academic Press, New York, 1977 (1977)

18 A. S. Barabash and A. I. Bolozdynya, *Liquid Ionization Detectors (in Russian)*, EnergoAtomizdat, Moscow, 1993

19 A. Belonoshko, R. Ahuja and B. Johansson, Phys. Rev. Lett. **87**, 165505 (2001)

20 J. D. Bernal, Proc. Royal Soc. A **280**, 299–322 (1964)

21 A. Baldini, C. Bemporad, F. Cei, T. Doke, M. Grassi, T. Haruyama, K. K. et al., 'Transparency of a 100 liter liquid xenon calorimeter prototype and measurement of its energy resolution for 55 MeV photons,' in *Proc. 2005 IEEE Int. Conf. Diel. Liquids, 26 Jun - 1 Jul, Portugal, Coimbra*, pages 337–340, 2005

22 R. L. Platzman, Appl. Rad. Isot. **10**, 116–122 (1961)

23 T. Takahashi, S. Konno, T. Hamada, M. Miyajima, S. Kubota, A. Nakamoto, A. Hitachi, E. Shibamura and T. Doke, Phys. Rev. A **12**, 1771–1775 (1975)

24 A. I. Bolozdynya and V. L. Morgunov, IEEE Trans. Nucl. Sci. **45**, 1646–1655 (1998)

25 G. Manzo, J. Davelaar, A. Peacock, R. D. Adersen and B. G. Taylor, Nucl. Instrum. Meth. **177**, 595–603 (1980)

26 A. Bolozdynya, V. Egorov, A. Koutchenkov, G. Safronov, G. Smirnov, S. Medved and V. Morgunov, IEEE Trans. Nucl. Sci. **44**, 1046–1051 (1997)

27 M. O. Krause, J. Phys. Chem. Ref. Data **8**, 307 (1979)

28 Z. Ophir, B. Raz, J. Jotner et al., J. Chem. Phys. **62**, 650–665 (1975)

29 V. M. Byakov, *Ionization potentials of non-polar liquids (in Russian)*, vol. 165, Preprint, ITEP, Moscow, 1983

30 B. Raz and J. Jortner, Chem. Phys. Lett. **4**, 155–158 (1969)

31 T. Doke, 'Ionization and Excitation by high energy radiation,' in *Electronic Excitations in Liquid Rare Gases* (edited by F. Werner, W. F. Schmidt and E. Illenberger), pages 71–93, American Scientific Publishers, 2005

32 T. Doke, A. Hitachi, J. Kikuchi, K. Masuda, H. Okada and E. Shibamura, Jpn. J. Appl. Phys. **41**, 1538–1545 (2002)

33 A. Bolotnikov and B. Ramsey, Nucl. Instrum. Meth. A **396**, 360–370 (1997)

34 I. M. Obodovskii, S. G. Pokachalov and V. A. Shilov, Zh. Tech. Phys. (in Russian) **50**, 2028–2030 (1980)

35 E. Aprile, R. Mukherjee and M. Suzuki, Nucl. Instrum. Meth. A **302**, 177–185 (1991)

36 M. Miyajima, T. Takahashi, S. Konno, T. Hamada, S. Kubota, H. Shibamura and T. Doke, Phys. Rev. A **9**, 1438–1443 (1974)

37 M. Miyajima, T. Takahashi, S. Konno, T. Hamada, S. Kubota, H. Shibamura and T. Doke, Phys. Rev. A **10**, 1452 (1974)

38 T. Doke, K. Masuda and E. Shibamura, Nucl. Instrum. Meth. A **291**, 617–620 (1990)

39 T. Doke, A. Hitachi, S. Kubota, A. Nakamoto and T. Takahashi, Nucl. Instrum. Meth. **134**, 353–357 (1976)

40 T. Doke, Portugal Phys. **12**, 9–48 (1981)

41 T. Takahashi, S. Konno and T. Doke, J. Phys. C **7**, 230–240 (1974)

42 D. Akimov, A. Bolozdynya, D. Churakov, A. Koutchenkov, V. Kuzichev, V. Lebedenko, I. Rogovsky, M. Chen, V. Chepel and V. Sushkov, Nucl. Instrum. Meth. A **327**, 155–158 (1993)

43 W. F. Schmidt, IEEE Trans. Nucl. Sci. **19**, 389–418 (1984)

44 N. Schwentner, M. Skibowski and W. Steinmann, Phys. Rev. B **8**, 2965–2968 (1973)

45 E. E. Koch, V. Saile, N. Schwentner and M. Skibowski, Chem. Phys. Lett. **28**, 562 (1974)

46 I. M. Obodovskii and S. G. Pokachalov, Low Temp. Phys.(in Russian) **5**, 829–836 (1974)

47 S. P. Ahlen, Rev. Mod. Phys. **52**, 121–173 (1980)

48 E. Aprile, A. Bolotnikov, D. Chen, and R. Mukherjee, Phys. Rev. A **48**, 1313–1318 (1993)

49 D. F. Anderson, T. T. Hamilton, W. H. Ku and R. Novick, Nucl. Instrum. Meth. **163**, 125–134 (1979)

50 G. D. Alkhazov, Zh. Tekh. Fiz. (in Russian) **41**, 1949 (1972)

51 G. D. Alkhazov, Sov. Tech. Phys. **16**, 1995 (1972)

52 N. Ishida, J. Kikuchi, T. Doke and M. Kase, Phys. Rev. A **46**, 1676 (1992)

53 G. Jaffe, Ann. der. Phys. **42**, 303 (1913)

54 D. Lee, Proc. Cambrige Phil. Soc. **30**, 80–101 (1934)

55 H. A. Kramers, Physica **18**, 665–675 (1952)

56 A. E. Bolotnikov, V. V. Dmitrenko, A. S. Romanuk, S. I. Suchkov and Z. M. Uteshev, Sov. J. Tech. Phys. **33**, 449–457 (1988)

57 V. V. Egorov, V. K. Ermilova and B. U. Rodionov, *Spectrometry of gamma radiation at energies below or about 1 MeV in liquid xenon detectors (in Russian)*, vol. 166, Preprint, FIAN, Moscow, 1982

58 A. E. Bolotnikov, V. V. Dmitrenko, S. E. Ulin et al., 'Properties of compressed Xe gas as the detector medium of high-pressure Xe spectrometers,' in *2004 IEEE Nucl. Sci. Symp. & Med. Imag. Conf. Record, 30 Oct - 5 Nov, Norfolk, Virginia*, vol. 1, pages 74–78, 1994

59 L. Onsager, Phys. Rev. **54**, 544–557 (1938)

60 E. Aprile, W. H. M. Ku and J. Park, IEEE Trans. Nucl. Sci. **35**, 37–41 (1988)

61 J. Thomas, D. A. Imel and S. Biller, Phys. Rev. A **38**, 5793–5800 (1988)

62 E. Shibamura, K. Masuda, T. Doke and A. Hitachi, Jpn. J. Appl. Phys. **34**, 1897–1900 (1995)

63 U. Fano, Phys. Rev. **72**, 26 (1947)

64 D. G. Alkhazov, A. P. Komar and A. A. Vorobiev, Nucl. Instrum. Meth. **48**, 1–12 (1967)

65 I. K. Bronic, J. Phys. B **25**, L215–L218 (1992)

66 T. Doke, 'Basic properties of high pressure xenon gas as detector medium,' in *Proc. XeSAT*, pages 92–99, 2005

67 V. V. Dmitrenko, A. S. Romanuk and Z. M. Uteshev, Sov. J. Tech. Phys. **28**, 1440 (1983)

68 C. Levin, J. Germani and J. Markey, Nucl. Instrum. Meth. A **332**, 206–214 (1993)

69 P. Laporte and I. T. Steinberger, Phys. Rev. A **15**, 2538–2544 (1977)

70 A. Bolozdynya, A. Bolotnikov, J. Richards and A. Proctor, Nucl. Instrum. Meth. A **522**, 595–597 (2004)

71 A. Bolozdynya and A. Bolotnikov, IEEE Trans. Nucl. Sci. **53**, 595–597 (2006)

72 K. Masuda, F. Nishikido, E. Shibamura, J. Kikuchi, T. Doke and T. Murakami, 'Fluctuation in energy loss measurement in allene-doped liquid argon for heavy ions,' in *Proc. 2005 IEEE Int. Conf. Diel. Liquids, 26 Jun - 1 Jul, Portugal, Coimbra*, pages 325–328, 2005

73 J. Engel, Phys. Lett. B **264**, 114–119 (1991)

74 J. D. Lewin and P. F. Smith, Astropart. Phys. **6**, 87–112 (1996)

75 M. G. Boulay, A. Hime and J. Lidgard, *Design constrains for a WIMP dark matter and pp Solar neutrino liquid neon scintillation detector*, Preprint arXiv:nucl-ex/0410025v1, 2004

76 R. Bernabei, P. Belli, F. Montecchia, A. Incicchitti, D. Prosperi, C. J. Dai, M. Angelone, B. P. and M. Pillon, Phys. Lett. B **436**, 379–388 (1998)

77 F. Arneodo, B. Baiboussinov, A. Badertscher, P. Benetti et al., Nucl. Instrum. Meth. A **449**, 147–157 (2000)

78 D. Akimov, A. Bewick, D. Davidge, J. Dawson, A. S. Howard, I. Ivaniouchenkov, W. G. Jones, J. Joshi, V. A. Kudryavtsev, L. T. B. et al., Phys. Lett. B **524**, 245–251 (2002)

79 E. Aprile, G. K. L., P. Majewski, K. Ni, M. Yamashita, R. Hasty, A. Manzur and D. N. McKinsey, Phys. Rev. B **72**, 072006 (2005)

80 C. W. Fabian and F. Gianotti, Rev. Mod. Phys. **75**, 1243–1284 (2003)

81 D. Schinzel, Nucl. Instrum. Meth. A **419**, 217–229 (1998)

82 C. W. Fabian and T. Lundlam, Ann. Rev. Nucl. & Part. Sci. **32**, 335–389 (1982)

83 L. G. H. Huxley and R. W. Crompton, *The Diffusion and Drift of Electrons in Gases*, John Wiley & Sons, New York, 1974

84 R. E. Robson, Austral. J. Phys. **25**, 685–693 (1972)

85 S. R. Hunter, J. G. Carter and L. G. Christophorou, Phys. Rev. A **38**, 5539–5551 (1998)

86 A. Pierset and F. Sauli, *Drift and diffusion of electrons in gases: a compilation*, Preprint CERN 84-08, Exp. Phys. Div., 1984

87 A. G. Khrapak and I. T. Yakubov, *Electrons in dense gases and plasma (in Russian)*, Nauka, Moscow, 1981

88 A. F. Borghesani, 'Electron and ion transport in dense gases,' in *Proc. 2005 IEEE Int. Conf. Diel. Liquids, 26 Jun - 1 Jul, Portugal, Coimbra*, pages 13–20, 2005

89 J. P. Hernandez, Rev. Mod. Phys. **63**, 675–697 (1991)

90 V. Atrazhev, J. Appl. Phys. **41**, 1572–1578 (2002)

91 V. V. Dmitrenko, A. S. Romanuk and Z. M. Uteshev, 'Compressed xenon as working medium for detection of low energy gamma quanta,' in *Elementary Particles and Cosmic Rays*, vol. 5, pages 72–83, Atomizdat, Moscow, 1980

92 K. N. Pushkin, N. Hasebe, S. Kobayashi, C. Tezuka, M. Mimura, T. Hosojima, M. N. Kobayashi, T. Doke, M. Miyajima, T. Miyachi, E. Shibamura, S. E. Ulin and V. V. Dmitrenko, 'Scintillation Yield in High Pressure Xenon and Xenon Doped with Methane,' in *2004 IEEE Nucl. Sci. Symp. & Med. Imag. Conf. Rec., 16 - 22 Oct*, vol. 1, pages 550 – 553, 2004

93 R. C. Lanza, W. Rideout, F. Fahey and R. E. Zimmerman, IEEE Trans. Nucl. Sci. **34**, 406–409 (1988)

94 O. Okudaira, C. Chong, N. Hasebe, T. Igarashi, T. Miyachi, H. Okada, S. Kobayashi, M. Takenouchi, E. Yokoyama, T. Doke, E. Shibamura, V. V. Dmitrenko, V. M. Grachev, S. E. Ulin and K. F. Vlasik, 'Measurements of electron drift velocity in the mixture of Xe and He for a new high-pressure Xe gamma-ray detector,' in *Proc. Sci. Sess. MEPhI-2003 Int. Sem. "High pressure xenon"*, vol. 7, pages 202–203, MEPhI, Moscow, 2003

95 R. N. Varney, Phys. Rev. **88**, 362–364 (1952)

96 G. W. C. Kaye and T. H. Laby, *Tables of Physical and Chemical Constants, 16th ed.*, Longman Sc & Tech, 1995

97 W. F. Schmidt, *Liquid State Electronics of Insulating liquids*, CRC Press LLC, 1997

98 T. Wada, K. Shinsaka, H. Namba and Y. Hatano, Can. J. Chem. **55**, 2144–2152 (1977)

99 W. Tauchert, H. Jungblat and W. F. Schmidt, Can. J. Chem. **55**, 1860–1866 (1977)

100 J. Jortner and A. Gaaton, Can. J. Chem. **55**, 1801–1818 (1977)

101 L. S. Miller, S. Howe and W. F. Spear, Phys. Rev. **166**, 871–878 (1968)

102 E. M. Guschin, A. A. Kruglov and I. M. Obodovsky, Zh. Eksper. Teor. Fiz. **82**, 1114–1125 (1982)

103 K. Yoshino, U. Sowada and W. F. Schmidt, Phys. Rev. A **14**, 438–444 (1976)

104 V. M. Atrazhev, A. V. Berezhnov, D. O. Dunikov, I. V. Chernysheva, V. V. Dmitrenko and G. Kapralova, 'Electron transport coefficients in liquid xenon,' in *Proc. 2005 IEEE Int. Conf. Diel. Liquids, 26 Jun - 1 Jul, Portugal, Coimbra*, pages 329–332, 2005

105 H. Schnyders, S. A. Rice and L. Meyer, Phys .Rev. **150**, 127–145 (1966)

106 T. Kimura and G. R. Freeman, Can. J. Phys. **52**, 2220–2222 (1974)

107 E. Shibamura, K. Masuda and T. Doke, *Measurement of the ratio of D_T/D_L for electrons in liquid xenon (in Japanese)*, vol. 62540284, Res. Rep. Ministry Ed. Sci. Sport & Cult. for Grant-in-Aid for Sci. Res., 1987-1988

108 S. E. Derenzo, T. S. Mast, H. Zaklad and R. A. Muller, Phys. Rev. A **9**, 2582–2590 (1974)

109 J. Lekner, Phys. Rev. **158**, 130–137 (1967)

110 M. H. Cohen and J. Lekner, Phys. Rev. **158**, 305–309 (1967)

111 J. Gryko and J. Popielawski, Phys. Rev. A **16**, 1333–1336 (1977)

112 G. Ascarelli, J. Chem. Phys. **71**, 5030–5033 (1979)

113 R. M. Minday, W. F. Schmidt and H. T. Davis, J. Chem. Phys. **51**, 3112–3125 (1971)

114 A. G. Khrapak, W. F. Schmidt and E. Illenberger, 'Localized Electrons, Holes and Ions,' in *Electron Escitations in Liquidfied Rare Gases* (edited by W. F. Schmidt and E. Illenberger), pages 239–273, American Scientific Publishers, 2005

115 J. L. Levine and T. M. Sanders, Phys. Rev. **154**, 138–149 (1967)

116 K. R. Atkins, Phys. Rev. **116**, 1339–1343 (1959)

117 P. G. Le Comber, R. J. Loveland and W. E. Spear, Phys. Rev. B **11**, 3124–3130 (1975)

118 O. Hilt and W. F. Schmidt, J. Phys. Cond. Matt. **6**, L735–L738 (1994)

119 O. Hilt, W. F. Schmidt and A. G. Khrapak, IEEE Trans. Diel. Elect. Insul. **4**, 648–656 (1994)

120 W. E. Spear and P. G. Le Comber, 'Electronic transport properties,' in *Rare Gas Solids* (edited by M. L. Klein and J. A. Venables), vol. 2, pages 1118–1149, Academic Press, London, 1977

121 I. Adamczewscki, *Ionization, Conductivity, and Breakdown in Dielectric Liquids*, Taylor & Francis, London, 1969

122 K. W. Schwarz, Phys. Rev. A **6**, 837–844 (1972)

123 H. T. Davis, S. A. Rice and L. Meyer, J. Chem. Phys. **37**, 947–956 (1962)

124 W. F. Schmidt and K. Yoshino, 'Electric discharge,' in *Electron Escitations in Liquified Rare Gases* (edited by W. F. Schmidt and E. Illenberger), pages 295–315, American Scientific Publishers, 2005

125 K. Wamba, C. Hall, R. Conley, A. Odian, C. Y. Prescott, P. C. Rowson, J. Sevilla, K. Skarpaas, R. DeVoe et al., Nucl. Instrum. Meth. A **555**, 205–210 (2005)

126 A. J. Walters and L. W. Mitchell, J. Phys. D **36**, 1323–1331 (2003)

127 F. Bloch and N. E. Bradbury, Phys. Rev. **48**, 689–696 (1935)

128 G. Bakale, U. Sowada and W. F. Schmidt, J. Chem. Phys. **80**, 2556–2559 (1976)

129 A. S. Barabash, A. A. Golubev, O. V. Kazachenko and B. M. Ovchinnikov, Nucl. Instrum. Meth. A **234**, 451–454 (1985)

130 A. I. Bolozdynya and V. N. Stekhanov, *Capture of quasi-free electrons by oxygen*

in condensed krypton (in Russian), vol. 27, Preprint, ITEP, Moscow, 1984

131 A. V. Kirilenov and S. P. Konovalov, *Xenon of high density in detectors for ionizing radiation (in Russian)*, vol. 149, Preprint of Lebedev Phys. Inst., 1981

132 H. Zaklad, *A purification system for the removal of electronegative impurities from noble gases for noble-liquid nuclear-particle detectors*, Preprint LRL USRL-20690, Berkeley, 1971

133 I. Obodovskiy, 'Solutes in rare gas liquids,' in *Electron Excitations in Liquefied Rare Gases* (edited by W. F. Schmidt and E. Illenberger), pages 95–132, American Scientific Publishers, 2005

134 E. Aprile, K. L. Giboni and C. Rubbia, Nucl. Instrum. Meth. A **241**, 62–71 (1985)

135 H. S. W. Massey, *Negative ions, 2nd ed.*, University Press, Cambridge, 1950

136 L. V. Gurvich, G. B. Karachentsev and V. N. Kondratiev, 'Breaking energy of chemical bonds,' in *Ionization potential and electron affinity (in Russian)*, Nauka, Moscow, 1974

137 H. Shimamori and Y. Hatano, Chem. Phys. **21**, 187–201 (1977)

138 A. P. L. Policarpo, V. Chepel, M. I. Lopes, V. Peskov, P. Geltenbort, R. Ferreira Marques, H. Araujo, F. Fraga, M. A. Alves, P. Fonte, E. P. Lima, M. M. Fraga, M. Salte Leite, K. Silander, A. Onofre and J. M. Pinhao, Nucl. Instrum. Meth. A **365**, 568–571 (1995)

139 J. G. Kim, S. M. Dardin, R. W. Kadel, J. A. Kadyk, V. Peskov and W. A. Wenzel, Nucl. Instrum. Meth. A **534**, 376–396 (2004)

140 G. Carugno, Nucl. Instrum. Meth. A **419**, 617–620 (1998)

141 N. G. Goleminov, B. U. Rodionov and V. Y. Chepel, *Timing method of position-sensitive registration of gamma radiation in electroluminescence detector (in Russian)*, vol. 030, Preprint, MEPI, Moscow, 1985

142 N. G. Goleminov, B. U. Rodionov and V. Y. Chepel, Pribory i Tekhnika Eksperimenta (in Russian) **2**, 61–64 (1986)

143 C. S. N. Conde, 'Gas Proportional Scintillation Counters for X-ray Spectrometry,' in *X-Ray Spectrometry: Recent Technological Advances* (edited by K. Tsuji, J. Injuk and R. Van Grieken), John Wiley & Sons, USA, 2004

144 S. Belogurov, A. Bolozdynya, D. Churakov, A. Koutchenkov, V. Morgunov, V. Solovov, G. Safronov and G. Smirnov, 'High pressure gas scintillation drift chamber with photomultipliers inside working medium,' in *1995 IEEE Nucl. Sci. Symp. & Med. Imag. Conf. Rec., San Francisco*, vol. 1, pages 519–523, 1995

145 A. Bolozdynya, *About electron emission from liquid isooctane (in Russian)*, vol. 103, Preprint, ITEP, Moscow, 1986

146 A. Bolozdynya, V. Egorov, B. Rodionov and V. Miroshnichenko, IEEE Trans. Nucl. Sci. **42**, 565–569 (1995)

147 A. F. Borghesani, G. Carugno, M. Cavenago and E. Conti, Phys. Lett. A **149**, 481–484 (1990)

148 E. M. Guschin, A. A. Kruglov and I. M. Obodovsky, Zh. Eksper. Teor. Fiz. (in Russian) **82**, 1485–1490 (1982)

149 A. I. Bolozdynya, 'Transport of excess electrons through and along a condensed krypton interface,' in *Proc. 3rd Int. Conf. Prop. & Appl. Diel. Mat., July 8-12, Tokyo, Japan*, pages 841–844, 1991

150 S. N. Anisimov, A. I. Bolozdynya and V. N. Stekhanov, JETP Lett. **40**, 829–832 (1984)

151 L. Bruschi, B. Maravigkia and F. E. Moss, Phys. Rev. Lett. **17**, 682–684 (1966)

152 C. M. Surko and F. Reif, Phys. Rev. **175**, 229–241 (1968)

153 W. Schoepe and G. W. Rayfield, Phys. Rev. A **7**, 2111–2121 (1973)

154 L. Bruschi, G. Mazzi and G. Torzo, J. Phys. C **8**, 1412–1422 (1975)

155 F. Ancilotto and F. Toigo, Phys. Rev. B **50**, 12820–12830 (1994)

156 C. M. Surko and F. Reif, Phys. Rev. Lett. **20**, 582–585 (1968)

157 W. Schoepe and K. Dransfeld, Phys. Lett. A **29**, 165–166 (1969)

158 P. Z. Leiderer, Phys.B **98**, 303–308 (1995)

159 P. Leiderer, M. Wanner and W. Schoepe, J. de Physique **39**, 1328–1333 (1978)

160 A. I. Bolozdynya, 'Two-phase electron emission radiation detectors,' in *Proc. 2005 IEEE Int. Conf. Diel. Liquids, 26 Jun*

- *1 Jul, Portugal, Coimbra*, vol. 26, pages 309–312, 2005

161 B. Cabrera, R. M. Clarke, P. Colling et al., Appl. Phys. Lett. **73**, 735–737 (1998)

162 V. N. Trofimov, Nucl. Instrum. Meth. A **370**, 168–170 (1996)

163 A. Bolozdynya, Nucl. Instrum. Meth. A **422**, 314–320 (1999)

164 F. P. Boyle and D. A. J., J. Low Temp. Phys. **23**, 477–486 (1976)

165 B. Halpern and R. Gomer, J. Chem. Phys. **51**, 1031–1047 (1969)

166 A. S. Barabash, A. A. Golubev, O. V. Kazachenko, V. M. Lobashev, B. M. Ovchinnikov and B. E. Stern, Nucl. Instrum. Meth. A **236**, 69–81 (1985)

167 D. M. Chernikova, Low Temp. Phys. **2**, 1374–1378 (1976)

168 A. M. Troyanovky, A. P. Volodin and M. S. Khaikin, JETP Lett. **29**, 65–68 (1979)

169 A. V. Benderskii, R. Zadoyan, N. Schwentner and V. A. Apkarian, J. Chem. Phys. **110**, 1542–1557 (1999)

170 J. B. Birks, *The Theory and Practice of Scintillating Counting*, The Macmillan Company, New York, 1964

171 A. Arodzero, A. Bolozdynya and J. Richards, IEEE Trans. Nucl. Sci. **51**, 322–327 (2004)

172 Y. Salamero, A. Birot, H. Brunet et al., J. Phys. B **21**, 2015–2025 (1988)

173 G. Bressi, G. Carugno, E. Conti, D. Iannuzzi and A. T. Meneguzzo, Nucl. Instrum. Meth. A **440**, 254–257 (2000)

174 P. G. Wilkinson and E. T. Byram, Appl. Opt. **4**, 581–588 (1965)

175 R. E. Packard, F. Reif and C. M. Surko, Phys. Rev. Lett. **25**, 1435–1439 (1970)

176 R. E. Huffman, J. C. Larrabee and Y. Tanaka, Appl. Opt. **4**, 1581–1588 (1965)

177 H. A. Koehler, L. J. Ferderber, D. L. Redhead and P. J. Ebert, Phys. Rev. A **9**, 768–781 (1974)

178 M. Stockton, J. W. Keto and W. A. Fitzsimmons, Phys. Rev. A **5**, 372–380 (1972)

179 C. M. Surko, R. E. Packard, C. J. Dick and F. Reif, Phys. Rev. Lett. **24**, 657–659 (1970)

180 I. Fugol, Pure & Appl. Chem. **69**, 1219–1226 (1997)

181 O. Chesnovski, B. Raz and J. J. Jortner, Chem. Phys. **59**, 5554–5561 (1973)

182 D. Akimov, A. Bolozdynya, B. A. et al., 'Time characteristics of scintillations excited in xenon doped liquid Krypton by relativistic particles,' in *1996 IEEE NSS Conf. Rec., 2 - 9 Nov, Anaheim, California*, vol. 1, pages 80–83, 1996

183 O. Chesnovsky, B. Raz and J. J. Jortner, Chem. Phys. **57**, 4628–4632 (1972)

184 J. Jortner, L. Meyer, S. A. Rice and E. G. J. Wilson, Chem. Phys. **42**, 4250–4253 (1965)

185 E. Boursey, J. Y. Roncin and H. Damany, Phys. Rev. Lett. **25**, 1279–1280 (1970)

186 G. Baldini, Phys. Rev. **128**, 1562–1567 (1962)

187 J. E. Simmons and R. B. Perkins, 'Use of a liquid helium scintillator as a neutron polarimeter,' in *Proc. Symp. Nucl. Instr.*, pages 62–66, Academic Press, New York, 1962

188 S. N. Anisimov, A. I. Bolozdynya and V. N. Stekhanov, Pribory i Tekhnika Eksperimenta (in Russian) **6**, 51–55 (1984)

189 A. Baldini, C. Bemporad, F. Cei, T. Doke, M. Grassi, A. Grebenuk, D. Grigoriev, T. Haruyama, K. K. et al., Nucl. Instrum. Meth. A **545**, 753–764 (2005)

190 D. Y. Akimov, A. I. Bolozdynya, D. L. Churakov, V. N. Afonasiev, S. G. Belogurov, A. D. Brastilov, A. A. Burenkov, V. H. Dodohov, L. G. Gusev, A. V. Kuchenkov, V. F. Kuzichev, V. N. Lebedenko, T. A. Osipova, I. A. Rogovsky, G. A. Safronov, S. A. Simonychev, V. N. Solovov, V. S. Sopov, G. N. Smirnov and V. P. Tchernyshev, IEEE Trans. Nucl. Sci. **42**, 2244–2249 (1995)

191 D. Y. Akimov, V. N. Afonasyev, S. G. Belogurov, A. I. Bolozdynya, A. D. Brastilov, A. A. Burenkov, D. L. Churakov, L. N. Gusev, V. F. Kuzichev, V. N. Lebedenko, T. A. Osipova, I. A. Rogovsky, A. Safronov, A. Simonychev, V. N. Solovov, V. S. Sopov, G. N. Smirnov, V. P. Tchernyshev, R. A. Minakova, V. M. Shershukov and V. H. Dodohov, *LKr Scintillation Calorimeter (in Russian)*, vol. 97, Preprint, ITEP, Moscow, 1993

192 N. Ishida, M. Chen, T. Doke, K. Hasuike, A. Hitachi, M. Gaudreau, M. Kase, Y. Kawada, J. Kikuchi, T. Komiyama, K. Kuwahara, K. Masuda, H. Okada, Y. H. Qu, M. Suzuki and T. Takahashi, Nucl. Instrum. Meth. A **384**, 380–386 (1997)

193 G. M. Seidel, R. E. Lanou and W. Yao, Nucl. Instrum. Meth. A **489**, 189–194 (2002)

194 A. Braem, A. Gonidec, D. Scginzel, W. Sedel, E. F. Clayton, G. Davies, G. Hall, R. Payne, S. Roe, J. Striebig, T. S. Virdee and D. J. A. Cockerill, Nucl. Instrum. Meth. A **320**, 228–237 (1992)

195 V. Y. Chepel et al., Nucl. Instrum. Meth. A **349**, 500–505 (1994)

196 V. Chepel, M. I. Lopes, H. M. Araújo, R. Ferreira Marques, M. A. Alves and A. J. P. L. Policarpo, 'First tests of a liquid xenon multiwire drift chamber for PET,' in *Conf. Rec. IEEE Nucl. Sci. Symp. & Med. Imag. Conf., Norfolk*, vol. 3, pages 1155–1159, 1994

197 K. Saito, H. Tawara, T. Sanami, E. Shibamura and S. Sasaki, IEEE Trans. Nucl. Sci. **49**, 1674–1680 (2002)

198 S. Kobayashi, N. Hasebe, T. Igarashi et al., Nucl. Instrum. Meth. A **531**, 327–332 (2004)

199 T. Doke, H. J. Crawford, C. R. Gruhn, A. Hitachi, J. Kikuchi, K. Masuda, S. Nagamiya, E. Shibamura and S. Tamada, Nucl. Instrum. Meth. A **235**, 136–141 (1985)

200 H. J. Crawford, T. Doke, A. Hitachi, J. Kikuchi, P. J. Lindstrom, K. Masuda, S. Nagamiya and E. Shibamura, Nucl. Instrum. Meth. A **256**, 47–54 (1987)

201 E. Shibamura, H. J. Crawford, T. Doke, J. M. Engelarge, I. Flores, A. Hitachi, J. Kikuchi, P. L. Lindstrom, M. K. and K. Ogura, Nucl. Instrum. Meth. A **260**, 437–442 (1987)

202 T. Doke, H. J. Crawford, A. Hitachi, J. Kikuchi, P. J. Lindstrom, K. Masuda, E. Shibamura and T. Takahashi, Nucl. Instrum. Meth. A **269**, 291–296 (1988)

203 A. Hitachi, T. Doke and A. Mozumder, Phys. Rev. B **46**, 436 (1992)

204 M. Tanaka, T. Doke, A. Hitachi, T. Kato, J. Kikuchi, K. Masuda, T. Murakami, F. Nishikido, H. Okada, K. Ozaki, E. Shibamura and E. Yoshihira, Nucl. Instrum. Meth. A **457**, 454–463 (2001)

205 T. Doke, E. Shibamura and S. J. Kubota, Phys. Soc. Jpn. **68**, 2433–2438 (1999)

206 T. Doke and K. Masuda, Nucl. Instrum. Meth. A **420**, 62–80 (1999)

207 M. Miyajima, S. Sasaki and H. Tawara, IEEE Trans. Nucl. Sci. **40**, 417–423 (1993)

208 R. A. Michniak, R. Alleaume, D. N. McKinsey and J. M. Doyle, Nucl. Instrum. Meth. A **482**, 387–394 (2002)

209 S. Kubota, M. Hishida, M. Suzuki and J. Ruan(Gen), Phys. Rev. B **20**, 3486–3496 (1979)

210 H. A. Roberts and F. L. Hereford, Phys. Rev. A **7**, 284–291 (1973)

211 A. C. Sinnock and B. L. Smith, Phys. Rev. **181**, 1297–1307 (1969)

212 L. M. Barkov, A. A. Grebenuk, N. M. Ryskulov, P. Y. Stepanov and S. G. Zverev, Nucl. Instrum. Meth. A **379**, 482–483 (1996)

213 N. H. Gale, Nucl. Phys. **38**, 252–258 (1962)

214 S. Heron, R. W. P. McWhirter and E. H. Rhoderick, Nature **174**, 564 (1954)

215 S. Heron, R. W. P. McWhirter and E. H. Rhoderick, Proc. Roy. Soc. A **234**, 565–583 (1956)

216 P. Lindblom, T. Olsson, K. Aho and O. J. Solin, Phys. B **25**, 3489–3503 (1992)

217 D. N. McKinsey, C. R. Brome, S. N. Dzhosyuk et al., Phys. Rev. A **67**, 062716 (2003)

218 D. N. McKinsey, C. R. Brome, J. S. Butterworth, S. N. Dzhosyuk, P. R. Huffman, C. E. H. Mattoni, J. M. Doyle, R. Golub and K. Habicht, Phys. Rev. A **59**, 200–204 (1999)

219 T. Suemoto and H. Kanzaki, J. Phys. Soc. Jap. **46**, 1554 (1979)

220 S. Himi, T. Takahashi, J. Ruan (Gen) and S. Kubota, Nucl. Instrum. Meth. **203**, 153–157 (1982)

221 A. Hitachi, T. Takahashi, N. Funayama, K. Masuda, J. Kikuchi and T. Doke, Phys. Rev. B **27**, 5279–5285 (1983)

222 S. Kubota, M. Hishida and J. J. Ruan(Gen), Phys. C **11**, 2645–2651 (1978)

223 W. Baum, S. Götz, H. Heckwolf, P. Heeg, M. Muttere and J. P. Theobald, IEEE Trans. Nucl. Sci. **35**, 102–104 (1988)

224 D. Y. Akimov, A. I. Bolozdynya, D. L. Churakov, V. A. Lamkov, A. A. Sadovsky, G. A. Safronov and G. N. Smirnov, Nucl. Instrum. Meth. A **327**, 575–576 (1993)

225 S. Kubota, M. Hishida, M. Suzuki and J. Ruan(Gen), Nucl. Instrum. Meth. **196**, 101 (1982)

226 T. Doke, *Decay Shape of scintillation due to electromagnetic showers in liquid xenon*, Ann. Rep. 1992, Inst. Nucl. Study Univ. Tokyo, 1993

227 D. Varding, J. Becker, L. Frankenstein, B. Peters, M. Runne, A. Schr¨der and G. Zimmerer, L. Temp. Phys. **19**, 427–436 (1993)

228 A. E. Grün and E. Z. Schopper, Naturforsch **6A**, 698 (1951)

229 E. H. Thorndike and W. J. Shlaer, Rev. Sci. Instrum. **30**, 838 (1959)

230 H. Fleishman, H. Einbinder and C. S. Wu, Rev. Sci. Instrum. **30**, 1130–1131 (1959)

231 C. E. Engelke, Trans. Nucl. Sci. **NS-7**, 32 (1960)

232 S. A. Baldin and V. V. Matveev, Pribory i Tekhnika Eksperimenta (in Russian) **4**, 5–18 (1963)

233 R. L. Aamodt, L. J. Brown and G. M. Smith, Rev. Sci. Instrum. **37**, 1338–1340 (1966)

234 A. E. Evans and J. J. Malanify, *^{4}He gas scintillator for prompt-neutron fissile assay of small samples*, LA-5885-PR Progress Report, UC-15, 1975

235 A. E. Evans, *Development of a high-pressure He-3 neutron scintillator spectrometer*, Tech. Note LA-Q2TN-82-109, Los Alamos Nat. Lab, 1982

236 M. S. Derzon, D. E. Slaughter and S. G. Prussin, IEEE Trans. Nucl. Sci. **33**, 247–249 (1986)

237 P. R. Huffman, C. R. Brome, J. S. Butterworth, K. J. Coakley, M. S. Dewey, S. N. Dzhosyuk, R. Golub, G. L. Greene, K. Habicht, S. K. Lamoreaux, C. E. H. Mattoni, D. N. McKinsey, F. E. Wietfeldt and J. M. Doyle, Nature **403**, 62–64 (2000)

238 M. I. Lopes and V. Chepel, 'Rare Gas Liquid Detectors,' in *Electronic Excitations in Liquefied Rare Gases* (edited by W. F. Shmidt and E. Illenberger), pages 331–388, American Scientific Publishers, 2005

239 E. Aprile, R. Mukherjee and M. Suzuki, IEEE Trans. Nucl. Sci. **37**, 553–558 (1990)

240 M. Minerskjöld, T. Lindblad and B. Lund-Jensen, Nucl. Instrum. Meth. A **336**, 373–377 (1993)

241 N. Funayama et al., Ionizing Radiation (in Japanese) **8**, 62 (1982)

242 V. N. Solovov, A. Hitachi, V. Chepel, M. I. Lopes, R. Ferreira Markus and A. J. P. L. Policarpo, Nucl. Instrum. Meth. A **488**, 572–578 (2002)

243 K. Ni, E. Aprile, D. Day, K. L. Giboni, J. A. M. Lopes, P. Majewski and M. Yamashita, Nucl. Instrum. Meth. A **551**, 356–363 (2005)

244 I. R. Barabanov, V. N. Gavrin and A. M. Pshukov, Nucl. Instrum. Meth. A **254**, 355–3607 (1987)

245 I. R. Barabanov, V. N. Gavrin, S. V. Girin, V. N. Kornoukhov and A. M. Pshukov, JETP Lett. **43**, 166–167 (1986)

246 E. Aprile, K. L. Giboni, P. Majewski, K. Ni and M. Yamashita, IEEE Trans. Nucl. Sci. **51**, 1986–1990 (2004)

247 F. Neves, V. Chepel, V. Solovov, A. Pereira, M. I. Lopes, J. P. daCunha, P. Mendes, A. Lindote, C. P. Silva, R. F. Marques and A. J. P. L. Policarpo, IEEE Trans. Nucl. Sci. **52**, 2793–2800 (2005)

248 S. Mihara, T. Doke, Y. Kamiya, T. Mashino, T. Mori et al., IEEE Trans. Nucl. Sci. **49**, 588–591 (2002)

249 M. Chen, C. Dionisi, Y. Galaktionov, G. Herten, P. LeCoultre, Y. Kamyshkov, K. Luebelsmeyer, W. Walraff and R. K. Yamamoto, Nucl. Instrum. Meth. A **267**, 43–48 (1988)

250 W. Braunschweig et al., Part. Fields **33**, 13 (1986)

251 M. Chen, M. Mullins, D. Pelly, K. Sumorok, D. Akyuz, E. Chen, M. P. J. Gaudreau, A. Bolozdynya et al., Nucl. Instrum. Meth. A **327**, 187–192 (1993)

252 T. Doke, T. Haryayama, T. Ishida, A. Maki, T. Mashimo, S. Mihara, T. Mitsuhashi, T. Mori, H. Nishiguchi, W. Ootani, S. Orito, K. Ozone, R. Sawada, S. Suzuki, K. Terasawa, M. Yamashita,

J. Yashima and T. Yoshimura, Nucl. Instrum. Meth. A **503**, 199–202 (2003)

253 T. Doke, T. Haryayama, K. Kasami, A. Maki, T. Mashimo, S. Mihara, T. Miyazawa, T. Mori, H. Nishiguchi, W. Ootani, S. Orito, K. Ozone, R. Sawada, S. Suzuki, K. Terazawa, M. Yamashita and J. Yashima, Nucl. Instrum. Meth. A **503**, 280–294 (2003)

254 S. Mihara, Nucl. Instrum. Meth. A **518**, 45–48 (2004)

255 M. L. Brooks, Y. K. Chen, M. D. Cooper, P. S. Cooper, M. Dzemidzic et al., Phys. Rev. Lett. **83**, 1521–1524 (1999)

256 Y. Kuno and Y. Okada, Rev. Mod. Phys. **73**, 151–202 (2001)

257 L. Lavoie, Medical Physics **3**, 283–293 (1976)

258 F. Nishikido, T. Doke, J. Kikuchi, T. Mori, K. Takizawa and M. Yamamoto, Jpn. J. Appl. Phys. **43**, 779–784 (2004)

259 F. Nishikido, T. Doke, J. Kikuchi, T. Mori, H. Murayama, T. Ooshita and H. Takahashi, Jpn. J. Appl. Phys. **44**, 5193–5198 (2005)

260 T. Doke, F. Nishikido and J. Kikuchi, Nucl. Instrum. Meth. A, to be published (2006)

261 M.-L. Gallin-Martel, P. Martin, F. Mayet, J. Ballon, G. Barbier, C. Barnoux, J. Berger, D. Bondoux, O. Bourrion, J. Collot, D. Dzahini, R. Foglio, L. Gallin-Martel, A. Garrigue, S. Jan, P. Petit, P. Stassi, F. Vezzu and E. Tourbefier, *Experimental study of a liquid xenon PET prototype module*, Preprint arXiv:physics/0511065v1, 2005

262 V. Y. Chepel, Nucl. Tracks Rad. Meas. **21**, 47–51 (1993)

263 E. Aprile, E. A. Baltz, A. Curioni, K.-L. Giboni, C. J. Hailey, L. Hui, M. Kobayashi, K. Ni, W. W. Craig, R. J. Gaitskell, U. Oberlack and T. Shutt, *A 1-tonne liquid xenon experiment for a sensitive dark matter search*, Preprint astro-ph/0207670, 2002

264 D. Cline, Y. Seo, F. Sergiampietri and H. Wang, IEEE Trans. Nucl. Sci. **49**, 1238–1242 (2002)

265 M. Yamashita, T. Doke, J. Kikuchi and S. Suzuki, Astropart. Phys. **20**, 79–84 (2003)

266 W. Schockley, J. Appl. Phys. **9**, 635–636 (1938)

267 S. Ramo, Proc. IRE **27**, 584 (1939)

268 D. S. McGregor, Z. He, H. A. Seifert and D. K. Wehe, Appl. Phys. Lett. **72**, 792–794 (1998)

269 Z. He, Nucl. Instrum. Meth. A **463**, 250–267 (2001)

270 C. R. Hill, Nucl. Instrum. Meth. **12**, 299–306 (1961)

271 V. V. Dmitrenko, A. G. Dvornyak, V. M. Gratchev, O. N. Kondakova, K. V. Krinova, A. Y. Papchenko, D. V. Sokolov, S. E. Ulin, Z. M. Uteshev and K. F. Vlasik, Nucl. Instrum. Meth. A **422**, 326–330 (1999)

272 O. Bunemann, T. E. Cranshaw and J. A. Harvey, Can. J. Res. A **27**, 191 (1949)

273 H. Okada, T. Doke, T. Kashiwagi, J. Kikuchi, M. Kobayashi, K. Masuda, E. Shibanura, S. Suzuki, T. Takashima and K. Terasawa, Nucl. Instrum. Meth. A **451**, 427–438 (2000)

274 M. Kase, T. Akioka, H. Mamyoda, J. Kikuchi and T. Doke, Nucl. Instrum. Meth. **227**, 311–317 (1984)

275 A. J. P. L. Policarpo, M. A. F. Alves, M. Salete, S. C. P. Leite and M. C. M. Dos Santos, Nucl. Instrum. Meth. **118**, 221–226 (1974)

276 T. Doke, N. Ishida and M. Kase, Nucl. Instrum. Meth. B **36**, 373 (1992)

277 V. V. Dmitrenko, A. E. Bolotnikov, I. V. Chernysheva, A. M. Galper, G. V. M., O. N. Kondakovs, S. V. Krivov, S. I. Sutchkov, S. E. Ulin, Z. M. Uteshev, K. F. Vlasik and Y. T. Yurkin, 'Compressed gaseous xenon gamma-ray detector with high energy resolution,' Proc. SPIE **1734**, 90–97 (1992)

278 J. Kikuchi and T. Doke, Nucl. Instrum. Meth. **99**, 469–475 (1972)

279 K. Masuda, A. Hitachi, Y. Hoshi and T. Doke, Nucl. Instrum. Meth. **174**, 439–446 (1980)

280 T. Doke, T. Hayashi et al., Nucl. Instrum. Meth. A **237**, 475–485 (1985)

281 V. M. Aulchenko, S. G. Klimenko, G. M. Kolachev et al., Nucl. Instrum. Meth. A **289**, 468–474 (1990)

282 P. N. Luke, IEEE Trans. Nucl. Sci. **42**, 207–213 (1995)

283 C. J. Sullivan, Z. He, G. K. Knoll, G. Tepper and D. K. Wehe, Nucl. Instr. Meths. A **505**, 238–241 (2003)

284 A. Bolotnikov, A. Bolozdynya, R. DeVito and J. Richards, IEEE Trans. Nucl. Sci. **51**, 1262–1269 (2004)

285 S. Hustache-Ottini, C. Monsanglant-Louvet, S. Haan, V. Dmitrenko, V. Grachev and S. Ulin, 'New trends in the high pressure xenon ionization chamber development,' in *Proc. Sci. Sess. MEPhI-2003 Int. Sem. "High pressure xenon"*, vol. 7, pages 216–217, MEPhI, Moscow, 2003

286 C. Rubbia, *The Liquid-argon time projection chamber: a new concept for Neutrino Detector*, CERN Report CERN-EP/77-08, 1977

287 G. Carugno, G. Bressi, S. Cerdonio, E. Conti, A. T. Meneguzzo, R. Onofrio, D. Zanello, U. Beriotto, S. De Biasia, N. M. et al., Nucl. Instrum. Meth. A **376**, 149–154 (1996)

288 E. Aprile, A. Curioni et al., Proc. SPIE **4140**, 333–343 (2000)

289 U. Oberlack, E. Aprile, A. Curioni and K. L. Giboni, IEEE Trans. Nucl.Sci. **48**, 1041–1047 (2001)

290 K. Takisawa, T. Doke, J. Kikuchi, K. Masuda, N. Matsuoka, F. Nikishido, H. Okada and E. Shibamura, Proc. SPIE **4851**, 1294–1301 (2002)

291 E. Conti, R. DeVoe, G. Gratta, T. Koffas, S. Waldman, J. Wodin, D. Akimov, G. Bower, M. Breidenbach, R. Conley, M. Danilov, Z. Djurcic, A. Dolgolenko, C. Hall, A. Odian, A. Piepke, C. Y. Prescott, P. C. Rowson, K. Skarpaas, J.-L. Vuilleumier, K. Wamba and O. Zeldovich, Phys. Rev. B **68**, 054201 (2003)

292 E. Aprile, K. L. Giboni, S. Kamat, P. Majewski, K. Ni, B. Singh and M. Yamashita, 'Measurement of the ionization and scintillation yield of nuclear recoils in liquid xenon,' in *Proc. 2005 IEEE Int. Conf. Diel. Liq. 26 Jun - 1 Jul, Coimbra, Portugal*, pages 313–316, 2005

293 A. Hitachi, H. Ichinose, J. Kikuchi, T. Doke, K. Masuda and E. Shibamura, Phys. Rev. B **55**, 5742–5748 (1997)

294 H. Ichinose, T. Doke, A. Hitachi, J. Kikuchi, K. Masuda and E. Shibamura, Nucl. Instrum. Meth. A **322**, 216–224 (1992)

295 T. Doke, Nucl. Instrum. Meth. B **234**, 203–209 (2005)

296 V. V. Dmitrenko, V. N. Lebedenko, A. S. Romanuk and Z. M. Uteshev, Pribory i Tekhnika Eksperimenta (in Russian) **5**, 49 (1981)

297 V. V. Dmitrenko, A. S. Romanuk, Z. M. Uteshev and V. K. Chernyatin, Pribory i Tekhnika Eksperimenta (in Russian) **1**, 51 (1982)

298 V. V. Dmitrenko, A. S. Romanuk, S. I. Suchkov, Z. M. Uteshev and V. K. Chernyatin, Pribori I Tekhhnika Eksperimenta (in Russian) **1**, 20–23 (1986)

299 M. Z. Iqbal, H. E. Henrikson, L. W. Mitchell, B. M. G. O'Callaghan, J. Thomas and H. T. k. Wong, Nucl. Instrum. Meth. A **259**, 459–465 (1987)

300 A. S. Barabash, V. M. Novokov and B. M. Ovchinnikov, Nucl. Instrum. Meth. A **77-79**, 77–79 (1991)

301 S. E. Ulin, V. Dmitrenko, A. E. Bolotnikov, K. F. Vlasik and A. M. Galper, Instr. Exper. Techiques **37**, 142–145 (1994)

302 G. Tepper and J. Losee, Nucl. Instrum. Meth. A **356**, 339–346 (1995)

303 G. Tepper and J. Losee, Nucl. Instrum. Meth. A **368**, 862–864 (1996)

304 A. Bolozdynya, V. Egorov, A. Koutchenkov, G. Safronov, G. Smirnov, S. Medved and V. Morgunov, Nucl. Instrum. Meth. A **385**, 225–238 (1997)

305 G. C. Smith, W. R. Kane and J. R. Lemley, IEEE Trans. Nucl. Sci. **NS-45**, 1024–1033 (1998)

306 A. Bolotnikov and B. Ramsey, Nucl. Instrum. Meth. A **383**, 619–623 (1996)

307 R. Kessick and G. Tepper, Nucl. Instrum. Meth. A **490**, 243–250 (2002)

308 A. E. Bolotnikov, R. Austin, A. Bolozdynya and J. Richards, Proc. SPIE **5540**, 216–224 (2004)

309 S. D. Kiff, Z. He and G. C. Tepper, IEEE Trans. On Nucl. Sci. **52**, 2932–2939 (2005)

310 J. L. Lacy, A. Athanasiades, N. N. Shehad, L. Sun, T. D. Lyons, C. S. Martin and L. Bu, 'Cylindrical high pressure xenon spectrometer using scintillation light pulse correction,' in *2004 IEEE Nucl. Sci. Symp. & Med. Imag. Conf. Rec. 16 - 22 Oct, Rome, Italy*, vol. 1, pages 16–20, 2004

311 V. Radeka, Ann. Rev. Nucl. Part. Sci. **38**, 217–277 (1988)

312 A. I. Bolozdynya and R. DeVito, IEEE Trans. Nucl. Sci. **51**, 931–933 (2004)

313 A. J. P. L. Policarpo, Space Sci. Instr. **3**, 77–107 (1977)

314 A. Parsons, T. K. Edberg, B. Sadoulet, S. Weiss, J. Wilkerson, K. Hurley, R. P. Lin and G. Smith, IEEE Trans. Nucl. Sci. **37**, 541–546 (1990)

315 G. F. Knoll, *Radiation Detection and Measurement, 3rd ed.*, John Wiley & Sons, New York, 2000

316 J. A. M. Lopes, J. M. F. Dos Santos and C. A. N. Conde, Nucl. Instrum. Meth. A **454**, 421–425 (2000)

317 J. F. C. A. Veloso, J. M. F. dos Santos and C. A. N. Conde, Nucl. Instr. Meth A. **457**, 253–261 (2001)

318 C. A. N. Conde and A. J. P. L. Policarpo, Nucl. Instrum. Meth. **53**, 7 (1967)

319 D. A. Goganov and A. A. Schultz, Nucl. Instrum. Meth. A **394**, 151–156 (1997)

320 F. I. Borges, J. M. dos Santos, T. H. Dias, F. P. Santos, P. J. Rachinhas and C. A. Conde, Nucl. Instrum. Meth. A **422**, 321–325 (1999)

321 J. C. Van Staden, M. Mutterer, J. Pannicke, K. P. Schelhaas, J. Foh and J. P. Theibald, Nucl. Instrum. Meth. **157**, 301–304 (1978)

322 A. J. Campos, IEEE Trans. Nucl. Sci. **31**, 133–135 (1984)

323 P. Mine, Nucl. Instrum. Meth. A **343**, 99–108 (1994)

324 P. A. Bagryanskii, V. S. Belkin, V. G. Dudnikov and E. I. Shabalov, Pribory i Tekhnika Eksperimenta (in Russian) **1, 4**, 43–45, 49–52 (1985)

325 D. Akimov, S. Belogurov, A. Bolozdynya, D. Churakov, M. Chumakov, Y. Grishkin, S. Pozdnyakov and V. Solovov, 'Xenon Scintillation Drift Chamber with Microstrip Readout,' in *Proc. Int. Works. Micro-strip Gas Chamb. 13 - 14 Oct 1994, Legnaro, Italy* (edited by G. Della Mea and F. Sauli), pages 215–216, Edizioni Progetto, Padova, 1994

326 C. M. B. Montiero, J. F. C. A. Veloso, J. M. F. dos Santos and C. A. N. Conde, IEEE Trans. Nucl. Sci. **49**, 907–911 (2002)

327 V. Dangendorf, A. Breskin, R. Chechik and H. Schmidt-Bocking, Nucl.Instr. Meth. A **289**, 322–324 (1990)

328 A. I. Bolozdynya and R. A. Austin, Proc. SPIE **5540**, 206–215 (2004)

329 G. Charpak, Ann. Rev. Nucl. Sci. **20**, 195–254 (1970)

330 C. Cavalleri, E. Gatti and G. Redaelli, Il Nuovo Cemento **XXV**, 1282–1291 (1962)

331 P. Gorenstein and K. Topka, IEEE Trans. Nucl. Sci. **24**, 511–514 (1977)

332 M. Suzuki, T. Takahashi, Y. Awaya, M. Oura, M. Yamamoto, T. Uruga, T. Mizogawa and K. Masuda, Rev. Sci. Instrum. **66**, 2336–2338 (1995)

333 F. Sauli, Nucl. Instrum. Meth. A **522**, 93–98 (2004)

334 F. A. F. Fraga, L. M. S. Margato, S. T. G. Fetal, M. M. F. R. Fraga, R. Ferrera Marques and A. J. P. L. Policarpo, Nucl. Instrum. Meth. A **513**, 379–387 (2003)

335 A. J. P. L. Policarpo, Nucl. Instrum. Meth. **196**, 53–62 (1982)

336 G. Charpak, G. Peterson, P. Policarpo and F. Sauli, Nucl. Instrum. Meth. **148**, 471 (1978)

337 W. H.-M. Ku, C. J. Hailey and M. H. Vartanian, Nucl. Instrum. Meth. **196**, 63–67 (1982)

338 W. J. C. Okx, C. W. E. Eijk, R. Ferreira Marques, R. W. Hollander, D. Langerveld and A. Stanovni, IEEE Trans. Nucl. Sci. **33**, 391–394 (1986)

339 K. S. K. Lum, D. H. Lee and W. H.-M. Ku, IEEE Trans. Nucle. Sci. **35**, 506–510 (1988)

340 G. Charpak and G. A. Renard, J. Phys. Radium **17**, 585 (1956)

341 G. Charpak, W. Dominik, J. P. Fabre, J. Gaudaen, V. Peskov, F. Sauli and M. Suzuki, IEEE Trans. Nucl. Sci. **35**, 483–486 (1988)

342 A. Breskin, R. Chechick, V. Dangendorf, S. Majevski, G. Malamud, A. Pansky and D. Varitsky, Nucl. Instrum. Meth. A **310**, 57–69 (1991)

343 P. Astier, A. Breskin, G. Charpak, W. Dominik, P. Fonte, J. Gaudaen, Y. Giomataris, A. Gougas, V. Peskov, F. Sauli, N. Soloimey and N. Zaganidis, IEEE Trans. Nucl. Sci. **36**, 300–304 (1989)

344 R. A. Austin, T. Minamitani and B. D. Ramsey, Proc. SPIE **2010**, 118–125 (1993)

345 G. Charpak, H. N. Ngoc and A. Policarpo, *Neutral radiation detection and localization*, United States Patent 4,286,158, August 25, 1981

346 H. Bräuning, A. Breskin, R. Chechik, V. Dangendorf, A. Demian, K. Ulmann and H. Schmidt-Böcking., Nucl. Instrum. Meth. A **348**, 223–227 (1994)

347 G. Manzo, S. Giarrusso, A. Santangelo, F. Ciralli, G. Fazio, S. Piraino and A. Segreto, Astronomy & Astrophysics Suppl. Ser. **122**, 341–356 (1997)

348 M. Gubarev, B. Ramsey and J. Apple, Proc. SPIE **5501**, 339–345 (2003)

349 H. Nguyen Ngoc, Nucl. Instrum. Meth. **154**, 597–601 (1978)

350 H. Nguyen Ngoc, J. Jeanjean, H. Itoh and G. Charpak, Nucl. Instrum. Meth. **172**, 603–608 (1980)

351 H. Nguyen Ngoc, J. Jeanjean, J. Jacobe and P. Mine, Nucl. Instrum. Meth. **188**, 677–679 (1981)

352 B. G. Taylor, J. Davelaar, G. Manzo and A. Peacock, IEEE Trans. Nucl. Sci. **28**, 857–860 (1981)

353 V. Egorov, Instrum. Exp. Techn. (in Russian) **1**, 53–57 (1988)

354 T. Ohashi, K. Ebisawa, Y. Fukazawa, K. Hiyoshi, M. Horii et al., Publ. Astron. Sic. Japan **48**, 157–170 (1996)

355 A. J. P. L. Policarpo, M. A. F. Alves and C. A. N. Conde, Nucl. Instrum. Meth. **55**, 105–119 (1967)

356 I. B. Keirim-Markus, A. K. Savinsky, V. G. Tchaikovsky and A. S. Yakovlev, Instr. Exp. Tech. **15**, 46–48 (1972)

357 M. Suzuki and S. Kubota, Nucl. Instrum. Meth. **164**, 197–199 (1979)

358 G. Charpak, S. Majevski and F. Sauli, Nucl. Instrum. Meth. **126**, 381–389 (1975)

359 V. I. Baskakov, V. K. Chernjatin, B. A. Dolgoshein, V. N. Lebedenko, A. S. Romanyuk, V. P. Pustovetov, A. P. Shmeleva and P. S. Vasiljev, Nucl. Instrum. Meth. **158**, 129–135 (1979)

360 B. U. Rodionov and V. Y. Chepel, *USSR invention certificate No.888706*, vol. 26, Byul. Izobreteniy, 1983

361 D. Y. Akimov, A. A. Burenkov, V. F. Kuzichev, V. L. Morgunov and V. N. Solovov, IEEE Trans. Nucl. Sci. **45**, 497–501 (1998)

362 A. J. P. L. Policarpo, M. A. F. Alves, M. C. M. Dos Santos and M. J. T. Carvalho, Nucl. Instrum. Meth. **102**, 337–348 (1972)

363 A. Bolozdynya, C. E. Ordonez and W. Chang, 'A concept of cylindrical Compton camera for SPECT,' in *1977 IEEE NSS & MIC Record, M06-08, 9 - 15 Nov*, vol. 2, pages 1047–1051, 1997

364 A. Lansiart, A. Seigneur, J.-L. Moretti and J. P. Morucci, Nucl. Instrum. Meth. **135**, 47 (1976)

365 M. Miyajima, K. Masuda, A. Hitachi, T. Doke, T. Takahashi, S. Konno, T. Hamada, S. Kubota, A. Nakamoto and E. Shibamura, Nucl. Instrum. Meth. **134**, 403–405 (1979)

366 K. Masuda, S. Takasu, T. Doke, T. Takahashi, A. Nakamoto, S. Kubota and E. Shibamura, Nucl. Instrum. Meth. **160**, 247–253 (1979)

367 P. Crespo, J. van der Marel, V. Chepel, M. I. Lopes, D. Santos, L. Janeiro, V. Solovov, R. Ferreira Marques and A. J. P. L. Policarpo, IEEE Trans. Nucl. Sci. **47**, 2119–2126 (2000)

368 M. Miyajima, K. Masuda, A. Hitachi, T. Doke, T. Takahashi, S. Konno, T. Hamada, S. Kubota, A. Nakamoto and E. Shibamura, Nucl. Instrum. Meth. **134**, 403–407 (1976)

369 B. A. Dolgoshein, V. N. Lebedenko and B. U. Rodionov, JETP Lett. **11**, 513–516 (1970)

370 I. A. Boriev, A. A. Balakin and B. S. Yakovlev, Khimiya Vysokih Energiy **12**, 1514 (1978)

371 A. I. Bolozdynya, *Excess electron emission from condensed krypton and other nonpolar dielectrics (in Russian)*, vol. 172, Preprint, ITEP, Moscow, 1986

372 S. N. Anisimov, A. S. Barabash, A. I. Bolozdynya and V. N. Stekhanov, Atom. Energia (in Russian) **66**, 415–417 (1989)

373 B. A. Dolgoshein, V. N. Lebedenko and B. U. Rodionov, Elementary Particles and Cosmic Rays (in Russian) **3**, 86 (1973)

374 A. I. Bolozdynya, V. N. Lebedenko, B. U. Rodionov et al., Zh. Tekh. Fiz. (in Russian) **48**, 1514 (1978)

375 D. F. Anderson, G. Charpak, R. A. Holroyd and D. C. Lamb, Nucl. Instrum. Meth. A **261**, 445–448 (1987)

376 S. N. Anisimov, A. I. Bolozdynya, V. V. Egorov and V. N. Stekhanov, *Application of mixtures of krypton and methane in emission detectors (in Russian)*, vol. 104, Preprint, ITEP, Moscow, 1986

377 A. Bondar, A. Buzulutskov, L. Shekhtman, R. Snopkov and Y. Tikhonov, Nucl. Instrum. Meth. A **524**, 130–141 (2004)

378 A. I. Bolozdynya, O. K. Egorov, A. A. Korshunov, V. P. Miroshnichenko, B. U. Rodionov, L. I. Sokolov and V. V. Sosnovtsev, JETP Lett. **25**, 375–378 (1977)

379 A. I. Bolozdynya, O. K. Egorov, A. A. Korshunov et al., 'Solid Krypton Emission Chamber,' in *Solid State Nuclear Track Detectors* (edited by H. Francois et al.), pages 29–32, Pergamon Press, Oxford-New York, 1980

380 A. I. Bolozdynya, O. K. Egorov, V. P. Miroshnichenko, B. U. Rodinov and E. N. Shuvalova, 'Observation of abnormal trecks in emission chamber (in Russian),' in *Elementarnye Chastitsy i Kosmicheskie Luchi*, vol. 5, pages 65–70, Atomizdat, Moscow, 1980

381 S. N. Anisimov, A. S. Barabash, A. I. Bolozdynya and V. N. Stekhanov, Pribory i Tekhnika Eksperimenta (in Russian) **1**, 79–82 (1989)

382 B. A. Dolgoshein, A. A. Kruglov, V. N. Lebedenko et al., Elemementanye Chastitsy Atomnogo Yadra (in Russian) **1**, 167 (1973)

383 A. V. Abramov, B. A. Dolgoshein, A. A. Kruglov and R. B. U., JETP Lett. **21**, 82 (1975)

384 A. I. Bolozdynya, V. P. Miroshnichenko and B. U. Rodionov, Zh. Tekh. Fiz. (in Russian) **2**, 64 (1977)

385 E. M. Guschin, A. A. Kruglov, I. M. Obodovsky et al., Pribory i Tekhnika Eksperimenta (in Russian) **3**, 49–52 (1982)

386 V. V. Egorov, V. P. Miroshnichenko, B. U. Rodionov, A. I. Bolozdynya, S. D. Kalashnikov and V. L. Krivoshein, Nucl. Instrum. Meth. **205**, 373–374 (1983)

387 A. I. Bolozdynya, V. V. Egorov, S. D. Kalashnikov, V. L. Krivoshein, V. Miroshnichenko and B. Rodionov, Pribory i Tekhnika Eksperimenta (in Russian) **4**, 43–45 (1985)

388 D. Cline, A. Curioni, A. Lamarina et al., Astropart. Phys. **12**, 373–377 (2000)

389 N. J. T. Smith, Nucl. Instrum. Meth. A **513**, 215–221 (2003)

390 M. Yamashita, T. Doke, K. Kawasaki, J. Kikuchi and S. Suzuki, Nucl. Instr. Meth A **535**, 692–698 (2004)

391 M. Hori, Nucl. Instr. Meth A **522**, 420–431 (2004)

392 M. P. Lorikyan and N. N. Trofimchuk, Nucl. Instrum. Meth. **140**, 505 (1977)

393 A. N. Arvanov, A. G. Akhperdzhanyan and V. G. Gavalyan, Pribory i Tekhnika Eksperimenta (in Russian) **4**, 58 (1981)

394 R. U. Martinelli and D. C. Fischer, Proc. IEEE **62**, 1339–1360 (1974)

395 B. A. Dolgoshein, Int. Meet. On Proport. and Drift Chamb. in Dubna **1** (1975)

396 E. M. Guschin, *Investigation of electron dynamics in position-sensitive detectors based on condensed argon and xenon (in Russian)*, PhD thesis, MEPI, Moscow, 1981

397 V. N. Afanasiev, V. V. Barmin, A. A. Burenkov et al., Phys. Atom. Nucl. **66**, 500–502 (2003)

398 C. collaboration, *The SuperCDMS Experiment*, Preprint arXiv:astro-ph/0502435 v1, 2005

399 S. Amerio, S. Amoruso, M. Antonello, P. Aprili et al., Nucl. Instrum. Meth. A **527**, 329–410 (2004)

400 V. D. Ashitkov, A. S. Barabash, S. G. Belogurov et al., Nuclear Physics B (Proc. Suppl.) **70**, 233–235 (1999)

401 A. S. Barabash, V. V. Kuzminov, V. M. Lobashev, V. M. Novikov, B. M. Ovchinnikov and A. A. Pomansky, Phys. Lett. B **223**, 273–276 (1989)

402 S. N. Anisimov, A. S. Barabash, A. I. Bolozdynya and V. N. Stekhanov, *Installation for spark purification of up to 100 liters of noble liquids (in Russian)*, vol. 106, Preprint, ITEP, Moscow, 1987

403 V. V. Dmitrenko, V. M. Grachev, S. E. Ulin, Z. M. Uteshev and K. F. Vlasik, Appl. Rad. Isot. **52**, 739–743 (2000)

404 V. Solovov, V. Chepel, A. Pereira, M. I. Lopes, R. Ferreira Marques and A. J. P. L. Policarpo, Nucl. Instrum. Meth. A **477**, 184–190 (2002)

405 F. Costantini, Nucl. Instrum. Meth. A **409**, 570–574 (1998)

406 A. Bondar, A. Buzulutskov, D. Pavlyuchenko, R. Snopkov and Y. Tikhonov, Nucl. Instrum. Meth. A **548**, 439–445 (2005)

407 F. A. F. Fraga, S. T. G. Fetal, M. M. F. R. Fraga, E. F. S. Balau, L. M. S. Margato, R. Ferreira Marques, A. J. P. L. Policarpo and F. Sauli, Nucl. Instrum. Meth. A **525**, 57–61 (2004)

408 A. Bondar, A. Buzulutskov, A. Grebenuk, D. Pavlyuchenko, R. Snopkov and Y. Tikhonov, Nucl. Instrum. Meth. A **556**, 273–280 (2005)

409 J. M. Maia, D. Mormann, A. Breskin, R. Checgik and J. F. C. A. J. M. F. dos Santos, Nucl. Instr. Meth A. **523**, 334–344 (2004)

410 A. I. Pipko, V. Y. Pliskovsky and E. A. Penchko, *Design and calculations of vacuum systems (in Russian)*, Energia, Moscow, 1979

411 C. Benvenutti, 'Non-evaporable getters: from pumping strips to thin film coatings,' in *Proc. EPAC, Stockholm, June*, 1998

412 A. S. Barabash and V. N. Stekhanov, Nucl. Instrum. Meth. A **327**, 168–170 (1993)

413 N. Ishida, T. Doke, J. Kikuchi, K. Kuwahara, T. Kashiwagi, M. Ichige, K. Hasuike, K. Ito, S. Ben, A. Hitachi, Y. H. Qu, K. Masuda, M. Suzuki, M. Kase, T. Takahashi, M. Chen, S. Sumarok, M. Gaudreau and E. Aprile, Nucl. Instrum. Meth. A **327**, 152–154 (1993)

414 Y. Tanaka, H. Inoue and S. S. Holt, Publ. Atsron. Soc. Japan **46**, L37–L41 (1994)

415 G. Bressi et al., Nucl. Instrum. Meth. A **292**, 585–592 (1990)

416 H. Zaklad, S. E. Derenzo, R. A. Muller, G. Smadja, R. G. Smith and L. W. Alvarez, IEEE Trans. Nucl. Sci. **19**, 206–212 (1972)

417 G. Bressi, G. Carugno, E. Conti, E. D'Uscio and D. Zanello, Nucl. Instrum. Meth. A **327**, 163–167 (1993)

418 I. M. Obodovsky and V. A. Shilov, 'Electrical breakdown of liquid xenon (in Russian),' in *Experimental Methods in Nuclear Physics*, vol. 6, pages 43–46, Atomizdat, Moscow, 1980

419 S. G. Pokachalov, M. A. Kirsanov, A. A. Kruglov and I. M. Obodovsky, Nucl. Instrum. Meth. A **327**, 159–162 (1993)

420 A. E. Bolotnikov, V. V. Dmitrenko, A. S. Romanuk, S. I. Suchkov and Z. M. Uteshev, Instrum. Exp. Tech. **29**, 802–806 (1986)

421 A. Bolotnikov and B. Ramsey, Nucl. Instrum. Meth. A **383**, 619–623 (1996)

422 T. Namba, Nucl. Phys. B (Proc. Suppl.) **143**, 506 (2005)

423 E. Barrelet, B. Andrieu, A. Babaev, E. Banas, P. Bederede et al., Nucl. Instrum. Meth. A **490**, 204–222 (2002)

424 P. Benetti et al., Nucl. Instrum. Meth. A **329**, 361–364 (1993)

425 V. N. Solovov, V. Chepel, M. I. Lopes, A. Hitachi, R. Ferreira Markus and A. J. P. L. Policarpo, Nucl. Instrum. Meth. A **516**, 462–474 (2004)

426 V. R. Weidner and J. J. Hsia, J. Opt. Soc. Am. G **71** (1981)

427 J. E. Proctor and P. Y. Barnes, J. Res. NIST **101**, 619–627 (1996)

428 P. Kadkhoda, D. Ristau and F. von Alvensleben, Proc. SPIE **3578**, 544–554 (1998)

429 D. N. McKinsey, C. R. Brome, J. S. Butterworth, R. Golub, K. Habicht, P. R. Huffman, S. K. Lamoreaux, C. E. H. Mattoni and J. M. Doyle, Nucl. Instrum. Meth. B **132**, 351–358 (1997)

430 V. Kumar and A. K. Datta, Appl. Opt. **18**, 1414–1417 (1979)

431 S. Duncan, M. Kuss, R. van der Meer and B. Wojtsekhowski, *Effect of p-TP coating to the Quantum Efficiency of Burle 8854 Photomultiplier Tubes*, Jefferson Lab Tech. Note JLAB-TN-98-006, 1998

432 H. M. Araujo, V. Y. Chepel, M. I. Lopes, J. van der Marel, R. Ferreira Marques and

A. J. P. L. Policarpo, IEEE Trans. Nucl. Sci. **45**, 542–549 (1998)

433 H. M. Araujo, V. Y. Chepel, M. I. Lopes, R. Ferreira Marques and A. J. Policarpo, Rev. Sci. Instrum. **68**, 34–40 (1997)

434 K. Terasawa, T. Doke, J. Kikuchi, Y. Kuno, A. Maki, T. Mashimo, K. Masuda, T. Miyazawa, T. Mori, H. Okada, S. Orito, Y. Sugimoto, S. Takenaka, S. Tanaka, M. Yamashita and K. Yoshimura, *Technical Report No.98-12*, Adv. Res. Inst. for Sci. & Eng., Waseda Uni., 1998

435 H. M. Araujo, A. Bewisk, D. Davidge et al., Nucl. Instrum. Meth. A **521**, 407–415 (2004)

436 K. Masuda, A. Aprile, H. L. Ding, T. Doke, S. S. Gau, M. P. J. Gaudreau, A. Hitachi, H. Ichinose, N. Ishida, M. Kase, T. Kashiwagi, J. Kikuchi, T. Nakasugi, E. Shibamura, K. Sumorok and T. Takahashi, Nucl. Instrum. Meth. A **309**, 489–496 (1991)

437 T. Kashiwagi, T. Doke, J. Kikuchi, N. Ishida, H. Onabe and M. Obinata, Nucl. Instrum. Meth. A **327**, 148–151 (1993)

438 G. Bressi, G. Carugno, E. Conti, C. Del Noce and D. Iannuzzi, Nucl. Instrum. Meth. A **461**, 378–380 (2001)

439 H. Rabus, U. Kroth, M. Richter, G. Ulm, J. Friese, R. Gernhause, A. Kastenmuller, P. Maier-Komor and K. Zeitelhack, Ann. Rev. Nucl. Part. Sci. **38**, 217–277 (1988)

440 T. Meinschad, L. Ropelewski and F. Sauli, Nucl. Instrum. Meth. A **547**, 342–345 (2005)

441 E. Aprile, A. Bolotnikov, D. Chen, F. Xu and V. Peskov, Nucl. Instrum. Meth. A **353**, 55–58 (1994)

442 Y. Tanaka, Adv. Space Res. **5**, 81–89 (1985)

443 Y. Ueda, T. Takahashio, H. Inque et al., J. Astrophys. **518**, 656–671 (1999)

444 B. D. Ramsey, C. D. Alexander, J. A. Apple, C. M. Benson, K. L. Dietz et al., J. Astrophys. **568**, 432–435 (2002)

445 R. A. Austin, B. D. Ramsey, C. L. Tse and C. G. Zirnstein, Proc. SPIE **3765**, 714–720 (1999)

446 S. E. Ulin, K. F. Vlasik, A. M. Galper, V. M. Grachev, V. V. Dmitrenko, V. I. Liagushin, Z. M. Uteshev and Y. T. Yurkin, Proc. SPIE **3114**, 499–504 (1997)

447 E. Aprile, A. Curioni, K. L. Giboni, M. Kobayashi, U. G. Oberlack, S. Ventura, E. L. Chupp, P. P. Dunphy, T. Doke and J. Kikuchi, N. Astr. Rev. **48**, 257–262 (2004)

448 E. Aprile, U. G. Oberlack, A. Curioni, V. Egorov, K. L. Giboni, S. Ventura, T. Doke, J. Kikuchi, K. Takizawa, E. L. Chupp and P. P. Dunphy, *Preliminary results from the 1999 baloon flight of the liquid xenon gamma-ray imaging telescope (LXeGRIT)*, Preprint astro-ph/0012398, 1998

449 E. Aprile, U. G. Oberlack, A. Curioni, V. Egorov, K.-L. Giboni, S. Ventura, T. Doke, J. Kikuchi, K. Takizawa, E. L. Chupp and P. P. Dunphy, Proc. SPIE **4140**, 344–359 (2000)

450 E. Aprile, C. A., K.-L. Giboni, U. Oberlack and S. Ventura, IEEE Trans. Nucl. Sci. **48**, 1299–1305 (2001)

451 E. Aprile, C. A., K.-L. Giboni, M. Kobayashi, K. Ni and U. Oberlack, IEEE Trans. Nucl. Sci. **50**, 1303–1308 (2003)

452 A. Curioni, *Laboratory and balloon flight performance of the liquid xenon gamma ray imaging telescope (LXeGRIT)*, PhD thesis, Columbia University, 2001

453 E. Aprile, V. Egorov, K. Giboni, T. Kozu, F. Xu, T. Doke et al., Nucl. Instrum. Meth. A **412**, 425–436 (1998)

454 D. N. McKinsey and K. J. Cookley, Astropart. Phys. **22**, 355–368 (2005)

455 C. collaboration, Phys. Rev. D **66**, 122003 (2002)

456 A. Barabash and A. Bolozdynya, JETP Lett. **49**, 356–359 (1989)

457 X. collaboration, 'The XENON dark matter search: status of XENON10,' in *Proc. TAUP 10-14 September, Zaragosa*, 2005

458 Y. Takeuchi, 'Distillation purification of xenon for krypton and measurement of radon contamination in liquid xenon,' Proc. XeSAT (2005)

459 N. Spooner, 'Dark matter searched at Boulby Mine - towards 1 tonne xenon and directional detectors,' in *SLAC Sum. Inst., 28 Jul - 8 Aug, Stanford.*, 2003

460 W. Collaboration, 'WARP: a double phase Argon parogramme for Dark Matter detection,' in *EP2005 Int. Europhys. Conf.*

High En. Phys., 21-27 July 2005, Lisboa, Portugal, 2005

461 J. F. Beacom and P. Vogel, Phys. Rev. Lett. **83**, 5222–5224 (1999)

462 M. Baldo-Ceolin, G. Puglierin, V. Barmin, A. Barabash, A. Bolozdynya, A. Dolgolenko, V. Nozik, A. Starostin, V. Shebanov, G. Tumanov and O. Zeldovish, 'Large volume liquid Xe detector for anti-neutrino magnetic momentum measurement from electron/anti-neutrino scattering at nuclear reactor,' in *Proc. III Int. Symp. Weak Electromag. Interact. Nucl., 15 - 22 Jun, Dubna, Russia*, page 753, 1992

463 A. Drukier and L. Stodolsky, Phys. Rev. D **30**, 2295–2309 (1984)

464 C. Hagmann and A. Bernstein, IEEE Trans. Nucl. Sci. **51**, 2151–2156 (2004)

465 S. R. Elliot and P. Vogle, Annu. Rev. Nucl. Part. Sci. **52**, 115–151 (2002)

466 V. A. Artemiev, E. V. Brakchman, M. A. Ivanovskii, A. K. Karelin, V. V. Kirichenko, O. M. Kozodaeva, A. V. Kuchenkov, V. A. Lyubimov, A. I. Mitin, T. N. Tsvetkova and O. Y. Zeldovich, Phys. Atom. Nucl. **63**, 1238–1241 (2000)

467 V. A. Artemiev, V. A. Belov, E. V. Brakhman, O. Y. Zel'dovich, A. Karelin, V. V. Kirichenko, O. M. Kozodaeva, A. V. Kuchenkov, V. A. Lyubimov, A. I. Mitin and T. N. Tsvetkova, Instrum. Exp. Tech. **48**, 177–188 (2005)

468 R. Luescher, J. Farine, F. Boehm, J. Busto, K. Gabathuler, G. Gerasio, H. E. Henrikson, V. Jörgens, K. Lou, A. Paic, D. Schenker, A. Tadsen, M. Treichel, J.-L. Vuilleumier, J.-M. Vuilleumier and H. Wong, Phys. Lett. B **434**, 407–414 (1999)

469 M. Danilov, R. DeVoe, A. Dolgolenko, G. Giannini, G. Gratta, P. Picchi, A. Piepke, F. Pietropaolo, P. Vogel, J.-L. Vuilleumier, Y.-F. Wang and O. Zeldovich, Physics Lett. B **480**, 12–18 (2000)

470 A. Barabash, A. Bolozdynya and V. Stekhanov, *On possibility of investigation of double beta decay with liquid ionization chambers (in Russian)*, vol. 154, Preprint, ITEP, Moscow, 1986

471 V. D. Ashitkov, A. S. Barabash, S. G. Belogurov et al., Part. Nucl. Lett. **3**, 69–73 (2001)

472 Y. B. Zeldovich and M. Y. Khlopov, JETP Lett. **34**, 141–145 (1981)

473 C. Sáenz, E. Cerezo, E. García, A. Morales, J. Morales, R. Núñez Lagos, A. Ortiz de Solórzano, J. Puimedón, A. Salinas, M. L. Sarsa, J. A. Villar, A. Klimenko, V. Kuzminov, N. Metlinsky, V. Novikov, A. Pomansky and B. Pritychenko, Phys. Rev. C **50**, 1170–1174 (1994)

474 S. C., E. Cerezo, E. Garcia et al., Nucl. Instrum. Meth. A **356**, 220–229 (1995)

475 V. B. Anikeev, S. V. Belikov, S. N. Gurshiev, A. G. Denisov, S. P. Denisov, N. N. Fedyakin, V. I. Kochetkov, V. M. Korablev, K. V. I. et al., Nucl. Instrum. Meth. A **419**, 596–601 (1998)

476 C. Cerry, S. P. Denisov, R. N. Krasnokutsky, S. A. Medved, V. Mikhailov, N. I. Naumov, S. A. Polovnikov, E. A. Rasuvaev, F. Sergiampietri and R. S. Shivalov, Nucl. Instrum. Meth. **214**, 217–235 (1983)

477 C. Cerry, S. P. Denisov, R. N. Krasnokutsky, S. A. Medved, V. Mikhailov, N. I. Naumov, S. A. Polovnikov, E. A. Rasuvaev, F. Sergiampietri and R. S. Shivalov, Nucl. Instrum. Meth. **227**, 227–236 (1984)

478 V. B. Anikeev, S. N. Gurshiev, S. P. Denisov, O. S. Zolina, S. R. Kelner, T. M. Kirina, R. P. Kokoulin, V. V. Lipaev, A. A. Petrukhin, A. M. Rybin, Sergiampietri and E. E. Yanson, Phys. Atom. Nucl. **68**, 259–266 (2005)

479 B. Andrieu, A. Babayev, J. Ban, E. Banas, E. Barrelet et al., Nucl. Instrum. Meth. A **336**, 460–498 (1993)

480 P. Puzo, Nucl. Instrum. Meth. A **494**, 340–345 (2002)

481 B. Lund-Jensen, IEEE Trans. Nucle. Sci. **51**, 2181–2186 (2004)

482 B. Aubert et al., Nucl. Instrum. Meth. A **500**, 178–201, 202–231 (2003)

483 G. D. Barr, C. Bruschini, C. Bocquet, P. Buchholz, D. Cundy, N. Doble, W. Funk, L. Gatignon, A. Gonidec, B. Hallgren et al., Nucl. Instrum. Meth. A **370**, 413–424 (1996)

484 V. M. Aulchenko, A. K. Barladyan, A. E. Bondar, S. Ganzhur, G. Y. Kezerashvili, S. G. Klimenko, G. M. Kolachev et al., Nucl. Instrum. Meth. A **379**, 475–477 (1996)

485 V. V. Anashin, V. M. Aulchenko, B. O. Baibusinov, V. Balashov, E. M. Baldin et al., Nucl. Instrum. Meth. A **428**, 420–425 (2002)

486 A. Baranov, V. Baskakov, G. Bondarenko et al., Nucl. Instrum. Meth. A **294**, 439–445 (1990)

487 A. A. Grebenuk, Nucl. Instrum. Meth. **453**, 199–204 (2000)

488 W. J. Willis and V. Radeka, Nucl. Instrum. Meth. **120**, 221–236 (1974)

489 J. Kotcher, 'Design, performance and upgrade of D0 Calorimeter,' in *Proc. 1994 Beijing Calorim. Symp. IHEP, 25 - 27 Oct, Beijing, China*, 1994

490 L. Apanasevich, J. Bacigalupi, W. Baker, G. Ballocchi, M. Begel, R. Benson, S. Blisk, C. Bromberg et al., Nucl. Instr. Meth. A **417**, 50–68 (1998)

491 G. S. Abrams, C. H. Broll, W. C. Carithers, R. G. DeVoe, C. Y. Pang, S. R. Shannon and E. N. Vella, IEEE Trans. Nucl. Sci. **25**, 309–311 (1978)

492 D. Grigoriev, *CMD-2 detector upgrade*, Preprint arXiv:hep-ex/0106009v1, 2001

493 H. E. Johns, A. Festner, D. Plewes, J. W. Boag and P. N. Jeffery, Brit. J. Radiol. **47**, 519–529 (1974)

494 S. A. Dubrovin, V. E. Klyuch, A. F. Novikova and N. G. Shishkanov, 10th All-Union Congress of Radiologist pages 572–575 (1977)

495 D. J. Drost and A. S. Fenster, Med. Phys. **9**, 224–230 (1982)

496 D. J. Drost and A. S. Fenster, Med. Phys. **11**, 602–609 (1984)

497 R. E. Zimmerman, B. L. Holman, F. H. Fahey, R. C. Lanza, C. Cheng and S. Treves, IEEE Trans. Nucl. Sci. **28**, 55–56 (1981)

498 J. L. Lacy, A. D. LeBlanc, J. W. Babich, M. W. Bungo, L. A. Latson, R. M. Lewis, L. R. Poliner, J. R. H. and P. Johnson, J. Nucl. Med. **25**, 1003–1021 (1984)

499 R. J. Ott, M. A. Flower, J. W. Babich and P. K. Marsden, 'The physics of radioisotope imaging,' in *The Physics of Medical Imaging* (edited by S. Webb), pages 142–318, The Institute of Physics, London, 1992

500 F. Sauli, Nucl. Instrum. Meth. A **422**, 257–262 (1999)

501 R. A. Muller, S. E. Derenzo, G. Smadja, D. B. Smith, R. G. Smits, H. Zaklad and L. W. Alvarez, Phys. Rev. Lett. **27**, 532–535 (1971)

502 V. Y. Chepel, Instr. Exp. Tech. **33**, 497–614 (1990)

503 J. Colot, S. Jan and E. Taumefier, 'A liquid xenon PET camera for neuron-science,' in *Proc. IX Int. Conf. Calorim. Part. Phys. "Annecy 2000"*, vol. 21, page 305, 2001

504 S. Jan, J. Collot, M.-L. Gallin-Martel, P. Martin, F. Mayet and E. Tounefeir, IEEE Trans. Nucl. Sci. **52**, 102–206 (2005)

505 S. Mihara, T. Doke, T. Haruyama, K. Kasai, A. Maki, T. Mitsuhashi, T. Mori, H. Nidshiguchi, W. Oootani, K. Ozone, R. Sawada, S. Suzuki, K. Terasawa and T. Yoshimura, Cryogenics **44**, 223–228 (2004)

506 K. Masuda and E. Shibamura, Phys. Rev. A **39**, 4732–4734 (1989)

507 G. Torantola, F. Zito and P. Gerundina, J. Nucl. Med. **44**, 756–769 (2003)

Index